MECHANICS OF RIVER EROSION

AND ITS EFFECTS ON

FLOODPLAIN BIOGEOCHEMISTRY

Thesis by

Madison M. Douglas

In Partial Fulfillment of the Requirements for

the Degree of Doctor of Philosophy

Caltech

CALIFORNIA INSTITUTE OF TECHNOLOGY

Pasadena, California

2023

(Defended April 18, 2023)

Madison M. Douglas
ORCID: 0000-0002-0762-4719

ACKNOWLEDGEMENTS

The research projects that comprise my PhD are the result of a period of immense scientific and personal growth. Here, I wish to acknowledge the people who shaped my experience.

First, I am deeply grateful to my advisor, Mike Lamb. You have time and again supported me by working side-by-side in the field, diving into the weeds on scientific problems, and providing excellent advice. Watching you has been a masterclass on how to run a lab, identify and tackle new research questions, and follow unexpected results to novel discoveries. Our scientific questions have led us into the fields of carbon geochemistry and environmental microbiology, and it was inspiring to watch you learn new disciplines alongside me. Most of all, I admire how your deliberate approach to training students and investigating the unknown is underlain by a joy and passion for the day-to-day work of research.

Next, I want to thank my thesis committee members: Woody Fischer, Josh West, and John Grotzinger. I selected you all as my committee because I admired you both personally and professionally. During these years, you have given me encouragement, honest advice, and held me to the highest scientific standards. I am grateful to have had such excellent mentors throughout my PhD.

None of the work described in this thesis could have been accomplished without the support of fellow graduate students and postdocs, particularly the Lamb group. From braving windy days in Death Valley and sleepless nights in Alaska to discussions over coffee and donuts, you have supported me and provided role models for how to be great community members as well as great scientists.

I would also like to thank the staff at Caltech who have managed the logistics for my PhD so that I could focus on research. In particular, I wish to thank Mark Garcia, Janice Grancich, Julie Lee, Mary Scott, and Julia Zuckerman.

I also wish to thank Glenn Price, Paul Asimow, Hye Sung Choe, and the members of the Caltech Wind Orchestra and Chamber Music programs. Playing and performing with you has been a source of joy throughout my PhD.

This thesis would not have been possible without the support of my friends. Through days in the office to unprecedented times, you became my family away from home. You lifted me up when I struggled and we celebrated successes together. Thank you for being a source of comfort and happiness throughout my time at Caltech.

When I began the final year of my PhD, I expected to write papers and travel to remote wilderness, but did not anticipate a romantic relationship. Thank you, David Millard, for being my partner on this wonderful and unexpected journey.

Most of all, I want to thank my family. From ski trips in Colorado to Lego and board game nights in Concord, you have kept me grounded and provided constant love, support, and

ABSTRACT

Rivers transport water, sediment, and nutrients across Earth's surface. They shape landscapes, eroding mountain ranges and building floodplains, simultaneously providing important resources and posing a hazard to nearby communities. Here, I present field work, flume experiments, numerical models, and laboratory analyses addressing three main themes: permafrost river and floodplain dynamics, river meandering without plants, and rates of bedrock incision. Arctic rivers migrate rapidly across their floodplains and their migration rates are predicted to increase as permafrost thaws due to climate change. However, no mechanistic model is capable of predicting permafrost riverbank annual erosion rates. To address this knowledge gap, I developed a calibrated numerical model for permafrost riverbank erosion. A previously published theory assumes that permafrost erosion rates are limited by pore-ice thaw, but underestimates thaw rates due to bank roughness increasing heat transfer from the river to its banks (Chapter 3). Results indicate that thaw-limited erosion is orders of magnitude higher than observed erosion rates, and permafrost riverbank erosion must instead be limited by sediment entrainment and the collapse of overhanging blocks to match observed rates (Chapter 2). Based on experimental results, I developed a 1D numerical model that includes roughness-dependent permafrost thaw and sediment entrainment and tracks how heat transfer within the riverbank can form a thawed layer (Chapter 4). Results indicate that permafrost riverbank erosion rates respond to changes in river discharge due to climate change, which affect both bank thaw and entrainment rates, and are only sensitive to changes in water temperature via thawed layer failure. As a case study, I conducted fieldwork along the Koyukuk River in Alaska, which is located in discontinuous permafrost. I found that changes in riverbank erosion rates may more rapidly erase permafrost from floodplains (Chapter 7) and change the spatial patterns of floodplain methane emissions (Chapter 5). While riverbank erosion releases eroded organic carbon to be oxidized as greenhouse gases or transported downstream, a portion of this carbon is re-deposited in the floodplain, modulating the effects of river migration on regional carbon cycling (Chapter 6). To understand the effects of vegetation on river migration rates and fluvial stratigraphy, I conducted long-term monitoring of the unvegetated, ephemeral Amargosa River in Death Valley, California (Chapter 8). This study found that the Amargosa is actively meandering at very slow rates and frequently avulses, producing muddy stratigraphy with isolated sand bodies that is thought to be unique to vegetated meandering rivers. Sediment transport has also been proposed as a primary control on bedrock river incision rates, where saltating grains gradually abrade the channel bed over geologic timescales. However, uncertainty about long-term sediment supply and the frequency of floods that cause significant bedrock incision has prevented using saltation-abrasion to model landscape evolution. Using a global data compilation, I calculated a best-fit sediment supply-normalized flood intermittency parameter so that the saltation-abrasion model can be broadly applied (Chapter 9). Together, these studies advance understanding of how riverine sedimentary transport governs permafrost riverbank erosion, Arctic floodplain biogeochemistry, stratigraphic deposits of unvegetated rivers, and bedrock incision rates.

PUBLISHED CONTENT AND CONTRIBUTIONS

Douglas, M. M., Dunne, K. B. J., & Lamb, M. P. (2023). Sediment Entrainment and Slump Blocks Limit Permafrost Riverbank Erosion. *Geophysical Research Letters, 50*(11), e2023GL102974. https://doi.org/10.1029/2023GL102974

> M.M.D. participated in the conception of the project, wrote the numerical model code, participated in analyzing model results, and lead the writing of the manuscript.

Douglas, M. M., Miller, K. L., Schmeer, M. R., Lamb, M. P. Frozen flume experiments indicate rapid permafrost riverbank erosion depends on bank roughness. In review at: *Journal of Geophysical Research: Earth Surface.*

> M.M.D. participated in the conception of the project, planned and executed experiments, analyzed resulting data, and lead the writing of the manuscript.

Douglas, M. M., Lingappa, U. F., Lamb, M. P., Rowland, J. C., West, A. J., Li, G., et al. (2021). Impact of river channel lateral migration on microbial communities across a discontinuous permafrost floodplain. *Applied and Environmental Microbiology*, *87*(20), AEM.01339-21. https://doi.org/10.1128/AEM.01339-21

> M.M.D. participated in the conception of the project, planned and executed sample collection, extracted DNA for 16S sequencing, analyzed resulting data, and lead the writing of the manuscript.

Douglas, M. M., Li, G. K., Fischer, W. W., Rowland, J. C., Kemeny, P. C., West, A. J., et al. (2022). Organic carbon burial by river meandering partially offsets bank erosion carbon fluxes in a discontinuous permafrost floodplain. *Earth Surface Dynamics*, *10*(3), 421–435. https://doi.org/10.5194/esurf-10-421-2022

> M.M.D. participated in the conception of the project, planned and executed sample collection, prepared and analyzed samples, analyzed resulting data, and lead the writing of the manuscript.

TABLE OF CONTENTS

LIST OF FIGURES AND TABLES

C h a p t e r 1

INTRODUCTION

Rivers transport water and sediment across Earth's surface, shaping landscapes from human to geologic timescales. Understanding fluvial mechanics is crucial to the billions of people living along rivers, who rely on them for water, transport, and resources. In turn, rivers have been significantly altered by human activity, whether directly by dam and levee construction or indirectly via anthropogenic climate change (Best, 2019; Dethier et al., 2022). These short-term changes have profound implications for local riparian ecosystems in addition to altering fluxes of nutrients from the land to Earth's oceans and impacting global geochemical cycles (Galy et al., 2015). On geologic timescales, bedrock rivers set the longevity of mountain ranges by carving channels over millions of years (Whipple, 2004). Alluvial rivers construct vast floodplains, filling in valleys produced by tectonic activity and building sedimentary deposits that enter the rock record and can record or shred signals of past terrestrial environments (Paola et al., 2018). Rivers are incredibly dynamic–flowing water can pick up, transport, and deposit sediment, which in turn changes the channel geometry and alters the flow of water in a cycle termed fluvial morphodynamics. This feedback cycle produces characteristic landforms and river behavior, but the mechanics of river erosion and deposition and their implications for terrestrial biogeochemical cycles remain poorly understood.

In this thesis, I explore the physical, chemical, and biological processes active in rivers from the hottest to the coldest environments on Earth's surface. This introduction (Chapter 1) provides an overview of three broad themes. The first theme is the migration of alluvial rivers with permafrost in their floodplains. My work addresses the questions, how do rivers erode their banks in permafrost environments (Chapters 2-4), and how does river migration influence floodplain organic carbon cycling and microbial ecology? (Chapters 5-7). The second theme focuses on unvegetated meandering rivers to understand how they migrate across their floodplains and build new sedimentary deposits (Chapter 8). The third theme consists of the intermittency of bedrock river incision (Chapter 9). In the conclusions (Chapter 10), I reflect on the broader observations and implications from this collected work.

1.1 Permafrost rivers and floodplains

Permafrost is ground that has remained frozen (below 0°C) for at least two years, and is typically overlain by an active layer which seasonally thaws (French & Shur, 2010). Permafrost regions span almost a quarter of the Northern Hemisphere (Obu et al., 2019) and preserve very high soil carbon stocks (Hugelius et al., 2014). These regions are currently experiencing rapid air and ground temperature warming due to polar amplification of climate change (Serreze & Barry, 2011). This warming is causing widespread permafrost thaw (Biskaborn et al., 2019), threatening local communities and infrastructure due to ground subsidence and accelerated erosion (Hjort et al., 2018). Permafrost thaw might also produce a positive feedback on climate warming if organic carbon that has been frozen since the last

glacial maximum (LGM) is released as carbon dioxide or methane (Ewing et al., 2015). Rates of organic carbon thaw and oxidation are modulated by landscape dynamics such that areas with rapid ground collapse and erosion tend to be hotspots for greenhouse gas production (Turetsky et al., 2020). Therefore, the key challenges facing permafrost science are: how will landscapes change in response to warming and how much carbon will be released as greenhouse gases when permafrost thaws?

1.1.1 Mechanics of permafrost riverbank erosion

Permafrost landscapes contain some of the largest river systems in the world, which are already experiencing climate change via increases in water temperature and discharge associated with climate change (Blaen et al., 2013; Peterson et al., 2002). Simultaneously, numerous Arctic communities are under threat of increased flooding, permafrost thaw, and riverbank erosion, and some have already been forced to relocate entirely (Bronen & Chapin, 2013; UAF & USACE, 2019). Predicting how rivers will respond to the changing Arctic environment requires developing and calibrating mechanistic models (Rowland & Coon, 2016). However, previous models for permafrost riverbank erosion predict kilometers of channel migration per year (Costard et al., 2003), orders of magnitude greater than observed erosion rates (Rowland et al., 2019). Therefore, developing a calibrated theory for permafrost riverbank erosion is a crucial step towards hazard prediction and community planning as the Arctic warms.

To address this knowledge gap, I developed and calibrated a new theory for permafrost riverbank erosion. First, I proposed that permafrost riverbank erosion can switch between two regimes: thaw-limited and entrainment-limited erosion (Chapter 2). During thaw-limited erosion, sediment can be picked up and washed downstream more rapidly than the river thaws permafrost in its banks, so bank erosion is a function of the thermal properties of the bank and the river, similar to previous models (Randriamazaoro et al., 2007). During entrainment-limited erosion, the rate of permafrost thaw exceeds the river's ability to entrain and transport sediment downstream, in line with field observations of riverbanks in mid-summer (Scott, 1978). I developed a numerical model including both regimes, which can reproduce observed bank erosion rates along the Yukon River for realistic input parameters (Chapter 2). However, thaw-limited erosion rates depend on the coefficient of heat transfer between the flowing water and frozen bank and is expected to vary with bank roughness. To calibrate this coefficient, I ran a series of hydraulically scaled frozen flume experiments at varying water temperatures (Chapter 3). I used this calibrated relation to develop a numerical model for bank erosion that includes heat transfer within the riverbank and used this model to calculate thaw layer thickness during entrainment-limited conditions (Chapter 4). Results indicate that thaw layers are generally tens of cm thick, and that entrainment-limited erosion rates are sensitive to water temperature if banks become unstable and fail past a critical thawed layer thickness. The calibrated model indicates that permafrost riverbank erosion will increase with river discharges, since both thaw- and entrainment-limited erosion depend on flow velocity. Bank erosion rates will not vary significantly with changes in water temperature, since bank erosion in summertime is primarily entrainment-limited, except for cases when the bank becomes unstable at very low thawed layer thicknesses.
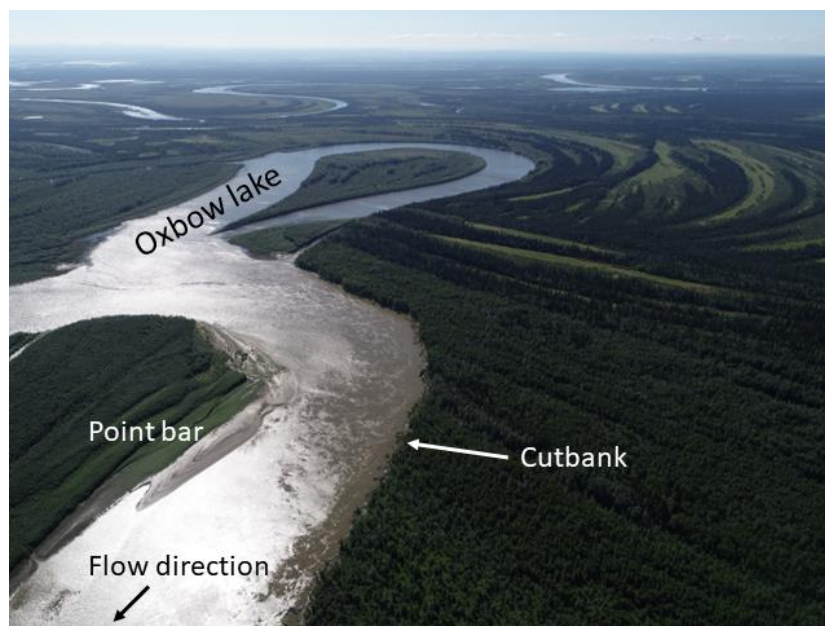
Figure 1.1. Discontinuous permafrost floodplain and oxbow lake formed by the meandering Koyukuk River, AK. Oblique aerial image from summer 2018 facing northeast. Channel is approximately 200 m wide.

1.1.2 Effects of river migration on permafrost biogeochemistry

The role of river floodplains in regional carbon cycling remains largely unexplored in Arctic environments. While eroding one bank, rivers also build new deposits on their accreting banks and floodplain. Floodplain deposits serve as a short- or long-term source or sink for particulate organic carbon (OC) associated with river sediment (Hilton et al., 2015; Repasch et al., 2021). In addition, river sediments may gain carbon due to primary productivity or lose it from microbial respiration while they are stored in floodplain deposits (Scheingross et al., 2021; Wang et al., 2020). Independently, river migration across Arctic floodplains and deltas is observed to set spatial patterns of permafrost occurrence and groundwater flow (Crampton, 1979; Smith, 1975; Stephani et al., 2020). Permafrost re-growth is linked to organic carbon storage by floodplain ecology, which follows a succession from willows to spruce and peat bogs after floodplain sediment is deposited (Jorgenson et al., 2001). Therefore, permafrost floodplain morphology is intimately linked to spatial patterns of OC fixation by plants, storage in soil and biomass, and release by microbial respiration (Treat et al., 2018).

To understand how floodplain landforms co-vary with soil microbial communities, OC stocks, and permafrost occurrence, I studied the floodplain of the Koyukuk River near Huslia, AK. Following field work in summer 2018 and spring and fall 2022, I analyzed floodplain sediments for grain size, total OC content, OC stable isotopes, and 16S microbial DNA sequencing (Chapters 5-6). Using remote sensing imagery, I produced maps of the relative age of floodplain deposits from cross-cutting relations produced by river channel migration,

as well as floodplain geomorphic landforms (Chapter 7). In addition, I submitted samples for optically stimulated luminescence and radiocarbon dating to quantify floodplain deposit ages and produced a permafrost occurrence map consistent with field observations.

I used these analyses to put floodplain carbon cycling in the context of spatial patterns of river migration. First, I evaluated how soil microbial communities varied across the river floodplain (Chapter 5). I found that most taxa from eroding banks and depositing bars were similar and consisted primarily of facultative or obligate anaerobes, likely because the floodplain was uniformly saturated. I observed that taxa capable of producing methane, verified by qPCR analysis for the methyl-coenzyme reductase subunit A (mcrA) gene, were only found in areas of the floodplain containing permafrost. Next, I compared OC stocks between eroding and newly deposited banks of the Koyukuk River to evaluate if river migration caused a net source or sink of carbon (Chapter 6). My results indicate that in the present day, young floodplain deposits have similar OC stocks to older deposits because a portion of particulate OC eroded from cutbanks is redeposited in point bars and any OC lost during transport is rapidly replaced by vegetation growing on the floodplain. Therefore, while riverbank erosion produces OC fluxes much larger than floodplain net ecological productivity to the Koyukuk River, much of this is subsequently reburied or replaced by new biomass, so river migration produces little net OC flux at present day.

Although river migration erodes permafrost and deposits sediment in unfrozen, unvegetated point bars, permafrost and vegetation can re-grow in river deposits symbiotically (Viereck, 1970). This is important because OC stocks and preservation potential can co-vary as floodplain sediment is deposited, vegetation becomes established, and the initially unfrozen deposits gradually re-form permafrost. Forest succession from willows and poplars to white spruce and mosses insulates the ground and allows permafrost to grow over hundreds of years, eventually forming the peat bogs and black spruce "drunken forests" characteristic of permafrost terrain. However, this progression of landscape change makes it difficult to evaluate the impact of climatic warming on floodplain permafrost formation. In Chapter 7, I investigated interactions between vegetation, river dynamics, and permafrost on the Koyukuk River floodplain using radiocarbon and OSL dating, field measurements, geomorphic mapping, and simple numerical model for permafrost growth on river deposits. Based on the presence of ice-rich permafrost in deposits as young as 1 ka, I inferred that permafrost growth did not cease at the end of the last glacial period and continued almost to present day. However, the extreme patchiness of permafrost in young deposits indicated that Koyukuk floodplain permafrost began degrading in recent years as the climate warmed. Therefore, similar to many Arctic rivers, the Koyukuk floodplain will be fundamentally changed in coming decades as permafrost is thawed by increasing air temperatures, changes in vegetation, increased flooding, and rapid river channel migration.

1.2 Morphodynamics of unvegetated meandering rivers

Meandering rivers, which erode one bank while simultaneously depositing sediment on their opposite bank, are ubiquitous on the surface of modern Earth. However, the characteristic muddy floodplain sedimentary deposits produced by meandering only become common in

the rock record after the evolution of land plants (Davies & Gibling, 2010a). Field data compilations (Millar, 2000) and flume experiments (Braudrick et al., 2009; Tal & Paola, 2007) indicate vegetation significantly increases bank strength and may encourage single-thread channel formation. River meandering requires shear stresses on the channel bed far in excess of the threshold of motion, and vegetation may stabilize channel banks against high fluid stresses (Davies & Gibling, 2010b). However, the discovery of meandering river deposits on Mars as well as in terrestrial deserts lacking vegetation implies that bank strength may also be provided by mud, salt crusts, or permafrost (Matsubara et al., 2015). Chapters 1 through 3 discuss the influence of permafrost on riverbank stability but conclude that riverbanks are not significantly stabilized by permafrost during summer months. Therefore, bank strength must instead be provided by mud or salt crusts.
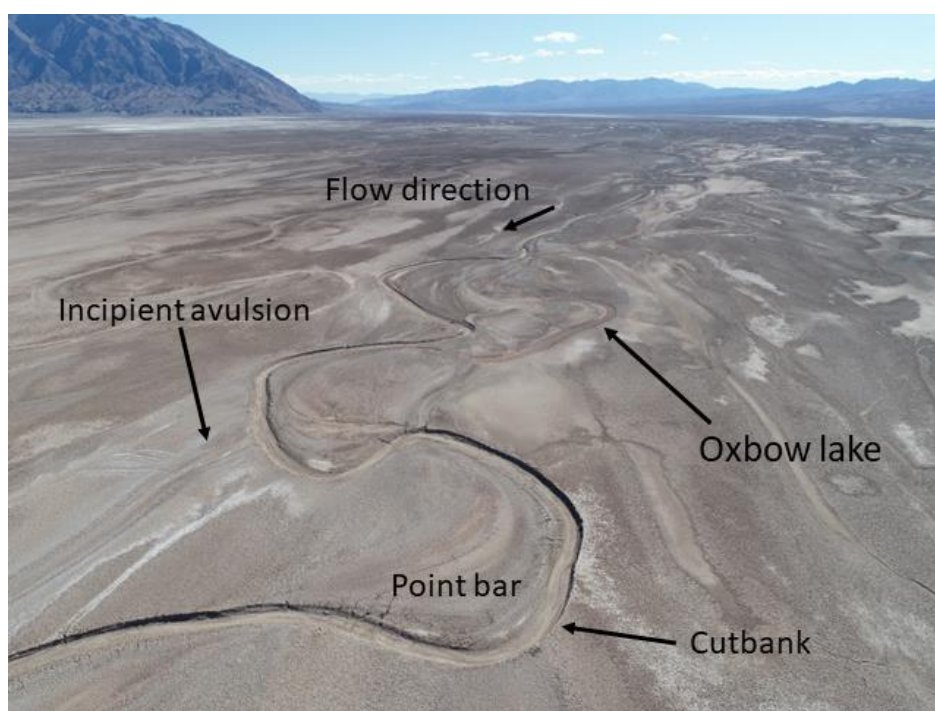
Figure 1.2. Barren, sinuous channels of the Amargosa River in Death Valley, CA that have similar morphology to vegetated meandering rivers. Oblique aerial image taken January 24, 2021 looks south (upstream) along the ~20 m-wide channel.

To investigate the mechanics of river meandering in unvegetated rivers, I monitored the Amargosa River in Death Valley National Park, CA (Chapter 8). My study reach was located upstream of Badwater Basin, lacked vegetation on eroding banks, and was highly sinuous, containing apparent cutoffs. Previous work argued that this reach of the Amargosa was actively meandering at rates up to 1 m/yr (Ielpi, 2018). The authors used similar methods to argue for active meandering in other arid catchments (Ielpi et al., 2020; Ielpi & Lapôtre, 2019) and proposed that meandering rivers without vegetation migrate more rapidly than

those with vegetated banks (Ielpi & Lapôtre, 2020). However, none of these studies actually measured rates of bank erosion and sediment deposition, sediment grain size distributions, and channel hydraulics during flow events. To address this knowledge gap, I monitored bank erosion along the Amargosa using cameras, water stage and conductivity sensors, and erosion pins, recording changes to channel morphology up to 5.5-year recurrence interval flows, including a bankfull flood. I also sampled intact bank sediment and directly measured sediment entrainment rates and settling velocities using a novel laboratory experimental setup. Results indicated that the study reach meanders slowly, at 5 cm/yr, and abruptly changes course via avulsion to gradually fill in Death Valley. This implies that unvegetated rivers may produce muddy floodplains with isolated sand bodies, commonly thought to be characteristic of vegetated channels (Davies & Gibling, 2010a). However, my results were not able to reproduce previously reported, rapid erosion rates (Ielpi, 2018), calling into question whether modern unvegetated channels migrate more rapidly than vegetated channels (Ielpi & Lapôtre, 2020).

1.3 Intermittency of bedrock river incision

Bedrock rivers gradually incise into their beds, potentially recording tectonic and climatic change over millions of years (Whipple et al., 1999; Wobus et al., 2006). Catchment-averaged bedrock incision rates are obtained by exposure age using cosmogenic nuclides, such as ^{10}Be, that form naturally in minerals near the surface from bombardment by high-energy subatomic particles formed by the interaction of cosmic rays with Earth's atmosphere (von Blanckenburg, 2005; Portenga & Bierman, 2011). While fluvial bedrock erosion is known to occur by sediment abrasion, cavitation, and direct plucking or toppling of fractured rock, the frequency of these processes over relevant timescales remains poorly understood (Lamb et al., 2015; Whipple et al., 2000). As a result, two distinct approaches for modeling bedrock river incision have emerged.

In the first approach, bedrock river incision is assumed to scale with stream power, which is then reformulated as a function of channel slope (S, m/m), drainage area (A, m^2), and empirical coefficients K, m, and n (Snyder et al., 2000):

$$E = KA^mS^n. \tag{1.1}$$

This empirical scaling was originally proposed based on field observations (Howard & Kerby, 1983), and is supported by cosmogenic exposure ages (Cyr et al., 2010; DiBiase et al., 2010; Roda-Boluda et al., 2019). Importantly, assuming values of K, m, and n and that the landscape is in topographic steady state, when tectonic uplift (U, m/kyr) equals erosion rate (E, m/kyr), allows direct calculation of uplift rates from topography (Whipple, 2001). This approach is incredibly powerful, and the stream power model is widely used to infer changes in climate and tectonics from bedrock river longitudinal profiles worldwide (Fox et al., 2014; Goren et al., 2014; Lague et al., 2005; Willett et al., 2018) as well as detect changes in river networks due to stream capture (Willett et al., 2014). However, there is little physical basis for values of K, m, and n, making it challenging to disentangle the roles of climate,

bedrock strength, tectonic environment, and autogenic processes in bedrock river evolution (DiBiase & Whipple, 2011; Ferrier et al., 2013; Harel et al., 2016; Scheingross et al., 2019).
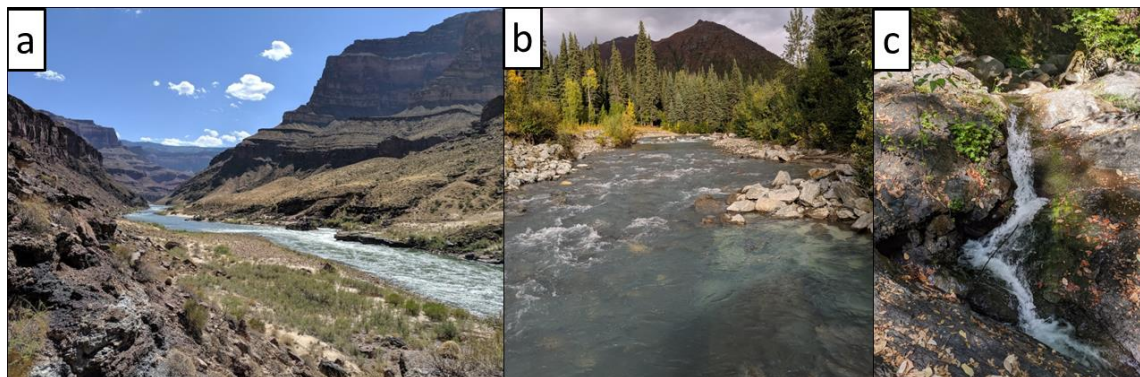
Figure 1.3. Bedrock rivers have a range of morphology and sediment supply, but all slowly incise into underlying rock. Field photos of bedrock rivers in **(a)** the Grand Canyon, AZ, **(b)** Marion Creek, AK (approximately 10 m wide), and **(c)** the Eel River, CA (waterfall approximately 2 m high).

A parallel approach to modeling bedrock river incision has developed out of field observations and flume experiments (Lamb et al., 2015). Channel bed abrasion by sediment being transported downstream has been extensively investigated in flume experiments (Chatanantavet & Parker, 2008; Scheingross et al., 2014; Sklar & Dietrich, 2001). These experiments imply that sediment can act as both a tool to incise bedrock and a cover to protect underlying bedrock and prevent incision (Gilbert, 1877). Bedrock incision rates from abrasion were formalized in the saltation-abrasion model (Sklar & Dietrich, 2004), which has since been extended to include sediment travelling suspended in the water column in the total load model (Lamb, Dietrich, & Sklar, 2008) and plucking (Chatanantavet & Lamb, 2014; Chatanantavet & Parker, 2011). However, applying the saltation-abrasion model requires measurements of sediment characteristics and supply as well as characteristic floods over geologic timescales (Sklar & Dietrich, 2006). This severely limits application this model, which has only been used at its calibration site on the Eel River (Sklar & Dietrich, 2004).

My work sought relations for the characteristic flood and sediment supply necessary to implement the saltation-abrasion model more broadly (Chapter 9). To do so, I used developments to in steep channel hydrodynamics to quantify channel friction and the threshold stress for sediment entrainment (Ferguson, 2007; Lamb, Dietrich, & Venditti, 2008). I applied these relations to simplify the saltation-abrasion model so that it could be solved using quantities measurable in the field and remote sensing datasets. Using a global compilation of measurements, I divided [10]Be cosmogenic erosion rates by the calculated incision rates to directly compute the sediment supply-normalized intermittency of channel-forming floods. This factor increases with channel slope, indicating that steeper rivers

experience floods less frequently. My closure relation for the saltation-abrasion model has comparable predictive power to the stream power model and offers the significant advantage of being based on the mechanics of physical processes. This result enables the saltation-abrasion model to be used for large-scale landscape evolution simulations.

C h a p t e r   2

SEDIMENT ENTRAINMENT AND SLUMP
BLOCKS LIMIT PERMAFROST RIVERBANK
EROSION

Madison M. Douglas, Kieran B. J. Dunne, Michael P. Lamb

Key Points:

- A new model shows that permafrost bank erosion depends both on pore ice thaw and sediment entrainment.
- Sediment entrainment from thawed banks and slump blocks can be rate-limiting in some cases, which helps explain slow bank migration rates.
- Where limited by sediment entrainment, decadal erosion rates may be less sensitive to warming river water than predicted previously.

2.1 Abstract

Climatic warming and permafrost thaw are predicted to increase Arctic riverbank erosion, threatening communities and accelerating sediment, carbon and nutrient cycling between rivers and floodplains. Existing theory assumes that pore-ice thaw sets riverbank erosion rates, but overpredicts observed erosion rates by orders of magnitude. Here, we developed a simple model that predicts more modest rates due to a sediment-entrainment limitation and riverbank armoring by slump blocks. Results show that during times of thaw-limited erosion, the river rapidly erodes permafrost and undercuts its banks, consistent with previous work. However, overhanging banks generate slump blocks that must thaw and erode by sediment entrainment. Sediment entrainment can limit bank and slump block erosion rates, producing seasonally-averaged rates more consistent with observations. Importantly, entrainment-limited riverbank erosion is nearly independent of water temperature, indicating that decadal erosion rates may be less sensitive to warming than predicted previously.

2.2 Plain-language Summary

Riverbank erosion in the Arctic is a major hazard for riverside communities and infrastructure. Arctic rivers flow through regions of permanently frozen ground, and this ground is thawing as the climate warms. Therefore, there is major concern that riverbank erosion will accelerate in the future because the ground loses its strength when thawed. However, in order for a riverbank to erode, the river must satisfy two conditions: it must thaw the frozen ground and entrain the thawed sand and mud. Our model and analyses

suggest that riverbank erosion in many Arctic rivers can be limited by the river's ability to entrain and transport the sand and mud, rather than the canonical view that erosion is limited by the rate of ground thaw. Applying our model to the Yukon River indicates that thaw rates are so fast that they cannot set the rate of erosion for the melt season. Instead, bank erosion for part of the time is controlled by the ability of the river to move the bank sediment, making riverbank erosion less sensitive to warming river waters.

2.3 Introduction

Major river systems flow through the Arctic, contributing approximately 10% of freshwater and 1% of sediment flux to Earth's oceans (Gordeev, 2006). These rivers flow through permafrost regions, which contain a seasonally-thawed active layer underlain by frozen ground (Obu et al., 2019). Arctic rivers can migrate rapidly (Rowland et al., 2019), eroding floodplain material that affects the carbon cycle (Turetsky et al., 2020) and threatens riverside communities and infrastructure (Bronen & Chapin, 2013; UAF & USACE, 2019).

Riverbank erosion in permafrost is thought to be limited by rates of pore-ice melting, implying that erosion rates could dramatically increase as the climate warms (Costard et al., 2003). This theory matches observed erosion rates along the Lena River in Siberia of 2-40 m/yr during the period after river ice break-up (Costard et al., 2014). However, Costard et al. (2014) only modeled erosion through the end of June, when predicted erosion rates approached 6 m/day. If the same 6 m/day rate applies until freeze-up in the fall, the model predicts over 500 m/yr of erosion, an order of magnitude greater than the fastest observed rates. Therefore, there must be a mechanism that substantially reduces bank erosion rates from the thaw-limited case.

Here we explore two mechanisms that might slow seasonally-averaged permafrost bank erosion rates compared to the thaw-limited end-member. Field studies of permafrost rivers in late summer show that banks have an order-meter-thick layer of thawed sediment at their surface (Scott, 1978), indicating erosion was limited by the river's ability to entrain sediment from the bank (i.e., entrainment-limited bank erosion) rather than being limited by pore-ice thaw. In addition, bank undercutting and slump block generation is common in Arctic rivers (Figure 2.1). These blocks can prevent further bank erosion until the fallen material has been entrained and transported downstream. We incorporate these two mechanisms into a model for riverbank erosion and discuss their implications for the fate of rivers in a warming Arctic.

2.4 Model development

We developed a 2D model for permafrost riverbank erosion where erosion rates may be thaw- or sediment entrainment-limited, and bank erosion only occurs when the permafrost bank is not shielded by slump blocks (Figure 2.2). The model was motivated by field observations near Beaver, AK in summer 2022. In the early summer following ice break-up, we observed that permafrost banks were often undercut by meter-deep erosional niches (Figure 2.1a). Rotational and shear failure generated slump blocks approximately 3-7 m wide along the bank (Figure 2.1b). Permafrost banks without erosional niches typically showed

armoring from thawed remnants of previous bank failures, suggesting erosion was limited by sediment entrainment (Figure 2.1c).
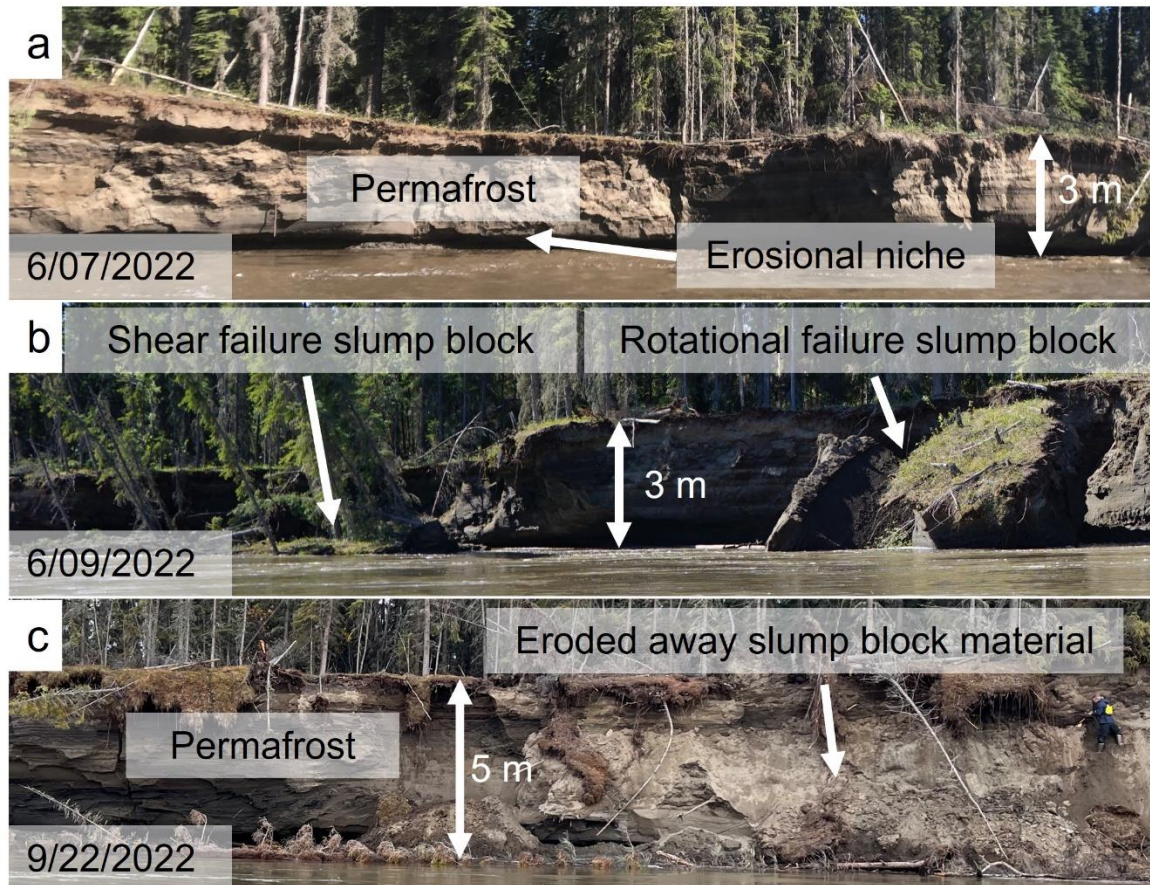
Figure 2.1. Field photos of the same permafrost river bank near Beaver, AK (66.3316°N, 147.6156°W) taken on different dates. Bank stands approximately 3.5 m above the water level. The majority of exposed bank face is permafrost with pore ice. The active layer on top of the bank is between 0.5-1 m deep. (**a**) Flowing water undercut the bank, creating an erosional niche (6/07/2022). (**b**) Shear failure and rotational failure-generated slump blocks (6/09/2022). (**c**) Slump block material armors the bank and prevents the development of an erosional niche until the material has been eroded away (9/22/2022). Photo Credit: Kieran Dunne (**a, c**), Michael Lamb (**b**).

We modeled the instantaneous riverbank erosion rate E_{bank} (m/s) as the minimum of thaw-limited (E_{thaw}; m/s) and sediment-entrainment-limited erosion rates (E_{ent}; m/s):

$$E_{bank} = \min(E_{thaw}, E_{ent}) \tag{2.1}$$

We calculated E_{thaw} using the model of Costard et al. (2003) with thermal properties for saturated permafrost calculated following Dupeyrat et al. (2011):

$$E_{thaw} = \frac{A Pr^{\alpha} Re^{\beta} \kappa_w (T_w - T_f)}{H \rho_b (L_f + c_p (T_f - T_i))} \tag{2.2}$$

where the numerator is the rate of heat transfer from the river water to the bank and the denominator is the heat required to thaw the bank. In equation (2.2), A, α, and β are empirical coefficients; $Pr = v/\chi$ is the Prandtl number, where v (m^2/s) is the kinematic viscosity and χ is the thermal diffusivity (m^2/s) of water; $Re = HU/v$ is the Reynolds number, where U (m/s) is the mean river flow velocity; κ_w (W/m/°C) is water thermal conductivity; T_w is river water temperature (°C); T_f (°C) is the freezing point of water; H (m) is the flow depth; ρ_b (kg/m^3) is permafrost bulk density; L_f (J/kg) is permafrost latent heat of fusion; c_p (J/kg/°C) is permafrost heat capacity; and T_i (°C) is the initial temperature of floodplain permafrost. We calculated $L_f = f_{ice} L_{ice}$, where f_{ice} (kg/kg) is the mass fraction of water ice in permafrost and L_{ice} (J/kg) is the water ice latent heat of fusion.

We modeled E_{ent} using a threshold-based model after Partheniades (1965),

$$E_{ent} = \frac{M}{\rho_b f_{sed}} \left(\frac{\tau_{bank}}{\tau_{crit}} - 1 \right)^n \tag{2.3}$$

where M (kg/m^2/s) and n (dimensionless) are empirical coefficients, τ_{bank} (Pa) is the fluid shear stress on the bank, τ_{crit} (Pa) is the critical shear stress to entrain bank sediment, and f_{sed} (kg/kg) is the mass fraction of sediment: $f_{sed} = 1 - f_{ice}$. We do not include detailed calculations on the river bend geometries or hydraulics, which would modify τ_{bank} for any given bend. We implemented the erosion equations for a 2-D cross-sectional elevation profile of a riverbank, tracking the water depth, H, throughout an annual hydrograph (see Section 3). The river has a bankfull depth of H_{bf} (m), and we defined a vertical coordinate system with the river thalweg at $Z=0$ and the top of the bank at $Z=H_{bf}$. At each time step, the bank was eroded horizontally (in the positive Y direction) at the rate E_{bank} (equation (2.1)) using finite differences everywhere on the submerged portion of the bank ($Z<H$) (Figure 2.2).

As the bank erodes during falling water level, the model generates overhangs that fail, producing slump blocks. We assessed bank failure following Patsinghasanee et al. (2018), which allows for rotational and shear failure of overhangs along a vertical plane (Figure 2.2b-c). We calculated the factor of safety (F_s) as the maximum of the factor of safety for rotational failure ($F_{s,rot}$; dimensionless) and shear failure ($F_{s,shear}$; dimensionless):

$$F_s = \max(F_{s,rot}, F_{s,shear}) \tag{2.4}$$

where $F_s > 1$ indicates that the driving forces exceed the bank strength and failure occurs. For rotational failure,

$$F_{s,rot} = \frac{2 \rho_b g A_{block} L_b}{\sigma_C L_c^2 + \sigma_T L_t^2} \tag{2.5}$$

where g is gravitational acceleration (9.81 m/s^2); σ_C (Pa) and σ_T (Pa) are the compressive and tensile strengths of permafrost, respectfully; L_c (m) and L_t (m) are the lengths of the failure plane under compressive stress and tensile stress, respectfully; and L_b (m) is the horizontal distance from the slump block's center of mass (Y_{COM}; m) to the failure plane. We assumed that the failure plane is vertical and occurs in the subaerial portion of the overhanging bank, such that $L_{fail}=H_{bf}-H$ at the time of failure (Figure 2.2a). Thus, $L_t=H_{bf}-Z_{COM}$, where Z_{COM} (m) is the height of the slump block's center of mass, and $L_c=L_{fail}-L_t$. The factor of safety for shear failure was calculated from the weight of the block divided by block shear strength (σ_S; Pa) along the failure plane:

$$F_{s,shear} = \frac{\rho_b g A_{block}}{\sigma_S L_{fail}}. \tag{2.6}$$

The cross-sectional area of the failed block, A_{block}, was found by integrating the bank profile elevation above the water line to the failure plane (Figure 2.2a).

To implement bank failures in our model, at each timestep, we evaluated if bank failure occurred using equations (2.4)-(2.6). If failure occurred ($F_s>1$), the overhanging material was removed from the bank cross-sectional profile, a slump block was generated, and the slump block was assumed to armor the bank and protect it from erosion ($E_{bank}=0$ when $E_{block}>0$). Slump block material was tracked separately from the bank and eroded at a rate E_{block} (m/s), which was either thaw- or entrainment-limited such that

$$E_{block} = \min(E_{thaw}, E_{ent}) \tag{2.7}$$

with E_{thaw} and E_{ent} evaluated using equations (2.2) and (2.3). We assumed that the block was fully submerged and eroded from an initial area A_{block} at rate $E_{block}H$. After the slump block was eroded away, $E_{block}=0$, and E_{bank} was assessed again using equation (2.1). We calculated the mean annual erosion rate E_{avg} (m/yr) as the total area of bank and block material eroded over the year normalized by H_{bf}.
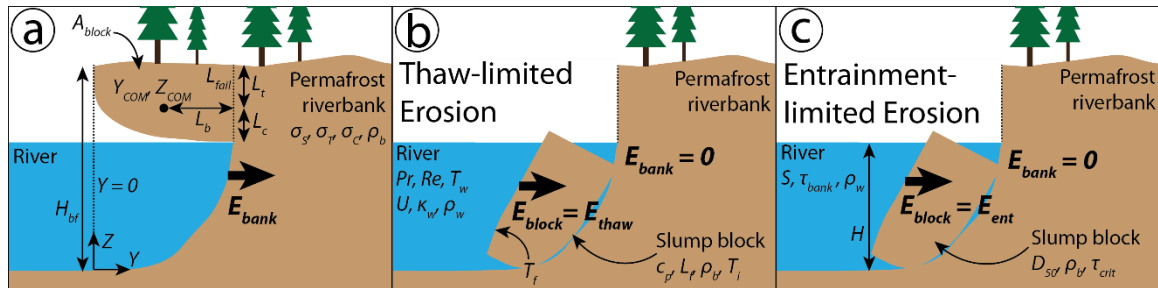
Figure 2.2. Illustration of the permafrost riverbank erosion model setup. (**a**) We define a coordinate system where the bank erodes horizontally from an initial position of $Y=0$ m and elevation is measured from the channel thalweg ($Z=0$ m) to the top of the bank ($Z=H_{bf}$ m). The riverbank erodes below the water surface at an erosion rate (E_{bank}; m/s) equal to the minimum of the thaw-limited (E_{thaw}; m/s) and entrainment-limited (E_{ent}; m/s) erosion rates. The bank overhang has a total failure plane length (L_{fail}; m) with sections under tension (L_t;

m) and compression (L_c; m); area of the overhang A_{block} (m^2); distance L_b (m) from the block center of mass at (Y_{COM}, Z_{COM}) to the failure plane; and permafrost bulk density (ρ_b; kg/m^3), shear strength (σ_S; Pa), tensile strength (σ_T; Pa), and compressive strength (σ_C; Pa). When slump blocks are present, $E_{bank} = 0$ and the block is eroded at rate E_{block} (m/s), which may be thaw-limited (**b**) or entrainment-limited (**c**). (**b**) E_{thaw} depends on the river Prandtl number (*Pr*; dimensionless), Reynolds number (*Re*; dimensionless), mean flow velocity (*U*; m/s), temperature (T_w; °C), thermal conductivity (κ_w; W/m/K), density (ρ_w; kg/m^3), and temperature of fusion (T_f; °C); as well as permafrost temperature (T_i; °C), specific heat capacity (c_p; J/kg/°C), and latent heat of fusion (L_f; J/kg). (**c**) E_{ent} depends on the shear stress on the bank (τ_{bank}; Pa), which depends on the water depth (*H*; m) and channel slope (*S*; m/m); the slump block median grain size (D_{50}; m); and the critical shear stress to entrain bank material (τ_{crit}; Pa).

2.5 Model implementation

We used input values for the model based on the Yukon River between Stevens Village, AK and Beaver, AK as an example case (Table 2.S1). Here the river traverses discontinuous permafrost and transitions from an anabranching to single-threaded channel morphology. The channel is gravel-bedded (D_{50}~10 mm) with slope $S=1.6\times10^{-4}$ (Clement, 1999). However, not all model parameters are known for this site, nor was the model locally calibrated. Our goal is to show an illustrative example of model behavior, not predictive results for any given river bend.

We used water discharge and temperature data from USGS gage 15453500 near Stevens Village. The daily discharge timeseries spans 1976-present and water temperature data exist intermittently from 1970-2005. We produced a representative annual timeseries of water velocity and depth from the discharge timeseries using power law fits to available paired measurements (Figure 2.S1). An average annual daily water temperature timeseries was found by combining sparse water temperature measurements from Steven's Village (*n*=214) with daily water temperature measurements from nearly Pilot Station, AK (USGS gage 15565447). We computed the median water temperature for each day of the year where data are available then smoothed the data using a Savitzky-Golay filter. Water temperature was set to 0°C for days in the spring with no available measurements, likely during ice breakup (Figure 2.S1).

We assumed bankfull depth equals the median annual maximum flow depth of 9.8 m. The shear stress on the bank (τ_{bank}) was calculated as $\tau_{bank}=\tau_{bed}/(1+\varepsilon)$, with $\varepsilon=0.2$ (Parker, 1978). We assumed normal flow conditions, so that $\tau_{bed}=\rho_w gHS$, where ρ_w (kg/m^3) is the density of water.

We modeled a representative sandy permafrost riverbank (D_{50}=1 mm). The initial condition was a vertical cutbank. We followed Costard et al. (2014) and used empirical coefficients of *A*=0.0078, α=0.3333, β=0.9270 (equation (2.2)) from experiments by Lundardini (1986), and set *Pr*=10. Using values typical for permafrost, we set T_f =0°C, σ_C=11.2±4.1 MPa (±1SD) and σ_T=2.4±0.2 MPa (±1SD) for frozen silt and sand (Bragg & Andersland, 1981;

Wolfe & Thieme, 1964), and σ_S=5×10^4 Pa (Arenson & Springman, 2005). We used measured values of ρ_b=861 kg/m^3 and f_{ice}=0.2362 for soils in the study region (Lininger et al., 2019). Background permafrost temperature, T_i=-1°C, was determined from borehole data for Stevens Village at 3 m depth (Biskaborn et al., 2015). For sediment entrainment, we used n=1 (Partheniades, 1965) and M=2.5×10^{-5} kg/m^2/s to represent river sediment with some cohesion (Winterwerp et al., 2012). We calculated τ_{crit}=0.28 Pa for D_{50}=1 mm (Parker et al., 2003).

2.6 Results

2.6.1 Yukon River example case

High water discharge for a typical hydrograph on the Yukon River near Stevens Village begins following ice breakup (day 120) and peaks around day 150 (since Jan. 1), before slowly declining to freeze-up around day 300 (Figure 2.3a). The water temperature gradually increases after ice breakup, peaking at a value of approximately 18°C in mid-summer (around day 200) before declining back to 0°C in the winter (Figure 2.3b). With these inputs, the model produces daily riverbank erosion rates (E_{bank}; Figure 2.3c) that are thaw-limited throughout the winter and the earliest part of the melt season (approximately 5 days) when the river water is cold (T_w<0.1°C). After day 125, the thaw rate accelerates as the water warms, making bank erosion limited by sediment entrainment, rather than thaw, despite the rise in water discharge and the increase in entrainment rate. The bank remains entrainment-limited until day 300, shortly before freeze-up. Erosion rates closely track water discharge, and are relatively insensitive to water temperature during summer months when rates are set by sediment entrainment. While a small fraction of bank erosion occurs under thaw-limited conditions (<1%), permafrost still plays a crucial role in preventing erosion from occurring during winter months when T_w=0°C. During this time, the river would entrain sediment if it was thawed, but temperatures are too low to permit thaw.

Rising and falling water levels form an overhang in the permafrost which collapses to form a slump block whose geometry is visible in plots of the riverbank profile through time (Figure 2.3e). The model produces bank profiles with a curved overhang reaching to the recent high-water level, similar to natural overhangs (Figure 2.1). Over the melt season, the model predicts one bank collapse event due to shear failure with a 10-m top length, consistent in scale with observed slump blocks. The slump block causes E_{bank} to vanish and E_{block} to abruptly increase while bank material is protected by the slump block (Figure 2.3c-d). The slump block shields the bank from direct erosion for 39 days, persisting because water levels are decreasing, which makes block erosion less efficient. The block has a large area because L_{fail} is set by the subaerially exposed portion of the bank that generates failures. Block erosion is limited by the rate of sediment entrainment because it occurred as the hydrograph is declining and water temperatures are warm, so permafrost thaw rates are rapid (Figure 2.3d).

For our example scenario, the thaw-limited model (equation (2.2)) alone produces a mean annual bank erosion rate greater than 8×10^3 m/yr, which is not realistic. Allowing both thaw- and entrainment-limited erosion and slump block armoring of the bank predicts 10 m/yr of

riverbank erosion. For comparison, reach-averaged values derived from Landsat imagery indicate erosion rates of 1.48±2.73 m/yr (mean±1SD) and a maximum of 36.04 m/yr for the Yukon River between Beaver and Stevens Village (Rowland et al., 2019). Thus, the example scenario produces erosion rates that fall within the range of observed rates and represent an improvement by multiple orders of magnitude compared to assuming thaw-limited conditions. The exact erosion rates are sensitive to model input parameters, which we explore next.
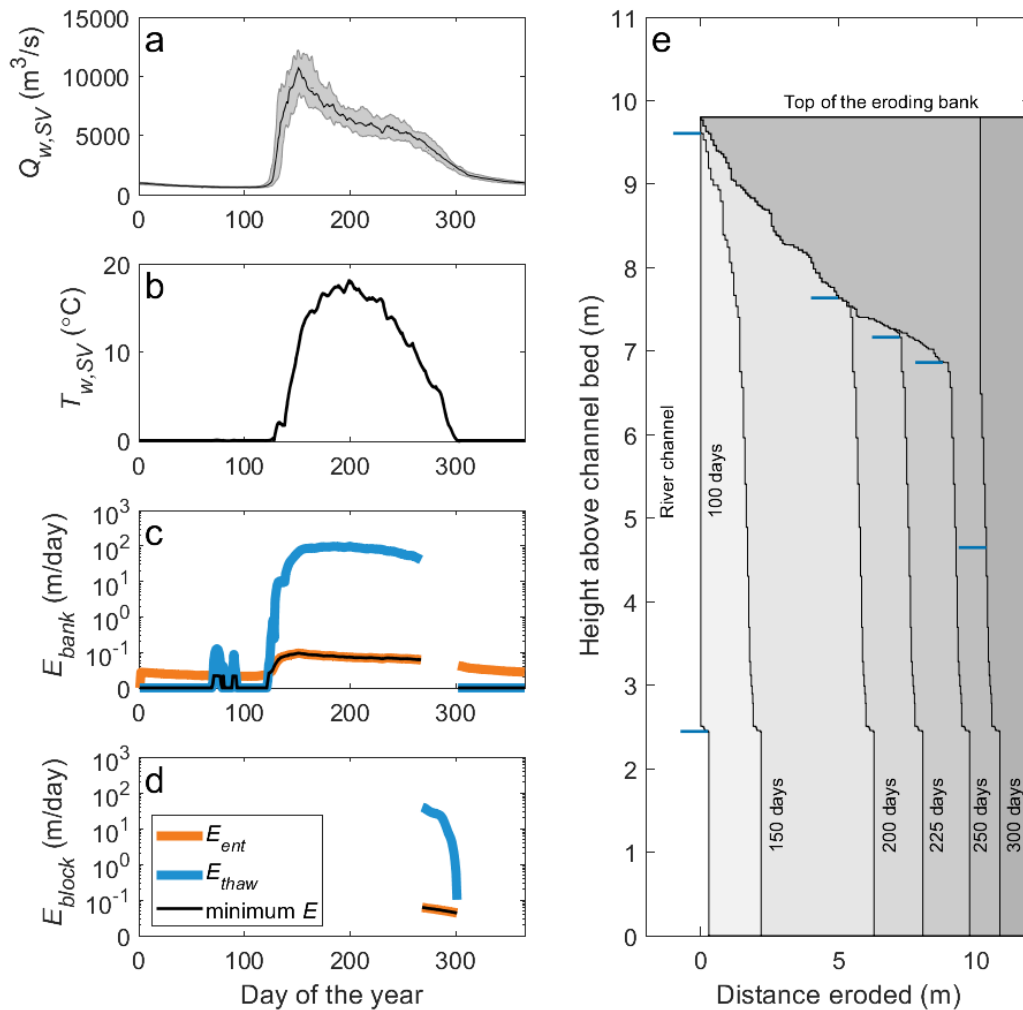
Figure 2.3. Riverbank erosion over the course of an annual hydrograph for sandy permafrost near Stevens Village along the Yukon River. (**a**) Median daily water discharge (Q_w; m^3/s) with the 25th to 75th percentiles shaded in gray (days since Jan. 1st). (**b**) Median daily water temperature (T_w; °C) for Stevens Village and Pilot Station. (**c**) Riverbank erosion rate (E_{bank}; m/day), with E_{ent} and E_{thaw} shown in orange and blue, respectively. Bank erosion is zero when a slump block shields the bank. (**d**) Model of slump block erosion rate (E_{block}; m/day), E_{ent},

and E_{thaw} versus day of the year. (**e**) Eroding riverbank profiles shaded light to dark gray through time with water level shown as a blue dash on each profile.

2.6.2 Model sensitivity analysis

We systematically changed the thaw and entrainment-limited erosion rate coefficients while holding all other parameters constant. Entrainment rates are highly variable (de Leeuw et al., 2020) and depend on the particle size, sediment cohesion, and vegetation that can bind sediment. The Yukon River floodplain is poorly sorted, with grain size ranging from pebbles (τ_{crit}~10 Pa) to cohesive silt and clay (τ_{crit}~0.01 Pa), so we varied M and τ_{crit} over a wide range of values that are representative of the natural variability for these materials (Parker et al., 2003; Winterwerp et al., 2012). When entrainment rates are very low, the river rapidly switches from thaw- to entrainment-limited erosion and the number of days with thaw-limited erosion decreases (Figure 2.4a). In contrast, when sediment is easily entrained, the number of days with thaw-limited bank erosion increases and E_{avg} increases. The E_{avg} contours are not linear in log-log space because changing E_{ent} also changes the number of days when thaw-limited erosion occurs. The interplay between rates of thaw- and entrainment-limited erosion and number of days in each state provides a negative feedback on E_{avg} that limits runaway permafrost thaw or sediment entrainment. Overall, these results suggest that the model produces erosion rates consistent with the observations (2-3 m/yr) depending on the values of M and τ_{crit}, which are poorly constrained. Changing coefficients A and β in the permafrost thaw model, or permafrost temperature, over a range of reasonable values had little effect on the model results for this scenario since the thaw-limited conditions were brief (Figure 2.S2 and 2.S3).

Water discharge and temperature are increasing as the climate warms (Docherty et al., 2019; Peterson et al., 2002). To investigate potential climatic changes, we ran model scenarios multiplying the Stevens Village water discharge timeseries ($Q_{w,SV}$) and the water temperature timeseries ($T_{w,SV}$) by a dimensionless scalar ranging from 0.5-1.5 and 0.7-1.3, respectively (Figure 2.4b). These ranges exceed observed variations in Arctic river discharge over the last 7 kyr (A. Wagner et al., 2011) and span modern river water temperatures for Arctic and temperate climates (Wanders et al., 2019). Model results indicate bank erosion rates increase with greater water discharge but are insensitive to water temperature. These trends emerge because permafrost riverbank erosion is only thaw-limited during summer months for a short period immediately after ice break-up, and otherwise bank erosion is entrainment-limited (Figure 2.4b). Bank and slump block erosion rates increase rapidly with respect to water discharge because both thaw- and entrainment-limited erosion rates depend on discharge (Figure 2.4b). Thaw-limited erosion rates are proportional to flow velocity (equation (2.2)) while entrainment-limited erosion rates are proportional to flow depth via shear stress (equation (2.3)), which both increase with discharge. In addition, more of the bank is exposed to erosion at higher water depths.

Slump block material may be more or less erodible relative to the underlying bank (Parker et al., 2011). For instance, slump blocks could be easier to erode because they have more surface area exposed to flow, they are comprised of weaker material, or the blocks break

apart during failure. In contrast, slump blocks might be more difficult to erode than their underlying bank because they contain finer, more cohesive sediment and organics such as tree roots from the upper floodplain. To understand these effects, we multiplied entrainment-limited erosion rates by a dimensionless scalar from 0.1-10 (simulating blocks that range from 10% to 10-fold the strength of the bank material) and examined how bank erosion rates varied with block erodibility and bank shear strength (Figure 2.4c). Intuitively, E_{avg} increased when slump blocks were easier to erode than their underlying material and decreased when slump blocks were more difficult to erode (Figure 2.4c). Therefore, the presence of cohesive materials, such as mud and plant roots, within slump blocks provides an additional mechanism to slow bank erosion rates, consistent with non-permafrost rivers (Parker et al., 2011). In our modeled scenarios, most slump blocks were eroded under entrainment-limited conditions, thus the results are not strongly affected by whether or not the slump block was initially frozen.
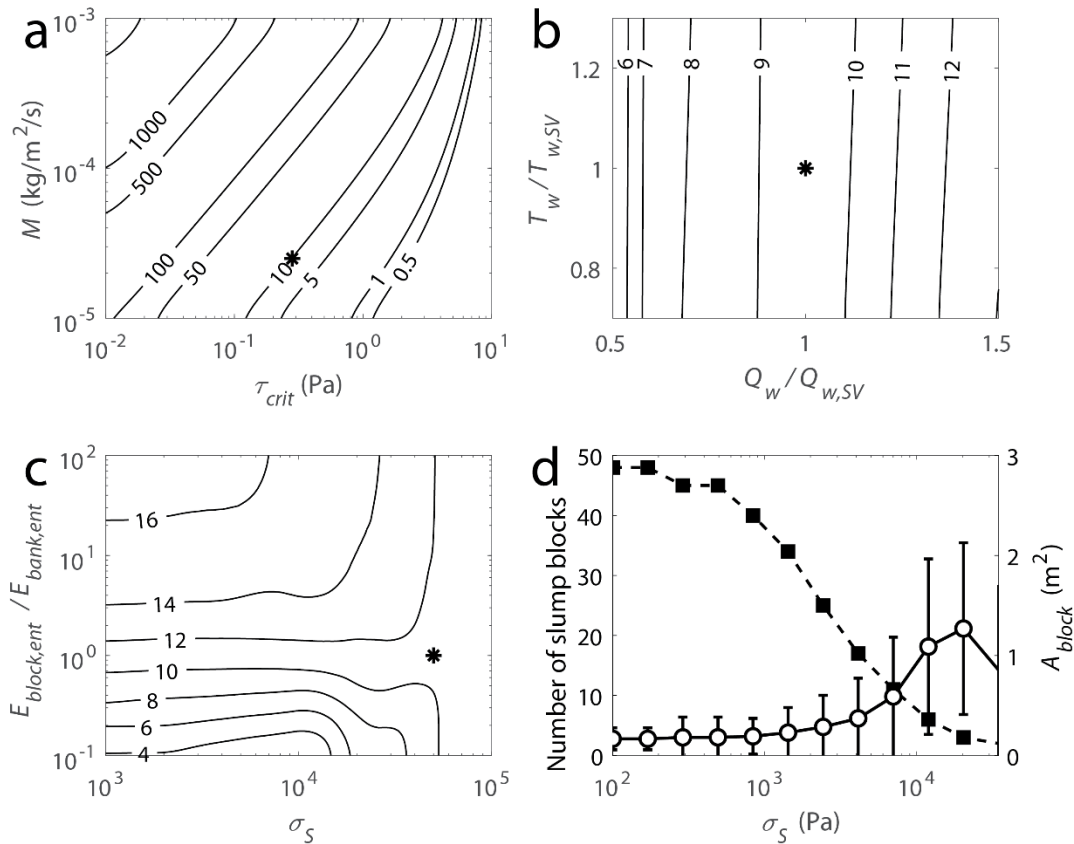
Figure 2.4. Contour plots of mean annual erosion rate E_{avg} (m/yr) smoothed with a 2-D gaussian filter with 1SD = 0.05 and the modeled example case displayed as a star (*). (**a**) E_{avg} contours for changing sediment entrainment coefficient M and τ_{crit}. (**b**) E_{avg} contours for changes in the magnitude of water temperature and discharge. (**c**) E_{avg} contours for the ratio of block versus bank M and bank shear strength. (**d**) The number of slump blocks (black

squares) and slump block area (white circles with 1SD error bars) as a function of bank shear strength.

Since bank failures in our modeled scenarios were due to shear rather than rotational failure, we explored the effect of changing shear strength on model results. We examined a broad range of strengths (σ_S=1-1,000 kPa): laboratory values give a range over multiple orders of magnitude for frozen sand with varying ice content and temperature (Arenson & Springman, 2005), and observations of overhanging, vertical, and low-angle banks imply bank strength spans a wide range of values. Overall, higher σ_S decreases the number of slump blocks and increases their size (Figure 2.4d). This occurs because a weaker bank requires less of an overhang to form before it fails, producing numerous small collapses over the course of the summer, while stronger banks need large overhangs to form before bank shear strength is exceeded. Despite shear strength strongly affecting the number of slump blocks and their residence time, it has a small effect on mean annual erosion rates when blocks have similar erodibility as the banks (Figure 2.4c). Slump blocks instead modulate the instantaneous rate of bank erosion, rather than the mean annual bank erosion rate. However, when blocks are resistant to entrainment, erosion rates first increase then decrease as shear strength increases. In contrast, for blocks that are highly erodible, average bank erosion rates first decrease then increase as shear strength increases. This occurs because increasing bank strength makes slump block failures occur later in the summer, and slump blocks that cover the bank when erosion rates peak during in early summer will most significantly increase (for weak blocks) or decrease (for strong blocks) annual erosion rates.

2.7 Discussion

Our model indicates slump blocks and entrainment-limited conditions can help to explain overestimates of permafrost riverbank erosion by thaw-limited theory. Using simple block collapse and sediment entrainment formulations, the model produces erosion rates similar to observations along the Yukon River. The model is simple by design to illustrate the important role that sediment entrainment and slump blocks play in modulating thaw-induced bank erosion rates. A predictive model may require additional physical processes, for instance, bank gouging by ice jams (Vandermause et al., 2021). In addition, our model does not track heat transferred to the bank during periods of entrainment-limited erosion. This may be important because sustained low flows could thaw the bank, allowing for rapid erosion during late-summer floods (McNamara et al., 2008). In addition, bank thaw may cause permafrost with very high pore-ice content to collapse, increasing erosion rates compared to our model. We also neglected form drag from slump blocks and fallen trees (Figure 2.1), which could slow near-bank flow, reducing bank shear stresses and erosion rates (Kean and Smith, 2004). Finally, our model neglects channel bend, bed, and bar morphodynamics, which can change bank stresses and modulate bank erosion rates on seasonal and inter-annual timescales (Naito & Parker, 2019, 2020).

Model results qualitatively match field observations, producing rapid, thaw-limited erosion in early summer and slower, entrainment-limited erosion with a large slump block as river discharge declines in mid- to late summer (Figure 2.1). Importantly, entrainment-limited

erosion slows bank erosion by two orders of magnitude, while slump block armoring changes erosion rates when slumped material is more or less resistant to entrainment than the underlying bank. Erosion was entrainment-limited for $T_w>0.1°C$, indicating that even catchments in continuous permafrost could be entrainment-limited for summer months. Since entrainment is important in setting the erosion rate, permafrost bank erosion in some rivers may behave more similarly to rivers in non-permafrost settings than previously thought.

Previous efforts to understand the effects of permafrost on channel mobility indicate that rivers are capable of rapidly eroding banks locally (Fuchs et al., 2020; Kanevskiy et al., 2016) yet erode more slowly when averaged spatially over river reaches and temporally over decadal timescales (Rowland et al., 2019). Spatial heterogeneity in riverbank and slump block strength and erodibility as well as channel hydraulics and curvature may account for some of these differences (Sylvester et al., 2019). Unfortunately, many of these parameters are poorly constrained for permafrost and non-permafrost rivers alike (Arenson & Springman, 2005; Bragg & Andersland, 1981; Wolfe & Thieme, 1964). For example, entrainment relations in non-permafrost settings commonly overpredict erosion rates, leading to proposals that plants, cohesive mud, or muddy slump blocks play important roles in throttling bank erosion rates (Parker et al., 2011). In addition, the interplay of thaw- and entrainment-limited erosion and the number of days per year that each process dominates may produce localized, rapid erosion over a few days following ice break-up but little to no erosion over the rest of the year, potentially reconciling fast short-term and slow long-term erosion rates along Arctic rivers. Thus, by allowing mixed entrainment-limited and thaw-limited behavior over the melt season, our model might help to reconcile observations of thaw-limited behavior (e.g., erosion rates depend on water temperature or pore ice content) with much slower averaged rates than predicted by purely thaw-limited conditions.

Arctic warming is increasing surface water temperatures (Docherty et al., 2019) and changing riverine hydrographs (Peterson et al., 2002). Our results show that, where partially entrainment limited, river morphodynamics may be less sensitive to warming of river water if thaw-limited conditions only persist for a few days after ice break-up, as in our modeled scenario. Moreover, thaw rates should increase with warming water temperature, which would result in them outpacing entrainment rates more often, further limiting the days in which erosion is thaw-limited. However, even if bank erosion rates are set by sediment entrainment, Arctic rivers will still respond to climate change through changing hydrographs. Increases in discharge and the size and frequency of late-summer storms, when riverbanks are thawed, can increase erosion rates (McNamara et al., 2008). Permafrost riverbanks also differ from non-permafrost banks because thaw rates are negligible during winter months, since water temperatures remain close to 0°C. As ice breakup occurs earlier in the year (Beltaos & Burrell, 2021), we expect that the number of days with non-zero erosion will increase, raising average annual erosion rates even if daily rates remain similar. Finally, regional permafrost thaw should reduce riverbank strength, resulting in smaller and more frequent slump blocks. Taken together, these changes may increase bank erosion hazards and

change that cadence of cycling of floodplain materials including sediment, carbon, and pollutants.

2.8 Conclusions

Arctic rivers can erode rapidly, damaging infrastructure and forcing some communities to relocate. Understanding the physical processes that govern permafrost bank erosion is a crucial step towards predicting and mitigating hazards from climate change. Here, we introduced a model that includes thaw-limited permafrost erosion as well as limits on erosion rates through slump block failure and sediment entrainment. The purely thaw-limited model produces unrealistically large erosion rates. However, simple representations of sediment entrainment and slump blocks reduce these rates by orders of magnitude, making predictions more comparable to observations. We also found that entrainment-limited conditions can occur over most of the summer in some cases, such that permafrost riverbank erosion can be sensitive to changes in water discharge but not water temperature. However, even in these scenarios, riverbank erosion may still accelerate if a warming climate leads to larger floods, potentially increasing hazards to riverside communities and the release of carbon currently stored in permafrost.

2.9 Acknowledgments

2.10 Open Research Statement

Soil bulk density and water content data were downloaded from doi:10.25675/10217/187212. Data for ground temperature were downloaded for site ID US O-82 from the Global Terrestrial Network for Permafrost (GTN-P) Database at http://gtnpdatabase.org/boreholes. Yukon River temperature and discharge data were downloaded from https://waterdata.usgs.gov/monitoring-location/15565447/ and https://waterdata.usgs.gov/monitoring-location/15453500/. Model code was written in Matlab R2022a under an academic license to the California Institute of Technology and code to run the model will be published using Zenodo after manuscript publication.

2.11 Supplemental Material

The supporting information includes a figure of the raw data and representative hydrograph and water temperature timeseries for the Yukon River at Stevens Village, AK and Pilot Station, AK (Figure 2.S1). We also include a supplemental table summarizing the variable inputs to the model and their values for our base case (Table 2.S1). Total bank erosion rates vary in response to changing empirical parameters in the thaw-limited erosion coefficient of heat transfer (Figure 2.S2) and permafrost temperature and mass fraction ice (Figure 2.S3).
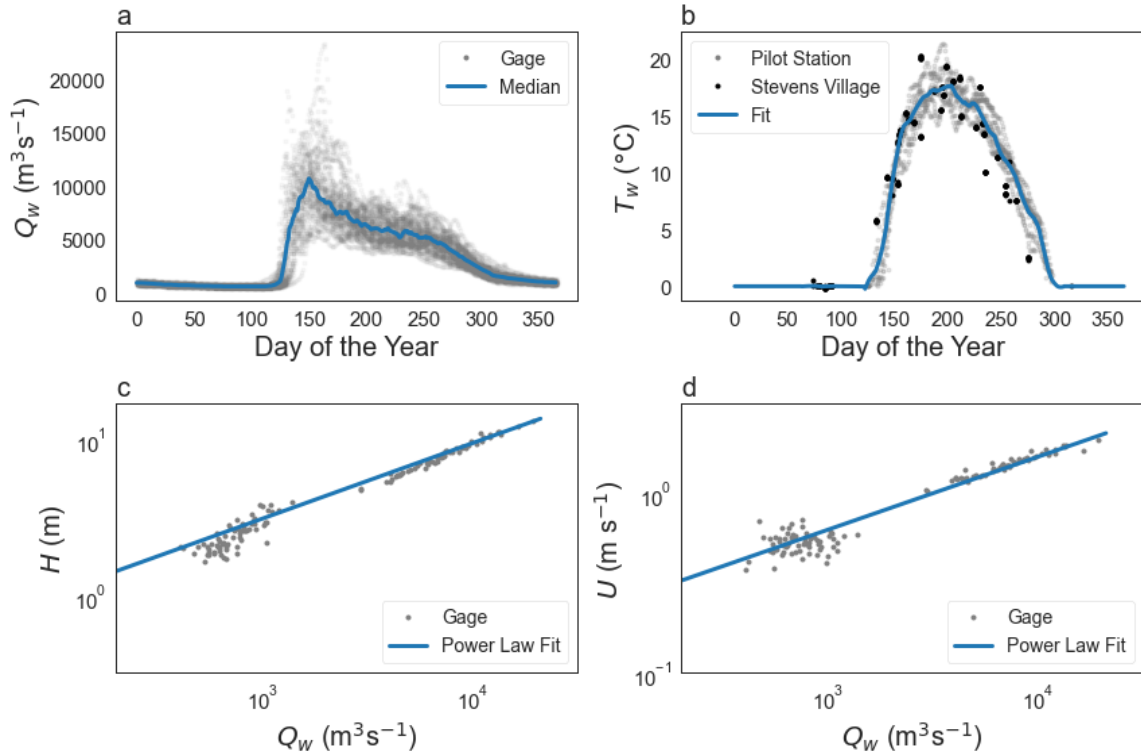
Figure 2.S1. (a) Daily average discharge for Stevens Village (USGS gage 15453500) from 1976-2022 (gray) with calculated median daily discharge (blue). **(b)** Daily average water temperature for Pilot Station from 1976-2022 (gray), intermittent water temperature measurements at Stevens Village gage from 1970-2005 (black), and average annual daily water temperature time series from combined datasets (blue). **(c)** Paired water discharge and water depth measurements at Stevens Village gage (gray). Power law fit to data: $H=-0.97Q_w^{0.41}$ (blue). **(d)** Paired water discharge and water velocity measurements at Stevens Village gage (gray). Power law fit to data: $U=-1.42Q_w^{0.49}$ (blue).

Table 2.S1. Numerical model variables and their values for the base case, with uncertainties shown as ±1SD. All references can be found in the main text.

Variable	Description	Value	Units	Source
ρ_b	bulk density of mineral sediment	861	kg/m^3	Lininger et al., 2019

f_{ice}	mass fraction of ice for mineral sediment	0.2362	kg/kg	Lininger et al., 2019
T_i	initial bank temperature	-1	°C	Global Terrestrial Network for Permafrost
S	channel slope	0.00016	m/m	Clement, 1999
σ_S	Shear strength	50000	Pa	Arenson & Springman, 2005
σ_C	compressive strength	$1.12 \times 10^7 \pm 4.1 \times 10^6$	Pa	Bragg and Andersland, 1981
σ_T	tensile strength	$2.40 \times 10^6 \pm 0.2 \times 10^6$	Pa	Bragg and Andersland, 1981
D_{50}	Median grain size	1.00×10^{-3}	m	
A	dimensionless constant	0.0078		Lunardini et al., 1986
α	dimensionless constant	0.3333		Lunardini et al., 1986
β	dimensionless constant	0.927		Lunardini et al., 1986
κ_w	thermal conductivity of water	0.6	W/m/°C	
v	kinematic viscosity of water	1.00×10^{-6}	m²/s	
T_f	Fusion temperature for water ice	0	°C	
Pr	Prandtl number	10		Costard et al., 2003
g	gravitation acceleration	9.81	m/s²	
ρ_s	density of sediment	2765	kg/m³	
ρ_w	density of water	1000	kg/m³	
M	coefficient for entrainment equation	2.5×10^{-5}	kg/m²/s	Partheneides, 1965
n	exponent for entrainment equation	1		Partheneides, 1965
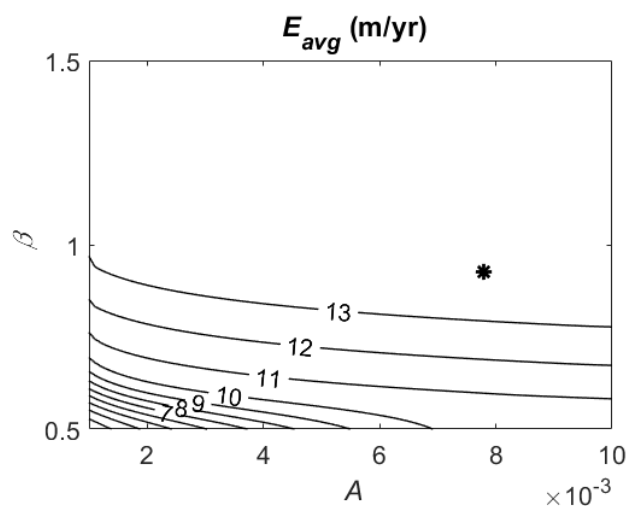
Figure 2.S2. Contour plots of mean annual erosion rate E_{avg} (m/yr) for changing dimensionless coefficient (A) and exponent (β) in equation (2.2) to compute E_{thaw}. E_{avg} is smoothed with a 2-D gaussian filter with 1SD = 0.05 and the modeled example case displayed as a star (*).
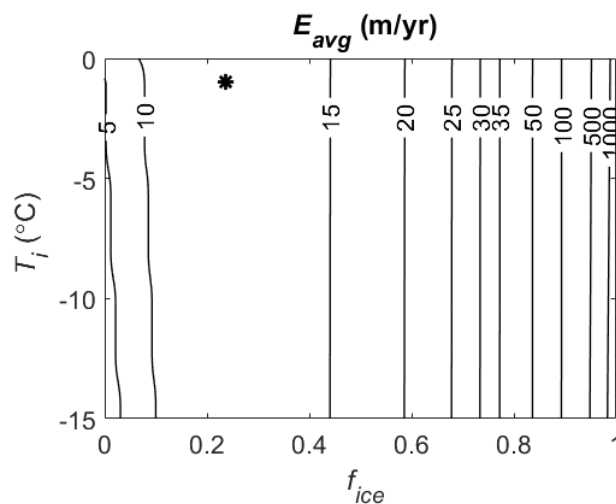
Figure 2.S3. Contour plots of mean annual erosion rate E_{avg} (m/yr) for changing permafrost temperature (T_i, °C) and mass fraction ice (f_{ice}, dimensionless). E_{avg} is smoothed with a 2-D gaussian filter with 1SD = 0.05 and the modeled example case displayed as a star (*). For model runs with $f_{ice} < 0.20$, sand with a typical 40% volumetric porosity is expected to have under-saturated pore space. Therefore, we set a maximum $f_{sed} = 0.80$ for all model runs with $f_{ice} < 0.20$. The base case has $f_{ice} = 0.2362$, so we expect that bank sediments on the Yukon River near Stevens Village are near saturation and have $f_{sed} = 0.7638$.

Chapter 3

ABLATION-LIMITED EROSION RATES OF
PERMAFROST RIVERBANKS

Madison M. Douglas, Kimberly Litwin Miller, Maria N. Schmeer, Michael P. Lamb

This chapter has been modified from a version submitted to *JGR: Earth Surface*.

Key Points:

- Flume experiments with frozen, erodible riverbanks were used to test and revise theory.
- Erosion rates were 3-fold faster than predicted by theory due to bank roughness.
- Ablation-limited bank erosion increases with water temperature, decreases with pore ice content, and is insensitive to bank temperature.

3.1 Abstract

Permafrost thaw is hypothesized to increase riverbank erosion rates, which threatens Arctic communities and infrastructure. However, existing erosion models have not been tested against controlled flume experiments with open-channel flow past an erodible, hydraulically rough permafrost bank. We conducted temperature-controlled flume experiments where turbulent water eroded laterally into riverbanks consisting of sand and pore ice. The experiments were designed to produce ablation-limited erosion such that any thawed sediment was quickly transported away from the bank. Bank erosion rates increased linearly with water temperature, decreased with pore ice content, and were insensitive to changes in bank temperature, consistent with theory. However, erosion rates were approximately a factor of three greater than expected. The heightened erosion rates were due to a greater coefficient of heat transfer from the turbulent water to the permafrost bank caused by hydraulically rough banks. A revised ablation-limited bank erosion model with a heat transfer coefficient that includes bank roughness matched our experimental results well. Results indicate that bank erosion along Arctic rivers can accelerate under scenarios of warming river water temperatures for cases where the cadence of bank erosion is set by pore-ice melting.

3.2 Plain-language summary

Many rivers in the Arctic have banks made up of permanently frozen sand and ice (permafrost) that are susceptible to erosion when they thaw. To understand how bank erosion may change with a warming Arctic climate, we conducted laboratory experiments using a channel with an erodible frozen bank. We found that warmer river water and a lower bank-ice content produced faster erosion rates. In contrast, bank erosion was insensitive to the ground temperature. Bank erosion rates were three-fold faster than predicted by existing theory. We attribute the faster-than-expected erosion to a greater transfer of heat from the

river water due to bank roughness. Our results imply that warming river water may increase riverbank erosion rates in permafrost regions, threatening communities and infrastructure built along Arctic rivers.

3.3 Introduction

Permafrost riverbank erosion threatens the homes, infrastructure, and livelihoods of people living in the Arctic (Hjort et al., 2018; Karjalainen et al., 2019). Permafrost regions contain 22% of Earth's landmass (Obu, 2021; Obu et al., 2019) and ground temperatures are warming rapidly due to climate change (Biskaborn et al., 2019; Isaksen et al., 2016). These regions also contain major river systems which can erode their banks up to tens of meters per year (Rowland et al., 2019) (Figure 3.1). Hundreds of Alaskan communities experience a combined risk of bank erosion, permafrost thaw, and flooding (UAF & USACE, 2019), and it is uncertain how much these hazards will increase as the Arctic warms. Riverbank erosion has already caused some communities to relocate entirely (Bronen & Chapin, 2013; Maldonado et al., 2013), but studies disagree whether erosion rates will increase (Costard et al., 2014; Kokelj et al., 2013) or decrease (Ielpi et al., 2023) in response to climate change. Accurate mechanistic models of permafrost riverbank erosion are needed to predict bank erosion hazards and develop mitigation strategies.

Theory has been developed for permafrost riverbank erosion based on the one-dimensional Stefan solution (Costard et al., 2003; Randriamazaoro et al., 2007). In this scenario, the erosion rate is assumed to be ablation-limited, such that heat transfer and pore-ice melting set the erosion rate, and sediment is assumed to be easily and immediately entrained following thaw (Figure 3.2). It is also possible that bank erosion is limited by sediment transport or slump blocks (Douglas et al, 2023; Kanevskiy et al., 2016), but our focus here is to evaluate the ablation-limited end member. For ablation-limited erosion, bank erosion rates should depend on river flow velocity and water temperature because these parameters are the primary control on heat transfer from the river to the bank (Costard et al., 2003). Therefore, since Arctic rivers are experiencing increases in water temperature and discharge (Brabets & Walvoord, 2009; Liu et al., 2005; Peterson et al., 2002), riverbank erosion rates might significantly increase as the Arctic warms. The theory of Costard et al. (2003) for ablation-limited erosion compares well to observed erosion of up to 40 m measured over 1-2 months for islands in the Lena River (Costard et al., 2014), but it over-predicts annual rates by hundreds of meters of erosion per year if applied over the entire open-water summer season. This partial disagreement between theory and observations motivates our investigation of ablation-limited erosion theory using flume experiments.

There have been few laboratory tests of permafrost bank erosion theory. The Costard et al. (2003) model used an empirical coefficient to parameterize heat transfer from the river water to the riverbank, based on experiments of flowing water over ice (Lunardini, 1986). However, it is unclear if the same heat transfer coefficient applies to a sediment bank with pore-ice, which is typical of permafrost floodplains. Other experiments measured erosion of a small block of frozen sand and ice that was lowered into a smooth-walled pressurized pipe or duct (Alexander, 2008; Costard et al., 2003; Dupeyrat et al., 2011). They found that higher

water temperatures, greater water discharge, and lower permafrost ice content increased the erosion rate of the sample, consistent with theory. However, hydraulics are different in a pressurized duct compared to an open channel, and thaw rates in these experiments may have been affected by any protrusion of the sample into the pipe as well as the change in roughness from the hydrodynamically smooth wall to the rough sample. For instance, the size, shape, spacing, and orientation of roughness elements are known to affect heat transfer by thinning and disrupting the thermally diffusive fluid sublayer (Miyake et al., 2001; Shishkina & Wagner, 2011; Yaglom & Kader, 1974).

Here we present results from a permafrost river flume experiment designed to investigate the erosion rate of a hydraulically rough and erodible frozen riverbank under open-channel flow. First, we present existing theories for ablation-limited bank erosion and heat transfer from a turbulent fluid to a rough wall. Next, we show the experimental methods and results used to test the theories and evaluate the heat transfer coefficient. Finally, we discuss how the theory applies to natural rivers and the implications for Arctic riverbank erosion in a warming climate.
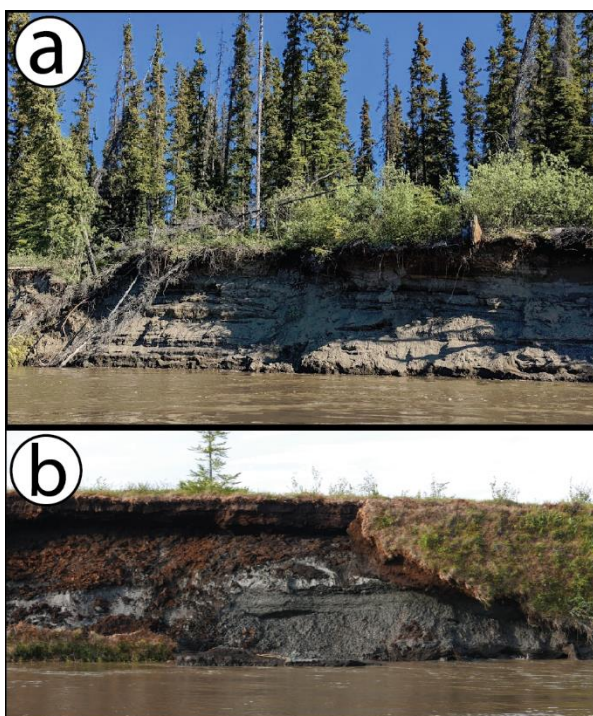
Figure 3.1. (a) Field photo of eroding permafrost sand and gravel riverbank along the Yukon River near Beaver, AK. The exposed bank is approximately 3 m tall. **(b)** Field photo of eroding permafrost silt and peat riverbank along the Koyukuk River near Huslia, AK. The exposed bank is approximately 1.5 m tall.

3.4 Theory for permafrost riverbank erosion

3.4.1 Ablation-limited erosion theory

Existing theory for permafrost riverbank erosion typically assumes ablation-limited conditions; that is, the erosion rate is set by the rate of bank thaw (Costard et al., 2003; Dupeyrat et al., 2011; Randriamazaoro et al., 2007). This is analogous to theory developed for the geometry and evolution of subglacial and supraglacial channels, where the channel geometry is set by heat transfer between the flow and a pure ice boundary (Gulley et al., 2014; Karlstrom et al., 2013), but instead uses bank material properties that reflect a mixture of sediment and ice. Following Randiamazaoro et al. (2007), we derive the position of the thawing bank ($y = s$; m) and the bank temperature (T; °C) at a given time for the 1-D case (Figure 3.2a). The control volume consists of a thawing portion of a frozen riverbank with thickness ds (m) (Figure 3.2a). Following the conservation of heat,

$$\rho_b c_{p,b} \frac{dT}{dt}\bigg|_{y=s} ds + q_f = q_w - q_r, \tag{3.1}$$

where q_f (J/m^2/s) is the latent heat flux into the bank, q_w (J/m^2/s) is the heat flux from the flowing river water to the bank, q_r (J/m^2/s) is the sensible heat flux conducted from the control volume to the frozen bank, ρ_b (kg/m^3) and $c_{p,b}$ (J/kg/°C) are the bulk density and specific heat of the bank material, and y is the coordinate normal to the bank. Equation (3.1) assumes a 1-D heat budget where the only heat source is water flowing past the bank. This assumption is supported by field observations that flowing water cuts deep thermoerosional niches and creates characteristic overhangs in permafrost riverbanks, implying that the heat flux from the air is a relatively minor component of bank erosion (Walker & Hudson, 2003). Bank material properties are assumed to be spatially and temporally homogeneous, so that ρ_b and $c_{p,b}$ are constants.

A thawing bank should be at the melting temperature, such that $T|_{y=s} = T_f$, where T_f (°C) is the temperature of fusion of pore ice; thus, in equation (3.1), $\frac{dT}{dt}\bigg|_{y=s} = 0$. In addition, the heat flux due to fusion is

$$q_f = \rho_b L_f \frac{ds}{dt}, \tag{3.2}$$

where L_f (J/kg) is the latent heat of fusion of the frozen bank. Substituting these expressions into equation (3.1) and rearranging results in

$$\rho_b L_f \frac{ds}{dt} = q_w - q_r. \tag{3.3}$$

To evaluate q_r in equation (3.3), heat flow is modeled by conduction within the frozen bank (i.e., where $y \geq s$), such that

$$-\rho_b c_{p,b} \frac{\partial T}{\partial t} = \frac{\partial q}{\partial y}, \tag{3.4}$$

with q as the heat flux (J/m²/s) within the frozen bank. Heat conduction occurs from $y = s$ to $y = s + \delta$, and beyond $y = s + \delta$ the bank temperature is set to a constant background value T_0 (°C) (Costard et al., 2003). Integrating equation (3.4) from $y = s$ to $y = s + \delta$ and using the chain rule results in:

$$\rho_b c_{p,b} \int_s^{s+\delta} \frac{\partial T}{\partial y} \frac{\partial y}{\partial t} dy = \int_s^{s+\delta} \frac{\partial q}{\partial y} dy. \tag{3.5}$$

As the bank erodes, δ (m) is assumed to remain constant, so the thermal gradient within the bank translates in the y-direction at the rate of bank erosion; thus, $dy/dt = ds/dt$. Then, equation (3.5) can be solved and rearranged using the boundary conditions $T(t, y = s + \delta) = T_0$, $T(t, y = s) = T_f$, $q(t, y = s + \delta) = 0$, and $q(t, y = s) = q_r$, to find,

$$q_r = \rho_b c_{p,b} \frac{ds}{dt} (T_f - T_0). \tag{3.6}$$

The latent heat of fusion in equations (3.2) and (3.3) for a saturated sand-ice mixture (Dupeyrat et al., 2011) depends on the mass fraction of ice in the bank (f_{ice}; kg ice/kg frozen bank) and the latent heat of fusion of ice ($L_{f,ice}$; J/kg):

$$L_f = f_{ice} L_{f,ice}. \tag{3.7}$$

The specific heat of the bank ($c_{p,b}$) is calculated as a sum of the specific heat of ice ($c_{p,ice}$; J/kg/°C) and the specific heat of quartz sand ($c_{p,s}$; J/kg/°C) weighted by the mass fraction of ice:

$$c_{p,b} = f_{ice} c_{p,ice} + (1 - f_{ice}) c_{p,s}. \tag{3.8}$$

Typically, the latent heat of fusion for ice is orders of magnitude greater than its specific heat, so we expect that the phase change and not the permafrost temperature should set the rate of pore-ice thaw.

The heat transfer from a turbulent fluid to a wall depends on fluid velocity, U (m/s), and an empirical coefficient that describes the efficiency of heat transfer (Nield & Bejan, 2017). Thus, q_w in equation (3.3) can be written as,

$$q_w = C_h \rho_w c_{p,w} U (T_w - T_b), \tag{3.9}$$

where C_h (dimensionless) is the heat transfer coefficient, ρ_w (kg/m³) is water density, $c_{p,w}$ (J/kg/°C) is the specific heat of water, T_b (°C) is the bank temperature, and T_w (°C) is the water

temperature. In the transient solution, T_b may change in response to q_w, but the ablation-limited solution given by equation (3.3) requires $T_b = T_f$.

The final expression is found from substituting equation (3.6) for q_r in equation (3.3), equation (3.9) for q_w in equation (3.3), and using equations (3.7)-(3.8) to account for the fraction of pore ice (f_{ice}) in the latent heat of fusion and heat capacity. Solving for the bank erosion rate $E \equiv \dfrac{ds}{dt}$ for the 1-D ablation-limited case results in (Randriamazaoro et al., 2007):

$$E = \frac{C_h \rho_w c_{p,w} U (T_w - T_f)}{\rho_b (f_{ice} L_{f,ice} + (f_{ice} c_{p,ice} + (1 - f_{ice}) c_{p,s})(T_f - T_0))}. \tag{3.10}$$
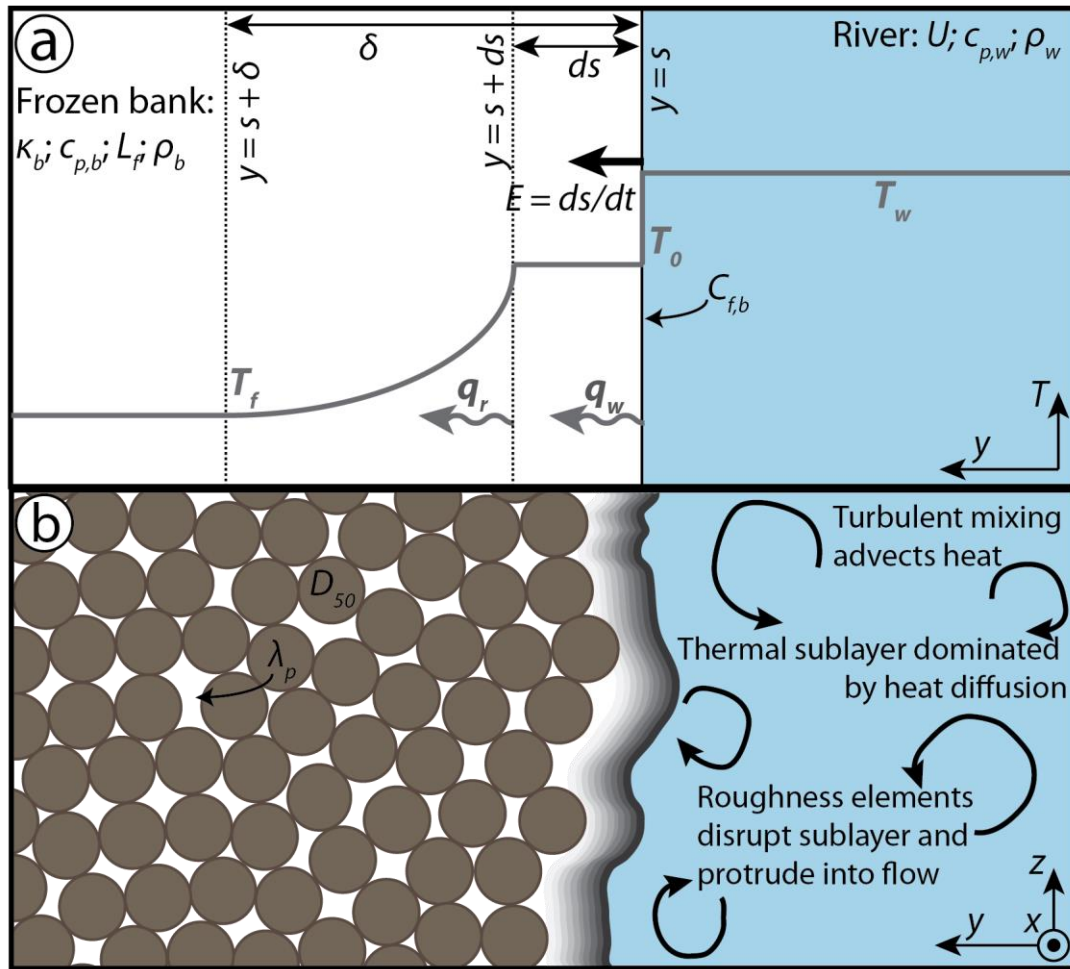
Figure 3.2. 1-D model for permafrost bank erosion ($E = ds/dt$; m/s) by ablation. **(a)** Schematic 1-D cross-section showing a temperature profile (T) into a bank (y-direction) with the river flowing into the page. The erosion model considers heat fluxes from the flowing water to the bank (q_w; J/m^2/s) in a control volume of width ds (m). Heat flux from the river depends on water flow velocity (U; m/s), temperature (T_w; °C), density (ρ_w; kg/m^3), specific heat capacity ($c_{p,w}$; J/kg/°C), and the bank coefficient of friction ($C_{f,b}$; dimensionless). The permafrost bank has a constant thermal conductivity (κ_b; W/m/°C), specific heat capacity

($c_{p,b}$; J/kg/°C), latent heat of fusion (L_f; J/kg), and bulk density (ρ_b; kg/m^3). The bank temperature in the control volume is at the temperature of fusion (T_f; °C) and decreases to the background temperature (T_0; °C) over a distance δ (m) driven by conduction (q_r; J/m^2/s). **(b)** Cartoon cross-section of the bank showing how roughness affects heat transfer from a fully turbulent fluid (flowing out of the page) to a hydraulically rough wall. The bank has median grain size D_{50} (m) and volumetric ice content λ_p (m^3/m^3). Far from the wall, heat transfer is dominated by heat advection in turbulent eddies, while heat transfer near the bank occurs by molecular diffusion through a thin sublayer. Roughness elements cause more rapid heat transfer to the bank by thinning or protruding through the diffusive sublayer.

3.4.2 Heat flux parameterizations

Applying equation (3.10) requires specifying the heat transfer coefficient C_h. Different empirical relations have been proposed for C_h. Costard et al. (2003) and Dupeyrat et al. (2011) calibrated C_h based on a series of frozen flume experiments to evaluate the rate of heat transfer from the water to a frozen bank. Both coefficients were calculated as a function of the thermal conductivity of water (κ_w; J/m/s/°C), the Prandtl number (Pr), and the Reynolds number (Re), using flow depth as the characteristic length scale:

$$C_h = A\kappa_w Pr^\alpha Re^\beta /(\rho_w c_{p,w} UH). \tag{3.11}$$

The Prandtl number ($Pr = \rho c_{p,w} v/\kappa_w$) represents the dimensionless ratio of momentum diffusivity over thermal diffusivity and depends on the fluid kinematic viscosity (v; m^2/s). The Reynolds number is the non-dimensional ratio of fluid inertial forces over viscous forces, with $Re = UH/v$. Costard et al. (2003) used values of $A = 0.0078$, $\alpha = 0.3333$, and $\beta = 0.9270$ constrained from flume experiments of water flowing over pure ice (Costard et al., 2003; Lunardini, 1986). During these experiments, the ablating ice developed scallops on the scale of tens of centimeters, so heat transfer may have been influenced by form drag from the scallops (Lunardini, 1986). In this case, $\beta \sim 1$, so C_h is mostly independent of flow velocity (in equation (3.11), $Re/UH \sim 1/v$).

Yaglom and Kader (1974) proposed an alternative formulation for C_h that considers explicitly how wall roughness affects heat transfer. They used the Reynolds analogy and asymptotic mapping of the thermal and viscous sublayers analogous to the derivation of the log law (Figure 3.2b). Their formulation has been used extensively in sea-ice models (Malyarenko et al., 2020), but has not been applied previously to permafrost riverbanks. Assumptions in their theory include a negligible longitudinal pressure gradient and homogeneous wall roughness. They used linear interpolation to find a solution that includes hydrodynamically rough flow (roughness Reynolds number, $Re_{k_s} = k_s u^*/v > 100$, with $u^* = U\sqrt{C_{f,b}}$) as well as hydrodynamically smooth flow. These are reasonable assumptions for permafrost rivers, which are fully typically turbulent with hydraulically rough banks due to coarse sand and gravel grains and morphological roughness elements such as slump blocks and vegetation (Figure 3.1). Their final expression when integrated over the flow field is (Yaglom & Kader, 1974; their equations (22) and (23)):

$$C_h = \frac{\sqrt{C_{f,b}}}{-\alpha \ln \eta_1 + \beta_1 + \beta_t}. \tag{3.12}$$

C_h depends on the bank coefficient of friction ($C_{f,b}$; dimensionless), the relative roughness element height ($\eta_1 = k_s/H$; dimensionless), the von Kármán constant ($\kappa = 0.41$), and empirical constants from the law of the wall ($\alpha = 2.12$; $\beta_1 = 0.5$). For hydraulically rough flows ($Re_{ks} > 100$), $\beta_t = \beta_r$, with $\beta_r = \sqrt{Re_{k_s}}\left(b_1 Pr^{\frac{2}{3}} - b_2\right)$. For smooth to transitional flow ($Re_{ks} \leq 100$), $\beta_t = \beta_r(Re_{ks}/100) + \beta_s(1 - Re_{ks}/100)$, where $\beta_s = 12.5Pr^{2/3} - 6$. Next, we describe the experimental approach and methods to test the bank erosion model (equation (3.10)) and the two different relations for the heat transfer coefficient (equations (3.11) and (3.12)).

3.5 Methods

3.5.1 Experimental goals and approach

The goal of our frozen flume experiments was to evaluate the relations for the heat transfer coefficient for conditions similar to permafrost rivers. We simulated ablation-limited permafrost riverbank erosion, where permafrost was directly in contact with the flowing river water. The experiments were not intended to be scale models of any specific river, but we did consider important dimensionless numbers so that the experiments had similar thermal and hydraulic states as natural permafrost rivers. The experiments were conducted under fully turbulent ($Re \sim 10^5$) and subcritical (Froude number < 1) flow with hydraulically rough bed and banks ($Re_{k_s} > 100$) (Table 3.1). We also scaled our flume experiments to the thermal regimes of natural permafrost rivers. We used the Biot number to compare heat transfer to the bank versus conduction within the bank ($Bi = C_h\rho_w c_{p,w} UH/\kappa_b$), where κ_b is the bank thermal conductivity (W/m/°C), and the Stefan number to compare heat transfer to the bank ($St = c_{p,w}(T_w - T_f)/H$). Using calculated values for bank thermal conductivity and best-fit model results for C_h (see Section 3.6.2), we find $Bi \sim 0.15$ and $St \sim 130 - 660$. For comparison, we estimated similar values ($Bi \sim 0.40$ and $St \sim 8 - 80$) from field measurements of the gravel-bedded Atigun River, Alaska, using data from Scott, (1978).

We conducted five experiments to vary water temperature, bank temperature, and mass fraction of water ice while holding the other variables approximately constant. The effect of water temperature was evaluated by comparing Experiments 1-3; bank temperature was evaluated by comparing Experiments 3 and 4; pore-ice fraction was evaluated by comparing Experiments 2 and 5 (Table 3.2).

Table 3.1. Experimental hydraulic conditions for all frozen banks. Water discharge and channel width were increased throughout each experiment as the channel widened.

Variable	Symbol	Units	Values
Bank median grain size	$D_{50,bank}$	m	0.00026132
Bank 84th percentile grain size	$D_{84,bank}$	m	0.00036361
Bed median grain size	$D_{50,bed}$	m	0.019

Bed 84th percentile grain size	$D_{84,bed}$	m	0.021
Water discharge	Q_w	m^3/s	0.00221 to 0.00756
Channel depth	H	m	0.056
Channel width	B	m	~ 0.10 - 0.30
Average water flow velocity	U	m/s	~ 0.6 - 0.7
Water Reynolds number	Re	Dimensionless	~ 3.04×10^5
Bank roughness Reynolds number	Re_{k_s}	Dimensionless	~ 90
Water Froude number	Fr	Dimensionless	~ 0.83
Prandtl number	Pr	Dimensionless	10
Stefan number	St	Dimensionless	~130 - 660
Biot number	Bi	Dimensionless	~0.33

Table 3.2. Frozen bank properties for each experiment, with variability reported as 1 standard deviation (SD).

Experiment	Bed slope (m/m)	Water temperature (ºC)	Bank temperature (ºC)	Fraction ice (wt%)	Bulk density (g/cm^3)	Measurement time interval (stage 1) (min:sec)	Bank erosion rate (mm/s)
Experiment 1	0.0156	1.9±0.1	-5.8±0.7	33.0±0.5	1.54±0.04	40:06	0.075±0.032
Experiment 2	0.0144	6.9±1.5	-4.1±0.8	23.6±1.1	1.57±0.06	19:32	0.16±0.07
Experiment 3	0.0249	8.8±0.6	-4.4±0.7	27.7±5.7	1.71±0.09	6:52	0.26±0.06
Experiment 4	0.0149	6.3±1.0	-7.1±0.6	21.4±0.5	1.65±0.36	15:00	0.19±0.06
Experiment 5	0.0205	6.2±0.2	-8.2±0.9	31.3±2.9	2.05±0.16	5:46	0.23±0.03

3.5.2 Experimental methods

The experiments were designed to simulate a straight half-width channel by using one fixed hydrodynamically smooth wall and one erodible permafrost bank in the Caltech Earth Surface Dynamics Laboratory (Figure 3.3). We placed the channel along the smooth wall, rather than in the middle of the flume, to suppress meandering or braiding. The smooth plexiglass wall had minimal friction relative to the rough bed and sediment bank, and therefore the half-width experiment can be considered representative of a full-width channel with two sediment banks that is twice as wide (Pitlick et al., 2013).

The flume was 0.75 m wide and 7.60 m long ending in a reservoir filled with chilled water. We evaluated bank erosion within a test section 0.70 m long centered in a 1.8 m reach bound by the clear, plexiglass wall of the flume on river right and an erodible bank consisting of a frozen mixture of sand and ice on river left. The bankfull channel was initially set to 0.056 m depth and 0.10 m width for each experiment. During the experiment, the channel width increased due to bank erosion to a final value of about 0.3 m. We increased water discharge to maintain a constant water depth as bank erosion progressed and the channel widened and used a backwater model (see Section 3.11.3) to account for variations in channel hydrodynamics throughout the experiment.

We controlled water temperature and bank temperature using a Mokon AL Iceman chiller. The chiller recirculated a 30% mixture of glycol in water through flexible pipes and mats

arranged in the end tank and end barrels to chill the water, and in the channel under the bed material and on the river-left flume wall to freeze the bank material (Figure 3.3). The experiments were not conducted in a climate-controlled room, so air temperature was variable.

We constructed the frozen, erodible bank and floodplain in layers to make a uniform mixture of sand (D_{16} = 0.16198 mm, D_{50} = 0. 26132 mm, and D_{84} = 0.36361 mm; Figure 3.S1) and pore ice. We used a 0.1 m wide mold along the length of the sandy bank to form the initial channel on river right. We filled the region between the mold and the river-left flume wall with the sand-water mixture and placed it on top of a graded gravel bed. We built the bank material by laying ~1.5 cm thick layers of saturated sand, graded each layer to parallel the bed slope, and then covered it with insulation to freeze overnight. Temperature sensors (Minco S667PFZ40BC resistance temperature detectors (RTDs) with ±0.2ºC resolution) were placed in the bank material before stacking the next layer (Table 3.S1). Three arrays of sensors in the bank were located in upstream (x = 2.5 cm), middle (x = 22.5 cm), and downstream (x = 42.5) locations extending perpendicular to the channel (in the y-direction). The upstream and downstream arrays consisted of one line of sensors spaced 3 cm apart at an elevation above the thalweg of z ~ 3 cm. The middle array consisted of three lines of sensors with similar spacing in the y-direction at z ~ 1 cm, 3 cm, and 5 cm plus additional sensors at the base of the bank (z = 0 cm) and near the frozen wall (y = 67.5 cm). Finally, a temperature sensor was placed protruding into the channel to measure water temperature at z ~ 5 cm at each sensor array x-coordinate.

The channel bed was composed of gravel (D_{16} = 18 mm, D_{50} = 19 mm, and D_{84} = 21 mm; Figure 3.S1), and the same gravel was used as river-left bank material for 1.2 m upstream and 0.9 m downstream of the sand-banked section. The gravel banks prevented erosion near channel headbox or outlet and helped to condition the flow and reduce spatial accelerations as it entered and exited the test section. The experiments were designed such that the gravel was below the threshold of motion. The gravel-banked reaches had a bankfull depth identical to the test section (0.056 m) and a bankfull width of 0.25 m. The gravel bed in the test section was graded by hand to a slope that ranged from 1.5% to 2.5% in different experiments (Table 3.2). Some pore ice formed in the gravel reaches, but the large pore spaces made the gravel drain relatively efficiently. The gravel banks maintained an angle of ~25°, slightly below the angle of repose.
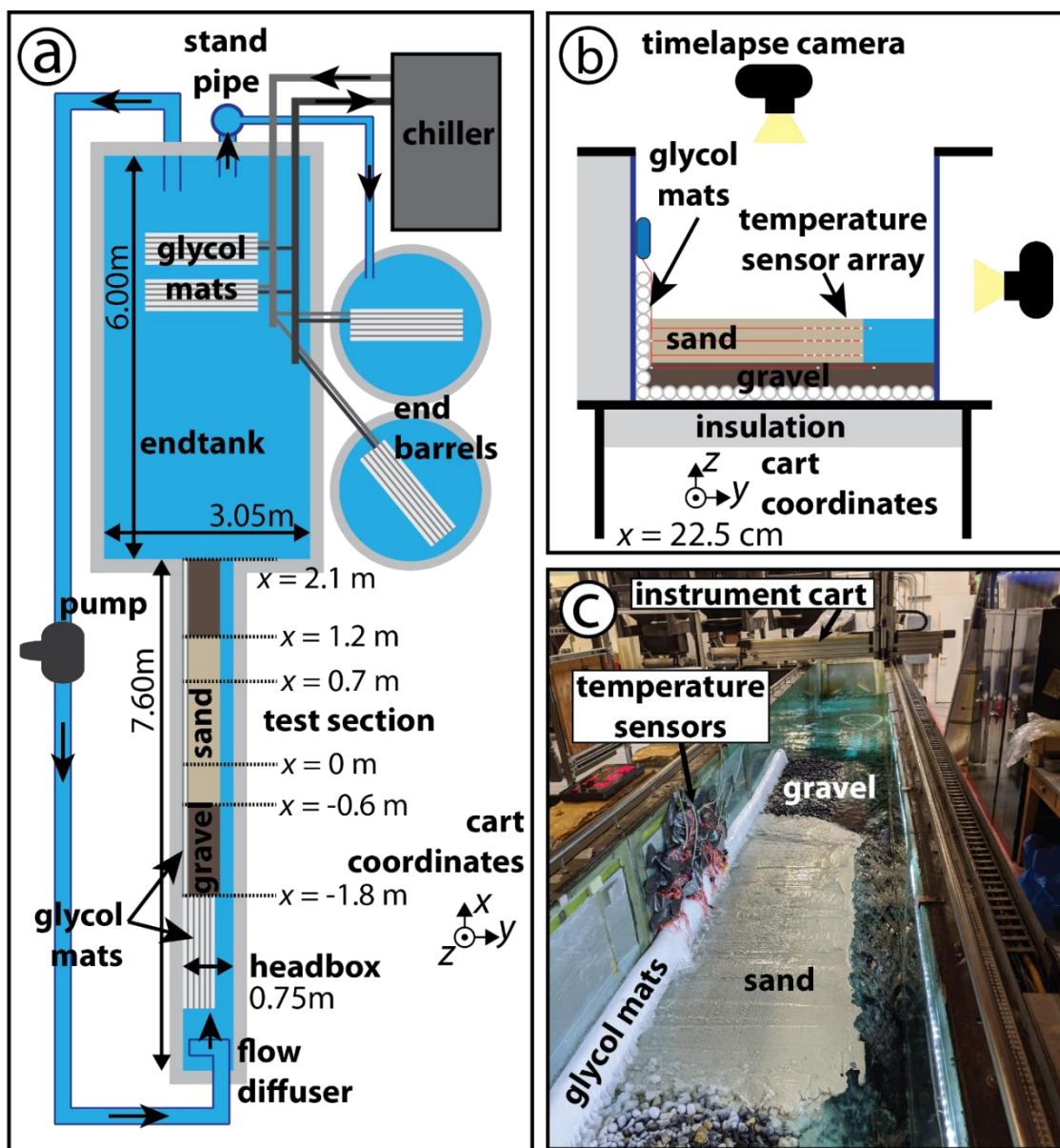
Figure 3.3. Frozen channel experimental setup in Caltech Earth Surface Dynamics Laboratory. **(a)** Top-down cartoon of the flume setup. Glycol was cooled by the chiller and circulated through a set of flexible pipes and mats to freeze the bank and cool the water in the end tank. Water was circulated by the pump from the end tank through the flow diffuser and into the experiment headbox, where it flowed past gravel and sand. Overflow of the stand pipe went into external barrels. **(b)** Side-looking cartoon of the flume test section. Glycol mats line the side and base of the flume, and the exterior of the flume was covered by insulation. An array of temperature sensors was frozen into the eroding, sandy bank, and we recorded 10-sec timelapse imagery using down- and side-looking cameras. **(c)** Photograph during a flume experiment. The glycol mats and temperature sensors are visible protruding up past the bank. The instrument cart ran on rails (visible in the lower right foreground) and

carried a laser to measure topography as well as a sonar to measure water slope throughout the experiments.

We sampled the sandy bank material using a chisel and calculated a bulk density (ρ_b) and mass fraction of ice (f_{ice}) for each experiment (Table 3.1). We obtained the volume of the samples by differencing 1x1 mm gridded laser elevation scans, with a vertical accuracy of ~10 microns, before and after sampling. The samples were weighed before and after oven drying at 70 °C to find the mass of sand and ice (Table 3.2).

To calibrate the temperature sensors, we submerged them in an ice water bath at 0ºC for multiple hours. Each sensor showed little temperature variation, typically giving a standard deviation of less than 0.1ºC, which was smaller than the reported precision of ±0.2ºC. However, some sensors showed offset from 0ºC. Therefore, we took the mean temperature of each sensor and subtracted that from the sensor with the lowest standard deviation whose mean temperature was closest to 0ºC. We used this correction offset while processing data for all experiments.

Temperature data were recorded using MicroDAQ data acquisition cards at 2 Hz. The initial bank temperature (T_0) was found by taking the mean±1SD of the middle layer of the middle section bank temperatures for 5 min before the experiment started. The mean±1SD of the water temperature was measured at the middle section during the period of uniform bank erosion when we calculate erosion rates. For subsequent analyses, we used a 10-sec (20-measurement) smoothing window to average the temperature data over a similar interval to our timelapse imagery.

Water discharge was recorded every 10-sec using an in-line flowmeter and controlled during each experiment using a variable frequency drive. We accounted for the time delay between the discharge at the flow meter and the discharge in the test section. We calibrated the water discharge by taking the time to fill a 5-gal container ($n = 4$ to 6) at 4 different discharges. We calculated uncertainty by making a linear fit to 1SD of the measured discharge versus the flowmeter. This uncertainty was propagated through subsequent calculations.

To measure the evolving channel width during the experiment, we took overhead photographs (Nikon D750, 300 dpi resolution) every 10 sec synchronized using DigiCamControl (Figure 3.4; Movies S3.1-S3.5). The water was dyed blue to enhance the contrast between the flowing water and eroding bank. Images were corrected for distortion using grids surveyed in with the cart to ~0.1 mm precision using Adobe Photoshop CS4 (Figure 3.4b). The blue band was used to isolate the water and bank material using the Matlab v2020a image processing package (Figure 3.4c; Table 3.S2). Images were cropped to isolate the test section and exclude portions of the bank that formed overhangs during each experiment. Incorrect classification on the bank material (e.g., from exposed temperature sensors or glint) was eliminated using the Matlab function imfill.m (Figure 3.4d) and by eye (Figure 3.4e). We summed the wetted top area of the channel, A_T (m^2), and then used this measurement to find the average bank erosion rate (m/s) as

$$\bar{E} = \frac{\Delta A_T}{L\Delta t},$$ (3.13)

where the test section length is $L = 0.70$ m. The timelapse had $\Delta t = 10$ sec, and erosion rates were smoothed using a moving average with 1-min window size and 1SD uncertainty (Figure 3.6).

We also used the channel-width, flow discharge, and flow depth measurements to calculate the cross-sectionally averaged flow velocity (U). We used mass balance (Figure 3.3d) such that $Q_w = A_{xs}U$, where A_{xs} (m^2) is the channel cross-sectional area. We estimated $A_{xs} = CHB$, where $B = A_T/L$ is the channel top width (m), and C is a correction factor to account for any deviation in cross-section shape from rectangular. Using the topographic scans of the channel topography when dry, confirmed that $C \sim 1$ within 5% uncertainty, which we used for all the experiments.

To calculate the friction coefficient on the eroding wall, we linearly partitioned the total frictional stress between components for the gravel bed, smooth flume wall, and grain and form drag on the eroding frozen bank using the approach of Vanoni & Brooks (1957). For the smooth flume wall, we evaluated the skin friction coefficient using Blasius (1950). To find the friction coefficient corresponding to the immobile gravel, we conducted a series of additional experiments where the entire river-left bank of the test section was composed of immobile gravel rather than frozen sand (Section 3.11.2.1). For these gravel-banked experiments, we fit the 1-D backwater equation to measured water surface data, to find the total frictional resistance for different water discharges (Section 3.11.2.2). We then subtracted the friction due to the smooth wall from the total frictional stress to find the stresses acting on the gravel bed and gravel bank. Weighting by the relative area of the bed and bank, we found values for the coefficient of friction for the gravel (Section 3.11.2.3). These data compared well to the Ferguson (2007) variable-power equation (VPE) for shallow and rough flow,

$$C_{f,g} = \frac{a_1^2 + a_2^2(H/k_s)^{5/3}}{a_1^2 a_2^2(H/k_s)^2}$$ (3.14)

using the recommended non-dimensional constants of $a_1 = 6.5$ and $a_2 = 2.5$ with $k_s = 2.5D_{84}$ (Figure 3.S2).

For the permafrost experiments, we followed the same procedure to isolate the frictional stress on the eroding permafrost bank. We used the 1-D backwater equation fit to find the total frictional stress in the test section (Section 3.11.3.1), subtracted off the stress components due to the smooth wall (Blasius, 1950) and the gravel bed (using equation (3.14)), and solved for the remaining frictional stress on the eroding permafrost bank. This coefficient of friction related to the bank stress ($C_{f,b}$) represents both grain drag and any morphologic form drag (Lamb, Dietrich, & Venditti, 2008) from scallops that developed on the eroding bank (described in Section 3.11.3.2). To calculate the component due to grain

drag ($C_{f,bg}$) on the sand bank, we followed the method of Wright & Parker (2004), solving the Manning-Strickler equation,

$$\frac{U}{u^*_{bg}} = 8.32 \left(\frac{H_{bg}}{k_{s,bg}}\right)^{1/6}, \tag{3.15}$$

with $k_{s,bg} = 3.5D_{84}$ and $u^*_{bg} = \sqrt{gH_{bg}S}$. We differenced the grain component from the total bank stress to find any remaining drag which we assign to morphologic form drag ($C_{f,bm}$). We then needed to determine the appropriate roughness lengthscales ($k_{s,b}$ and $k_{s,bm}$) to substitute into equation (3.12) and evaluate C_h for total and morphologic bank drag. To solve for the effective roughness lengthscale for total bank drag ($k_{s,b}$), we set $u^*_b = U\sqrt{C_{f,b}}$ and solve equation (3.15), substituting H for H_{bg}, u_b^* for u_{bg}^*, and $k_{s,b}$ for $k_{s,bg}$. To solve for the roughness lengthscale for morphologic form drag ($k_{s,bm}$), we set $C_{f,bm}U^2 = \sqrt{gH_{bm}S}$ and solve for the flow depth attributed to morphologic drag (H_{bm}, m). We then solve equation (3.15), substituting $u^*_m = U\sqrt{C_{f,bm}}$ for u_{bg}^*, H_{bm} for H_{bg}, and $k_{s,bm}$ for $k_{s,bg}$.
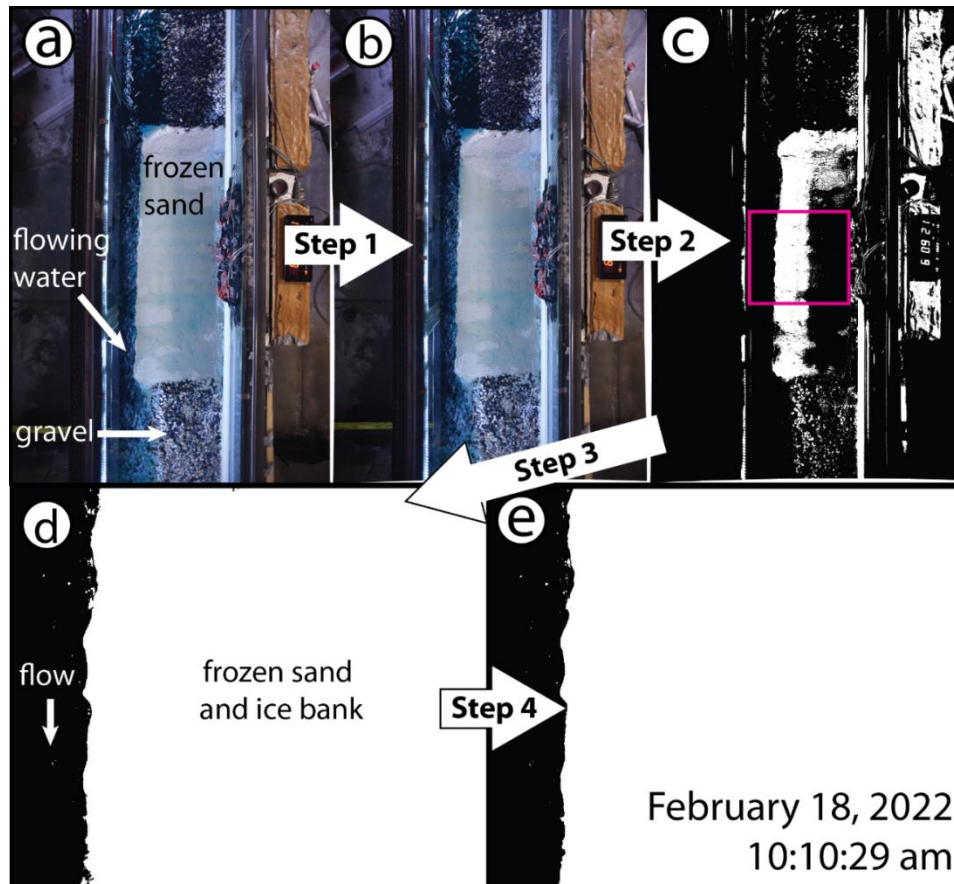
Figure 3.4. Steps for image processing to extract channel width and bank erosion rates. **(a)** Original image from overhead, down-looking camera. Blue dyed water flows from the top to the bottom of the image. **(b)** The image is corrected for camera lens distortion so that the

pixels are at known values of the carriage coordinates. **(c)** Thresholded red band of the .jpg image, with light pixels considered part of the eroding bank. **(d)** The thresholded image is clipped to the test section (70 cm channel length, outlined in pink in panel c) and the interior of the bank top is filled in. **(e)** The image is reviewed and small artifacts are manually removed.

3.5.3 Comparing experiments and theory

We used our measurements of the bulk density of permafrost (ρ_b), its mass fraction of ice (f_{ice}), and its initial temperature (T_0) in the ablation-limited erosion theory (equation 3.10). We assumed constant bulk densities of sediment ($\rho_s = 2650$ kg/m^3) and ice ($\rho_{ice} = 920$ kg/m^3), latent heat of fusion of ice ($L_{f,ice} = 333{,}550$ J/kg), fusion temperature ($T_f = 0°$C), and specific heat of sand ($c_{p,s} = 730$ J/kg/°C) and ice ($c_{p,ice} = 2093$ J/kg/°C). We used the average water flow velocity (U) and temperature (T_w), and assumed a constant water specific heat capacity ($c_{p,w} = 4184$ J/kg/°C) and density ($\rho_w = 1000$ kg/m^3).

We solved equation (3.10) using four different values of the heat transfer coefficient, C_h. The first used equation (3.11) (Costard et al., 2003). The other three values used equation (3.12) (Yaglom & Kader, 1974) with the wall drag parameterized as the total bank drag from the stress partitioning, bank grain drag calculated from equation (3.15) and bank morphologic form drag that is the difference between total bank drag and bank grain drag. Our experiments had hydraulically rough flow, with Re_{ks} ~ 100 for both scallop and grain roughness lengthscales. To evaluate equation (3.11), we inserted the flow depth (H) and the channel-averaged fluid flow velocity (U) to solve for the coefficient of heat transfer (C_h) assuming a constant Prandtl number ($Pr = 10$, varies from 9-13 over the temperature range we investigated) and fluid kinematic viscosity ($v = 10^{-6}$ m/s^2). We used $A = 0.0078$, $\alpha = 0.3333$, and $\beta = 0.9270$ (Lunardini, 1986), similar to the Costard et al. (2003) experiments. To solve equation (3.12) for the three scenarios, for total bank drag we used the total bank friction coefficient ($C_{f,b}$), constrained by a backwater model and stress partitioning, set $u_b^* = U\sqrt{C_{f,b}}$ and solved for $k_{s,b}$ using equation (3.15). For grain drag ($C_{f,bg}$), we set $k_{s,bg} = 3.5D_{84}$ and solved equation (3.15) so that $u_{bg}^* = U\sqrt{C_{f,bg}}$. The morphologic drag ($C_{f,bm}$) was constrained by stress partitioning, and we set $u_{bm}^* = U\sqrt{C_{f,bm}}$ and solved for $k_{s,bm}$ using equation (3.15).

3.6 Results

In this section, we first describe the stages that occurred during each experiment, using Experiment 1 as an example (Section 4.1). In Section 4.2 we evaluate the heat budget for the experiments. Then we compare bank erosion rates from our experiments with theoretical rates calculated using heat transfer coefficients evaluated using the total bank friction and the bank friction due to grain and morphologic drag to understand the effects of bank roughness (Section 4.3). Finally, we compare the effects of changing water temperature, bank temperature, and bank ice content on modeled and experimental bank erosion rates (Section 4.4).

3.6.1 Experiment progression

All frozen experiments proceeded through similar stages. Prior to the experiment (stage 0), we filled the channel to bankfull conditions. Experimental runtime is defined as the time since the start of stage 1. During stage 1, the channel remained at bankfull flow conditions as it widened and we increased the water discharge. At the end of the first stage, the frozen sand eroded back so that the channel was the same width as in the gravel reaches (Figure 3.5c). The end of stage 1 had the highest quality data because there was a smooth transition between the gravel reaches and the frozen reach, which minimized flow acceleration. In stage 2, water discharge was held constant as the bank continued to erode, such that the flow depth decreased in time as the channel widened. Stage 2 ended when sediment accumulated at the base of the eroding bank. We do not evaluate bank erosion theory for stage 2 because it experienced non-uniform and unsteady flow, and decreasing erosion rates due to declining bank and bed stresses.

Experiment 1 serves as an example case; processes were qualitatively similar in all experiments (Figures 3.S1-3.S4; Movies 3.S1-3.S5), but experiments with warmer water proceeded more rapidly (Table 3.2). In stage 0 of Experiment 1, there was near-normal flow conditions as we raised the water level, where the water surface slope in the test section was parallel to the channel bed. During the beginning of stage 1, the erodible-banked channel was narrower than the gravel-banked channel. This produced localized bank overtopping and undercutting by the flowing water at the upstream and downstream portions of the erodible bank. These reaches were not included in the test section analyzed for bank erosion rates because of their variable hydraulic conditions. The eroded sand was rapidly transported downstream as suspended load and the bank and bed did not accumulate any sediment. At the end of stage 1 ($t = 24$ min) the water experienced minimal spatial accelerations as the erodible sand bank and gravel sections had nearly equal widths. This marked the end of ablation-limited bank erosion conditions in Experiment 1, and afterward sand began accumulating at the toe of the bank.

Flow depth (Figure 3.6a) and water surface slope (Figure 3.6b) remained relatively constant throughout stage 1 of Experiment 1 as the channel widened because we increased water discharge (Figure 3.6c) to maintain near bankfull conditions. Discharge was increased in stage 0 at an irregular rate to fill the headbox and subsequently the channel with a low flow velocity. As the channel approached bankfull, we increased discharge to establish the water surface slope at $t = 3$ min. The bank was overtopped at $t = 3$ min, so we slightly decreased the discharge and kept it at a constant value until $t = 9$ min to avoid further overtopping. The discharge was then increased until $t = 24$ min and stage 1 ended. Water flow velocity remained relatively constant at 0.7 m/s through stage 1 (Figure 3.6d).

The sandy channel doubled in width during the experiment, from less than 10 cm to over 20 cm, with nearly constant bank erosion rates in the latter part of stage 1 (Figure 3.6). The bank eroded back as a near vertical wall, maintaining a nearly rectangular cross-section with flow depths within 10% of 5.2 cm, which was nearly bankfull (bankfull depth was 5.6 cm). Shallow flow undercut the bank in stage 0, causing a delay between the start of water flowing

through the experiment and erosion being recorded (Figure 3.6e). Once the water depth stabilized near bankfull (stage 1), erosion remained relatively constant, except for a brief peak in erosion rates 2 min into stage 1 when the undercut bank collapsed. The erosion rate decreased at the start of stage 2 when the discharge reached its maximum value and the water surface slope began to drop, before erosion rates returned to zero when the experiment ended.
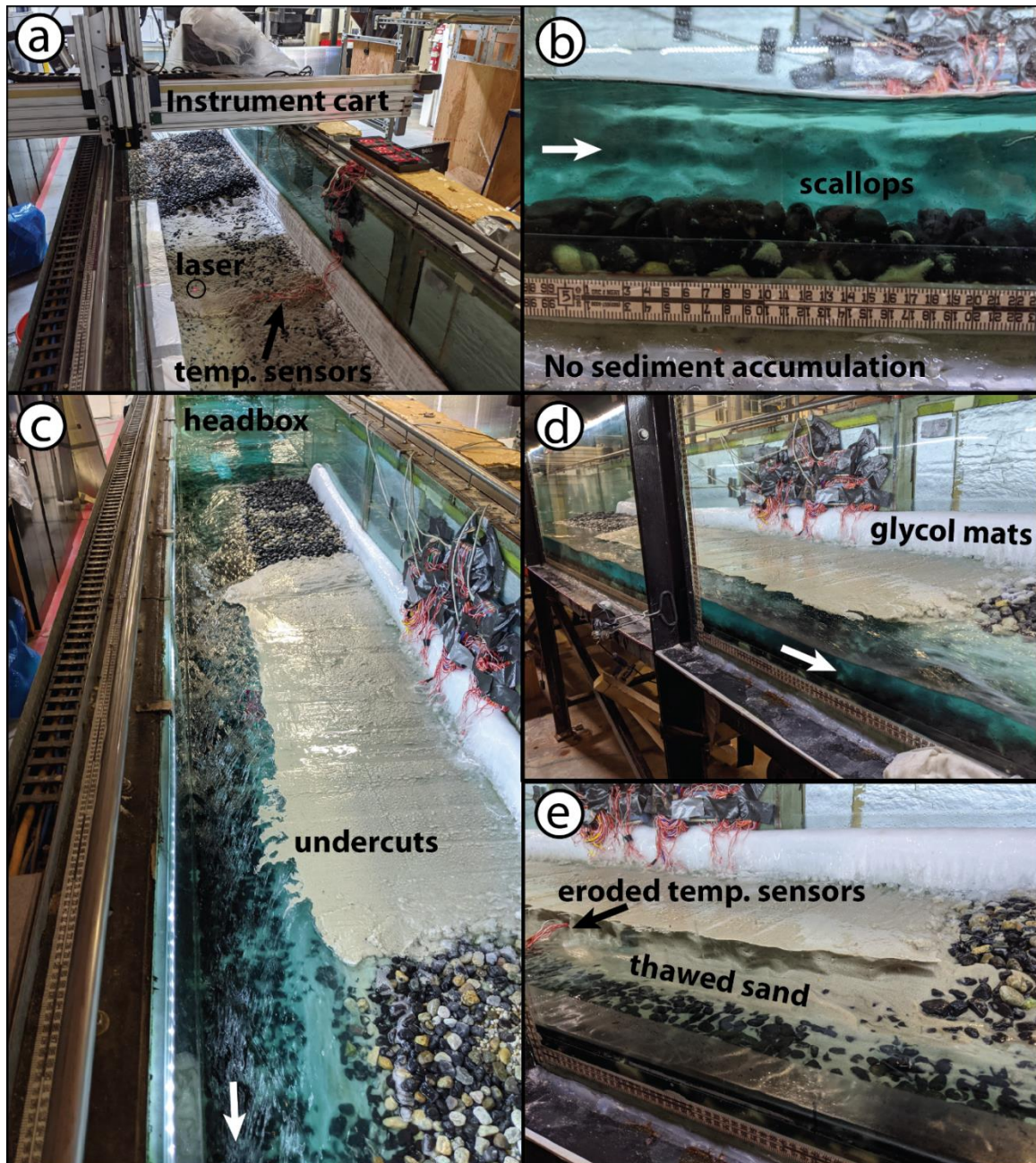
Figure 3.5. Setting up and running frozen bank Experiment 1, with water flow direction indicated by a white arrow. **(a)** Temperature sensors were laid out in an array using the Keyence laser on the instrument cart to set their position accurately. The bank was

constructed of layers of frozen sand and ice with temperature sensors sandwiched between each layer, and the initial channel width was the thickness of the silver insulation mold to the left of the laser. **(b)** As water filled the channel, scallops rapidly formed on the bank. During this stage, all sediment was transported in suspension and did not accumulate on the gravel bed. **(c)** As the experiment progressed, the frozen bank eroded back until it was even with the immobile gravel in the test section. The upstream and downstream sections of the channel experienced unsteady water levels as the bank eroded, leading to undercuts that are cropped from during image processing steps. As the channel eroded, some thawed sand began to be deposited at the base of the bank and transported as bedload. **(d)** The downstream end of the bank continued to be undercut due to flow expansion, forming a thermoerosional niche just upstream of the gravel section. **(e)** After sand accumulated at the base of the eroding bank, we terminated the experiment and drained the channel and headbox, exposing the eroded temperature sensors, thawed sand, and scallops on the exposed, and still-frozen bank.

In all experiments, we observed features that mimicked thermoerosional niches observed in natural permafrost riverbanks (Figure 3.5b). Thermoerosional niches occur where frozen banks are undercut, forming ledges that extend meters (in the field) or centimeters (in our experiments) above the channel (Walker et al., 1987). In our experiments, they formed during stage 0 of the experiment and where the erodible bank meets the upstream and downstream gravel so the water level was lower than the top of the bank. During our experiments, we also observed erosional scallops ~5 cm long forming on the submerged bank. These appeared analogous to the scallops that form other on ice-fluid interfaces, such as in subglacial channels (Bushuk et al., 2019).

The temperature of the frozen bank varied throughout Experiment 1 (Figure 3.7). In general, temperature sensors closer to the surface of the bank were warmer since a thermal gradient developed between the glycol mats lining the channel bed and the warmer air. The average bank temperature increased over the course of the experiment due to heat fluxes from the flowing water and the warm air into the bank (q_a and q_c in Figure 3.7). By the end of the experiment, the bank temperature had increased from around -7°C to near 0°C, indicating that bank temperature in Experiment 1 was buffered by the latent heat of fusion.
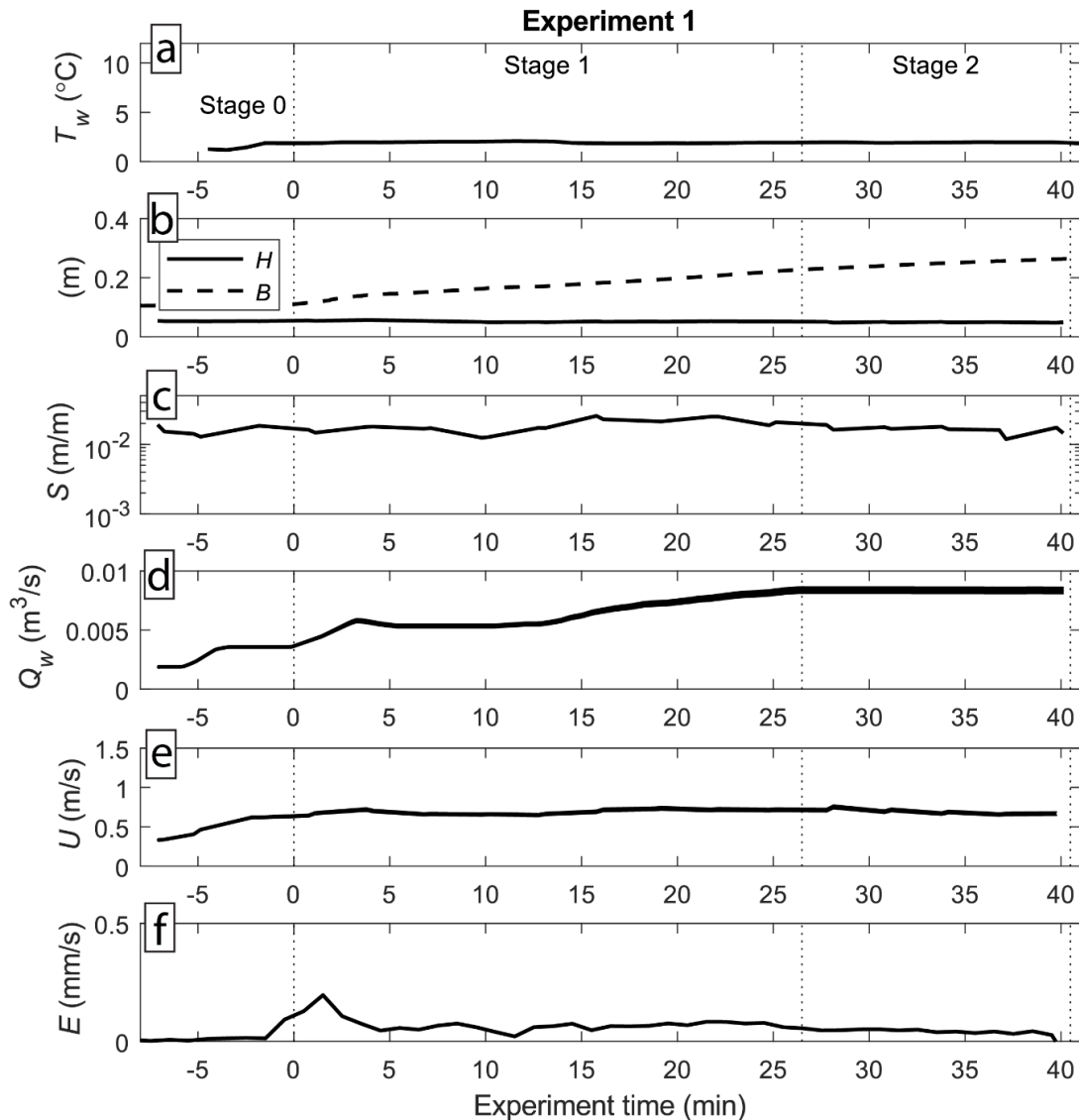
Figure 3.6. Measured and calculated thermal and hydraulic variables over the course of frozen flume Experiment 1. **(a)** Water depth (H) and channel width (B) measured in meters at $x = 22.5$ cm downstream using downstream Massa sonar scans. **(b)** Water surface slope (m/m) measured using a linear fit to water surface elevation from $x = 0 - 70$ cm downstream. **(c)** Water discharge (m^3/s) past the central temperature sensors. Discharge (Q_w) was measured using timelapse imagery at the channel inlet and corrected using the headbox dimensions and mean discharge velocity to the distance along the experimental bank. Line width includes 1SD uncertainty in the discharge calibration. **(d)** Mean water flow velocity at the central temperature sensor array with line width enclosing 1SD uncertainty. **(e)** Erosion rates were calculated by differencing the total bank area from 10-sec timelapse images and averaging over a 1-min window.
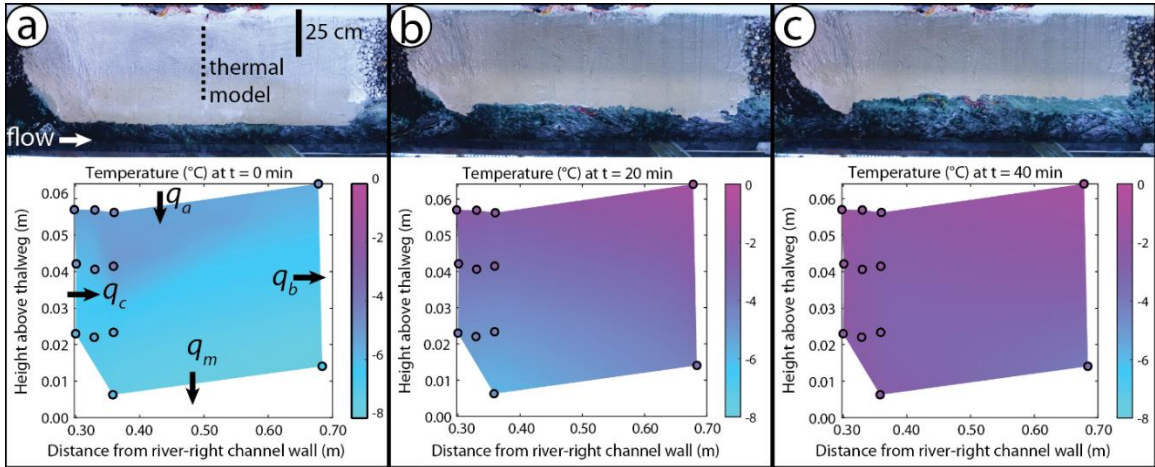
Figure 3.7. Overhead images and bank temperatures at the **(a)** start, **(b)** middle, and **(c)** end of Experiment 1. The overhead images have water flowing left to right. The lower panel shows the measurements from temperature sensors that did not erode in the experiment (circles) and a heat conduction model (shaded region). The heat conduction model was then used to calculate the heat fluxes from the air (q_a) and conducted into the un-eroded bank (q_c), glycol mats at the base of the bank (q_m), and the edge of the flume (q_b), as described in Section 4.2. We compared them to the latent heat of fusion (q_f) required to thaw the bank at observed erosion rates.

3.6.2. Heat budget

The theory for permafrost bank erosion presented in Section 2.1 is valid for a homogeneous bank with constant background temperature T_0, where the bank is eroding at a constant rate and its temperature profile has been established and translates uniformly at the same rate the bank is eroding (Randriamazaoro et al., 2007). These assumptions should be met when heat flow is primarily in 1-D, from the water into the bank material in the y-direction, without other sources of heat.

The assumption of homogeneous bank material was satisfied in our experiments, as the standard deviations were small for the bank bulk density and mass fraction of ice for each experiment (Table 3.2). In addition, we only analyzed data from the period during the experiments when erosion rates were roughly constant in time (stage 1), satisfying the constant rate constraint. Evaluating the 1-D heat flux assumption requires more consideration.

We fit a heat conduction model to the temperature sensor data at $x = 22.5$ cm far from the river channel to solve for the heat fluxes into the bank material. In particular, we solved for the heat flux from the air to the bank (q_a; J/m^2/s), from the frozen bank to the underlying glycol mats (q_m; J/m^2/s), from the frozen bank to the glycol mats where the bank is frozen to the flume wall (q_b; J/m^2/s), and conducted from the eroding bank (q_c; J/m^2/s) (Figure 3.8a). The conduction model solves the 2-D heat equation,

$$\rho_b c_{p,b} \frac{\partial T}{\partial t} - \nabla \cdot (\kappa_b \nabla T) = 0, \tag{3.16}$$

using Matlab's thermal PDE toolbox. The boundary conditions for temperature were set by the temperature sensor data (placed as the vertices of the control volume in the model domain) and the edges of the model domain were imposed using linear interpolation of temperature between the sensors (Figure 3.8a). We used measurements of f_{ice} to calculate $c_{p,b}$ (equation (3.8)). For saturated sediments, heat conduction occurs in parallel through sand and ice, producing a power-law relation for thermal conductivity of the frozen bank (κ_b; W/m/°C) (Farouki, 1981):

$$\kappa_b = \kappa_{ice}^{\lambda_p} \kappa_{sed}^{1-\lambda_p} \tag{3.17}$$

with the thermal conductivity of sediment of $\kappa_{sed} = 3.00$ W/m/°C (Powell et al., 1966), the thermal conductivity of ice of $\kappa_{ice} = 2.14$ W/m/°C (Bonales et al., 2017), and the bank volume fraction ice (λ_p; dimensionless). Bank volumetric porosity for saturated sediment is solved as:

$$\lambda_p = f_{ice} \rho_b / \rho_{ice}. \tag{3.18}$$

We compared modeled conductive heat fluxes to the heat flux required to thaw the eroded bank material,

$$q_f = E L_f \rho_b, \tag{3.19}$$

which provides a minimum bound on the heat flux from the flowing water to the bank, q_w, since $q_w = q_f + q_r$ and q_r equals the sum of q_c and the heat required to warm the bank material between the eroding bank and the heat conduction model domain (Figure 3.8a). This comparison showed that q_f was greater than q_a, q_c, q_b, and q_m by at least two orders of magnitude (Figure 3.8b; Figure 3.S9), validating the assumption in equation (3.10) that the heat balance is dominated by heat flux from the river water to the bank.

We also used the temperature sensors in the bank material to validate the ablation-limited bank erosion model assumptions that the temperature profile maintains a similar curvature over a conduction lengthscale δ and translates in the y-dimension in concert with the eroding bank. The temperature data for Experiment 1 (Figure 3.8c) shows that δ is approximately 0.1 m, and temperature ranges from a value near zero at the bank to a background value of T_0. The temperature gradient remains approximately constant in time, especially during stage 1 ($0 < t < 40:06$ for Experiment 1). Throughout the experiment, T_0 slightly increased due to warming of the bank material by the air, which accounts for deviation of the temperature profile from a purely 1D Stefan solution. However, as constrained above, the heat flux from the air was negligible compared to the heat flux from the water to the bank (Figure 3.5b). Thus, we conclude that the experimental setup achieved a heat balance that was sufficiently

1-D and that the temperature profile translated in step with the eroding bank, such that the experiments should provide a robust test of equation (3.10).
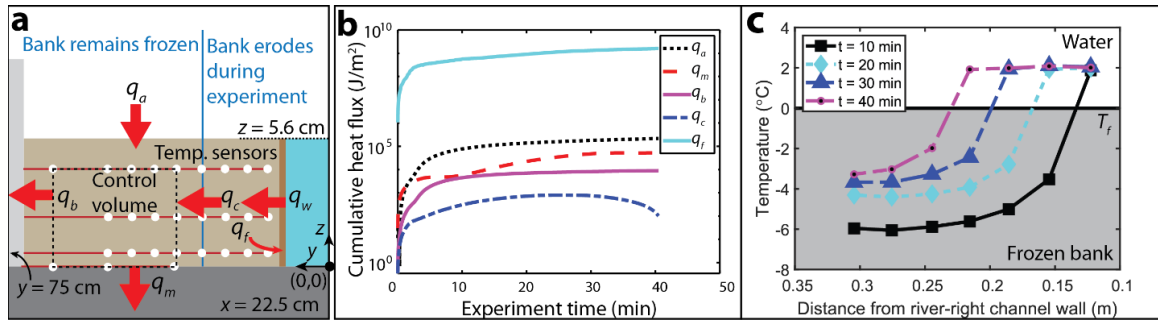
Figure 3.8. Cumulative heat fluxes in frozen region of the bank during Experiment 1. **(a)** Cartoon looking downstream of the heat conduction model control volume labeled with temperature sensors, y and z axes, and heat fluxes. Flux q_w is the heat flux to the bank, q_f is the heat of fusion required to thaw the bank at the observed erosion rates, q_a is the flux from the air to the top of the bank, q_c is the flux conducted past the thaw front and into the fixed control volume, q_b is the heat conducted to the mats on the side of the flume, and q_m is the flux conducted down into the gravel underlying the frozen bank. **(b)** The relative magnitude of cumulative heat fluxes throughout Experiment 1. **(c)** The bank temperature at 10, 20, 30, and 40 minutes into Experiment 1 for the line of sensors at $x = 22.5$ cm, $z \sim 3$ cm.

3.6.3 Bank erosion rates and comparison to theory

We compared our experimental measurements during stage 1 of the experiments to ablation-limited theory (equation (3.10)) using four different methods to calculate the coefficient of heat transfer (C_h): empirical fits from Costard et al. (2003) (equation (3.11)), the formulation of Yaglom & Kader (1974; equation 3.12) using k_s and C_f calculated for the total bank friction, bank grain drag, and bank morphologic drag from scallops (see Section 3.5). Experimental measurements agree well with the ablation-limited erosion model (equation (3.10)) of permafrost riverbank erosion with C_h evaluated for rough banks using grain drag roughness (Figure 3.9a). Heat transfer coefficients calculated using scallop morphologic drag predicted ablation rates significantly higher than observed erosion rates (Figure 3.9b). Heat transfer coefficients including both bank form and grain drag produced erosion rates approximately threefold greater than those observed (Figure 3.9c). Measured erosion rates were significantly higher than those predicted using C_h from equation (3.11) based on the closed pipe experiments (Costard et al., 2003; Lunardini, 1986) (Figure 3.9d). In addition, the Yaglom & Kader (1974) heat transfer coefficient better captures the range of erosion rates seen in experiments, with 1SD of modeled erosion rates scaling well with the variation observed in measured erosion rates. This implies that grain roughness significantly disrupts the diffusive sublayer and allows more rapid heat transfer to the frozen bank.
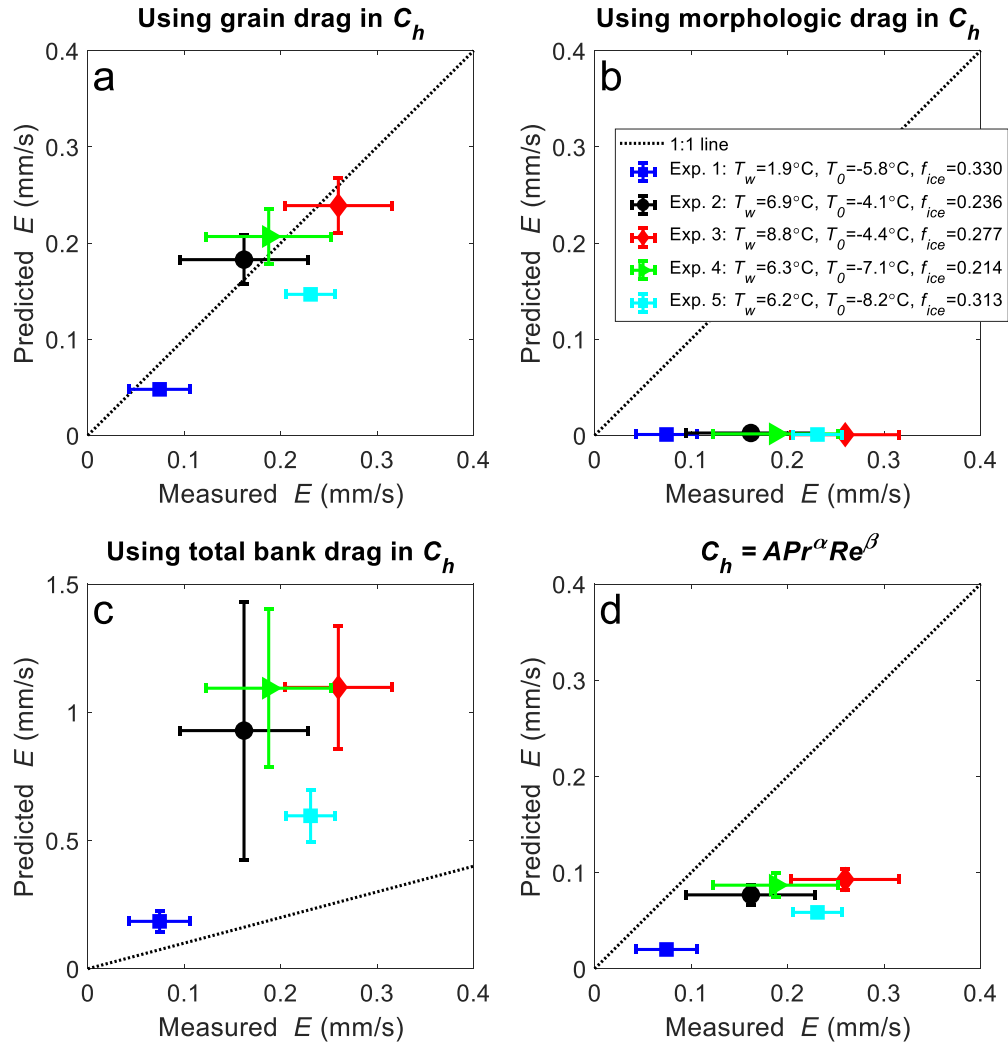
Figure 3.9. Comparison of experiments with modeled ablation-limited bank erosion rates calculated using heat transfer coefficients from **(a)** equation (3.12) evaluated for bank grain roughness, **(b)** equation (3.12) evaluated for bank morphologic roughness, **(c)** backwater modeling of total channel friction to evaluate total sand bank drag, and **(d)** equation (3.11) using $A = 0.0078$, $\alpha = 0.3333$, and $\beta = 0.9270$. Error bars contain 1 SD of variability in measured and modeled erosion rates throughout each experiment.

3.6.4 Effect of water temperature, bank temperature, and pore ice content

Our results suggest that evaluating bank erosion rates using equation (3.10) with a heat transfer coefficient calculated using the grain roughness lengthscale in equation (3.12) best matches our experimental results (Figure 3.9a). Erosion rates calculated using bank morphologic drag predicted unrealistically large roughness lengthscales, leading to poor

prediction of experimental results, while rate calculated using the total bank drag significantly over-predicted experimental results (Figure 3.9b-c). Rates calculated using a heat transfer coefficient from equation (3.11) matched results well (Figure 3.9d). Therefore, we compare the grain roughness bank erosion model to our data to isolate results on the effects of water temperature, bank temperature, and pore ice content.

Experiments 1-3 were designed to vary water temperature with all other parameters held approximately constant. To account for slight differences in conditions aside from water temperature both between experiments and during the course of each experiment, we ran the erosion model for the measured thermal and hydraulic conditions as a function of time for each experiment. The shaded region represents the mean $\pm$ 1 SD for model results accounting for observed variations in all parameter except water temperature. Water temperature was a significant control on bank erosion rates, with warmer temperatures causing more rapid erosion (Figure 3.10a). Our observed erosion rates agree with calculated erosion rates (equation (3.10)) within 1 SD when temporal variability in thermal and hydraulic conditions is accounted for. Results support that erosion rates scale linearly with the water temperature.
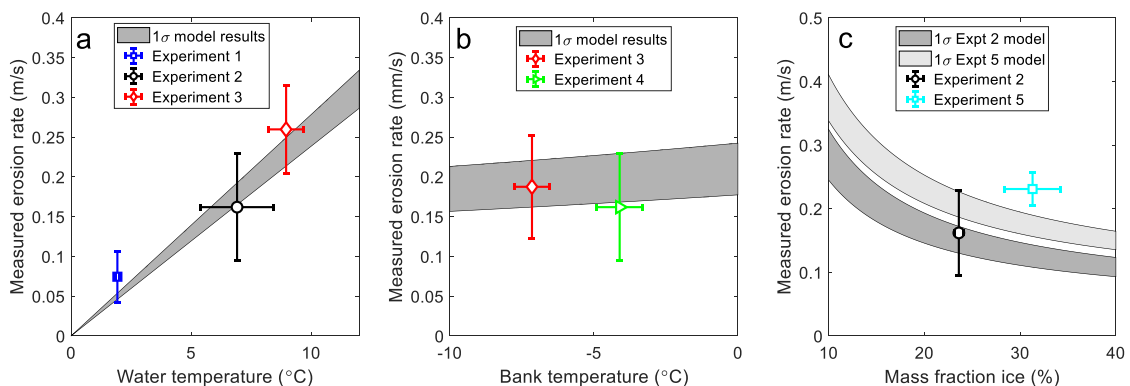
Figure 3.10. (a) Measured erosion rates versus water temperature for Experiments 1-3. The grey-shaded region encloses 1 SD of the Yaglom & Kader (1974) erosion rate model results calculated using grain drag for all 3 experiments, including variability in all parameters except water temperature. **(b)** Measured erosion rates versus bank ice content for Experiments 3 and 4, with the grey-shaded region enclosing 1 SD variability in the Yaglom & Kader (1974) grain drag erosion rate model results. **(c)** Measured erosion rates versus bank ice content for Experiments 2 and 5. The grey-shaded region encloses 1 SD of parameter variability for the Yaglom & Kader (1974) bank erosion model, with results calculated using grain drag, for each experiment.

Experiments 3 and 4 were designed to vary bank temperature with all other parameters held approximately constant (Figure 3.10b). The temperature of the permafrost riverbank did not have a significant effect on measured erosion rates, despite varying nearly twofold (from -7 to -4.1°C) between Experiments 3 and 4. This spanned the range of most natural permafrost terrain (Biskaborn et al., 2019), suggesting a negligible role in warming the bank material, compared to melting pore ice, in ablation-limited bank erosion. These results also support

that q_a and q_m (equation (3.1)) can be neglected when comparing theory and our experiments (Figure 3.8).

Experiments 2 and 5 were designed to vary mass ice fraction with all other parameters held approximately constant (Figure 3.10c). Bank ice content ranged from 20.7 to 33.0 wt% (Table 3.2), and the difference in erosion rates between Experiments 2 and 5 can be explained by their difference in the mass fraction of ice. Slight differences in thermal and hydraulic conditions cause Experiment 5 to have a higher modeled bank erosion rates than modeled erosion rates for Experiment 2 for the same ice content. Therefore, Experiment 5 has slightly higher erosion rates than Experiment 2, despite its bank containing 10 wt% less ice than the bank in Experiment 2. Both experiments agree with ablation-limited bank erosion theory, which indicates that higher ice content produces lower erosion rates with all else being equal.

3.7 Discussion

Our results indicate that the main driver of ablation-limited bank erosion in our experiments was water temperature, which may drive increases in bank erosion rates as the Arctic warms. Previous experiments (Costard et al., 2003) and theoretical predictions (Randriamazaoro et al., 2007; Yaglom & Kader, 1974) found that frozen bank erosion rates increased linearly with water temperature, in agreement with our results. Arctic river water temperatures are primarily set by an initial temperature near 0°C for snow- and ice-melt, and river waters are subsequently warmed by heat transfer from the air (Blaen et al., 2013; Yang & Peterson, 2017; Zhilyaev & Fofonova, 2016). Arctic air temperatures are warming rapidly due to polar amplification (England et al., 2021), and corresponding increases in water temperature have been observed in many permafrost rivers (Docherty et al., 2019; Liu et al., 2005). Therefore, erosion rates, where set by pore-ice melting, should increase proportionally to air temperature as the Arctic warms.

The bank erosion model, heat conduction model, and experiments are in agreement that ablation-limited permafrost riverbank erosion is dominated by phase change from ice to water in the heat budget rather than heating the bank material. Our results support the previous findings of Costard et al. (2003), who observed little change in erosion rates for experiments conducted over a 10°C difference in bank temperature because the latent heat of fusion is orders of magnitude greater than the heat capacity of permafrost (Figure 3.11). Additional work demonstrated that ablation-rates decrease with bank ice content (Dupeyrat et al., 2011), though the authors found an inflection point at low ice contents and Reynolds numbers beyond which flow was not strong enough to transport all of the sediment downstream and ablation rates declined. However, our experiments and prior work did not address conditions when sediment is under-saturated (air is present in pore space), and it remains poorly understood whether these conditions can be modeled with existing theory.

To test the ablation-limited bank erosion theory, we took care to model thermal diffusion through the frozen bank and ensure that heat transfer was 1-D (Figure 3.7). We constructed a wide floodplain so that the temperature gradient in the floodplain material could fully develop and translate with the eroding bank. We found that heat was transferred from the

bank to the frozen ground across a lengthscale $\delta = 10$ cm. If this holds for field cases with banks comprising similarly well-sorted sand with pore ice, it implies that heat transfer is primarily in 1-D for natural riverbanks, unless the bank geometry is highly 3-D at the decimeter scale. In addition, we found that the heat flux from warm air on top of the bank was measurable but small during our experiments (Figure 3.7b). Most Arctic rivers are much deeper than our experiments (meter versus cm-scale channel depths) which indicates that top-down seasonal thaw by warm air should not significantly alter permafrost bank erosion rates. Instead, we hypothesize that thaw by warm air may actually slow riverbank erosion at low water levels by thawing upper layers of the banks and causing slump block failure that subsequently insulates the submerged portion of the riverbank. Thus, while we expect heat transfer within frozen riverbanks is dominantly 1-D in our experiments and in nature, higher-dimensional bank geometry and erosional events may also influence the bank thermal profile.

One unexpected result from our experiments was the development of scallops on the frozen bank. The scallops appear strikingly similar to ripples and scallops developed by water flowing past pure ice, which have been produced in the lab (Bushuk et al., 2019; Camporeale & Ridolfi, 2012) as well as observed migrating along the underside of river ice cover (Ashton & Kennedy, 1972). While we did not observe the scallops migrating, they are known to grow and migrate in response to spatial patterns in flow turbulence (Bushuk et al., 2019), and they deserve further investigation on permafrost riverbanks in nature and in experiments.
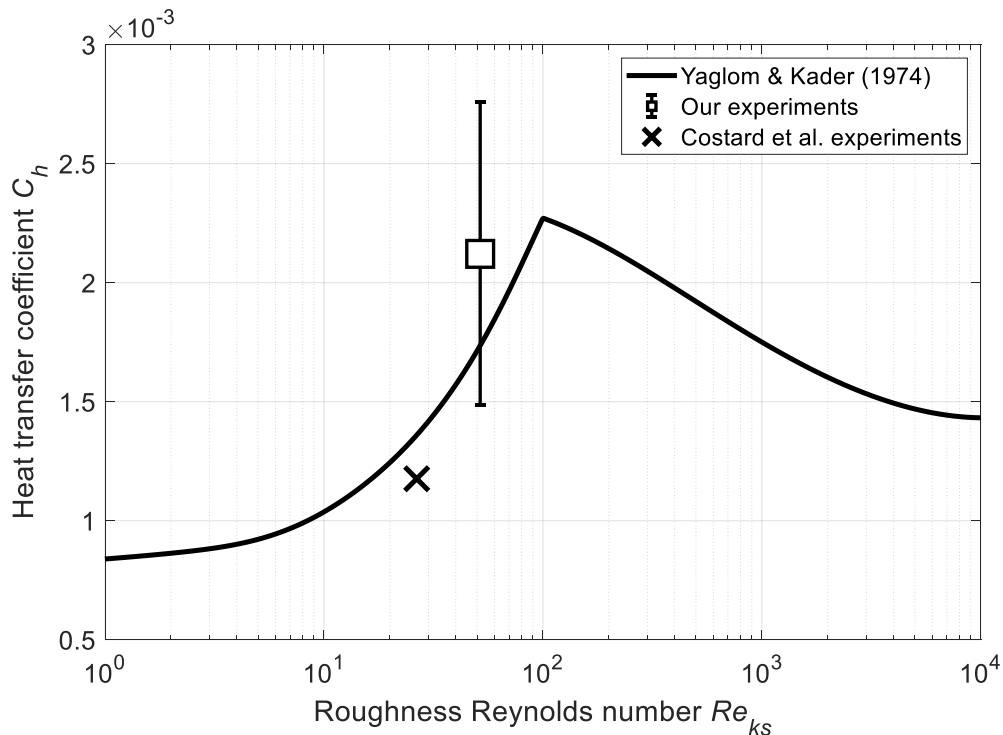
Figure 3.11. Heat transfer coefficient for fully turbulent flow (equation (3.12)), calculated for a range of k_s and u^* using empiricisms from Afzal et al. (2013) and Yaglom & Kader (1974). The mean and 1SD error bars for C_h back-calculated from Experiments 1-5 are

plotted as a black square. For comparison, a representative value for the Costard et al. (2003) experiments are shown with Re_{ks} values for the sand used during the experiment ($k_s = 3.5(2.2D_{50})$, $H = 0.1$ m, Re $= 1.5\times10^4$) as a black 'x'.

Our results demonstrate that accurately accounting for bank roughness is important for predicting ablation-limited erosion of permafrost riverbanks. Using equations (3.12) and (3.15), with all other variables kept constant, heat flux should increase with roughness in the hydrodynamically smooth flow regime and decrease in the hydrodynamically rough flow regime, with a peak value near the transition (Figure 3.11). Our experiments had roughness Reynolds numbers that place them very close to the theoretical peak in C_h. The rate of heat transfer in our experiments was higher by a factor of three than indicated by previous experiments (Costard et al., 2003; Randrimazaoro et al., 2007), primarily due to the development of a turbulent sublayer between the rough bank and the flow. Our model also matches previous results from Costard et al. (2003) when we calculate the rate of heat transfer to the block using reported values of flow Reynolds number, sediment D_{50}, and pipe dimensions. Their experiments had a lower roughness Reynolds number than ours, which we do not expect is representative of natural rivers with hydraulically rough banks. As a result, their experiments found slower ablation rates than ours because of their experimental setup, but these results are still consistent with our model for ablation as a function of grain-scale roughness.

Our results indicate that heat transfer in fully developed boundary layers depends on sediment grain-scale bank roughness because sediment grains disrupt the boundary layer in which heat conduction is dominated by molecular diffusion and receive more efficient heat transfer through advection in the turbulent flow (Figure 3.2b) (Yaglom & Kader, 1974). Larger grains or slumps cause a decrease in rates of heat transfer because they cause flow separation, and heat transfer is relatively inefficient in these turbulent wakes (Yaglom & Kader, 1974). Natural rivers contain a range of roughness scales, and larger scales of roughness disproportionately affect channel hydrodynamics. A substantial proportion of shear stress in natural rivers and flume experiments can be taken up by morphologic drag from the largest roughness elements, leaving only a minority able to directly entrain and erode sediment as grain drag (Darby et al., 2010; Kean & Smith, 2006a, 2006b). Likewise, our experiments developed scallops at the scale of the channel depth, and we calculated the morphologic drag from these scallops using a backwater equation fit with stress partitioning. Our experiments were not designed to measure scallop geometry or their effect on the near-bank flowfield and boundary layer, though scallops likely significantly alter the structure of the hydraulic and thermal boundary layers (Figure 3.2b), particularly because their sharp peaks are likely to cause flow separation. Our results indicate that the coefficient of heat transfer in our experiments is likely set by small-scale turbulence and is not significantly impacted by autogenic scallops (Figure 3.9). This makes sense since we did not observe the scallop geometry changing rapidly throughout the experiments, which would be expected if portions of the scallops thawed more rapidly than others. In natural rivers, cohesive slump blocks and vegetation may provide a similar source of morphologic drag, since they are of similar order to channel depth, and could affect heat transfer indirectly by slowing near-bank

flow velocities. Therefore, while our experimental erosion rates agreed with ablation-limited model calculations using the average channel flow velocity in equation (3.10), using a near-bank flow velocity to calculate grain drag would better account for the multiple scales of roughness present on natural riverbanks.

Both this work and previous experiments on ablation-limited erosion generated rates much higher than field measurements of permafrost riverbank erosion averaged over many years (Rowland et al., 2019). Some of the highest reported permafrost riverbank erosion rates are along the Lena River (Costard et al., 2014): 2 to 40 m/year occurring over a period of 6 to 39 days during ice break-up. Our slowest-eroding experiment (Experiment 1) produced erosion rates of 0.1 mm/s, or 52 m over a 6-day period and 340 m over a 39-day period. For a 4-month long open water season between ice break-up and freeze-up, continuous ablation-limited erosion would produce over 1 km of bank erosion, two orders of magnitude greater than the highest observed rates. We hypothesize that a process, different from pore-ice ablation, must limit bank erosion large parts of the year. Such a limitation could come from sediment entrainment (Roux et al., 2017; Scott, 1978; Shur et al., 2021), the collapse of cohesive slump blocks (Barnhart et al., 2014; Parker et al., 2011), or root reinforcement of bank sediments (Ielpi et al., 2023). Our evaluation of the ablation-limited end member provides a foundation to start to disentangle the role of other erosion processes and develop a more complete model for long-term erosion rates in permafrost rivers.

3.8 Conclusions

Arctic rivers are experiencing increases in water temperature due to climate change that have the potential to thaw permafrost banks. In this study, we evaluated theory for ablation-limited riverbank erosion using flume experiments in which a frozen sand and ice mixture was exposed to erosion by a fully turbulent, open-channel flow for a range of water temperatures, bank temperatures, and bank ice content. Erosion rates were most sensitive to water temperatures showing a linear increase; they also increased with lower volumetric ice content, and were relatively insensitive to bank temperature. Permafrost thaw is dictated in part by a heat transfer coefficient that describes the efficiency of heat transfer from the turbulent river to the bank. Using stress partitioning, we considered the effect of different scales of roughness of the eroding bank on heat transfer, and found that a parameterization based on grain roughness best matched experimental results. Using the revised heat transfer coefficient, the experimental erosion rates were well-described by 1-D ablation-limited bank erosion theory. Thus, results support that where permafrost bank erosion is ablation-limited, erosion rates should increase with increasing river water temperatures, threatening Arctic communities and infrastructure. However, ablation-limited theory predicts unrealistically high erosion rates when compared to seasonal averages, highlighting that additional processes beyond pore-ice thaw need to be incorporated to accurately model bank erosion rates in permafrost.

3.9 Acknowledgments

3.10 Open Research Statement

Original photographs, laser topography scans, sonar measurements, discharge measurements, bank weight fraction water, grain size measurements, temperature sensor data, and instrument calibrations are available for download at https://data.ess-dive.lbl.gov/datasets/doi:10.15485/1972218.

3.11 Supporting information

Supporting information includes videos of timelapse images of the frozen flume experiments (Movies 3.S1-3.S5) and the red bank RGB threshold used to process each image (Table 3.S1). Section 3.11.1 and Figure 3.S1 describe the sand and gravel grain size distributions and measurement methods. Sections 3.11.2 and 3.12.3 and Figures 3.S2 to 3.S3 detail methods for determining the gravel bed and sand bank coefficients of friction. Figures 3.S4 to 3.S8 display summaries of measurements from Experiments 2 through 5 versus time (similar to Figure 3.6 in the main text). Figure 3.S9 compares heat fluxes to evaluate the 1-D thermal conduction model for each experiment (similar to Figure 3.8b in main text).

Movie 3.S1-3.S5. Timelapse imagery was taken at 10-sec intervals from an overhead camera for running frozen flume experiments will be made available for download with the published manuscript.

Table 3.S1. Red image threshold values for the eroding bank top for each experiment.

Experiment	Bank top threshold (blue band)
Experiment 1	140
Experiment 2	110
Experiment 3	140
Experiment 4	100
Experiment 5	150

3.11.1 Grain size measurements of gravel bed and sand bank

We measured the grain size of the gravel bed using a Wolman pebble count (n = 100) of grain intermediate b-axes to a precision of 1 mm. We measured the grain size of the eroding sand bank using the Camsizer P4 with the X-Fall attachment for dry sediment ($n > 10^6$) and calculated the median grain size by linear interpolation in semilog space.
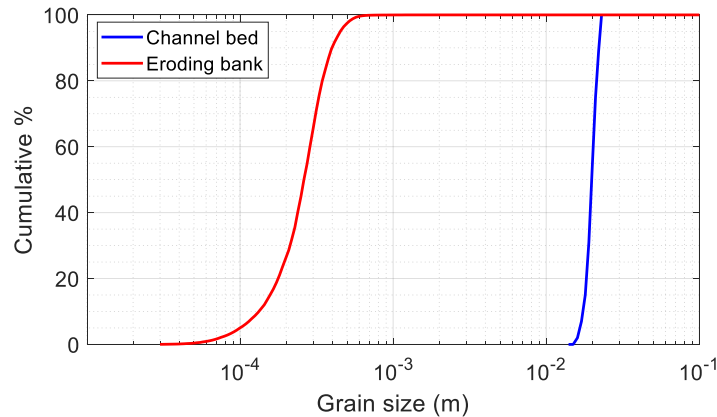
Figure 3.S1. Cumulative distribution function of b-axis grain size for the sandy eroding bank and gravel channel bed.

3.11.2 Coefficient of friction of immobile gravel

To accurately partition fluid stress between the flume wall, eroding bank, and immobile gravel bed we conducted a series of unfrozen, fixed-bank experiments to determine the coefficient of friction for the gravel. We fit the backwater equation to account for spatial accelerations in an immobile channel, varying flow depth, velocity, and discharge while holding all other variables constant (Section 3.11.2.1). Fitting measurements of the water surface slope in the test section with a backwater equation, we calculated the channel total coefficient of friction (Section 3.11.2.2) and partitioned stress between the smooth flume wall and gravel bed and banks (Section 3.11.2.3). We then compared these results to the Ferguson (2007) VPE and determined a best-fit coefficient of friction for the coarse, immobile gravel (Section 3.11.2.4).

3.11.2.1 Gravel fixed-bank experiments

We conducted unfrozen, fixed-bank experiments using the same coarse gravel that made up the channel bed in frozen experiments to determine its coefficient of friction for grain drag. The experiments were run without freezing the bed or banks so that we could run them for long periods without changing thermal or hydraulic conditions. The gravel bed and bank were graded to a slope of 0.01288, measured using a 1 mm-resolution Keyence scan down the center of the channel. No sediment feed was used during these experiments. We ran experiments for water discharges of 0.0070 and 0.0079 m^3/s. Discharge was measured using the same relation for pump variable frequency drive versus discharge described in Section 3.5.2. The fixed bank experiments were run for up to 45 min at each discharge condition to ensure that the entire basin had reached a constant water surface slope in time, verified by three 1 mm-resolution Massa measurements of water surface slope taken 5 min apart. After the experiments, we measured a 4x10 mm scan of the gravel bed and bank using a Keyence laser scanner.

We calculated the maximum water flow depth by subtracting the channel bed elevation from the water surface elevation. Flow maximum depths and slopes increased with increasing

discharge, motivating the application of a backwater equation (Section 3.11.2.3) since the flow was steady but spatially non-uniform. Since the gravel was not frozen, the bank was slightly below the gravel angle of repose and the channel cross-section was not rectangular. The channel depth (H; m), top-width (B; m), and cross-sectional area (A_{xs}; m^2) were calculated using Massa data during each experiment and from a 4x10 mm Keyence scan taken after the experiment. The flow top-width (B), cross-sectional area (A_{xs}), and gravel wetted perimeter (P_w; m) were calculated at each location along the channel by finding the intersection of the water surface and gravel bank elevations using the 2D Keyence scan. The average flow depth (H_{avg}; m) was calculated as $H_{avg} = A_{xs}/B$ and was typically ~1 cm less than the maximum depth (H).

3.11.2.2 Backwater equation fitting to find total friction coefficient

To calculate the total coefficient of friction for the immobile channel, we iteratively fit a backwater equation over the test section ($x = 0 - 70$ cm) to account for spatial acceleration (Figure 3.S1). We used the following backwater formulation for gradual changes in flow depth:

$$\frac{dH}{dx} = \frac{S_{bed} - C_{f,tot}Fr^2 + Fr^2 \frac{H_{avg}}{B}\frac{dB}{dx}}{(1 - Fr^2)} \tag{3.S1}$$

where S_{bed} (m/m) was the channel bed slope, and H_{avg} (m) and B (m) were the top-width and average flow depth at each location. The Froude number at each location was calculated as:

$$Fr^2 = \frac{Q_w^2}{B^2 gH_{avg}^3}\frac{B}{B_{avg}}, \tag{3.S2}$$

where B_{avg} was the mean channel top-width along the test section. Solving equation (3.S2) required the test section outlet flow depth, channel bed elevation, water discharge, channel width, and the total coefficient of friction ($C_{f,tot}$). The backwater equation was then used to calculate the flow depth for each node moving upstream using an upwinding scheme. We used nodes spaced 1 mm apart to capture the resolution of Massa and Keyence scans. To calculate the best fit for $C_{f,tot}$, we input a range of values, ran the backwater fit, and selected the value that most closely matched the measured water surface elevation (based on R^2 values) and remained subcritical ($Fr < 1$) through the test section. Since the backwater equation was very sensitive to changes in the channel geometry, we smoothed the channel bed elevation, width, and flow depth by taking the moving mean over a window $4\times H$ (22.4 cm ~ B).

3.11.2.3 Stress partitioning

We determined the coefficient of friction due to the gravel bed and bank. For the immobile gravel experiments, the momentum balance as a total stress on the channel boundary (τ_{tot}; Pa) was balanced by gravel grain drag on the channel bed and bank (τ_g; Pa) and skin friction on the smooth flume wall (τ_w; Pa) according to the Einstein (1956) stress decomposition.

The total boundary stress can be calculated as:

$$\tau_{tot} = \rho_w C_{f,tot} U^2.$$ (3.S3)

Assuming that the flow velocity in regions influenced by the walls and bed were similar, the stress on the gravel bed and bank can be calculated as:

$$\tau_g = \rho_w C_{f,g} U^2,$$ (3.S4)

and the stress on the flume wall as:

$$\tau_w = \rho_w C_{f,w} U^2.$$ (3.S5)

We assumed that the morphologic drag of the gravel bed and bank were negligible since they were graded to lack large-scale roughness such as grain clusters or barforms. Similarly, the smooth flume wall should not experience morphologic or grain drag.

To partition stress between the smooth flume wall and gravel bed and bank, we used the Vanoni & Brooks (1957) sidewall correction:

$$(H + P_w)C_{f,tot} = HC_{f,w} + P_w C_{f,g},$$ (3.S6)

where P_w (m) is the wetted perimeter of the gravel calculated from the Keyence topographic scan of the immobile channel. The total coefficient of friction ($C_{f,tot}$) was previously solved for in Text S2.2 using an iterative backwater equation fit. The skin friction for the flume wall can be calculated using the Blasius (1913) relation for the Darcy friction factor, where

$$C_{f,w} = 0.03955 Re^{-1/4}$$ (3.S7)

and Re is the Reynolds number of the channel. Here, we calculated $Re = UH_{avg}/v$, where v is the kinematic viscosity of water ($v = 10^{-6}$ m/s). Therefore, we can evaluate $C_{f,w}$ using equation (3.S7), substitute it into equation (3.S6), and re-arrange to solve for the grain drag of the gravel bank and bed:

$$C_{f,g} = \frac{H(C_{f,tot} - C_{f,w}) + P_w C_{f,tot}}{P_w}.$$ (3.S8)

3.11.2.4 Relation for gravel coefficient of friction

We compared the Ferguson (2007) variable-power equation (VPE; their equation (20)) to our data. Ferguson's relation for the coefficient of friction is:

$$C_f = \frac{a_1^2 + a_2^2 (H_{avg}/k_s)^{5/3}}{a_1^2 a_2^2 (H_{avg}/k_s)^2}$$ (3.S9)

and incorporates two dimensionless empirical parameters, a_1 and a_2.

At average flow depths of 4.62 and 4.84 cm, the gravel coefficient of friction matches the VPE well for the author-recommended values of $a_1 = 6.5$ and $a_2 = 2.5$ and with $k_s = 2.5D_{84}$. Since the frozen flume experiments use a higher $H_{mean} \sim 5.6$ cm, the results from the gravel experiments indicate that the VPE can be used to predict channel bed grain drag in frozen flume experiments.
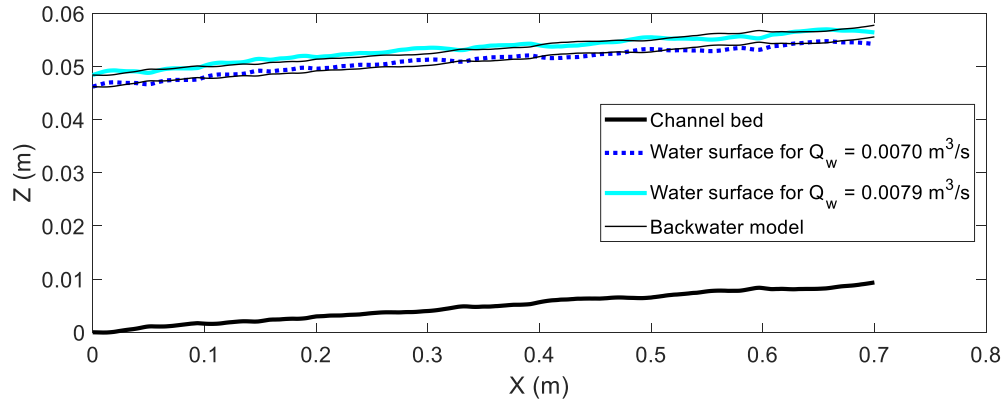
Figure 3.S2. Backwater equation best-fit results from unfrozen, immobile gravel bank experiment used to calibrate the immobile gravel coefficient of friction. Calculated water surface elevations from the backwater equation match measured water surface elevations within the test section well for best-fit $C_{f,tot}$.
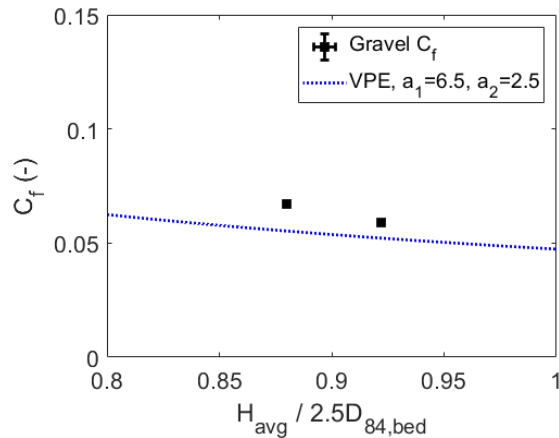
Figure 3.S3. Partitioning total stress between the channel bed, bank, and flume wall allowed us to calculate the $C_{f,g}$ for gravel, which agreed well with the Ferguson (2007) VPE. Error bars are 1SD water depth propagated through the VPE.

3.11.3 Coefficient of friction of the eroding bank

The frozen flume experiments had multiple scales of roughness, including skin friction on the flume wall, grain drag on the gravel channel bed, and grain drag and morphologic form drag on the eroding sand bank. The morphologic form drag arose because the eroding bank developed scallops approximately 5 cm long with ~1-2 cm relief. In this section, we show how we estimated the grain drag and morphologic form drag on the eroding wall.

3.11.3.1. Backwater equation fitting to find total friction coefficient

We ran a backwater equation fit for our frozen flume experiments to calculate the total coefficient of friction of the test section ($x = 0 – 70$ cm). During the frozen experiments, the temporal acceleration terms for shear stress due to channel widening were negligible ($< 1\%$ of total shear stress). However, spatial acceleration of flow was significant, due to variable bank erosion rates along the channel and flow contraction and expansion where the erodible bank met the immobile gravel (Figure 3.3). Therefore, we ran a backwater equation and iteratively solved for the best fit $C_{f,tot}$ to experimental results along our test section.

We used the same backwater equation formulation and iterative solution scheme from the immobile experiments, though we assumed that the channel maintained a rectangular cross-section. We assumed a rectangular channel geometry ($H = H_{avg}$ in equations (3.S1) and (3.S2)) because the initial channel geometry was set up to be rectangular and observed to remain rectangular throughout stage 1 of the experiments, when the best erosion rate data was collected. We were only able to make channel cross-sectional geometry measurements before the start and after the end of the experiments, so we could not accurately measure cross-sectional geometry during stage 1. However, the cross-sectional geometry during stage 2 (when thawed sediment accumulated along the base of the eroding bank) had values of $HB / A_{xs} < 1.15$. Therefore, the maximum uncertainty due to our assumption of a rectangular cross-sectional geometry was 15% of the maximum flow depth.

3.11.3.2 Stress partitioning

We calculated the total coefficient of friction for the eroding bank using the Vanoni & Brooks (1957) sidewall correction scheme. This formulation assumes normal flow conditions and uses the Einstein stress decomposition, with the same assumptions outlined in Section 3.11.2.3. The stress on the flume wall can be calculated using equation (3.S5), the stress on the gravel bed using equation (3.S4), and the stress on the eroding sand bank can be calculated as:

$$\tau_b = \rho_w C_{f,b} U^2. \tag{3.S10}$$

The total boundary friction can be linearly partitioned using coefficients of friction for the gravel bed ($C_{f,g}$; unitless), smooth wall of the flume ($C_{f,w}$; unitless), and eroding bank ($C_{f,b}$; unitless) and assuming a rectangular cross-section:

$$(2H + B)C_{f,tot} = BC_{f,g} + HC_{f,w} + HC_{f,b}. \tag{3.S11}$$

We then re-arranged the equation and substituted values for the gravel bed grain drag (equation (3.S9)) and the wall skin friction (equation (3.S7)) to solve for the total eroding bank coefficient of friction:

$$C_{f,b} = \frac{B(C_{f,tot} - C_{f,g}) + H(2C_{f,tot} - C_{f,w})}{H}. \tag{3.S12}$$

This bank coefficient of friction includes both the grain drag on the sand and the morphologic drag on the scallops. Next, we used the Ferguson (2007) VPE (equation (3.S10)) to solve for the grain drag of the eroding bank ($C_{f,bg}$) and estimate the morphologic drag due to scallops ($C_{f,bm}$) by subtracting $C_{f,bg}$ from $C_{f,b}$. The values of $C_{f,b}$, $C_{f,bg}$, and $C_{f,bm}$ are used to evaluate the coefficient of heat transfer, with results displayed in Figure 3.9 in the main text.

Figure 3.S4-3.S8. Measured and calculated thermal and hydraulic variables over the course of frozen flume Experiments 2 - 5. **(a)** Water temperature was measured with temperature sensors next to the bank test section. **(b)** Water depth (H) and channel width (B) were measured in meters at the central temperature sensor array ($x = 22.5$ cm downstream) using downstream Massa sonar scans. **(c)** Water surface slope (m/m) measured using a linear fit to water surface elevation from $x = 0$-70 cm downstream. **(d)** Discharge (Q_w) past the test section was measured using timelapse imagery at the channel inlet and corrected using the headbox dimensions and mean discharge velocity to the distance along the experimental bank. Line thickness includes 1 SD of uncertainty in the discharge calibration. **(e)** Mean water flow velocity at the central temperature sensor array with 1 SD uncertainty. **(f)** Erosion rates were calculated by differencing the total bank area from 10-sec timelapse images and averaging over a 1-min window.

Experiment 2

Experiment 3

Experiment 4
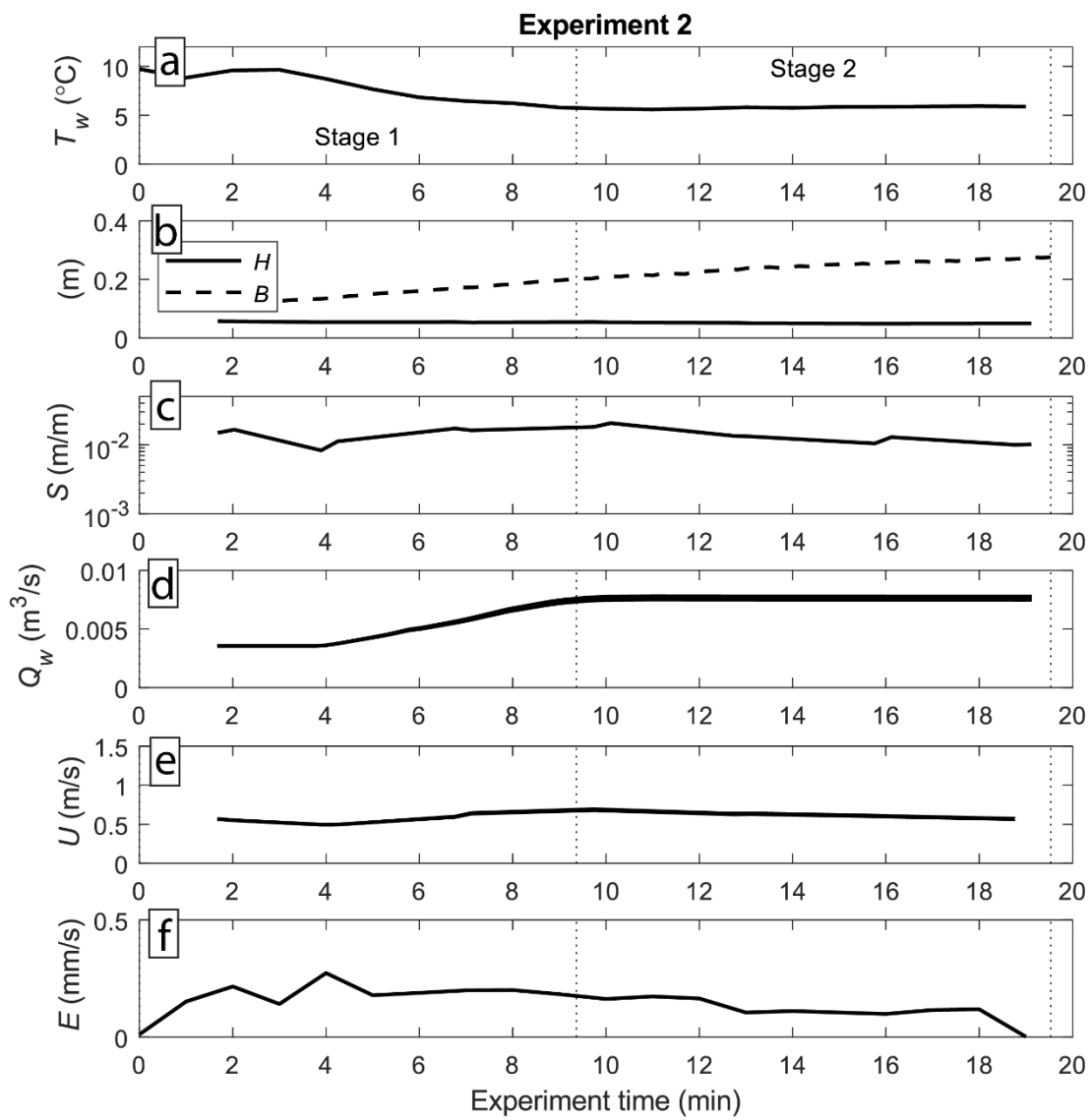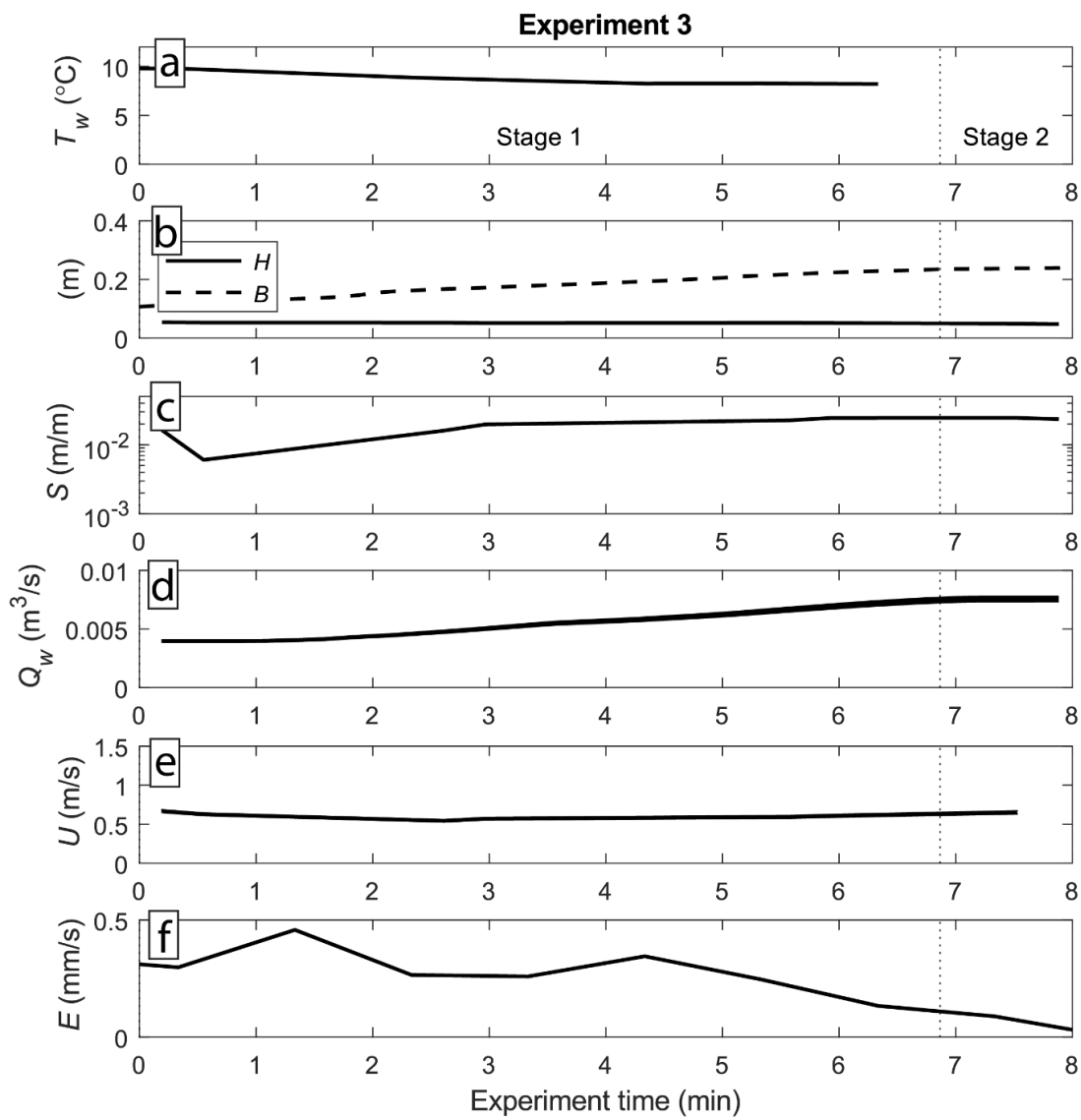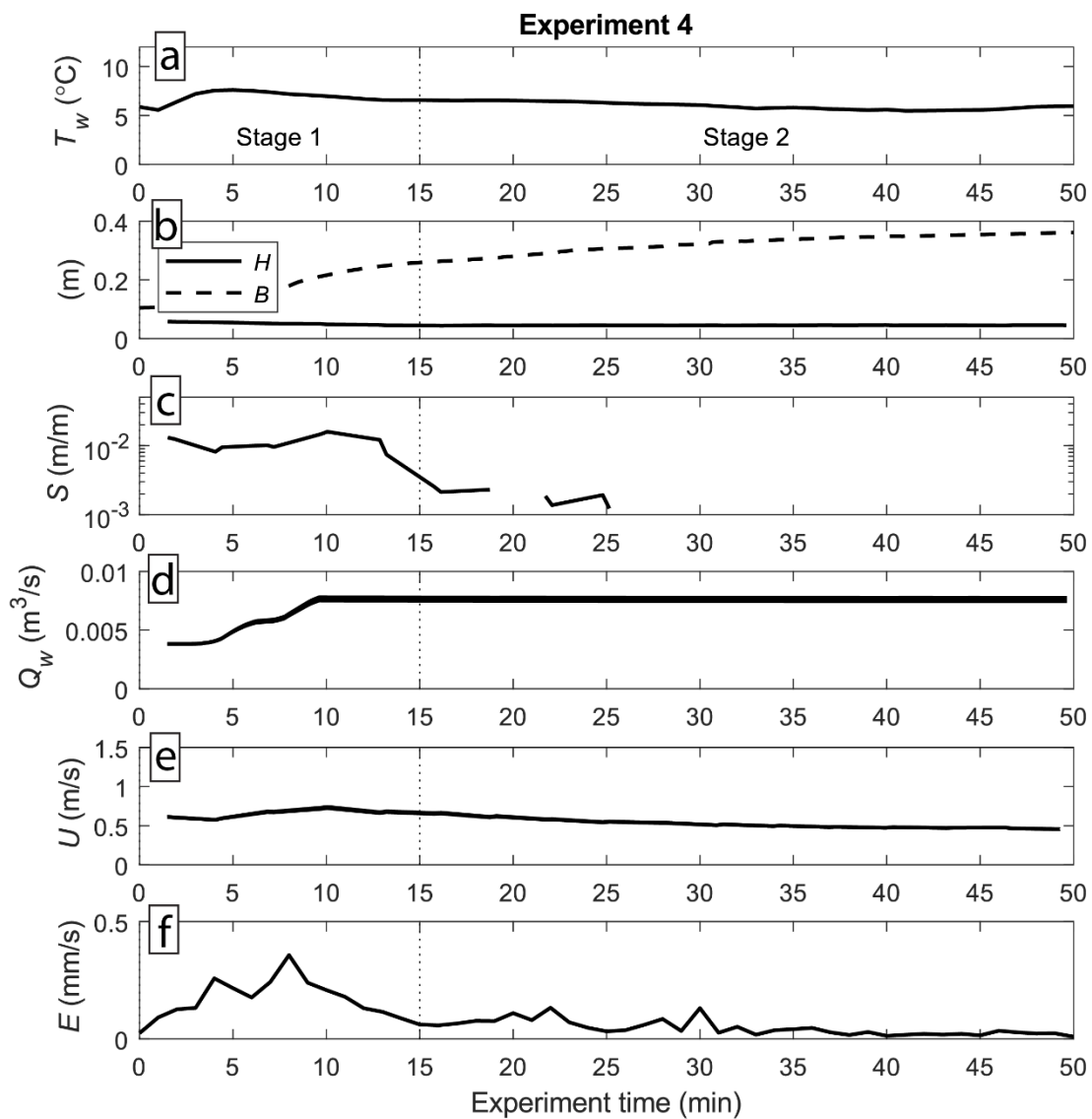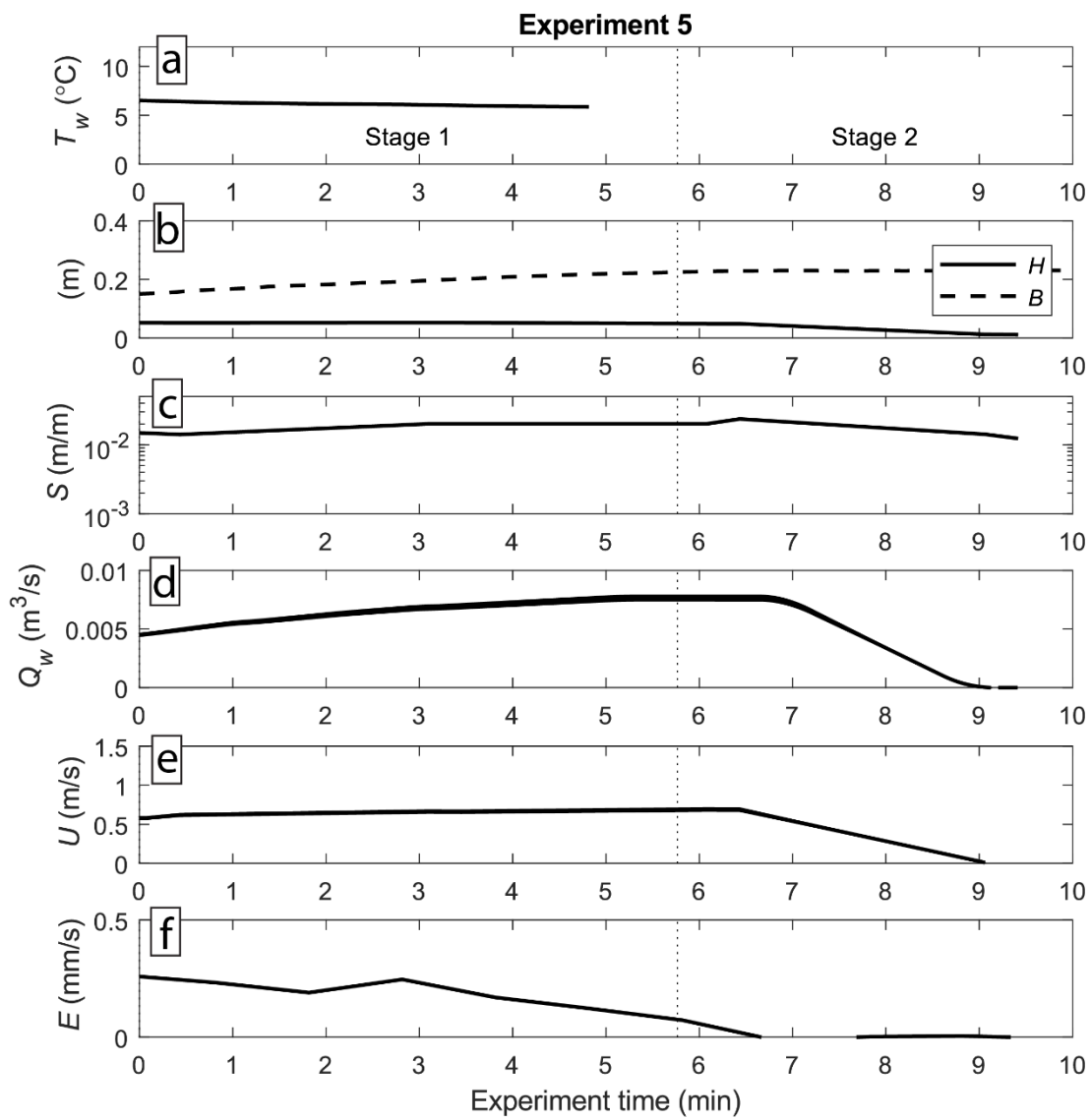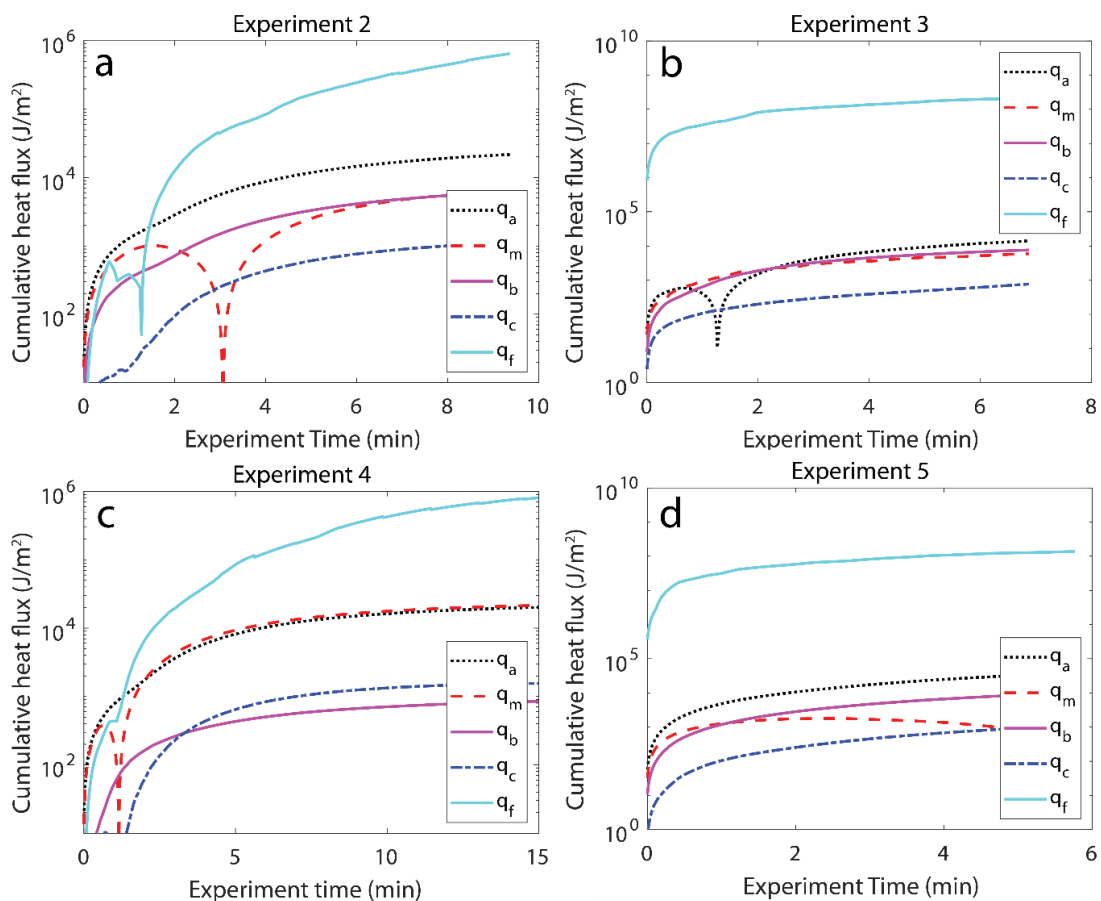
Experiment 5

Figure 3.S9. Cumulative heat fluxes due to air (q_a), latent heat of fusion (q_f), and thermal conduction from the thawing layer (q_r), underlying gravel (q_m), and flume wall (q_b) for the frozen portion of the bank at $x = 22.5$ cm for **(a)** Experiment 2, **(b)** Experiment 3, **(c)** Experiment 4, and **(d)** Experiment 5.

C h a p t e r   4

A MODEL FOR THAW AND EROSION OF
PERMAFROST RIVERBANKS

Madison M. Douglas & Michael P. Lamb

Key Points:

- We develop a 1D permafrost riverbank erosion model that works across the thaw- and entrainment-limited regimes.
- Thawed sediment insulates permafrost and produces a steady state where sediment entrainment and permafrost thaw occur at the same rate.
- Periodic thaw-layer failure produces realistic erosion rates that are sensitive to river water temperature.

4.1 Abstract

Arctic rivers are bounded by permafrost and there is concern that riverbank erosion will increase with warming. Canonical theory assumes erosion is limited by pore-ice thaw but can predict rates much greater than observed. One possible solution is that erosion is slowed by a layer of thawed sediment on the bank surface that buffers heat transfer. We developed a 1D model for this thawed layer, which reveals three regimes for permafrost riverbank erosion. Thaw-limited erosion occurs in the absence of a thawed layer, such that pore-ice melting sets the pace of erosion, consistent with existing theory. In contrast, entrainment-limited erosion occurs when pore-ice melting outpaces bank erosion, resulting in a thawed layer, and entrainment of sediment sets the pace of erosion similar to non-permafrost rivers. A third intermediate regime occurs when the thawed layer goes through cyles of growth and mass wasting, leading to a transient thermal buffer that slows erosion to rates more consistent with observations. Distinguishing between these regimes is important because thaw-limited erosion is highly sensitive to water temperature, whereas entrainment-limited erosion is not. The buffered regime produces a thawed layer like the entrainment regime, but erosion rates remain temperature sensitive. Results suggest the potential for accelerating erosion in a warming Arctic where bank erosion is presently thaw-limited or buffered. Moreover, rivers can experience all regimes annually and transition between regimes with warming, changing their sensitivity to future warming.

4.2 Plain-language summary

Large river systems flow through regions containing permafrost (permanently frozen ground), which stabilizes riverbanks. As the climate warms, Arctic riverbank erosion processes and rates might change, threatening the homes and livelihoods of communities living along permafrost rivers. Previous work determined that permafrost riverbank erosion

can be limited by rates of permafrost thaw or sediment entrainment, whichever process is slower, but did not track heat transfer within the riverbank or the development of a layer of thawed sediment on the bank when erosion was entrainment-limited. To address this knowledge gap, we developed a 1D model for permafrost thaw, thawed sediment entrainment, and heat transfer within the thawed and frozen portions of the riverbank. We found that banks form thin layers of thawed sediment, which insulate permafrost and dramatically slow thaw and erosion rates. For the case where thawed sediment was unstable and fails past a threshold thickness, the thawed layer remained thin and bank erosion was sensitive to water temperature, even for the entrainment-limited erosion regime. Therefore, Arctic rivers may experience higher bank erosion rates as river water warms with climate change, even if most erosion occurs under entrainment-limited conditions.

4.3 Introduction

The Arctic contains major river systems that supply 10% of riverine water to the Earth's oceans (Peterson et al., 2002; Whitefield et al., 2015) and flow through catchments underlain by permafrost (Obu et al., 2019). Permafrost can dramatically strengthen riverbanks, since frozen sand-ice mixtures have tensile strengths of approximately 0.5 – 1 MPa (Akagawa & Nishisato, 2009; Lange & Ahrens, 1983; Litwin et al., 2012), similar to sandstone bedrock (Sklar & Dietrich, 2001). This has led to the idea that thawing pore ice is the rate-limiting step in permafrost riverbank erosion (Costard et al., 2003; Randriamazaoro et al., 2007). If Arctic riverbank erosion is thaw-limited, it has broad implications as the climate warms because bank erosion rates are predicted to be highly temperature sensitive. This can induce a climate feedback since bank erosion can liberate permafrost carbon (Douglas et al., 2022; Kanevskiy et al., 2016; Turetsky et al., 2020). In addition, bank erosion threatens communities and infrastructure in the Arctic (Hjort et al., 2018; Karjalainen et al., 2019; UAF & USACE, 2019), and disproportionately affects the livelihoods of Indigenous communities (Bronen, 2013; Cozzetto et al., 2014).

Thaw-limited bank erosion models make a critical assumption: that the stress exerted on the riverbank is sufficient to pick up sediment as soon as its pore ice has thawed, therefore continually and directly exposing the pore-ice front to warm river water (Costard et al., 2003; Randriamazaoro et al., 2007). Under these conditions, the rate of bank erosion depends on the heat flux from the river water to the frozen bank, with warmer water and higher flow velocities causing more efficient heat transfer into the bank. Bank erosion rates also depend on the heat required to warm and thaw pore ice, which is primarily a function of the volume of pore ice present in the bank (Dupeyrat et al., 2011). However, applying numerical models of thaw-limited conditions over an annual hydrograph generate erosion rates on the order of km/yr, much higher than observed rates of up to tens of m/yr (Rowland et al., 2019). Additionally, Arctic river migration rates may be declining, in direct opposition to predictions from thaw-limited erosion models (Ielpi et al., 2023). Therefore, another process beyond pore-ice thaw must limit riverbank erosion rates in permafrost regions.

One possibility is that erosion rates are limited by sediment entrainment, rather than thaw (Douglas et al., 2023). For example, during the summer along the Atigun and Saganovirktok

Rivers on the North Slope of Alaska, a layer of thawed sediment tens of cm thick formed on eroding riverbanks (Scott, 1978). The layer of thawed sediment suggests that bank erosion could have been entrainment-limited; that is, limited by the rate of entrainment of thawed sediment from the bank, rather than by the rate of pore-ice thaw (Douglas et al., 2023). Other studies also documented rivers switching from thaw- to entrainment-limited erosion, such as a bluff along the Itkilik River which eroded very rapidly until it built up a protective apron of sediment (Kanevskiy et al., 2016; Shur et al., 2021). On the beds of permafrost rivers, where sediment entrainment is generally balanced by deposition, a stable thaw layer called a talik forms (Hollingshead et al., 1978; Smith, 1975; Stephani et al., 2020). A similar layer may form along river banks; ground temperature and electrical resistivity surveys on part of the Yukon River indicated that the riverbank is unfrozen year-round (Laxton & Coates, 2010). Conceptual models developed based on these observations include multiple stages of bank thaw, collapse, and sediment entrainment grouped together as thermomechanical erosion (Shur et al., 2021; Tananaev, 2016).

If the rate of thaw outpaces the rate of sediment entrainment, then river banks should develop a layer of thawed sediment between river water and the permafrost that likely influences erosion mechanics. Previous models have tracked the pore-ice front without dynamically tracking the erosion front (Douglas et al., 2023; Ensom et al., 2012; Ohara et al., 2022; Zheng et al., 2019), or assumed that the thawed sediment was rapidly transported away such that a thawed layer did not develop (Costard et al., 2003, 2014; Randriamazaoro et al., 2007). Here, we developed a numerical model to dynamically track thaw of the pore-ice front and sediment entrainment from the riverbank surface to create a dynamic thawed layer. We compared the model to a compilation of observations from Arctic rivers, used the model to investigate the phase space for thaw-limited erosion, entrainment-limited erosion, and explored a new regime in which the thawed layer grows and fails through mass wasting which buffers thaw and erosion rates.

4.4 Conceptual model

Here we explore the idea that the thawed layer plays an important role in modulating bank erosion rates. For example, the thawed layer can create a thermal buffer between permafrost and the flowing water, which can slow thaw rates as this layer thickens. Changes in the thawed layer thickness, in turn, are controlled by the relative rate of thaw compared to sediment entrainment. Arctic rivers commonly have a period of warm, low flows in mid-summer, which may promote development of a thawed layer on the bank (under entrainment-limited conditions) that insulates the deeper pore ice (Figure 4.1). We hypothesize that late season floods then might experience thaw-limited erosion conditions once that thawed layer is fully eroded.
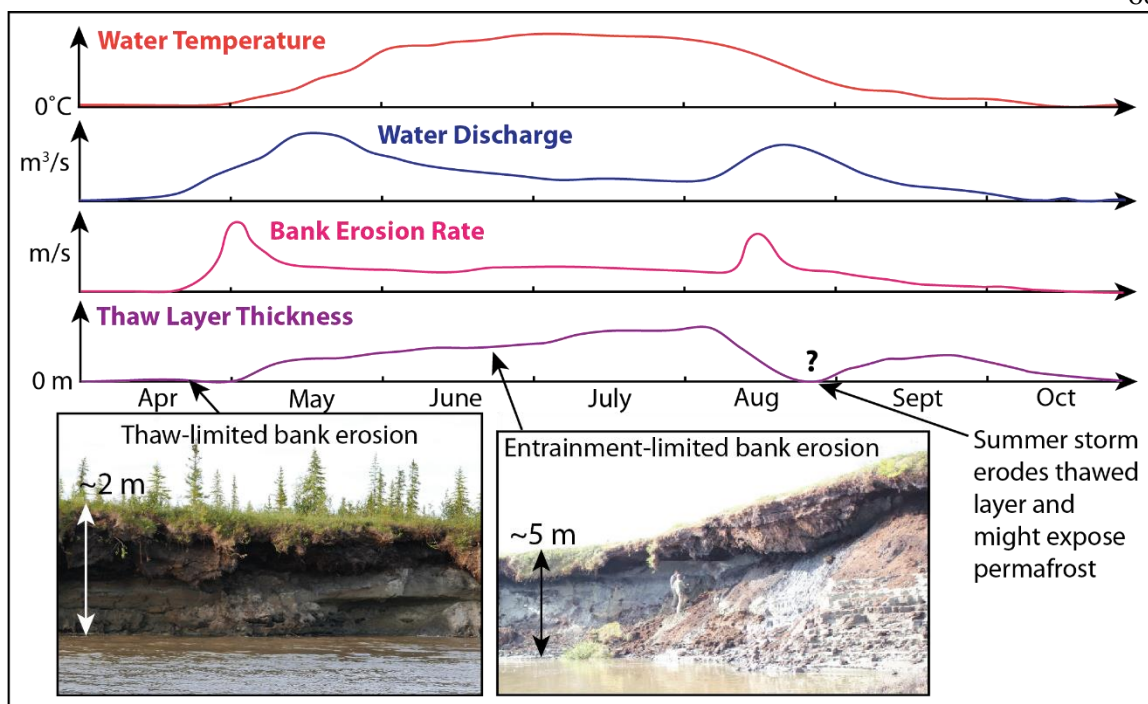
Figure 4.1. Schematics of water temperature (red curve) and discharge (blue curve) characteristic of Arctic rivers and the resulting riverbank erosion rates (pink curve) and thaw layer thickness (purple curve). Annotation of our hypothesized thaw layer thickness plot shows thaw- and entrainment-limited erosion using field photos taken along the Koyukuk River near Huslia, Alaska.

To establish intuition for the formation and thickness of this thawed layer, we report selected field measurements made by the authors along the Koyukuk River near Huslia, AK and by Scott (1978) along the Atigun River, AK (Figure 4.2). Scott (1978) found that noncohesive channel bed and bank material typically formed thawed layers 0-70 cm thick except at at the channel thalweg and apices of thermoerosional niches, where no thawed layer was present (Figure 4.2a-b). In contrast, cohesive bed and bank material formed thawed layers less than 20 cm thick, except in places where erosion was keeping pace with thaw (at the apexes of thermoerosional niches). From May to mid-June, Scott (1978) found that submerged coarser sediment formed a thicker thawed layer than submerged silt, and that banks exposed to air had slightly higher (~20%) thicker thawed layers than submerged channel banks and bed. To assess the change in thawed layer thickness throughout an entire season, we measured the thickness of the thawed layer exposed to air in June and September 2022 near Huslia, AK (see Section 4.12.1). We were unable to measure the submerged thawed layer thickness because the river thalweg is over 10 m deep at the measurement site (Figure 4.2c), but we assumed that the portion of the bank exposed subaerially has a similar thaw layer thickness to the submerged bank, following the results of Scott (1978). Our measurements indicate that the thawed layer has significant variation in its thickness early in the thaw season, then has a uniform thickness of ~ 50 cm in the fall (Figure 4.2d). For comparison, we also plotted the measured thaw depth of the floodplain active layer. At the start of the season the active layer

is much thinner than the thawed layer on the bank, but it reaches a similar median thaw depth by the fall. This indicates that thaw occurs much more quickly laterally on exposed banks in the spring than vertically, likely due to a lack of insulating vegetation on the exposed bank face. During summer, the bank thawed layer does not significantly change its thickness but converges to a value similar to that of the floodplain (Figure 4.2d).

Based on these field observations, we propose that erosion rates maybe dictated by different processes depending on the existence and dynamics of the thawed layer (Figure 4.1). When the sediment entrainment rate (E_{ent}; m/s) is persistently higher than the pore ice thaw rate (E_{thaw}; m/s), sediment should be swept from the riverbank as soon as it thaws, and a thawed layer should not form. This case has been treated extensively in previous theory, models and physical experiments (Costard et al., 2003; Dupeyrat et al., 2011; Randriamazaoro et al., 2007). The rate of thaw-limited erosion is governed by rate of heat transfer from the turbulent river to the pore-ice and the heat needed to warm and melt the pore ice (Randriamazaoro et al., 2007), and rates are linearly proportional to water temperature and flow velocity (Costard et al., 2003; Dupeyrat et al., 2011).

In contrast, in cases where a thawed layer develops because the pore-ice thaw rate (E_{thaw}) exceeds the sediment entrainment rate (E_{ent}), bank erosion may be set by the rate of sediment entrainment (Douglas et al., 2023). In the entrainment-limited regime, the rate of change of thaw layer thickness (η; m) is set by the difference between E_{thaw} and E_{ent}. The presence of the thawed layer slows down the rate of thaw because heat transfer through the thawed layer is less efficient than heat transfer from the turbulent river to the bank surface (Roux et al., 2017). Thus, under constant forcing, we expect η can eventually reach a steady thickness, $\eta = \eta_{ss}$, where sediment entrainment and thaw occur at the same rate. Bank erosion rates when entrainment-limited depend on the flow strength relative to the sediment size and cohesion, similar to non-permafrost rivers, and importantly should be insensitive to water temperature. An intermediate regime might occur if the thawed layer erosion occurs by mass failure (Patsinghasanee et al., 2018; Zhao et al., 2021) rather than by grain-by-grain entrainment. In this case, the thaw layer could be in a state of transient growth while $E_{thaw} > E_{ent}$, with mass failure occurring before the layer reaches a steady state thickness. In this regime, the rate of bank erosion is set by the rate at which the thawed layer grows, which increases with the difference between E_{ent} and E_{thaw}. Therefore, this regime might be sensitive to the parameters that affect both pore-ice thaw and sediment entrainement, including water temperatures, despite the presence of a thawed layer. However, thaw rates will be reduced in comparison to the thaw-limited regime because the thawed layer will thermally buffer the permafrost from the river water.
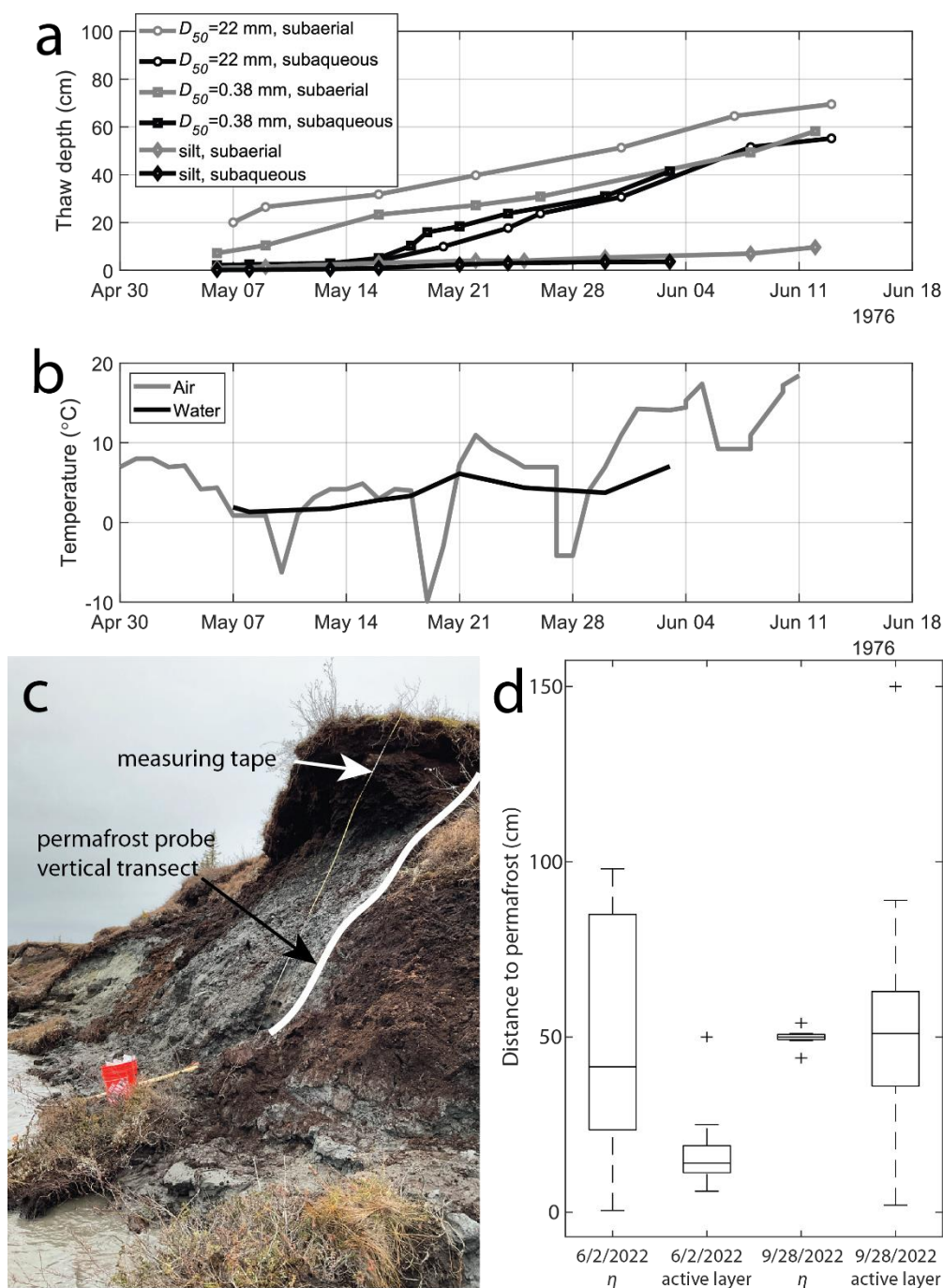
Figure 4.2. Field examples of thawed layer thickness measured subaerially and subaqueously. **(a)** Subaerial (grey) and subaqueous (black) measurements of early-season thawed layer thickness along the Atigun River by Scott (1978). **(b)** River water and air and water temperatures for the Atigun River in summer 1976. **(c)** Site of thawed layer (measured horizontally into bank along white line) and active layer (measured vertically from top of bank on floodplain) measurements. Site is located at 65.70167° N and 156.3942° W near the village of Huslia, AK. Photograph was taken 9/28/2022 by Josh West of ~6 m tall bank. **(d)**

Thawed layer thickness measurements of thaw layer thickness (η) and active layer thickness in on 6/2/2022 and 9/28/2022.

Regardless of the regime, the thawed layer exerts an important 'memory' on the system during transient changes in forcing that can introduce lags in erosion response. For example, a thick thawed layer may form due to slow, warm water and low sediment entrainment rates during the late summer. A late season flood might have predicted $E_{ent} \gg E_{thaw}$, which would suggest thaw-limited erosion at steady state. However, bank erosion may still be entrainment limited until the thaw layer has been eroded completely. Thus, $E_{ent} > E_{thaw}$ is a necessary but not a sufficient condition to produce thaw-limited erosion; in addition, the thaw-layer thickness must be zero (i.e., $\eta = 0$). This thought experiment illustrates the importance of modeling thaw layer dynamics.

4.5 Theory development

In this section, we develop a 1-D mathematical framework for permafrost riverbank erosion that is as simple as possible while accurately capturing the thaw and entrainment processes discussed in our conceptual model. In Section 4.5.1, we describe the evolution equation for the thaw layer and describe how to calculate rates of bank sediment entrainment and thaw. In Section 4.5.2, we describe how heat is transferred through the thawed and frozen regions of the riverbank. Section 4.5.3 details a non-dimensional framework for the bank erosion model and identifies key controlling variables, and Section 4.5.4 derives a model for steady-state thaw layer thickness. All model variables, units, and constants are summarized in Tables 4.S1-4.S3.

4.5.1 Riverbank thaw layer thickness

To determine the thickness of the thawed layer, the model tracks two moving boundaries: the pore ice melting front and the bank erosion front. The evolution of the thawed layer thickness can be found from mass balance as:

$$\frac{d\eta}{dt} = E_{ent} - E_{thaw}. \tag{4.1}$$

The permafrost riverbank must be thawed before sediment can be entrained, so $\eta \geq 0$ for all physically possible cases.

We calculate the sediment entrainment rate using a classic approach (Partheniades, 1965):

$$E_{ent} = M(\tau_b/\tau_c - 1), \tag{4.2}$$

where τ_b is the fluid shear stress on the bank (Pa), τ_c is the critical shear stress for bank sediment entrainment (Pa), and M is a rate coefficient (m/s). Eq. (2) has been used to describe riverbank erosion where τ_c and M can be affected by mud cohesion and vegetation (Ternat et al., 2008; Winterwerp et al., 2012) and implicitly assumed constant bank material properties.

Following Costard et al. (2003), the rate of permafrost riverbank thaw,

$$E_{thaw} = \frac{q_w}{\rho_{ic}(L_f + c_{p,ic}(T_f - T_0))},$$ (4.3)

depends on heat flux to bank (q_w; J/m^2/s), the permafrost bulk density (ρ_{ic}; kg/m^3), permafrost latent heat of fusion (L_f; J/kg), the specific heat of the permafrost ($c_{p,ic}$; J/kg/°C), the temperature of fusion for water ice ($T_f = 0$°C), and the background permafrost temperature (T_0; °C). From mass balance, the bulk density of permafrost (Anisimov et al., 1997),

$$\rho_{ic} = \rho_s(1 - \lambda_p) + \rho_{ice}\lambda_p,$$ (4.4)

depends on the density of quartz sand ($\rho_s = 2650$ kg/m^3), the density of water ice ($\rho_{ice} = 990$ kg/m^3), and the volumetric porosity (λ_p; unitless). Following Dupeyrat et al. (2011), we assume that the volumetric pore space is completely filled with ice, so that

$$\lambda_p = \frac{V_{ice}}{V_{ice} + V_s},$$ (4.5)

where V_{ice} is the volume of ice and V_s is the volume of sediment within the bank. For example, permafrost alluvial deposits commonly consist of sediment with its pore space filled with ice or sediment is suspended in an ice matrix (Douglas et al., 2022; Lininger, et al., 2018). The latent heat of fusion for permafrost (L_f; J/kg) is (Dupeyrat et al., 2011):

$$L_f = \lambda_p L_{f,ice}\, \rho_{ice}/\rho_{ic},$$ (4.6)

where the latent fusion of ice ($L_{f,ice}$) is 333,550 J/kg. The specific heat of the sediment-ice mixture ($c_{p,ic}$; J/kg/°C) is (Dupeyrat et al., 2011):

$$c_{p,ic} = c_{p,ice}\, \rho_{ice}/\rho_{ic} + c_{p,s}\, \rho_s/\rho_{ic},$$ (4.7)

with the specific heat of ice, $c_{p,ice} = 2093$ J/kg/°C, and the specific heat of quartz sand, $c_{p,s} = 730$ J/kg/°C.

Heat flux to the bank (Kader & Yaglom, 1972),

$$q_w = c_{p,w}\rho U C_h(T_w - T_b),$$ (4.8)

is a function of water specific heat ($c_{p,w} = 4.184$ J/kg/°C), water density ($\rho = 1000$ kg/m^3), average water velocity (U; m/s), a heat transfer coefficient (C_h; unitless), and the difference in temperature between the water (T_w; °C) and sediment at the bank surface (T_b; °C). For cases where permafrost is directly in contact with the flowing river ($\eta = 0$), $T_b = T_f$, but T_b may exceed 0°C for cases when a layer of thawed sediment develops on the bank. Heat lost by thawing the riverbank is typically not significant compared to the latent heat of the river water, so we assume that T_w is not a function of heat lost in thawing the riverbank (q_w).

We use a heat transfer coefficient, C_h, from Yaglom and Kader (1974) that has performed well compared to numerical experiments (Kuwata, 2021), natural environments (McPhee, 1992), and our own frozen flume experiments (Chapter 3).

$$C_h = \frac{\sqrt{C_{f,b}}}{-\alpha \ln \eta_1 + \sqrt{Re_{ks}}\left(b_1 Pr^{\frac{2}{3}} - b_2\right) + C + \beta_1 - \frac{1.5\alpha}{(1-\eta_1)^2} + \alpha A \sqrt{C_{f,b}}\left(3.5 - \frac{2.25}{(1-\eta_1)^2}\right)},$$

(4.9)

where $C_{f,b}$ is the wall coefficient of friction (unitless), and empirical constant $\alpha = 2.12$, $A = 1/0.41$, $\beta_1 = 0.5$, $C = 9.5$, $b_1 = 0.55$, $b_2 = 1/11$. The model depends on the roughness Reynolds number,

$$Re_{ks} = k_s u^*/\nu,$$

(4.10)

which varies as a function of the roughness element height (k_s; m), the near-wall fluid shear velocity (u^*; m/s), and the fluid kinematic viscosity (ν). The parameterization is valid for fully turbulent flow ($Re > 10^3$) past hydraulically rough banks ($Re_{ks} > 100$), and is a function of roughness element height, $\eta_1 = k_s/H$, where H is the flow depth (m).

To model the thawed layer failure, we assume for simplicity that the thawed layer destabilizes and collapses when it grows beyond a critical thickness, η_{fail} (m). In reality, failure may occur through rotational or translational displacement, and depend on bank geometry and substrate mechanical properties (Patsinghasanee et al., 2018; Zhang et al., 2021; Zhao et al., 2021). We chose a simpler representation because our model is 1-D and we are assuming homogeneous and constant mechanical properties.

4.5.2 Heat transfer within riverbank

We divide the bank material into three regions to model heat transfer: the mixing region, where the flow of river water may cause faster heat transfer via advection through sediment pore space; the diffusive region, consisting of the deeper thawed region with negligible subsurface pore flow; and the frozen permafrost bank material (Figure 4.3). The presence of a mixing region is consistent with borehole measurements of riverbed thermal diffusivity, which found zones of elevated effective diffusivity tens of cm thick near the surface of cobble-bedded rivers on the Mackenzie River delta (Wankiewicz, 1984).

For scenarios where $\eta > 0$, a layer of thawed sediment insulates permafrost from the flowing river water (Figure 4.3). We assume that heat is primarily transferred through the bank via conduction (Kudryavtsev et al., 1977; Roux et al., 2017), so

$$\frac{\partial H}{\partial t} = \kappa \frac{\partial T}{\partial x}$$

(4.11)

where T (°C) is bank temperature, H (J) is enthalpy, and α (m^2/s) is the thermal diffusivity. This assumption is not valid for coarse sediment with high permeability, where heat fluxes within the bank may be dominated by advection of pore water, or alternatively the diffusivity

must be considered an effective diffusivity that accounts for pore water flow. Similar to previous efforts to model phase change in porous media, we assume that the sediment, pore ice, and water have the same temperature at each location within the bank and calculate bulk thermal diffusivity and conductivity (Beckermann & Viskanta, 1988).
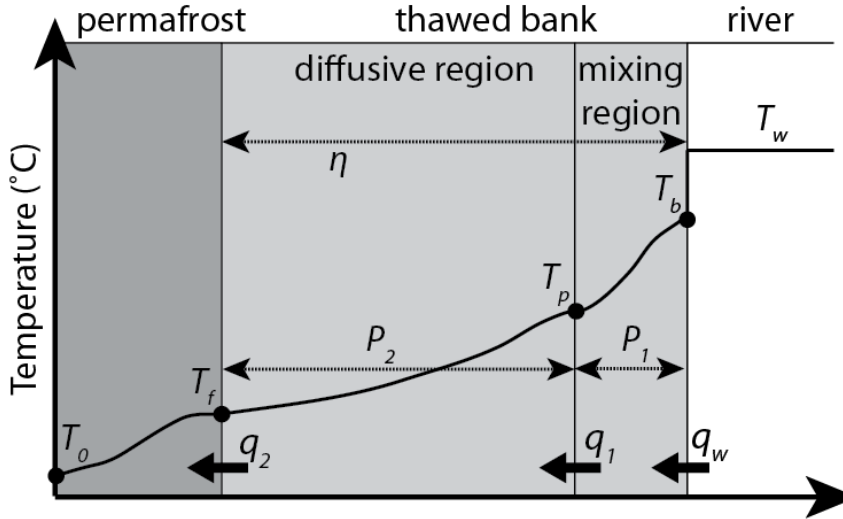
Figure 4.3. Regions of bank with a representative temperature profile. The river water has temperature T_w, the bank surface has temperature T_b, the temperature at the boundary between the diffusive and mixing regions is T_p, the temperature at the permafrost thaw front is the fusion temperature for water ice ($T_f = 0°C$), and permafrost outside the thermal influence of the river has a temperature of T_0. The heat fluxes between each region are q_w, q_1, and q_2 while the thaw layer thickness (η) is equal to the sum of the diffusive (P_2) and mixing region (P_1) thicknesses.

We can convert between bank enthalpy and temperature using permafrost bulk density and specific heat (equations (4.4) and (4.7)). The thermal conductivity of permafrost (W/m/°C) is

$$K_{ic} = K_s^{1-\lambda_p} K_{ice}^{\lambda_p} \tag{4.12}$$

using the bank volumetric porosity (λ_p) and thermal conductivities of water ice ($K_{ice} = 2.18$ W/m/°C) and quartz sand ($K_s = 3.00$ W/m/°C), following a widely used power-law relation (Slusarchuk & Watson, 1975). Thermal conductivity for the diffusive thawed region is calculated using an analogous equation,

$$K_{ts} = K_s^{1-\lambda_p} K_w^{\lambda} \tag{4.13}$$

for a constant value of $K_w = 0.606$ W/m/°C. Assuming that the density of the bank does not change significantly upon thaw (Beckermann & Viskanta, 1988; Kudryavtsev et al., 1977), since water and ice have similar densities near freezing, the bulk density of the thawed bank (ρ_{ts}; kg/m^3) is:

$$\rho_{ts} = \rho_s(1 - \lambda_p) + \rho\lambda_p. \tag{4.14}$$

and the specific heat of thawed permafrost ($c_{p,ts}$; J/kg/°C) is:

$$c_{p,ts} = c_{p,w}\,\rho_w/\rho_{ts} + c_{p,s}\,\rho_s/\rho_{ts}. \tag{4.15}$$

For the outermost mixing region, we consider that the exchange of pore water with the river water might cause heat advection into the bank. Here, we use relations for the exchange region depth, hydraulic conductivity, and subsurface flow validated in flume experiments to calculate an effective thermal diffusivity (Lamb et al., 2017). The mixing regime depth for a densely packed, porous media (Ghisalberti, 2009) follows

$$P_1 = \frac{2D_{50}}{9C_D(1-\lambda_p)} \tag{4.16}$$

and scales with the bank roughness element height (we use the median bank grain size so that $k_s=D_{50}$), the bank porosity, and a drag coefficient ($C_D=1$ for granular beds) (Ghisalberti, 2009). We calculate an effective thermal conductivity (K_{eff}; W/m/°C) that accounts for heat advection and diffusion to substitute for K_{ts} in equation (4.13) and evaluate the effective thermal diffusivity ($\alpha_{ts} = \alpha_{eff}$; m^2/s). Accounting for dispersion from drag and turbulence within pores (Hsu & Cheng, 1990),

$$K_{eff} = K_w D_t U_{sub} \frac{D_{50}}{\alpha_w} \tag{4.17}$$

and depends on the conductivity of water ($K_w = 0.606$ W/m/°C), an experimental constant ($D_t = 0.12$), the mean subsurface flow velocity (U_{sub}; m/s), the bank median grain size (D_{50}; m), and the thermal diffusivity of water ($\alpha_w = 1.32\times10^{-7}$ m^2/s). Since we expect that the exchange region will primarily occur in very coarse-grained riverbanks, the subsurface flow is likely non-Darcian. Therefore, we calculate the mean subsurface flow velocity using a modified Forchheimer equation for layer-averaged flow (Lamb et al., 2017):

$$U_{sub} = \frac{1}{2}\sqrt{\left(\frac{1}{C_1 KF^*}\right)^2 + \frac{4S}{C_1 F^*}\left(\frac{H}{P_1}+1\right)} - \frac{1}{2}\frac{1}{C_1 KF^*}, \tag{4.18}$$

which depends on the channel slope (S; unitless), the hydraulic conductivity (K; m/m) the thickness of the exchange region (P_1; equation (4.16)), the non-dimensional Forchheimer parameter (F^*), and empirical coefficients. Following Lamb et al. (2017), we take $C_1 = 2$ assuming that negligible pore water flow occurs past the outer mixing layer. We evaluate the non-dimensional Forchheimer parameter

$$F^* = \frac{F\lambda_p}{g\sqrt{K}} \tag{4.19}$$

using the Forchheimer coefficient ($F = 5\times10^{-3}$; Lamb et al., 2017) and the hydraulic conductivity,

$$K = \frac{k\mu}{\rho g},$$ (4.20)

which varies with water dynamic viscosity ($\mu = 0.0015$ kg/m/s) and bank hydraulic permeability (k; m^2). Compilations of hydraulic permeability (Barree & Conway, 2004; Bear, 1972; Lapotre & Lamb, 2018; Shepherd, 1989) found good fits to alluvial deposits where

$$k = \frac{a_b v}{g(1+Re_b)} D_{50}^{b_b}$$ (4.21)

and the Reynolds number for the pore space is (Baree & Conway, 2004):

$$Re_b = \frac{2U_{sub}D_{50}}{v}$$ (4.22)

Since a wide range of experimental hydraulic conductivities are observed for a given grain size, we took the mean value of the functions proposed by Lapotre and Lamb (2018) to bound the maximum ($a_b = 6695$ and $b_b = 1.85$) and the minimum ($a_b = 11.9$ and $b_b = 1.5$) for given grain size and fluid flow characteristics.

4.5.3 Non-dimensionalization of bank erosion model

To compare across scales, we develop a non-dimensional version of the model. We non-dimensionalize the sediment entrainment rate as

$$E_{ent}^* = \frac{E_{ent}}{\sqrt{RgD_{50}}},$$ (4.23)

where the sediment submerged specific gravity (R) depends on the density of sediment ($\rho_s = 2650$ kg/m^3) and density of water ($\rho = 1000$ kg/m^3) as $R = \rho_s/\rho - 1 = 1.65$.

We non-dimensionalize E_{thaw} using the independent variables in equation (4.3). Permafrost temperature is non-dimensionalized as $T_0^* = T_0 c_{p,ic}/L_f$, and the non-dimensional temperature of fusion is similarly $T_f^* = T_f c_{p,ic}/L_f$. Substituting these variables into equation (4.3) produces

$$E_{thaw}^* = \frac{\rho_{ic}L_f E_{thaw}}{q_w} = \frac{1}{1+T_f^*-T_0^*}.$$ (4.24)

Here, $E^*_{thaw} = 1$ when the permafrost is at its thawing point and thaw rate is determined by the latent heat of fusion alone. In terrestrial permafrost environments, T_f is very close to 0°C so $T_f^* = 0$. In addition, $c_{p,ic}$ is two orders of magnitude less than L_f, so E^*_{thaw} is usually close to 1.

We then substitute equations (4.25)-(4.26) into equation (4.1) and derive a nondimensional governing equation for permafrost riverbank erosion:

$$\frac{d\eta^*}{dt^*} = q^* E_{thaw}^* - E_{ent}^*. \tag{4.25}$$

Here, $\eta^* = \eta/D_{50}$ and $t^* = t\sqrt{D_{50}/Rg}$. The parameter q^* quantifies the relative rates of permafrost thaw versus sediment entrainment, such that

$$q^* = \left(\frac{q_2}{\rho_{ic}L_f}\right)\left(\frac{1}{\sqrt{RgD_{50}}}\right). \tag{4.26}$$

Therefore, when $q^* < 1$ the time required to thaw the bank is shorter than the time required to erode it, and vice versa when $q^* > 1$. When $q^* = 1$, sediment entrainment and permafrost thaw occur at the same rate. For the case when the bank is at steady-state and the thaw layer thickness is not changing in time, $E^*_{thaw} \sim 1$ and $q^* \sim E^*_{ent}$

4.5.4 Steady-state bank erosion model

In this section we derive the steady-state condition for η^* when the permafrost thaw rate equals the sediment entrainment rate from the surface of the bank. The trivial solution, when $E^*_{ent} = E^*_{thaw} = 0$, occurs when the river is frozen over, so $T_w^* = 0$ and $\eta^* = 0$. For the case when $\frac{d\eta^*}{dt^*} = 0$, the model predicts a steady-state with constant thaw layer thickness through time and

$$E_{ent}^* = q^* E_{thaw}^*. \tag{4.27}$$

Since P_1 is typically much thinner than P_2, we assume that $\eta \sim P_2$. To derive the thickness of the diffusive region, P_2, we assume the temperature gradient with respect to distance from the riverbank is the constant through time and that the flux within the bank can be approximated as linear conduction with a multiplicative shape factor s because heat is rapidly diffused through this layer. For this case, heat flux through the thermally diffusive region (q_2; J/m^2/s) is:

$$q_2 = \frac{s\kappa_{ts,2}(T_b - T_f)}{\eta}, \tag{4.28}$$

with T_b (°C) being the bank temperature exposed to the water (Figure 4.3).

At steady-state conditions, the mixing region must maintain a constant heat flux to the adjacent regions while increasing its temperature to maintain a constant thermal profile as the bank is eroded. Therefore, the heat flux into the bank (q_b; J/m^2/s) equals

$$q_b = q_2 + E_{ent}c_{p,ts}\rho_{ts}(T_b - T_f). \tag{4.29}$$

Re-arranging and substituting equations (4.27) to (4.29) with the sediment entrainment rate (equation (4.2)) and erosion rate under thaw-limited conditions (equation (4.8)) gives an analytical solution for the thickness of the thawed diffusive region under steady-state conditions.

We define $U^* = U/\sqrt{RgD_{50}}$, so that the flow velocity scales with the bank sediment settling velocity when $U^* = 1$, and a non-dimensional heat transfer coefficient between flowing water and permafrost so that:

$$C_h^* = \frac{\rho c_{p,w} C_h}{\rho_{ic} c_{p,ic}}. \tag{4.30}$$

In addition, we non-dimensionalize the ratio of thermal properties for thawed and frozen bank sediment as the variable C^*_{ts}:

$$C_{ic}^* = \frac{\rho_{ic} c_{p,ic}}{\rho_{ts} c_{p,ts}}, \tag{4.31}$$

and the thermal conductivity for the diffusive region such that:

$$\kappa_{ts,2}^* = \frac{\kappa_{ts,2}}{\rho_{ts} c_{p,ts} \sqrt{RgD_{50}^3}}. \tag{4.32}$$

Then, we substitute equations (4.30)-(4.32) and simplify algebraically to solve for steady-state η^*.

We assume $T_f^* = 0°C$, to produce a simplified equation for η^*:

$$\eta^* \sim \frac{s\kappa_{ts,2}^* \left(C_h^* U^* T_w^* - E_{ent}^*(1-T_0^*)\right)}{E_{ent}^*(1-T_0^*)\left(C_{ic}^* C_h^* U^* + E_{ent}^*\right)}. \tag{4.33}$$

In this case, we can see that larger values of T_0^*, T_w^*, and $\kappa^*_{ts,2}$, or smaller values of C^*_{ic} and E_{ent}^* will cause a thicker thaw layer to develop. The effects of C_h^* and U^* depend on the relative magnitudes of the other variables, since they appear as positive values in the both the numerator and denominator.

In thaw-limited cases, the erosion rate rapidly becomes constant in time after any thawed sediment has been eroded away from the riverbank. For entrainment-limited cases, the sediment entrainment rate, and therefore total bank erosion rate, immediately reaches a constant value. In contrast, the permafrost thaw rate is initially rapid but decreases as the thaw layer becomes thicker and heat must be conducted through this layer. There is also a delay to establish the thermal gradient through the thaw layer as the heat flux into the riverbank decreases to approach a relatively steady rate.

We derive the timescales to establish a thaw layer and develop a linear temperature profile to evaluate when the steady-state solution should be a reasonable approximation of the unsteady solution. We define the timescale to form the thawed layer as $t_\eta = \eta/E_{ent}$ and the timescale to develop a linear temperature profile in the thawed layer as $t_T = \eta^2/\alpha_{ts}$. The ratio of these timescale is

$$\frac{t_\eta}{t_T} = \frac{\alpha_{ts}}{\eta E_{ent}},\tag{4.34}$$

where the analytical steady-state approximation (equation (4.33)) is a good approximation when this ratio is < 1 and will underestimate the thaw layer thickness when this ratio exceeds 1.

4.6 Data compilation and model implementation

4.6.1 Arctic rivers compilation

Implementing the model requires characterizing the bank thermal properties and the channel hydraulics. To do so, we complied data from published channel hydraulics, sediment characteristics, and ground thermal properties to identify a reasonable range of parameters to run the model. The database consists of 27 sites from 6 rivers with latitude greater than 62° N and ranging from discontinuous to continuous permafrost regions. We also report new permafrost probe measurements of active layer and thawed layer thicknesses near Huslia (see Section 4.12.1). The model requires the background permafrost temperature (T_0), volumetric porosity (λ_p), mean water velocity (U) and depth (H) or the total water discharge (Q_w), channel slope (S), either the riverbed median grain size ($D_{50,bed}$) or total coefficient of friction ($C_{f,tot}$), bank median grain size (D_{50}), and the water temperature (T_w). To determine model sensitivity to each parameter, we varied each while holding the others constant for fully turbulent cases ($Re_{ks} > 100$). To span the range of values in our compilation (see Section 4.12.2, Tables 4.S4-4.S5), we ran the model for $D_{50,bank}$ from 10^{-5} to 10^{-1} m, $D_{50,bed}$ from 10^{-4} to 10^{-1} m, S from 10^{-5} to 10^{-2}, λ_p from 0 to 1, T_w from 0 to 20°C, T_0 from -15 to 0°C, U from 0 to 3 m/s, and H_r from 0 to 20 m.

4.6.2 Yukon River case study

In order to understand the response of riverbank erosion to seasonal and inter-annual variability, we examined bank erosion in a scenario modeled roughly after the Yukon River between Stevens Village, Alaska and Beaver, Alaska. Here, the Yukon River flows through discontinuous permafrost and has an anabranching morphology that converges to a single channel at Stevens Village. The erosion rates along this reach are 2-3 m/yr (Rowland et al., 2019).

Field measurements (Biskaborn et al., 2015; Clement, 1999; Lininger et al., 2019) allowed us to run the full model and compare to measured bank erosion rates. We computed the median daily water temperature or discharge then smoothed the medians using a Savitzky-Golay filter. Water temperature was assumed to be 0°C during periods when no

measurements were taken due to ice cover. For discharge, we used the daily timeseries for the Yukon River USGS gage 15453500 at Stevens Village, which is available from 1976 to the present. Water depth and velocity were measured periodically, and we calculated a power-law relation to discharge and used that to obtain daily H and U for the USGS gage at Stevens Village (see Figure 4.S2). Water temperature data were only available sporadically from 1970-2005 at Stevens Village ($n=214$), so we combined this dataset with daily water temperature measurements from the downstream gage at Pilot Station, Alaska (USGS gage 15565447).

Over this reach, the Yukon River flows over a gravel bed ($D_{50} \sim 10$ mm) with a slope $S = 1.6 \times 10^{-4}$ (Clement, 1999). We modeled a representative sandy permafrost riverbank with $D_{50} = 1$ mm and $T_f = 0°C$. We used measurement values of $\rho_b = 861$ kg/m^3 and $f_{ice} = 0.2362$, corresponding to $\lambda_p = 0.22$, for mineral soils on the Yukon Flats between Beaver and Stevens Village (Lininger et al., 2019). For the farfield permafrost temperature, we use $T_0 = -1°C$, determined from 3 m borehole data for Stevens Village (Biskaborn et al., 2015). To run the model with time-varying discharge and water temperature, we kept channel bank and riverbed properties – such as bank and bed porosity, grain size, permafrost temperature, channel width, and channel slope – constant (Section 4.6.1).

4.6.3 Model implementation

We implemented the model numerically using second-order finite differences in space and time. We tracked the thaw front, erosion front, enthalpy and temperature throughout the bank and the fraction of each bank node that has been eroded or thawed. To ensure that the results were non-grid size and time spacing dependent, we compared bank erosion rates, thaw rates, and thaw layer thickness for spatial steps (dx) ranging from 10^{-4} to 10^{-1} m and timesteps (dt) ranging from 10^{-3} to 10^2 sec. We also evaluated the model for numerical stability using the von Neumann and Courant-Friedrich-Lewy criteria. Based on these numerical experiments and stability criteria, we selected $dx = 0.01$ m and $dt = 1$ s.

Model runs begin with a riverbank with constant temperature T_0 and a thaw layer thickness of $\eta = 0$, and subsequently evolves with time-varying boundary conditions. The boundary node within the bank does not have a fixed temperature and may respond to heat diffused through the bank. However, the model terminates if this node begins to thaw.

To solve equation (4.2) for E_{ent}, we used an erosion coefficient of $M = 2.5 \times 10^{-5}$ m/s, representative for mixtures of sand and silt (Winterwerp et al., 2012). Shear stress on the channel banks is a function of the total shear stress (τ_{tot}; Pa),

$$\tau_b = \frac{1}{(1+\varepsilon)} \tau_{tot}, \tag{4.35}$$

where $\varepsilon = 0.2$, characteristic of a self-formed channel (Parker, 1978). We assumed normal flow conditions and a wide channel, such that $\tau_{tot} = \rho g H S$. The critical shear stress for entrainment was evaluated as (Parker et al., 2003):

$$\tau_c = (\rho_s - \rho)gD_{50}(0.11Re_p^{-0.6} + 0.03 \times 10^{-7.7Re_p^{-0.6}}), \tag{4.36}$$

with the particle Reynolds number

$$Re_p = \frac{\sqrt{gRD_{50}^3}}{\upsilon}. \tag{4.37}$$

To evaluate equation (4.3) for E_{thaw}, we assumed normal flow so that the shear velocity on the wall $u^* = U\sqrt{C_{f,b}}$. The total flow depth is

$$H = \frac{C_{f,tot}U^2}{gS}, \tag{4.38}$$

with $C_{f,tot}$ (unitless) the total coefficient of friction, U (m/s) the mean flow velocity, and S (unitless) the water surface slope. We assumed that most bank roughness is due to the grain size of sediment in the bank, and evaluate the coefficient of friction from grain drag using the variable power equation (VPE) (Ferguson, 2007):

$$C_{f,b} = \frac{a_1^2 + a_2^2(H/k_s)^{5/3}}{a_1^2 a_2^2(H/k_s)^2}. \tag{4.39}$$

We used the author-recommended nondimensional constants of a_1=6.5 and a_2=2.5 and roughness height (k_s; m) set at $k_s = 2.5 \times (2.2D_{50})$ (Rickenmann & Recking, 2011). Values of H and $C_{f,b}$ are substituted into equations (4.8) and (4.9) to compute the heat transferred from the water to the riverbank.

Heat was supplied to the boundary node at the edge of the eroding bank using equation (4.3) and diffused through the bank across a fixed grid. At each timestep, we assigned the thermal and mechanical properties at each node of the eroding bank by evaluating equations (4.4)-(4.7) for the bank's thermal properties. For the case when $\eta > 0$ (Figure 4.3), we used equations (4.16)-(4.22) to compute the P_1 thickness and thermal properties and equations (4.11)-(4.15) for P_2. For nodes containing the thaw front and boundary between the diffusive and exchange regions, we calculated their properties according to the fraction of the node comprising each layer (Beckermann & Viskanta, 1988). For instance, a node may contain fraction f_a of layer a and f_b of layer b so $f_a + f_b = 1$. For this node, its specific heat $c_{p,ab} = f_a c_{p,a} + f_b c_{p,b}$, its bulk density $\rho_{ab} = f_a \rho_a + f_b \rho_b$, and its thermal conductivity $K_{ab} = (f_a/K_a + f_b/K_b)^{-1}$. After calculating the thermal and material properties throughout the bank, we propagated heat using an upwinding finite differences scheme for thermal diffusion (equation (4.11)). For the node at the thaw front, heat in excess of 0°C was used to partially thaw that node. After updating the bank temperature and thaw front, we calculated the rate of total riverbank erosion using equation (4.2) and updated the erosion front to reflect this new value. Then, we compared the locations of the new erosion and thaw fronts, setting the erosion front equal to the thaw front if the bank had eroded further than it had thawed. After

a node eroded, its temperature was set equal to the river water temperature and the boundary node at the water-bank interface moved. The temperature, enthalpy, and locations of the erosion and thaw fronts were then used to calculate next timestep. When running the model to steady-state, we selected a threshold value of $\zeta_{crit} = 10^{-5}$. We used a reference value of thaw layer thickness, η_{ref}, that is the mean of the previous 10^3 timesteps. If $\varepsilon = (\eta_{ref} - \eta)/\eta_{ref}$ was less than ζ_{crit}, the model was considered to have reached steady-state.

4.7 Results

In this section we illustrate model response to the range of conditions observed in terrestrial permafrost river systems. First, we investigate model transient behavior under constant forcing for the base case scenario, as well as related scenarios with different grain size and bank ice content, without allowing thaw-layer failure (Section 4.7.1). Next, we show the model results for controls on steady-state thaw layer thickness by changing parameters from a base case, again while not allowing failure (Section 4.7.2). After exploring model behavior under steady forcing, we ran the model for transient forcing typical of Arctic rivers. Section 4.7.3 describes experimental results obtained using an annual hydrograph and water temperature curve typical for the Yukon River in Alaska. Section 4.7.4 includes results from models run for a typical hydrograph with cold water temperatures. Then, we investigate the bank failure regime for different bank failure thresholds (Section 4.7.5) and evaluate how periodic bank failure changes the sensitivity of erosion rates to water temperature.

4.7.1 Model behavior for a base case

To illustrate the behavior of the numerical model through time, we ran the model for a base case, varied grain size, and varied bank volumetric ice contents. The base case, which was scaled after the Yukon River (Table 4.1), had moderate cold water temperatures ($T_w = 10°C$), low volumetric ice content ($\lambda_p = 0.22$), and coarse sand banks ($D_{50,bank} = 1$ mm; Figure 4.4). In each model run, the thaw rate was initially rapid and then declined to equal the sediment entrainment rate so that a constant thaw layer thickness persisted through time, and bank erosion was entrainment limited. For the case where $\lambda_p = 0.22$ (Figure 4.4a), the model shows slow entrainment and a 16 cm thick thawed layer. In the higher ice content cases ($\lambda_p = 0.80$; Figure 4.4b-c), erosion was more rapid than the base case due to the lower volume of sediment per unit bank. However, the thaw layer was thinner (6 and 2 cm for $\lambda_p = 0.50$ and 0.80) because the heat required to thaw the bank increased with ice content.
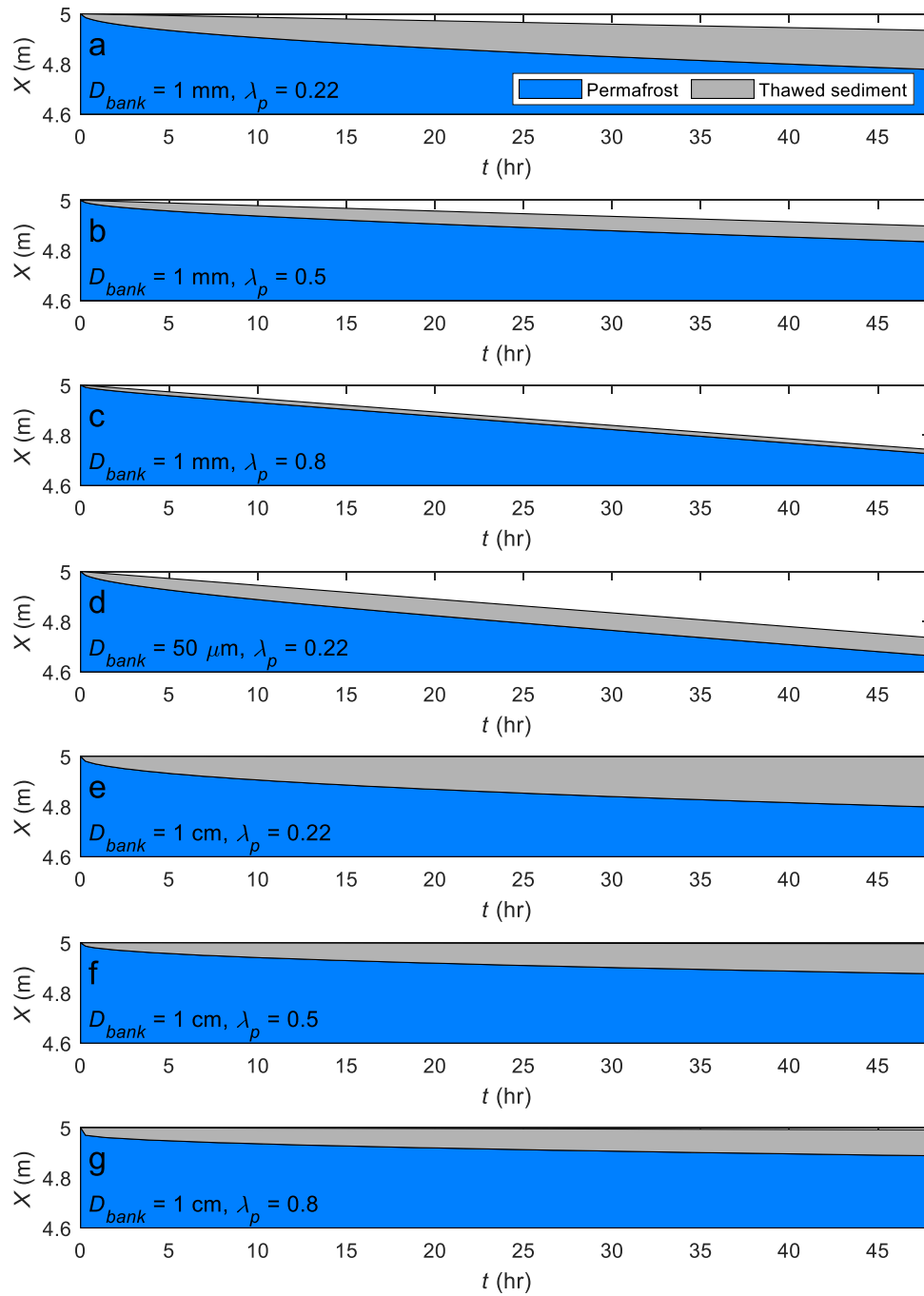
Figure 4.4. Model results for riverbank thaw and erosion under constant hydraulic conditions. The thawed layer (grey) and permafrost (blue) retreat from their initial position of $X = 5$ m (y-axis) during the 1-hour model run (time on x-axis). The model was run for the Yukon River base case conditions for varying bank grain size ($D_{50,bank}$) and volumetric porosity (λ_p). Model runs include: **(a)** $D_{50,bank} = 1$ mm and $\lambda_p = 0.22$, **(b)** $D_{50,bank} = 1$ mm and $\lambda_p = 0.50$, **(c)** $D_{50,bank} = 1$ mm, and $\lambda_p = 0.80$, **(d)** $D_{50,bank} = 50$ μm and $\lambda_p = 0.22$, **(e)** $D_{50,bank} = 1$ cm and $\lambda_p = 0.22$, **(f)** $D_{50,bank} = 1$ cm and $\lambda_p = 0.50$, and **(g)** $D_{50,bank} = 1$ cm and $\lambda_p = 0.80$.

Model input variables	Symbol	Yukon River (base case)	Compilation range
Bank median grain size	D_{50}	1×10^{-3} m	7.70×10^{-6} to 2.80×10^{-4} m
River water surface slope	S	1.6×10^{-4}	2.71×10^{-5} to 4.3×10^{-4}
Permafrost porosity	λ_p	0.22 m³/m³	0 to 1 m³/m³
River water temperature	T_w	1°C	0 to 20°C
Background permafrost temperature	T_0	-1°C	-6.6 to -0.1°C
Mean river water flow velocity	U	1.0 m/s	0.7 to 1.49 m/s

Table 4.1. Numerical model input values for the base case of the Yukon River and the range of nautral rivers in our data compilation.

For a finer bank median grain size of 0.050 mm, viscous forces were significant but grain inertia is small. This resulted in more rapid entrainment rates (6.5 cm/day) and entrainment-limited erosion conditions when compared to sand banks with similar ice content (Figure 4.4a, d). The small grain size also caused low bank roughness, and therefore slow rates of thaw and a thinner thaw layer compared to sand and gravel with the same porosity. Overall, heat transfer to thaw the bank still outpaced sediment entrainment so the model predicted that a thaw layer 7 cm thick would develop as entrainment-limited bank erosion proceeds. For coarser, gravel riverbanks ($D_{50,bank}= 1$ cm), base case conditions are below the threshold of entrainment and erosion is zero (Figure 4.4e-g). By definition, these channels are entrainment-limited and cannot reach a steady-state η since thawed layer will always thicken through time. A 20 cm-thick thaw layer formed within 2 days when $\lambda_p = 0.22$ (Figure 4.4e). Similar to the sandy bank, the thaw layer thickness decreased (to 16 then 7 cm) when we increased λ_p to 0.5 and 0.8.

4.7.2 Steady state thaw-layer thickness

To explore the parameter space of steady thaw layer thickness produced by our bank erosion equations, we took our base case and varied single parameters over a range that spanned our data compilation. In each analysis, we held all variables constant from our base case (Table 4.1) and varied one parameter at a time for hydraulically rough conditions ($Re_{ks} > 100$).

We found that bank erosion rates were highest for small grain sizes that produced bank roughness just above the transitional flow regime (Figure 4.5a). Fine sediment did not produce hydraulically rough conditions and had a high critical Shields number due to viscous effects, so it eroded more slowly than sand and was not included in Figure 4.5. As grain size increased beyond sand, bank erosion rates decreased. This is because very coarse sediment has a large volume relative to its surface area and therefore is more difficult to pick up. When sediment grew large enough to become immobile, the erosion rates dropped to 0 m/s. The dimensionless heat flux to the bank (q^*) showed that increasing grain size increased bank

roughness but decreased heat fluxes from the water to the bank (Figure 4.5b). The decrease in $q*$ was sublinear because larger roughness elements disrupted the fluid boundary layer in which heat transfer was governed by molecular diffusion, increasing heat fluxes, and slowed near-bank flow, which significantly decreased heat fluxes. These two competing processes caused a rollover in the dimensionless heat flux to the bank at steady-state. For conditions in which sediment was mobile, the timescale to erode the thaw layer was much greater than the timescale to establish a linear temperature profiles, so the analytical solution was a very poor approximation for η_{ss} (Figure 4.5c). However, cases with immobile sediment never reached steady-state, which is the case for $D_{50}>10^{-2}$ m. Models that reached steady-state produced η_{ss} up to ~100 grain diameters (Figure 4.5d). The value of $\eta*_{ss}$ decreased since the thaw layer got thicker less rapidly than grain size increased, which caused the denominator of $\eta*_{ss}$ to increase more rapidly than the numerator. Therefore, dimensionless thaw layer thickness generally decreased with grain size but its rate depended on small-scale interactions between bank roughness and near-bank fluid flow.
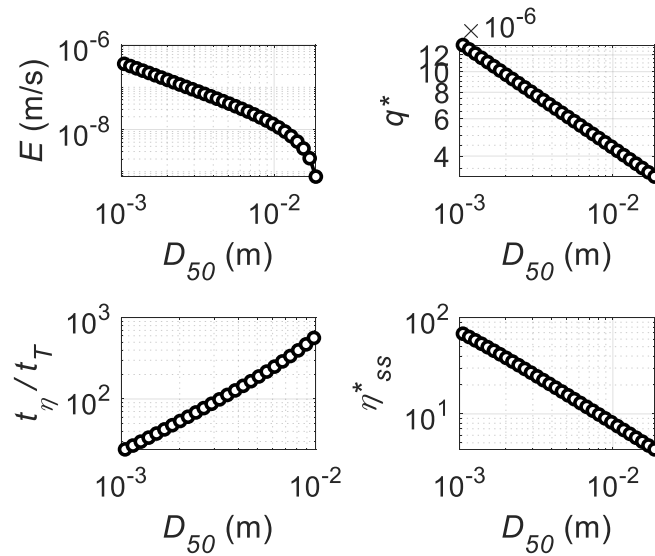
Figure 4.5. Effect of riverbank median grain size (D_{50}) on riverbank erosion processes. **(a)** Riverbank erosion rates versus D_{50}, with $Re_{ks}>100$. **(b)** Dimensionless heat transfer rate ($q*$) versus D_{50}. **(c)** Timescale to reach steady-state versus D_{50}. **(d)** Steady state thickness $\eta*$ versus D_{50}.

Next, we evaluated the sensitivity of modeled riverbank erosion rates to pore ice content (Figure 4.6a). We ran the model for 0 to 100 vol% pore ice (corresponding to 100 to 0 vol% quartz sand) to span the range of observed permafrost volumetric ice contents (Section 4.6.1). The bank was entrainment-limited for all cases except $\lambda_p=1$. At low pore ice contents, the thaw rate was high because the latent heat of fusion was proportional to the amount of water ice in the bank (Figure 4.6a). As pore ice content increased, thaw rate decreased inversely. In contrast, entrainment rates were initially lower because there was more sediment to entrain per unit volume of riverbank and the entrainment rate was inversely correlated to $1-\lambda_p$ (equation (4.2)). Therefore, as the porosity increased, riverbank erosion rates increased while

the bank remained entrainment-limited and the thaw layer thinned. This caused $q*$ to fall and then rise with λ_p as the thaw rate decreased and the entrainment rate increased (Figure 4.6b). For this range of parameters, the bank changed its thawed layer thickness slightly faster than the linear temperature profile became established (Figure 4.6c). The steady-state η declined from ~200 to 2 grain diameters as ice content increased (Figure 4.6d). For $\lambda_p=1$, the thickness of the thawed layer went to zero since bank erosion was thaw-limited. Therefore, the base case maintained entrainment-limited conditions for all ice contents, with the exception of pure ice such as that found in ice wedges.
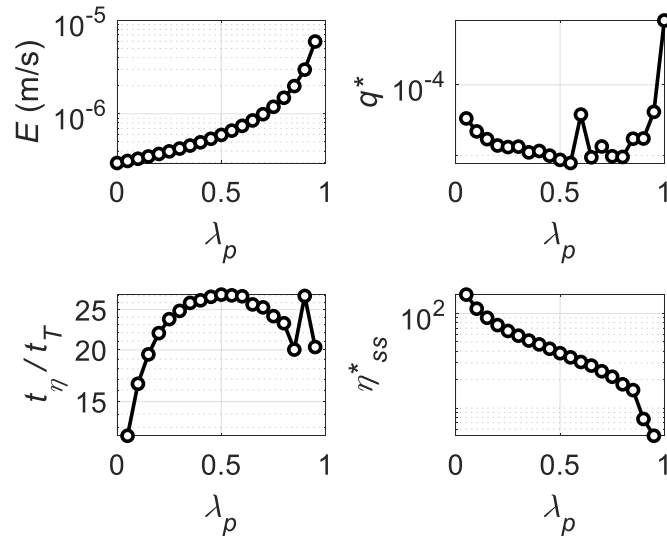
Figure 4.6. Effect of riverbank ice content (λ_p) on riverbank erosion processes. **(a)** Riverbank erosion rates versus λ_p, with $Re_{ks}>100$. **(b)** Dimensionless heat transfer rate ($q*$) versus λ_p. **(c)** Timescale to reach steady-state versus λ_p. **(d)** Steady state thickness $\eta*$ versus λ_p.

Permafrost temperature had little influence on the thaw rate and no influence on the entrainment rate, causing no change in bank erosion rates since the case study was entrainment-limited for all permafrost temperatures (Figure 4.7a). Therefore, decreasing bank temperature within the range of present-day permafrost measurements could not cause a transition to thaw-limited conditions, shown by low values of $q*$ that slightly decreased as the bank temperature increases due to the presence of a warmer thawed layer (Figure 4.7b). For this range of parameters, the bank reached its steady-state erosion rate within hours but that state was poorly approximated by a linear temperature profile (Figure 4.7c). Increasing bank temperature did cause a slight increase in thaw layer thickness, from ~50 to ~75 grain diameters (Figure 4.7d). Permafrost thaw rate did not significantly change with bank temperatures because the latent heat of fusion for water ice is two orders of magnitude higher than the specific heat of ice (equation (4.3)). Therefore, any changes in heat required to raise the pore ice to its melting point at 0°C would be significantly less than the permafrost latent heat of fusion.
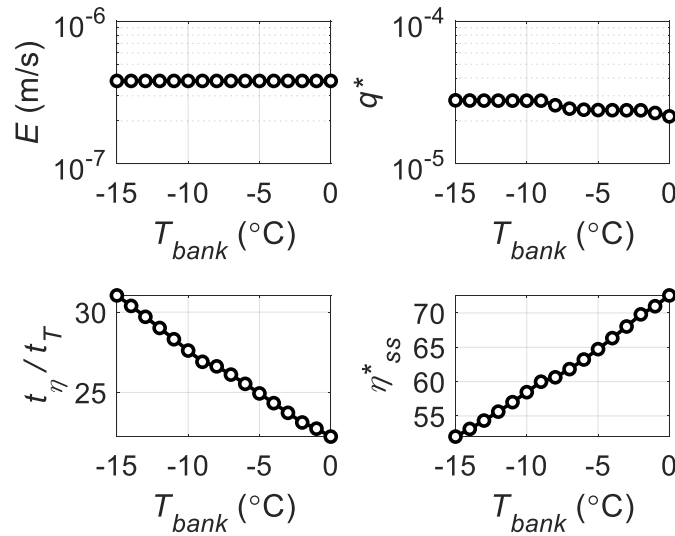
Figure 4.7. Effect of permafrost temperature (T_{bank}) on riverbank erosion processes. **(a)** Riverbank erosion rates versus T_{bank}, with $Re_{ks}>100$. **(b)** Dimensionless heat transfer rate (q^*) versus T_{bank}. **(c)** Timescale to reach steady-state versus T_{bank}. **(d)** Steady state thickness η^* versus T_{bank}.
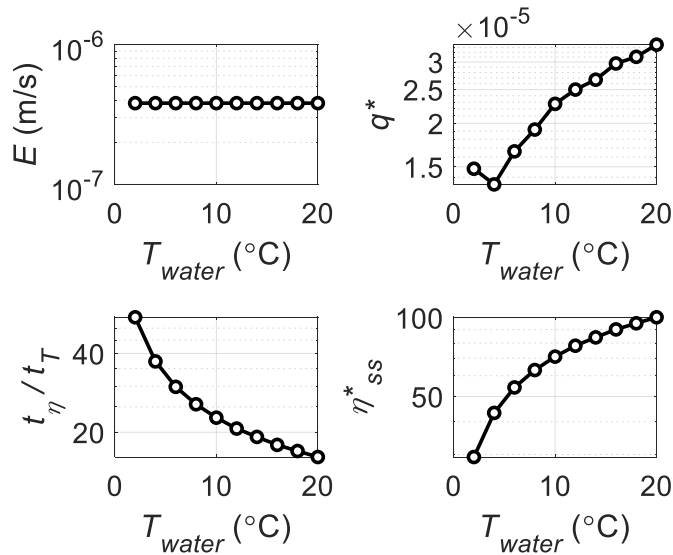
Figure 4.8. Effect of river water temperature (T_{water}) on riverbank erosion processes. **(a)** Riverbank erosion rates versus T_{water}, with $Re_{ks}>100$. **(b)** Dimensionless heat transfer rate (q^*) versus T_{water}. **(c)** Timescale to reach steady-state versus T_{water}. **(d)** Steady state thickness η^* versus T_{water}.

Since the Yukon River example case was almost always entrainment-limited for $T_{water}>0°C$, river water temperature also did not have a significant effect on bank erosion rates (Figure 4.8). When $T_{water}=0°C$, no erosion occurred since the bank did not thaw, so $E=0$ m/s (Figure

4.8a). For the non-zero values of T_{water} we evaluated, the bank was entrainment-limited so erosion rates were not temperature-dependent. This produced generally low values of $q*$ that increased with sub-linearly water temperature (Figure 4.8b). When the thaw layer remained within the surface node, the model maintained the bank surface temperature at 0°C which caused a high heat flux due to the large difference between water and bank surface temperature (equation (4.8)). The time required to reach a linear temperature profile was less than the time to erode the thawed layer by an order of magnitude, and the time to form a linear profile increased as the water temperature decreased (Figure 4.8c). Resulting thaw layer thicknesses increased linearly for higher water temperatures, from ~12 to 110 grains thick, because the rate of heat transfer from the water to the bank was higher for warmer water (Figure 4.8d). These results indicate permafrost riverbanks respond to warmer water temperatures by developing thicker thawed layers on their banks within hours.
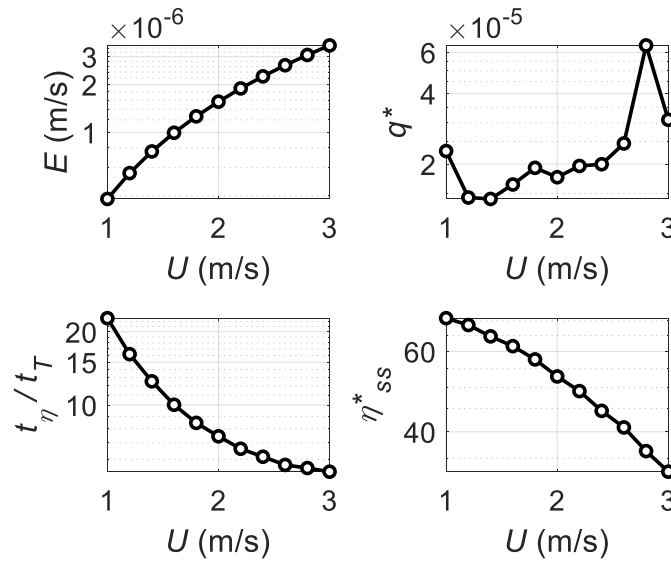
Figure 4.9. Effect of river water flow velocity (U) on riverbank erosion processes. **(a)** Riverbank erosion rates versus U, with $Re_{ks}>100$. **(b)** Dimensionless heat transfer rate ($q*$) versus U. **(c)** Timescale to reach steady-state versus U. **(d)** Steady state thickness $\eta*$ versus U.

Increasing water flow velocity increased both thaw and entrainment rates (equations (4.3) and (4.8)). For cases with $Re_{ks}>100$, erosion rates increased with flow velocity because sediment entrainment rates depend linearly on excess shear stress, which scales roughly as U^2 (Figure 4.9a). Heat flux to the bank generally increased with flow velocity, although there was an irregular trend of $q*$ with U because varying thaw layer thickness altered the bank surface temperature (Figure 4.9b). Increasing thaw and entrainment rates caused the temperature profile to approach linear at higher flow velocities (Figure 4.9c). The steady-state thaw layer thickness decreased with U in a concave-down trend (Figure 4.9d). This trend reflects competition between thaw and entrainment rates, however, $\eta*_{ss}$ had a stronger concavity with respect to U than entrainment rates. Therefore, we inferred that the rapid removal of thawed sediment from the bank outpaces the increasing heat flux due to the lower

bank surface temperature, reducing the thickness of the thaw layer by around 1/3. Together, these results imply that floods should cause rapid bank erosion due to high rates of both permafrost thaw and sediment entrainment.
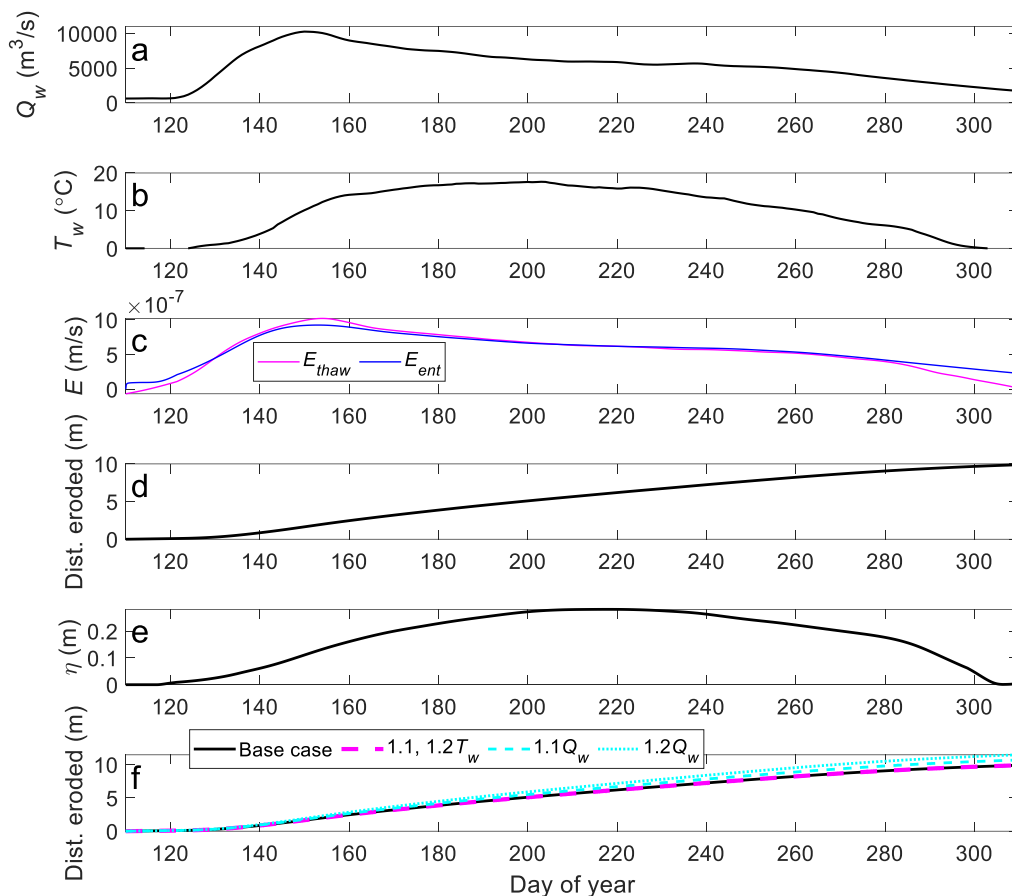
Figure 4.10. Bank erosion for Yukon River as a function of discharge and water temperature through its annual hydrograph. **(a)** Median daily water discharge versus measurement day of the year from the Yukon River USGS stream gage at Stevens Village, Alaska. **(b)** Median daily water temperature measurements from Stevens Village, which were taken intermittently, combined with measurements from Pilot Station. **(c)** Modeled erosion rates for the modern hydrograph of the Yukon River. **(d)** Cumulative bank erosion versus day of the year. **(e)** Modeled thaw layer thickness versus day of the year for the modern hydrograph. **(f)** Predictions for cumulative distance eroded for 110% and 120% water temperature (T_w) and discharge (Q_w), with other variables held constant.

4.7.3 Seasonal variations in thaw-layer thickness

To understand the processes limiting riverbank erosion over an annual hydrograph, we ran the model for the Yukon River (Figure 4.10). At the start of the summer, water temperature

began near 0°C, peaks mid-summer, and then dropped back to zero as the river ices over in the fall (Figure 4.10a). Water discharge started from zero with complete ice cover then peaked in the early summer with the spring snowmelt and ice break-up before subsiding to a relatively constant discharge mid-summer and declining in the fall (Figure 4.10b). Erosion occurred throughout the summer, and thaw rates were slower than entrainment rates only for the days immediately after ice break-up and before freeze-up – otherwise erosion was entrainment-limited (Figure 4.10c). The thawed layer remained relatively thin (<30 cm) throughout the summer but slows bank thaw rates so that they equaled entrainment-limited erosion rates (Figure 4.10e). Importantly, the thawed layer prevented thaw-limited conditions in fall when water temperatures and discharges declined, which occurred after day 280 in (Figure 4.10c). Therefore, the presence of this thin thawed layer was important to limit permafrost bank erosion rates.

To assess the potential effects of climate change on bank erosion along the Yukon River, we ran the model at steady-state for conditions of 110% and 120% water temperature (T_w) and discharge (Q_w). We took the cumulative sum of the minimum of the entrainment- and thaw-limited erosion rates to get the predicted erosion through the summer (Figure 4.10f). There was no change in erosion rates with increases in water temperature. However, increasing water discharge by 10% increased erosion rates to 10.68 m/yr, and a 20% increase in discharge caused 11.46 m/yr of erosion. Increases in discharge caused a roughly proportional increase in erosion rate because most erosion occurred under entrainment-limited conditions, and the rate of sediment entrainment increased linearly with shear stress, which scales linearly with depth and approximately linearly with discharge. Therefore, although water temperature played an important role in limiting bank erosion during winter months, the thawed layer protected the bank during the summer and bank erosion instead responds to changes in water discharge.

4.7.4 Effect of colder water temperatures

To investigate whether bank erosion rates and processes differed while varying water temperature but keeping all variables constant, we decreased water temperature by 80% while maintaining the same hydrograph from Stevens Village (Figure 4.11a-b).

Model results indicated that sediment entrainment rates exceeded permafrost thaw rates throughout the summer and fall, except immediately after ice break-up and before freeze-up, similar to model results for warmer water temperatures (Figure 4.11c). However, erosion rates remain thaw-limited later into the spring and become thaw-limited earlier in the fall, reducing the total bank erosion rate slightly. Total erosion rates did not significantly vary for 110% and 120% water temperature, but were 10.68 m/yr for 110% of the water discharge and 11.46 m/yr for 120% annual discharge (Figure 4.11d, f). The thawed layer developed during the flood peak in the spring then gradually thinned and disappeared throughout the summer (Figure 4.11e). These results indicate that summer floods must be coupled with very low water temperatures (approaching 0°C) for thaw-limited erosion to occur.
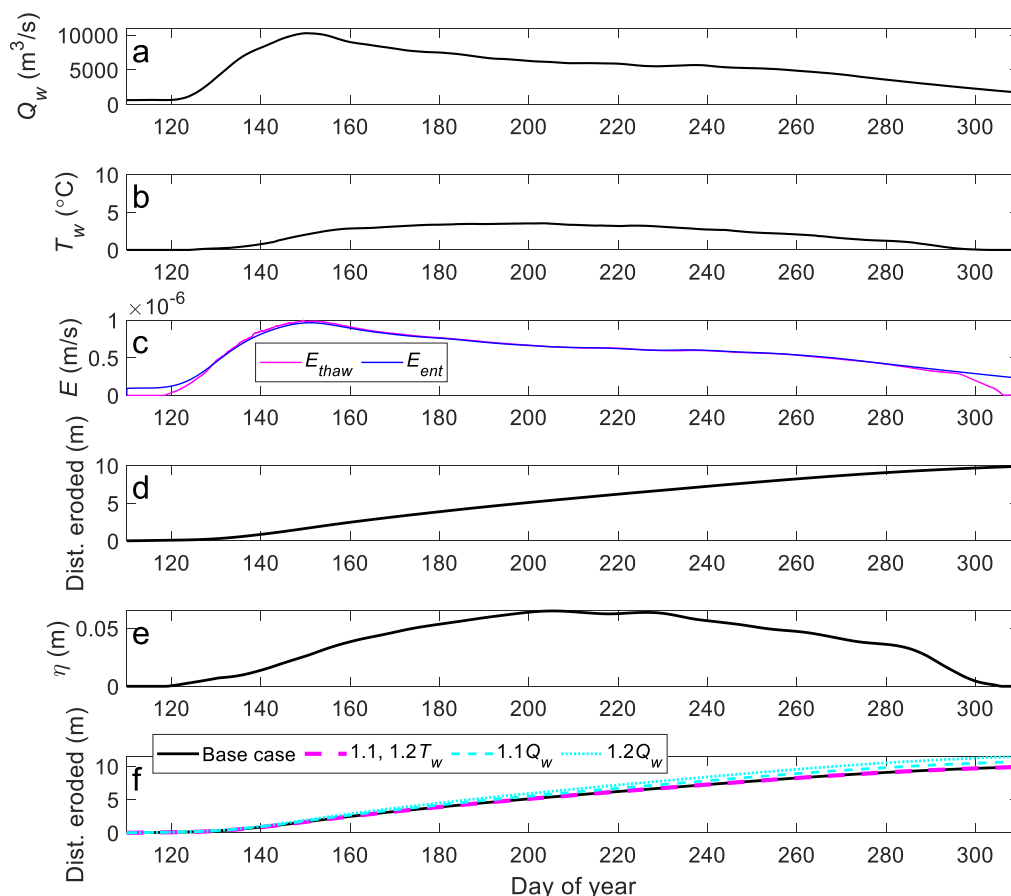
Figure 4.11. Steady-state bank erosion for Yukon River as a function of discharge and water temperature, with its hydrograph flipped so discharge peaks in late summer. **(a)** Median daily water discharge versus measurement day of the year from the Yukon River USGS stream gage at Stevens Village, Alaska. **(b)** Median daily water temperature measurements from Stevens Village, which were taken intermittently, combined with measurements from Pilot Station and multiplied by 0.2 to simulate colder climates such as those in continuous permafrost. **(c)** Modeled erosion rates for the inverted hydrograph of the Yukon River. **(d)** Cumulative bank erosion versus day of the year. **(e)** Modeled thaw layer thickness versus day of the year for the inverted modern hydrograph. **(f)** Predictions for cumulative distance eroded for 110% and 120% water temperature (T_w) and discharge (Q_w) for the inverted hydrograph, with other variables held constant.

4.7.5 Intermittent bank failure

To understand how periodic failures of the thawed layer, which are commonly observed in permafrost environments, might affect bank erosion rates we added a criterion to the model where thawed sediment will be removed whenever a critical thickness (η_{fail}; m) is exceeded

(Figure 4.12). We ran the 1 mm sand and 1 cm gravel models for our base case hydraulics. We maintained a constant 10°C water temperature over 1 day and modeled a range of η_{fail}. Hydraulic conditions in our base case were insufficient to entrain 1 cm gravel, so no erosion occurred except due to bank failure, but flow was sufficient to erode 1 mm sand. We compared model results to a case with no failures for 1mm sand, where the thaw layer developed to a steady-state thickness. For the 1 cm gravel, we compared erosion rates for different water temperatures and failure thresholds.
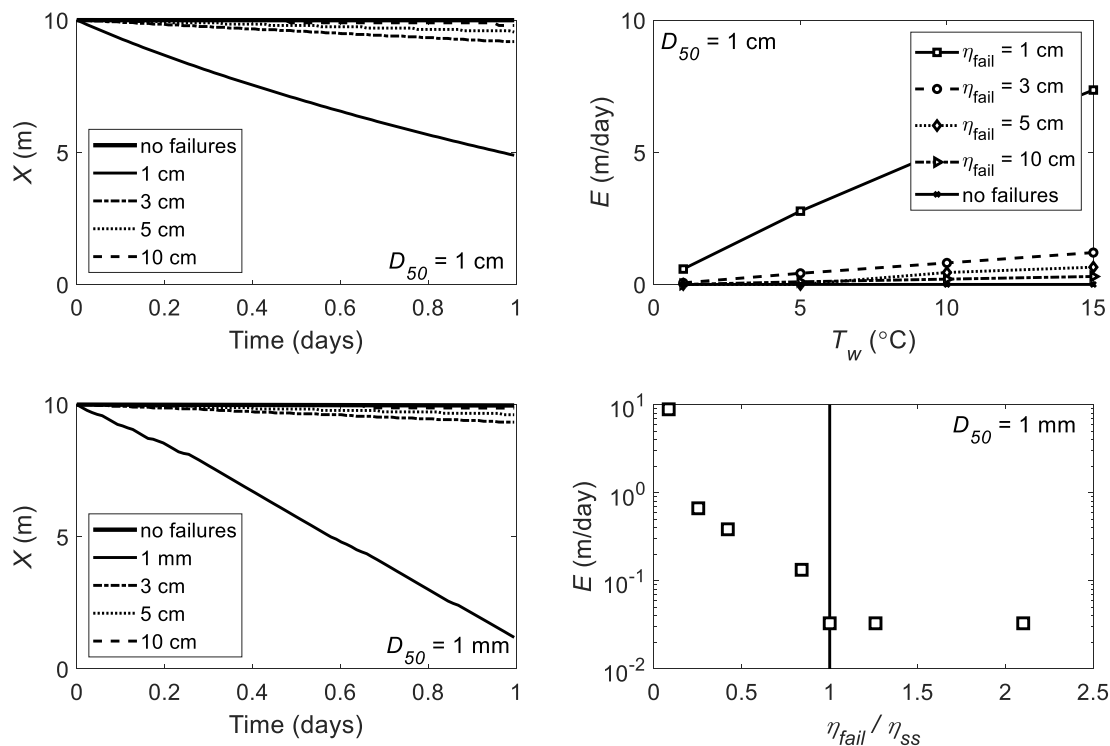
Figure 4.12. Model results with periodic thawed-layer failure. **(a)** Bank front location for immobile 1 cm diameter gravel with 10°C river water models with imposed threshold for failure when the thickness of the thawed layer exceeds 1, 3, 5, and 10 cm, and a case without failure. **(b)** Erosion rates for 1 cm gravel with varying η_{fail} versus water temperature. **(c)** Bank front location for mobile 1 mm coarse sand with 10°C river water models with imposed threshold for failure when the thickness of the thawed layer exceeds 0.1, 3, 5, and 10 cm, plus a case without failure. **(d)** Erosion rates for 1 mm sand with varying ratios of η_{fail}/η_{ss}.

For the 1 cm gravel case, we found that banks with a low threshold of failure for thawed sediment tended to erode very rapidly, while banks with a high failure threshold did not experience any failures and do not erode (Figure 4.12a). For the 1 mm sand case, very slow bank erosion occurred in the absence of failure but bank erosion with failure produced rates orders of magnitude higher that approach 10 m/day (Figure 4.12c). In both cases, as the thawed layer thickened, the bank surface temperature increased, decreasing total heat flux to the bank, and the temperature gradient within the thawed layer decreased. These effects caused a decrease in thaw rate for permafrost in banks with larger η. However, small values

of η_{fail} maintained conditions where permafrost thaw was rapid and the bank rapidly eroded. When η_{fail} was greater than η_{ss}, we saw constant entrainment-limited erosion rates, while a decreasing ratio of η_{fail} / η_{ss} caused a nonlinear increase in erosion rates due to the persistence of a high thermal gradient within the thawed portion of the bank (Figure 4.12d).

Next, we varied water temperature and η_{fail} for the 1 cm gravel case (Figure 4.12b). Higher water temperatures produced faster bank erosion rates for the same relative bank stability (η_{fail} / η_{ss}) due to a higher thermal gradient within the thawed region of the bank. While these banks all experienced sediment entrainment-limited erosion, which was not dependent on water temperature, bank failure frequency was a function of water temperature and therefore provided a mechanism for water temperature-dependent entrainment-limited conditions.

4.8 Discussion

Our 1D mechanistic permafrost riverbank erosion model includes both thermal and mechanical erosion processes, and indicates that a very thin layer of thawed sediment may significantly limit bank erosion rates on most Arctic rivers. Thawed layer thickness is largely set by the thickness of the zone of heat advection into the bank, with coarser materials having thicker layers dominated by advection, in agreement with temperature profiles of river taliks obtained from borehole data (Wankiewicz, 1984). During low flows, when fluid shear is insufficient to entrain sediment, the thaw layer grows through time, which agrees with observations that large rivers may have regions of bank that are perpetually thawed (Laxton & Coates, 2010). To model the case when riverbanks become unstable upon thaw, we imposed a critical thaw layer thickness for bank failure (Figure 4.12). Since warmer water temperature causes the banks to reach this critical thickness more rapidly than cold water temperatures, model results indicate that warmer water temperatures cause more rapid bank erosion rates for smaller critical thicknesses and warmer water temperatures.

Our analysis assumes hydraulically rough banks and homogeneous bank material properties, which are not true in some instances. One shortcoming of our analysis is that riverbank pore water does not freeze uniformly at 0°C, reflecting pore water chemistry (Greenwald et al., 2008; Kokelj & Burn, 2005) as well as the physical chemistry of ice crystallization (Schulson & Duval, 2009). This effect could be accounted for in our current framework by adjusting the fluid temperature of fusion (T_f) and other physical properties to be specific to the pore fluid composition. Our model also does not include sediment cohesion at fine grain sizes through the formulation of the critical Shields number as a function of particle Reynolds number (Vanoni, 2006). While this is a poor assumption for clays such as kaolinite and montmorillonite, it may accurately capture the difficultly in entraining glacial flour and loess, which are abundant in Arctic catchments (Jensen et al., 2016) and have experienced extensive physical but little chemical alteration when they reach a fine grain size. Fine-grained banks may also experience transitional or laminar, instead of hydraulically rough, near-bank fluid flow ($Re_{ks} < 100$), which is expected to decrease the coefficient of heat transfer (equation (4.8)) and thus the rate of bank thaw (Yaglom & Kader, 1974).

Our model provides an explanation for field observations of very rapid riverbank erosion at ice-rich bluffs. Many well-studied field sites are composed of thaw slumps in yedoma, where excess pore ice volume drives rapid transport of sediment into the river (Kokelj et al., 2013; Lantz & Kokelj, 2008; Littlefair et al., 2017; Shakil et al., 2020). Since these banks consist of sediment suspended in a matrix of ice, they are expected to collapse upon thaw, and correlate to model runs with $\eta_{fail} \sim 0$. After episodes of rapid thaw, water drains from the riverbank and the thawed layer collapses, so that when the sediment re-freezes in the winter, it has a lower volume fraction of ice than previously. The lower ice-content, refrozen bank would have higher thaw rates but slower entrainment rates the next summer, providing a negative feedback on riverbank collapse similar to slowing erosion rates observed over multiple field seasons (Shur et al., 2021). Therefore, our model might explain field observations of rapid erosion at single locations (Fuchs et al., 2020; Kanevskiy et al., 2016) yet overall slow rates of permafrost riverbank erosion (Rowland et al., 2019).

Results indicates that both thaw- and entrainment-limited erosion may be sensitive to changes in water temperature and discharge due to climate change. River discharge (Peterson et al., 2002) and water temperature (Liu et al., 2005; Yang & Peterson, 2017) are increasing in response to climate warming. Water temperature affects the rate of heat transfer between the river and the bank, and effects on the sediment entrainment rate can be accounted for using existing theory (Syvitski et al., 2019). River discharge increases flow depth and velocity, and is predicted to cause an increase in both thaw-limited and entrainment-limited bank erosion rates via equations (4.2) and (4.8)). Increases to river discharge will generally enhance the entrainment-limitation while decreases to discharge will promote thaw-limited conditions. Since H and U increase with Q_w and $E_{thaw} \sim U$ while $E_{ent} \sim U^2$, we expect that late-summer floods with warm water temperatures will enhance entrainment-limited conditions. Therefore, late-summer floods must be associated with low water temperatures, such as glacial or pro-glacial lake outburst floods, in order for thaw-limited conditions to occur. Including a threshold for bank failure in our model introduces a new mechanism where entrainment-limited erosion rates increase with water temperature. Therefore, riverbanks the stability of riverbanks after thaw should be a primary control on how much erosion rates should change as the climate warms.

The effects of thaw- versus entrainment-limited erosion should also have a significant influence on Arctic river geochemistry. The value of η sets the dimensions of the potential hyporheic zone and may influence the composition and radiocarbon age of riverine dissolved organic carbon (Walvoord et al., 2012; Zarnetske et al., 2008). The bank erosion rate determines the mass of particulate carbon locally supplied to the river (Beel et al., 2020; Kokelj et al., 2013; Littlefair et al., 2017; Shakil et al., 2020). Organic matter supplied to the river by pore water flow or bank erosion can then be transported downstream (Behnke et al., 2021; McClelland et al., 2016) or oxidized in the river to form greenhouse gases (Striegl et al., 2012). Differences in the rates of bank erosion and hyporheic zone extent with water temperature and discharge may explain spatial variations in dissolved and particulate carbon fluxes and composition that have been detected in Arctic river systems (Koch et al., 2022; Wild et al., 2019).

The recognition that sediment transport processes, and not permafrost thaw, may dominate permafrost riverbank erosion changes the expected river response to global warming. Our results indicate that increases in water temperature will increase bank erosion rates immediately following ice breakup and for banks that are highly unstable upon thaw. Rising permafrost temperatures will not alter bank erosion rates due to the dominance of the latent heat of fusion over the specific heat of permafrost. In contrast, a longer open-water season and higher discharges may significantly increase bank erosion rates, and potentially cause transient channel widening (Ashmore & Church, 2001). Higher magnitude and more frequent extreme floods would cause higher erosion, as well as widespread permafrost thaw across the floodplain, enhancing the dominance of entrainment-limited conditions (Zheng et al., 2019). Finally, rivers continue to thaw permafrost in their floodplains under entrainment-limited conditions, which is likely a significant control on the characteristics and longevity of permafrost as well as groundwater hydrology in Arctic floodplains.

4.9 Conclusions

Field observations and numerical models disagree on the governing processes and rates of permafrost riverbank erosion. To address this knowledge gap, we developed a 1D model that includes bank sediment erosion, heat transfer from the river to the bank, and phase changes within the frozen bank. The model produces three regimes: thaw-limited erosion, entrainment-limited erosion, and periodic thaw-layer failure. Thaw-limited erosion only occurs during winter months and immediately following ice break-up, when water temperatures are very low and riverine sediment transport capacity is very high. When banks become entrainment-limited for much of the summer, the model produces a thin thawed layer that reaches a constant thickness to match bank erosion rates, or grows indefinitely when river flow is insufficient to erode thawed bank sediment. When periodic bank failure occurs, entrainment-limited rates are rapid and remain sensitive to water temperature. We found the model is very sensitive to bank material properties, such as grain size and pore ice content, but relatively insensitive to bank temperature. Higher water temperatures increase rates of thaw-limited and periodic failure driven erosion, while higher discharges increase all erosion mechanisms. A comparison to annual hydrologic data at Stevens Village on the Yukon River suggests that our model produces plausible bank erosion rates over the course of annual water temperature and discharge cycles. This model explains observed patterns of rapid erosion in ice-rich permafrost but slow average rates throughout the Arctic, and predicts that both thaw- and entrainment-limited erosion rates may be sensitive to increases in permafrost river temperature and discharge as the climate warms.

4.10 Acknowledgments

4.11 Data Availability Statement

The scripts to run this model will be posted on Zenodo upon publication. Water discharge and temperature data for the Yukon River at Pilot Station and Stevens Village can be downloaded at https://waterdata.usgs.gov/monitoring-location/15565447/ and https://waterdata.usgs.gov/monitoring-location/15453500/. Soil bulk density and water content data can be downloaded from doi:10.25675/10217/187212. Data for ground temperature are available for site ID US O-82 from the Global Terrestrial Network for Permafrost (GTN-P) Database at http://gtnpdatabase.org/boreholes.

4.12 Supporting Information

The supporting information contains 5 tables summarizing empirical constants (Table 4.S1), input variables (Table 4.S2), and output variables (Table 4.S3) for the permafrost riverbank erosion model. We describe permafrost probe methods (Section 4.12.1) and measurements (Table 4.S4) to assess the seasonal variability of thawed layer thickness for a permafrost riverbank near Huslia, AK. This also contains the locations (Table 4.S5), calculations (Section 4.12.2), and relevant hydrologic and temperature information (Table 4.S6) required to run the model for a compilation of Arctic rivers.

Constants	Symbol	Values	Units
Water ice latent heat of fusion	$L_{f,ice}$	333.55	kJ/kg
Density of water ice	ρ_{ice}	920	kg/m^3
Density of quartz sediment grains	ρ_s	2650	kg/m^3
Density of river water	ρ	1000	kg/m^3
Sediment submerged specific gravity	R	2.65	kg/kg
Specific heat of water ice	$c_{p,ice}$	2093	J/kg/°C
Specific heat of quartz sediment	$c_{p,s}$	730	J/kg/°C
Specific heat of water	$c_{p,w}$	4.184	J/kg/°C
Water ice thermal conductivity	K_{ice}	2.18	W/m/°C
Sediment grain thermal conductivity	K_s	3.00	W/m/°C
Liquid water thermal conductivity	K_w	0.591	W/m/°C
Water thermal diffusivity	α_w	1.32×10^{-7}	m^2/s
Gravitational acceleration	g	9.81	m/s^2
Water kinematic viscosity	ν	1×10^{-6}	m^2/s

Water dynamic viscosity	μ	0.0015	kg/m/s
Coefficient for sediment entrainment equation	M	5×10^{-5}	m/s
Fusion temperature for water ice	T_f	0	°C
Coefficient for effective hydraulic conductivity	a	11.9 to 6695	variable
Exponent for effective hydraulic conductivity	b	1.5 to 1.85	dimensionless
Inverse of von Karman constant	A	1/0.41	dimensionless
Heat transfer coefficient from experiments	α	2.12	dimensionless
Heat transfer coefficient from experiments	β_1	0.05	dimensionless
Heat transfer coefficient from experiments	b_1	0.55	dimensionless
Heat transfer coefficient from experiments	b_2	1/11	dimensionless
Heat transfer coefficient from experiments	C	9.5	dimensionless
Velocity profile exponent in mixing layer	C_1	2	dimensionless
Bed drag coefficient	C_D	1	dimensionless
Empirical thermal diffusion coefficient	D_t	0.12	dimensionless
Empirical coefficient for hydraulic conductivity	a_b	11.9 to 6695	dimensionless
Empirical exponent for hydraulic conductivity	b_b	1.5 to 1.85	dimensionless

Table 4.S1. Empirical constants used in numerical model for permafrost riverbank thaw.

Model input variables	Symbol	Values	Units
Bank median grain size	D_{50}	10^{-5} to 10^{-1}	m
Bed median grain size	$D_{50,bed}$	10^{-4} to 10^{-1}	m
River water surface slope	S	10^{-5} to 10^{-2}	m/m
Permafrost porosity	λ_p	0 to 1	m³/m³
Volume fraction of water ice	V_{ice}	0 to 1	m³/m³
Volume fraction of sediment grains	V_s	0 to 1	m³/m³
River water temperature	T_w	0 to 20	°C
Background permafrost temperature	T_0	-15 to 0	°C
Mean river water flow velocity	U	0 to 3	m/s
Height of roughness elements on bank	H_r	0 to 20	m
Channel width	B	100 to 2890	m
Water discharge	Q_w	Time-variant	m³/s

Table 4.S2. Input parameters for permafrost riverbank erosion model and the range of values observed in natural Arctic rivers from the data compilation.

Model output variables	Symbol	Units
Bulk density of permafrost ice cement	ρ_{ic}	kg/m³
Bulk density of thawed bank	ρ_{ts}	kg/m³
Specific heat of permafrost	$c_{p,ic}$	J/kg/°C
Specific heat of thawed bank	$c_{p,ts}$	J/kg/°C
Permafrost latent heat of fusion	L_f	kJ/kg
Permafrost thermal conductivity	K_{ic}	W/m/°C
Thawed bank thermal conductivity	K_{ts}	W/m/°C

Effective thawed bank thermal conductivity	K_{eff}	W/m/°C
Riverbank thermal diffusivity	α	m²/s
Permafrost thermal diffusivity	α_{ic}	m²/s
Thawed bank thermal diffusivity	α_{ts}	m²/s
Thawed bank hydraulic permeability	k	m²
Thawed bank hydraulic conductivity	K	m/m
Subsurface flow velocity	U_{sub}	m/s
84th percentile bank grain size	D_{84}	m
Characteristic roughness lengthscale	k_s	m
River flow depth	H	m
Relative roughness height	η_1	m/m
Roughness element Reynolds number	h	dimensionless
Bank particle Reynolds number	Re_p	dimensionless
Bank pore water Reynolds number	Re_β	dimensionless
Heat transfer coefficient	C_h	dimensionless
Channel coefficient of friction	$C_{f,tot}$	dimensionless
Bank coefficient of friction	$C_{f,b}$	dimensionless
Bank sediment entrainment rate	E_{ent}	m/s
Permafrost thaw rate	E_{thaw}	m/s
Thaw layer thickness	η	m
Fluid shear velocity	u^*	m/s
Forcheimer coefficient for non-Darcian flow	F	dimensionless
Dimensional Forcheimer ratio	F^*	s²/m²
Shear stress on riverbank	τ_b	Pa
Critical shear stress to entrain riverbank sediment	τ_c	Pa
Bank surface temperature	T_b	°C
Heat flux into permafrost	q_1	J/m²
Heat flux into thawed sediment layer	q_2	J/m²
Heat flux into thawed sediment exchange layer	q_w	J/m²
Thickness of thawed sediment mixing layer	P_1	m
Thickness of thawed sediment diffusive layer	P_2	m
Bank temperature at base of mixing layer	T_p	°C
Temperature at bank surface	T_b	°C

Table 4.S3. Intermediate and output values for permafrost riverbank model.

4.12.1. Permafrost probe measurements

We measured the thickness of the thawed layer formed over the course of the summer on an eroding permafrost riverbank along the Koyukuk River near Huslia, AK. Huslia has a mean annual air temperature of -3.6°C (Daly et al., 2018) and is located in a region of discontinuous permafrost (Obu et al., 2019). We visited Huslia in June and September 2022 to make measurements following ice break-up on May 8, 2022 (Alaska-Pacific River Forecasting

Center, 2023). We measured the thawed layer thickness as horizontal distance to permafrost along a vertical transect and the active layer thickness as the vertical depth to permafrost along a transect on the floodplain ground surface (see Table 4.S4). Measurements were made using a 1 m permafrost probe on June 2, 2022 and a 2 m probe on September 28, 2022 at 65.70167° N and 156.3942° W near the village of Huslia, AK. Multiple measurements at one location were taken within 10 cm of each other to assess reproducibility.

June 2, 2022		September 28, 2022	
Depth in vertical transect (cm)	Horizontal distance to permafrost (cm)	Horizontal transect (m)	Depth to permafrost (cm)
0	>100	1	54
0.8	1	2	51
25	40	3	50
50	73	4	49
75	85	5	50
100	97	5	84
130	88	6	44
150	90.5	6	89
170	0.5	7	50
170	4	7	89
200	98	8	36
250	24	9	36
250	23	10	32
250	23.5	11	30
250	25	12	20
250	39.5	13	2
290	43	14	20
300	67	15	56
350	64.5	16	52
		17	70
		18	81
		19	63
		20	62
		21	64
		22	55
		23	33
		24	19
		25	51
		26	62
		27	150

		28	>210
		29	>210
		30	>210
June 2, 2022		**September 28, 2022**	
Horizontal transect (m)	**Depth to permafrost (cm)**	**Depth in vertical transect (cm)**	**Horizontal distance to permafrost (cm)**
0.00	50	100	54
0.80	15	200	51
1.20	13	300	50
1.60	14	400	49
2.14	12	500	50
2.80	25	600	44
3.50	19	700	50
4.00	9		
4.50	16		
5.00	19		
6.00	7		
7.00	6		
7.00	13.5		

Table 4.S4. Measurements of active layer and thawed layer depth along the Koyukuk River near Huslia, AK.

4.12.2 Permafrost rivers compilation

Implementing the thaw-layer model requires characterizing the bank thermal properties and the channel hydraulics. Here we complied data from previously published field studies and publicly available stream gage data for the purpose of identifying a reasonable range of parameters to run the model. The key variables for the permafrost thermal properties (Section 4.5.3) include the background permafrost temperature (T_0) and the volumetric porosity (λ_p), where we assume that all pore space is filled with ice or water. To characterize channel hydraulics (Sections 4.5.2-4.5.4), the model requires either the mean water velocity (U) and depth (H) or the total water discharge (Q_w), channel slope (S), and the riverbed median grain size ($D_{50,bed}$), used to calculate the total coefficient of friction ($C_{f,tot}$). To characterize heat transfer from the river to the bank (Section 4.5.3), the model requires the bank median grain size (D_{50}) and the water temperature (T_w). In this analysis, we assume that the grain-scale bank roughness sets the rate of heat exchange, but the model can be run assuming other roughness scales are significant.

To evaluate the model behavior for these parameters over the range of modern Arctic Rivers, we compiled instantaneous and long-term data from the following locations where there have been sufficient measurements made to run the model (Table 4.S4). We identified the following locations that span permafrost rivers of varying properties: the Atigun River, Alaska (Scott, 1978) (USGS Gage 15905100); the Peel and Mackenzie Rivers, Northwestern

Territory (Outhet, 1974) (ArcticGRO gage data); the Koyukuk River, Alaska (Douglas et al., 2022) (USGS Gage 15564900); the Lena River, Siberia (Gautier et al., 2018; Liu et al., 2005) (ArcticGRO gage); Colville River, Alaska (Arnborg et al., 1967); Itkillik River, Alaska (Kane et al., 2014; Kanevskiy et al., 2016). The Itkillik River is a tributary of Colville Delta, so we assume that it follows similar seasonal variations in water temperature and discharge to the Colville (Arnborg et al., 1967).

Most of these rivers were missing values for $C_{f,tot}$ and either H, S, or U for the instantaneous discharge datasets (Table 4.S5). Since the model assumes normal flow conditions, we used the balance of flow resistance and momentum under normal flow conditions,

$$C_{f,tot}U^2 = gHS, \tag{4.S1}$$

in conjunction with the Ferguson (2007) variable power equation (VPE),

$$\frac{U}{\sqrt{gHS}} = \frac{a_1^2 + a_2^2(H/k_s)^{5/3}}{a_1^2 a_2^2 (H/k_s)^2}, \tag{4.S2}$$

with a_1=6.5, a_2=2.5, and $k_s = 2.5 \times (2.2 D_{50,bed})$ to solve for the missing variables iteratively (starred values in Table 4.S5). We observed large sand dunes on the bed of the Koyukuk River, so k_s is likely proportional to bedform height and not grain size in equation (4.S2). However, no other papers mention the presence or absence bedforms, so we are unable to satisfactorily partition morphologic drag versus skin friction. Similarly, river deltas are influenced by the backwater effect, so flow acceleration terms may be significant for the Mackenzie and Colville Deltas.

The compiled rivers have a range of characteristics for their instantaneous and time-invariant parameters (Figure 4.S1). The bank grain size ranges over 4 orders of magnitude, from clay to fine pebbles (Figure 4.S1a). Channel bed grain sizes were generally coarser, ranging from silt to coarse pebbles (Figure 4.S1b). The channel slope varies from 5×10^{-5} to 5×10^{-3}, with lowland rivers having lower slopes and upland rivers having steeper slopes (Figure 4.S1c). Flow depth varied significantly, from <1 m to 9 m, but these values do not reflect the cross-sectional average depth (Figure 4.S1d). Similarly, the range of water velocity from 0 to over 2 m/s reflects instantaneous, and not bankfull, velocities (Figure 4.S1e). The bank erosion rates range from 0 to 28 m/yr and represent the total bank erosion rate integrated over the annual hydrograph (Figure 4.S1f).

The background temperature of permafrost did not vary significantly in our compilation, ranging from -6.6 to 0°C (Table 4.S5). As a result, we evaluate the model from 0 to -13°C to span global measured permafrost temperatures in the modern Arctic (Biskaborn et al., 2019; Isaksen et al., 2016).
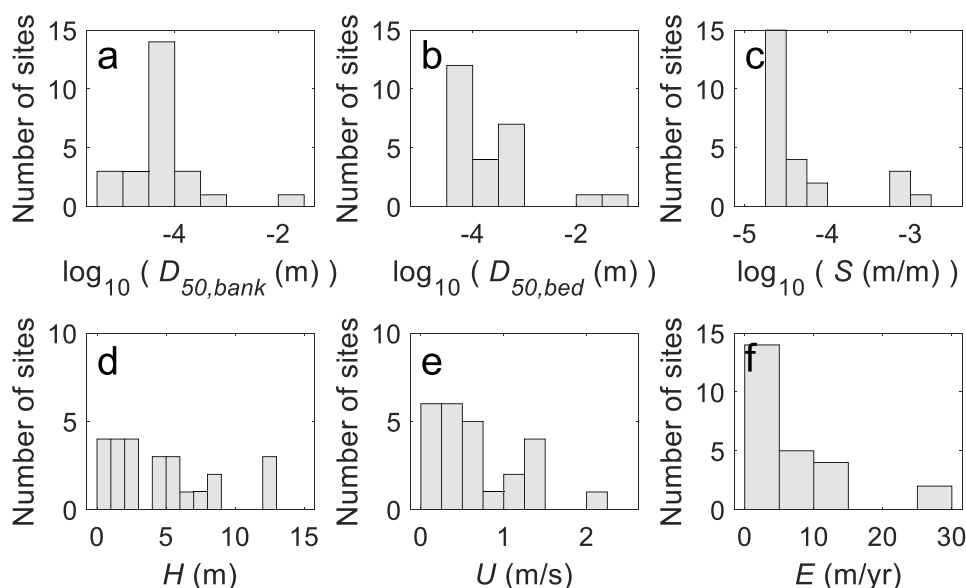
Figure 4.S1. Histograms of model parameters from permafrost rivers. The histograms show the range of compiled riverbank **(a)** median grain size ($D_{50,bank}$; m), **(b)** channel bed median grain size ($D_{50,bed}$; m), **(c)** channel slope (S; m/m), **(d)** water flow depth (H; m), **(e)** water velocity (U; m/s), and **(f)** riverbank erosion rate (E; m/yr).

Our compilation revealed significant variability in water-ice content within single sites. For example, the Colville Delta has water contents in alluvial deposits ranging from 29 to 75 wt% (Stephani et al., 2020). The Itkillik River exhibits a wider range of ice content, from 37 to 100 wt% in yedoma containing ice wedges (Kanevskiy et al., 2016). Therefore, we choose a representative volumetric ice fraction of 80 vol% (58 wt%) and evaluate the model from 0 to 100 vol% ice to span the range commonly observed in alluvial deposits. Evaluating the model over the range of compiled grain sizes, channel slopes, and flow conditions in tandem with globally observed ranges of permafrost temperatures and riverbank ice contents will span the range of terrestrial permafrost riverbank erosion behavior (Table 4.S2).

Site Name	n	Latitude (°N)	Longitude (°E)
Atigun River, Alaska, USA	3	68.4444	-149.3713
Tabaga Gage, Lena River, Russia	1	62.0272	129.7181
Peel and Mackenzie Rivers, Canada	15	67.8780	-134.3325
Koyukuk River, Alaska, USA	3	65.7012	-156.3844
Coleville River, Alaska, USA	4	70.2411	-150.8425
Itkillik River, Alaska, USA	1	68.4383	-150.6878

Table 4.S5. Locations of sites in Arctic rivers data compilation.

Location	U (m/s)	H (m)	B (m)	S (m/m)	T_0 (°C)	$D_{50,bank}$ (m)	$D_{50,bed}$ (m)	$C_{f,tot}$	E (m/yr)
Atigun River (A1)	0.71*	0.57	100+	8.80×10^{-4}	-1.02	2.20×10^{-2}	2.20×10^{-2}	9.7×10^{-3}*	0.687
Atigun River (A2)	1.4*	0.57	100+	8.80×10^{-4}	-1.02	6.25×10^{-5}	4.10×10^{-4}	2.6×10^{-3}*	0.253
Atigun River (A3)	1.4*	0.57	100+	8.80×10^{-4}	-1.02	3.80×10^{-4}	3.80×10^{-4}	2.5×10^{-3}*	0.253
Lena River (Tabaga Gage, 1B)	1.3635	8	2890	2.0×10^{-4}	-2.0	1.20×10^{-4}	3.63×10^{-4}	8.3×10^{-3}*	10
Lena River (Tabaga Gage 1C)	1.3635	8	2890	2.0×10^{-4}	-2.0	2.80×10^{-4}	3.63×10^{-4}	8.3×10^{-3}*	10
Mackenzie River (A)	0.154	0.171*	2070+	2.90×10^{-5}	-1.9	7.00×10^{-5}	6.25×10^{-5}	2.0×10^{-3}*	25.0
Mackenzie River (B)	0.450	0.852*	230+	2.90×10^{-5}	-1.9	7.00×10^{-5}	6.25×10^{-5}	1.2×10^{-3}*	28.0
Mackenzie River (C)	0.410	0.741*	380+	2.90×10^{-5}	-1.9	7.00×10^{-5}	6.25×10^{-5}	1.3×10^{-3}*	6.2
Mackenzie River (D)	0.463	0.889*	210+	2.90×10^{-5}	-1.9	7.00×10^{-5}	6.25×10^{-5}	1.2×10^{-3}*	6.5
Mackenzie River (E)	0.381	0.664*	2550+	2.90×10^{-5}	-1.9	7.00×10^{-5}	6.25×10^{-5}	1.3×10^{-3}*	12.6
Mackenzie River (F)	0.335	0.547*	870+	2.90×10^{-5}	-1.9	7.00×10^{-5}	6.25×10^{-5}	1.4×10^{-3}*	11.8
Mackenzie River (H)	0.153	0.169*	2660+	2.90×10^{-5}	-1.9	7.00×10^{-5}	6.25×10^{-5}	2.1×10^{-3}*	7.0
Mackenzie River (I)	0.390	0.687*	580+	2.90×10^{-5}	-1.9	7.00×10^{-5}	6.25×10^{-5}	1.3×10^{-3}*	7.5
Mackenzie River (J)	0.236	0.324*	240+	2.90×10^{-5}	-1.9	9.00×10^{-5}	6.25×10^{-5}	1.7×10^{-3}*	7.0
Mackenzie River (K)	0.122	0.120*	-	2.90×10^{-5}	-1.9	7.00×10^{-5}	6.25×10^{-5}	2.3×10^{-3}*	4.7
Mackenzie River (N)	0.214	0.279*	220+	2.90×10^{-5}	-1.9	7.00×10^{-5}	6.25×10^{-5}	1.7×10^{-3}*	2.5
Mackenzie River (O)	0.222	0.295*	-	2.90×10^{-5}	-1.9	7.00×10^{-5}	6.25×10^{-5}	1.7×10^{-3}*	1.0
Koyukuk River (sand)	0.8	12.4	175	2.71×10^{-5}	-0.1	1.33×10^{-4}	4.42×10^{-4}	1.4×10^{-3}*	0.5
Koyukuk River (silt)	0.8	12.4	175	2.71×10^{-5}	-0.1	2.67×10^{-5}	4.42×10^{-4}	1.4×10^{-3}*	0.5
Koyukuk River (peat)	0.8	12.4	175	2.71×10^{-5}	-0.1	3.15×10^{-5}	4.42×10^{-4}	1.4×10^{-3}*	0.5
Colville River Delta (I)	1.49	4.6	960	4.0×10^{-4}	-6.6	7.70×10^{-6}	2.00×10^{-4}	8.1×10^{-3}*	1.21
Colville River Delta (II)	1.43	4.1	200	4.3×10^{-4}	-6.6	1.00×10^{-5}	2.00×10^{-4}	8.5×10^{-3}*	1.59

Colville River Delta (IX)	0.7	2	76	2.7×10^{-4}*	-6.6	9.07×10^{-6}	2.00×10^{-4}	1.07×10^{-2}*	3.8
Colville River (X)	0.79	2.2	243	3.0×10^{-4}*	-6.6	9.70×10^{-6}	2.00×10^{-4}	1.04×10^{-2}*	2.2
Itkillik River	2.04	1.49	106	1.27×10^{-3}	-5.1	3.52×10^{-5}	6.5×10^{-2}	4.5×10^{-3}	3.3

*solved iteratively using equations (4.S1) and (4.S2)

[+]not reported in sources, top width measured in Google Earth at reported study sites using 1985 Landsat imagery

Table 4.S6. Data compilation of hydraulic and thermal parameters necessary to run our numerical model for Arctic rivers in permafrost regions.
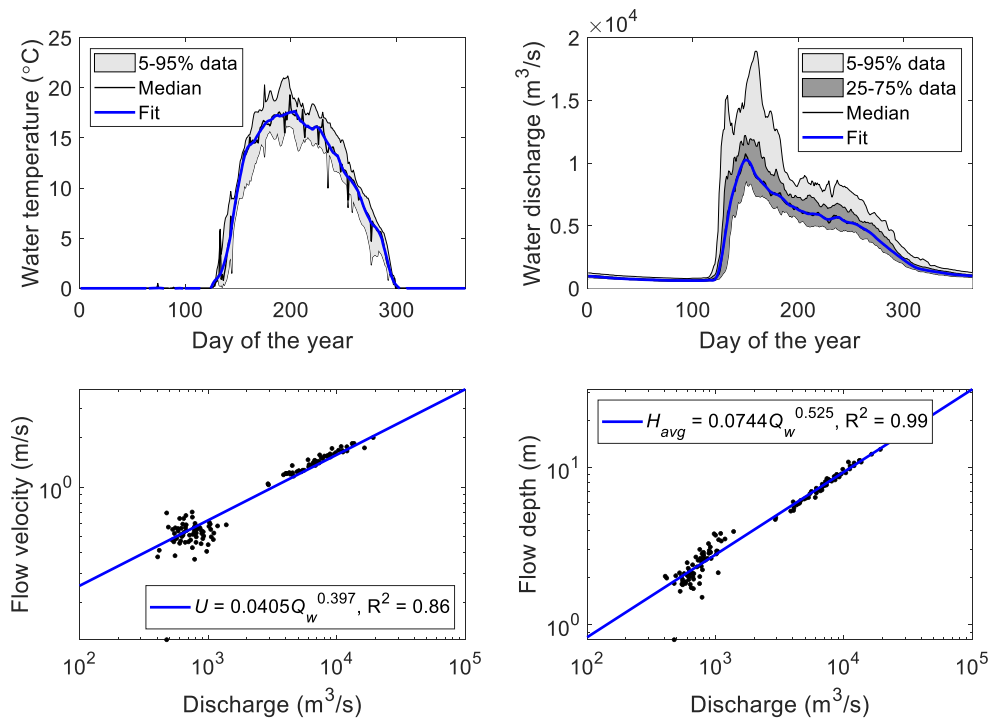
Figure 4.S2. (a) Daily average water temperature for Pilot Station (1976-2022) and Stevens Village (1970-2005). The 5% to 95% range of measurements (gray shading), the daily median (black line), and a smoothed curve produced using a Savitsky-Golay filter (21-day window, 3rd degree polynomial) are plotted versus day of the calendar year. **(b)** Daily average discharge for Stevens Village (USGS gage 15453500) from 1976-2022 versus day of the year. The 5-95% and 25-75% data ranges are shaded in gray, the moving median traced in black, and the blue line shows data smoother using a Savitsky-Golay filter (21-day window, 3rd degree polynomial). **(c)** Field measurements of water discharge and mean velocity at Stevens Village (black dots) and power law fit to data (blue line). **(d)** Field measurements of water discharge and temperature at Stevens Village (black dots) and power law fit to data (blue line).

C h a p t e r   5

IMPACT OF RIVER CHANNEL LATERAL
MIGRATION ON MICROBIAL
COMMUNITIES ACROSS A
DISCONTINUOUS PERMAFROST
FLOODPLAIN

5.1 Abstract

Permafrost soils store approximately twice the amount of carbon currently present in Earth's atmosphere and are acutely impacted by climate change due to the polar amplification of increasing global temperature. Many organic-rich permafrost sediments are located on large river floodplains, where river channel migration periodically erodes and redeposits the upper tens of meters of sediment. Channel migration exerts a first-order control on the geographic distribution of permafrost and floodplain stratigraphy and thus may affect microbial habitats. To examine how river channel migration in discontinuous permafrost environments affects microbial community composition, we used amplicon sequencing of the 16S rRNA gene on sediment samples from floodplain cores and exposed riverbanks along the Koyukuk River, a large tributary of the Yukon River in west-central Alaska. Microbial communities are sensitive to permafrost thaw: communities found in deep samples thawed by the river closely resembled near-surface active-layer communities in non-metric multidimensional scaling analyses but did not resemble floodplain permafrost communities at the same depth. Microbial communities also displayed lower diversity and evenness in permafrost than in both the active layer and permafrost-free point bars recently deposited by river channel migration. Taxonomic assignments based on 16S and quantitative PCR for the methyl coenzyme M reductase functional gene demonstrated that methanogens and methanotrophs are abundant in older permafrost-bearing deposits but not in younger, nonpermafrost point bar deposits. The results suggested that river migration, which regulates the distribution of permafrost, also modulates the distribution of microbes potentially capable of producing and consuming methane on the Koyukuk River floodplain.

5.2 Importance

Arctic lowlands contain large quantities of soil organic carbon that is currently sequestered in permafrost. With rising temperatures, permafrost thaw may allow this carbon to be consumed by microbial communities and released to the atmosphere as carbon dioxide or methane. We used gene sequencing to determine the microbial communities present in the

floodplain of a river running through discontinuous permafrost. We found that the river's lateral movement across its floodplain influences the occurrence of certain microbial communities—in particular, methane-cycling microbes were present on the older, permafrost-bearing eroding riverbank but absent on the newly deposited river bars. Riverbank sediment had microbial communities more similar to those of the floodplain active-layer samples than permafrost samples from the same depth. Therefore, spatial patterns of river migration influence the distribution of microbial taxa relevant to the warming Arctic climate.

5.3 Introduction

Permafrost environments cover 24% of land area in the Northern Hemisphere and contain significant amounts of organic carbon in soil and sedimentary deposits (Schuur et al., 2015; Zhang et al., 1999). This organic carbon (OC) has been largely isolated from microbial consumption, in some cases for thousands of years, due to low subsurface temperatures and ice-cemented sediment pore spaces (Jansson & Taş, 2014). Currently, polar amplification of increases in global air temperature is causing rapid permafrost thaw that exposes previously sequestered organic carbon stores to greater rates of microbial degradation (Serreze & Barry, 2011). The upper "active layer" of Arctic soils thaws each summer, in contrast to underlying permafrost, i.e., ground that has remained below 0°C for at least 2 years. As the active layer deepens interannually across the Arctic due to higher temperatures, labile OC becomes available for respiration by permafrost microbial communities, and active-layer microbes may penetrate deeper soil horizons. This soil carbon reservoir can be released to the atmosphere as methane (CH_4) or carbon dioxide (CO_2) or remain sequestered in Arctic sediments, depending on the affinities and activities of microbes present in permafrost environments (Schädel et al., 2016).

Predicting microbial responses to permafrost thaw requires understanding changes in soil microbiomes with warming over decadal timescales within heterogeneous landscapes. Most understanding of permafrost microbial activity comes from laboratory incubation studies simulating deepening of the active layer. Previous work documented an initial spike in CO_2 emissions in the days following permafrost thaw, with peak CH_4 emissions occurring years after thaw (Knoblauch et al., 2013; Monteux et al., 2018; Schädel et al., 2016). However, incubation studies range widely in their predictions of CO_2-C equivalent emissions, primarily due to challenges in mapping results from laboratory incubations to the three-dimensional structure of landscapes (Knoblauch et al., 2018; Monteux et al., 2018). Furthermore, understanding the vertical structure of permafrost microbiomes requires time-integrated tracking of the depths of the active layer, water table, and seasonal frost, all of which may generate vertical discontinuities in microbial community composition (Barbier et al., 2012; Zona et al., 2016).

In addition to vertical variations in soil structure and microbial community, permafrost landscapes are laterally heterogeneous (Treat et al., 2018). Previous work correlating microbiome and landform heterogeneity focused on variations in soil saturation of ice wedge polygons near Barrow, AK (Taş et al., 2018), and in Stordalen Mire, Sweden (Kuhn et al.,

2018; Liebner et al., 2015; McCalley et al., 2014; Mondav et al., 2014). However, many organic-matter-rich permafrost deposits are located in the floodplains of large rivers, where fluvial processes control the transport of carbon and sediment and the resulting architecture of the deposits (Lininger & Wohl, 2019; Torres et al., 2017, 2020). In particular, river channel migration may introduce additional variability to the permafrost soil microbiome by eroding the active layer and upper tens of meters of underlying permafrost and by building new deposits elsewhere on the floodplain (Shur & Jorgenson, 2007).

Arctic rivers can migrate laterally by meters per year (Rowland et al., 2019), and river migration controls spatial patterns of grain size, surface water in lakes, and deposit age across floodplains (Mann et al., 1995). Meandering streams erode previous river channel deposits on the outside of bends in their sinuous channel paths, forming a steep cutbank (Fig. 5.1E). In locations with permafrost, the river must first thaw its cutbanks before being able to erode the thawed sediment (Costard et al., 2003). Most bank thaw and erosion occur during the spring snowmelt flood following ice breakup, which removes unconsolidated sediment and exposes permafrost to thawing by the river (Costard et al., 2014). At the same time that cutbanks are eroding, the river deposits sediment on the inside of bends, forming shallowly sloping point bars and maintaining a roughly constant channel width (Fig. 5.1C to E). These erosion and depositional processes gradually increase curvature until the channel eventually cuts itself off and subsequently begins the process anew. Point bar deposits display systematic, predictable trends in grain size: coarser sand or gravel occurs at depth, reflecting the size of sediment transported along the bed of the river, while deposits closer to the surface of the floodplain contain fine sand, silt and clay transported in the upper portion of the river water column (Miall, 2013).

In this study, we examined microbial community variation throughout various floodplain deposits of the Koyukuk River—a major tributary of the Yukon River that runs through a floodplain underlain by discontinuous permafrost (Fig. 5.1A). The river is thawing and eroding permafrost along cutbanks exposed at the outside of its bends and depositing sediment on its inner bends without permafrost, generating a juxtaposition of permafrost, active-layer (including laterally thawed sediment on the riverbanks), and nonpermafrost environments with the same local climate (Fig. 5.1E, with scroll bars highlighted and direction of river migration indicated). Here, we compared the microbial community compositions of sediments from different landforms across the river floodplain to see if newly built, unfrozen point bar deposits contained a microbial community similar to that of their opposing, eroding permafrost cutbanks (Fig. 5.1B).
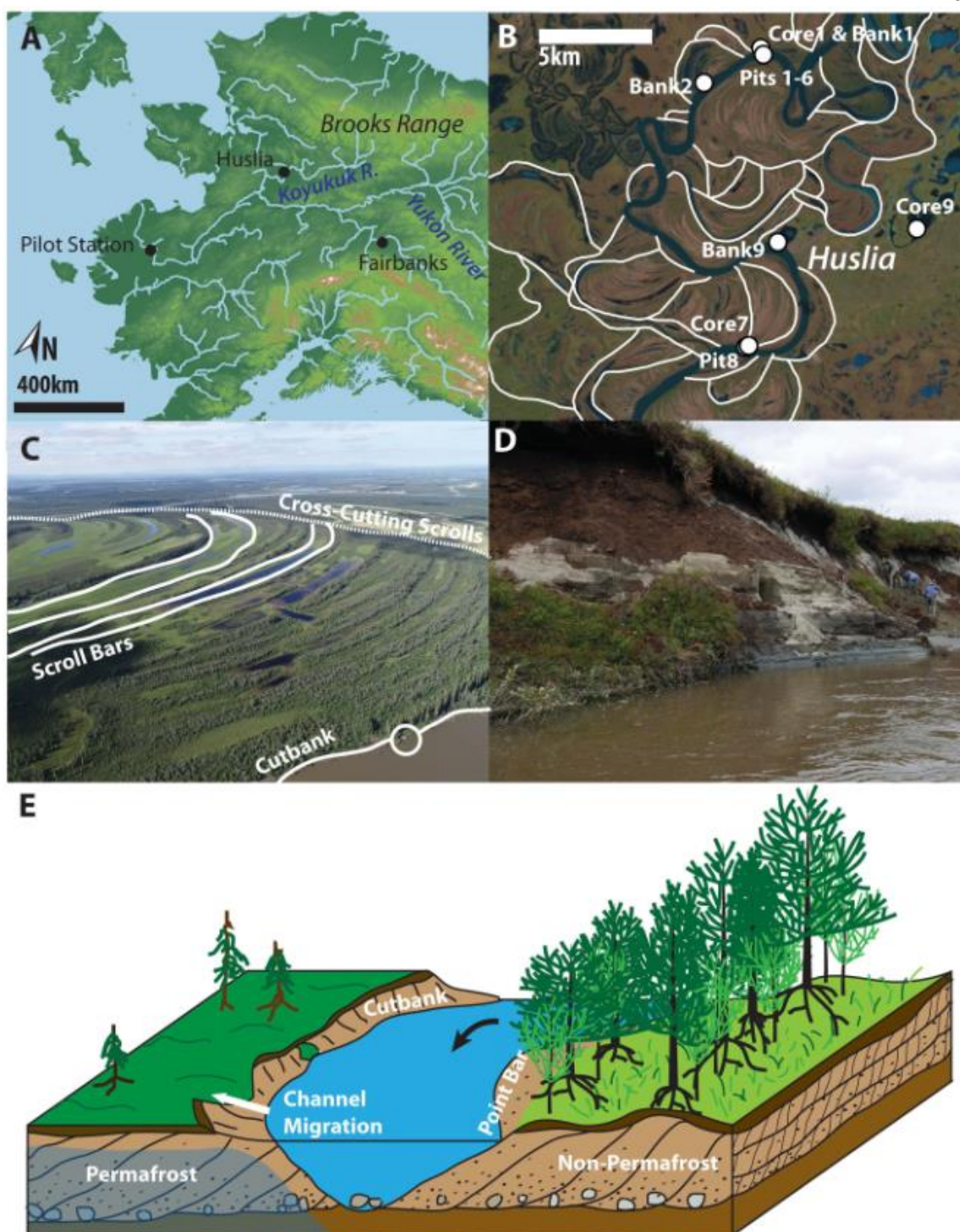
Figure 5.1 Sample site context and field photos of the Koyukuk River floodplain near Huslia, Alaska. **(a)** Map of Alaska, with the study location near the village of Huslia on the Koyukuk River, a major tributary of the Yukon River. Base map generated in QGIS 3.4 using USGS GTOPO30 30 arc-second digital elevation model (Earth Resources Observation And Science (EROS) Center, 2017) and the HydroSHEDS 15 arc-second Arctic regional river shapefile

(Lehner et al., 2008) projected in WGS 84/NSIDC Sea Ice Polar Stereographic North. **(b)** Satellite imagery of the Koyukuk Flats floodplain marked with sampling locations and contacts between scroll bar complexes that illustrate cross-cutting relationships indicating their relative age. Core 1 was sampled approximately 10 m from the river cutbank, while bank 1 was sampled at the cutbank. Note the abundant scroll bar complexes that trace out past locations of the river channel as it migrated across the floodplain. **(c)** Oblique UAV photograph taken at 243 m above ground level of a meander bend on the Koyukuk River, with the boat circled for scale and water flowing away from the viewer. Unfrozen sediment is deposited on the sandy point bar and then becomes vegetated in alternating grass lake troughs and elevated, forested scrolls. **(d)** Field photo of permafrost river cutbank at sampling location bank 9, with undercut peat deposits over permafrost and a thick apron of thawed sediment containing slump blocks armoring the bank. **(e)** Schematic of river channel migration, with the river eroding an outer cutbank composed of former point bar deposits while depositing new sediment on the point bar on the right. The river flows out of the page (flow direction shown by black arrow), constructing cross-bedded strata in the point bar deposits that are coarser at the base of the channel and fine upwards. The river is migrating to the left (white arrow), eroding permafrost deposits (with permafrost shaded in blue and the active layer near the surface on the floodplain and the channel bank) with peat and black spruce vegetation, while the point bar consists of scrolls with ridges containing white spruce and deciduous trees alternating with troughs containing grasses.

5.4 Materials and Methods

5.4.1 Field site

The Koyukuk River is a major tributary of the Yukon River and runs south from its headwaters in the Brooks Range, meandering through discontinuous permafrost in the west-central Alaska lowlands (Fig. 5.1A) (Nowacki et al., 2003). The region had an arid climate during the last ice age and was unglaciated, instead hosting a more extensive predecessor of the modern Nogahabara dune field (Barclay et al., 2009). In the present day, permafrost typically underlies black spruce, birch-ericaceous shrubs, and tussock sedge bogs in wet soils with thick upper strata of peat that can extend more than 1 m below the surface. Nonpermafrost areas contain denser stands of white spruce, balsam poplar, alder, and willow trees in well-drained locations and form wet sedge meadows in saturated soils (Nowacki et al., 2003). The vegetation on the Koyukuk floodplain highlights the topography of successive abandoned levees known as scroll bars (Mason & Mohrig, 2019), with trees growing on the ridges and grasses and moss occupying the troughs between successive levees (Fig. 5.1C). The floodplain contains numerous lakes, and soils are frequently saturated. The region experiences wildfires with an approximately 180-year recurrence interval, and microbial communities in the underlying deposits have been potentially impacted by fires through combustion of upper-soil organic horizons and a temporary increase in active-layer thickness (O'Donnell et al., 2012).

Our field sampling centered on the Koyukuk River floodplain near the village of Huslia (Fig. 5.1A). Huslia has a mean annual temperature of -3.6°C and mean annual precipitation of 31

cm/year rainfall or snow water equivalent, measured from 1981 to 2010 (Daly et al., 2015, 2018). Analysis of Landsat imagery indicated that the Koyukuk channel migrates at rates up to 11 m/year, with average rates of 0.53 m/year in the reach indicated in Fig. 5.1B (Rowland et al., 2019). The highest erosion rates occurred at the apices of the more tightly curved meander bends.

5.4.2 Field sampling

We collected samples on the Koyukuk River floodplain near Huslia, AK, in June and July of 2018 (Fig. 5.1A). During sampling, we measured a mean thaw depth of approximately 0.75 m, with a range from 0.40 m to over 1.00 m, based on cores and surveys with a 1-m-long permafrost probe. We classified samples taken from cores as permafrost versus seasonal frost by the presence of ice cement and frozen material without thawed intervals at depths greater than 1 m, in contrast to observed intervals of seasonal frost 0.2 m thick at a 2-m depth that did not contain ice cement and had thawed sediment both above and below them.

Samples of channel banks and shallow unfrozen sediment were collected using a hand trowel (bank 1, bank 2, and bank 9 samples, collected from cutbanks; pit 1, pit 2, pit 5, pit 6, and pit 8 samples, collected on active point bars), deep unfrozen cores were collected using a hand auger (core 7), and frozen cores were collected using a gas-powered US Snow, Ice and Permafrost Research Establishment (SIPRE) corer and split in the field on a plastic tarp using a hacksaw (core 1 and core 9 samples). Sample sites were chosen to include floodplain areas with different relative ages, which were defined based on cross-cutting relationships between scroll bar sets in aerial images (Fig. 5.1B and C). Scroll bars are levees abandoned through channel lateral migration that tend to record the approximate location of the river inner bank through time, though a single scroll develops over multiple flood events and does not record a single instance of formation (Fig. 5.1E) (Miall, 2013). In contrast, to compare microbial communities within a single scroll bar complex, pits 1, 2, 5, and 6 were sampled along a transect perpendicular to the river centerline, extending from the point bar. Sampling locations were chosen to include permafrost and unfrozen deposits, as well as material from the riverbank and floodplain spanning the youngest (PB1 and PB2) to oldest (core 9) mappable units on the floodplain within constraints required for access by boat. Sample collection extended up to a 4-m depth, and sampling depths were selected after characterizing the stratigraphic section to span the grain size and sedimentological units present at each location (Table 5.3). Nitrile gloves were worn during sample collection, and sampling implements were rinsed with deionized water between samples. Samples were refrigerated in coolers in the field and transferred to an ice chest in the evening, before being flown back to the laboratory in coolers and stored in a cold room at 215°C. The core 1 samples showed signs of partial thaw during transport from the field; we estimate that the samples were potentially unfrozen for up to about 8 h.

5.4.3 Deposit characteristics

Each sample was dried in precombusted Al foil at 55 to 60°C, then gently homogenized in a mortar and pestle, and subsampled using a riffle splitter. Prior to grain size analysis, samples

were treated to remove carbonate and organic material (Gee & Or, 2002). A sample split was decarbonated in 1 M HCl in a sterile polypropylene Falcon tube, centrifuged for 15 min at 4,000 rpm, and then decanted by hand. Each sample was then rinsed twice with 45 ml of deionized (DI) H2O, centrifuged, and decanted before redrying of the Falcon tubes in the oven at 55 to 60°C. To remove organic matter, each sample was transferred to a Pyrex beaker sitting at 85°C on a hot plate and treated with 20 ml of 30% H_2O_2 until oxidation reactions ceased (based on visual inspection of bubbling). Larger, floating organic matter was removed using a microspatula. After removal of organic matter, each sample was transferred back into its original Falcon tube and rinsed three times with centrifuging and decanting before being dried in the oven. Sediment grain size distribution was measured using laser diffraction. DI water and Calgon were added to each sample to rehydrate and prevent flocking; clumps of sediment were broken up by sonicating each sample for 3 min. The samples were then split while wet and run for grain size on a Malvern Mastersizer 2000, calibrated using a laboratory silica carbide standard. Replicate analysis of the silica carbide standard yielded a median grain diameter (D_{50}), of 13.184 ± 0.105 mm.

Total organic carbon (TOC), stable carbon isotope ratios, and total nitrogen (TN) were measured from dried sample splits. Approximately 3 mg of each sample was weighed out into a silver capsule. The sample was acidified by fumigation with HCl, and then carbon and nitrogen content and carbon stable isotopes were measured on a Costech elemental analyzer coupled to a MAT 253 isotope ratio mass spectrometer (IRMS). Isotope ratios ($R = {}^{13}C/{}^{12}C$) are reported in standard notation relative to Vienna Pee Dee Belemnite (VPDB) ($\delta^{13}C = (R_{sample}/R_{VPDB}) - 1$, reported in per mille). The measurements were calibrated using laboratory standards of peach leaves (1570a; TOC = 44.65%, measured at $44.33 \pm 0.96\%$; $\delta^{13}C = -25.95‰$, measured at $-26.13 \pm 0.08‰$; TN = 2.83%, measured at $3.31 \pm 1.27\%$), urea (Eurovector; TOC = 20.00% measured at $17.98 \pm 0.37\%$; TN = 46.65% measured at $45.88 \pm 0.88\%$) and 2,5-bis(5-tert-butyl-2-benzo-oxazol-2-yl) thiophene (BBOT; Eurovector; TOC = 72.53%, measured at $69.59 \pm 2.05\%$; $\delta^{13}C = -26.6‰$, measured at $-26.6 \pm 0.01‰$; TN = 6.51%, measured at $6.82 \pm 0.24\%$) for TOC and TN and cellulose (IAEA-C3; $\delta^{13}C = -24.91‰$, measured at $-24.82 \pm 0.06‰$), sucrose (IAEA-C6; $\delta^{13}C = -10.8‰$, measured at $-10.7 \pm 0.03‰$), and oxalic acid (IAEA-C8; $\delta^{13}C = -18.3‰$, measured at $-18.5 \pm 0.06‰$) for C stable isotopes. Measured blanks were below peak detection limit.

Table 5.1 Sample location metadata, with median grain size measured using laser diffraction.

Sample	Permafrost Classification	Depth (cm)	Median Grain Size (μm)	Sediment Class	Landform
Pit1-1	Non-Permafrost	1	-	silt*	Point Bar
Pit2-10	Non-Permafrost	10	70.664	sand	Point Bar
Pit5-20	Non-Permafrost	20	24.262	silt	Point Bar
Pit6-0	Non-Permafrost	surface	-	silt*	Point Bar
Pit6-60	Non-Permafrost	60	90.390	sand	Point Bar

Pit8-40	Non-Permafrost	40	32.250	silt	Point Bar
Core7-0-5	Non-Permafrost	2	17.669	topsoil	Floodplain
Core7-85-95	Non-Permafrost	90	56.611	silt	Floodplain
Core7-390-400	Non-Permafrost	395	57.561	silt	Floodplain
Bank2-10	Non-Permafrost	10	33.413	silt	Bank
Bank2-230	Non-Permafrost	230	111.183	sand	Bank
Bank1-Peat	Active Layer	35	9.139	peat	Bank
Bank1-120	Active Layer	120	10.685	silt	Bank
Core1-22-28	Active Layer	25	10.101	silt	Floodplain
Core1-105-111	Permafrost	108	10.718	silt	Floodplain
Bank9-Peat	Active Layer	75	47.659	peat	Bank
Bank9-220	Active Layer	200	207.325	sand	Bank
Bank9-350	Active Layer	330	154.874	sand	Bank
Bank9-510	Active Layer	490	52.863	silt	Bank
Core9-0	Active Layer	surface	-	peat*	Floodplain
Core9-33-38	Active Layer	35	51.129	peat	Floodplain
Core9-44-46-R1	Active Layer	45	-	peat*	Floodplain
Core9-44-46-R2	Active Layer	45	-	peat*	Floodplain
Core9-44-46-R3	Active Layer	45	-	peat*	Floodplain
Core9-58-67	Permafrost	63	-	peat*	Floodplain
Core9-75-83	Permafrost	79	-	peat*	Floodplain
Core9-90-97	Permafrost	95	16.947	peat	Floodplain
Core9-109-115-R1	Permafrost	112	-	peat*	Floodplain
Core9-109-115-R2	Permafrost	112	-	peat*	Floodplain
Core9-109-115-R3	Permafrost	112	-	peat*	Floodplain
Core9-123-130	Permafrost	127	-	peat*	Floodplain
Core9-130-137	Permafrost	134	-	silt*	Floodplain
Core9-169-174	Permafrost	172	28.044	silt	Floodplain

*sediment class based on field observations, grain size not measured using laser diffraction

5.4.4 DNA extraction

To characterize variations in microbial community across the Koyukuk floodplain, small subsamples were collected for DNA extraction after bulk samples were thawed overnight at 4°C and before core homogenization for geochemistry measurements. To assess microbial community variability within a single core, evaluate sequencing reproducibility, and assess the potential for contamination during field sampling, multiple subsamples were collected from the same 1-cm interval within core 9. For each sample, ~250 mg of sediment was bead beaten in a DNA stabilization buffer (DNA/RNA Shield in BashingBead lysis tubes; Zymo) to dislodge and lyse microbial cells associated with the sediment. Samples were frozen for up to 6 weeks between bead beating and DNA extraction. Upon thawing, DNA was extracted from the lysate using a soil/fecal DNA miniprep kit (Zymo). Procedural blanks were run alongside the samples to characterize contamination during DNA extraction and amplification.

5.4.5 Amplification and sequencing

A segment of the V4-to-V5 hypervariable region of the 16S rRNA gene was amplified by PCR using archaeal/bacterial primers 515f and 926r (Parada et al., 2016), with Illumina adapters on the 59 ends. PCRs were set up in 15-ml volumes with Q5 Hot Start high-fidelity 2× master mix (New England Biolabs), with annealing at 54°C and 30 cycles. Selected samples (Core9-44-46-R1, Core9-44-46-R3, Core9-58-67, Core9-75-83, Core9-109-115-R1, Core9-109-115-R2, and Core9-109-115-R3) were diluted 10× with MilliQ water before amplification after an initial amplification generated faint bands during PCR amplification. A 2.5-ml portion of each product was barcoded with Illumina Nextera XT index 2 primers that include unique 8-bp barcodes (P5 59-AATGATACGGCGACCACCG-AGATCTACACXXXXXXXXTCGTCGGCAGCGTC-39 and P7 59-CAAGCAGAAG-ACGGCATACGAGATXXXXXXXXGTCTCGTGGGCTCGG-39). PCR amplification with barcoded primers was conducted in 25-ml reactions with annealing at 66°C and 10 cycles. Barcoded products were purified using a Millipore-Sigma MultiScreen plate with vacuum manifold and quantified using the Thermo Fisher Scientific QuantIT PicoGreen double-stranded DNA (dsDNA) assay kit on the Bio-Rad CFX96 Touch real-time PCR detection system. Barcoded samples were combined in equimolar amounts in a single tube and purified with a Qiagen PCR purification kit before submission to Laragen for 2×250-bp paired-end analysis on Illumina's MiSeq platform.

5.4.6 qPCR

Quantitative real-time PCR (qPCR) was conducted on samples from core 9 and core 7 to examine the presence and abundance of methyl-coenzyme M reductase (MCR), encoded by a functional marker gene commonly used to assess methane cycling in environmental samples (Morris et al., 2014; Zeleke et al., 2013). Quantitative PCRs were conducted in 10 ml volumes with iTaq universal SYBR green supermix (Bio-Rad), using the MCR a-subunit (*mcrA*) primers ME1 and ME2 (Hales et al., 1996), with parallel reactions using the 16S primers described above. Reactions were run in triplicate in a CFX96 real-time PCR detection system (Bio-Rad), with an initial denaturation step of 3 min followed by 39 cycles

of 10 s denaturation at 95°C and 30 s annealing/extension at 55°C. Fluorescence readout was measured following each cycle, and the cycle at which the target gene crossed the threshold of a detectable amplification curve (C_q) was determined using the CFX Manager software (Bio-Rad). C_q values were normalized to negative controls for each target gene ($\Delta C_q = C_{q\_neg} - C_{q\_sample}$), and *mcrA* was normalized to 16S ($\Delta C_{q\_MCR}/\Delta C_{q\_16S}$).

5.4.7 Data processing

Sequence data were processed using QIIME version 1.8.0 (Caporaso et al., 2010) following a previously published protocol (Mason et al., 2015). Raw sequence pairs were joined and quality trimmed using the default parameters in QIIME. Sequences were clustered into de novo operational taxonomic units (OTUs) with 97% similarity using the UCLUST open reference clustering protocol. Clustering sequences using the same protocol at 99% similarity did not significantly change OTU assignments or the main results of our analysis. The most abundant sequence was chosen as representative for each de novo OTU (Edgar, 2010). Taxonomic identification for each representative sequence was assigned using the Silva-119 database (Quast et al., 2013). Tables of both absolute and relative abundance were generated for each sample. To further interrogate taxonomy of certain OTUs, we compared their representative sequences against the National Institutes of Health (NIH) BLASTn database using a standard nucleotide BLAST for highly similar sequences using the Megablast algorithm on 24 September 2019.

Before analysis of microbial community trends across environment and depth, the de novo OTUs were singleton filtered, and unassigned and eukaryotic OTUs were removed. In addition, OTUs with over 50 reads in each respective extraction and amplification blank were removed. Nonmetric multidimensional scaling (NMDS) plots were constructed using the vegan ecology package in RStudio for a Bray dissimilarity matrix calculated based on the square root of taxon abundance. NMDS plots were generated by rank ordering n OTUs present in different samples and projecting the samples on the plane in n-dimensional space defined by the two vectors accounting for most of the variation in the sample set. The OTU vectors on each NMDS plot were extracted using the envfit function from vegan, run for 99,999 permutations. We plotted the NMDS with vectors of de novo OTUs with *p* values less than 10^{-5}.

Alpha diversity calculations (observed OTUs, Shannon diversity index, Chao 1, Fisher's alpha, Simpson's index, and Simpson's evenness) were carried out in QIIME1.8.0 (alpha_diversity.py), on datasets rarefied by random subsampling to a consistent depth (single_rarefaction.py). Figures and results presented used data sets rarefied to 4,500 counts (5 permafrost, 11 active-layer, and 7 nonpermafrost samples), but a similar pattern was obtained by rarefying to 1,000 counts (10 permafrost, 14 active-layer, and 9 nonpermafrost samples). The diversity metrics calculated using data sets rarefied to 4,500 counts were compared to soil chemistry and sampling location metadata using scaled principal-component analysis (sPCA) in Matlab 2018b.

Table 5.2. Diversity metrics for the 16S amplication data, rarefied to 4500 reads.

Sample	Observed OTUs	Shannon Diversity Index	Chao 1	Fisher's Alpha	Simpson's Index	Simpson's Evenness
Non-Permafrost						
Pit2-10	2686	11.129	3,579	2,808	0.9992	0.4874
Pit5-20	2720	11.006	4,894	2,910	0.9991	0.4050
Pit6-60	2552	10.599	5,820	2,444	0.9964	0.1093
Pit8-40	2777	11.018	6,275	3,090	0.9991	0.4158
Core7-0-5	2099	10.239	3,102	1,531	0.9973	0.1739
Core7-85-95	1573	8.960	3,178	859	0.9795	0.0310
Core7-390-400	1032	8.505	1,848	419	0.9932	0.1421
Active Layer						
Bank2-10	2977	11.260	5,887	3,835	0.9994	0.5849
Bank2-230	2157	9.989	4,619	1,626	0.9900	0.0461
Bank9-Peat	877	6.225	1,901	325	0.9122	0.0130
Bank9-220	1656	9.662	3,646	946	0.9939	0.0989
Bank9-350	2215	9.141	4,477	1,727	0.9569	0.0105
Bank9-510	1010	7.469	1,955	405	0.9686	0.0316
Bank1-Peat	2171	10.277	3,422	1,650	0.9973	0.1683
Bank1-120	2308	10.209	7,344	1,901	0.9977	0.1850
Core1-22-28	2352	10.529	3,894	1,989	0.9981	0.2201
Core9-33-38	1759	9.055	5,969	1,063	0.9938	0.0913
Core9-44-46-R1	1474	8.807	2,965	763	0.9895	0.0648
Permafrost						
Core1-105-111	678	5.606	1,674	222	0.9016	0.0150

Core9-58-67	1099	7.470	1,722	464	0.9410	0.0154
Core9-90-97	2059	9.466	5,570	1,468	0.9915	0.0573
Core9-109-115-R2	1268	7.596	3,417	587	0.9631	0.0214
Core9-169-174	1364	7.786	3,892	666	0.9724	0.0265

This sequencing approach does not distinguish active cells from dead or extracellular DNA and in some examples has been shown to underestimate the abundance of certain taxa and functional groups, particularly Deltaproteobacteria and Firmicutes (Coolen & Orsi, 2015; Mackelprang et al., 2016). Fully characterizing microbial activity and absolute abundance under present and changing climatic conditions requires qPCR and live/dead assays from incubations in addition to *in situ* measurements of redox conditions and gas fluxes (Burkert et al., 2019; Crevecoeur et al., 2017; Liebner et al., 2015). However, recent work quantifying the abundance of live, dead, and dormant cells across a permafrost chronosequence indicated that removal of DNA from dead cells did not significantly change taxonomic relative abundance down to the family level, despite a significant decrease in 16S rRNA gene reads after treatment with increasing permafrost age (Burkert et al., 2019). Our field sampling also captured a snapshot of the landscape before peak thaw in late summer and thus did not address potential seasonal changes in the microbial communities. Based on previous work on monthly variation seen by 16S sequencing of permafrost on Svalbard, we may have overestimated the abundance of Cyanobacteria, candidate division AD3 organisms, and Alphaproteobacteria, but other taxa are expected to exhibit little seasonal variation (Schostag et al., 2015).

5.4.8 Data availability

All sequences are available at NCBI Sequence Read Archive, under BioProject accession number PRJNA728135.

5.5 Results

Microbial community diversity. Comparison of amplicon sequences to reference taxa indicated that members of the *Acidobacteria*, *Actinobacteria*, and *Proteobacteria* (mainly *Alphaproteobacteria* and *Betaproteobacteria*) were the most dominant phyla, followed by *Bacteriodetes*, *Chloroflexi*, and *Firmicutes* (Fig. 5.2). This is taxonomically consistent with previous studies of permafrost microbial communities (Jansson & Taş, 2014; Kim et al., 2016; Taş et al., 2018).

A distinction between permafrost versus active-layer and nonpermafrost deposits was reflected in certain taxonomic groups. The families *Caldisericaceae*, vadinHA17 (*Bacteroidetes*), and *Clostridiaceae 1* are relatively abundant in our permafrost samples, while few representatives are present in nonpermafrost or active-layer samples (Fig. 5.3). Other groups, such as *Rhizobiales*, *Planctomycetaceae*, and *Gemmatimonadaceae*, displayed

the opposite trend and were more abundant in nonpermafrost deposits (Fig. 5.3). Few groups exhibited consistent trends with depth, likely due to discontinuities in soil conditions at the base of the active layer (for permafrost samples) or at the depth of annual frost formation in nonpermafrost samples (Taş et al., 2018). Both permafrost and nonpermafrost samples contained *Anaerolineaceae*, while *Syntrophaceae* were more abundant in active-layer and permafrost deposits (Fig. 5.3). These taxa were classified into families associated with anaerobic taxa, including obligate anaerobes, suggesting that while anoxic conditions were common across the floodplain, there were potentially more reducing conditions in permafrost (Galushko & Kuever, 2019; Yamada & Sekiguchi, 2018). Archaea typically accounted for ~1% of sequence reads in nonpermafrost deposits (Fig. 5.2). In permafrost, several of our subsurface samples from below the active layer contained more than 10% of reads belonging to the *Archaea*. Archaeal abundance was driven by members of the *Euryarchaeota*, which made up a mean of 85% of archaeal reads in permafrost, 88% in the active layer, and 68% in nonpermafrost deposits. The remaining archaeal operational taxonomic units (OTUs) consisted of unclassified *Thaumarchaeota*, particularly "*Candidatus* Nitrosoarchaeum." Previous studies of ice wedge polygons found that autotrophic ammonia oxidizers from the *Nitrososphaerales* dominate the *Thaumarchaeota* found in permafrost, implying that Archaea may play an important role in nitrogen cycling in permafrost environments (Allan et al., 2014). Fewer than 1% of archaeal reads consisted of *Crenarchaeota* or other phyla (e.g., Asgard taxa).
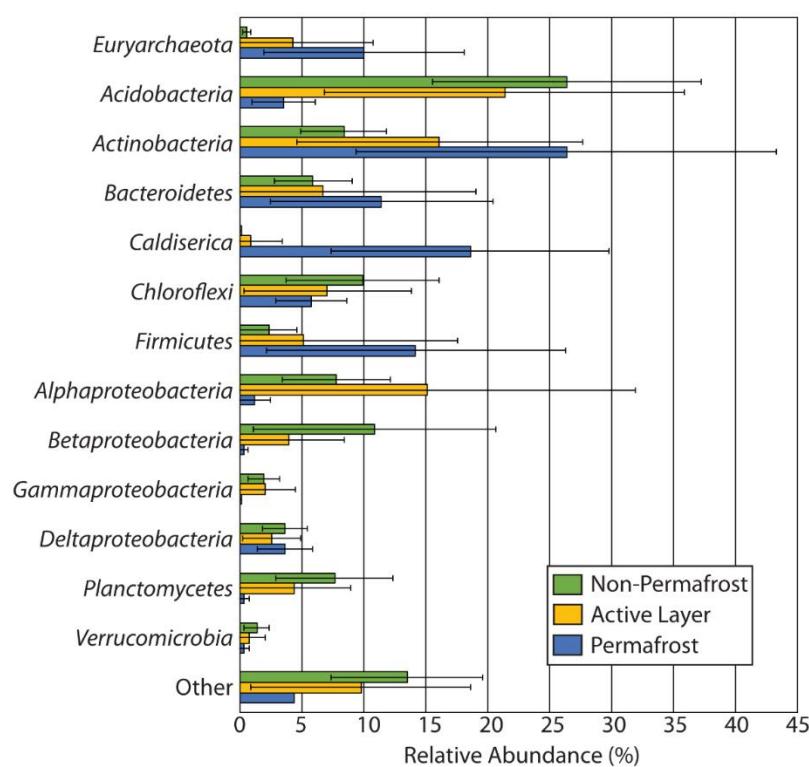
Figure 5.2. Mean relative taxa abundances for permafrost, active layer and non-permafrost samples, with error bars from the standard deviation of relative abundance within each

grouping. The permafrost samples contained ice cement (n = 8: Core1-105-111, Core9 > 58 cm depth), active layer samples were overlying ice cement (n = 6: Core1, Core9 > 58cm depth) or located on riverbanks with ice cement (n = 8: Bank1, Bank2, Bank9) and non-permafrost scroll bars were unfrozen (n = 9: Core7, Pit1, Pit2, Pit5, Pit6, Pit8).
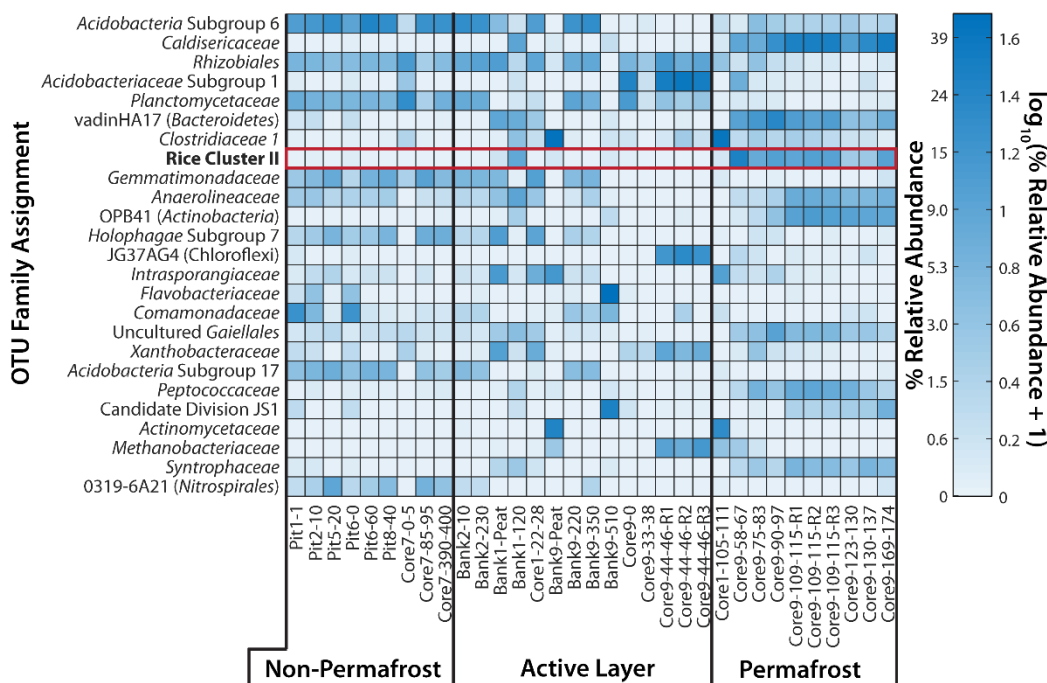
Figure 5.3. Heat map of dominant families in each sample—note that the methanogenic Rice Cluster II (outlined in red) were abundant in permafrost and rare in non-permafrost deposits. Sample core, pit or bank number and depth in centimeters are indicated in sample name, and replicates are denoted as R1, R2 and R3. Non-permafrost samples come from all depths in locations without observed permafrost, active layer samples come from the zone of seasonal thaw on river banks or sediment overlying permafrost, and permafrost samples contained ice cement. Samples moving from left to right trend from more recent (non-permafrost) river deposits to the oldest permafrost floodplain, and the samples at each location are listed moving from shallow to deep.

Replicate sample splits analyzed from Core9-44-46 and Core9-109-115 generated highly similar relative OTU abundances (Fig. 5.4), which we quantified as the standard deviation of relative abundance for the most abundant listed taxa at the phylum and family level. In comparison to Core9-44-46-R1 and -R3, Core9-44-46-R2 displayed slightly higher *Acidobacteria* and *Chloroflexi* relative abundances and smaller amounts of *Euryarchaeota*, *Actinobacteria*, and *Alphaproteobacteria*. The differences in relative abundance contributed to the higher uncertainty in reads for Core9-44-46 (2.0% at the phylum level and 1.4% at the family level) versus Core9-109-115 (0.50% at the phylum level and 0.44% at the family

level). However, the similar and consistent OTU occurrence and relative abundance between replicates indicates relatively low uncertainty due to potential sample contamination as well as DNA extraction, amplification, and sequencing.
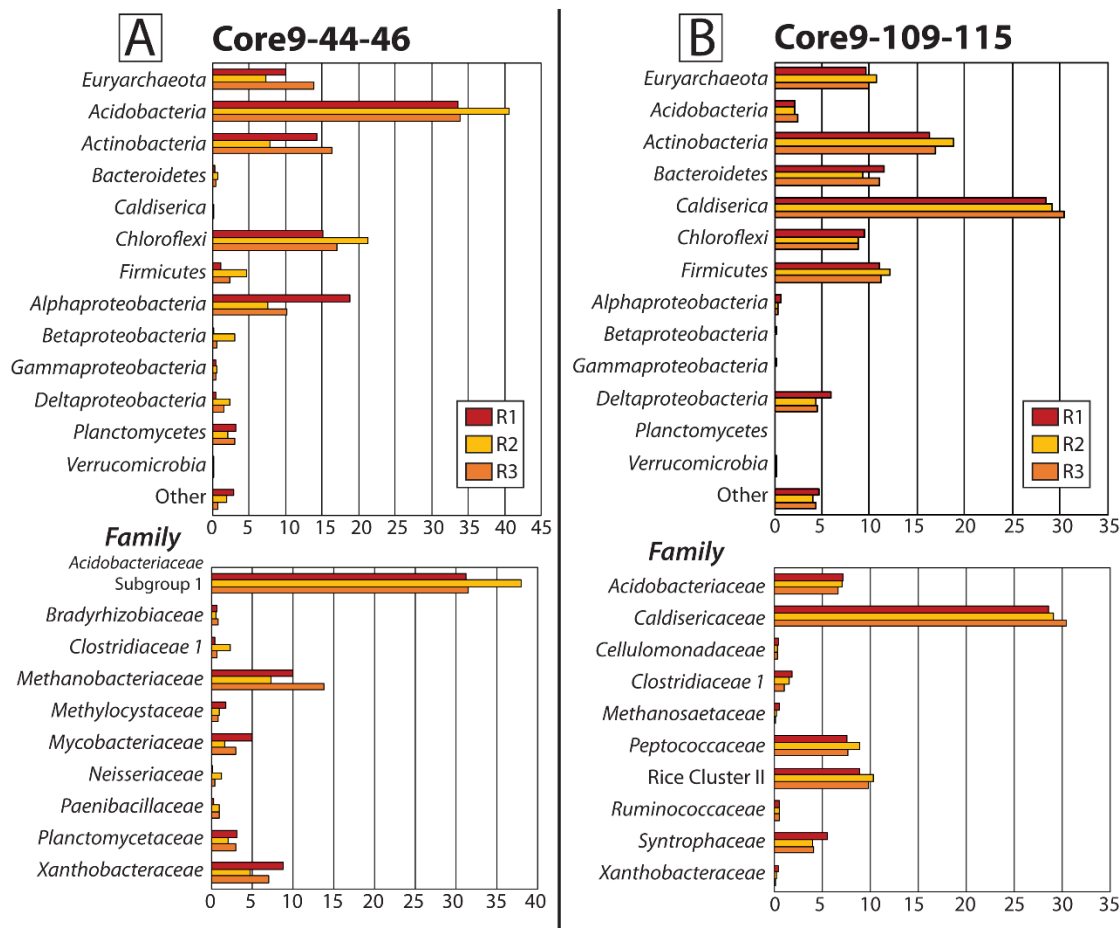
Figure 5.4. Comparison of replicate samples analyzed from **(A)** Core9-44-46 and **(B)** Core9-109-115 at the phylum and family taxonomic levels, displaying the 10 most abundant families for each sample.

5.5.2 Microbial community diversity

We observed lower microbial diversity in permafrost than in active-layer samples and the highest diversity and evenness in nonpermafrost samples (Table 5.1; Fig. 5.5). We rarefied the data to 4,500 reads and did not conduct diversity analyses on samples with fewer reads out of concern that low reads were due to an error in sequencing and the data are not representative of the sample. However, we note that rarefying to 1,000 reads did not significantly change our results. The number of observed OTUs and the Shannon diversity index, Chao 1, Fisher's alpha, Simpson's evenness, and Simpson's index all indicated decreased diversity when transitioning from nonpermafrost to active-layer and permafrost

samples. Active-layer samples from the floodplain cores and cutbanks showed similar diversity and evenness: floodplain active-layer samples had a Fisher's alpha of $1,272 \pm 703$ (mean $\pm$ 1 standard deviation) and a Simpson's evenness of 0.1254 ± 0.0830, while cutbank active-layer samples had a Fisher's alpha of $1,552 \pm 1,106$ and a Simpson's evenness of 0.1423 ± 0.1912 (Table 5.1). The floodplain and cutbank active-layer samples differed by ~3% of the mean value of all other diversity metrics and had intermediate diversity between permafrost and nonpermafrost samples. Therefore, we inferred that the regions of the Koyukuk River floodplain that contain no permafrost hosted a greater variety of taxa. In contrast, permafrost and active-layer sediment contained microbial communities dominated by fewer taxa (Table 5.1; Fig. 5.5).
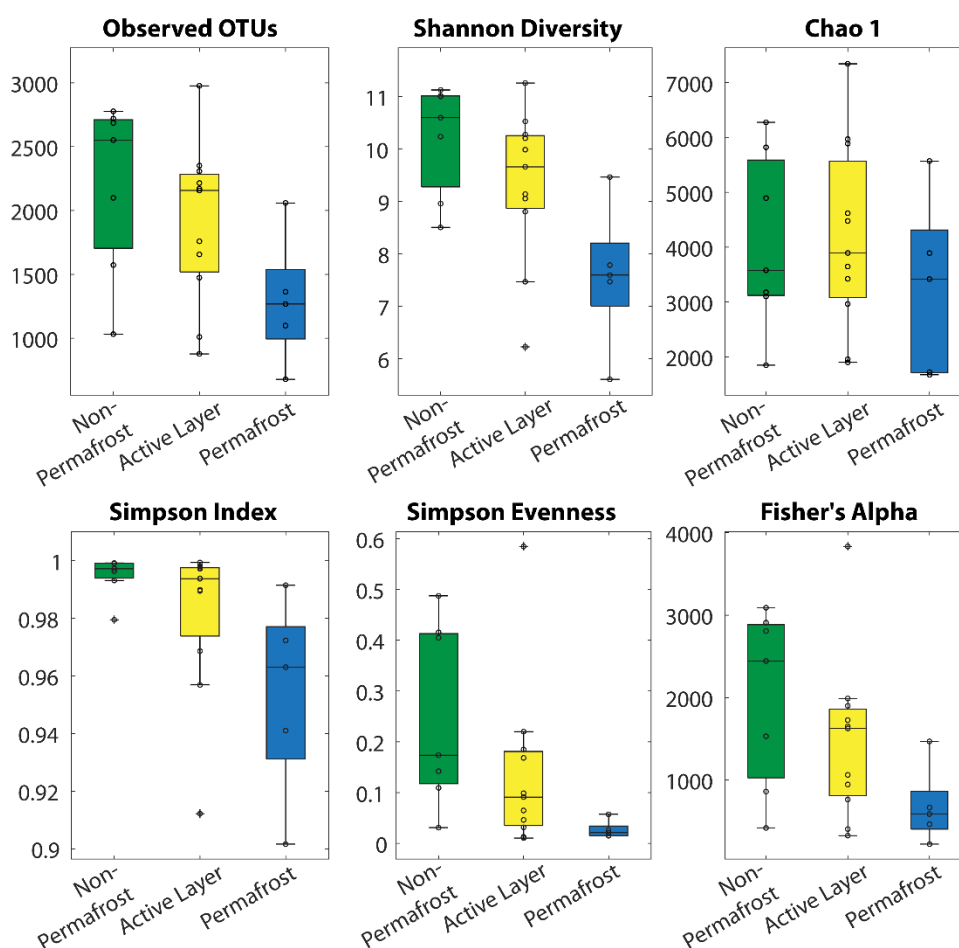
Figure 5.5. Box-and-whisker plots indicating the median, 25 and 75 percentiles of diversity index distributions. Samples are grouped as non-permafrost (no ice cement, only seasonal frost; n = 7), active layer (permafrost cutbanks or samples overlying permafrost; n = 11) and permafrost (ground containing ice cement; n = 5), rarefied to 4500 OTU reads.
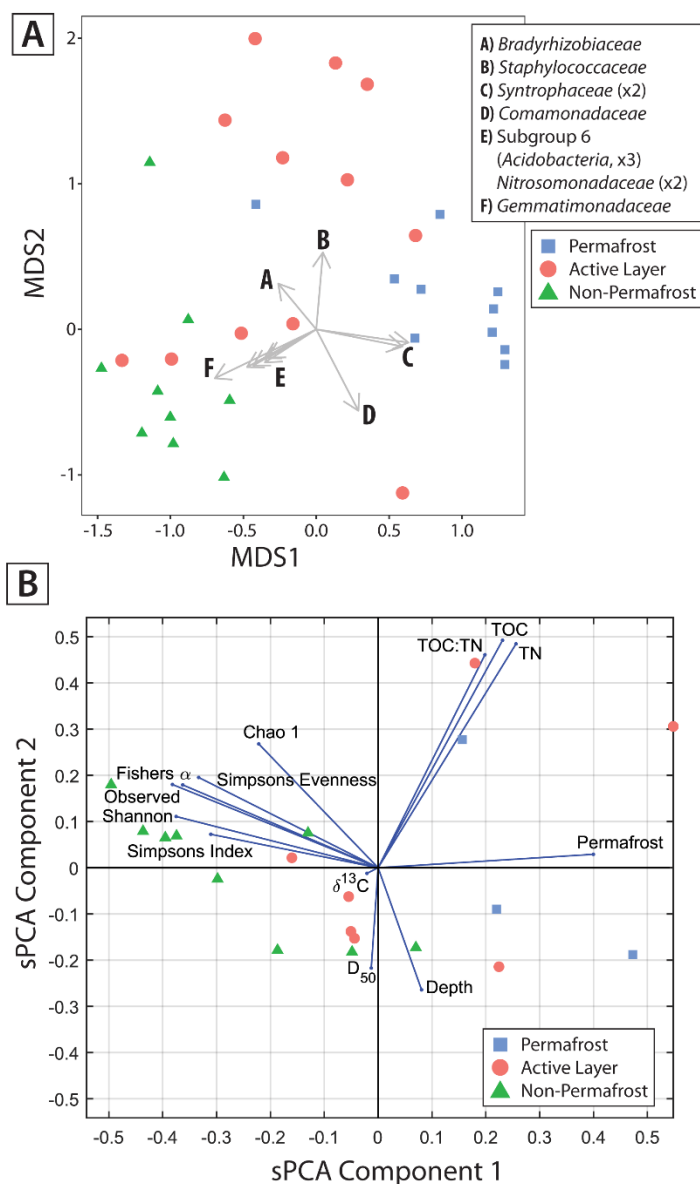
Figure 5.6. Statistical comparison of microbial communities with their sample site environment. **A)** NMDS analysis of microbial communities, color-coded by sample classification as permafrost, active layer, or non-permafrost, and demonstrating that microbial communities vary depending on permafrost presence. The samples are plotted for MDS vectors from a Bray matrix calculated to maximize the difference between samples based on the rank order of the square root of taxon abundance for each sample. The vectors for OTUs with p-values $< 10^{-5}$ are displayed, with the family-level taxonomic classification for each vector in the legend and the number of vectors for each family shown in parentheses. **B)** Results of scaled principle components analysis (sPCA), with diversity metrics for samples rarefied to 4500 OTU reads, geochemical analyses, and metadata vectors plotted

against the first and second principle components (accounting for 47% and 19% of sample variability, respectively).

Nonmetric multidimensional scaling (NMDS) analyses of the microbial community data found distinct differences between the microbial communities of permafrost, active-layer, and nonpermafrost deposits, with active-layer samples spanning the space between isolated clusters of permafrost and nonpermafrost samples (Fig. 5.6A). Plotting the vectors of the most significant de novo taxa showed that most were from *Gemmatimonadaceae*, *Xanthobacteraceae*, *Syntrophaceae* (genus *Smithella*), and *Acidobacteria* subgroup 6. Some taxa commonly associated with nitrogen cycling, in particular *Bradyrhizobiaceae* and *Nitrosomonadaceae*, were highly significant and preferentially associated with nonpermafrost and active-layer deposits. We focused further analyses on the differences between permafrost, active-layer and nonpermafrost deposits in sequences assigned to families of biogeochemical interest but noted that large contributions to these differences come from sequences assigned to uncultured families and *Acidobacteria* subgroup 6.

5.5.2 Taxa involved in methane biogeochemistry

Community analyses revealed that relative abundances of both methanogens and methanotrophs decrease upon permafrost thaw over seasonal timescales (Fig. 5.3). The main methanogenic taxa in our data belong to Rice Cluster II, which contains "*Candidatus* Methanoflorens stordalenmirensis" (100% similarity to IonTorrent metagenome SRA096214 using BLASTn)—a hydrogenotrophic methanogen whose abundance strongly correlated with soil methane concentrations in Stordalen Mire, Sweden (McCalley et al., 2014; Mondav et al., 2014). OTUs assigned to Rice Cluster II were abundant in permafrost samples in this study, including those from core 1, bank 1, and core 9, accounting for up to 28.0% of reads (Fig. 5.3). We also observed less abundant taxa from the hydrogenotrophic genus *Methanobacterium* (up to 13.7% of reads) and the acetoclastic methanogenic genera *Methanosaeta* (up to 0.5% of reads) and *Methanosarcina* (up to 0.3% of reads) in core 9, core 1, bank 1, bank 9, and pits 1 to 8. In cutbanks that had been thawed by river migration, methanogen abundance was near or below the limit of detection (Fig. 5.7). Previous studies found similar trends with the hydrogenotrophic methanogens *Methanobacterium* and *Methanocellales* as well as the acetoclastic methanogens *Methanosarcina* and *Methanosaeta* (Barbier et al., 2012; Liebner et al., 2015).

The main methanotrophic taxa in our data belong to GoM Arc I, which contains "*Candidatus* Methanoperedens nitroreducens," a species of ANME 2d. These are anaerobic methanotrophic (ANME) archaea that in cultured strains have a metabolism coupling methane oxidation to nitrate/nitrite reduction (Haroon et al., 2013). OTUs assigned to GoM Arc I were abundant in one sample, Bank1-120, where they made up 10.9% of reads. ANME 2d archaea have been previously detected in permafrost microbial communities (Johnston et al., 2019), often located in soil horizons slightly above horizons rich in methanogens (Lipson et al., 2015). However, locations with abundant methanogens often contained few ANME archaea (e.g., core 9, <0.2% ANME relative abundance), while bank 1 contained a high relative abundance of ANME archaea but a low relative abundance of methanogens.

We observed rare reads of potential aerobic methanotrophs in both permafrost and nonpermafrost deposits, classified as members of the alphaproteobacterial families *Methylocystaceae* and *Methylobacteriaceae*, the betaproteobacterial family *Methylophilaceae*, and the gammaproteobacterial families *Crenotrichaceae* and *Methylococcaceae* (see Table 5.S1 in the supplemental material). However, these taxa were very low in abundance (taken together, 2.5% of reads in Core1-105-111 and <1% of reads in other samples) and therefore are likely to be minor contributors to methane consumption.
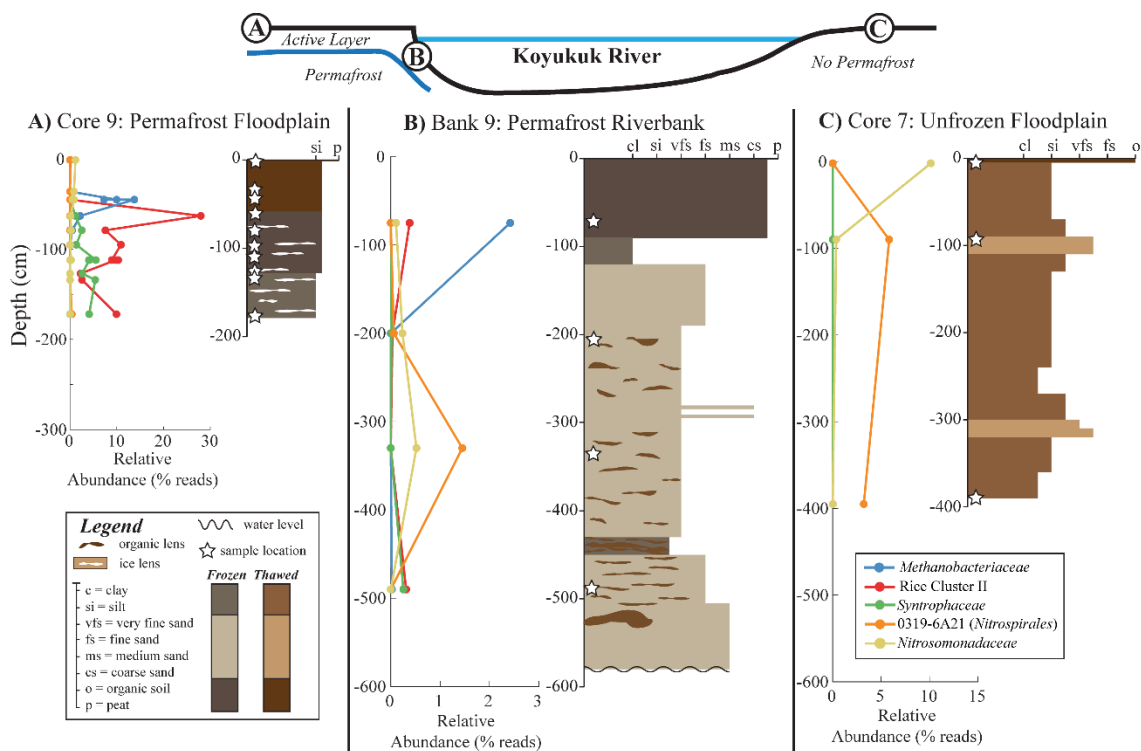
Figure 5.7. Idealized cross-section of the Koyukuk River. Steep, permafrost-bearing cutbanks first thawed by the river, forming the active layer, before being eroded, and sediment is deposited on the opposing point bar without permafrost as the river migrates, maintaining approximately equal channel width. The locations of representative stratigraphic sections for our sampling locations across the permafrost floodplain (Core 9, stratigraphic column A), permafrost riverbank (Bank 9, stratigraphic column B), and non-permafrost floodplain (Core 7, stratigraphic column C) show sediment grain size classification versus depth. Grain size was classified in the field into clay (cl), silt (si), very fine sand (vf), fine sand (f), medium sand (m), coarse sand (c) and organic-rich horizons. For each location, the relative abundance of select orders inferred to be involved in methanogenesis (Rice Cluster II and *Methanobacteriaceae*), sulfate reduction (*Syntrophaceae*), nitrite oxidation (*Nitrospirales*), and nitrogen fixation (*Bradyrhizobiaceae*) are plotted versus sample depth, with sampling locations shown as stars on the stratigraphic columns.

As a complementary approach to corroborate the presence of methanogenic and anaerobic methanotrophic taxa, we conducted qPCR analyses to examine the abundance of the methyl-coenzyme M reductase a-subunit functional gene (*mcrA*). Samples with abundant *Methanomicrobia* 16S amplicons (largely Rice Cluster II with minor contributions from other methanogenic taxa and GoM Arc I) also contained high abundances of the *mcrA* functional gene by qPCR (Fig. 5.8A), with the relative abundance of *mcrA* following trends with depth similar to those of the relative abundance of *Methanomicrobia* OTUs (Fig. 5.8B). Some samples (Core9-0, Core9-33-38, and Core9-44-46-R3) showed delayed amplification of *mcrA* (indicating the rare presence of the gene) but contained few or no amplicons attributed to known methanogenic or anaerobic methanotrophic taxa. We interpreted this to mean that these samples contained a very low abundance of such taxa (<0.001 relative abundance) whose presence was revealed by qPCR amplification. The samples with the highest *mcrA* gene abundances of samples with low or no methane-cycling taxa identified by 16S overlay sediment that both *mcrA* and 16S analyses indicated contains abundant *Methanomicrobia*, with the exception of Core7-85-95. Therefore, while qPCR results suggested that microbes carrying the *mcrA* gene may in fact be present in these samples at very low abundance, overall *mcrA* qPCR results lend support to metabolic inferences based on taxonomic classification of methanogen prevalence between sampling sites across the landscape (Fig. 5.8B).

We note that complete characterization of methane cycling on the Koyukuk floodplain requires constraining the activity, and not just the presence, of methanogens and methanotrophs (Steinberg & Regan, 2009). Previous work found that methanogenesis pathways inferred from 16S sequencing correlated with methane fluxes and δ^{13}C measurements made in permafrost at Stordalen Mire (McCalley et al., 2014). Our findings indicated that concentrations of methanogen and methanotroph DNA detectable via 16S sequencing and correlated abundance of the *mcrA* functional gene—a minimum constraint for methane production and consumption—were found only in permafrost terrain far from the river channel. Improved understanding of covariance of landscapes with microbial communities can guide further analysis—such as field- and laboratory-based measurements and incubations to measure methane flux—required to further characterize and quantify methanogen and methanotroph activity (Blake et al., 2015).
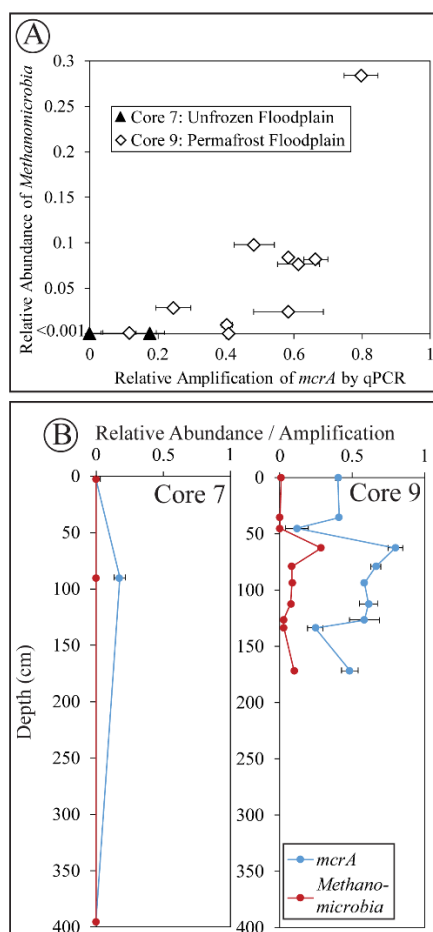
Figure 5.8. Results from qPCR. **A)** Relative abundance of *Methanomicrobia* versus relative amplification of methyl-coenzyme M reductase (*mcrA*; functional gene for methanogenesis and anaerobic methanotrophy). Samples plotting at relative abundance < 0.001 mark a bound indicating that no OTUs were assigned to *Methanomicrobia* taxa, but may contain other taxa with *mcrA* gene not assigned to *Methanomicrobia* or at very low abundance. Data for samples Core7-0-5 and Core7-390-400 overlap at the origin, and error bars represent ±1 standard deviation. **B)** Depth profiles of relative abundance of *Methanomicrobia* and relative amplification of *mcrA* from qPCR using 16S rRNA as a control marker gene.

5.5.2 Soil geochemistry

To evaluate how sediment properties might influence microbial diversity, we conducted scaled principal-component analysis (sPCA) on our diversity metrics and metadata, including OC content, stable isotope ratios, sample depth, and median grain size (Tables 5.2 and 5.3). The first two sPCA components accounted for 47% and 19% of the variance in community composition, respectively. Our results show that the first component depended primarily on diversity indices (observed OTUs, Chao 1, Simpson's evenness, Fisher's alpha, Shannon index, and Simpson's index) and sample classification as permafrost, active layer, or nonpermafrost (Fig. 5.5). The second component is mainly dependent on total organic carbon (TOC), total nitrogen (TN), and the TOC/TN ratio, with secondary contributions for

sample depth and median grain size (Fig. 5.6B). Many of these variables are highly correlated; we observed higher TOC and TN contents in finer-grained sediment, similar to previous studies on sediments from other Arctic rivers (Galy et al., 2008; Hilton et al., 2015). In turn, point bar deposits tended to be finer grained closer to the floodplain surface (Miall, 2013), so TOC content was also weakly anticorrelated with sample depth. However, sample classification as permafrost, active layer, or nonpermafrost appeared to dominate variations in sediment geochemistry in determining taxa presence and diversity (Fig. 5.5). We also noted that in our study area, vegetation varies with permafrost occurrence (Nowacki et al., 2003), so the changes in microbial community between frozen and unfrozen sediment may also be a result of different ecological niches available in the permafrost and nonpermafrost rhizospheres (Zhang et al., 2014).

We compared soil geochemistry to examine differences between permafrost, active-layer, and nonpermafrost sediments (Table 5.2). On average, organic matter in permafrost samples had a slightly lower $\delta^{13}C$ value of -28.13 ± 1.29‰ (measurement mean with uncertainty reported as one standard deviation) compared to -26.89 ± 1.21‰ for active-layer samples and -26.96 ± 0.49‰ for nonpermafrost samples. TOC was more strongly correlated with grain size than permafrost presence, with nonpermafrost, active-layer, and permafrost samples having mean TOC values of 2.61 ± 2.49%, 14.22 ± 19.44%, and 9.42 ± 9.80%, respectively. TN exhibited similar variation within classes; nonpermafrost samples had a mean TN value of 0.21 ± 0.12%, while active-layer and permafrost samples had values of 0.46 ± 0.40% and 0.58 ± 0.45%, respectively. However, permafrost samples displayed TOC/TN ratios slightly higher than those of nonpermafrost samples and with less variability than in the active layer. Mean TOC/TN ratios for permafrost samples were 11.8 ± 5.3, while TOC/TN ratios were 21.1 ± 19.8 for active-layer samples and 17.1 ± 6.1 for nonpermafrost samples. Therefore, permafrost, active-layer, and nonpermafrost samples show a similar N content, potentially indicating that N bioavailability is insensitive to permafrost thaw by either deepening of the active layer or bank erosion in the Koyukuk floodplain.

Table 5.3. Chemical and physical data of the sequenced sediment samples with ±1σ uncertainty.

Name	TOC (wt%)	$\delta^{13}C$ (‰)	TN (wt%)	Molar Ratio TOC:TN
Non-Permafrost				
Pit2-10	2.88±0.07	-27.3±0.1	0.22±0.01	15.4±0.8
Pit5-20	1.46±0.04	-26.8±0.1	0.18±0.01	9.6±0.5
Pit6-60	1.05±0.03	-27.4±0.1	0.12±0.01	10.5±0.6
Pit8-40	1.10±0.03	-26.6±0.1	0.14±0.01	9.0±0.5
Core7-0-5	7.74±0.19	-27.7±0.1	0.44±0.02	20.6±1.1
Core7-85-95	0.56±0.01	-26.6±0.1	0.10±0.00	6.6±0.4
Core7-390-400	5.25±0.13	-26.2±0.1	0.36±0.02	17.0±0.9
Bank2-10	3.20±0.06	-27.3±0.1	0.27±0.02	13.9±0.9
Bank2-230	0.27±0.01	-26.7±0.1	0.08±0.01	3.8±0.3

Active Layer

Bank1-Peat	6.45±0.13	-27.1±0.1	0.44±0.03	17.2±1.2
Core1-22-28	2.30±0.05	-29.2±0.1	0.26±0.02	10.3±0.7
Bank9-Peat	43.80±0.86	-26.5±0.1	1.03±0.07	49.5±3.3
Bank9-220	0.16±0.00	-27.3±0.1	0.05±0.00	3.5±0.2
Bank9-350	0.17±0.00	-25.8±0.1	0.05±0.00	3.8±0.3
Bank9-510	5.59±0.11	-25.5±0.1	0.44±0.03	14.7±1.0
Core9-33-38	41.07±1.01	-26.8±0.1	0.98±0.05	48.9±2.6
Permafrost				
Core1-105-111	3.50±0.07	-29.6±0.1	0.40±0.03	10.3±0.7
Core9-90-97	20.73±0.51	-27.20±0.1	1.09±0.05	22.2±1.2
Core9-169-174	4.04±0.10	-27.6±0.1	0.25±0.01	18.7±1.0

5.5.3 Effects of river migration

The differences in microbial communities between permafrost, active-layer, and nonpermafrost samples were greater than the variability within river deposits grouped into coeval scroll bar complexes. Samples from pits 1 to 6 were taken in a transect moving away from the river shoreline within a single scroll bar complex; these exhibited similar relative abundances of taxa at the family level (Fig. 5.3). Similarly, bank 1 and core 1 samples were also taken from the same scroll bar complex that is currently being eroded by the river; again, samples taken from similar depths (Bank1-Peat and Core1-22-28; Bank1-120 and Core1-111-115) displayed similar microbial community compositions at the family level. In contrast, permafrost, active-layer, and nonpermafrost samples contained distinct communities, reflecting how variations in permafrost occurrence between scroll bar complexes govern microbial community, more so than variability within a scroll bar complex. Since scroll bar complex age and permafrost presence were strongly correlated, we were not able to deconvolve changes in microbial community due to deposit age from the presence or absence of permafrost.

To understand how river channel migration influences the geographic distribution of microbial communities, we compared samples from a permafrost section of floodplain and eroding riverbank to a nonpermafrost point bar (Fig. 5.7). As the Koyukuk River migrated, it eroded permafrost bank 9 while migrating toward core 9 (located on a distal permafrost floodplain approximately 5.5 km from the modern river channel) and depositing new sediment on the nonpermafrost opposing point bar at core 7 (Fig. 5.7). We observed high relative abundances of OTUs classified as Rice Cluster II and *Methanobacteriaceae* methanogens in addition to anaerobic *Syntrophaceae* on the permafrost floodplain (core 9), as well as greater relative amplification of the *mcrA* gene. In contrast, samples taken on a partially frozen cutbank (bank 9) and unfrozen point bar (core 7) contained lower abundances of Rice Cluster II, *Methanobacteriaceae*, and *Syntrophaceae* and much lower relative amplification of *mcrA*.

The only taxa associated with methane cycling in bank 9 were located closer to the surface in the stratigraphic column; this pattern may be because peat is more insulating than sand and can preserve low temperatures in the upper soil column, even as underlying sand is thawed and eroded by the river. Alternatively, an anoxic layer could be generated close to the surface of the thawed permafrost cutbank as aerobic and facultative anaerobic taxa become established and multiply in the newly thawed active-layer community. In contrast, expected nitrogen cyclers, such as members of the *Nitrospirales* and *Nitrosomonadaceae*, were rare in permafrost floodplain deposits (core 9) but more abundant in the river cutbank and point bar (bank 9 and core 7). *Nitrospirales* had slightly higher relative abundances with depth, and we did not observe a clear trend in *Nitrosomonadaceae* with depth. The scarcity of families associated with nitrogen cycling coincided with lower TOC/TN ratios in active-layer and nonpermafrost deposits. Our observations also indicated that riverbanks along the Koyukuk experienced thaw during summer months, forming a lateral active layer with much greater grain sizes and lower organic content than typical surface soil horizons. Therefore, the Koyukuk River introduces lateral heterogeneity in floodplain microbial communities by seasonally thawing its banks.

5.6 Discussion

5.6.1 Mechanisms of community change

We found that samples taken from thawed river cutbanks have microbial communities similar to those in the active layer overlying permafrost deposits (Fig. 5.3). Since Arctic riverbanks erode at spatially variable rates up to meters per year (Rowland et al., 2019)—in stark contrast to the deepening of the active layer overlying permafrost, which occurs at millimeters to centimeters per year (Luo et al., 2016)—cutbank thaw provides a natural experiment to evaluate the timescales of microbial community adjustment to permafrost thaw. Results indicated that microbial communities at the time of sampling (late June to early July 2018) had adjusted to unfrozen, well-drained, and aerobic conditions since the spring 2018 floods (May 2018). If microbial communities responded to permafrost thaw more slowly than the pace at which the river erodes its cutbank (which is approximately equal to the active-layer thickness per year), we would have seen samples taken on cutbanks with a microbial community structure similar to that in samples from the permafrost floodplain. Instead, calculated diversity indices (number of observed OTUs, Shannon diversity index, Chao 1, Simpson's index, and Fisher's alpha) showed that permafrost samples have lower diversity than active-layer and nonpermafrost samples (Fig. 5.5). The Simpson evenness values indicated that a few abundant taxa dominate permafrost environments but a characteristic active-layer community can develop within a single thaw season. Thus, we propose that samples from thawed, actively eroding permafrost cutbanks, showing more species and a higher Simpson evenness (such as samples from bank 1, bank 2, and bank 9), likely developed active-layer communities more rapidly than the river could erode newly thawed cutbank sediment. This interpretation agrees with incubation studies that found that microbial communities in thawing permafrost and active-layer samples converged on a timescale of days (Mackelprang et al., 2011).

While motile or rapidly reproducing microbes may be able to change the makeup of a microbial community on small, incubation spatial scales, the transport of water and sediment across river floodplains may similarly help transport active-layer communities to newly thawed permafrost. For unfrozen channel banks directly in contact with the river, microbes transported by the river itself or pore fluid flow may homogenize bank microbial communities. Another mechanism that may help homogenize microbial communities not in contact with the river is cryoturbation, where seasonal freeze-thaw cycles physically mix floodplain sediments.

5.6.2 Importance of landscape heterogeneity

We found that OTU diversity decreases from the active layer to permafrost—a pattern consistent with previous studies (Lipson et al., 2015; Taş et al., 2018; Yergeau et al., 2010). However, we discovered that thawed riverbank samples were more similar in OTU diversity to samples from the floodplain active layer than samples taken from permafrost at a similar depth below the ground surface (Fig. 5.7). Permafrost samples generally had a lower number of OTU reads than nonpermafrost samples from active layers, though our approach is not calibrated to provide a quantitative metric of absolute abundance. While some methanogens were observed in the upper peat layer of bank 9, deeper unfrozen sandy samples more closely resembled the nonpermafrost point bar sampled in core 7. Therefore, we argue that as the Koyukuk migrates and exposes deposits that had been previously buried meters underground to surface conditions, this thawing disrupts permafrost microbial communities. These initial results suggest the interpretation that heterogeneous thaw and erosion of permafrost landscapes can disrupt established vertical trends in microbial diversity and community composition.

5.6.3 Effect of river channel migration on carbon cycling

We observed abundant methanogens in permafrost samples, including both hydrogenotrophic and acetoclastic taxa; this contrasted with only rare observations of methanogenic OTUs in nonpermafrost deposits. The occurrence of both acetoclastic and hydrogenotrophic methanogenic pathways has been globally documented in permafrost environments (Burkert et al., 2019; Hodgkins et al., 2015; Liebner & Wagner, 2007). We observed methanogen abundance from 16S classification peaking near the base of the active layer, in agreement with some previous studies (Barbier et al., 2012; Kotsyurbenko et al., 2004; Liebner et al., 2015; Tripathi et al., 2018). However, the active layer of core 9 contained *mcrA* genes amplified by qPCR (Fig. 5.8), which may indicate the presence of methanogens throughout the sediment column, possibly due to interannual variability in the active-layer thickness or relict environmental DNA (eDNA) persisting in the deposits. We also found fewer methanotrophs in core 9, though they were relatively abundant in bank 1, which may indicate a lack of methanotrophs in the soil column (possibly due to a high water table) or that our vertical sampling intervals are too coarse to pick specific depths at which methanotrophs might have been more abundant (Wagner et al., 2007). We emphasize that our study did not include direct measurements of the absolute abundance or activity of methane cycling within our samples. Further work is therefore required to determine if the

stark differences observed in the relative abundance of methane cycling taxa between permafrost and nonpermafrost river sediment translate into absolute differences in the methane fluxes as river migration transforms this landscape (McCalley et al., 2014).

Since only permafrost samples contained abundant methanogens and methanotrophs, and spatial patterns of Koyukuk River migration control the distribution of permafrost and nonpermafrost environments, we propose that river migration influences the fraction of floodplain area with potential for microbial methane cycling. River channel migration alters microbial communities in the Koyukuk River floodplain, giving insight into the floodplain's potential to respire CO_2 and methane in a warming climate. While we found evidence for methane cycling taxa only in older floodplain deposits that contained permafrost, all samples contained abundant anaerobic taxa.

Therefore, we anticipate that river erosion of permafrost deposits will gradually decrease the area of the floodplain with potential to release methane. The taxa that we observed in point bar deposits would instead remineralize newly thawed carbon as CO_2, though likely at a low rate due to their anaerobic conditions and cold average temperatures, generating a weaker positive feedback to climate warming due to permafrost thaw (Moni et al., 2015; Waldrop et al., 2010). For instance, if thawing permafrost destabilizes Arctic riverbanks (Costard et al., 2003), causing bank erosion rates to double, we expect that rivers would more rapidly decrease the floodplain area with significant relative abundance of methanogens, though at less than double the previous rate, as rivers tend to preferentially rework deposits near the channel (Torres et al., 2017). Our observations provide a framework and opportunity for future studies to use patterns of river channel migration to examine the influence of active landscape change on potential climate feedbacks in the Arctic.

5.7 Conclusions

In order to determine the effects of river channel migration on microbial communities in discontinuous permafrost floodplains, we collected samples from the Koyukuk River floodplain and investigated differences in microbial community compositions across the landscape using 16S amplicon sequencing and qPCR. Spatial patterns of river migration allowed us to evaluate how the floodplain microbial communities are responding to ongoing thaw and erosion of permafrost soils and deposition of unfrozen river sediment. We found that permafrost samples had lower microbial community diversity and evenness than active-layer and nonpermafrost samples, as well as higher TOC/TN ratios. During summer months, thawed channel banks develop an active-layer microbiome distinct from that of unthawed permafrost deposits found at a similar depth, suggesting that permafrost microbial communities adjust to thawed conditions in active-layer communities within the timescale of river cutbank thaw and erosion. Among these distinctions, we noted that methanogens and methanotrophs are abundant in permafrost samples and rare in active-layer and nonpermafrost sediments and that this interpretation was supported by the relationship between relative amplification of the *mcrA* functional gene and abundance of taxa assigned to the *Methanomicrobia*. Therefore, the cadence and spatial pattern of river migration influence the rate of change of microbial communities with potential roles in biogeochemical

cycling, for instance, by eroding the floodplain area that hosts microbial communities with potential for substantial methane cycling.

5.8 Acknowledgements

5.9 Supplementary material

Supplemental file 1 (8.8 MB Microsoft Excel xlsx file) is available for download online at: https://doi.org/10.1128/AEM.01339-21.

Chapter 6

ORGANIC CARBON BURIAL BY RIVER
MEANDERING PARTIALLY OFFSETS
BANK EROSION CARBON FLUXES IN A
DISCONTINUOUS PERMAFROST
FLOODPLAIN

6.1 Abstract

Arctic river systems erode permafrost in their banks and mobilize particulate organic carbon (OC). Meandering rivers can entrain particulate OC from permafrost many meters below the depth of annual thaw, potentially enabling the production of greenhouse gases. However, the amount and fate of permafrost OC that is mobilized by river erosion is uncertain. To constrain OC fluxes due to riverbank erosion and deposition, we collected riverbank and floodplain sediment samples along the Koyukuk River, which meanders through discontinuous permafrost in the Yukon River watershed, Alaska, USA, with an average migration rate of 0.52 m yr^{-1}. We measured sediment total OC (TOC) content, radiocarbon activity, water content, bulk density, grain size, and floodplain stratigraphy. Radiocarbon activity and TOC content were higher in samples dominated by silt as compared to sand, which we used to map OC content onto floodplain stratigraphy and estimate carbon fluxes due to river meandering. Results showed that the Koyukuk River erodes and re-deposits a substantial flux of OC each year due to its depth and high migration rate, generating a combined OC flux of a similar magnitude to the floodplain net ecological productivity. However, sediment being eroded from cutbanks and deposited as point bars had similar OC stocks (mean ± 1 SD of 125.3 ± 13.1 kg OC m^{-2} in cutbanks versus 114.0 ± 15.7 kg OC m^{-2} in point bars) whether or not the banks contained permafrost. We also observed radiocarbon-depleted biospheric OC in both cutbanks and permafrost-free point bars. These results indicate that a substantial fraction of aged biospheric OC that is liberated from floodplains by bank erosion is subsequently re-deposited in point bars rather than being oxidized. The process of aging, erosion, and re-deposition of floodplain organic material may be intrinsic to river–floodplain dynamics, regardless of permafrost content.

6.2 Introduction

The warming climate is changing Arctic landscapes, inducing complex feedbacks in the global carbon cycle as permafrost soils thaw (Schuur et al., 2015; Turetsky et al., 2020).

Changes in air temperature and precipitation have increased the thickness of the active layer (ground overlying permafrost that experiences seasonal freeze–thaw cycles), allowing respiration of soil organic carbon (OC) previously frozen for thousands of years (Biskaborn et al., 2019; Isaksen et al., 2016; Romanovsky et al., 2010). Organic carbon is also lost from permafrost through lateral erosion by Arctic rivers – the six largest Arctic rivers contribute ~ 3 Tg of river particulate OC (POC) to the Arctic Ocean annually (McClelland et al., 2016). Since a substantial portion of eroded POC is thought to be prone to oxidation (Schreiner et al., 2014), river erosion of POC could play an important role in the greenhouse gas fluxes associated with permafrost thaw (Toohey et al., 2016; Walvoord & Kurylyk, 2016).
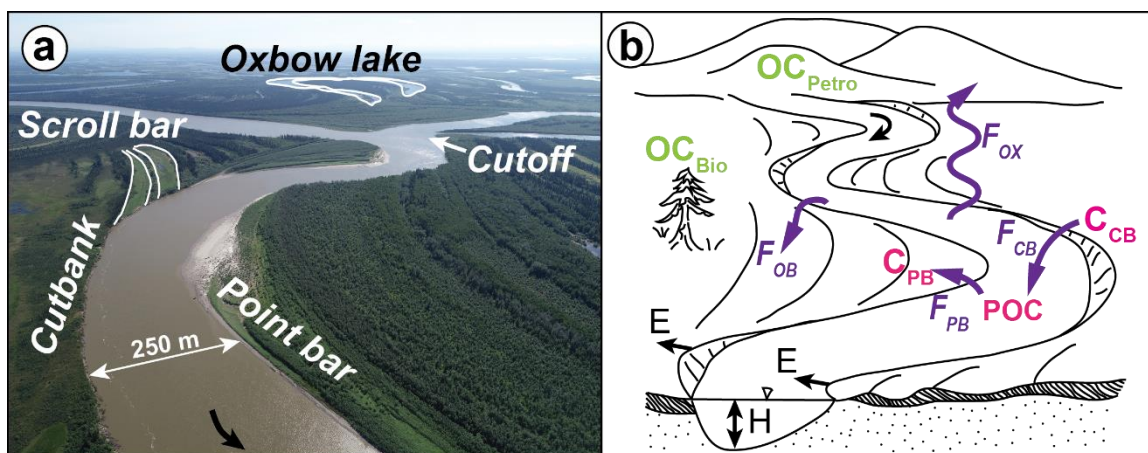
Figure 6.1. Overview of sediment erosion and deposition patterns in meandering river floodplains and important variables influencing the regional carbon cycle. **(a)** Drone photograph taken looking east across the Koyukuk River floodplain, Alaska (location marked with a white star in Fig. 6.2). The river flows south toward the bottom of the image (indicated by black arrow), eroding the cutbank on the outside of the river bend and depositing sediment on the point bar. Channel migration generates bands of higher and lower elevation sections of floodplain called scroll bars. As the river migrates, an individual bend becomes more sinuous, eventually cutting itself off and abandoning a section of channel, which becomes an oxbow lake. **(b)** Schematic of a meandering river floodplain, with channel geometry variables shown in black and particulate organic carbon reservoirs and fluxes into and out of the river control volume shown in purple. The river has bankfull depth H and migrates laterally at rate E, maintaining a constant channel width. Organic carbon is stored in the river cutbanks (C_{CB}) and point bars (C_{PB}) and is transported in the river as particulates (POC). These reservoirs are mixtures of radiocarbon-dead (Fm = 0) petrogenic organic carbon (OC$_{Petro}$) and biospheric organic carbon (OC$_{Bio}$) that has been stored in permafrost (low Fm) or been recently fixed by the biosphere (Fm $\geq$ 1). Fluxes of organic carbon into and out of the river control volume include cutbank erosion (F_{CB}), point bar deposition (F_{PB}), overbank deposition (F_{OB}), and oxidation of POC and DOC (F_{OX}).

As Arctic rivers migrate laterally across permafrost floodplains, they can mine sediment and organics from over 10 m below the active layer (Kanevskiy et al., 2016; Spencer et al., 2015). Permafrost floodplains are thus an important source of POC to rivers (Kanevskiy et al., 2016;

Lininger et al., 2019; Lininger, Wohl, et al., 2018; Loiko et al., 2017). After mobilization by a river, POC can be oxidized during transport (Denfeld et al., 2013; Serikova et al., 2018; Striegl et al., 2012) or re-buried in floodplains (Torres et al., 2020; Wang et al., 2019). Alternatively, POC can be delivered downstream to the ocean, where it may be oxidized to CO_2, reduced to CH_4, or buried in deltaic sedimentary deposits (Hilton et al., 2015; Torres et al., 2020). Riverbank erosion may be limited by the rate of permafrost thaw (Costard et al., 2003; Dupeyrat et al., 2011; Randriamazaoro et al., 2007), implying that erosion rates could increase with warming air and river water temperatures. Therefore, more rapid riverbank erosion resulting from warming temperatures has the potential to increase fluvial POC fluxes and oxidation, resulting in a positive feedback on the concentration of atmospheric carbon dioxide (Denfeld et al., 2013; Serikova et al., 2018; Striegl et al., 2012). The magnitude and timescale of this feedback are highly uncertain but may be important to consider for predicting and mitigating impacts from anthropogenic climate change.

Floodplain POC stocks are vulnerable to erosion by Arctic rivers (Parmentier et al., 2017; Vonk et al., 2019). For instance, Lininger et al. (2018, 2019) mapped OC contents and stocks across the Yukon Flats and found significant variability in OC contents between riverine landforms (Lininger et al., 2018) as well as underestimation of floodplain OC stocks in previous data compilations (Lininger et al., 2019). Their work built on previous studies that characterized vegetation and permafrost succession through a time series of floodplain surfaces that had been progressively abandoned by river migration (Shur & Jorgenson, 2007). Yet major questions remain about the magnitude of POC fluxes due to bank erosion and bar deposition in permafrost river systems as well as the physical processes that govern these fluxes (Lininger & Wohl, 2019).

Alluvial rivers commonly maintain an approximately constant channel width, eroding one bank while depositing sediment at a commensurate rate on the opposite bank (Fig. 6.1a) (Dietrich et al., 1979; Eke et al., 2014). Riverbank erosion has been shown to contribute substantially to downstream POC fluxes (Kanevskiy et al., 2016). However, it is unclear to what extent the OC released by bank erosion is compensated by OC burial in depositional bars as opposed to being transported downstream or oxidized during transport within river systems (Fig. 6.1b) (Scheingross et al., 2021; Wang et al., 2019). To quantify POC storage and mobilization, we investigated the Koyukuk River in the Yukon River watershed, Alaska, USA (Fig. 6.2), which is an actively meandering river in discontinuous permafrost. We quantified OC stocks using measurements of OC content in field samples and extrapolated these across the floodplain using floodplain stratigraphy and correlations between grain size and OC content. We then used a one-dimensional mass-balance model to quantify net fluxes of OC into and out of the river due to bank erosion and bar deposition. To attribute OC to biospheric versus rock-derived (petrogenic) sources, we used radiocarbon measurements to infer the presence of a petrogenic OC end-member and compared the range of biospheric radiocarbon compositions in permafrost and non-permafrost sediment samples and landforms.
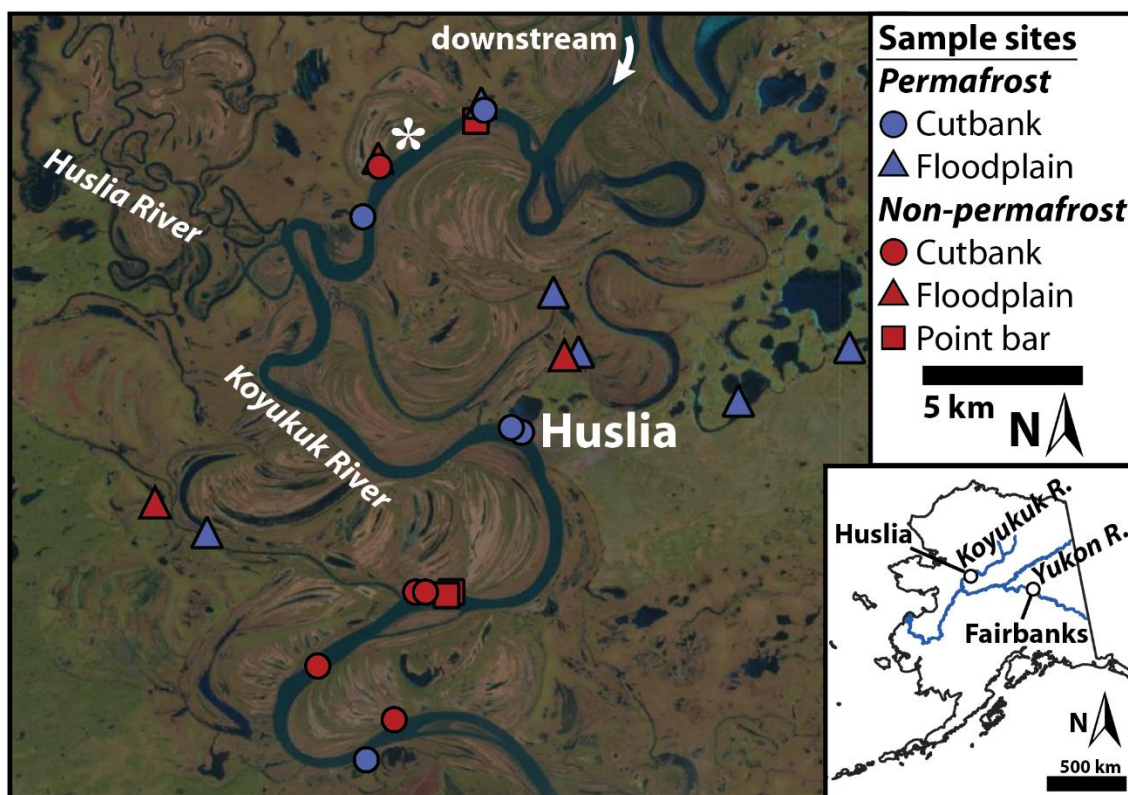
Figure 6.2. Sample locations on the Koyukuk River floodplain. Locations are coded for sites where we sampled ice-cemented permafrost versus ice-poor ground inferred to be non-permafrost. Sample sites are located near the village of Huslia, in central Alaska, and the river flows towards the south past the town. Sampling locations are mapped on Landsat imagery, with the white star marking the location of Fig. 6.1a (drone photo taken looking east). The inset map was generated using the "Alaska Coast Simplified" and "Major Rivers" shapefiles from the Alaska State Geo-Spatial Data Clearinghouse.

6.3 Approach

To understand cycling of POC between rivers and floodplains, we developed an approach to ascertain OC sources and determined if OC eroded from river deposits was transported downstream or re-buried (Fig. 6.1b). Eroding banks can source OC from modern vegetation and organic horizons near the bank surface as well as deeper sediment that may be depleted in radiocarbon. Radiocarbon provides an effective tracer of OC aging in floodplains (Galy & Eglinton, 2011; Torres et al., 2017), but several processes can produce depleted radiocarbon signals. First, many Arctic permafrost deposits are relicts from colder climatic conditions (O'Donnell et al., 2012). These deposits have low radiocarbon activity, expressed as fraction modern (Fm = $A_{sample,norm}/(0.95 A_{Ox,norm})$; $A_{sample,norm}$ indicates sample ^{14}C activity normalized for isotope fractionation to $\delta^{13}C_{VPDB} = -25$ ‰ (VPDB – Vienna Pee Dee Belemnite), while $A_{Ox,norm}$ indicates NBS Oxalic Acid I normalized to $\delta^{13}C_{VPDB} = -19$ ‰, with $\delta^{13}C_{VPDB} = (R_{sample}/R_{VPDB} - 1) \times 1000$ reported in per mill (‰)) (Reimer et al., 2004). If mobilized permafrost POC is reburied in bars without the addition of newly fixed biospheric OC, then

bar sediment should also have OC with low Fm values inherited from permafrost carbon. Second, sediment can contain a radiocarbon-dead, petrogenic OC component that contributes to low Fm values (Blair et al., 2003). We expected a petrogenic OC contribution in floodplain sediments throughout the Koyukuk River system, since the headwaters of the Koyukuk River contain outcrops of shale bedrock rich in kerogen (Dumoulin et al., 2004; Slack et al., 2015; Wilson et al., 2015). Third, river–floodplain interactions generate organic carbon with low Fm values via transient OC storage, independent of the presence of either permafrost or petrogenic OC (Torres et al., 2020). For example, floodplain deposits can remain in place over millennial timescales before being reworked by the river channel due to the stochastic nature of river lateral migration (Repasch et al., 2020; Torres et al., 2017). Therefore, radiocarbon measurements provide insight into OC sources but require de-convolving petrogenic OC from biospheric OC and assessing aging of OC by storage in permafrost versus non-permafrost floodplain deposits.
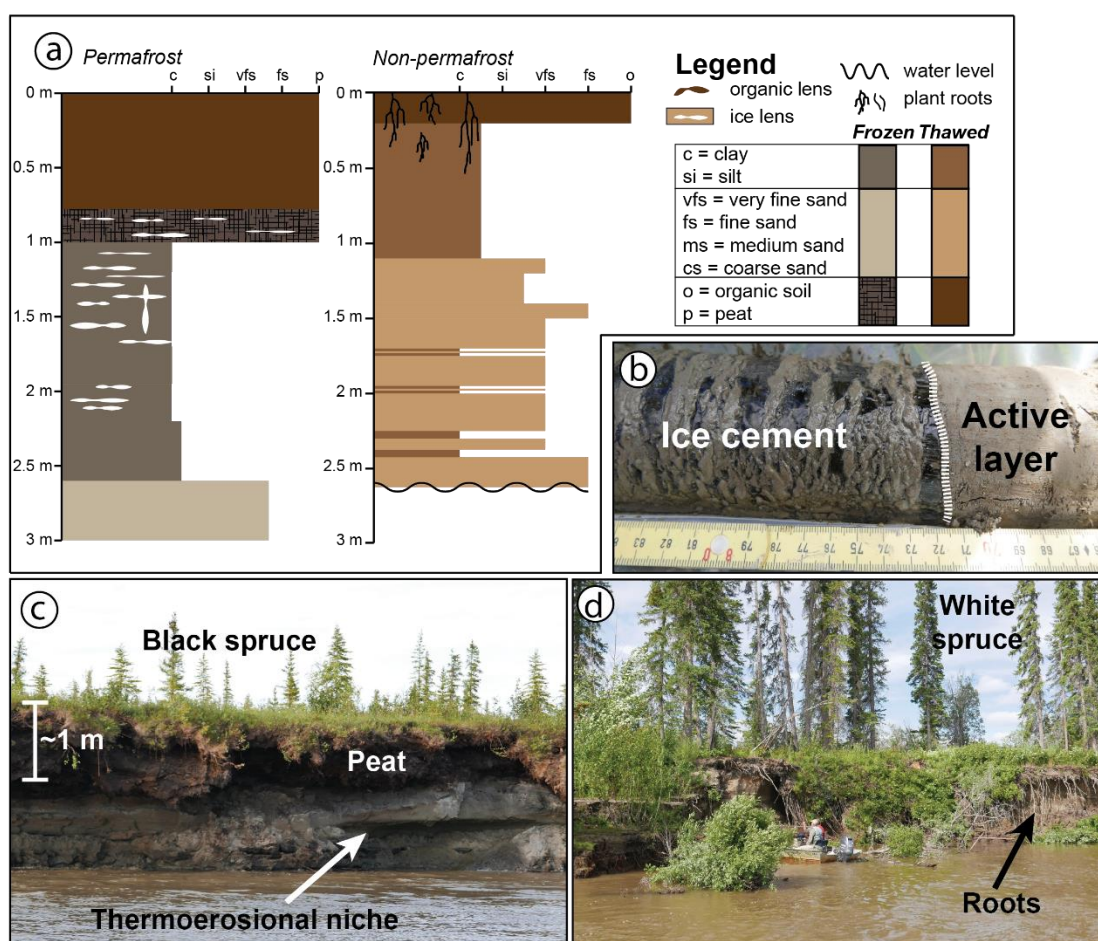
Figure 6.3. Field observations of Koyukuk riverbanks and floodplain stratigraphy. **(a)** Representative stratigraphic columns from nonpermafrost (Bank 2) and permafrost (Bank 6) cutbanks. **(b)** Field photo of boundary between permafrost ice cement and the overlying active layer in Core 4. **(c)** Thermoerosional niche formed in a permafrost cutbank, with silty

permafrost overlain by a layer of peat and black spruce trees. **(d)** Eroding riverbank without permafrost, hosting a white spruce forest with roots that reach deep into the bank sediment. Complete stratigraphic sections and additional field photos are in Figs. 6.S2 and 6.S3.

We used sediment total OC (TOC) and Fm measurements to calculate the Fm of the biospheric OC end-member as well as the contribution of petrogenic OC to our samples. This calculation allowed us to determine if low Fm values were due to a high content of radiocarbon-dead rock-derived OC or preservation and aging of OC in permafrost or in the river floodplain (Fig. 6.1b) (Scheingross et al., 2021). Both radiocarbon-dead OC derived from bedrock erosion (TOC_{petro}) and aging of biospheric OC (TOC_{bio}) in permafrost and river floodplain deposits will yield sediment OC with low Fm values (Fig. 6.1b). We partitioned the TOC contents measured in each sample (TOC_{meas}) into a two endmember mixture of biospheric ($TOC_{bio} = f_{bio} \times TOC_{meas}$) and petrogenic OC ($TOC_{petro} = f_{petro} \times TOC_{meas}$) fractions (Fig. 6.4c) (Blair et al., 2003; Cui et al., 2016):

$$TOC_{bio} + TOC_{petro} = TOC_{meas}, \tag{6.1}$$

$$f_{bio} + f_{petro} = TOC_{bio}TOC_{meas} + TOC_{petro}TOC_{meas} = 1, \tag{6.2}$$

where f_{bio} and f_{petro} are the fraction of organic carbon from biospheric and petrogenic sources. Changes in the ratio of biospheric to petrogenic OC, as well as aging of the biospheric pool, will change the measured fraction modern in sediment OC (Fm_{meas}; unitless ratio) (Galy et al., 2008). By mass balance,

$$TOC_{meas}Fm_{meas} = TOC_{bio}Fm_{bio} + TOC_{petro}Fm_{petro}. \tag{6.3}$$

The petrogenic OC end-member was assumed to be radiocarbon-dead ($Fm_{petro} = 0$), and Eqs. (6.1) and (6.2) substituted into Eq. (6.3) yield

$$Fm_{meas} = Fm_{bio}(TOC_{meas} - TOC_{petro})TOC_{meas}. \tag{6.4}$$

A nonlinear optimization of Eq. (6.4) for Fm_{meas} versus TOC_{meas} was used to calculate 95 % confidence intervals around Fm_{bio} (effectively the mean radiocarbon activity of biosphere-derived carbon) and the TOC_{petro} content in cutbank and point bar sediment samples (Fig. 6.4c) (Hemingway et al., 2018; Wang et al., 2019). We reported a range of fitted Fm_{bio} end-members to compare biospheric OC eroding from cutbanks to that being deposited in point bars because cutbanks comprise a mixture of permafrost and non-permafrost terrain with varying Fm values that are homogenized during transport in the river. This optimization also considers a range of TOC_{petro} content end-members for cutbanks and point bars. We do not expect that geographic location on the Koyukuk floodplain has a strong control on sediment OC_{petro} content. While recent work found evidence for petrogenic OC oxidation during riverine transport of sediment (Bouchez et al., 2010; Horan et al., 2019), these studies focused on river reaches spanning hundreds of kilometers, 1 order of magnitude longer than our study

reach. Even over hundreds of kilometers, Horan et al. (2019) found that less than half of petrogenic OC eroded from the Mackenzie River catchment was oxidized during transport. Therefore, it is reasonable to assume that the production and oxidation of rock-derived OC is limited within our study reach and a single TOC_{petro} endmember is appropriate for cutbanks and another for point bars.

6.4 Materials and methods

6.4.1 Field sampling methods

We collected samples from 33 locations along the Koyukuk River near the village of Huslia, Alaska, during June–July 2018 (Fig. 6.2 inset; Fig. 6.S1 in the Supplement). Near Huslia, the mean annual air temperature is $-3.6°C$ (Daly et al., 2015, 2018; Nowacki et al., 2003). The Koyukuk is a meandering river in discontinuous permafrost (portions of the floodplain are underlain by ground below $0°C$ while others are not) with well-defined scroll bars (former levees) (Mason & Mohrig, 2019) that demarcate clear spatial patterns of channel lateral migration (Fig. 6.2) (Shur & Jorgenson, 2007). Bands of vegetation outline scroll bars on the floodplain that were abandoned due to channel lateral migration and meander-bend cutoff (Fig. 6.1). Seasonal variations in temperature cause an annual freeze–thaw cycle in sediment near the ground surface across the landscape, called the active layer, while the ground below, in areas of permafrost, is perennially at sub-zero temperatures. To represent the diversity of floodplain geomorphology, permafrost occurrence, and deposit ages, we selected eight permafrost cutbanks, six non-permafrost cutbanks, six permafrost floodplain cores, four non-permafrost floodplain cores and pits, and nine nonpermafrost cores and pits in transects across two point bar complexes to characterize floodplain stratigraphy and carbon geochemistry (Fig. 6.2; Tables 6.S1 and 6.S2 in the Supplement). We categorized permafrost as ice-cemented sediment observed during our summer field season, often containing ice lenses and other structures indicative of permafrost (Fig. 6.3a and b) (French & Shur, 2010). Permafrost cutbanks often had an undercut marking the high water level where bank sediment was directly thawed by the river and collapsed as well as abundant toppled trees indicating active bank erosion. We classified terrain without ice cement observed to the depth of coring or sampling as non-permafrost (Fig. 6.3a and c), although this category might also include perennial sub-zero ground that lacked pore water to form ice cement. Bank samples were collected by digging into cutbanks and point bars, and cores were taken using a hand auger in nonpermafrost deposits and a Snow, Ice, and Permafrost Research Establishment (SIPRE) auger in permafrost (Fig. 6.2). All samples were recorded in stratigraphic columns to determine the thickness of each stratigraphic unit. Samples were stored in sterile Whirl-pak bags and frozen within 12 h of collection and then transported frozen back to a cold room ($-15°C$) at Caltech for laboratory analyses.

River bathymetry was characterized using a Teledyne RioPro acoustic Doppler current profiler (ADCP). We calculated a river depth of 12.4 m as the mean of the deepest measured value (i.e., the thalweg) for eight ADCP river cross-sectional transects across a representative meander bend. Mean bank erosion rates for the portion of the Koyukuk we studied were 0.52 m yr^{-1} averaged over the time period of 1978–2018 (Rowland et al., 2019). Over the same

time interval, channel width varied from 173 ± 43 m in 1978 to 179 ± 43 m in 2018 (median ± 1 SD), indicating a balance between cutbank erosion and point bar deposition over this period since net lateral erosion or deposition would change channel width (Fig. 6.S2).

6.4.2 Laboratory analyses

Samples were transferred to pre-combusted aluminum foil, weighed, and oven-dried at 55–60°C to calculate the mass fraction of water ($M_{H2O,i}$). For samples taken using the SIPRE auger with known volume, bulk density (ρ_i) was calculated from total mass divided by volume. The samples were gently homogenized using an agate mortar and pestle and then split using cone and quarter or a riffle splitter, to avoid grain size fractionation, for further analysis. Total organic carbon content (TOC_{meas} in Eq. 6.2), stable organic carbon isotopes, and total nitrogen (TN) content were measured on a Costech Elemental Analyzer coupled to a MAT 253 IRMS (isotope ratio mass spectrometer) at Los Alamos National Laboratory (LANL). Prior to analysis, samples were ground to a powder and approximately 3 mg of each sample was decarbonated by fumigation with HCl in silver capsules. Isotope ratios are reported relative to the VPDB ($\delta^{13}C$ = (Rsample/RVPDB − 1) × 1000; reported in per mill (‰)), and measured blanks were below the peak detection limit. Measurements were calibrated using laboratory standards of 2,5-Bis(5-tertbutyl-2-benzo-oxazol-2-yl) thiophene (BBOT, Eurovector; TOC = 72.53%, measured as 69.59% ± 2.05%; $\delta^{13}C$ = −26.6‰, measured as −26.6‰ ± 0.01‰; TN = 6.51%, measured as 6.82% ± 0.24%), peach leaves (1570a; TOC = 44.65%; measured as 44.33% ± 0.96%; $\delta^{13}C$ = −25.95‰, measured as −26.13‰ ± 0.08‰; TN = 2.83%, measured as 3.31% ± 1.27%), and urea (Eurovector; TOC = 20.00%, measured as 17.98% ± 0.37%; TN = 46.65%, measured as 45.88% ± 0.88%) for TOC and TN and cellulose (IAEA-C3; $\delta^{13}C$ = −24.91‰, measured as −24.82‰ ± 0.06‰), sucrose (IAEA-C6; $\delta^{13}C$ = −10.8‰, measured as −10.7‰±0.03‰), and oxalic acid (IAEA-C8; $\delta^{13}C$ = −18.3‰, measured as −18.5‰ ± 0.06‰) for stable OC isotopes, with uncertainties reported as 1 standard deviation (± 1 SD). Values of $\delta^{13}C$ and TN content are not discussed in the main text but are included in figures and tables in the Supplement.

Radiocarbon content was measured on a subset of sample at the National Ocean Sciences Accelerator Mass Spectrometry (NOSAMS) facility in Woods Hole. Sample splits for radiocarbon were ground to a powder and decarbonated at Caltech in pre-combusted glassware using 1 M HCl, sonicated for 10 min, and neutralized using 1 M NaOH. Splits were centrifuged for 10 min, and the supernatant was removed using a pipette. The samples were rinsed using 20 mL Milli-Q water, centrifuged and decanted twice before being lyophilized, and sent to NOSAMS to be measured for radiocarbon activity (Fm_{meas} in Eq. 6.3). NOSAMS also reported total organic carbon content (dry wt % with 5 % measurement uncertainty) and organic carbon stable isotope measurements (referenced to VPDB; $\delta^{13}C$ = (R_{sample}/R_{VPDB} − 1) × 1000; reported in per mill (‰)), and these produced similar results as LANL (Fig. 6.S5 and Table 6.S2). We used LANL OC contents in subsequent analyses because they reported smaller uncertainties and because we made measurements at LANL for all samples. NOSAMS data are used only for Fm values of the sample subset.

Sample splits for grain size analysis were placed into sterile polypropylene Falcon tubes to remove carbonate and organic materials (Gee and Or, 2002). Samples were acidified overnight with 1 M HCl and then centrifuged for 15 min at 4000 rpm and decanted; they were rinsed twice with DI (deionized) H_2O, centrifuged, and decanted before being oven-dried at 55–60°C; and they were then reacted with H_2O_2 on a hot plate at 85°C to remove organics. Floating pieces of organic material were removed using a microspatula rinsed with DI H_2O. Additional H_2O_2 was added until reactions ceased by visual inspection. Samples were rinsed and centrifuged three times before oven-drying. Each sample was re-hydrated using DI H_2O, ~10 mL of 10 g $(NaPO_3)_6$ (sodium hexametaphosphate) per 1 L DI H_2O was added to prevent flocculation, and samples were sonicated for 3 min. The samples were split while wet using a riffle splitter to the required sediment concentration for laser diffraction, and grain size was measured on a Malvern Mastersizer 2000, with measurements calibrated against a laboratory silica carbide standard (median diameter D_{50} = 13.184 ± 0.105 μm throughout our measurements). Grain size data confirmed our field observations of grain size that were made using a sand card and hand lens (Table 6.S5).

A subset of TOC and TN contents, stable OC isotopes, and grain size data was previously published in Douglas et al. (2021) (Table 6.S2).

6.5 Results

Permafrost cutbanks and floodplains generally displayed an organic-rich upper horizon, which extended up to 1.3 m below the ground surface in peat, underlain by silt that abruptly transitioned to sand (Fig. 6.3a and d; Fig. 6.S3). The thickness of the active layer, measured by trenching or using a 1 m permafrost probe (n = 53), ranged from 40 cm to greater than the length of the probe, with a median of measured values (n = 38) of approximately 75 cm. Non-permafrost cutbanks had a layer of organic topsoil overlying silt with abundant roots and organic-rich lenses that became interbedded and then transitioned to sand with increasing depth (Fig. 6.3a). All terrain types exhibited a trend of grain size fining upward, with medium sand (based on bed-material grab samples taken from a boat with a Ponar sampler) comprising the channel-bed material. We did not observe permafrost in active point bars, which had a thin to absent layer of organic topsoil at the land surface underlain by sandy deposits exhibiting ripple and dune cross stratification from sediment transport and deposition. Sediment TOC content and Fm values varied with sediment size. Silt samples had higher average TOC content than sandy samples, and peat had higher TOC content than topsoil (Fig. 6.4a). Although the organic horizons overlying permafrost had a higher TOC content than the organic horizons overlying non-permafrost deposits, sediment samples below the organic horizon did not show a significant difference in TOC content based on the presence or absence of permafrost for a given grain size (Fig. 6.4a and b). The strong dependence of TOC content on grain size allowed us to estimate OC stocks based on measured stratigraphic sections.
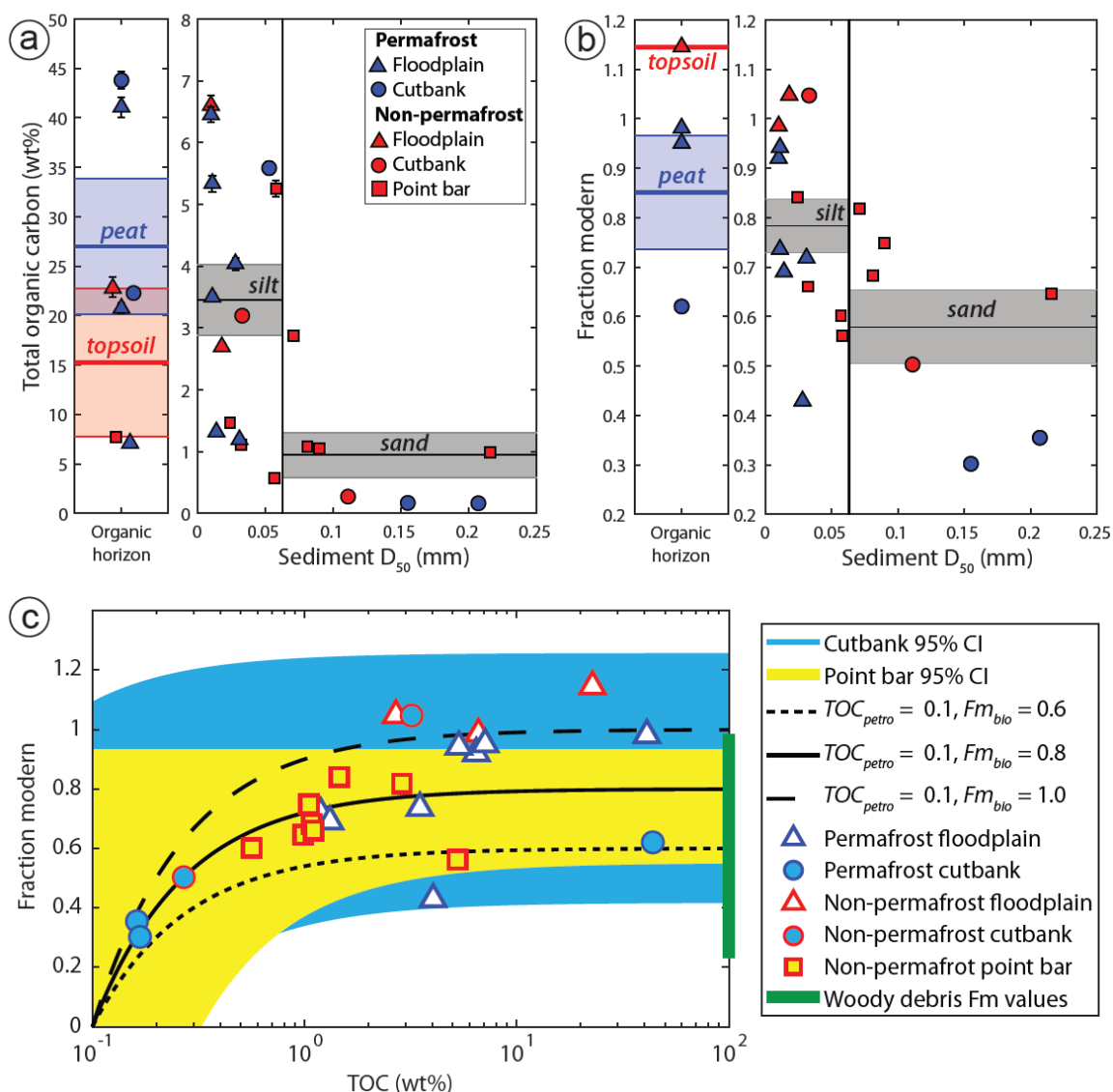
Figure 6.4. Floodplain sediment geochemistry results. **(a)** Total organic carbon versus median sediment grain size, with organic horizons split into ice-rich permafrost peat and non-permafrost topsoil, with 1 SD error bars. The horizontal lines indicate the mean and shaded region the standard error of the mean for the peat (n = 5, blue shading), topsoil (n = 2, red shading), silt (D_{50} < 0.63 mm, n = 14, gray shading), and sand (D_{50} > 0.63 mm, n = 7, gray shading) grain size classes. **(b)** Radiocarbon activity (reported as fraction modern, Fm) versus median grain size, with 1 SD error bars and shaded regions indicating the mean and standard error of the mean for peat (n = 3), topsoil (n = 1), silt (n = 13), and sand (n = 7). **(c)** Sediment sample fraction modern (Fm_{meas}) plotted against TOC content (TOC_{meas}) and fit using Eq. (6.4) to calculate end-members for biospheric radiocarbon fraction modern (Fm_{bio}) and petrogenic organic carbon content (TOC_{petro}). The 95 % confidence intervals (CI) for cutbanks and point bars are shaded in blue and yellow, with the horizontal upper bound on the point bar CI representing TOC_{petro} = 0.0 wt%. Black lines denote mixing between

representative values of TOC_{petro} and Fm_{bio}. The range of wood and plant debris Fm values is plotted on the right y axis, indicating the likely range of biospheric end-members.

Coarser sediment yielded lower Fm values – indicative of older organic carbon – with silt and organic horizons having higher Fm values (Fig. 6.4c). A petrogenic contribution can explain measured differences in sediment Fm and would be expected to be enriched in the coarser-size fraction (Galy et al., 2007). To calculate the range of TOC_{petro} and Fm_{bio} end-members for cutbank and point bar sediment OC, we fitted a nonlinear regression (nlinfit.m in Matlab 2017) between Fm_{meas} and TOC_{meas} using Eq. (6.4) and used the Jacobian to calculate 95 % confidence intervals (Fig. 6.4c). Fitting Fm_{meas} to TOC_{meas} gave a range of biospheric radiocarbon (Fm_{bio}) and petrogenic OC content (TOC_{petro}) end-members. Some cutbank samples had $\delta^{13}C$ greater than −20‰, raising concerns about incomplete decarbonation (see Table 6.S2). However, fitting Fm_{meas} to TOC_{meas} for cutbank and floodplain samples together but excluding samples with $\delta^{13}C$ greater than −20‰ (n = 13) generated a fit with similar end-members and confidence intervals. Therefore, due to the small number of radiocarbon activity, we did not exclude the high $\delta^{13}C$ samples from our analysis.

The 95 % confidence intervals for Fm_{bio} of the cutbanks and point bars overlapped with Fm values from centimeterscale wood fragments collected from bank samples and cores (Fm = 0.2319 ± 0.0015 to 0.9843 ± 0.0027, equivalent to radiocarbon ages of 11,750±55 to 125±20 yr BP). Since wood and plant debris is devoid of petrogenic OC, its Fm directly reflects storage and aging in these deposits. Therefore, we inferred that non-permafrost point bars also likely contained some aged biospheric OC.

6.6 Analysis: organic carbon cycling by river meandering

6.6.1 Carbon mass balance for a meandering river

To evaluate particulate OC fluxes into and out of the Koyukuk River, we used a mass-balance model applicable to single-threaded, meandering rivers (Fig. 6.1b), neglecting fluxes due to dissolved OC and wood and plant debris. Our model includes vertical variations in floodplain structure and their corresponding OC stocks, following similar floodplain-river exchange models (Lauer & Parker, 2008a). While other models exist that incorporate more complex boundary conditions and sediment tracking (Lauer & Parker, 2008a; Lauer & Willenbring, 2010; Malmon et al., 2003), we sought the simplest possible framework that could utilize our field data to constrain carbon fluxes. We considered POC fluxes into the river due to cutbank erosion (F_{CB}; kg yr^{-1}) and out of the river due to POC being deposited in point bars (F_{PB}; kg yr^{-1}) or overbank deposits (F_{OB}; kg yr^{-1}) or oxidized during transport and released to the atmosphere as CO_2 (F_{OX}; kg yr^{-1}; Fig. 6.1b) (Denfeld et al., 2013; Serikova et al., 2018; Striegl et al., 2012). This net budget is represented by

$$\frac{dPOC}{dt} = F_{CB} - F_{PB} - F_{OB} - F_{OX}. \tag{6.5}$$

In the subsequent sections, we estimate the organic carbon stocks to find F_{CB} and F_{PB} in Eq. (6.5) and then discuss the relative magnitudes of F_{OB} and F_{OX}.

6.6.2 Floodplain organic carbon stocks

To quantify the fluxes of carbon in and out of the river due to bank erosion and bar deposition, we first needed to estimate the carbon stocks in the floodplain. Our approach was to first take advantage of particle-size correlations with TOC content (Fig. 6.4a and b), as discussed in detail below, to estimate carbon contents for stratigraphic units where we only had grain size information. This process increased our sample size from 9 to 30 complete stratigraphic sections. Next, we used our mapping of floodplain stratigraphy and grain size to estimate carbon stocks integrated over a characteristic depth of the floodplain. We produced this analysis using two different characteristic depths for comparison. A depth of 1 m was used for comparison to previous studies that often only sampled in the top meter of the floodplain (Hugelius et al., 2014). The second depth we used was the depth of the Koyukuk River (12.4 m) because ultimately this is the thickness of floodplain material that is being eroded and deposited by the river. In Sect. 6.3, these depth-integrated carbon concentrations are used to estimate carbon fluxes due to bank erosion and bar deposition.

Measured stratigraphic sections were divided into four units (Fig. 6.S4): sand ($D_{50} > 63$ μm), mud ($D_{50} < 63$ μm), topsoil (organic horizons overlying non-permafrost sediment), and peat (organic horizons overlying permafrost). These stratigraphic units correlated with distinct magnitudes of mean TOC content (c_i) and mass fraction of water ($M_{H2O,i}$). We found the average TOC value from each unit and assigned these average values to the corresponding units for beds where we measured grain size but did not measure TOC. We quantified the uncertainty in c_i and $M_{H2O,i}$ using Gaussian error propagation of 1 standard deviation (Tables 6.S2–6.S4).

To estimate carbon stocks, total OC measurements and estimated values for each unit (Fig. 6.4a; Figs. 6.S6 and 6.S7) were integrated both over 1 m depth below the surface (Fig. 6.5a) and over a depth equivalent to the bankfull river depth (12.4 m; Fig. 6.5b). We calculated the depth-integrated OC stock using

$$C_{CB} = \sum_{i=1}^{n} \rho_i H_i c_i \left(1 - M_{H2O,i}\right). \tag{6.6}$$

We accounted for n beds of the four stratigraphic units in each measured stratigraphic section, where ρ_i is the mean unit bulk density (kg wet sediment per m^3), H_i is the unit thickness (m), c_i is the mass fraction of OC in the unit (kg OC per kg dry sediment of each unit), and $M_{H2O,i}$ is the mass fraction of water in the unit (kg H$_2$O per kg wet sediment of each unit). $M_{H2O,i}$ + $M_{dry,i} = 1$, with $M_{dry,i}$ being the mass fraction of dry sediment in the unit (kg dry sediment per kg wet sediment of each unit). Bulk densities measured from cores for mineral (mean ± 1SD of 989 ± 323 kg m^{-3}, n = 7) and organic (905±49 kg m^{-3}, n = 2) horizons were the same within uncertainty (Table 6.S2). Therefore, we used a constant mean bulk density ($\rho_i = 971$ ± 283) across all stratigraphic units (Table 6.S3).

Measurement and sampling were only possible on the exposed section of the riverbank, above the water level. Exposed sections represented 7%–47% of total bank height (as measured from channel thalweg to bank top). We assumed all sediment below the base of our stratigraphic sections consisted of sand, which was supported by our measurements of grab samples of the active channel and cores of the floodplain beyond 2 m depth (Fig. S3) and was consistent with downward-coarsening trends widely observed in meandering rivers and their deposits (Tables 6.S3–6.S4) (Miall, 2013).

Estimated permafrost cutbank and floodplain OC stocks integrated to 1 m depth were 31.1 ± 9.8 kg OC m^{-2} (mean $\pm$ 1 SD of OC stocks; n = 14), while nonpermafrost cutbanks, floodplains, and point bars contained 23.3 ± 4.8 kg OC m^{-2} (n = 10) (Fig. 6.5a). The Mann-Whitney U test found that OC stocks in permafrost and nonpermafrost deposits had similar organic content distributions ($p = 0.1669$). Grouping results by terrain type, permafrost and non-permafrost cutbanks had 30.2 ± 9.2 kg OC m^{-2} (n = 11), permafrost and non-permafrost floodplains had 28.8 ± 8.3 kg OC m-2 (n = 9), and non-permafrost point bars had 19.4 ± 5.2 kg OC m^{-2} (n = 4). The Mann–Whitney U test could not reject the null hypothesis of cutbank and floodplain OC stocks being drawn from the same distribution at 5 % confidence ($p = 0.7891$), but the test found weak evidence for point bars having distinctly lower OC stocks ($p = 0.0503$ for floodplains versus point bars, $p = 0.0601$ for point bars versus cutbanks). Therefore, floodplains and cutbanks generally had higher OC stocks in their upper 1 m of sediment than point bars, but we did not observe a significant difference in 1 m OC stocks between permafrost and non-permafrost deposits (Fig. 6.5a).

Estimated permafrost cutbank and floodplain OC stocks integrated over the channel depth were 125.1 ± 14.9 kg OC m^{-2} (mean $\pm$ 1 SD of OC stocks; n = 14), while non-permafrost cutbanks, floodplains, and point bars contained 116.1 ± 11.4 kg OC m^{-2} (n = 10) (Fig. 6.5b). The Mann–Whitney U test could not reject the null hypothesis that OC stocks in permafrost and non-permafrost deposits had the same organic content distributions ($p = 0.3641$). Grouping results by terrain type, permafrost and non-permafrost cutbanks had 125.3 ± 13.1 kg OC m^{-2} (n = 11), permafrost and non-permafrost floodplains had 121.0 ± 13.5 kg OC m-2 (n = 9), and non-permafrost point bars had 114.0 ± 15.7 kg OC m^{-2} (n = 4). Again, the Mann–Whitney U test could not reject the null hypothesis of all landform OC stocks being drawn from the same distribution at 5 % confidence ($p = 0.3619$ for floodplains versus cutbanks, $p = 0.8252$ for floodplains versus point bars, $p = 0.2799$ for point bars versus cutbanks). Therefore, the distribution of OC stocks integrated to channel depth for cutbanks was indistinguishable from the distribution of measured stocks of newly deposited point bars (Fig. 6.5b).
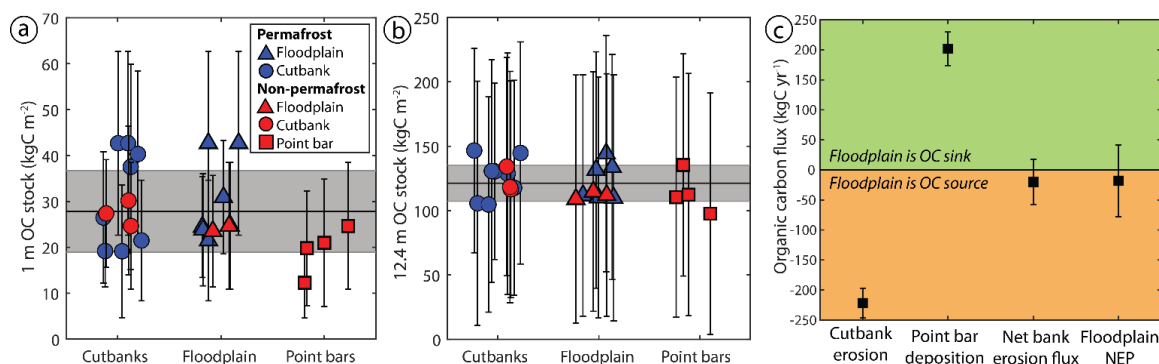
Figure 6.5. Carbon cycling due to river meandering. **(a)** Total organic carbon (OC) in each stratigraphic column integrated to 1 m below surface, with unmeasured portions of the section assumed to be sand; horizontal lines indicate the mean and shaded regions 1 SD for the complete dataset. **(b)** Total organic carbon in each stratigraphic column integrated to mean channel depth (12.4 m) using the same assumptions and uncertainty. **(c)** The net OC flux due to channel migration is comparable to floodplain net ecological productivity (NEP), and both are zero within uncertainty. The net flux of OC into the river due to erosion of cutbanks and out of the river due to sediment deposition in point bars in the Koyukuk River is calculated as the mean OC stock for each landform (with ±1 SD OC stock uncertainty for that landform) multiplied by an average channel migration rate for a 1 m downstream section of riverbank. The cutbank and point bar fluxes are differenced to calculate the net bank erosion flux. Floodplain NEP is calculated for a 10 km wide, 1 m downstream distance section of floodplain using previously reported regional NEP and uncertainties (Potter et al., 2013).

6.6.3 Carbon fluxes from river meandering

We used the OC stocks calculated to channel depth to quantify POC fluxes due to lateral channel migration (F_{CB} and F_{PB} in Eq. 6.5). We averaged the lateral migration rate over 83 km river length comprising eight meander bends (Fig. 6.2) to capture the characteristic sediment transport distances between depositional events (Pizzuto, 2014), variation in local erosion rate due to channel curvature (Howard & Knutson, 1984; Sylvester et al., 2019), and the formation of cutoffs and oxbow lakes. We calculated the mean bank erosion rate by averaging the area of floodplain eroded (1.60 km^2) and accreted (1.85 km^2) from previously published erosion masks generated using Landsat imagery (Rowland et al., 2019). Dividing this area by the length of the channel reach centerline (82.823 km) and the measurement interval for the erosion masks (2018–1978) resulted in a mean lateral migration rate of 0.52 m yr^{-1}.

We approximated the flux into the river due to cutbank erosion as $F_{CB} = L \times E \times C_{CB}$, where L is a unit river reach length (1 m), E is the bank erosion rate (0.52 m yr^{-1}), and C_{CB} is the cutbank carbon stock (kg OC m^{-2}). The point bar carbon flux was similarly calculated using $F_{PB} = L \times E \times C_{PB}$, where C_{PB} is the carbon stock of the point bar (kg OC m^{-2}). Using OC stocks integrated to channel depth, we estimated fluxes of POC due to bank erosion as F_{CB}

$= 65.2 \pm 7.3$ kg OC yr^{-1} and due to point bar deposition as $F_{PB} = 59.3 \pm 8.2$ kg OC yr^{-1} (Fig. 6.5c). This result means that OC fluxes due to bank erosion and bar deposition were equal within uncertainty.

We used radiocarbon measurements to evaluate if (1) the OC being eroded from cutbanks was oxidized during transport (F_{OX}), (2) the eroded OC was re-deposited in bars via lateral accretion (F_{PB}) or overbank deposits (F_{OB}), or (3) new biospheric OC was being added to point bars and floodplains by vegetation growth after sediment deposition. Similar to TOC and TN contents, Fm displayed a trend of higher values for finer grain sizes – a pattern consistent with prior findings that reflects the greater proportional petrogenic OC contribution in coarser material (Galy et al., 2007; Hilton et al., 2015). Coarser sediment tended to have lower TOC content, potentially indicating that low Fm values are in part due to a greater fraction of petrogenic OC (f_{petro}). When we fit a range of mixing models to assess sediment biospheric radiocarbon activity, we found that sediment from cutbanks and point bars had similar ranges of potential biospheric OC end-members (Fig. 6.4c). This observation matched the range of aged wood and plant debris found at sediment sampling locations.

Our mass-balance calculation and the presence of aged Fm_{bio} in newly deposited point bars both support the hypothesis that a significant fraction of OC eroded from cutbanks is re-deposited in the floodplain and not oxidized during transport. In addition to point bar deposition, OC could be lost from the river via overbank deposition (F_{OB}). In this case, one would expect the carbon stocks to increase on floodplain surfaces of increasing age due to the deposition of silt units near the surface. Our measurements did indicate a slight increase in 1 m OC stocks between recently deposited point bars and floodplain inferred to be older based on their distance to the river (Fig. 6.5a), but they did not show a significant increase in OC stock when integrated to channel depth (Fig. 6.5b). One possible explanation could be that F_{OB} is substantial but that this carbon has been remineralized and lost to the atmosphere. To constrain the frequency of overbank flooding along the Koyukuk River near Huslia, we examined the Landsat image record and did not find instances of overbank flooding. Ice jams, where floating ice piles up and causes high water during spring break up along Arctic rivers, occurred only four times near Huslia from 1967-2019, and in these cases, overbank flooding did not occur (White & Eames, 1999). Therefore, historical records suggest that sediment fluxes due to overbank sediment deposition are relatively minor compared to fluxes due to channel migration. Our stratigraphic observations showing a similar thickness of capping silt units in floodplain stratigraphy (with a mean of 1.29 m for cutbank, 0.92 m for floodplain, and 1.55 m for point bar samples; Table 6.S4), and the low mass fraction of siliciclastic sediment in organic horizons (based on high mass fraction TOC; Fig. 6.4a) also indicated that overbank deposition of sediment on the distal floodplain is relatively small.

Rather than additional OC from overbank flows, floodplains do appear to accumulate additional OC from biomass production. We observed an increase in organic horizon thickness, from a mean of 0.06 m in point bars to 0.45 m in cutbanks and 0.44 m in floodplain deposits, primarily driven by increasing thickness of peat horizons (Table 6.S4). The increase in organic horizon thickness can explain the cutbank and floodplain OC stocks summed to 1

m depth being slightly higher than the point bar 1 m OC stocks. Since OC stocks summed to channel depth were statistically similar between landforms, we expected that there was some oxidation of modern, labile OC during fluvial transport that was replaced after sediment was deposited in a point bar by biomass production. In spite of biospheric OC input to floodplain sediment through the growth of peat (on permafrost) and an organic-rich topsoil (on non-permafrost), observations of sediment containing old radiocarbon in both cutbanks and point bars indicate that point bar OC has been eroded from upstream and subsequently re-deposited, generating a reservoir of OC that has been aged by sediment storage along the Koyukuk River.

6.7 Discussion

Our mass-balance model indicated that channel migration generated substantial fluxes of OC into the river (> 50 kg OC yr^{-1} from cutbank erosion). If we assumed that all OC in point bars was deposited with river sediment, the calculated OC fluxes due to bank erosion and bar deposition balanced each other within uncertainty (Fig. 6.5c). However, our radiocarbon analyses indicated that a portion of the biospheric OC in point bars was fixed after deposition by local vegetation. This was reflected in slightly higher 1 m OC stocks in cutbanks and floodplain deposits versus point bars. If we instead assumed that around half of OC in eroding cutbanks was oxidized during river transport, we calculated the river must transport downstream or oxidize > 30 kg OC yr^{-1} per meter of river reach. For comparison, measurements of floodplain net ecological productivity (NEP) – the rate of OC fixation minus respiration – indicated that an equivalent 10 km wide, 1 m long river reach would emit 12.1 ± 39.9 kg OC yr^{-1} (mean $\pm$ 1 SD) (Potter et al., 2013). Therefore, the large depth (> 10 m) and migration rates (0.52 m yr^{-1}) of the Koyukuk River allow fluxes due to bank erosion and deposition to exceed floodplain NEP, despite the far smaller land area of erosion and deposition along the riverbanks compared to the expansive floodplain. In addition, our results indicate that $\sim 75\%$ of OC liberated by bank erosion comes from below the top meter. Therefore, large downstream OC fluxes from river migration can be attributed to rapid exposure and mobilization of a deep OC reservoir not readily accessible by top–down thaw.

The channel migration rates we measured reflect the river area eroded versus deposited from 1978–2018, and these migration rates are influenced by the cutoff of a narrow river reach that decreases channel length but slightly increases average width (Fig. 6.S2). Autogenic processes such as river response to cutoffs and re-visiting areas of the floodplain more or less frequently may cause transient changes in downstream OC fluxes along the Koyukuk. However, sparse observations indicate very high excess dissolved CO_2 and methane in Koyukuk River water, supporting that there is significant OC oxidation during transport (F_{OX}) (Striegl et al., 2012). Overall, significant work remains to understand the partitioning of OC loss between the dissolved and particulate loads as well as between petrogenic versus biospheric POC, particularly since DOC concentration and lability varies seasonally in the headwaters of the Koyukuk River (O'Donnell et al., 2010).

Our results indicated less variability in OC stocks across the Koyukuk River floodplain than previous work by Lininger et al. (2019), who found significant variations in OC stocks

between geomorphic units in the Yukon Flats. Lininger et al. (2019) report OC stocks to a depth of 1 m along the Yukon River and its tributaries and extrapolated the deepest measured mineral OC contents to 1 m based on similar OC content in a few samples taken at depth along cutbanks. Similar to their results, we found that newly deposited point bars without a thick organic horizon had slightly lower OC stocks for the upper 1 m of sediment. Our results also agree with Lininger et al. (2019) that the coarser sediment fraction contributes significant OC and that floodplain sediments can store OC for thousands of years between riverine transport events. However, we found little variation with geomorphic unit for OC stocks calculated to the channel depth (12.4 m). Though we included organic horizons extending below 1 m, the majority of our OC budget used to calculate fluxes due to channel migration was comprised of the more massive sandy deposits with low OC content. These differences point to the importance of river depth relative to the depth of significant floodplain biospheric OC production and the grain size of the floodplain material at depth. We hypothesize that cutbank and point bar OC stocks will be similar for rivers with coarser sediment and channels much deeper than the active layer and rooting depth of vegetation. In contrast, OC stocks in floodplains of fine-grained, shallow rivers might have a higher fraction of their OC oxidized after erosion from cutbanks and replaced after deposition in point bars.

The presence of aged biospheric OC in newly deposited, non-permafrost point bars along the Koyukuk River illustrated that floodplains are important reservoirs of aged OC in sediments both with and without permafrost. Rivers tend to rework younger floodplain deposits faster than older floodplain deposits, and this can yield a heavy-tailed distribution of deposit ages and carbon storage over thousands of years (Torres et al., 2017). Our results supported the idea that a fraction of particulate OC has experienced transient mobilization and deposition and thus becomes naturally aged during transport through the river–floodplain system. Therefore, particulate OC with old radiocarbon signatures might be attributed to OC storage in floodplains and may not be a diagnostic indicator of permafrost thaw. One might expect better preservation of carbon stocks in permafrost deposits. However, our field observations of bank sediment rapidly changing color from gray to orange when exposed to air imply that thawed floodplain sediments may be anoxic, which would reduce rates of organic matter respiration in non-permafrost deposits. When coupled with cold mean annual temperatures, anoxic non-permafrost terrain might be similarly effective as permafrost in preserving and aging biospheric OC stocks (Davidson et al., 2006). Thus, transient storage of particles in floodplains, potentially for thousands of years (Repasch et al., 2020; Torres et al., 2020), may delay or diffuse downstream signals of perturbations to the watershed's carbon cycle before reaching long-term monitoring stations at river mouths or sediment depocenters (Holmes et al., 2012; McClelland et al., 2016).

Climate change is expected to cause a decrease or disappearance of permafrost, which might alter rates of POC oxidation (F_{OX}), overbank deposition (F_{OB}), and ultimately downstream riverine POC fluxes. Permafrost thaw is also hypothesized to increase river lateral migration rates (Costard et al., 2003), although such changes have yet to be systematically documented. For the Koyukuk River, higher channel migration rates should, with all else equal, increase the magnitude of OC fluxes due to erosion and deposition and thereby decrease the residence

time and age of OC within the floodplain, but possibly with no net change in OC fluxes from the floodplain to the river. However, if, for example, climate change increases the relative importance of overbank deposition of OC-rich mud (higher F_{OB}) relative to sand bar accretion, then this change would cause a permanent increase in floodplain OC stocks, with associated decreases in OC river fluxes during the transient period of floodplain grain size fining. In contrast, an increase in channel lateral migration relative to overbank flooding would cause floodplains to become sandier and floodplain OC stocks to decline. Furthermore, climate change is altering flood discharge and frequency (Koch et al., 2013; Vonk et al., 2019; Walvoord & Kurylyk, 2016) as well as sediment supply, often associated with thaw slumps (Kokelj et al., 2013; Lantz & Kokelj, 2008; Malone et al., 2013; Shakil et al., 2020). Increases in flood magnitude could cause channel widening (Ashmore & Church, 2001; Walvoord & Kurylyk, 2016), which would increase cutbank OC fluxes relative to point bar fluxes ($F_{CB} > F_{PB}$), creating a transient increase in riverine OC flux. We expect that changes in floodplain hydrology and sedimentation due to climate change will alter downstream particulate OC fluxes and floodplain OC storage along deep, meandering Arctic rivers similar to the Koyukuk. In the process, sediment deposition in river bars should preserve radiocarbon-depleted OC and dampen positive feedbacks due to POC being released from permafrost by riverbank erosion as the climate warms.

6.8 Conclusions

To evaluate the role of riverbank erosion and bar deposition in liberating organic carbon (OC) from permafrost floodplains, we conducted a field campaign along the Koyukuk River in central Alaska, taking samples of riverbank and floodplain sedimentary deposits. Finer bank sediment had a systematically higher TOC content and Fm values than coarser sands. We combined measurements on individual samples with measured floodplain stratigraphic columns to calculate OC stocks for cutbanks, point bars, and floodplains summed to both 1 m below the surface and extrapolated to the 12.4 m river channel depth. We found that cutbanks had slightly higher OC stocks than point bars at shallow depths. However, OC stocks integrated to river channel depth did not significantly vary between river cutbanks, floodplain, and point bars or with the presence or absence of permafrost. As the Koyukuk River migrates, it is able to rapidly erode this deep OC reservoir, generating substantial OC fluxes from bank erosion and bar deposition. Net OC fluxes due to river migration are of the same order of magnitude as floodplain net ecological productivity, despite the river occupying a small fraction of the land surface. Our results indicate that floodplain processes generated an aged biospheric radiocarbon signature in newly deposited point bars, and variations in sediment Fm with grain size may be due to mixing with a petrogenic end-member. We conclude that a portion of biospheric OC that was eroded from cutbanks was preserved through transport and deposition. The presence of radiocarbon-depleted sediment in non-permafrost deposits indicates that aged POC in Arctic rivers is not a unique indicator for the presence of permafrost. Our results highlight that Arctic floodplains are significant reservoirs of OC, and their stratigraphic architecture and morphology influence POC fluxes and radiocarbon ages transmitted downstream. Therefore, sediment deposition in river bars should dampen positive feedbacks due to POC being released from permafrost by riverbank erosion as the climate warms.

6.9 Author contributions

M.P.L., J.C.R., W.W.F., A.J.W., G.K.L., and M.M.D. conceptualized the study. M.P.L., A.J.W., J.C.R. and G.K.L. determined the methodology. M.M.D., G.K.L., J.C.R., P.C.K., A.J.W., J.S., A.P.P., A.J.C., and M.P.L. collected field data. M.M.D., G.K.L., P.C.K., and A.J.W. assisted with geochemistry. M.P.L. supervised the work. M.M.D. conducted data analysis and wrote the original draft, and all authors contributed to the review and editing of the paper.

6.10 Acknowledgements

6.11 Supplemental Materials

Figure 6.S1. Sample locations. Georeferenced Landsat imagery with labelled sampling locations; C = core, B = bank, P = pit samples.
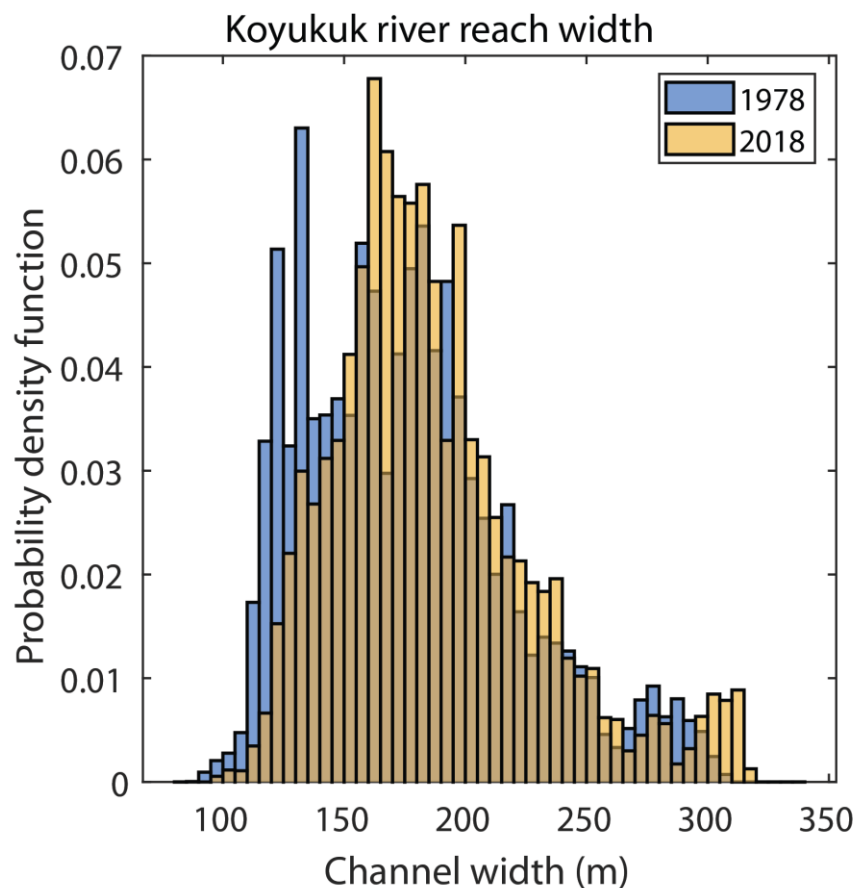
Figure 6.S2. Koyukuk River width. Probability distribution of width of channel masks generated from Landsat 30 m imagery, with widths calculated at each pixel along the channel centerline for the reach of the Koyukuk River pictured in Fig. S1 (Rowland et al., 2019). The reach maintained a roughly constant channel width over the Landsat record, from 173±43 m (median ± 1SD) in 1978 to 179±42 m in 2018, supporting our assumption that cutbank erosion and point bar deposition occur at the same rate.

Cutbanks

152
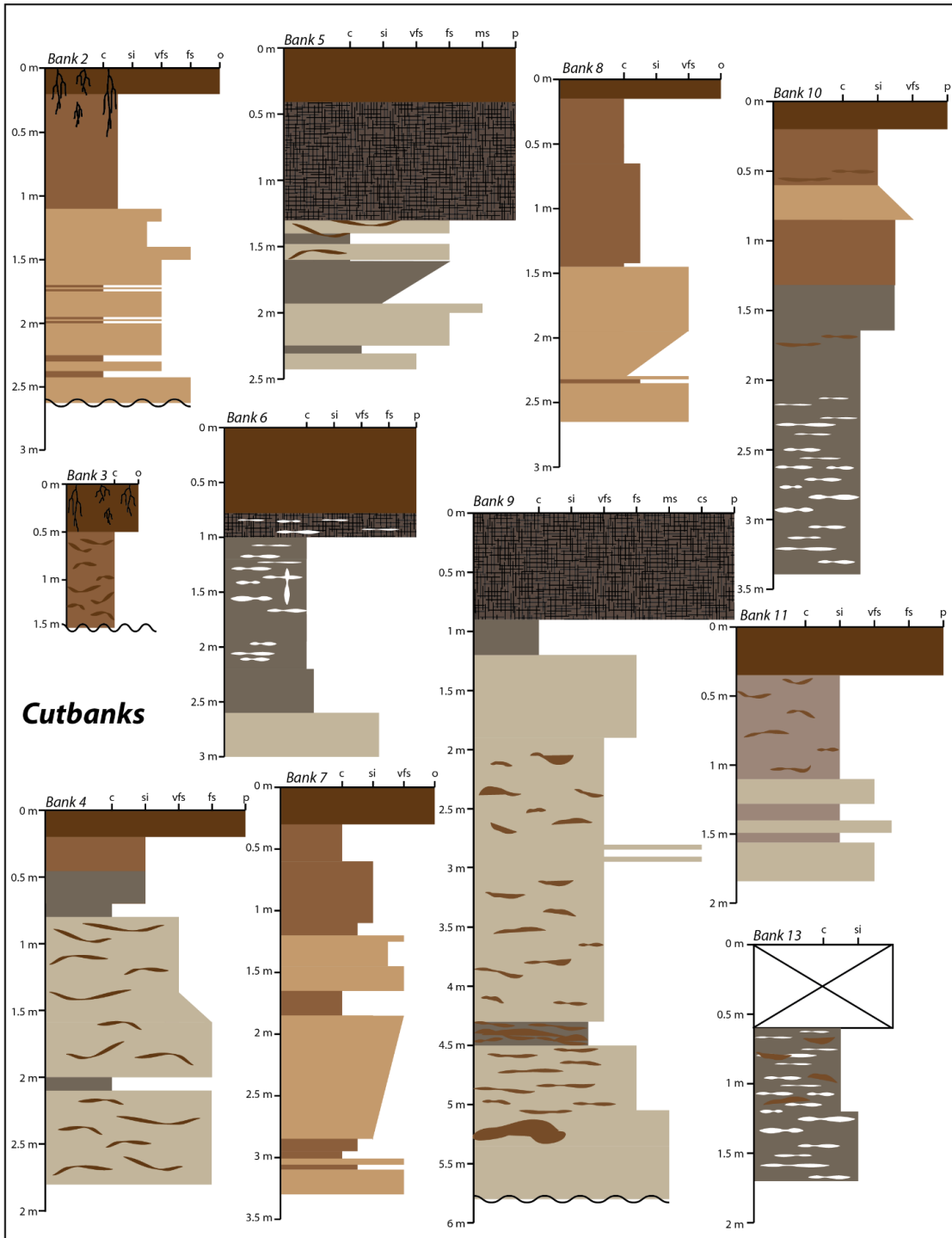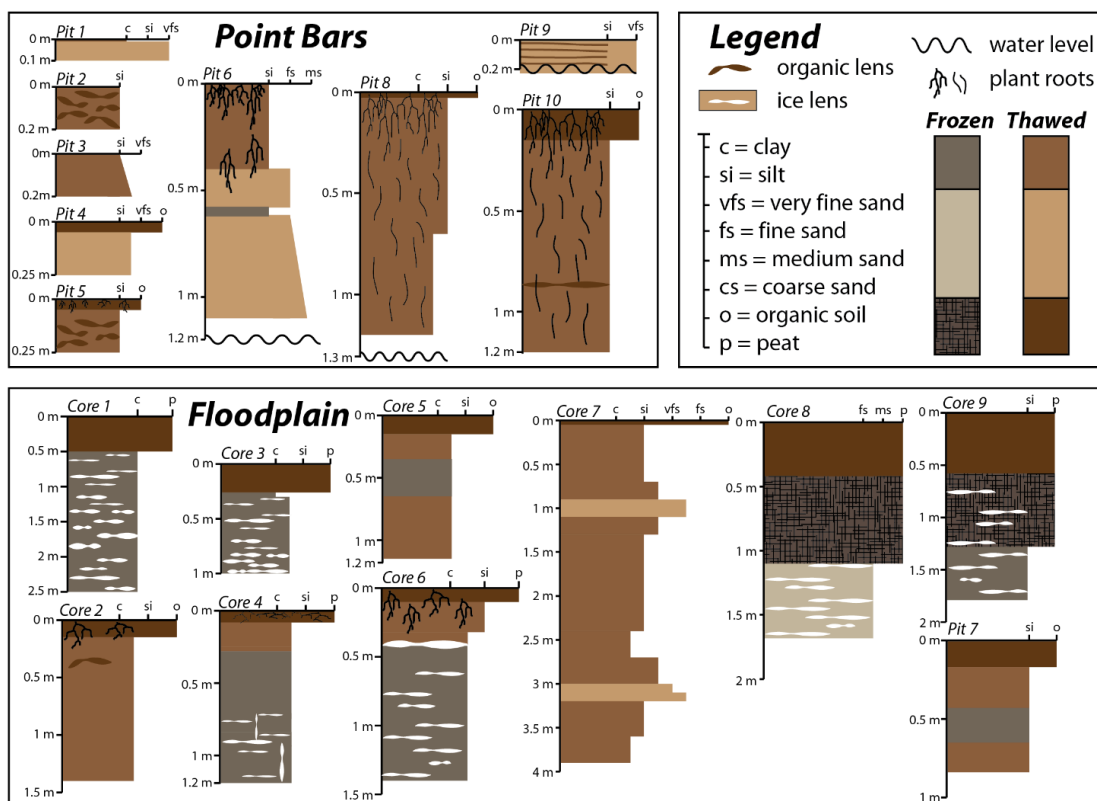
Figure 6.S3. Measured stratigraphic sections grouped by location on river floodplain. The river channel is eroding its cutbanks and depositing sediment on its point bars, which accrete to form the floodplain as the channel continues to migrate laterally. Note that deposits were generally sandy greater than 2 m depth below the floodplain surface, and that organic horizon thickness at the ground surface varies, though lenses of organic-rich sediment were prevalent meters below the surface. The active layer was shallower in permafrost units containing thick layers of peat, while locations without permafrost contained plant roots extending meters farther below the ground surface and lacked thermoerosional niches. Thicknesses of stratigraphic units were tabulated for each section in Table 6.S4.
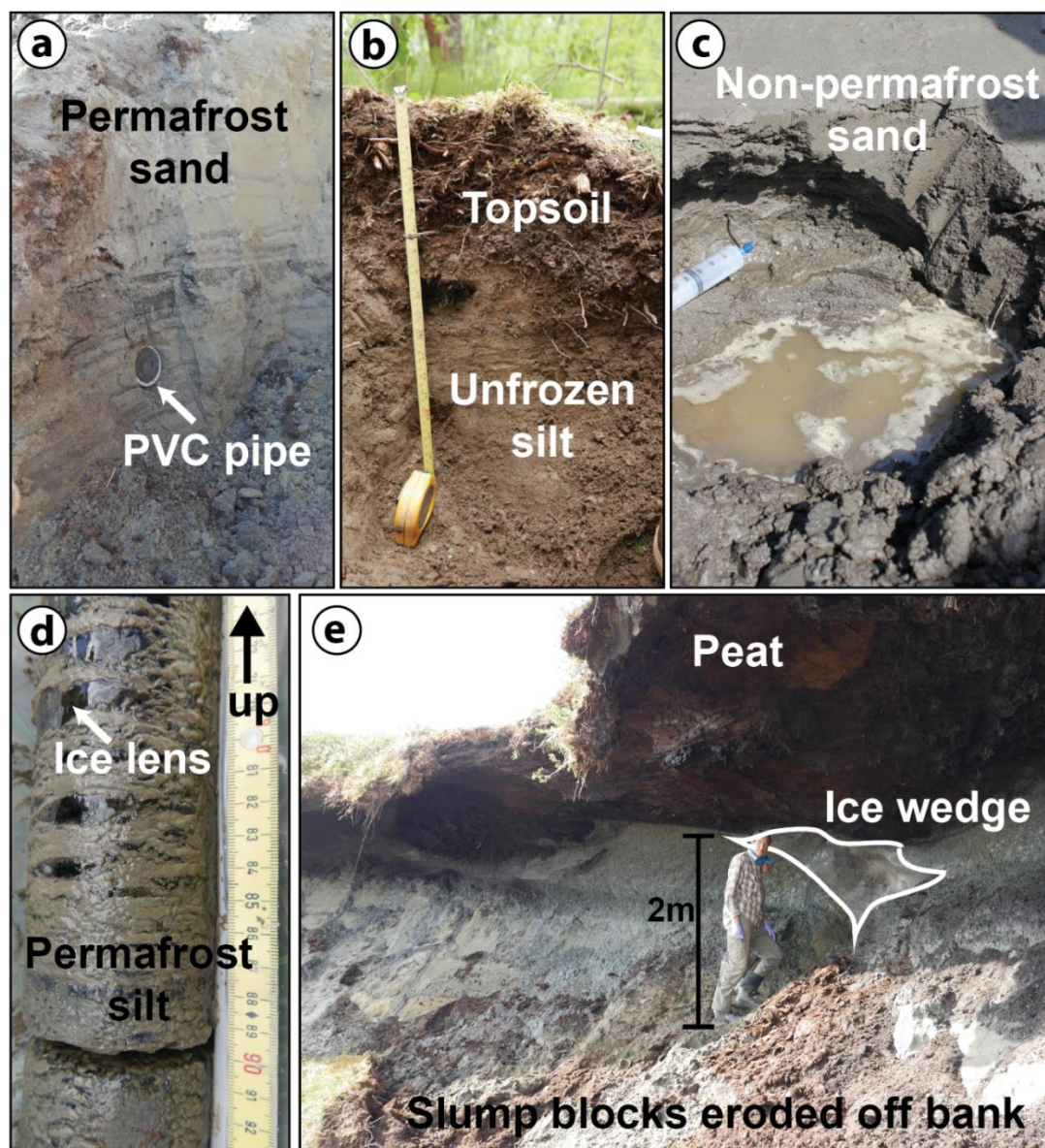
Figure 6.S4. Field photos of floodplain stratigraphic facies. **(a)** Permafrost sand in Bank 9 with 2 inch PVC pipe (outer diameter is 6.0 cm) installed in the bank for scale. **(b)** Pit dug in non-permafrost ground with root-rich topsoil overlying silt at Core 5. **(c)** Non-permafrost sandy deposits on a point bar beach at Pit 9. **(d)** Permafrost silt containing ice lenses in Core 4. **(e)** Overhung cutbank from Bank 9, with a layer of peat overlying an ice wedge surrounded by grey, frozen silt with slump blocks and intraclasts of thawed peat and silt forming a slope that shields the bank.
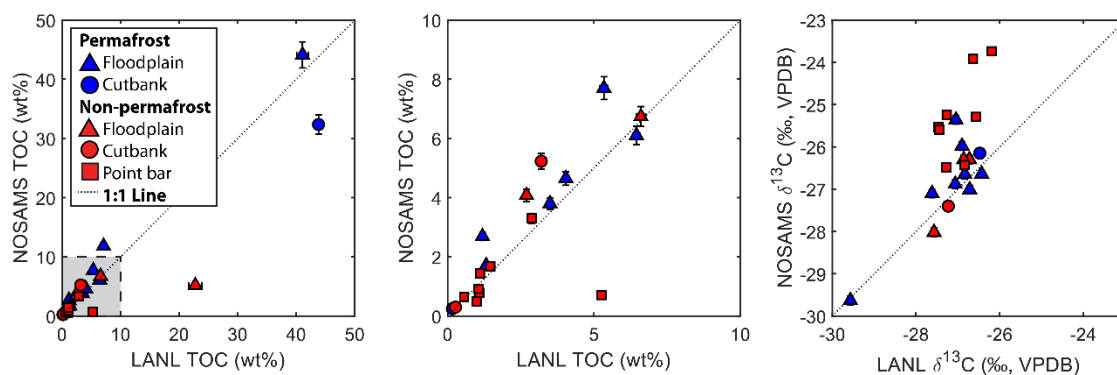
Figure 6.S5. Organic carbon measurement comparison. TOC and OC stable isotopes were measured at both NOSAMS and Los Alamos National Lab (LANL), with NOSAMS generally showing a slightly higher TOC and δ^{13}C. We attribute these differences to decarbonation procedures (see Materials and methods). All plots in the main text and supplemental materials use the LANL TOC and δ^{13}C values with NOSAMS radiocarbon measurements. **(a)** NOSAMS versus LANL TOC measurements, with error bars showing 1SD analytical uncertainty. **(b)** Zoomed in plot of shaded region in plot (a). **(c)** NOSAMS versus LANL OC stable isotope measurements, reported as per mille (‰) relative to VPDB with error bars showing 1SD analytical uncertainty.
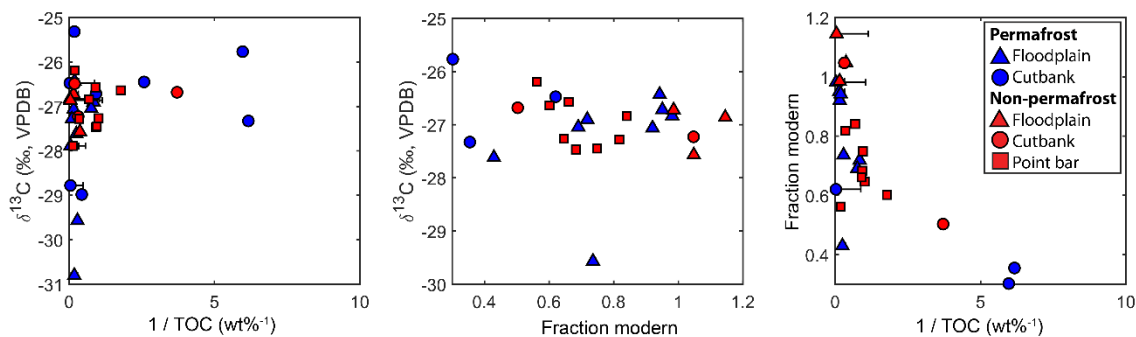
Figure 6.S6. Sediment OC characteristics. Stable organic carbon isotopes displayed no trends with total organic carbon (TOC) or radiocarbon fraction modern (Fm). Sediment δ^{13}C values spanned the range previously reported in peat and woody debris (from -23.2±0.2 ‰ to -28.6±0.2 ‰) on the Koyukuk River floodplain near its confluence with the Yukon River (O'Donnell et al., 2012). Stable organic carbon isotope values also incorporated a petrogenic end-member, and kerogen-rich sedimentary rocks in the Brooks Range had δ^{13}C ranging from -27.23±0.1 ‰ to -30.75±0.1 ‰ (Johnson et al., 2015). Measured δ^{13}C values are reported in units of per mille (‰) relative to the VPDB, with x and y error bars showing 1SD analytical uncertainty.
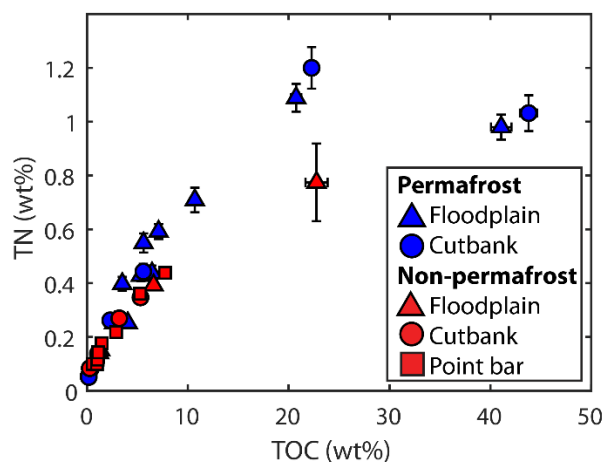
Figure 6.S7. Sediment total nitrogen. Total nitrogen (TN) versus total organic carbon (TOC) measured as dry weight % of samples, with error bars showing 1SD analytical uncertainty.

Table 6.S1. Sample site locations and characteristics.

Sample site	Landform	Latitude (°)	Longitude (°)	Frozen ground type
Bank 1	Cutbank	65.78014	-156.43661	Permafrost
Bank 2	Cutbank	65.76493	-156.49031	Non-permafrost
Bank 3	Cutbank	65.76519	-156.48964	Non-permafrost
Bank 4	Cutbank	65.75232	-156.50511	Permafrost
Bank 5	Cutbank	65.75232	-156.50511	Permafrost
Bank 6	Cutbank	65.75232	-156.50511	Permafrost
Bank 7	Cutbank	65.66093	-156.45087	Non-permafrost
Bank 8	Cutbank	65.66126	-156.44711	Non-permafrost
Bank 9	Cutbank	65.70265	-156.40977	Permafrost
Bank 10	Cutbank	65.61942	-156.48534	Permafrost
Bank 11	Cutbank	65.62931	-156.46198	Non-permafrost
Bank 12	Cutbank	65.64022	-156.50949	Non-permafrost
Bank 13	Cutbank	65.87132	-156.26283	Permafrost
Bank 14	Cutbank	65.70153	-156.40353	Permafrost
Core 1	Floodplain	65.78014	-156.43661	Permafrost
Core 2	Floodplain	65.76521	-156.49049	Non-permafrost
Core 3	Floodplain	65.72090	-156.37178	Permafrost
Core 4	Floodplain	65.73519	-156.38866	Permafrost
Core 5	Floodplain	65.67904	-156.61163	Non-permafrost
Core 6	Floodplain	65.67158	-156.58762	Permafrost
Core 7	Point bar	65.66046	-156.43256	Non-permafrost
Core 8	Floodplain	65.72552	-156.20992	Permafrost
Core 9	Floodplain	65.71100	-156.27473	Permafrost
Pit 1	Point bar	65.77817	-156.43370	Non-permafrost

Pit 2	Point bar	65.77764	-156.43364	Non-permafrost
Pit 3	Point bar	65.77688	-156.43394	Non-permafrost
Pit 4	Point bar	65.77636	-156.43342	Non-permafrost
Pit 5	Point bar	65.77483	-156.43354	Non-permafrost
Pit 6	Point bar	65.77756	-156.43381	Non-permafrost
Pit 7	Floodplain	65.72083	-156.37217	Non-permafrost
Pit 8	Point bar	65.65986	-156.43524	Non-permafrost
Pit 9	Point bar	65.65958	-156.43542	Non-permafrost
Pit 10	Point bar	65.66132	-156.43354	Non-permafrost

Table 6.S2. Sample descriptions and results of laboratory analysis.
TableS2.csv available for download at: https://esurf.copernicus.org/articles/10/421/2022/

Table 6.S3. Averaged sediment TOC concentrations and constants used in calculations of bank TOC integrated to channel depth.

	Sand	**Silt**	**Peat**	**Topsoil**
D_{50} (mm)	>0.063	<0.063	N/A	N/A
Water content (wt%)	18.1±6.1	46.6±15.6	87.5±7.4	62.2±1.0
TOC (wt%)	0.94±0.95	3.69±2.25	35.20±12.60	15.25±10.62
TOC (kgC/m^3)	7.49±8.27	19.1±14.4	42.7±20.0	55.9±42.2
TOC_{petro} (wt%)	0.108±0.045	0.108±0.045	0.108±0.045	0.108±0.045
TOC_{petro} (kgC/m^3)	0.86±0.52	0.56±0.34	0.13±0.07	0.40±0.20
TOC_{bio} (wt%)	0.83±0.95	3.58±2.25	35.09±12.60	15.14±10.62
TOC_{bio} (kgC/m^3)	6.63±8.13	18.57±14.29	42.55±20.00	55.52±42.18
Bulk density (kg/m^3)	971±283			
Channel Depth (m)	12.4			
Migration Rate (m/yr)	0.52			

Table 6.S4. Calculation of bank TOC, biospheric, and petrogenic components integrated to channel depth based on measured stratigraphic columns. Note that unmeasured section was assumed to consist of sand based on field observations.
TableS4.csv available for download at: https://esurf.copernicus.org/articles/10/421/2022/

Table 6.S5. Complete grain size distributions measured using laser diffraction tabulated in log-normal bins, with 10th-, 50th- and 90th-percentile grain size reported as D_{10}, D_{50}, and D_{90}.
Table5S.csv available for download at: https://esurf.copernicus.org/articles/10/421/2022/

Table 6.S6. Linear mixing calculations of fraction modern of biospheric OC and fraction of biospheric OC produced *in situ* (as opposed to being deposited in association with the sediment by the river). End-members for transported OC (Fm of oldest woody debris from a cutbank) and *in situ* produced OC (youngest topsoil Fm_{bio}) are italicized.

Sample Name	Sample Type	Biospheric fraction modern (Fm_{bio})
KY18-Bank2-10	Cutbank sediment	1.0837±0.0330
KY18-Bank2-230	Cutbank sediment	0.8398±0.1015
KY18-Bank9-Peat	Cutbank sediment	0.6217±0.0173
KY18-Bank9-220	Cutbank sediment	1.0631±0.1776
KY18-Bank9-350	Cutbank sediment	0.8509±0.1396
KY18-Core1-22-28	Floodplain sediment	0.9359±0.0265
KY18-Core1-105-111	Floodplain sediment	0.7593±0.0228
KY18-Core2-10-12	Floodplain sediment	1.0916±0.0413
KY18-Core2-35-37	Floodplain sediment	1.0018±0.0354
KY18-Core3-15-20	Floodplain sediment	0.9653±0.0340
KY18-Core3-84-89	Floodplain sediment	0.7899±0.0380
KY18-Core4-16-20	Floodplain sediment	0.9616±0.0342
KY18-Core4-105-110	Floodplain sediment	0.7521±0.0347
KY18-Core5-15	*Floodplain sediment*	*1.1507±0.0781*
KY18-Core7-85-95	Point bar sediment	0.7440±0.0551
KY18-Core7-390-400	Point bar sediment	0.5736±0.0205
KY18-Core9-33-38	Floodplain sediment	0.9837±0.0344
KY18-Core9-169-174	Floodplain sediment	0.4409±0.0160
KY18-Pit1-5	Point bar sediment	0.7253±0.0383
KY18-Pit2-10	Point bar sediment	0.8494±0.0319
KY18-Pit4-20	Point bar sediment	0.7588±0.0382
KY18-Pit5-20	Point bar sediment	0.9077±0.0401
KY18-Pit6-60	Point bar sediment	0.8343±0.0426
KY18-Pit8-40	Point bar sediment	0.7323±0.0365
KY18-Bank14	*Cutbank woody debris*	*0.2319±0.00152*

C h a p t e r   7

SLOW PERMAFROST FORMATION AND
RAPID DEGRADATION IN A MEANDERING
RIVER FLOODPLAIN

Madison M. Douglas[1], Gen K. Li[1,2], A. Joshua West[3], Yutian Ke[1], Joel C. Rowland[4],
Nathan Brown[5], Jon Schwenk[34], Preston C. Kemeny[1,6], Anastasia Piliouras[4,7], Woodward
W. Fischer[1], Michael P. Lamb[1]

[1]Division of Geological and Planetary Sciences, California Institute of Technology,
Pasadena, CA, 91125, USA
[2]Department of Earth Science, University of California, Santa Barbara, CA, 93106, USA
[3]Department of Earth Sciences, University of Southern California, Los Angeles, CA, 90089,
USA
[4]Los Alamos National Laboratory, Los Alamos, New Mexico, 87545, USA
[5]Department of Earth and Environmental Sciences, University of Texas at Arlington,
Arlington, TX, 76019, USA
[6]Department of the Geophysical Sciences, University of Chicago, Chicago, Illinois, 60637,
USA
[7]Department of Geosciences, Pennsylvania State, University Park, PA, 16802, USA

Key Points:

- The Koyukuk River erodes permafrost up to 10 ka and deposits unfrozen sediment while migrating across its floodplain.
- Permafrost reforms in new floodplain deposits over approximately 4,000 yrs and is more prevalent in older deposits over millennia.
- Koyukuk River deposits formed permafrost until recent decades, but younger deposits have patchy permafrost due to changing climate and active layer deepening.

7.1 Abstract

Permafrost regions cover 25% of land in the Northern Hemisphere, where permafrost stabilizes the ground beneath communities and infrastructure and sequesters carbon. However, the coevolution of permafrost occurrence, geomorphology and vegetation in Arctic environments remains poorly understood. In this study, we examined these dynamics in the Koyukuk River floodplain, located in discontinuous permafrost in central Alaska. We mapped geomorphic landforms and floodplain relative depositional ages from optical satellite imagery to understand how river processes and vegetation succession impact permafrost occurrence and floodplain morphology. We validated these maps using field observations of permafrost presence and absence, and dated sedimentary deposits using radiocarbon and optically-stimulated luminescence (OSL) ages. We found that the Koyukuk River erodes permafrost at cutbanks through lateral channel migration and deposits new land

as point bars. Point bar deposits span ages from 8 ka to the present, and permafrost is more abundant on older floodplain deposits. An idealized permafrost growth model revealed that this spatial pattern reflected relatively consistent formation of permafrost following river migration over at least the last 8 ka, with newly deposited sediment forming continuous permafrost after ~1.5 ka, and indicates likely top-down permafrost thaw decreasing permafrost extent by 40% in recent decades. Model results and field observations indicate that permafrost on the Koyukuk floodplain used to be governed by a balance between channel migration and regrowth but is now vulnerable to top-down thaw and increasing patchiness from rising air temperatures.

7.2 Plain-language summary

Arctic rivers constantly resurface their floodplains, eroding permafrost from one riverbank while depositing unfrozen sediment on the opposite bank where permafrost may eventually re-form. Therefore, while permafrost is often considered a stable reservoir for carbon or platform for construction of residential or commercial infrastructure, permafrost in river floodplains is continually being erased and re-formed. To better understand this process, we combined field measurements, dating techniques, and remote sensing to map active landscape processes and vegetation patterns pertaining to permafrost along the Koyukuk River in Alaska. By mapping floodplain deposit chronology and developing a simple numerical model, we determined that permafrost was present in floodplain deposits of all ages, indicating it has been eroding and re-forming continuously over at least the past 8,000 years. Permafrost is most abundant in older areas of the floodplain, where thick accumulations of moss insulate the ground from warm summer air temperatures. Younger areas of the floodplain display very patchy permafrost, which we attributed to localized differences in vegetation causing spatial variation in permafrost degradation from recently rising air temperatures. Our results illustrated how river processes shape floodplain vegetation succession and permafrost occurrence along the Koyukuk, and highlight that permafrost in Arctic floodplains will be vulnerable to degradation from a combination of warming air temperatures and river processes like increased flooding and bank erosion.

7.3 Introduction

Much of the northern hemisphere is underlain by permafrost – ground that has remained frozen for at least two years – but the age and material properties of permafrost vary widely (French & Shur, 2010; Jaroslav Obu et al., 2019). Determining which permafrost deposits will remain stable or will collapse upon thaw is critical for hazard prediction in the Arctic (Karjalainen et al., 2019). In addition, permafrost deposits are especially rich in organic carbon (OC), and the thaw and mobilization of these deposits might result in oxidation of this OC and provide a positive feedback on climate change (Schwab et al., 2020; Turetsky et al., 2020). Thus, the temporal and spatial scales over which permafrost forms and decays has a significant impact on the material properties and the abundance and lability of organic carbon in Arctic soils.
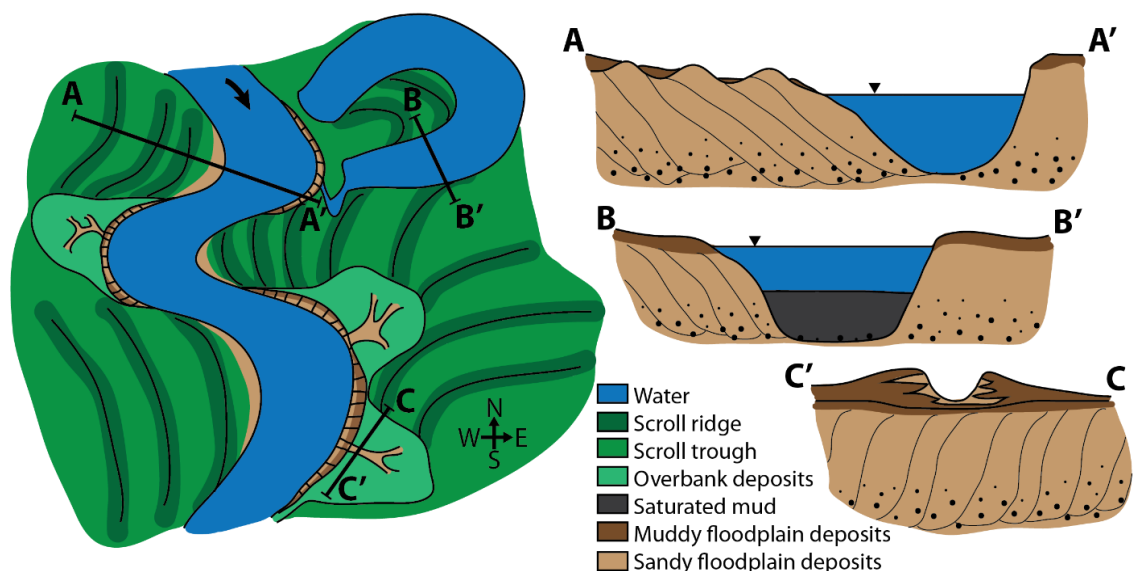
Figure 7.1. Schematic of a meandering river floodplain. Cross-section A-A' shows a transect of the river channel, which is eroding its steep outer bank (cutbank) at A' and depositing sediment on its low-slope bank (pointbar) in the center of the transect. Cross-section B-B' illustrates an oxbow lake gradually filling with mud being sourced from the river by a tie channel and overbank floods. Cross-section C-C' shows pointbar deposits overlain by deposits from a secondary distributary channel (crevasse splay) that sources a mixture of coarse and fine sediment during intervals of high water.

Arctic floodplains provide an opportunity to substitute space for time and study permafrost development under constant climatic and tectonic conditions. Permafrost river deposits contain landforms characteristic of meandering rivers globally as well as unique thermokarst landforms found in polar regions. Meandering rivers thaw permafrost in their cutbanks and below the riverbed, typically forming a through-talik (Crampton, 1979; Smith, 1976), though some rapidly migrating rivers in cold climates may not completely thaw permafrost beneath their beds (Kreig & Reger, 1982). River meandering produces a series of unfrozen scroll bars (inner bank levees) that trace out the past locations of the river (Figure 7.1, A-A') (Mason & Mohrig, 2019). While rivers tend to migrate without external forcing, they visit specific locations on the floodplain at irregular intervals, generating a heavy-tailed distribution of floodplain deposit ages (Lauer & Willenbring, 2010; Torres et al., 2017). Therefore, meandering river floodplains contain deposits with ages typically spanning millennia that have experienced the same climate and tectonic forces, setting up a natural experiment of deposit evolution through time.

River floodplains contain deposits with distinct terrain types, distinguished by variations in elevation and flood frequency, that might allow permafrost to grow at different rates on deposits of the same age. When river bends intersect themselves, they abandon a section of channel to form an oxbow lake extending to the channel depth (Figure 7.1, B-B'). The connection between the oxbow lake and the river is gradually filled in by a wedge of sand over hundreds of years (Rowland et al., 2005), then inter-bedded sand and finer sediments

accrete to produce a secondary tie channel that infills the lake (Ishii & Hori, 2016; Rowland et al., 2009; Toonen et al., 2012). Overbank floods also form channel splays where flow cross-cuts cutbank levees (Figure 7.1, C-C') or links abandoned oxbows together (Czuba et al., 2019; David et al., 2017). Permafrost floodplains contain distinctive topographic features generated by the collapse of ice-rich sediments, such as thermokarst lakes and thaw slumps (Vonk et al., 2015). Cryoturbation plus the formation of peat bogs on permafrost terrain may gradually render meandering river deposits unrecognizable (Shur & Jorgenson, 2007). Floods degrade permafrost due to advection and infiltration of warm water across the floodplain surface (Zheng et al., 2019), but also deposit a veneer of fine sediment (Lauer & Parker, 2008a, 2008b), which can subsequently insulate the underlying permafrost. Thus, river floodplains offer a diversity of terrain types to help understand favorable conditions for permafrost formation.

Discontinuous permafrost growth in newly deposited sediments has been observed to occur in tandem with ecological succession of forest regrowth but is primarily controlled by air temperatures. In discontinuous permafrost regions, pioneer willows, poplars, and grasses form on newly deposited bars within 10-15 years and are the primary vegetation for 50-100 years. Then, white spruce seedlings become established and form a canopy that prevents poplars from growing (Viereck, 1970). Spruce seedlings, understory shrubs, and moss are generally intolerant of silt deposited during floods, so they do not become established until the point bar has aggraded or river migrated sufficiently far to reduce the frequency of flooding (Gill, 1973; Kreig & Reger, 1982; Péwé et al., 1969). After predominantly white spruce replaces willow and poplar, moss begins to grow on the forest floor ~200-300 years after the deposit formed, and is hypothesized to provide sufficient insulation for permafrost to form under the floodplain (Viereck, 1970). Once permafrost starts to grow, it forms epigenetically from the surface downwards, gradually restricting rooting depth of plants as ice fills sediment pore space, causing a transition to a moss-rich (*Sphagnum*) bog, sparsely populated by black spruce (*Picea mariana*) trees (Kreig & Reger, 1982). In continuous permafrost regions, permafrost regrowth typically outpaces ecological succession, and localized vegetation growth can even cause localized increases in active layer depth (Smith, 1976). Therefore, air temperatures appear to be the primary control on permafrost occurrence, but vegetation growth influences the growth and persistence of permafrost in warmer regions (Jorgenson et al., 2008).

Permafrost occurrence on Arctic floodplains is governed by patterns of channel migration, fluvial deposit characteristics, and vegetation growth (Mann et al., 1995). However, the timescales for permafrost to re-form remain largely unknown. Modeling exercises indicate that thick layers of permafrost can form within decades to centuries (Delisle, 1998), but developing many of the characteristics of permafrost landscapes, such as ice-wedge polygons, are thought to form over millennia (Plug & Werner, 2002). The degree to which floodplain permafrost forms syngenetically with overbank deposits and moss growth versus epigenetically in sandy deposits after they are formed might determine the rate of growth – syngenetic permafrost growth following infilling of thermokarst lakes requires thousands of years (Jorgenson & Shur, 2007; Kanevskiy et al., 2014). Prior studies in riparian

environments focused on borehole and vegetation measurements at single cross-sections through one generation of floodplain deposits, neglecting older deposits (Shur & Jorgenson, 2007; Smith, 1975). Some efforts examined multiple generations of scroll bars for short river reaches (Jorgenson et al., 1998; Mann et al., 1995; Stephani et al., 2020), but these approaches have not been scaled up to large floodplains with complex networks of secondary channels, oxbow lakes, and thermokarst features (Pastick et al., 2014). Therefore, we lack a comprehensive understanding of the interactions between major Arctic rivers, their floodplain ecology, and permafrost occurrence.

In this study, we examined spatial patterns of permafrost, vegetation, and landforms in the discontinuous permafrost floodplain of the Koyukuk River, located in central Alaska, to better understand the temporal evolution of permafrost in the floodplain. We evaluated two alternative hypotheses for modern permafrost occurrence: (1) the floodplain contains relict permafrost from a prior, colder climate which is currently thawing from the top-down; or (2) permafrost is actively growing in the floodplain, likely with a delay between the deposition of new bars and permafrost formation. To test these hypotheses, we used satellite imagery and field observations to generate geomorphic and relative age maps of the Koyukuk floodplain. We combined these maps with radiocarbon ages, optically stimulated luminescence (OSL) ages, and permafrost probe measurements to produce permafrost and absolute age maps. We used observations of present-day permafrost extent to formulate an inverse problem and constrain potential permafrost growth and degradation histories over time, taking advantage of the shared climatic conditions experienced across the floodplain.

Figure 7.2. Field photos of the Koyukuk River, Alaska. **(a)** Map of Alaska with the Yukon River system shown in blue. **(b)** Aerial image showing scroll bar complexes outlined by vegetation across the Koyukuk River floodplain near Huslia, Alaska. Boat for scale (white circle) is the same boat depicted in (d). **(c)** Seasonally frozen bank with large white spruce and willow trees tipping into the river as the bank erodes. **(d)** Cutbank containing permafrost and ice wedges overlain by a thick layer of peat and mosses with few trees.

7.4 Field site: Koyukuk River, Alaska

The Koyukuk River flows south from its headwaters in the Brooks Range through lowlands containing discontinuous permafrost to join the Yukon River (Figure 7.2a). We selected the

Koyukuk as a field site because it is meandering and has deposited scroll bar complexes which enable a space-for-time substitution. The Koyukuk contributes 12% of the mean annual water and sediment discharge and makes up 11% of the catchment area of the Yukon River as measured at Pilot Station (Brabets et al., 2000). We conducted field work on a 30 km long reach of the river near the village of Huslia, Alaska in June to early July of 2018, and in May and late September in 2022. Huslia has a mean annual air temperature of -3.6°C and mean annual precipitation of 31 cm/year for the period of 1981-2010 (Daly et al., 2018). The village was built on eolian deposits from sand dunes that covered the region during the last ice age, predecessors to the present-day Nogahabara dunes. Climate reconstructions indicate that the region experienced an interval of colder air temperatures from ~13–11.5 ka during the Younger Dryas, then air temperatures stabilized at modern values in ~8 ka (Alley, 2004; Meyer et al., 2010). Today, the Koyukuk River primarily reworks sediment from its own prior fluvial deposits.

The Koyukuk River transits the floodplain near Huslia as a single-threaded, meandering channel (Figure 7.3a). The much smaller Huslia River is the only tributary to the Koyukuk within our study reach, and we assumed the Koyukuk has a similar water discharge, sediment supply, and grain size throughout this river reach. Borehole data indicates that permafrost in the Koyukuk floodplain is up to 31 m thick (Jorgenson et al., 2008), so the 12.4 m-deep Koyukuk River most likely thaws all permafrost present under its bed (producing a through-talik) as it migrates. The Koyukuk rarely experiences overbank flooding caused by ice jams (White & Eames, 1999), but portions of the floodplain are frequently inundated (Pekel et al., 2016).

Vegetation in the Koyukuk floodplain is closely tied to surface morphology. Trees commonly grow on the ridges of scroll bars, contrasting with grasses filling frequently inundated scroll swales, making scroll bars visible in drone and remote sensing imagery (Figure 7.2b). Floodplain areas with near-surface permafrost tend to contain sparse black spruce trees and thick layers of moss and peat at the ground surface as well as thermokarst lakes (Nowacki et al., 2003). Riverbanks containing permafrost are frequently overhung, where peat slumps down over thermoerosional niches thawed back at the water line (Figure 7.2d). In contrast, floodplain regions without permafrost contain willows, poplars, white spruce, and sparse black spruce (Figure 7.2c).

7.5 Methods

7.5.1 Field sampling and measurements

Measurements of permafrost depth were obtained using a 1 m (in summer 2018, spring 2022) or 2 m (in fall 2022) long permafrost probe. With practice, it was possible to distinguish permafrost from other obstructions, such as tree roots, cohesive mud, and pebbles. We also conducted two permafrost depth surveys in a random walk to characterize local variability in active layer thickness. In this study, we defined permafrost operationally as ground with sufficient pore-ice content to resist probing, consistent with ground control datasets for large-scale permafrost mapping (Pastick et al., 2015). Ground that did not resist permafrost probing

or contained only thin layers of frozen soil resistant to probing were classified as seasonally frozen but lacking permafrost.

Field samples were taken across a range of erosional and depositional environments on the floodplain (Figure 7.3a). Sampling methods and analysis were previously reported (Douglas et al., 2021, 2022), and are described briefly here. We used hand trowels to sample riverbanks and shallow bars, a hand auger for deep unfrozen sediment, and a snow, ice and permafrost research establishment (SIPRE) corer for permafrost. Optically stimulated luminescence (OSL) samples were collected using a mallet to pound in opaque PVC pipe to sandy bank sediment under an opaque tarp to avoid exposure to sunlight. Samples were kept cool in the field and transported frozen back to Caltech, where they were stored at -15°C.
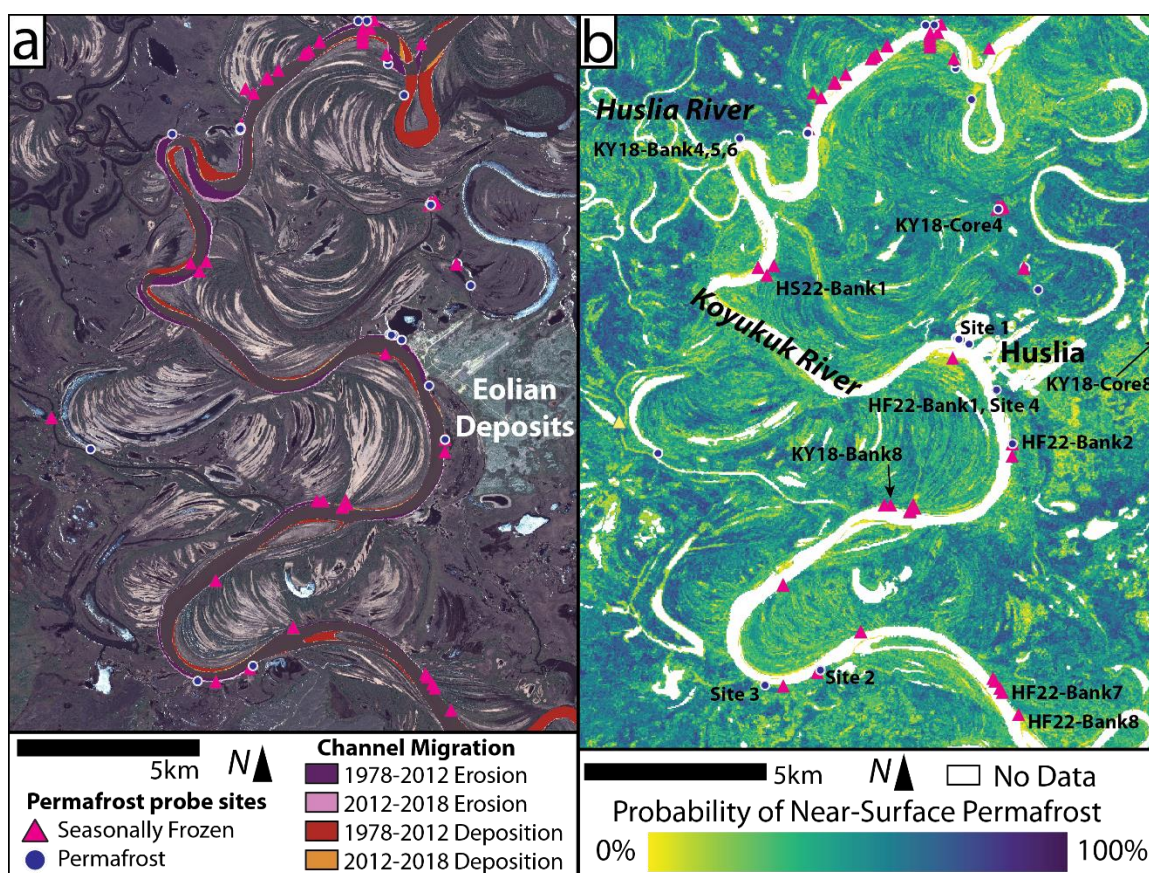
Figure 7.3. Permafrost occurrence and bank erosion along the Koyukuk River. **(a)** Floodplain sampling locations from summer 2018 field campaign near the village of Huslia, Alaska. Channel migration masks show areas of erosion and deposition calculated using SCREAM (Rowland et al., 2016) based on 1978-2012 and 2012-2018 Alaska High-Altitude Photography and Worldview imagery (Rowland & Stauffer, 2019). Basemap satellite imagery ©Maxar 2012. **(b)** Pastick et al. (2015) 30 m-resolution near-surface (within upper 1 m of soil column) permafrost probability map for the Koyukuk River floodplain. Sample sites mentioned in the main text are labeled. No Data values shown in white include rivers, lakes, and infrastructure within the town of Huslia.

7.5.2 Radiocarbon analysis

We analyzed the radiocarbon ages of individual fragments of synsedimentary woody debris to constrain the age of sedimentary deposits (Table 7.S1). We did not use sediment radiocarbon measurements, because sediment contains a mixture of modern biospheric carbon and a rock-derived, radiocarbon-dead component that do not reflect deposit ages (Douglas et al., 2022). Measurements and methods for the 2018 samples were previously described in Douglas et al. (2022). In brief, pieces of wood, peat, and plant material were rinsed with MiliQ water and stored in combusted glass vials. Samples were shipped to the National Ocean Sciences Accelerator Mass Spectrometry (NOSAMS) facility in Woods Hole (all 2018 samples) or UC Irvine (UCI) (spring 2022 (HS22) and fall 2022 (HF22) samples) for radiocarbon dating. At NOSAMS, peat samples were treated with 5-10 ml 1.2M hydrochloric (HCl) to remove carbonate, then neutralized with 0.5M NaOH, with a 1 hr water bath temperature at 60°C following each procedure. Samples were then dried in a 50°C oven for 24-36 hours and combusted. Peat samples analyzed at UCI (HS22 and HF22) were treated with an acid-base-acid sequence (1N HCl and 1N sodium hydroxide at 75°C) prior to combustion. Results from both facilities are reported as fraction modern (Fm) and uncalibrated radiocarbon years (BP) with uncertainties reported as ±1SD.

To convert radiocarbon Fm to calibrated ages (cal BP, defined as years before 1950), we used the web interface for CALIBomb (Reimer & Reimer, 2023). We calibrated the datasets on March 6, 2023 using the Intcal20 curve for pre-bomb samples and the unsmoothed Northern Hemisphere Zone 1 curve for post-bomb samples (Reimer et al., 2004, 2020). For converting radiocarbon to calendar ages, we reported the most probable midpoint age with 1SD variation (Table 7.S1) (del Valle et al., 2014). Full radiocarbon age calibration probabilities and CALIBomb results are found in Table 7.S2.

7.5.3 Optically stimulated luminescence

Sediment samples were prepared and measured for quartz optically stimulated luminescence (OSL) analysis at the University of California, Los Angeles Luminescence Laboratory in 2019 and the University of Texas at Arlington Luminescence Laboratory in 2023. Six of these samples were also prepared for K-feldspar post-infrared infrared stimulated luminescence (post-IR IRSL) analysis at UTA. Samples were wet-sieved to 100-150 μm and then separated by density using lithium metatungstate heavy liquid. Quartz grains were concentrated with densities from 2.62-2.68 g/cm^3 and K-feldspar grains with density <2.565 g/cm^3. Quartz grains were treated with 48% hydrofluoric acid for 60 min and then with 48% HCl for 24 hours under constant stirring. Sample discs were prepared by mounting a 2-mm-diameter monolayer of grains on Al aliquots with silicon oil. Samples were irradiated using ^{90}Sr/^{90}Y beta sources delivering a 0.1 and 0.2 Gy/s dose rate and measured using TL-DA-20 Riso automated reader (Bøtter-Jensen et al., 2000, 2003).

OSL measurements used a modified quartz single aliquot regenerative dose (SAR) protocol (Murray & Wintle, 2000, 2003). Aliquots were preheated to 220°C for 10 sec, then

stimulated at 125°C for 60 sec using IR diodes, then at 125°C for 60 sec using blue LEDs to measure the OSL signal. For test dose measurements, aliquots were preheated at 200°C for 10 sec and exposed to the same light stimulation as natural and regenerative measurements. Test measurements used a standard dose of 6 Gy, and aliquots were bleached with blue LEDs at 220°C for 40 sec at the end of each cycle. The single-grain post-IR IRSL SAR protocol incorporated a preheat of 250°C for 10 s after regenerative and test doses. The first IR stimulation was at 50°C for 3 s per grain and the second stimulation was at 225°C for 3 s. At the end of each cycle we included a hot bleach at 290°C with IR diodes on. The number of grains (K-feldspar) and aliquots (quartz) that were accepted and measured are listed in Tables 7.S3 and 7.S4.

To determine the equivalent dose for each sample and signal, we considered the over-dispersion (OD) of the population. When the OD value is low, we assume a single burial dose population and use the central age model (Galbraith et al., 1999). When the OD value is high, we assume incomplete bleaching before the most recent deposition event, and we use the minimum age model with three parameters (Galbraith et al., 1999). (Arnold & Roberts, 2009) OD values greater than 0.23 were considered high (Arnold & Roberts, 2009). For two samples, KY18-Bank9-350cm and HS22A-Bank3-OSL-90cm, negative equivalent dose results were measured for some aliquots and therefore, for those samples, the unlogged central age model was used.

To constrain the geologic dose rate for each sample, U and Th concentrations were measured by SGS Mineral Services using inductively-coupled plasma mass spectrometry (ICP-MS) and K was measured using inductively-coupled plasma optical emission spectrometry (ICP-OES). Conversion factors were used to calculate background radioactivity of the surrounding sediments for each sample (Guérin et al., 2011). Sample burial depth, latitude and elevation were used to calculate the cosmic ray background contribution (Prescott & Hutton, 1994). Burial ages for the OSL samples were calculated by dividing the equivalent dose by the background geologic dose. Analyses were performed in *R* using the luminescence dating statistical package (Kreutzer et al., 2012). The geologic dose rate and burial age were calculated using the online Dose Rate and Age Calculator (DRAC v. 1.2) and reported as age ±1SD error bars (Durcan et al., 2015).

7.5.4 Mapping and remote sensing

We compared field measurements of permafrost occurrence and active layer thickness with a previously published map of near-surface permafrost probability (Figure 7.3b) (Pastick et al., 2015). This map used decision and regression tree modeling on 17,000 permafrost probe measurements and 30 m resolution remote sensing data products to map near-surface permafrost (permafrost within the upper 1 m of soil) in Alaska (Pastick et al., 2015). While the training dataset contained a large number of data points, very few were located near our study site, motivating us to compare the map with our field measurements. To do so, we threholded the map so that probabilities less than 50% were considered nonpermafrost and probability greater or equal to 50% were permafrost, similarly to the analysis of Pastick et al. The thresholded map is expected to have 85% accuracy based on cross-validation tests

(Pastick et al., 2015). Since Pastick et al. (2015) generated their map using remote sensing products pre-dating our field work, some sampling locations are mapped as open water or barren ground and are assumed to lack permafrost (values reported as "NoData" in map). We used the map from Pastick et al. (2015) because we found better agreement between permafrost probe measurements with this map than one published specifically for the area near Huslia (Schwenk et al., 2023). Specifically, we found 22 true positives, 20 false positives, 23 true negatives, and 2 false negatives for an overall accuracy of 67% relative to the map of Schwenk et al. (2023).

We used satellite imagery to map floodplain deposit relative age and geomorphic units. From Landsat 30 m and Worldview 2 m resolution images, we relied on field observations of correlations between vegetation and geomorphology to manually map the floodplain in QGIS 3.4. We used cross-cutting scroll bar complexes to infer floodplain relative age, with scrolls that are truncated by other sedimentary deposits being older than the truncating deposit. Relative age mapping was internally consistent, with the youngest possible age class picked for each depositional surface. Importantly, gaps are present in cross-cutting scrolls where the Huslia River enters the main channel of the Koyukuk and eolian deposits are eroded by the river. Therefore, we observed a gap in cross-cutting relations between Koyukuk River deposits and inferred ages across these gaps using sites where scrolls are being deposited in one location while being eroded in another.

Mapping of geomorphic units was done manually, primarily on Maxar imagery (2 m, ©2012), Landsat imagery (30 m), and the National Land Cover Dataset (Wickham et al., 2021). The landscape was classified into the following units: eolian deposits, the town of Huslia, floodplain ridges, floodplain swales, lakes and secondary channels, overbank deposits, unvegetated bars, Huslia River deposits, and undifferentiated floodplain (areas that are former river deposits but lack distinct scroll bars). Units were distinguished by differences in vegetation and feature shape and dimensions. In addition to field observations of vegetation, we used the 2016 National Landcover Dataset produced by spectral classification of Landsat imagery (30 m) combined with ecological surveys (Wickham et al., 2021). Overbank units were grouped together because these expansive areas with homogeneous vegetation were primarily visible radiating from modern cutbanks, secondary channels, and the former cutbanks of oxbow lakes. We mapped the surficial extent of geomorphic units but did not attempt to estimate their thickness.

Using the relative age and geomorphic maps, we inferred previous locations of the Koyukuk River. After mapping the modern path of the river, we drew locations of newly formed and infilled oxbow lakes by hand. These lakes must have been connected by channels that did not cut across older floodplain deposits and had a roughly similar width and sinuosity to the modern Koyukuk River. In some cases, we were able to infer prior connections between oxbow lakes that appear consistent with the modern channel morphology. For reaches with large gaps between lakes, we did not interpolate the channel by eye. We could not accurately map past channel widths because previously abandoned channels had been filled in and overgrown with vegetation.

7.6 Results

7.6.1 Permafrost field measurements and mapping

Permafrost probe surveys revealed significant local variability in active layer thickness (Figure 7.4). The measurements (n = 35) near Core 4 converged to a bimodal distribution of active layer depth, with one mode at 65 cm depth and another mode for locations where permafrost may have been at depths greater than 1 m or absent altogether (Figure 7.4a). In contrast, the depths measured near Core 8 did not generate a centralized uni-modal distribution (Figure 7.4b), perhaps due to the lower number of measurements made (n=18 versus n=35). Measurements from both sites showed a minimum thaw depth of ~40 cm and a long tail of the distribution extending beyond 1 m depth. Our probe surveys found near-surface permafrost in 69% and 78% of measurements at the Core 4 and Core 8 sites, in comparison to predicted probabilities of 72% and 50% for the 1-2 pixels that contained each survey (Pastick et al., 2015).

We compared our field observations to the mapped probability of near-surface permafrost by Pastick et al. (2015) at each sampling location (Figure 7.4c). Overall, sites that lacked permafrost but are seasonally frozen (*n*=16) exhibited a much lower mapped probability of near-surface permafrost than sites with permafrost (*n*=14). Though there was significant scatter in the distributions of probabilities, their 25-75 percentiles did not overlap, which supports using the published permafrost map to extrapolate our field measurements across floodplain deposits.

In addition to comparing the spatial distribution of permafrost at single locations, we measured depth to permafrost in transects downwards and away from eroding cutbanks in fall 2022 (Figure 7.4d). We found that the bank had thawed back horizontally at least 40 cm from its surface at all four sites. Thus, an active layer developed on the surface of vertical cutbanks where sediment was thawed but not eroded. The floodplain active layer became steadily thinner over 5 to 10 m back from the edge of the bank. Beyond that distance, the active layer varied more with the rise and fall of scroll ridges (visible at Site 1) and was no longer monotonically decreasing in thickness (as at Site 3). We hypothesized that the active layer was deeper towards the edge of the bank because it was exposed to heat transferred from the river, sunlight, and warm air from multiple directions (Walker et al., 1987).
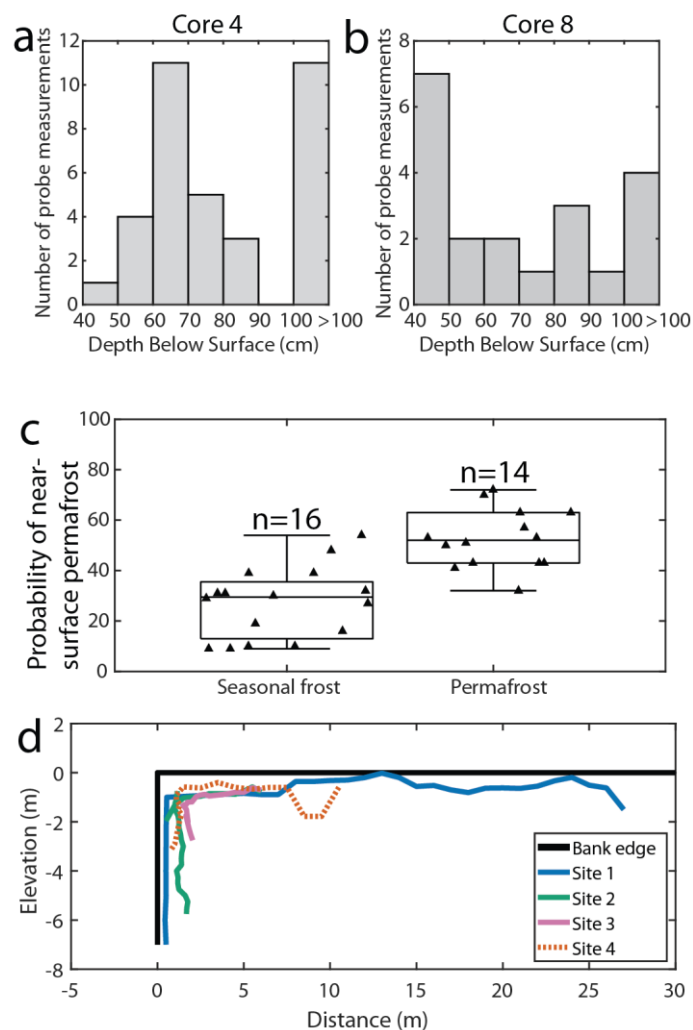
Figure 7.4. Field observations compared to remote sensing predictions of permafrost occurrence. **(a & b)** Histograms of permafrost depth surveys measured using a permafrost probe near **(a)** Core 4 (July 1, 2018) and **(b)** Core 8 (July 6, 2018). Measurements of >100 cm were recorded when the 1m long permafrost probe could be pushed flush with the ground surface. **(c)** Box & whisker plot of probability of permafrost for each sample site from Pastick et al. (2015) mapping, grouped by whether we observed permafrost or not. **(d)** Permafrost occurrence plotted as depth below the top of the cutbank versus distance along the top of the eroding cutbank at four different locations in September 2022. The edge of the bank is plotted as a black line, and the location of permafrost within each bank as colored lines, with the distance between the black and colored lines showing the thickness of the thawed layer along the eroding bank face or from the top of the floodplain downwards.
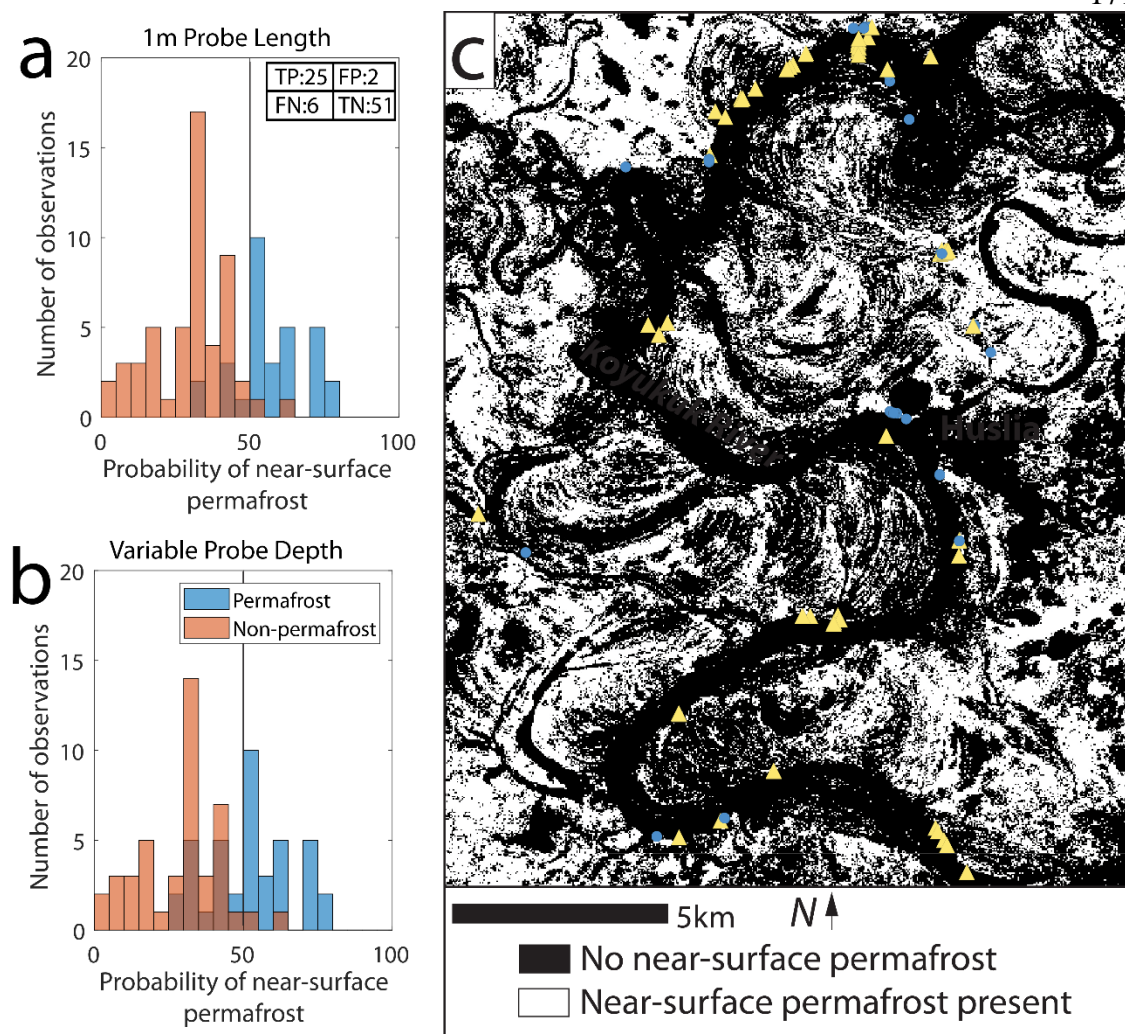
Figure 7.5. Comparison of permafrost field observations with Pastick et al. (2015) map of permafrost probability. **(a)** Observations of permafrost in the top 1 m of the soil column, with matrix in upper right corner showing number of true positives (TP), false positives (FP), false negatives (FN), and true negatives (TN) using a 50% probability threshold. **(b)** Observations of permafrost at any depth within the soil column. **(c)** Map of the probability of permafrost in the top 1 m of the soil column for the Koyukuk River floodplain near Huslia, AK (Pastick et al., 2015). Areas shaded white contain near-surface permafrost (≥50% probability) and areas shaded in black do not contain near-surface permafrost (<50% probability).

We compare field observations of permafrost across the entire floodplain area to evaluate using the 50% probability cutoff for near-surface permafrost presence to produce a floodplain-spanning permafrost map (Figure 7.3). This 50% probability cutoff to separate locations with and without near-surface permafrost was used by Pastick et al. to validate their analyses and map permafrost extent across Alaska, so we considered this to be the authors recommended probability cutoff. To compare our measurements to Pastick et al.'s map, we eliminated sites with multiple measurements per stratigraphic column or multiple measurements per pixel on the permafrost map. Since we only had a 2 m-long permafrost

probe in fall 2022, we compared the map probabilities to observations in the upper 1 m of the soil column (Figure 7.5a) and the entire measured section (Figure 7.5b). When only the top 1 m of soil was considered, the map mis-classified a total of 2 nonpermafrost sites and 6 permafrost sites out of 84, giving 90.5% accuracy. When considering permafrost below 1 m depth, the map misclassified the same 2 nonpermafrost sites as permafrost and misclassified 15 permafrost sites as nonpermafrost, giving 81% accuracy. Therefore, the Pastick et al. (2015) map is remarkably accurate for detecting near-surface permafrost (active layer <1 m deep) but mis-classifies an additional 10% of points with active layer thicknesses greater than 1 m.

The Pastick et al. (2015) map with a 50% threshold classified permafrost versus nonpermafrost terrain on the Koyukuk floodplain well, though the instances of misclassification pointed to specific limitations in the map. The misclassification of permafrost with active layer thicknesses greater than 1 m might reflect that the neural network for the map was trained on data primarily with active layers <1 m (Pastick et al., 2015). Since the training dataset also included vegetation characteristics from the National Land Cover Dataset, the model's performance may have reflected variation in the number of measurements for each land cover type or that regions with thinner active layers had a significant influence on surface vegetation. Abundant near-surface permafrost potentially decreased rooting depth and led to more saturated soils—both would be expected to engender shorter and/or fewer trees; which thicker active layers would have less effect on above-ground vegetation visible in satellite imagery. The map assumed that there was no near-surface permafrost in areas classified as barren land that lacks vegetation or open water (rivers, lakes), which agreed with field observations that permafrost was entirely absent on point bars. A second source of permafrost misclassification was proximity to lakes (responsible for 1 misclassification) and rivers. Since surface water typically does not contain near-surface permafrost, changes in lake and river extent, as well as spectral mixing in single pixels that span both water and land, increased misclassification along surface water boundaries. Misclassification also occurred due to sub-pixel topographic variability, particularly from overbank deposits and secondary channel levees (accounted for 4 misclassifications), which had lengthscales smaller than the map's 30 m pixel size. Another three misclassifications occurred in a sandy bank capped by 1.1 m of peat and mosses, providing insulation and preserving permafrost in a riverside location that otherwise was not predicted to form permafrost. In summary, the Pastick et al. (2015) map provided a useful classification of near-surface permafrost in this region of the Koyukuk floodplain, except for locations with significant sub-pixel variability in topography and/or surface-water occurrence.

7.6.2 Floodplain deposit ages

The combination of OSL and radiocarbon ages indicated that Koyukuk floodplain deposits post-date the last glacial maximum (~20 ka). OSL results directly dating the time since exposure to sunlight of floodplain sands gave ages up to 11.7±1.7 ka (Table 7.1). A timescale of ~12,000 years to resurface the entire floodplain was consistent with estimated floodplain resurfacing timescales of ~20 kyr, given modern reach-averaged channel migration rates of

~0.5 m/yr and a floodplain width of ~10 km near Huslia (Douglas et al., 2022). Therefore, the Koyukuk River was capable of completely re-surfacing its floodplain since the last glacial maximum at the river's current migration rates.

Table 7.1. Ages of optically stimulated luminescence samples from single-aliquot quartz. Site coordinates are in WGS84.

Sample name	Latitude (°)	Longitude (°)	Age (ka)	Relative Age
KY18-Core8-OSL-95cm	65.72552	-156.20992	9.3±2.0	7
KY18-Bank1-OSL-130cm	65.76492903	-156.490314	4.1±2.2	2
KY18-Bank5-OSL-100cm	65.75232	-156.50511	5.3±0.8	2
KY18-Bank5-OSL-260cm	65.75232	-156.50511	11.7±1.7	2
KY18-Bank8-OSL-260cm	65.66126	-156.44711	4.0±1.5	3
KY18-Bank9-OSL-350cm	65.70265	-156.40977	5.0±1.9	7
HS22A-Bank3-OSL-90cm	65.7806	-156.4287	0.9±0.6	4
HS22B-Bank4-OSL-222cm	65.7167	-156.5263	2.8±0.4	2

Single grain K-feldspar post-IR IRSL and single aliquot quartz OSL measurements of the same samples give consistent ages within 1σ for all samples, though the post-IR IRSL ages tend to be about 0.7 ka older than the OSL ages. This is probably due to incomplete bleaching of the post-IR IRSL signal (Colarossi et al., 2015; Jain et al., 2004). For this reason, in the remainder of the study, we use the quartz OSL results as more representative of the true burial age than the K-feldspar results.

Floodplain materials collected in 2018 did not provide consistent measurements of deposit age from radiocarbon dating. Radiocarbon ages of woody debris were relatively consistent for samples taken meters below the surface, with KY18-Bank5 having ages of 4728±38 cal BP (midpoint age with 1SD confidence interval) at 175 cm and 4598±33 cal BP at 240 cm below the surface (Table 7.S1). KY18-Bank4 and KY18-Bank6 were located within meters of KY18-Bank5, and KY18-Bank4 had a piece of woody debris sampled at 240 cm depth that was dated as 4601±37 cal BP, the same as the 240 cm sample from KY18-Bank5. The KY18-Bank6 sample was the most shallow, at 155 cm, and had an age of 3931± 30 cal BP. Though differences in sample age within the same stratigraphic section may reflect the timescale of channel migration and aggradation, these samples implied 1.3×10^{-4} m/yr vertical accretion rates, which are far below modern channel migration rates (~0.75 m/yr). Woody debris sampled from less than 100 cm depth in 2018 was frequently recent or modern, such as 88±35 cal BP at 60 cm depth and 300±39 cal BP at 250 cm depth below the surface in KY18-Bank 8, indicating they might be recently buried by overbank flood deposits or re-working of the surface soils by bio- or cryoturbation.

To better constrain depositional ages, in 2022, we only collected woody debris and leaf litter that was visibly imbricated in the bank, or layers of peat that had grown in place. This resulted in much tighter age distributions for each stratigraphic column, although radiocarbon ages of

woody debris still varied by as much as 1 kyr cal BP in many deposits. Since ^{14}C ages of woody debris could be older than the deposit since the trees had to die then fall in the river before being deposited, this scatter might reflect wood storage times before burial. Therefore, we selected the youngest ^{14}C ages for HS22-Bank1, HF22-Bank1, HF22-Bank2, HF22-Bank7, and HF22-Bank8 as most representative of the sedimentary deposit age. Woody debris ages range from modern to 13.6 cal kBP (see Tables 7.S1 and 7.S2). Permafrost ^{14}C ages were generally at least 4 cal kBP and the upper envelope of ^{14}C ages increases with deposit relative age.

7.6.3 Floodplain geomorphology

Abundant scroll bars revealed the spatial and temporal pattern of the Koyukuk River and its secondary channels re-surfacing the floodplain (Figure 7.6). The relative age map of the floodplain shows the spatial distribution of scroll bars, with 8 generations of deposits visible (Figure 7.6a). The extent of channel migration appears to have been limited by the vegetation eolian sands underlying Huslia and located to the southwest. In general, older deposits were observed farther from the modern river channel, indicating that areas closer to the channel may be re-worked with a higher frequency (Howard & Knutson, 1984) (Figure 7.6a). This mimicked the trend in preserved channel segments, where the remains of older channel cutoffs were preserved farther from the modern river (Figure 7.6b). Abundant lakes and secondary channels connected the main river to distant parts of the floodplain. Some of the secondary channels had meandered, generating their own scroll bars, while others were sinuous but showed little evidence of lateral migration (Figure 7.6c). Sinuous but apparently static tie channels (no visible scrolls) mainly occurred in oxbow lakes and grassy swales in moderately-aged floodplain deposits (Rowland et al., 2009).

In addition, we observed consistent differences in behavior and the types of geomorphic units generated by Koyukuk River bends with low versus high curvature (Figure 7.7). High-curvature reaches displayed the largest areas of floodplain eroded or deposited, consistent with studies indicating hydrodynamic effects of river curvature are the primary control on erosion rates in temperate and tropical environments (Furbish, 1988; Sylvester et al., 2019). Many high-curvature bends, such as the bend where the Huslia River enters the Koyukuk, were rapidly translating downstream, primarily eroding into deposits of previous translating bends (Figure 7.7b). They appeared to frequently cut themselves off, leaving oxbows linked by secondary channels that extend perpendicularly to the meander translating downstream (Figure 7.7b). Translating meanders primarily generated forested scroll deposits with overbank deposits extending from the secondary channels. Forested scrolls were typically classified as evergreen forest on younger deposits and forested wetlands on older deposits (Figure 7.6d). These bends did not show clear vegetation alternation with scroll ridges and troughs and instead showed signs of frequent inundation, indicating that a distinct vegetation-permafrost succession may occur for these floodplain deposits. In contrast, expanding bends migrated more slowly and generated successive levees of well-ordered alternating forested ridges with intervening grassy swales. Some expanding meanders displayed internal discontinuities that likely originated from changes in the direction of maximum meandering that generated slight erosion of the point bar (Figure 7.7a). Expanding bend deposits

appeared to follow the vegetation-permafrost succession characterized for other discontinuous floodplains (Kreig & Reger, 1982; Smith, 1976). It is unclear how the undifferentiated floodplain deposits form, but we hypothesize that a combination of overbank floods, sediment compaction, growth of mosses, and cryoturbation might create a surface without distinct scroll bars.

The geomorphic landforms making up the Koyukuk floodplain changed with the age of the deposits (Figure 7.8b-c). Forested scrolls comprised the majority of new floodplain deposits, and their proportion of floodplain area decreased roughly linearly with age (Figure 7.8c). Younger forested scroll deposits contain evergreen forest (Figure 7.6d), and we interpreted that the raised elevation of scroll ridges prevents flooding and allows white spruce forests to establish. Grassy swales (generally formed by expanding meanders) were moderately abundant on young deposits and then decreased with relative age for old deposits. These correspond roughly to the mixed forest classification on younger deposits and herbaceous wetlands on older deposits in the National Land Cover Dataset map (Figure 7.6d). We interpreted grassy swales to be frequently inundated in younger deposits, preventing white spruce trees from becoming established and instead grasses and deciduous trees persist. The transition to mixed forest then herbaceous wetlands might indicate the growth of white and then black spruce trees as permafrost forms under neighboring scroll ridges. Translating meanders generated a series of forested scroll ridges without intervening grassy swales, while expanding meanders generated both geomorphic landforms (Figure 7.7). In addition, translating meanders frequently contained secondary channels and overbank deposits. Translating meanders are occupied by mixed forest and woody wetlands but do not form a clear scroll pattern (Figure 7.6d). We infer that the presence of secondary channels distributed floodwaters throughout the translating deposits at irregular intervals, forming a patchwork of inundated deciduous areas in more frequently flooded areas with white spruce becoming established in less frequently flooded locations. For young floodplain deposits, translating meanders made up a slightly lower proportion of the scroll bar area than expanding meanders (Figure 7.8a). However, translating meanders were preferentially erased on older areas of the floodplain. Selective erosion or burial of deposits from translating bends could account for the decrease in forested scroll and increase in overbank deposit fractional area while other geomorphic units had a relatively constant fractional area for young floodplain deposits (Figure 7.8b-c).

The fraction of overbank deposits peaked at moderate floodplain ages, while the area of undifferentiated floodplain terrain increased monotonically with relative age (Figure 7.8b-c). The increase in overbank deposits with relative age may be due to flood deposits accumulating through time, causing a roughly linear increase in area while burying distinct scroll units. The area of floodplain covered by lakes remained roughly constant with deposit relative age (Figure 7.8b). Lakes comprised approximately 10% of the floodplain for all relative ages, though younger deposits had more arcuate oxbow lakes while older deposits contain round thermokarst lakes. We observed oxbows being filled in over time by overbank deposits and static secondary channels but did not observe secondary channels in thermokarst lakes.
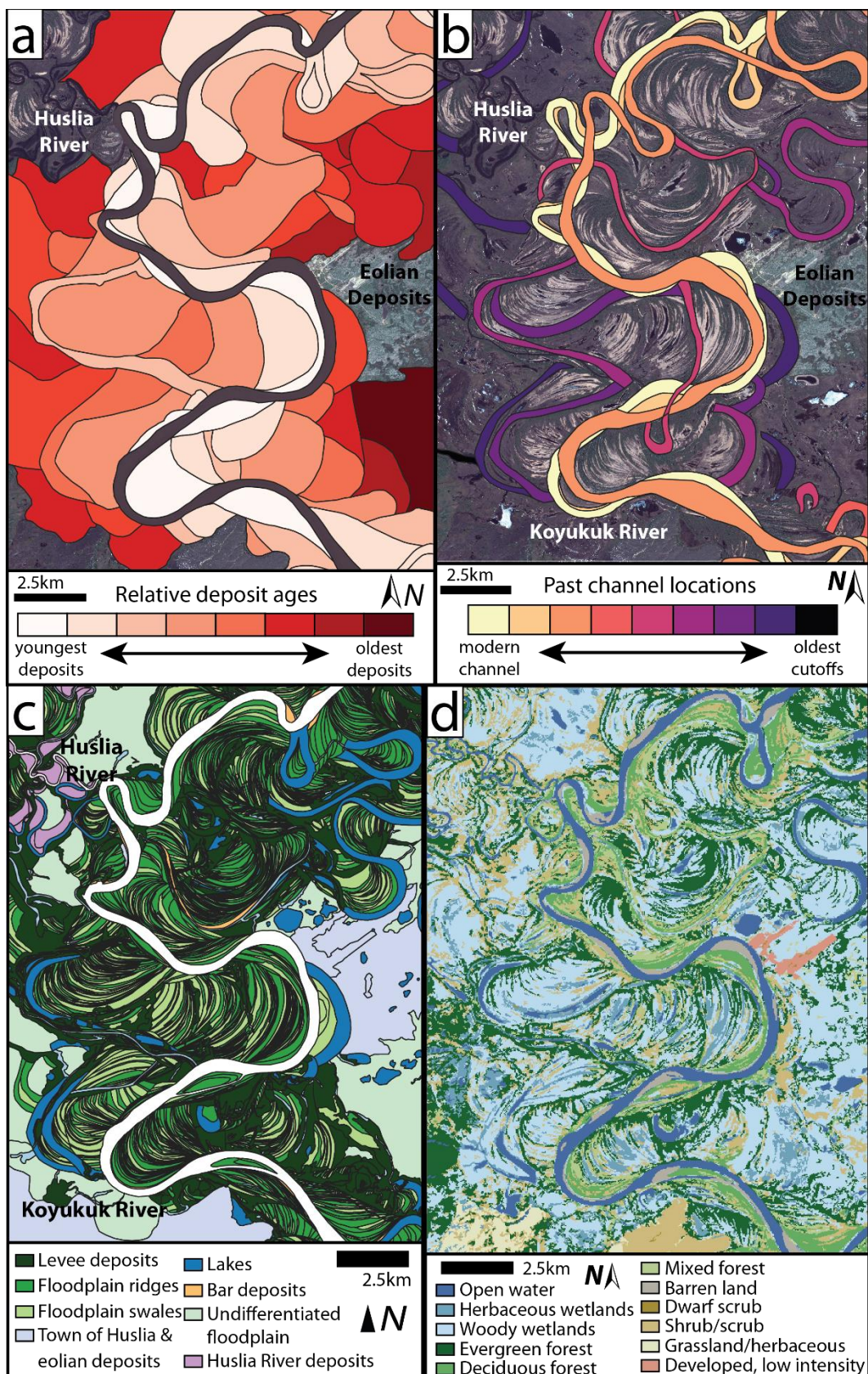
Figure 7.6. Hand-drawn geomorphic map of the Koyukuk River floodplain from satellite imagery. **(a)** Map of the relative age of floodplain deposits produced from cross-cutting relationships of scroll bars. **(b)** Inferred (and undated) previous locations of the Koyukuk River with satellite imagery basemap ©Maxar 2012. **(c)** Geomorphic map of Koyukuk River floodplain surrounding the village of Huslia, Alaska. **(d)** National Land Cover Dataset for the floodplain near Huslia, Alaska.
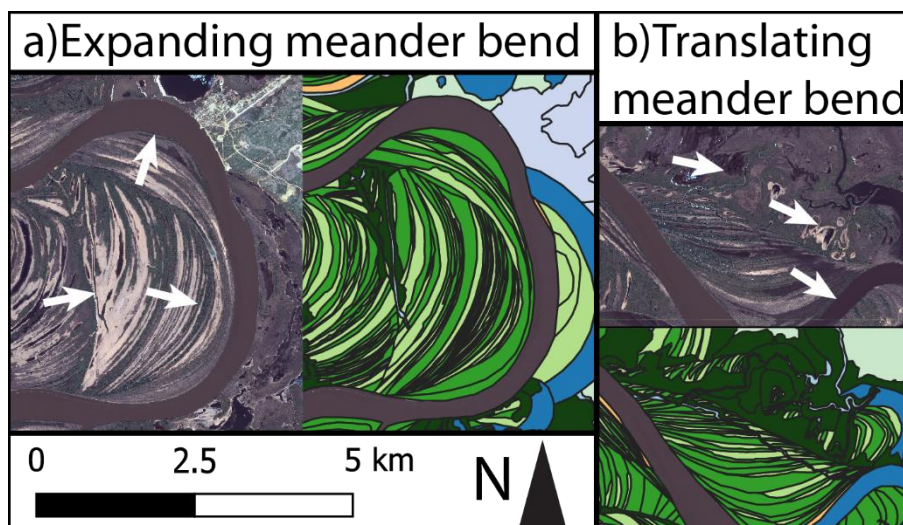
Figure 7.7. Worldview imagery and geomorphic mapping of **(a)** expanding and **(b)** translating meander bends, with white arrows showing migrating direction at different points in time.

Older floodplain units (>4 cal kBP) were predominantly comprised of undifferentiated terrain, in which clear scroll bar sequences have been re-surfaced, apparently by processes associated with permafrost. This corresponded to forested and herbaceous wetlands in the NLCD, indicating that this change in vegetation might be driven by reduced infiltration rates in permafrost. Permafrost might create intense cryoturbation, peat may gradually grow in saturated regions and smooth the floodplain, and cycles of formation and collapse of massive ground ice can disrupt the original floodplain stratigraphy (French & Shur, 2010; Kanevskiy et al., 2014). These undifferentiated deposits were barely present on terrain less than 4 cal kBP, raising the possibility that it takes 4 kyr for permafrost to form and significantly alter the Koyukuk floodplain through freeze-thaw and thermokarst processes. Alternatively, undifferentiated terrain may only be present in older landforms because these deposits were formed when air temperatures were colder (Marsicek et al., 2018), so permafrost, and not river migration, was the dominant control on floodplain landforms. For either case, the presence of a wetland ecology on older deposits but not on younger deposits implies that deposit age and permafrost occurrence might drive ecological succession, and not the other way around.
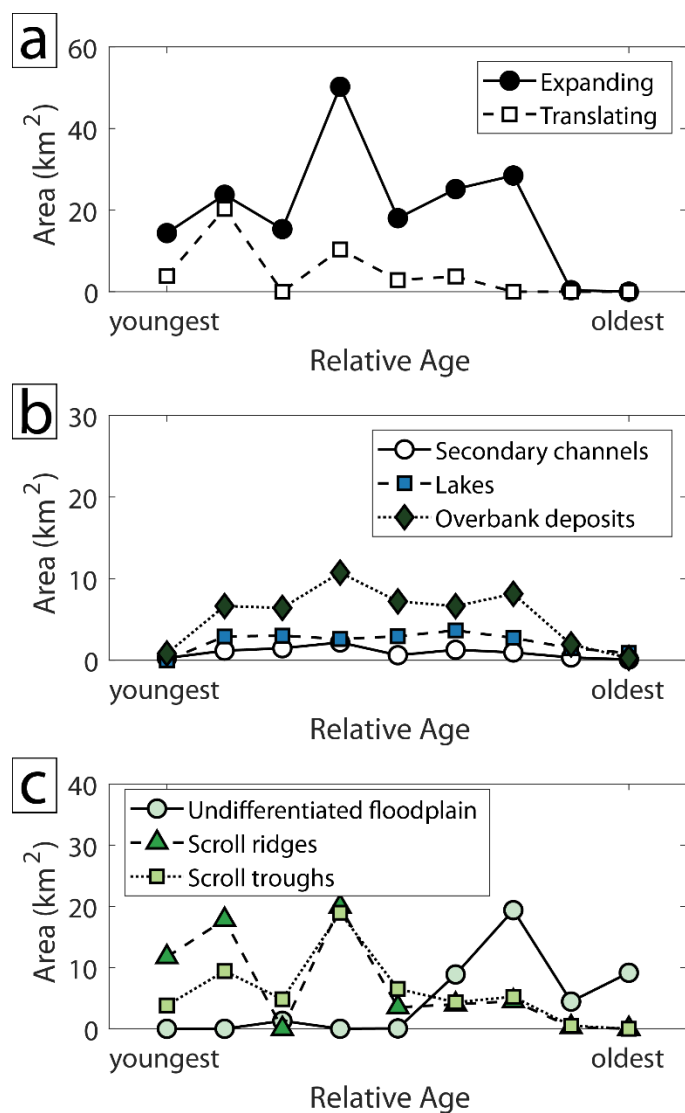
Figure 7.8. Variation in floodplain geomorphology with deposit age. Plots of the area of **(a)** translating versus expanding bends and **(b, c)** geomorphic landforms.
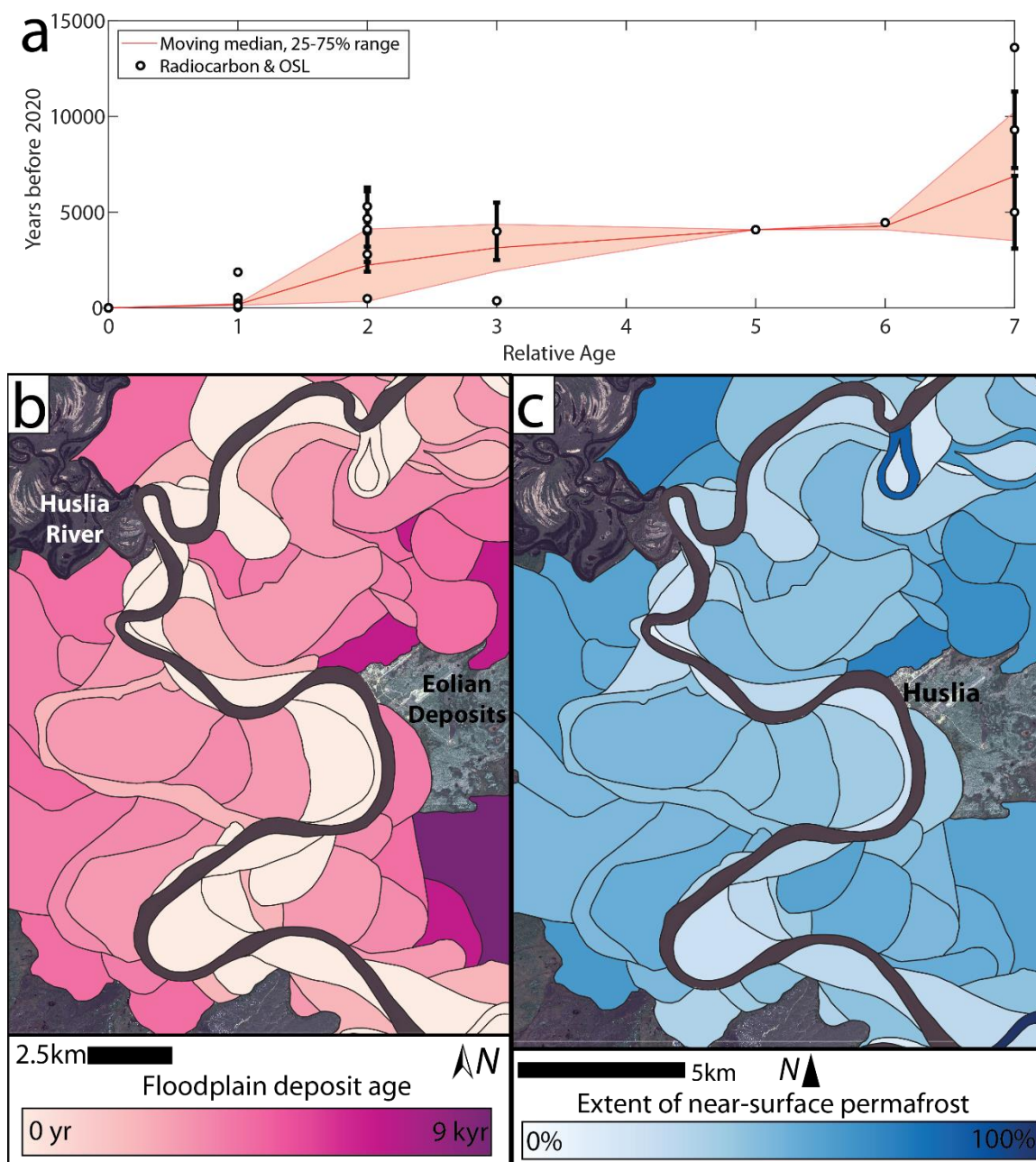
Figure 7.9. (a) Radiocarbon and OSL ages fit to deposit relative age (0 is youngest, 8 is the oldest) to develop an absolute age calibration for floodplain deposits shown as a moving median with 25-75% range envelopes in red. Maps of **(b)** absolute deposit age and **(c)** probability of permafrost in the top 1 m of the soil column for the Koyukuk River floodplain near Huslia, AK (Pastick et al., 2015). Each relative age unit is color-coded by the fraction of ground that contains near-surface permafrost (>50% probability in a given pixel).

7.6.4 Permafrost occurrence in floodplain through time

We computed a floodplain absolute versus relative age relation by plotting radiocarbon and OSL measurements of deposit age versus the mapped relative age of deposits (Figure 7.9a). To produce this relation, we excluded 5 of 37 radiocarbon measurements. Some results were excluded because they were inconsistent with cross-cutting relations. One OSL sample, KY18-Bank5-OSL-260cm, was kyr older than other samples in its relative age category and we hypothesize that this sediment was incompletely bleached during its last transport event. In contrast, HS22A-B04-S12-OSL-90cm had a very young age (<1 kyr) and old relative age, which support that this shallow sample might have been a sandy overbank deposit or channel splay. Other excluded samples consisted of very young (<200 years cal BP) KY18 samples from <1 m depth that are inconsistent with other samples in that deposit or the relative age mapping. We also excluded 3 HF22 samples taken from the same relatively young point bar, which had very low OC content (<1 wt%) and very old ages (~1, 9, and 14 kBP), indicating they likely contained radiocarbon-dead petrogenic OC. For samples where we had multiple measurements of woody debris ^{14}C content that were closely correlated (within hundreds of years), we selected the lowest age as most representative of the time of deposition and burial. Using the remaining samples, we use a moving median to fit deposit age versus relative age (Figure 7.9). We use a trailing 2 relative age bin window and report uncertainty as the 25 to 75% range for samples within each window. This fit was used to assign absolute ages to each floodplain deposit in the relative age map (Figure 7.9a).

Permafrost was most abundant on older landforms further from the modern channel (Figure 7.9b-c). The age of floodplain deposits did not increase linearly with relative age, and instead there were multiple generations of very young deposits and long gaps between older deposition ages (Figure 7.9b). The youngest floodplain deposits did not contain permafrost, excluding the possibility that permafrost formed syngenetically as sediment aggrades on point bars (Figure 7.9c). Therefore, any newly forming permafrost should have been detectable because it must be forming epigenetically (top-down) in pre-existing deposits. In contrast, older deposits had a much higher fraction of area containing near-surface permafrost. We observed ice-rich permafrost in deposits dated to ~4 ka, implying a minimum vertical permafrost formation rate of 12.4 m (depth of the Koyukuk) over 4 kyr, or a permafrost formation rate of at least 3.1 m/kyr. Satellite imagery indicated that the vegetation succession required to form permafrost in regions of discontinuous permafrost (~100-200 years) occurred within the first mapping unit, in agreement with its assigned deposit age of decades. However, permafrost extent is very patchy on the first and second mapping units (deposits <190 a) and only becomes prevalent for deposits >1 ka. The oldest units, which date to 8 ka, have ubiquitous permafrost and thermokarst terrain features.

One significant exception to the trend that permafrost extent increased with deposit age was the eolian sediment that underlay Huslia. We were unable to detect any near-surface permafrost in these deposits, even though they pre-dated formation of the floodplain. We inferred that their high elevation relative to their surroundings and composition of well-sorted sand created a significant hydraulic head and low resistance to pore flow, which together inhibited the formation of pore ice. Variability in permafrost presence within fluvial and

eolian deposits agreed with field observations across Alaska, which indicated that mean annual temperatures near Huslia should produce sporadic (10-50%) permafrost for both types of deposits (Jorgenson et al., 2008).
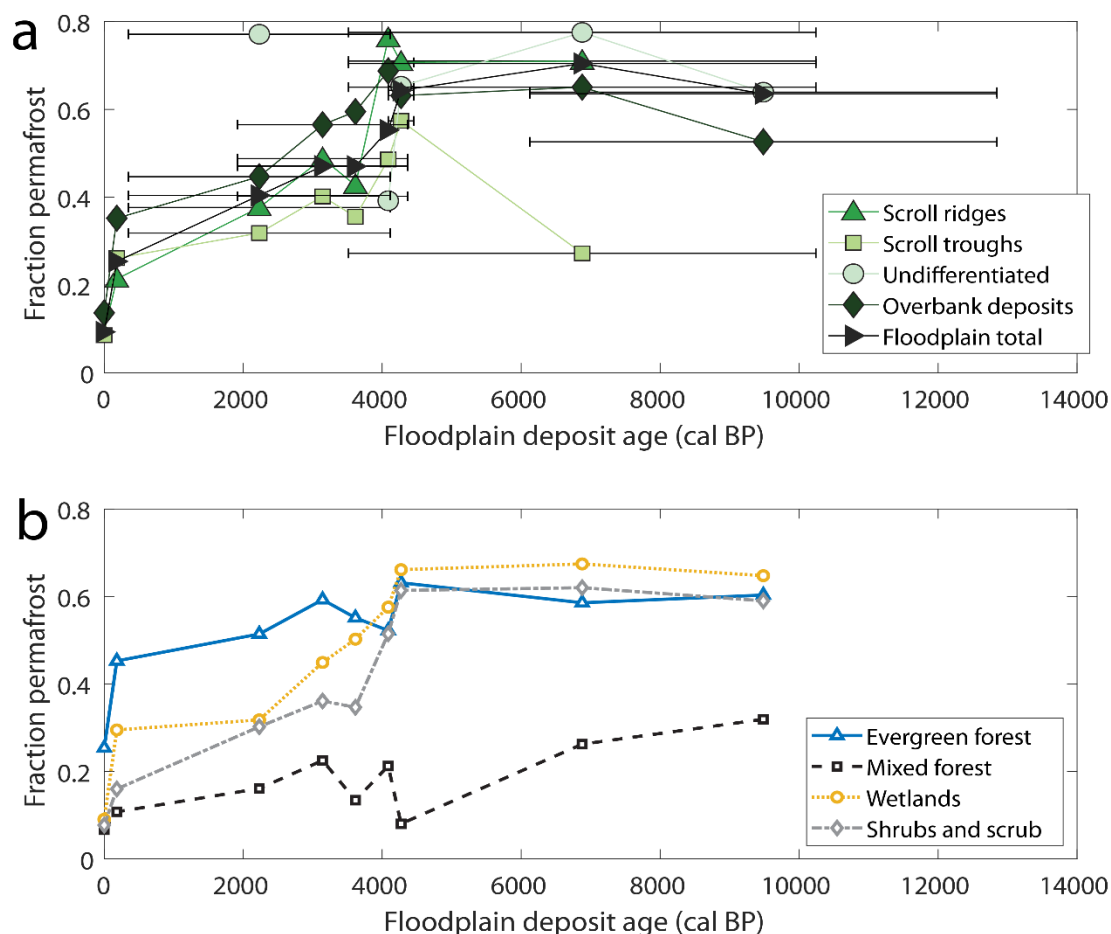
Figure 7.10. The fraction of deposits containing near-surface permafrost versus deposit age. **(a)** The fraction of ground of a specific terrain type consisting of permafrost landforms plotted versus floodplain deposit age. Horizontal error bars encompass 25-75% age distribution. (b) The fraction of ground containing permafrost for different vegetation classifications. From the National Land Cover Dataset, we plot four main vegetation classes: evergreen forest, deciduous and mixed forest, woody and herbaceous wetlands, and shrubs and scrub (including dwarf scrub, scrub/shrub, grassland/herbaceous).

In general, permafrost occurrence increased with deposit age, with overbank deposits and undifferentiated floodplain having the highest fractions of permafrost (Figure 7.10a). Scroll ridges had a similar permafrost extent as the floodplain average for each age, and scroll troughs had the lowest permafrost extent at a given age. This may be because permafrost formation or degradation was ongoing, and deposits with different grain size characteristics

had different ability to insulate the ground. Permafrost extent was below 20% for the youngest floodplain deposits, increased linearly to approximately 50% for deposits ~2 cal kBP old and briefly plateaued, then extended up to ~65% for deposits greater than 4 cal kBP old. Since the undifferentiated floodplain unit only occurs on older floodplain deposits, we expect that overbank flooding and vegetation succession gradually makes scroll ridges and troughs indistinguishable from each other. Most notably, although floodplain deposits experienced the same climate forcings over recent years, landforms deposited over the previous 4 ka have different permafrost extents. This implies that near-surface permafrost forms slowly, increasing in extent by approximately 15% per 1 kyr. Permafrost extent increases with deposit age, but no clear trends are visible between landforms that contain different vegetation with similar deposit ages.

To more directly compare permafrost formation, deposit age, and forest succession, we compared the fraction of land classified as evergreen forest, mixed or deciduous forest, wetlands, and shrub or scrub that contained permafrost for each deposit age (Figure 7.10b). Based on previous work (see Section 7.3), we expected that forest succession would occur as shrub and scrub, mixed forest, evergreen forest, then wetlands over approximately 200 years and that the fraction of ground containing permafrost would increase through this progression. Instead, results indicate that mixed and deciduous forest always correlates with a low permafrost coverage, and that permafrost coverage increases from shrubs and scrub through wetlands then evergreen forest (Figure 7.10b). This indicates that wetlands and shrubs might indicate inundated, unfrozen regions of the floodplain (such as grassy swales) as well as permafrost. Evergreen forest very commonly indicates underlying permafrost, as would be expected from forest succession. However, permafrost formation appears to be limited primarily by the age of the deposit and not forest succession. While evergreen trees are capable of growing within decades on floodplain deposits, all deposits younger than 3 ka have a low fraction of permafrost, regardless of vegetation cover. In addition, all vegetation types in deposits older than 4 kyr, with the exception of mixed and deciduous forest, have the same permafrost extent. Therefore, the dominant control on near-surface permafrost extent is age of deposit, not terrain type or ecological succession.

7.7 Analysis: Is permafrost re-forming or degrading on the Koyukuk floodplain?

Using our mapping and measurements, we evaluated our original hypotheses for permafrost occurrence on the Koyukuk River floodplain: (1) all permafrost was relict and thawing from the top-down, (2) permafrost was re-forming in new deposits, potentially after a temporal lag. We used observations of floodplain deposit ages and permafrost occurrence to frame an inverse problem to determine when and how rapidly permafrost has formed through time. Since the floodplain deposits are located next to each other, we assumed that they have experienced the same climatic history and should have the same rate of permafrost formation and degradation through time.

Based on mapping results, near-surface permafrost extent depends primarily on floodplain deposit age, rather than local variations in geomorphic landform or vegetation (Figure 7.10). Specifically, permafrost extent increases linearly with deposit age for areas of the floodplain

less than 4 ka, implying a roughly constant permafrost formation rate that we can solve for as an inverse problem. For example, if permafrost formed rapidly on new floodplain deposits, as is the case for continuous permafrost regions (Smith, 1975), we would expect the entire floodplain to have the same permafrost extent. Similarly, if permafrost formed over 10 kyr, we should not see permafrost extent stabilize for deposits >4 ka, where permafrost extent appears to saturate at 65%. Therefore, it appears that permafrost formation rates are relatively slow and take ~4 kyr to reach a saturation value but do not depend strongly on local landform and vegetation conditions, especially since vegetation succession occurs on much shorter (hundreds of years) timescales. However, the saturation value of 65% is much lower than expected for previous climatic conditions, when air temperatures were colder and the region likely experienced continuous permafrost (Jorgenson et al., 2008; Marsicek et al., 2018), which by definition would have 90 – 100% permafrost extent. Therefore, it is likely that this older terrain reached a higher saturation value for permafrost extent during colder climates but that recent climatic warming has caused uniform top-down thaw of permafrost across the floodplain, decreasing the extent of near-surface permafrost. While differences in vegetation might cause some local changes in permafrost degradation rates, we did not observe systematic differences in the apparent permafrost extent saturation value with landform and vegetation, implying that these are secondary effects. Therefore, we interpret Figure 7.10 to indicate that permafrost requires thousands of years to form in the floodplain, so that deposits formed within the past 5 ka never reached a saturation value for permafrost extent. In addition, deposits of all ages across the floodplain have likely experienced top-down thaw in recent decades due to climatic warming.

7.7.1 Permafrost growth model

To quantify these arguments, we used the data for deposit age and permafrost content to pose a linear inverse problem. The idea is to take advantage of the space-for-time substitution allowed by the floodplain deposits which experienced a shared history of similar climate forcing during the times that the deposits coexisted. To model the probability of floodplain deposits of a given age containing near-surface permafrost (ψ_{pf}, dimensionless probability between 0 and 1 to indicate no versus complete permafrost coverage), we defined a permafrost probability growth function G as:

$$G = \frac{d\psi_{pf}}{dt}. \tag{7.1}$$

We assume that permafrost can occupy a maximum fraction of the floodplain ψ_{max}, so that $G = 0$ when $\psi_{pf} = \psi_{max}$. We assume that permafrost growth follows:

$$G = C_1 T_{air} + C_2, \tag{7.2}$$

where the growth function has a linear dependence on mean annual air temperature (T_{air}; °C) and empirical constants C_1 and C_2. We infer that permafrost follows a linear growth trend based on Figure 7.10, where the probability of near-surface permafrost increases nearly linearly for all deposits over the first ~2 kyr. Numerous other factors—the amplitude of

annual air temperature variations, vegetation cover, and snow cover—are known to affect permafrost occurrence and active layer depth (Anisimov et al., 1997). However, for the purposes of evaluating possible trajectories of permafrost formation and degradation over millenia, mean annual air temperature provides a first-order control.

We calculate ψ_{pf} from 13 ka onwards using equations (7.1) and (7.2) in a forward model. We used Euler's method, so that at timestep $i+1$, the permafrost dimensionless probability is:

$$\psi_{pf,i+1} = \psi_{pf,i} + G \times dt \tag{7.3}$$

where $dt = 1$ year. We used absolute deposit ages calibrated from Figure 7.9 and tracked permafrost growth and degradation at each timestep for portions of the floodplain that had been deposited. We select $\psi_{max} = 1$, which corresponds to continuous permafrost with complete coverage of the landscape. Since we are not able to evaluate whether permafrost has stopped forming due to Arctic amplification, we introduced a parameter ψ_a which can range between -1 and 1 and is added from model runs in the final timestep to capture potential permafrost degradation due to anthropogenic warming. To determine best-fit parameters for C_1, C_2, and ψ_a we ran the model iteratively using Matlab nonlinear optimizer fmincon.m to find values with the highest R^2 with the total area of each unit containing permafrost in the present day ("floodplain total" points in Figure 7.10). No significant difference was found from including C_2 or not, so we set $C_2 = 0°C$. Using these best-fit values, we ran the model to evaluate the most likely history for permafrost formation and degradation in the Koyukuk floodplain.

We evaluated equation (7.2) using T_{air} estimates obtained from a compilation of pollen temperature anomaly estimates across North America and Europe and observed temperature anomalies for recent decades (Marsicek et al., 2018), which was linearly interpolated for model runs then shifted so that the temperatures at present reproduce mean values from 1981 – 2010 (-3.6°C at Huslia; Figure 7.11a) (Daly et al., 2018). Based on paleoclimate records from pollen in the northern hemisphere, air temperatures were significantly colder during the Younger Dryas (~13–11.5 ka), then rose steadily to pre-industrial ranges and were relatively consistent over ~8 ka until recent rises due to anthropogenic warming (Marsicek et al., 2018). Pollen records generally agree with temperature anomalies inferred from leaf wax measurements sampled in lakes on the north slope of Alaska, which indicated steady or slightly declining temperatures from 10 ka to present (Daniels et al., 2021; Longo et al., 2020). Paleotemperature records in Greenland and the Gulf of Alaska synchronized approximately 15 ka, indicating that climatic changes between the north Atlantic and Pacific have been similar since the oldest floodplain deposits were in place (Praetorius & Mix, 2014). In recent decades, air temperatures have dramatically increased due to polar amplification of climate change (England et al., 2021).

7.7.2 Permafrost model results

Fitting the permafrost growth model to datasets from mapping the Koyukuk River floodplain produce best-fit parameters of $C_1 = -1.00 \times 10^{-4}$ 1/°C/yr and $\psi_a = -0.446$. The small, negative

value of C_1 indicates that permafrost growth increases with decreasing annual temperatures, but that floodplain permafrost forms gradually over thousands of years. We were unable to fit the model results without including a decrease in permafrost extent attributed to climate change, indicating that permafrost is likely degrading in the present day.

Examining permafrost growth through time, the model captures how deposits initially lack permafrost and then gradually progress from sporadic to continuous permafrost over ~2 kyr (Figure 7.11b) (Jorgenson et al., 2008). Deposits greater than 2 ka reached $\psi_{pf} = \psi_{max}$, and permafrost growth ceases. In reality, these deposits are likely continuously forming and degrading permafrost at the local scale due to differences in snowfall, vegetation, fires, and groundwater flow, so ψ_{max} can be considered a dynamic equilibrium. In contrast, deposits younger than 2 ka are still forming additional permafrost up until the abrupt decline in permafrost extent due to ψ_a at the present. The model therefore captures how older deposits have very similar permafrost extents while a sharp increase in permafrost extent with deposit age is apparent for younger scroll bars (Figure 7.10).
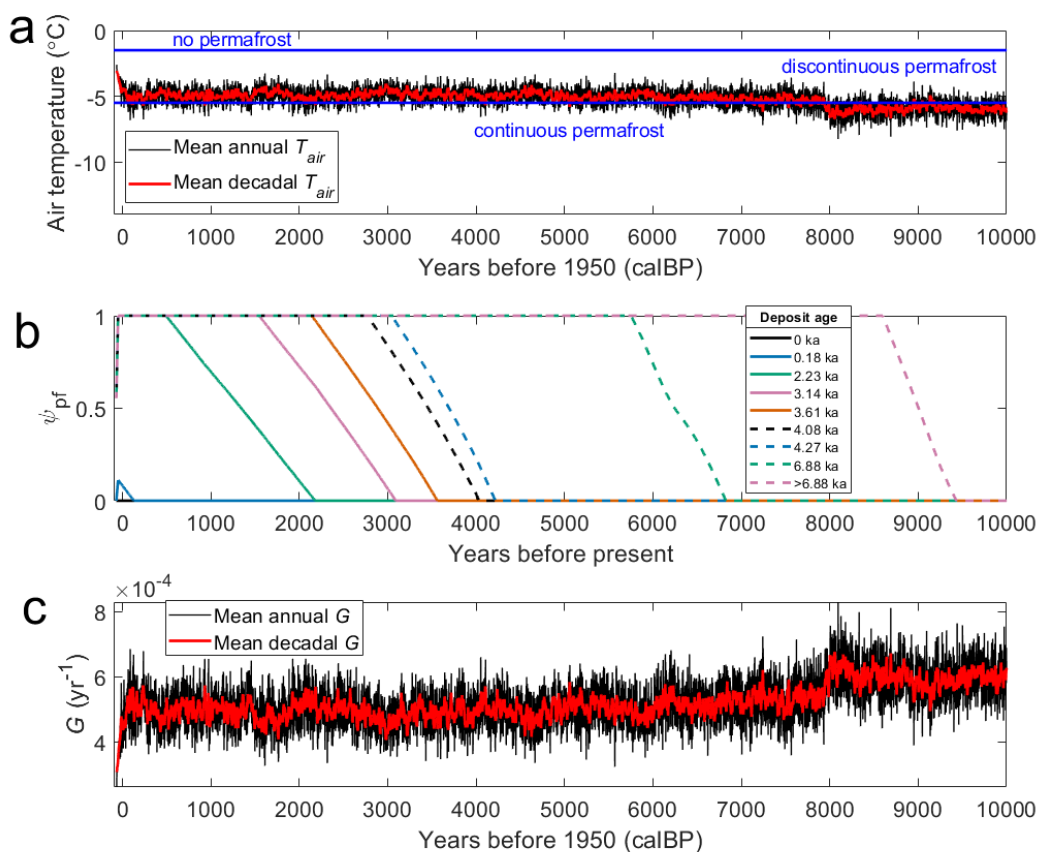
Figure 7.11. **(a)** Estimated mean annual air temperatures with 1SD shaded uncertainty for Huslia, AK based on values from Kielhofer et al., 2023. **(b)** The fraction of sedimentary deposits of different ages that are underlain by permafrost through time. **(c)** The rate of permafrost growth through time.

Model results agreed with observations that permafrost has been actively forming on the floodplain through recent history (rejecting hypothesis (1))—particuarly since field observations revealed permafrost in sedimentary deposits dated to <4 ka by both radiocarbon and OSL (Figure 7.6). To distinguish whether permafrost is currently being formed on the floodplain or not, we examined our map of permafrost occurrence with age (Figure 7.9) using our value of 90% accuracy as an estimate of the permafrost map uncertainty compared to permafrost probe observations at our study site. Examining Figure 7.10, new floodplain deposits had ~10% of their area covered by permafrost, at the edge of uncertainty of the map; we also did not observe any permafrost in these deposits while in the field. Floodplain deposits <2 ka contained sparse permafrost based both on field observations and the permafrost map (Figure 7.9), though it may have been missed in our field surveys due to its low prevalence. Recent warming might have caused a rapid decay of permafrost, though this implies that top-down thaw of permafrost must occur more rapidly than permafrost formation (Marsicek et al., 2018).

Since permafrost typically takes 100-200 years to begin forming on floodplain deposits in discontinuous permafrost regions (Kreig & Reger, 1982), recent sediment deposits are not expected to contain permafrost. Model results found a best-fit with 44.6% decrease in permafrost area due to climate change (Figure 7.11), providing tentative evidence for recent permafrost degradation, similar to sites across the Arctic. Based on these observations, we propose that permafrost was actively re-forming on the Koyukuk River floodplain until at least 200 years ago. Subsequent climatic warming has likely degraded thin permafrost on young sedimentary deposits to produce isolated patches of permafrost, since floodplain deposits are only expected to have 10% permafrost area after 200 years at -5°C. Therefore, sediment deposited in the last 200 years is not expected to contain significant permafrost, since its formation is limited by the rate of forest vegetation succession in similar discontinuous permafrost environments (Viereck, 1970), but we expect that permafrost formation has ceased in the present day due to climatic warming.

7.8 Discussion

7.8.1 Evolution of the Koyukuk River floodplain

The Koyukuk River has eroded eolian deposits to form its floodplain over the last ~9 ka. Radiocarbon and OSL ages of the oldest floodplain deposits were slightly younger than ages measured for deposits from the Nogahabara Dunefield, located 50 km west of Huslia. Radiocarbon measurements of vegetated eolian deposits being eroded by the Koyukuk River downstream of Huslia produced ages from 15,350 – 25,850 cal BP for when vegetation immobilized the dunes near Huslia (Farquharson et al., 2011). This was consistent with the dunes becoming vegetated and then being eroded by the river as the climate became warmer and wetter following the end of the Younger Dryas. Since ~9 ka, the Koyukuk has remained single-threaded and formed a floodplain where discontinuous permafrost is eroded by the river and then gradually re-forms in floodplain deposits, though permafrost appears to be degrading across the floodplain at present. The pattern of vegetation succession, from

willows and poplars to white spruce and eventually black spruce with mosses and bog, was similar to that observed in other discontinuous permafrost floodplains (Jorgenson et al., 1998; Mann et al., 1995). Permafrost regrowth was part-and-parcel of this succession, creating a natural delay of a couple centuries between when sediment is deposited and when it might form permafrost (Kreig & Reger, 1982).

The trend of floodplain deposit absolute age with respect to relative age implied that permafrost does not affect how frequently the Koyukuk River resurfaces its floodplain (Figure 7.9). The Koyukuk River was much deeper (12.4 m) than the floodplain active layer (~0.4-2 m) but shallower than the estimated thickness of permafrost (31 m) (Jorgenson et al., 2008), so permafrost might be expected to significantly impact spatial patterns of channel migration. For instance, bank migration might be limited by the rate at which ice-rich permafrost can be thawed, causing permafrost to slow channel migration (Rowland et al., 2023). Alternatively, this pattern may be entirely due to the stochastic nature of channel migration producing a heavy-tailed distribution of deposit ages (Torres et al., 2017; Yan et al., 2021). Simulations of a representative meandering river floodplain evolution indicated that for a representative cutoff timescale (T_{cut}), 90% of floodplain deposits were less than $10\times T_{cut}$ old and a heavy tail of deposits is up to $100\times T_{cut}$ old (Torres et al., 2017). For comparison, if we approximated T_{cut}~850 yr, and 90% of deposits are less than 8.5 ka, we found that the Koyukuk floodplain has a similar area of older deposits, that are likely to contain permafrost, compared to temperate floodplains.

Overbank floods cause top-down thawing of permafrost due to transport of warm water across the landscape (Zheng et al., 2019), yet overbank deposits had some of the highest predicted permafrost extents for each deposit age. This apparently contradictory result may be because of spatial patterns in flooding and sediment deposition on younger floodplain deposits or variable effects of flooding on active layer depth versus permafrost warming (Zhang et al., 2023). Channel levees typically contain coarse sediment that is rapidly deposited after the river overtops its banks, and then the water carrying the remaining load of fine sediment can be transported as sheet flow or via secondary channels across the floodplain (Day et al., 2008). Therefore, fine sediment deposition and long periods of standing water are likely most common in scroll bar troughs, causing these landforms to have the slowest formation and highest potential for rapid degradation of permafrost. On older floodplain deposits, surface water from thermokarst lakes and saturated ground was abundant. Therefore, we hypothesized that the thick layer of peat moss provides sufficient insulation to preserve underlying permafrost during periods of inundation.

Overall, permafrost cover on the Koyukuk floodplain was patchy, even for very old deposits (Figures 7.10 and 7.13). Some variability was likely due to differences in snowfall and redistribution of fallen snow by wind, since thicker snow coverage insulates the ground from cold winter air temperatures (Jafarov et al., 2018). Variations in vegetation cover, whether due to the growth of an insulating moss layer or direct changes in ground insolation, also cause local variation in active layer thickness (Domine et al., 2022; Wang et al., 2020). Wildfires significantly affect vegetation and permafrost, causing rapid thaw and decreasing

the accuracy of permafrost maps (Pastick et al., 2015). Secondary channels and lakes also play a role in directing warm river water away from the main river channel, particularly for oxbow lakes that remain connected to the Koyukuk via secondary channels. In some locations, fine sediment carried by secondary channels and overbank deposits can help to insulate permafrost, shown by the high occurrence of permafrost in overbank deposits (Figure 7.10). However, flood water tends to pond in the lower areas of the floodplain, which might cause permafrost to thaw and prevents its formation in scroll bar troughs (Figure 7.10). Therefore, spatial heterogeneity of permafrost and vegetation across the Koyukuk floodplain can be attributed to geomorphic and climatic processes.

7.8.2 Effects of climate change on permafrost floodplains

The Koyukuk River provided a case study for how understanding the fluxes and composition of OC transported by Arctic rivers required considering lateral movement of the river and fluxes of water and sediment within floodplains. The diversity of geomorphic features found on the Koyukuk floodplain indicated that organic carbon (OC) cycling and preservation may vary significantly within the deposits of one river. River migration was known to be a source of OC to the river, releasing carbon from permafrost thawed in cutbanks (Kanevskiy et al., 2016). However, river migration also produced permafrost-free bars that allow trees to persist far north in zones of continuous permafrost, enhancing primary productivity (Gill, 1973). Although expanding bend deposits followed well-established patterns of vegetation and permafrost succession, much of the Koyukuk floodplain was covered by translating bend deposits, secondary channels, overbank deposits, and lakes that do not follow the same succession (Figure 7.8). We mapped a large number of translating bends that were migrating rapidly and produced relatively short-lived deposits with ubiquitous secondary channels and overbank deposits (Figure 7.7). Similar bends in the Amazon contained finer sediment than average floodplain deposits (Sylvester et al., 2021), and therefore likely had much higher OC concentrations (Douglas et al., 2022). Similarly, oxbow lakes were identified as hotspots for OC deposition, with quiescent water causing settling out of fine-grained, OC-rich sediment and fostering productive aquatic ecosystems (Sutfin & Wohl, 2017). Since oxbow lakes were remnants of the main stem of the Koyukuk, they also likely had a through-talik that gradually re-freezes as the lakes fill in over thousands of years (Rowland et al., 2005), producing syngenetic instead of epigenetic permafrost (Lattaud et al., 2021).

Like other river systems in the Arctic, the morphology of the Koyukuk and its floodplain are anticipated to change in response to Arctic warming (Lininger & Wohl, 2019). Our model indicates that already, the floodplain is unlikely to re-form permafrost. Therefore, we expect that channel migration will determine the spatial patterns of relict permafrost and might completely erode permafrost from the floodplain within its re-surfacing interval (~9 kyr). However, removing permafrost from the channel banks may also alter river meandering rates and spatial pattern, and it is not clear how that would change the time between the river re-working sediment at a given location (Ashmore & Church, 2001; Lininger & Wohl, 2019). Other rivers currently in zones of continuous permafrost may also see a decrease in their area underlain by permafrost, which could significantly increase groundwater connectivity and alter biophysical feedbacks between permafrost and vegetation growth (Smith, 1975;

Viereck, 1970). Climatic warming is also causing river discharge to increase, potentially increasing flood frequency and inhibiting vegetation succession and permafrost regrowth (Brabets & Walvoord, 2009; Peterson et al., 2002).These feedbacks between river dynamics, permafrost occurrence, and vegetation indicate that climate change may significantly alter floodplain above and below-ground carbon storage.

7.9 Conclusions

The Koyukuk is a meandering river whose patterns of migration shape the vegetation and discontinuous permafrost present in its floodplain. To understand how river processes influence permafrost occurrence and vegetation succession, we produced detailed geomorphic and relative age maps of the floodplain. We used radiocarbon and OSL measurements to generate a deposit age map, and verified that the Pastick et al. (2015) near-surface permafrost map was accurate in the floodplain using permafrost probe measurements. Results indicate that river migration is the primary control on permafrost presence within the floodplain, with older deposits containing more permafrost and thermokarst landforms. Younger deposits contained patchy permafrost whose presence was controlled by vegetation succession and the formation of a thick layer of moss and organics to insulate the ground. By comparing permafrost observations, absolute age maps, and a simple numerical model, we determined that permafrost has been re-forming on the Koyukuk River floodplain for the last 9 ka, but is currently being degraded across the floodplain as the climate warms. Our results indicated that warming air temperatures, changing patterns of river migration, and increases in flood frequency due to climate change may significantly alter processes, patterns, and timing of vegetation succession and permafrost formation within Arctic floodplains.

7.10 Acknowledgments

7.11 Data availability statement

Geochemical data is available in this manuscript or is available at: https://data.ess-dive.lbl.gov/datasets/doi:10.15485/1910300. ESRI shapefiles of geomorphic and relative age maps plus a .csv file of permafrost probe measurements be made available upon publication in a peer-reviewed journal. Mapping was done on QGIS (https://www.qgis.org/en/site/) using the version 3.4.13 long-term release and analyses were done in Matlab v2021 under academic license to Caltech.

7.12 Supplemental materials
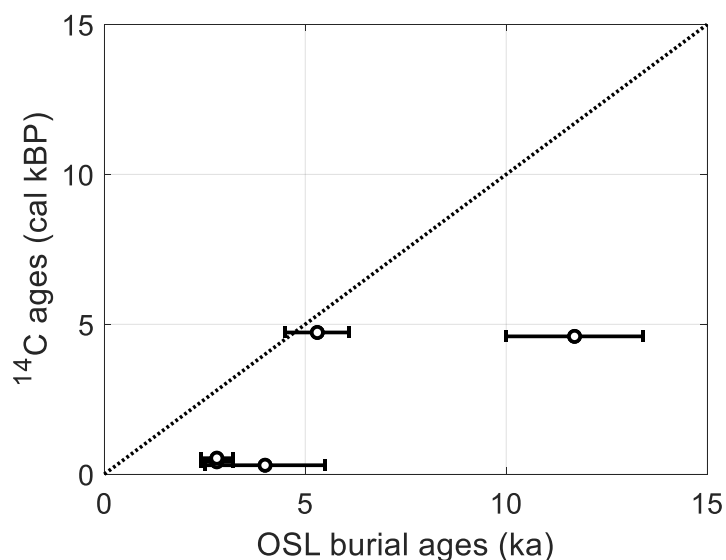
Figure 7.S1. Radiocarbon and OSL measurements plotted for the same sampling sites. Here, we plot OSL samples versus radiocarbon woody debris measurements: KY18-Bank5-OSL-100cm versus KY18-Bank5-175, KY18-Bank5-OSL-260cm versus KY18-Bank5-240, KY18-Bank8-OSL-260cm versus KY18-Bank8-250, and HS22B-Bank4-OSL-222cm versus HS22-Bank1-RC1, HS22-Bank1-RC2, HS22-Bank1-RC3, and HS22-Bank1-RC4. The HS22-Bank1 samples plot primarily on top of each other since the radiocarbon ages are very close.

Table 7.S1. Sampling site locations, permafrost occurrence and geomorphic map units from May and September 2022. GPS coordinates in WGS84. Frozen ground type classified based on field observations from fall. Relative age spans from the youngest deposits (zero) to the oldest sections of the floodplain (eight) mapped using cross-cutting relationships of scroll bars.

Sample Name	Landform	^{14}C Fraction modern (Fm)	^{14}C Age (calBP)	Latitude (°)	Longitude (°)	Permafrost	Relative Age	Geomorphic Unit
KY18-Bank3-101	Cutbank	0.9773 ± 0.0024	178 ± 23	65.76519	-156.48964	Seasonal Frost	1	Floodplain Swale
KY18-Bank4-240	Cutbank	0.5991 ± 0.0018	4601 ± 37	65.75232	-156.50511	Permafrost	2	Levee Deposit
KY18-Bank5-175	Cutbank	0.5945 ± 0.0018	4728 ± 38	65.75232	-156.50511	Permafrost	2	Levee Deposit
KY18-Bank5-240	Cutbank	0.5996 ± 0.0015	4598 ± 33	65.75232	-156.50511	Permafrost	2	Levee Deposit
KY18-Bank6-155	Cutbank	0.6354 ± 0.0015	3931 ± 30	65.75232	-156.50511	Permafrost	2	Levee Deposit
KY18-Bank8-60	Cutbank	0.9843 ± 0.0027	88 ± 35	65.66126	-156.44711	Seasonal Frost	3	Floodplain Swale
KY18-Bank8-250	Cutbank	0.9685 ± 0.0042	300 ± 39	65.66126	-156.44711	Seasonal Frost	3	Floodplain Swale
KY18-Bank12-140	Cutbank	0.9553 ± 0.0020	459 ± 23	65.64022	-156.50949	Seasonal Frost	1	Floodplain Ridge
KY18-Bank14	Cutbank	0.2319 ± 0.0015	13532 ± 62	65.70153	-156.40353	Permafrost	7	Undiff. Permafrost
KY18-Core4-80	Floodplain	0.9305 ± 0.0019	611 ± 20	65.73519	-156.38866	Permafrost	6	Levee Deposit
HS22-Bank1-RC1	Cutbank	0.9577 ± 0.0016	443 ± 21	65.71673	-156.52627	Seasonal Frost	2	Floodplain Ridge
HS22-Bank1-RC2	Cutbank	0.9526 ± 0.0014	482 ± 19	65.71673	-156.52627	Seasonal Frost	2	Floodplain Ridge
HS22-Bank1-RC3	Cutbank	0.9645 ± 0.0015	415 ± 16	65.71673	-156.52627	Seasonal Frost	2	Floodplain Ridge
HS22-Bank1-RC4	Cutbank	0.9363 ± 0.0016	535 ± 16	65.71673	-156.52627	Seasonal Frost	2	Floodplain Ridge
HS22-Bank2-RC1	Cutbank	1.2732 ± 0.0019	-30 ± 15	65.7578	-156.50223	Seasonal Frost	1	Floodplain Ridge
HF22-Bar1-RC1	Point bar	1.0104 ± 0.0017	-69 ± 15	65.697403	-156.413107	Seasonal Frost	0	Floodplain Ridge
HF22-Bar2-RC1	Point bar	1.0548 ± 0.0017	-58 ± 15	65.71853	-156.531532	Seasonal Frost	0	Floodplain Ridge
HF22-Bank1-RC1	Cutbank	0.6293 ± 0.0011	4017 ± 26	65.690546	-156.386102	Permafrost	5	Levee Deposit

HF22-Bank1-RC2	Cutbank	0.5892 ± 0.0022	4840 ± 38	65.690546	-156.386102	Permafrost	5	Levee Deposit
HF22-Bank1-RC3	Cutbank	0.6057 ± 0.0013	4465 ± 30	65.690546	-156.386102	Permafrost	5	Levee Deposit
HF22-Bank1-RC4	Cutbank	0.5617 ± 0.0010	5428 ± 20	65.690546	-156.386102	Permafrost	5	Levee Deposit
HF22-Bank2-RC1	Cutbank	0.7083 ± 0.0013	2864 ± 23	65.677454	-156.375384	Seasonal Frost	5	Floodplain Swale
HF22-Bank2-RC2	Cutbank	0.7840 ± 0.0014	1879 ± 19	65.677454	-156.375384	Seasonal Frost	5	Floodplain Swale
HF22-Bank2-RC3	Cutbank	0.7152 ± 0.0014	2772 ± 23	65.618867	-156.487252	Seasonal Frost	1	Floodplain Ridge
HF22-Bank2-RC4	Cutbank	0.7138 ± 0.0011	2834 ± 19	65.618867	-156.487252	Seasonal Frost	1	Floodplain Ridge
HF22-Bank2-RC5	Cutbank	0.7907 ± 0.0016	1803 ± 29	65.618867	-156.487252	Seasonal Frost	1	Floodplain Ridge
HF22-Bank3-RC1	Cutbank	0.6161 ± 0.0011	4386 ± 25	65.615178	-156.50727	Seasonal Frost	6	Undiff. Permafrost
HF22-Bank4-RC1	Cutbank	0.3354 ± 0.0008	9743 ± 47	65.619025	-156.381985	Seasonal Frost	1	Floodplain Ridge
HF22-Bank5-RC1	Cutbank	0.8515 ± 0.0033	1195 ± 39	65.61834	-156.380733	Seasonal Frost	1	Floodplain Swale
HF22-Bank5-RC2	Cutbank	0.9621 ± 0.0015	408 ± 23	65.61834	-156.380733	Seasonal Frost	1	Floodplain Swale
HF22-Bank6-RC1	Cutbank	0.9546 ± 0.0016	466 ± 21	65.61661	-156.377653	Seasonal Frost	1	Floodplain Ridge
HF22-Bank7-RC1	Cutbank	0.9773 ± 0.0017	178 ± 18	65.615627	-156.37607	Seasonal Frost	1	Floodplain Swale
HF22-Bank7-RC2	Cutbank	0.9704 ± 0.0017	296 ± 17	65.615627	-156.37607	Seasonal Frost	1	Floodplain Swale
HF22-Bank8-RC1	Cutbank	1.1812 ± 0.0019	-37 ± 15	65.769522	-156.417542	Permafrost	1	Floodplain Swale
HF22-Bank8-RC2	Cutbank	1.1695 ± 0.0018	-39 ± 15	65.769522	-156.417542	Permafrost	1	Floodplain Swale
HF22-Bank8-RC3	Cutbank	0.9826 ± 0.0015	92 ± 26	65.769522	-156.417542	Permafrost	1	Floodplain Swale
HF22-Bank9-RC1	Cutbank	0.9899 ± 0.0017	51 ± 17	65.772325	-156.418888	Seasonal Frost	1	Floodplain Ridge

Table 7.S2. Complete CALIBomb results for radiocarbon samples.

Sample Name	Landform	^{14}C Fraction modern (Fm±1SD)	^{14}C calendar age (% probability) for 68% confidence interval in CALIBomb
KY18-Bank3-101	Cutbank	0.9773±0.0024	1737.13 to 1754.93 cal AD (23.6%); 1760.57 to 1783.14 calAD (31.3%); 1666.04 to 1682.68 cal AD (22.3%); 1938.10 to 1949.19 cal AD (13.2); 1795.12 to 1800.94 cal AD (7.5%); 1930.28 to 1931.71 cal AD (1.4%)
KY18-Bank4-240	Cutbank	0.5991±0.0018	-2679.01 to -2623.34 cal BC (44.8%); -2848.57 to -2810.30 cal BC (31.6%); -2745.07 to -2727.95 cal BC (12.0%); -2696.01 to 2681.01 cal BC (9.7%); -2591.13 to -2589.01 cal BC (1.2%)
KY18-Bank5-175	Cutbank	0.5945±0.0018	-2807.21 to -2749.75 cal BC (56.7%); -2723.08 to -2700.25 cal BC (22.4%); -2876.84 to -2854.83 cal BC (21.0%)
KY18-Bank5-240	Cutbank	0.5996±0.0015	-2674.01 to -2621.00 cal BC (48.8%); -2844.96 to -2812.01 cal BC (30.8%); -2602.10 to -2582.50 cal BC (13.9%); -2741.51 to -2732.01 cal BC (6.5%)
KY18-Bank6-155	Cutbank	0.6354±0.0015	-2003.63 to -1958.44 cal BC (62.6%); -2033.50 to -2008.38 cal BC (37.4%)
KY18-Bank8-60	Cutbank	0.9843±0.0027	1832.71 to 1891.10 cal AD (52.3%); 1687.64 to 1708.21 cal AD (16.0%); 1906.14 to 1924.60 cal AD (15.5%); 1719.91 to 1729.73 cal AD (8.2%); 1807.31 to 1816.70 cal AD (7.5%)
KY18-Bank8-250	Cutbank	0.9685±0.0042	1633.60 to 1666.72 cal AD (57.1%); 1527.22 to 1551.55 cal AD (22.5%); 1782.44 to 1795.53 cal AD (16.7%); 1949.07 to1952.67 cal AD (3.7%)
KY18-Bank12-140	Cutbank	0.9553±0.0020	1473.76 to 1507.73 cal AD (59.2%); 1593.64 to 1618.14 cal AD (40.8%)
KY18-Bank14	Cutbank	0.2319±0.0015	-11610.07 to -11554.26 cal BC (48.3%); -11659.73 to -11621.98 cal BC (31.5%); -11785.78 to -11763.84 cal BC (12.4%); -11701.12 to -11685.92 cal BC (7.8%)
KY18-Core4-80	Floodplain	0.9305±0.0019	1326.15 to 1351.39 cal AD (79.7%); 1394.45 to 1400.90 cal AD (20.3%)

HS22-Bank1-RC1	Cutbank	0.9577±0.0016	1492.34 to 1521.53 cal AD (43.9%), 1576.48 to 1602.50 cal AD (36.0%), 1607.81 to 1622.26 cal AD (20.2%)
HS22-Bank1-RC2	Cutbank	0.9526±0.0014	1456.51 to 1479.46 cal AD (100.0%)
HS22-Bank1-RC3	Cutbank	0.9645±0.0015	1527.92 to 1541.29 cal AD (47.2%), 1544.70 to 1550.43 cal AD (15.1%), 1634.08 to 1643.91 cal AD (37.7%)
HS22-Bank1-RC4	Cutbank	0.9363±0.0016	1408.50 to 1421.30 cal AD (100.0%)
HS22-Bank2-RC1	Cutbank	1.2732±0.0019	1980.02 to 1980.78 cal AD (97.4%), 1962.08 to 1962.10 cal AD (2.6%)
HF22-Bar1-RC1	Point bar	1.0104±0.0017	2018.89 to 2019.20 cal AD (46.8%), 2018.20 to 2018.43 cal AD (36.2%), 1955.19 to 1955.33 cal AD (17.0%)
HF22-Bar2-RC1	Point bar	1.0548±0.0017	2007.87 to 2008.85 cal AD (88.7%), 2007.21 to 2007.39 cal AD (11.3%)
HF22-Bank1-RC1	Cutbank	0.6293±0.0011	-2088.22 to -2045.58 cal BC (67.9%), -2142.15 to -2130.79 cal BC (17.3%), -2191.73 to -2180.56 cal BC (14.9%)
HF22-Bank1-RC2	Cutbank	0.5892±0.0022	-2905.55 to -2874.86 cal BC (96.3%), -2792.46 to -2789.56 cal BC (3.7%)
HF22-Bank1-RC3	Cutbank	0.6057±0.0013	-2537.17 to -2491.84 cal BC (78.6%), -2574.59 to -2561.68 cal BC (21.4%)
HF22-Bank1-RC4	Cutbank	0.5617±0.0010	-3490.90 to -3464.56 cal BC (82.1%), -3374.63 to -3368.33 cal BC (17.9%)
HF22-Bank2-RC1	Cutbank	0.7083±0.0013	-931.17 to -897.19 cal BC (75.4%), -867.44 to -854.15 cal BC (13.9%), -967.77 to -956.95 cal BC (10.7%)
HF22-Bank2-RC2	Cutbank	0.7840±0.0014	59.26 to 82.82 cal AD (46.1%), 96.50 to 113.46 cal AD (30.6%), 28.76 to 43.30 cal AD (23.3%)
HF22-Bank2-RC3	Cutbank	0.7152±0.0014	-833.01 to -810.00 cal BC (80.5%), -891.21 to -881.60 cal BC (19.5%)
HF22-Bank2-RC4	Cutbank	0.7138±0.0011	-895.85 to -872.35 cal BC (50.1%), -838.19 to -818.41 cal BC (49.9%)

HF22-Bank2-RC5	Cutbank	0.7907±0.0016	126.17 to 167.99 cal AD (68.3%), 184.45 to 202.99 cal AD (29.8%), 180.88 to 182.11 cal AD (1.9%)
HF22-Bank3-RC1	Cutbank	0.6161±0.0011	-2455.85 to -2415.54 cal BC (44.4%), -2385.85 to -2344.45 cal BC (43.0%), -2410.47 to -2398.20 cal BC (12.6%)
HF22-Bank4-RC1	Cutbank	0.3354±0.0008	-7835.27 to -7750.41 cal BC (68.9%), -7938.81 to -7896.96 cal BC (31.1%)
HF22-Bank5-RC1	Cutbank	0.8515±0.0033	737.40 to 773.08 cal AD (51.7%), 670.93 to 705.60 cal AD (48.3%)
HF22-Bank5-RC2	Cutbank	0.9621±0.0015	1523.99 to 1560.01 cal AD (74.2%), 1563.98 to 1571.49 cal AD (12.7%), 1630.69 to 1637.47 cal AD (13.1%)
HF22-Bank6-RC1	Cutbank	0.9546±0.0016	1469.17 to 1499.83 cal AD (66.8%), 1600.01 to 1615.97 cal AD (30.8%), 1461.17 to 1462.83 cal AD (2.4%)
HF22-Bank7-RC1	Cutbank	0.9773±0.0017	1761.94 to 1782.20 cal AD (34.4%), 1739.26 to 1753.40 cal AD (23.3%), 1666.96 to 1681.07 cal AD (23.0%), 1795.67 to 1799.88 cal AD (6.8%), 1939.56 to 1941.26 cal AD (2.3%), 1941.93 to 1949.04 cal AD (9.7%), 1952.68 to 1953.10 cal AD (0.6%)
HF22-Bank7-RC2	Cutbank	0.9704±0.0017	1647.20 to 1661.54 cal AD (79.1%), 1787.59 to 1792.44 cal AD (20.9%)
HF22-Bank8-RC1	Cutbank	1.1812±0.0019	1987.01 to 1987.29 cal AD (70.9%), 1987.77 to 1987.90 cal AD (29.1%)
HF22-Bank8-RC2	Cutbank	1.1695±0.0018	1989.21 to 1989.72 cal AD (87.3%), 1988.74 to 1988.84 cal AD (12.7%)
HF22-Bank8-RC3	Cutbank	0.9826±0.0015	1836.57 to 1878.67 cal AD (42.2%), 1914.64 to 1927.92 cal AD (17.2%), 1953.28 to 1953.92 cal AD (0.6%), 1802.64 to 1811.67 cal AD (10.8%), 1756.64 to 1759.23 cal AD (2.1%), 1723.82 to 1733.71 cal AD (12.0%), 1684.07 to 1695.69 cal AD (15.1%)
HF22-Bank9-RC1	Cutbank	0.9899±0.0017	1891.35 to 1905.91 cal AD (37.8%), 1817.42 to 1832.51 cal AD (33.8%), 1708.71 to 1719.71 cal AD (27.1%), 1954.13 to 1954.59 cal AD (1.2%)

Table 7.S3. Single grain K-feldspar post-IR IRSL results (overdispersion abbreviated as "OD").

Sample name	Depth (m)	n	OD	Equivalent dose (Gy)			Age model	Dose rate (Gy/ka)			Age (ka)		
KY18-Bank3A-OSL	2.60	17/200	0.87	26.79	±	5.43	MAM-3	2.56	±	0.126	10.5	±	2.2
KY18-Bank1-130cm	1.30	17/300	0.83	15.20	±	3.97	MAM-3	2.82	±	0.139	5.4	±	1.4
KY18-Bank3A-1m	1.00	11/200	1.00	19.89	±	10.00	MAM-3	2.92	±	0.141	6.8	±	3.4
KY18-Bank6-350cm	2.60	13/200	0.40	12.12	±	3.32	MAM-3	1.93	±	0.111	6.3	±	1.8
HS22A-B04-S12-OSL-0.9m	2.22	16/200	1.00	4.55	±	2.97	MAM-3	2.83	±	0.137	1.6	±	1.1
HS22B-B01-S06-OSL-2.22m	0.90	6/200	0.97	13.04	±	5.65	MAM-3	3.17	±	0.140	4.1	±	1.8

Table 7,S4. Single aliquot quartz OSL results.

Sample name	Depth (m)	n	OD	Equivalent dose (Gy)			Age model	Dose rate (Gy/ka)			Age (ka)		
KY18-Core8	0.95	13/58	0.60	10.93	±	2.29	MAM-3	1.18	±	0.05	9.3	±	2.0
KY18-Bank5	2.40	7/57	0.35	8.07	±	3.07	MAM-3	2.01	±	0.09	4.0	±	1.5
KY18-Bank3A-OSL	2.60	12/12	0.22	20.95	±	2.91	CAM	1.79	±	0.076	11.7	±	1.7
KY18-Bank1-130cm	1.30	9/12	1.00	8.27	±	4.38	MAM-3	2.02	±	0.091	4.1	±	2.2
KY18-Bank3A-1m	1.00	11/12	0.23	11.27	±	1.64	CAM	2.12	±	0.094	5.3	±	0.8
KY18-Bank6-350cm	2.60	11/12	0.00	6.05	±	2.30	CAM-UL	1.22	±	0.053	5.0	±	1.9
HS22A-B04-S12-OSL-0.9m	2.22	11/12	0.00	1.81	±	1.19	CAM-UL	2.05	±	0.091	0.9	±	0.6
HS22B-B01-S06-OSL-2.22m	0.90	11/12	0.19	6.63	±	0.98	CAM	2.36	±	0.093	2.8	±	0.4

C h a p t e r   8

MIGRATION RATES AND BASIN STRATIGRAPHY FOR UNVEGETATED MEANDERING CHANNELS IN DEATH VALLEY

Madison M. Douglas, Kimberly Litwin Miller, Michael P. Lamb

8.1 Abstract

Vegetation is hypothesized to be a key source of riverbank cohesion, enabling the formation of sinuous and meandering channels with high depth-width ratios. However, early Earth and Mars contained many rivers without vegetation on their banks that appear to have meandered with similar slopes and width to depth ratios as vegetated meandering channels, and we lack long-term observations of river meandering in modern systems without vegetation. To address this knowledge gap, we conducted a multi-year field and remote sensing study of the Amargosa River in Death Valley National Park. The Amargosa has muddy channel banks coated in salt crusts and lacks significant vegetation. Its channel network contains both straight and highly sinuous, meandering reaches, where cutbanks erode into fine-grained silt deposits with sand lenses and clay drapes while the point bars contain ripple cross-stratified very fine sand and silt. We observed water flow using pressure and conductivity sensors and cameras in addition to opportunistic measurements of flow hydraulics, and directly measured cutbank erosion using erosion pins in meandering reaches. These measurements, along with radiocarbon dating of wood from a flood strandline and surveys following a bankfull flood in fall 2022, allowed us to relate local flood frequency to decadal stream discharge records from the USGS gage in Tecopa, CA. We found no erosion of the bed or bank following a 1-year recurrence flood, 2-3 cm of cutbank erosion for a flood with a 4-year recurrence interval, and 18.5 cm of cutbank erosion and 7 cm of point bar aggradation following a bankfull flood with a 5.5-year recurrence interval. We also conducted flume experiments using sampled intact riverbank to measure entrainment rates and calibrate an erosion law as a function of fluid shear velocity. We calculated shear velocities from observed floods and surveyed channel cross-sectional geometries to calculate bank erosion rates, and found they matched erosion pin data during flow pressure measurements. Field and experimental data agree that the channels migrate very slowly – only ~5 cm/yr. We extended our analysis using the USGS Tecopa gage and radiocarbon dating and predicted that most bank erosion occurs at conditions below bankfull when the threshold for sediment entrainment is exceeded. The water conductivity varies throughout each flood and fresh mud cracks were visible on the eroded surface, which imply that salt crusts do not significantly limit cutbank erosion. This indicates that mud alone is sufficient to provide bank cohesion required for channel meandering. When compared to previous cores of Death Valley and our newly acquired lidar topography, our observations suggest that the Amargosa slowly meanders and rapidly

aggrades, frequently avulsing to generate isolated sand bodies in a matrix of silt and mud over the last ~9.6 kyr.

8.2 Plain-language summary

Most rivers present on Earth today have plants on their banks, and vegetation is thought to reinforce riverbanks, allowing them to migrate laterally and form dynamic, sinuous paths. However, growing evidence for river meandering in places without plants, such as early Earth and Mars, implies that there may be ways to reinforce riverbanks to enable meandering without vegetation. To better understand how rivers can meander in the absence of plants, we studied the Amargosa River in Death Valley National Park. We used a combination of aerial and satellite datasets and field measurements and found that the river is actively meandering, which was supported by layers of sediment in the river banks and floodplain having a similar structure to meandering rivers with plants on their banks. Using field observations and laboratory experiments, we evaluated two potential sources of bank strength: salt crusts and mud. We found that salt crusts dissolve during floods but mud was very difficult to erode, enabling channel migration. However, the river flows infrequently and mud erodes very slowly over decadal timescales based on an analysis of flood frequency using long-term measurements of upstream water flow by the US Geological Survey. Therefore, the river would not be able to migrate across its current floodplain in the time since Death Valley was filled by a lake, when the climate was wetter during the last ice age (~10,000 years ago). Instead, the river is gradually filling in Death Valley by a combination of meandering (slow lateral migration) and avulsion (rapid changes in flow paths).

8.3 Introduction

Alluvial rivers form characteristic bankfull and planform geometries that are thought to be controlled by the threshold stress required to erode their banks while maintaining a mobile bed (Gary Parker, 1978). This threshold channel theory predicts channel geometries of coarse-grained rivers well, but requires that rivers with sandy channel beds have a source of bank strength beyond the weight of sediment grains to stabilize their banks (Trampush et al., 2014). The bank strength then sets channel width, with weak banks producing wider channels that form mid-channel bars and a braided planform geometry, while strong riverbanks maintain narrow, single-threaded channels that can migrate laterally and meander across their floodplain (Dunne & Jerolmack, 2020; Parker, 1976). However, the main factors controlling bank strength for sand-bedded alluvial rivers, and therefore the conditions for forming meandering rivers, remain unclear (Matsubara et al., 2015).

Riverbank cohesion sufficient to permit river meandering is often attributed to vegetation (Corenblit & Steiger, 2009; McMahon & Davies, 2018) or material cohesion (Kleinhans et al., 2018; Lapôtre et al., 2019), and isolating the role of each mechanism is difficult. Plants, mud, and meandering rivers are ubiquitous on the modern Earth and often occur together. Plant roots may provide significant mechanical reinforcement for riverbanks (Santos et al., 2019) and can alter bank hydrologic conditions, for instance by increasing soil porosity and rainfall infiltration rates, which help to decrease bank fluid pore pressures and maintain

stability (Pollen-Bankhead & Simon, 2010). Mud also increases bank strength and decreases erodibility for sediment at all depths of river cutbanks (Dunne & Jerolmack, 2020; Ternat et al., 2008). Meandering rivers are difficult to produce at laboratory scales, but planting alfalfa sprouts (Braudrick et al., 2009; Tal & Paola, 2010) or adding cohesive sediment (van Dijk et al., 2012; van Dijk et al., 2013; Peakall et al., 2007) to flume experiments can transform braided into meandering streams. The rock record also records a shift from amalgamated sandy channel bodies to isolated sand channel bodies in muddy floodplains with the evolution of land plants (Fig. 8.1) (Hajek et al., 2010), which has been interpreted to reflect a change in river planform geometry from sandy braid plains to meandering rivers (Almeida et al., 2016; Davies & Gibling, 2010b).

In recent years, the paradigm of meandering rivers co-evolving with land plants has been called into question. Reconstructing river morphology and planform geometry from stratigraphic deposits is challenging because meandering rivers may avulse in addition to migrating (Ielpi et al., 2020). Single-threaded rivers can also create amalgamated sandstone bodies with little preserved mudstone when they migrate laterally much faster than they aggrade vertically (Jerolmack & Mohrig, 2007). This behaviour can be captured quantitatively using a dimensionless channel mobility number (M):

$$M = \frac{\bar{h}v_c}{Bv_a},\qquad\qquad(8.1)$$

where $\bar{h}$ is the average channel depth (m), B is the channel width (m), v_c is the channel lateral migration rate (m/yr), and v_a is the vertical aggradation rate (m/yr). When $M \gg 1$ the channel transits its floodplain by migration and seldom avulses, forming amalgamated sandy channel bodies. For $M \ll 1$ the river only forms narrow channel belts and frequently avulses to new locations on the floodplain to keep up with aggradation rates, creating isolated sand bodies in mudstone. Thus, stratigraphic architecture may have more to do with the relative rates of river lateral migration and avulsion than it does with river morphology. Re-examination of pre-Silurian fluvial deposits indicates that deep, meandering rivers pre-dated plants (Ganti et al., 2019; Ielpi, & Rainbird, 2015; Santos & Owen, 2016). Evidence for meandering rivers has also been found in Martian sedimentary deposits (Malin & Edgett, 2003). In addition, numerous modern examples of meandering rivers occurring in drylands, where vegetation is sparse or absent, demonstrate that rivers can produce a meandering planform without plants on their banks (Ielpi, 2018; Ielpi et al., 2020; Ielpi & Lapôtre, 2019, 2020).

Since some unvegetated meandering rivers likely existed throughout Earth history, other potential sources of bank cohesion have been proposed, primarily mud and salt crusts (Matsubara et al., 2015; Millar & Quick, 1998; Parker et al., 2011). Mud has a high critical shear stress for entrainment and can provide cohesion directly, though its material strength (Hanson & Cook, 2004; Hanson & Simon, 2001; Ternat et al., 2008). Mud deposition may be enhanced through organic molecules produced by vegetation or microbial communities, which cause flocculation and increase mud settling velocity on the floodplain (Zeichner et al., 2021). Salt crusts provide cohesive strength by providing chemical cementation within the bank (Ritter et al., 2022) or increasing water salinity and causing mud flocculation, thus

increasing particle settling rates (Mietta et al., 2009; Nghiem et al., 2022). Therefore, salt crusts and mud have become favored mechanisms to enable river meandering in terrestrial drylands and on early Mars (Lapôtre et al., 2019; Matsubara et al., 2015; Millar, 2005).
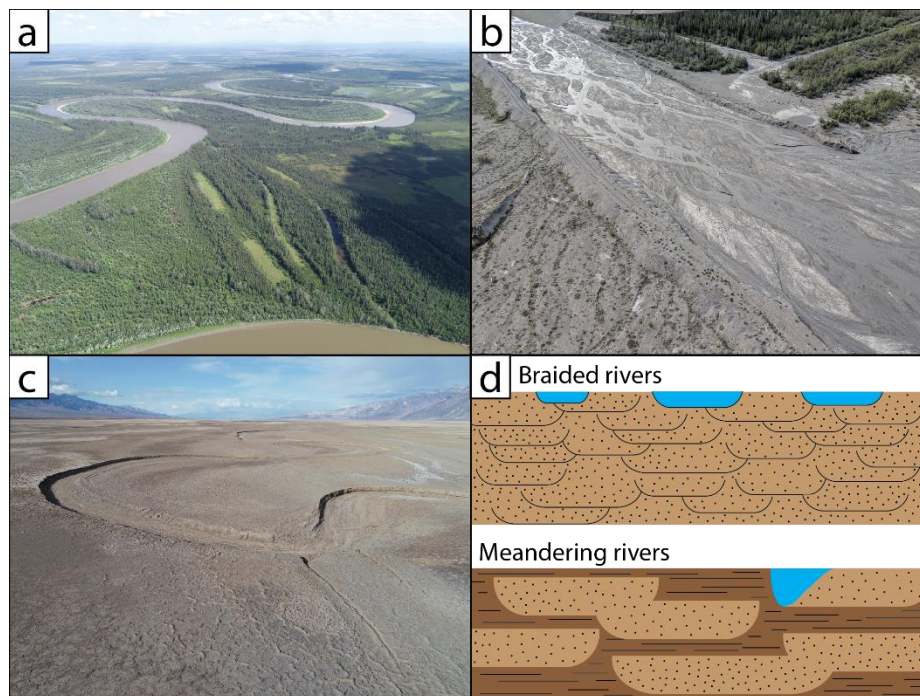
Figure 8.1: Contrasting river planform morphologies and stratigraphic architectures. **(a)** A meandering reach of the Koyukuk River near Huslia, AK. The aerial image was taken in summer 2018, and the river is approximately 300 m wide in the image. **(b)** Photo taken from small aircraft of the braided Kaskawulsh River, Yukon Territory, Canada. Photo by Madison Douglas. **(c)** Aerial image of an unvegetated, meandering reach of the Amargosa River, Death Valley, CA. The river cutbank is approximately 1 m high. **(d)** Cartoon of characteristic braided and meandering river stratigraphic architecture. Coarser sandy deposits are shown in speckled light brown, finer muddy deposits are dark brown with short lines, and active channels are shown at bankfull stage in light blue.

While meandering rivers without vegetation have been well-documented, the types and rates of fluvial processes that shape meandering dryland river systems are poorly understood. First, it remains unclear whether mud cohesion or salt crust dissolution is the primary control on bank erodibility, as well as if the bank strengths provided by mud and salt agree with threshold channel theory. Second, we lack direct measurements of flow events and erosional processes along these primarily ephemeral channels. Third, it is difficult to demonstrate that these rivers are meandering: specifically, building bars at similar rates to how rapidly banks are eroding and increasing their curvature to the point of cutoff. Finally, we lack comparisons between vertical aggradation and lateral migration rates to understand the resulting fluvial stratigraphic architecture.

To address these knowledge gaps, we conducted a multi-year field observation study on a meandering reach of the Amargosa River on the floor of Death Valley (Fig. 8.2). We measured bank erosion rates and observed floods and erosion processes with time-lapse cameras. In addition, we sampled the bank toe and developed a novel experimental setup to determine the threshold and rates of cohesive sediment entrainment. Then, we used our calibrated stream discharge and bank erosion model to extrapolate bank erosion rates over the decadal timescale using the USGS stream gage at Tecopa, CA. We used our decadal migration rates and valley aggradation rates from dated cores in Badwater Basin to calculate the channel mobility number (Eq. 8.1). We combined these insights with lidar observations of sinuous reaches and avulsions to understand the stratigraphic architecture of the lower Amargosa River.

8.4 Study site

Death Valley contains Badwater Basin, the lowest point in North America at 86 m below sea level, as well as the highest recorded temperatures of 57°C at the Furnace Creek weather station. Our study focused on the lower reach of the Amargosa, which drains directly to Badwater Basin, because it contains meandering reaches devoid of vegetation (Fig. 8.2). The site has previously been examined in geomorphic and remote sensing studies as a Mars analog (Anderson, 2005; Baldridge et al., 2004). The Amargosa has sinuous channels that were reported to actively meander at rapid, measurable rates up to 1.5 m/yr despite lacking vegetation along its cutbanks for tens of km (Ielpi, 2018). In Death Valley, the Amargosa is composed of a network of ephemeral, depositional channels with varying sinuosity. The lack of vegetation implies that salt crusts or mud present on the cutbanks must supply sufficient bank cohesion to enable meandering in portions of the network, enabling us to evaluate the role of bank cohesion in channel meandering and its signature in the stratigraphic record.

The Amargosa River originates in the Amargosa Valley, NV and flows south before turning and flowing north to Badwater Basin, CA (Fig. 8.2). Its watershed is largely protected from anthropogenic alteration because our study reach is in Death Valley National Park, much of watershed is protected through the Nevada National Security Site, and the reach between Shoshone and Dumott Dunes is designated as a Wild and Scenic River. The river reach in Death Valley is bounded on the west by Panamint Range and east by the Black Mountains, which supply water and sediment to the Amargosa via alluvial fans. Death Valley is downdropping along faults running north to south and bounding the eastern and western edges of the valley. The eastern fault is moving faster than the western bounding fault, causing long-term tilting of approximately 0.016°/kyr at present (Hooke, 1972).

Previous studies took a long core at Badwater Basin and short cores to understand the long-term aggradational history of the Valley. The most detailed results come from a 185 m core extracted from Badwater Basin and dated using U-series chronologic methods (Ku et al., 1998; Li et al., 1996; Lowenstein et al., 1999). These studies found that Death Valley has remained a mud flat and salt pan for the previous 10 ka, during which 7.7 m of mud with primary halite aggraded. During the last glacial period, Death Valley hosted Lake Manly, a perennial saline lake that deposited 10.3 m of sediment containing ostracods and subaqueous

halite crystal structures from 10 – 35 ka. Shorter cores extracted using a hand auger in transects across the valley found mostly brown silt and clay with ~1-2 m thick sand bodies (Hooke, 1972).
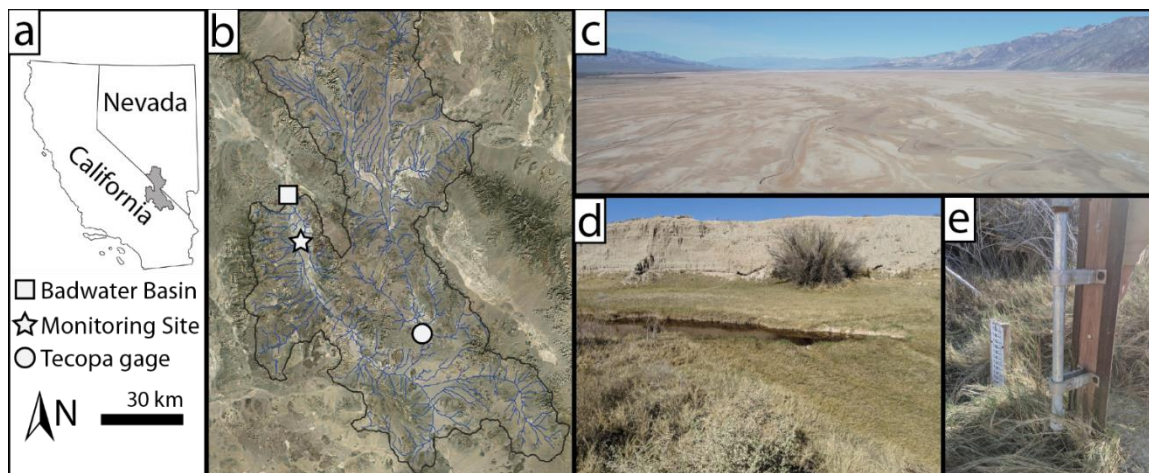
Figure 8.2: Context of Amargosa River and study bends. **(a)** The Amargosa watershed is shaded grey on the state outlines. **(b)** The Amargosa runs from the Amargosa Valley, NV to Badwater Basin in CA (square), past a USGS stream gage in Tecopa, CA (circle). The area of the catchment at our monitoring site (star) receives water from upstream as well as alluvial fans coming off the Black (east) and Panamint (west) ranges. **(c)** Aerial image taken looking north towards Badwater Basin overlooking the monitoring site (image taken January 2021). **(d-e)** Location and instrumentation for USGS Tecopa gage station (photos taken March 23, 2019).

8.5 Methods

8.5.1 Remote sensing and hydrologic data

We compiled remote sensing imagery and long-term hydrologic datasets for the lower Amargosa. The closest upstream river gage with a long period of record is located at Tecopa, CA (USGS 10251300) with a discontinuous record from September 26, 1962 to present. The closest rain gage is located in Furnace Creek, CA (NWS GHCND:USC00042319), with records from April 26, 1961 to present. We compared our monitoring data to stream and rain gage data to calibrate a relation between the gages and discharge in our study reach (Sect. 8.5.2).

We also compiled satellite and aerial imagery and topography to determine the prevalence of sinuous reaches, locations of previous cutoffs and infilled channels, and identify active versus inactive channels. We downloaded Planetlabs (3 m), Landsat (30 m), and National Agriculture Imagery Program (NAIP, 1 m) imagery and used it to map channels by hand and determine which were active during significant flood events in 2022. We considered active channels to have significant changes in the color and spatial distribution of salt crusts visible in satellite imagery between the end of July and start of September. We also acquired lidar

0.5 m resolution topography covering our study region from NCALM (OpenTopography, 2020).

8.5.2 Field monitoring

We conducted regular field monitoring at a sinuous reach of the Amargosa from November 2018 through July 2020, and then revisited the sites in March 2022 after large floods that water year. We focused monitoring and recurrent measurements on two bends along one active, highly sinuous channel. The primary study site, Bend 1, was located approximately 1 km north (downstream) of the Bend 2, the second site. Bend 2 had been previously reported to migrate at 1.5 m/yr (Ielpi, 2018), and we anticipated measuring significant bank erosion at this site.

We directly measured cutbank erosion rates using 51-cm long erosion pins (Table 8.S3). We visited sites and measured the exposure of pins installed at 2 locations with high curvature in Bend 1 and 3 locations in Bend 2 (Table 8.S3). The pins were pounded flush with the bank upon installation. We measured the length of pin exposed by fluvial erosion on the top and the bottom to mm precision and took the mean of these two values to determine erosion between visits before using a hammer to pound the pin flush with the bank. We initially anticipated that significant erosion and high flows could occur, so we did not install pins low enough (< 0.3 m) to capture the spring 2019 flood which exceeded the critical shear velocity for bank erosion. Cameras, pressure sensors, and a conductivity sensor collected images and measurements of water stage and conductivity between our site visits. The game cameras took photographs during daytime with a 5- or 10-min interval. The Onset HOBOware U24-002-C logger measured fluid conductivity and temperature at 10-min intervals to 5 mS/cm and 0.1°C resolution. Two Onset HOBOware U20L-02 loggers measured water and air pressure (to 1.2 kPa resolution) and temperature (to 0.44°C resolution). One sensor was attached to a game camera to record air pressure (P_{air}; Pa) and another was mounted at ~5 cm above the channel thalweg to measure water pressure (P_{water}; Pa) and avoid the sensor becoming buried by sediment deposits. We calculated flow depth (H; m) as:

$$H = \frac{P_{water} - P_{air}}{\rho g} + H_{sens},$$
(8.2)

where flow depth depends on the height to the pressure sensor (H_{sens}; m), fluid density (ρ; kg/m^3), and acceleration due to gravity ($g = 9.81$ m/s^2). Our calculations assume a constant fluid density of 1000 kg/m^3. The concentration of salt added to tap water required to produce conductivity of 30,000 mS/cm (representative of high values during floods) is less than 1 g/L, which would introduce ~1% error on the fluid density, of similar magnitude to pressure sensor measurement precision. We did not leave monitoring equipment in place during summer months because it was only rated up to ~110°F. When we left them out for early summer 2020, our game cameras recorded temperatures of 57°C (>135°F).

To calculate channel hydraulics during floods of varying stage, we measured downstream channel slope and cross-sectional geometry for each bend with Trimble R12 RTK GPS to 1

cm precision. From these measurements, we extracted the channel bed slope (S; m/m), top width (B; m), cross-sectional area (A_{xs}; m^2), wetted perimeter (P_w; m), and average depth ($H_{avg} = A_{xs}/B$) for cross-sections along our study reach. We then calculated a water discharge using Manning's equation:

$$Q_w = \frac{1.468}{n} S^{1/2} A_{xs}^{5/3} P_w^{-2/3}. \tag{8.3}$$

We calculated A_{xs} and P_w the channel wetted perimeter from measured cross-sections and the flow depth timeseries. We used Manning's $n = 0.039$ calculated from field measurements during a rare flow event in a nearby channel on March 3, 2023. Flow was shallow, so we used a RIGID ruler to measure flow depth at topographic inflection points spaced along the cross-section (Table 8.S1), calculating $A_{xs} = 0.15$ m^2 and $P_w = 1.83$ m. From doing 5 repeats of the orange-peel test along the channel centerline, we measured $U = 0.16\pm0.01$ m/s (1 SD uncertainty). Channel centerline slope was measured using a linear fit to lidar data as 5.26×10^{-4}. Substituting these measurements into equation (3), we calculated a best-fit Manning's $n = 0.039\pm0.003$ that is appropriate for use in relatively straight, smooth channels composed of fine sediment (Arcement & Schneider, 1989).

To calculate fluid shear stress on the cutbank, we assumed normal flow conditions and that the stresses on the channel bed and outer bank were similar. To calculate the channel bank stresses (τ_{bank}; Pa) we used the depth-slope product:

$$\tau_{bank} = \rho g R_h S \tag{8.4}$$

where the hydraulic radius $R_h = A_{xs} / P_w$. Defining a shear velocity for the banks (u_{bank}^*; m/s), $u_{bank}^* = \sqrt{\tau_{bank}/\rho}$, we substitute Eq. (8.4) and find that

$$u_{bank}^* = \sqrt{\frac{B+2H}{B/\varphi+2H} g R H_{avg} S}. \tag{8.5}$$

This relation allows us to evaluate the shear velocity on the eroding cutbanks for an arbitrary hydrograph or bankfull conditions.
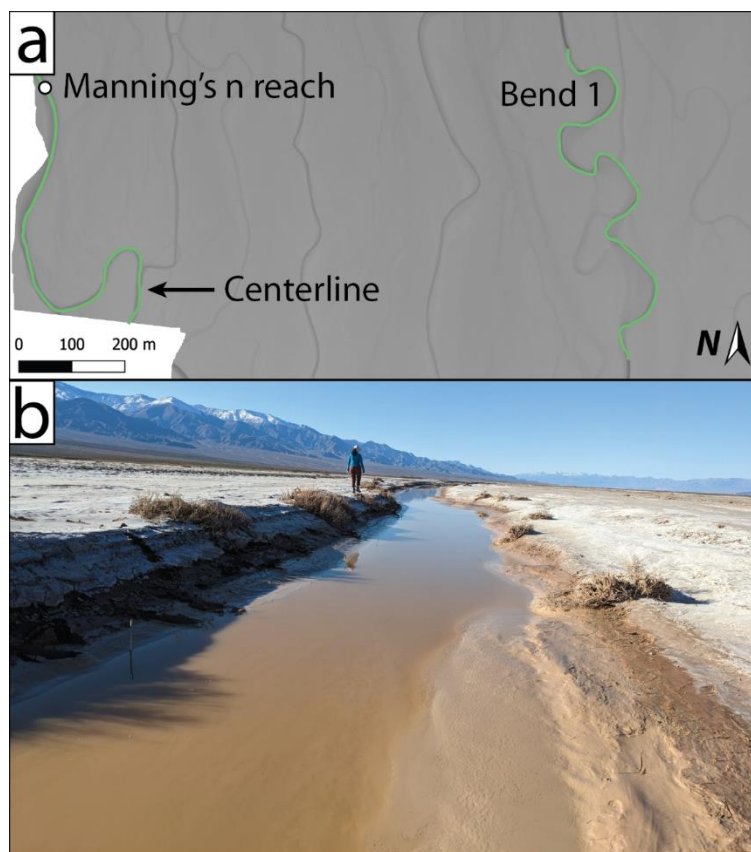
Figure 8.3: (a) Location of Manning's n channel measurement (36.11371203°N, 116.826681°W) in comparison to Bend 1. Basemap is 0.5 m lidar with channel centerlines used to calculate slope shown in green. **(b)** Field photo of measurement reach for channel hydraulics used to calculate Manning's *n*.

8.5.3 Sediment and radiocarbon sampling

To understand flood frequency of the Amargosa, we collected samples of plants and woody debris from a strandline on a point bar for radiocarbon analyses. We selected wood from a continuous strandline that was at ~1/2 bankfull depth in 2021, prior to the bankfull flood that occurred in 2022. We collected the samples in whirlpaks and rinsed them with MilliQ water before storing them in combusted glass vials and shipping them to WHOI NOSAMS for analysis. To convert from radiocarbon years (BP) to calendar years, we used CaliBomb with IntCal20 and the Hua et al. calibration for Northern Hemisphere Zone 1 (China Lake, very near field site) to extend radiocarbon record up to 2020 (Hua et al., 2022; Reimer et al., 2013; Reimer & Reimer, 2023).

To determine the grain size of the cutbanks, channel bed, and point bar we observed stratigraphy and collected sediment samples. At Bend 1, we dug two trenches in the point bars and measured ten stratigraphic columns, as well as recording seven cutbank stratigraphic columns and two stratigraphic columns for pits dug into the channel thalweg. At Bend 2, we measured two stratigraphic columns on the cutbank and one on the point bar, and recorded

five stratigraphic columns along other reaches of the river, measuring sediment grain size using a sand card and hand lens.

8.5.4 Grain size analysis

We collected samples to measure using laser diffraction and verify our field observations of sediment grain size. In the laboratory, we measured grain size using laser diffraction, in a Malvern Mastersizer 3000 with Hydro LV accessory to suspend and analyze fine sediment. First, we decarbonated sediment samples by adding 20 mL 1M HCl and having the samples sit unheated for 12 hours. We then centrifuged samples at 4000 rpm for 15 min and decanted the supernatant, then rinsed the sediment twice by adding ~40 mL deionized H_2O and repeating the centrifuging and decanting steps. Next, we removed organics by adding 25 mL of 30% hydrogen peroxide on hot plate (80°C) then repeated the centrifuge and rinse steps. Little reaction was observed for most samples, likely indicating low organic content. Finally, we ran samples on the Malvern Mastersizer 3000 at Caltech. Since we were concerned about potential for flocculation or the Malvern sonicator breaking the clay particles into small fragments, we did not use the sonicator but kept the propeller at 2000 rpm, and took measurements until at least 3 subsequent measurements had RSD < 5%.

8.5.5 Sediment entrainment experiments

To determine the entrainment threshold and rate of sediment on the toe of the riverbank, we ran physical experiments in an abrasion mill. To run sediment entrainment experiments, we sampled intact pieces of the eroding cutbank toe in our study reach (Fig. 8.4a). We removed salt crusts from the bank to expose the underlying sediment and used a sledgehammer to pound the PVC mill into the bank toe and collect a 10 cm deep sample of intact riverbank. The mill was dug out of the bank, and its base was secured to a flat board and the top of the mill was filled with soft packing material for transport back to the laboratory with minimal disturbance.

To set up the experiments, we prepared the abrasion mill with the sample inside so that it had two acrylic windows to let floodlights shine in and one spigot to siphon water and sediment (Fig. 8.4b-c). We attached a light sensor (Onset HOBOware MX Temp/Light Pendant with HOBOconnect application) to the inside of the mill to collect data at a 10-sec sampling interval throughout experiment. The mill bed sampled for its initial grain size, then filled it to 40 cm depth with saline solution. We produced the saline solution by dissolving salt crusts from the sampling site in tapwater until we reached a conductivity of ~30,000 μS/cm, which was representative for floods through the Amargosa based on our field monitoring.

We ran the experiment for a range of shear velocities, calibrated to the spinning rate of the flat plate driving fluid flow (calibrations in Supplemental Text 8.S2). For each $u*$ value in Table 8.S4, we increased the variable frequency drive, measured the rotor RPM with a tachometer, and covered with a black curtain to avoid fluctuations in light for 5 hours. After 5 hours, we measured fluid conductivity with the handheld probe then siphoned ~1L via the metal spigot into a clean, pre-weighed glass jar. We then gently topped off saline solution to

40 cm, increased the variable frequency drive to the next u^* value in Table 8.2, and repeated this step.

After running the experiment for all non-zero u^* values, we turned off the motor and let sediment settle for 24 hours. We siphoned a final sample after this interval determine the mass of dissolved salt in solution. Then, we siphoned all the water out of the mill and let it air dry before taking a sample of the final sediment bed to measure its grain size distribution.

We measured sediment concentrations and grain sizes from the samples taken before, during, and after the experiments. We weighed glass jars full of siphoned fluid, dried them in an oven at 70⁰C, and re-weighed the dried jars to get sediment concentration. We subtracted the weight of the jars and the weight of dried salt from the final 0 RPM siphoned jar to get sediment concentration in g/L, assuming a uniform fluid density 1000 kg/m^3. To measure samples for grain size, we scraped sediment out of the glass jars and into Falcon tubes using a microspatula. We then measured grain size for the siphoned and bed sediment using laser diffraction (Sect. 8.5.4) and calibrated a relation between light flux (lux) and sediment concentration (c; g/L) to 0.1 g/L precision (see Supplemental Text 8.S2.1). To calculate the sediment entrainment fluxes, we analyse the measured sediment concentrations through time. From conservation of mass, the change in sediment concentration is equal to the vertical sediment entrainment minus the settling flux (Garcia & Parker, 1991). Assuming a dilute suspension of sediment, flat channel bed, and sediment fine enough to be transported in suspension and follow fluid turbulence (Reynolds analogy), the net sediment flux at a reference height (F_a; m/s) is evaluated as:

$$F_a = w_s(E_a^* - c_a), \tag{8.6}$$

where the downwards flux of sediment is the concentration at $z = a$ (c_a; m^3 sediment/m^3 fluid) times the settling velocity (w_s; m/s), and the upwards flux of sediment is equal to the settling velocity multiplied by a dimensionless entrainment rate (E^*_a). Assuming a uniform vertical sediment concentration and grain size, w_s is constant throughout the water column such that:

$$\frac{\partial c_a}{\partial t} = w_s \frac{\partial c_a}{\partial z} - \frac{\partial E}{\partial z}, \tag{8.7}$$

with c_a averaged through time to account for turbulence. The assumption of uniform vertical sediment concentration and grain size is acceptable for our experiments based on calculations that indicate a dimensionless Rouse number ($P \sim w_s/u^*$) < 0.001 (see Supplemental Text 8.S2).

We designed our experiments to isolate the role of mud cohesion by setting different terms in Eq. (8.7) equal to zero. The mill setup was based on previous experimental work in abrasion mills for bedrock and alluvial systems (Scheingross et al., 2014; Sklar & Dietrich, 2001; Trower et al., 2017). We exerted a range of shear velocities and let the sediment

concentration stabilize at each concentration so that $\frac{\partial c_a}{\partial t} = 0$ and $E = w_s c_a$. We first calculated the particle settling velocity using the change in sediment concentration through time and compared this value to the theoretical Stokes settling velocity corrected for the Corey shape factor of natural sediments (Dietrich, 1982). Therefore, given the sediment concentration at a reference height and the settling velocity, we directly calculated a sediment entrainment rate. To determine c_a throughout the experiments, we took a sample of concentration directly and used this to calibrate a concentration versus lux curve from our light sensor measurements. To evaluate w_s, we turned off the mill (set $E = 0$) so that $\frac{\partial c_a}{\partial t} = w_s \frac{\partial c_a}{\partial z}$. Assuming all sediment settles as a front with constant average concentration (c_a) and settling velocity (w_s), we calculate settling velocity as the slope of a linear fit to sediment concentration versus time. Thus, the experiments let us solve for w_s, c_a, and E using two independent equations and laboratory measurements of sediment concentration.
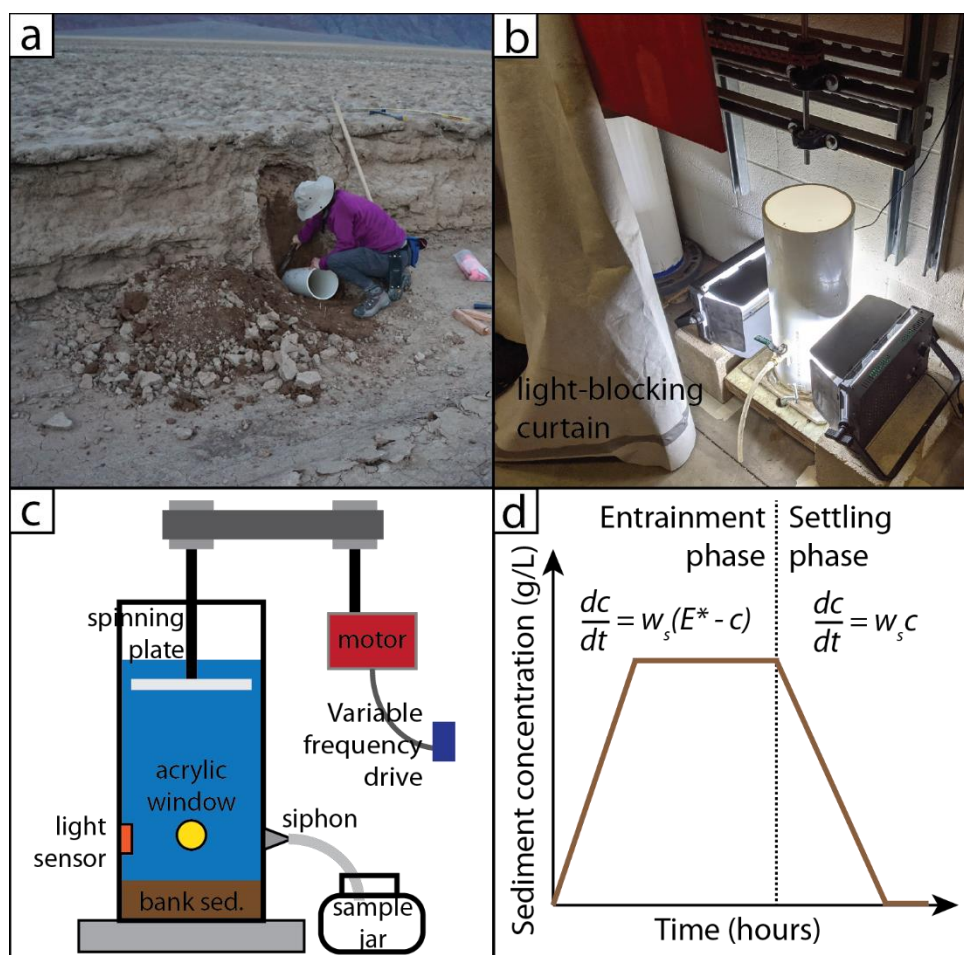
Figure 8.4: Sampling and experimental setup from abrasion mill tests on Amargosa bank sediment. **(a)** Digging out a PVC pipe that was pounded into the bank toe of the Amargosa River to collect intact riverbank. **(b)** Photo of experimental setup, where spotlights are shown through acrylic windows installed in the side of the PVC pipe and the setup is covered by a

light-blocking curtain. **(c)** Cartoon cross-section of experimental setup, where a variable frequency drive sets the speed of a motor that turns a spinning plate. This exerts shear on the bank sediment, picking up sediment that obscures light shining in through an acrylic window. Measurements of sediment concentration were made indirectly using a light sensor and directly by siphoning fluid into a glass jar. **(d)** Cartoon timeseries of expected sediment concentration (c; g/L) data during the entrainment and settling phases of an experimental run. During the entrainment phase, the change in concentration is a function of sediment settling velocity (w_s; m/s), entrainment rate (E^*; dimensionless), and sediment concentration (c). During the settling phase, $E^* = 0$.

8.6 Results

8.6.1 Remote sensing observations

As it traverses the floor of Death Valley, the Amargosa River divides into a complex network of channels (Fig. 8.5a). Most channels are active, and both the proportion of active channel and channel density measured on transects across the valley decrease approaching Badwater Basin (Fig. 8.5b). We hypothesize that channels may spread out because the valley widens and sediment is distributed across a wider region. In addition, inactive channels tend to cluster near the center of the valley, farthest from the bounding faults on its east and west edges.

Subtle topographic features visible in lidar data for our study reaches reveal the Amargosa's evolution through time. In Bend 2, we can clearly see the river forming asymmetrical channels with steep cutbanks and gently sloping point bars as it flows north (Fig. 8.5c). Scroll bars and a chute cutoff in the early stages of formation are visible, implying that the channel has migrated in the past and may be doing so at present. Where the channel bends to the west and flows south, we see that it overtopped its banks and re-occupied a shallow divot that traces the path of an infilled floodplain channel. We infer that an incipient avulsion is occurring this location because flow decelerates as it turns up-valley, causing an increase in water surface elevation and promoting overtopping of the bank.

While Bend 2 appears to be meandering, we did not observe the same evidence of rapid migration (up to 1.5 m/yr) detected by Ielpi (2019), as described in their Fig. 8.11b. We note that satellite imagery from the National Agriculture Imagery Program (NAIP) has 60 cm/pixel ground resolution but is only orthorectified so that 95% of data falls within 6 m of ground truth (Fig. 8.6). Therefore, migration rate errors of up to 10 pixels may be due to orthorectification errors. Since Ielpi (2019) does not describe a re-orthorectification procedure, we overlaid available NAIP imagery for this bend with its existing orthorectification. While we observe significant variation in salt crust appearance on the point bar surface, we do not observe point bar accretion or cutbank erosion beyond 6 m region of uncertainty.

Downstream (north) along the same active channel to Bend 1, we observe similar features, including steep cutbanks and point bars transitioning to scroll bar deposits (Fig. 8.5e). One

bend upstream of Bend 1, a channel bend appears to have been abandoned and then filled in by fluvial sediment. However, no other evidence of cutoffs is visible adjacent to the active channel. Just upstream of Bend 1, we also see evidence of channelized overbank flow where the river turns to slow south (up-valley). To the east of the active channel, we observed a shallow, inactive channel that appears to be an infilled meandering reach. From these observations, we infer a multi-stage history for the meandering reach. First, the channel avulsed at an upstream location, abandoning the eastern meanders which subsequently were filled in by floodplain material. Then, the active channel increased its sinuosity, producing scroll bars. When the channel became sufficiently sinuous that the river decelerated and overtopped its bank, it avulsed in a direction where it flowed back into the active channel. This formed a neck cutoff and abandoned channel bend, which was then slowly infilled. At present, the bend downstream of the cutoff (Bend 1) is highly sinuous and has begun overtopping its bank during high flows and incising a channel that will grow to form a stream avulsion.
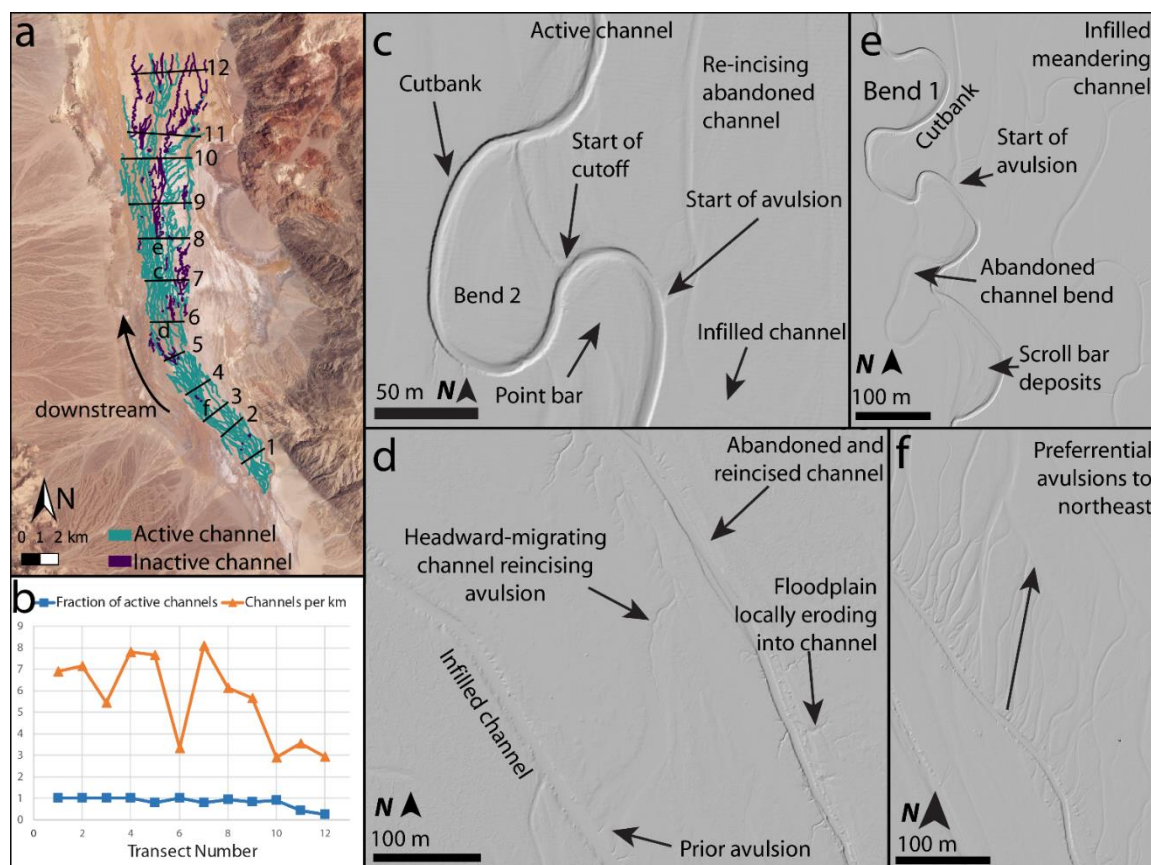
Figure 8.5: (a) Planetlabs 3m satellite imagery of Death Valley in August 2022 overlain with traces of active (teal) and inactive (purple) channels traced by hand from lidar imagery. Active channels showed significant change in ground color and salt crust distributions between the start and end of August 2022, when a significant flood event occurred. Transects where channel statistics are measured are shown as numbered black lines and the locations for panels (c) through (f) are indicated with the panel letter. **(b)** The fraction of active

channels intersecting each transect (orange triangles) and number of channels per km distance (blue squares) along each transect. Lidar hillshade topography of characteristic floodplain features along the Amargosa River for our two study sites, **(c)** Bend 2 (map lower right corner at 36.103°N, 116.813°W) and **(e)** Bend 1 (map lower right corner at 36.110°N, 116.812°W). **(d)** Example of shallow channels on the floodplain with secondary channels incising their banks (map lower right corner at 36.060°N, 116.803°W). **(f)** Secondary channels channels flow preferentially to the northeast (map lower right corner at 36.032°N, 116.785°W).
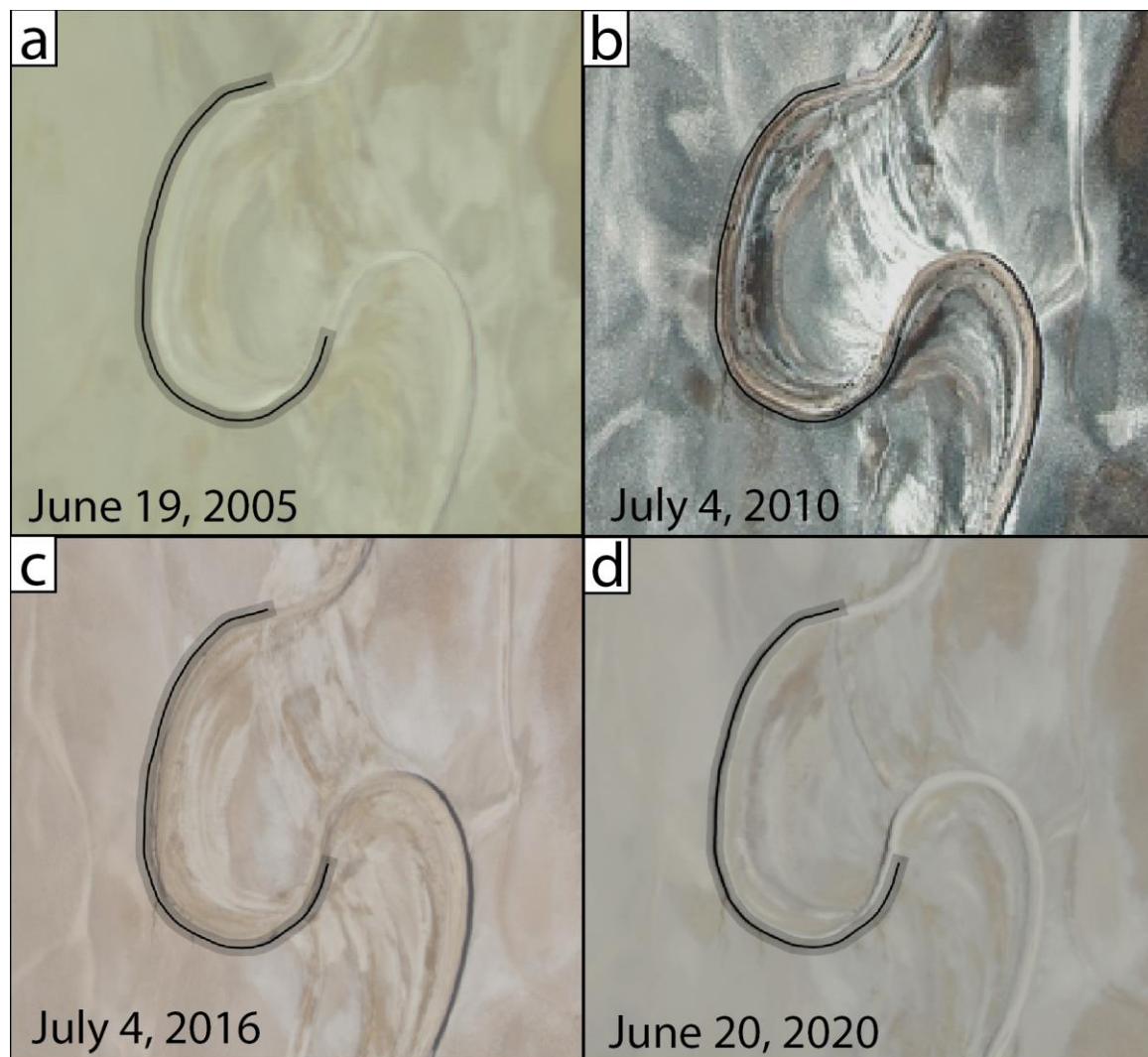
Figure 8.6: NAIP imagery of Bend 2. The cutbank from the June 20, 2020 image traced in black with a 6 m shaded region is shown on the image from each panel.

We observe similar patterns of channel abandonment by avulsion and subsequent re-incision along less sinuous reaches of the Amargosa as well. In Fig. 8.5d, the western channel is shallow, with a symmetric flat bottom, and has numerous short gullies along its edge. We interpret this feature as an abandoned channel that is slowly being infilled by floodplain

sediment and erosion of its banks by direct rainfall. The channel to the east similar morphology but with a narrow inner channel with steep banks. This may represent an abandoned channel that infilled and was subsequently re-occupied and incised. Shallow channels on the floodplain appear to contribute water to the active channel via complex networks grown by headward incision. From this example (Fig. 8.5d), we infer that the avulsion timescale is slightly shorter than the time required to infill a channel, and that secondary channels are crucial to routing water across the floodplain and go through periods of activity alternating with dormancy.

In general, avulsion preferentially produces a new channel path direction to the northeast (Fig. 8.5f). In many locations, avulsions cluster so that a large number of shallow channels radiate from the eastern bank of an active channel, join, and then incise a new flow path. The eastern bounding fault of Death Valley is subsiding more rapidly than the western fault, causing the valley to slowly tilt to the east (Hooke, 1972). We expect that the preferential avulsion direction is caused by the Amargosa re-routing towards the axis of maximum subsidence, then being forced to migrate back towards the center of the valley due to the sediment supplied by alluvial fans along the Black Mountains (Kim et al., 2011; Kopp & Kim, 2015).

8.6.2 Stratigraphy and topographic surveys

Our study reach contains many landforms common to perennial meandering rivers, including sinuous channels with steep, nearly vertical cutbanks and gently sloping point bars (Fig. 8.7). The cutbanks are periodically incised by secondary channels, and ripples migrate across the channel bed (Fig. 8.7b). We surveyed channel cross-sections at the apexes of Bends 1 and 2 and found that the channel has a bankfull depth of approximately 1 meter (Fig. 8.7; Fig. 8.8b-c). Cutbanks are higher than the point bars, and we defined bankfull depth to the inflection point on the point bar. We also traced channel centerlines of Bend 1 and Bend 2 and extracted their elevations from the lidar data (Fig. 8.3a). Fitting a line to these measurements, we find a downstream slope of 3.25×10^{-4} at Bend 1 (Fig. 8.8a).

We analyzed samples from both bends for grain size and found that the cutbank and channel thalweg are comprised of silt with some sand, while the point bar is much coarser (Fig. 8.8d-e). When sampling the channel thalweg, we noted thin layers of alternating silt and very cohesive clay. Water tends to pond in the apexes of bends as the channel dries up after a flood because they are deeper than the straight reaches between bends. Therefore, fine clays typically transported as washload will settle in these locations. These thin clay layers may armor the channel bed and prevent sediment motion for low flows, since we observed a footprint and mud cracks in January 2019 left from a previous trip that survived flow through the channel in the meantime (Fig. 8.7g).

Both bends had very sparse vegetation on their point bars but few roots visible in their stratigraphy and no plants visible on their cutbanks. Therefore, we do not expect the sparse, mostly dead vegetation to provide sufficient bank cohesion to enable meandering. We sampled intact plants from Bend 2 (Fig. 8.7d, f) as well as woody debris forming a strandline

and found that the plants likely grew following high flows in 2015 (Table 8.1). The strandline had calibrated ages ranging over hundreds of years, implying the wood had been stored in the catchment before being transported downstream.
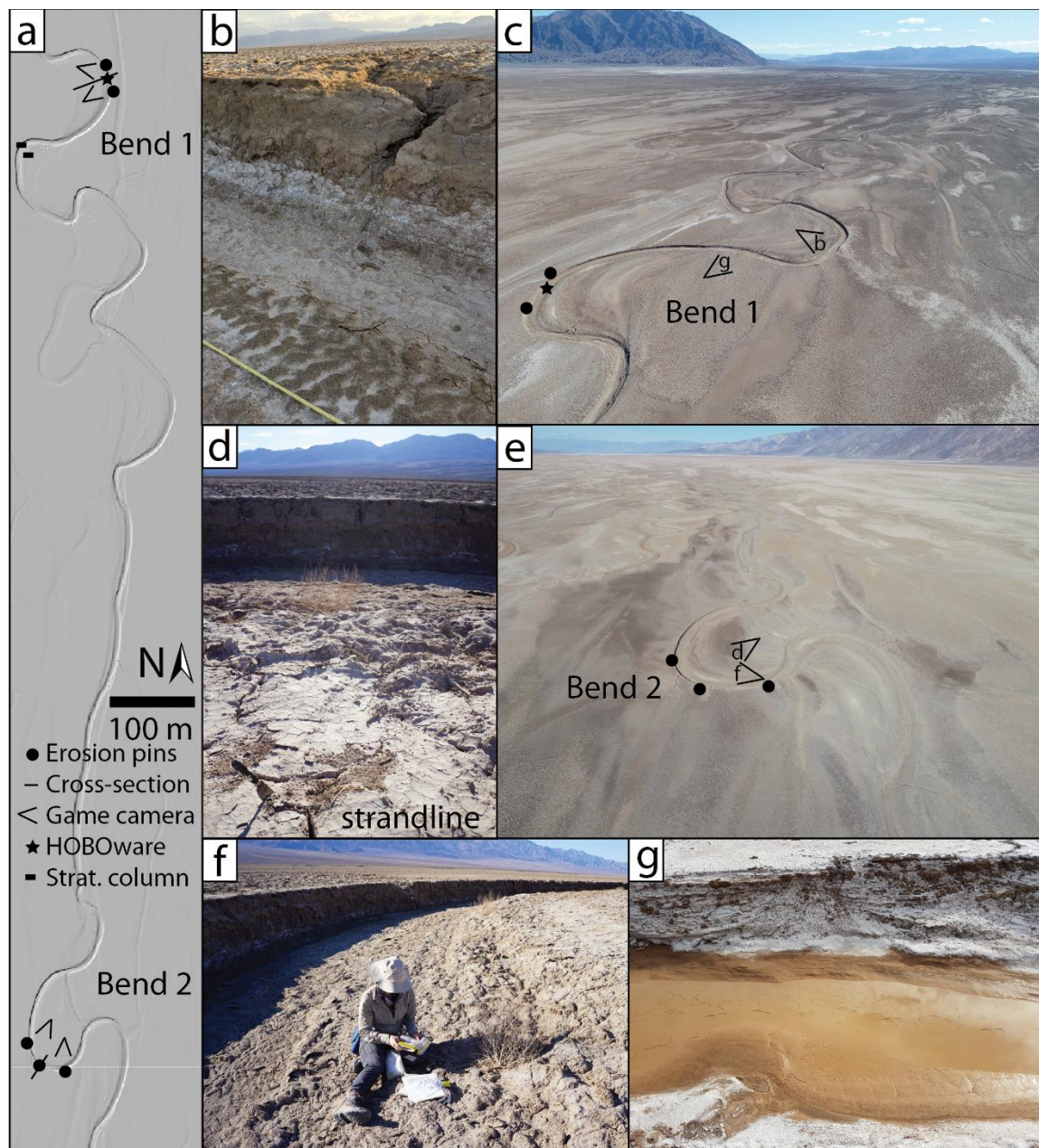
Figure 8.7: Overview of study bends along active reach of Amargosa River. **(a)** Lidar hillshade of study areas with measured cross-sections (thin line), HOBOware pressure and conductivity sensors (star), erosion pins (circles), game cameras (angle), and measured stratigraphic columns (rectangles) marked. **(b)** Photo of shallow channel draining from floodplain into channel and asymmetric ripples on the channel bed. **(c)** Aerial image of Bend 1 taken looking south (upstream). **(d)** Strandline of woody debris and dead vegetation on

point bar of Bend 2 that were sampled for radiocarbon dating. (**e**) Aerial image of Bend 2 looking to the north (downstream). (**f**) Sampling dead vegetation on point bar of Bend 2. (**g**) During our visit in January 2019, we observed footprints and mud cracks in a puddle of standing water left by the most recent flood (photo taken by Alex Beer).
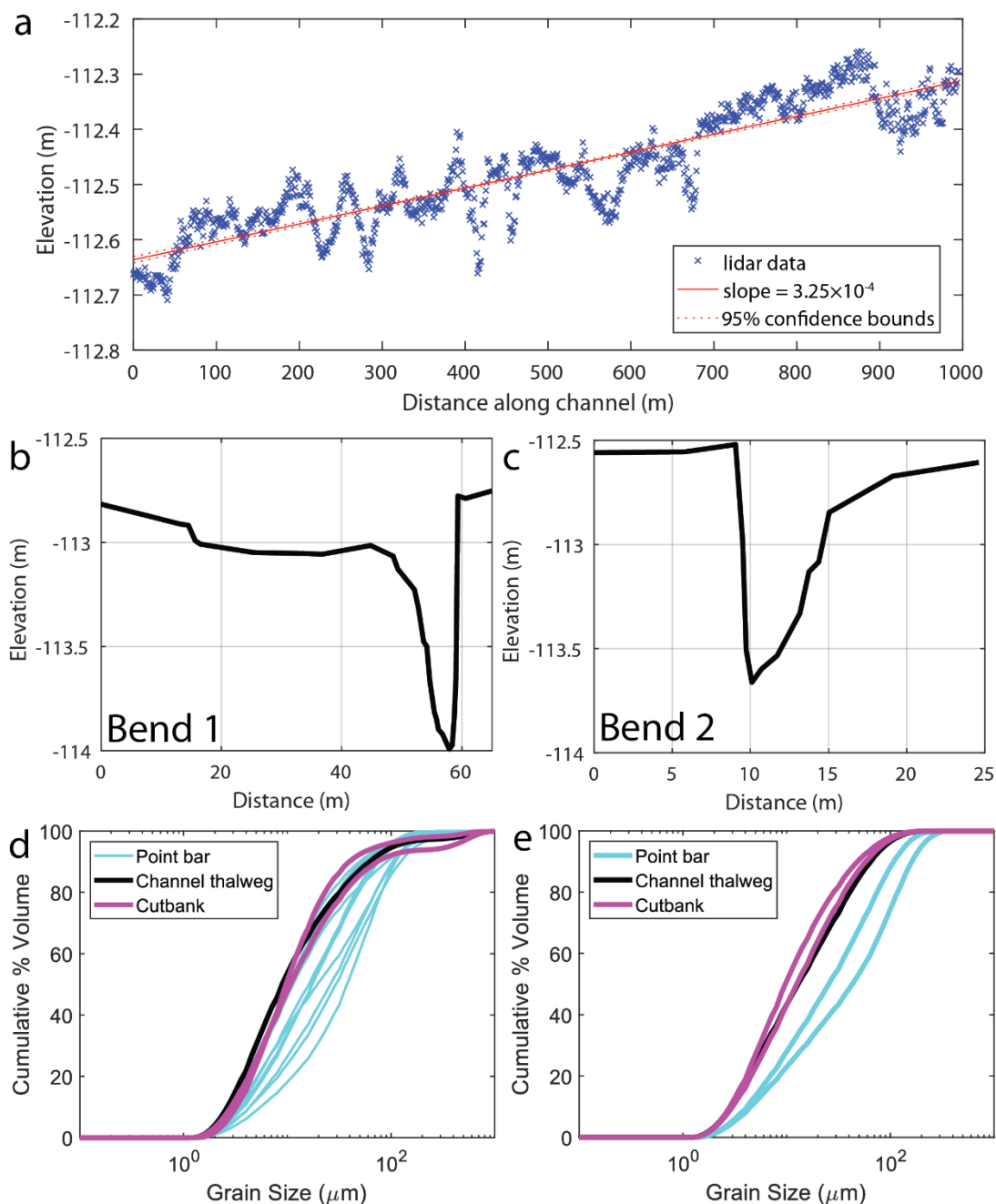
Figure 8.8: (**a**) Lidar elevation of channel centerline along the bends adjacent to Bend 1, from North to South bend in study reach, and the linear least-squares regression to calculate channel slope as a function of distance along the centerline (red dashed line). (**b**) Channel

cross section at Bend 1 surveyed using RTK GPS, 1SD measurement uncertainty (1 cm) within line thickness. **(c)** Cross-section of Bend 2 surveyed using RTK GPS, 1SD measurement uncertainty within line thickness. **(d)** Grain size measured using laser diffraction for 2 cutbank samples (magenta lines), 2 thalweg samples (black lines), and 11 point bar samples (thin blue lines) in Bend 1. **(e)** Grain size measured using laser diffraction for 2 cutbank samples (magenta lines), 1 thalweg sample (black line), and 2 point bar samples (blue lines) from Bend 2.

We observed contrasting stratigraphy on the channel cutbank and point bars (Fig. 8.9). The channels appear to be actively meandering, with clearly visible scroll bars as well as bedforms that migrate during each flow event, indicating active sediment transport (Fig. 8.9b). The cutbanks contain a mixture of silt and small deposits of cross-bedded very fine sand and are coated with a thick (~10 cm) salt crust, and we interpret them to be river floodplain deposits rather than sediment deposited by paleolake Manly. The channel point bars are primarily composed of ripple cross-stratified very fine sand, characteristic of active point bars in similar dryland river systems (Ielpi & Lapôtre, 2019). The channel bed and point bar had a surficial layer of crystallized salt but had not yet formed thick salt crusts like those present on the cutbank.
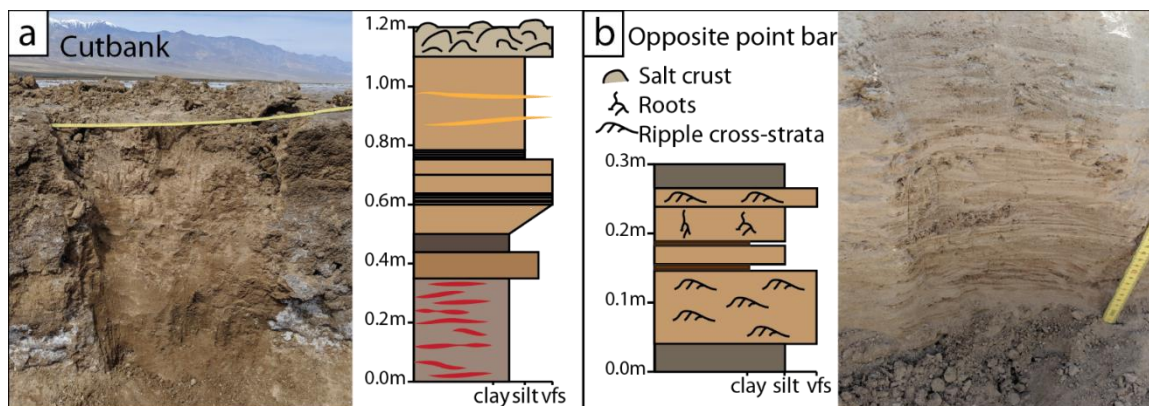
Figure 8.9: Field photographs of stratigraphic columns from cutbank **(a)** and point bar **(b).** Location of stratigraphic columns is marked on Fig. 8.7.

8.6.3 Observations from continuous monitoring

We set up HOBOware pressure and conductivity sensors as well as game cameras to record when the Amargosa flowed from November 2018 to March 2019, November 2019 to April 2020, and January 2021 to April 2021 (Fig. 8.10c). During these periods, we recorded three large flow events, all of which coincided with peaks in the discharge measurements for the Amargosa at Tecopa (Fig. 8.10). These flow events were poorly correlated with rainfall from Furnace Creek, potentially because these short localized thunderstorms did not source significant water to the Amargosa catchment. We calculated water discharge using Eq. (8.3) and shear velocity on the riverbank using Eq. (8.4)-(8.5) (Sect. 8.5.3). River discharge decreased between Tecopa and our study site by approximately a factor of five, either

because water infiltrates and evaporates as it flows downstream or a portion of flow is routed through other channels on the floor of Death Valley. We measured high water conductivity
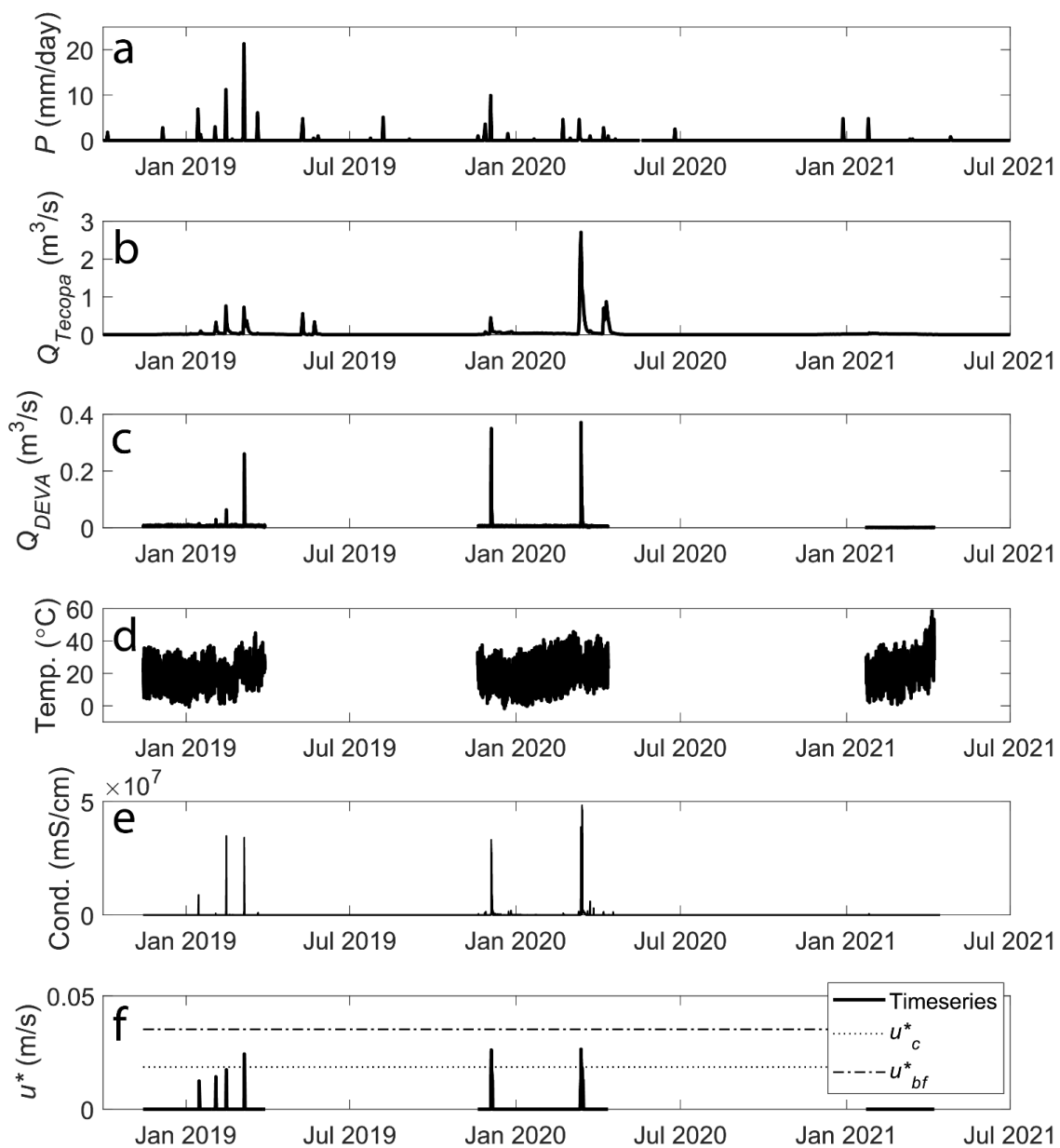
Figure 8.10: Timeseries of hydraulic measurements from November 2018 to July 2021. **(a)** Rain gage at Furnace Creek, CA. **(b)** Water discharge measured by USGS stream gage 10251300 in Tecopa, CA. **(c)** Water discharge calculated using Manning's equation and measured flow depths and cross-sectional geometry for our study reach. **(d)** Air temperature measured using HOBOware. **(e)** Fluid conductivity measured with at same location as stage height. **(f)** Fluid shear velocity timeseries on the channel banks at our study reach (solid line),

with critical shear velocity for entrainment determined from experiments ($u*_c$, dotted line) and the channel bankfull shear velocity ($u*_{bf}$, dashed line) shown for comparison.

that varied between and throughout floods (Fig. 8.10e). Calculated bank shear velocities increased with flow discharge at Bend 1 (Fig. 8.10f). Shear velocity increases sub-linearly with discharge because the channel widens as flow depth increases above the bed, so increasing water stage causes discharge (proportional to depth and width) to increase faster than bank shear stress, which is proportional to channel depth. Three flow events from our period of observation exceeded the bank erosion threshold calculated from experiments (see Sect. 8.6.4). All three events were far below bankfull conditions, which we did not observe during our monitoring period, but we did reconstruct a bankful event that occurred in 2022 (see Sect. 8.6.4).

The banks of the Amargosa are coated with a decimeter-scale thick of salt crusts which cover the underlying muddy sediment (Fig. 8.10a). However, the salt crusts appear to completely dissolve during flow events. At the bank toe, we observed erosion pins protruding through a layer of fine sediment with mud cracks but only a thin veneer of salt, indicating that the river was able to directly mobilize mud (Fig. 8.10b). During January 2020, we observed small amounts of flow in channels near our study reach, and saw that the salt crusts surrounding the channel had been dissolved (Fig. 8.10c). Our conductivity sensor measurements also support that salt is dissolved during flow events because water conductivity varied significantly within each flow event (Fig. 8.10d). We would expect conductivity to remain relatively constant if the water became saturated with salt and was not able to dissolve the crusts on its banks. From these lines of evidence, we infer that salt crusts fully dissolve during floods and do not supply the primary cohesive force to enable channel meandering.
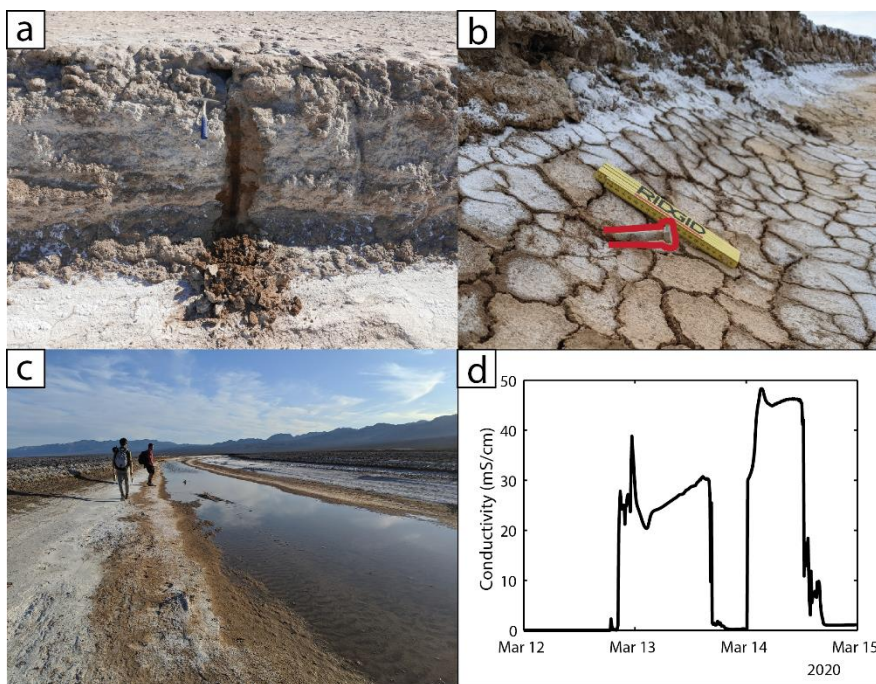
Figure 8.11: (a) Salt crusts on the river cutbank in Bend 1, with freshly exposed sediment appearing dark brown. **(b)** Erosion pin in Bend 1exposed by flow event sticking out of apron of mud cracks. **(c)** Water ponded in the channels dissolved the surrounding salt crusts. Photo taken along the channel where Manning's n was measured near measurement 36.1137°N, 116.8267°W. **(d)** Water conductivity (mS/cm) varied throughout a single flow event.
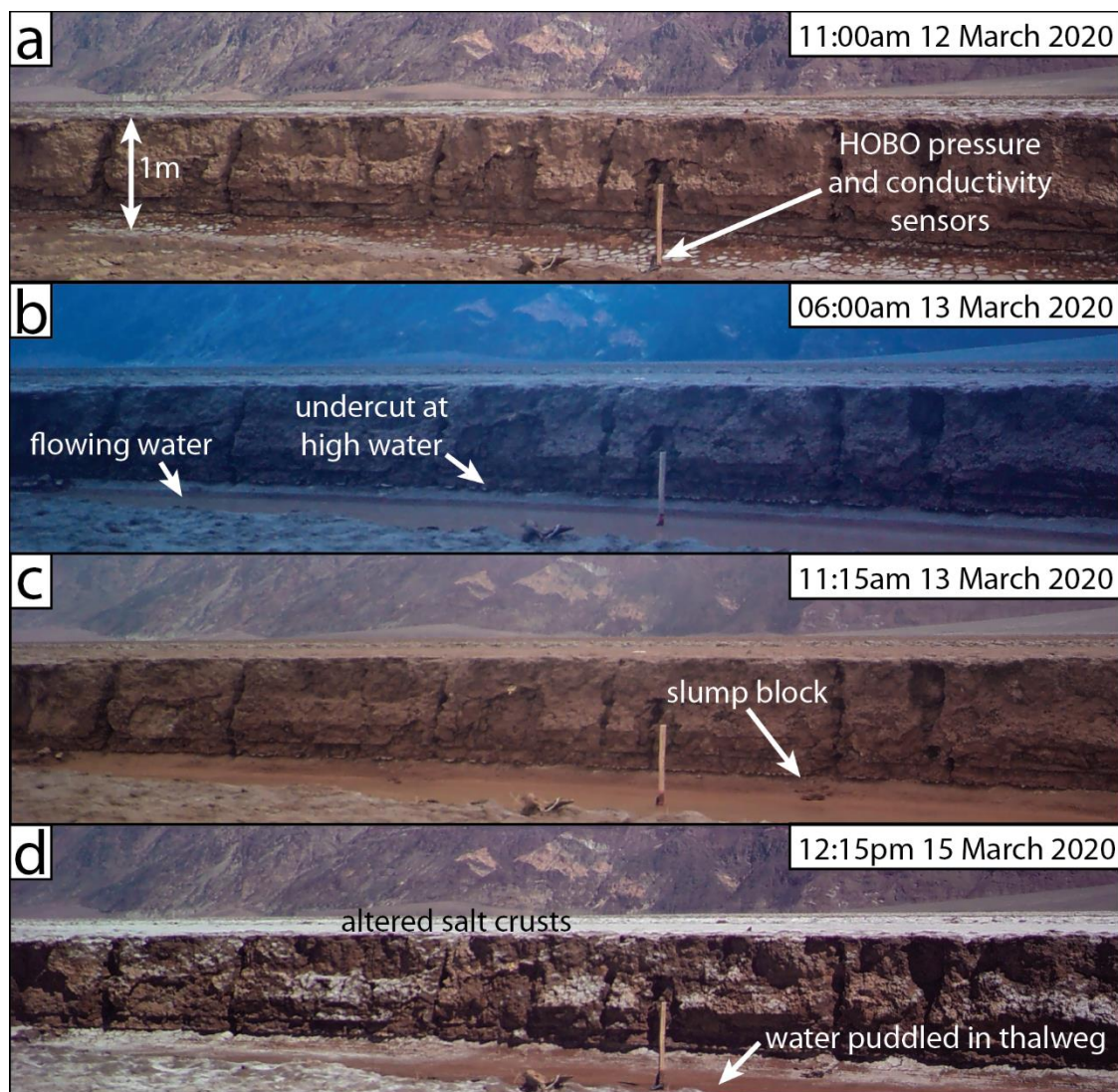
Figure 8.12: Game camera timelapse images of Bend 1 before **(a),** during **(b-c),** and after **(d)** a flood from March 13-15, 2020.

We directly measured cutbank erosion rates of 8-9 cm below the waterline and 0 cm above the waterline using erosion pins and attributed the erosion to the March 12-15 flood based on game camera footage (Fig. 8.12). The flood began overnight, with muddy water visible in the channel at dawn (Fig. 8.12b). As the water receded, we observed that it left a niche where salt crust dissolution and fluvial sediment entrainment had eroded the bank (Fig. 8.12c). We measured little erosion on the upper portions of the riverbank, though we

observed slump blocks with diameter ~10 cm failing in game camera timelapse footage (Supplemental Movie SM3). As the flood receded, water stagnated in the pool at the apex of the bend and surficial salt crusts re-crystalized in a pattern different from before the flood (Fig. 8.12a, d). From our erosion pin measurements, we concluded that sub-bankfull flows exceeded the threshold for bank toe sediment entrainment and could cause cutbank erosion.

8.6.4 Bankfull flood observations

A bankfull flood occurred in September 2022, which we captured using erosion pins, but we had ceased monitoring our study reach with game cameras and HOBO loggers (Fig. 8.13a). Lacking measurements from the HOBO pressure sensors, we determined that the maximum flow depth reached bankfull conditions from a strandline of woody debris present at the top of the cutbank and high on the point bar and slightly overhanging salt crusts extending immediately above the strandline (Fig. 8.13). The strandline provided a lower bound on the high water line and we expect that the overhanging salt crusts were not inundated, so these markers bracketed the maximum flood stage. This flood caused significant bank erosion, on average 18.5 cm from the 10 erosion pins, and completely eroded one 51-cm long erosion pin from the (Fig. 8.13c). Repeat RTK GPS cross-sectional surveys indicate that the river caused 7±3 cm (±1SD) of aggradation on the point bar and channel bed (Fig. 8.13b), supported by measurements of 7.5 cm deep mud cracks formed around plants buried by mud (Fig. 8.13d). Aggradation of the channel bed may account for lower erosion rates measured from erosion pins at the bank toe compared to higher on the cutbank (Table 8.S3).

Inundated portions of the floodplain were coated with a layer of bright white salt that highlighted places where the Amargosa overtopped its banks at Bends 1 and 2 (Fig. 8.13). While conditions were bankfull at the location where we previously installed our pressure sensor, we were able to track the maximum flow depth around each bend through variations in the height of the woody debris strandline. Banks were typically overhung with the strandline below bankfull when flow in the bend is directed downvalley. As the bends curved to flow across or up the valley, the strandline rose and series of overhangs ended until the strandline disappeared and white salt was visible extending from the channel onto the floodplain (Fig. 8.13f). One incipient avulsion formed just upstream of Bend 1 but narrowly avoided the bend. We hypothesize that if this avulsion intersected Bend 1 it would eventually form a neck cutoff, but since flow was not intercepted, this will eventually develop into an avulsion and abandon the river reach at Bend 1. Since the avulsion may be routed preferentially eastward by the tectonic tilting of the valley floor, this implies that active tectonics can promote channel avulsion over migration by impeding neck cutoff formation in lowland river systems.
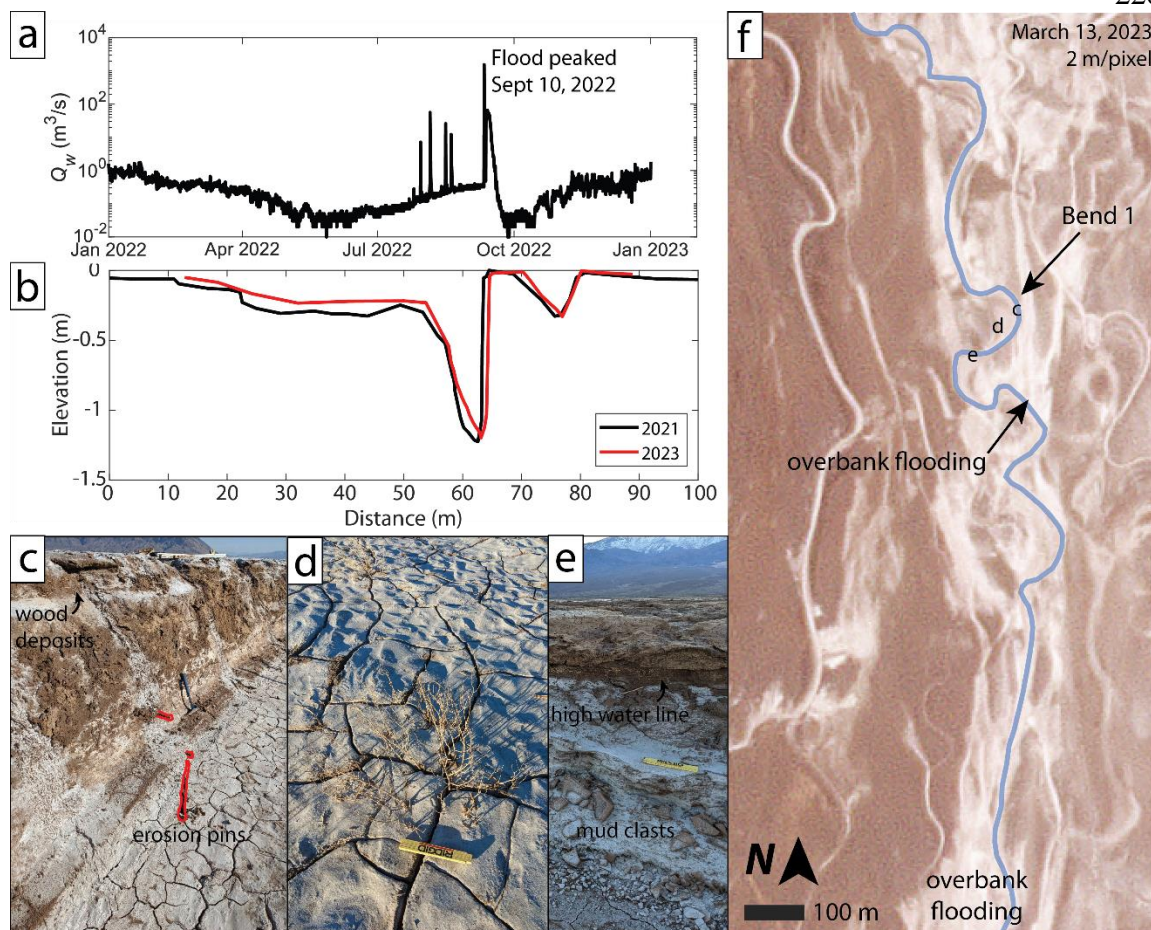
Figure 8.13: Field photos and remote observations following fall 2022 bankfull flood. **(a)** USGS gage at Tecopa records of 15-min average discharge for 2022. **(b)** RTK GPS measurements of channel cross-section at Bend 1 along the same transect from 2021 (black line) and 2023 (red line). **(c)** Erosion pins (outlined in red) and woody debris strandline at cutbank in Bend 1. **(d)** Plant buried by 7.5 cm of mud on point bar of Bend 1. **(e)** High water line marked by woody debris and mud clasts being eroded out of Bend 2. **(f)** Satellite imagery (2 m/pixel) taken by Planetlabs on March 13, 2023. The study reach is drawn in blue, and overbank deposits are visible as white salt deposits on the brown floodplain.

8.6.5 Experimental results

We analysed data from the entrainment and settling stages of the abrasion mill experiment to determine sediment entrainment rates. In the entrainment stages, the sediment concentration began to increase immediately after shear velocity was increased and stabilized to a steady-state value in <5 hours (Fig. 8.14a). Higher shear velocity caused a nonlinear increase in sediment concentration, and higher sediment concentrations took a longer time to stabilize at a constant value in time. For $u* = 0.0199$, the concentration curve becomes discretized as it approaches the resolution of the light sensor. In the settling stage, sediment concentration remains constant for a short period after we set $u* = 0$ m/s, then abruptly declines to less than 1 g/L, before slowly declining to 0 g/L after 2 hours (Fig. 8.14b). We

interpret this curve to mean that sediment settles as a uniform front, and the rapid decline occurs when the front passes the acrylic window where light shines through to the sensor. The subsequent slow decline is then any remaining fine sediment settling from the column which may have a very slow fall velocity.
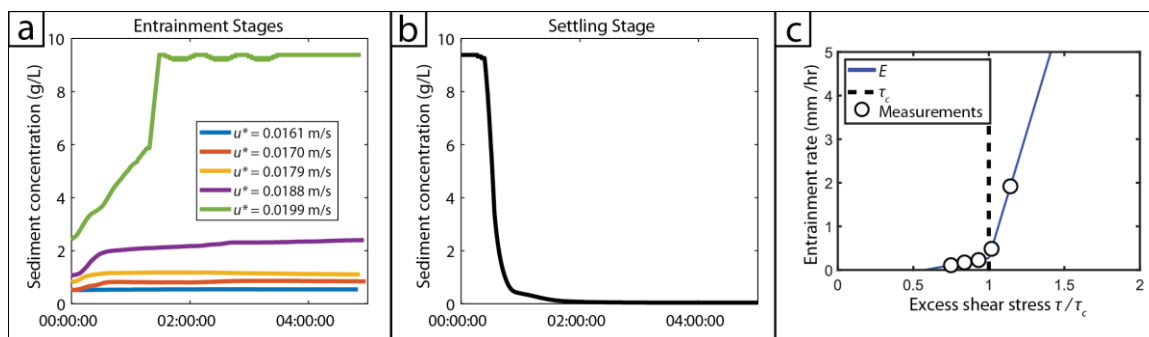
Figure 8.14: (a) Sediment concentration through time (hours) for each shear velocity (u^*; m/s) during the entrainment phase, smoothed using a 2-min moving mean filter. **(b)** Sediment concentration through time (hours) during the settling phase, smoothed using a 2-min moving mean filter. **(c)** Measured sediment entrainment rates as a function of shear stress (τ; Pa) divided by critical shear stress (τ_c; Pa) shown as white circles. We fit a piecewise function for entrainments rates as a function of fluid shear stress (Eq. 8.10, blue solid line) and calculated the threshold of entrainment (black dotted line) as their intersection.

The sediment concentration reflects a balance between sediment entrainment and settling velocity (Eq. 8.6). During the settling stage, no sediment is entrained so all changes in concentration reflect sediment settling out of suspension. We fit a linear regression to the period of rapid concentration decline during the settling stage and found $w_s = 1.51\times10^{-4}$ m/s, which corresponds to an effective siliciclastic grain diameter of 13.9 μm (Dietrich, 1982). For comparison, sediment siphoned from the final experimental interval had median grain size $D_{50} = 9.98$ μm, giving a predicted settling velocity of 7.39×10^{-5} m/s (Table 8.1). The actual settling velocity was approximately two times faster than the theoretical settling velocity, implying that some of the fine sediment in the mill may have been flocculated, as is expected for sediment in saline solutions (Mietta et al., 2009).

Table 8.1. Abrasion mill experimental parameters and grain sizes from siphoned samples at the end of each stage.

Sediment concentration (g/L)	Conductivity (mS/cm)	Suspended sediment D_{10} (μm)	Suspended sediment D_{50} (μm)	Suspended sediment D_{90} (μm)	RPM	Shear velocity (m/s)
Initial bed	-	0.832	8.608	35.659	0	0.000
0.75	30.4	0.643	4.901	19.747	124.5	0.016
1.05	29.7	0.433	4.386	20.312	152.1	0.017
0.69	30.6	0.664	5.890	23.198	177.9	0.018
2.45	31.6	0.717	5.676	22.668	199.5	0.019

9.38	33.0	0.557	5.058	21.867	227.8	0.020
Final bed	33.2	2.448	9.977	430.921	0.0	0.000

Next, we used experimental data to calculate sediment entrainment rates (Sect. 8.5.5) and calibrate an erosion relation for bank sediment in the meandering section of the Amargosa River. During the entrainment stages, sediment concentrations stabilized so that $\frac{\partial c_a}{\partial t} = 0$ and $E = w_s c_a$ (Eq. 8.7). Using w_s measured during the settling stage and the measured sediment concentration (c_a) at each u^* value, we calculate sediment entrainment rates (E). We assume that E is a linear function of excess shear stress (Partheniades, 1965). We observed some sediment entrainment at low shear velocities, and then a rapid increase in sediment entrainment past an apparent threshold shear velocity around ~0.018 m/s (Fig. 8.14c). Therefore, we used separate lines calculated for the nearly flat and steeply increasing portions of the sediment entrainment curve, such that

$$E = \begin{cases} 0 & \tau < 0.58\tau_c \\ 0.64\,\tau/\tau_c - 0.37 & 0.58\tau_c < \tau < \tau_c. \\ 11.5\,\tau/\tau_c - 11.23 & \tau \geq \tau_c \end{cases} \tag{8.10}$$

We identified the threshold shear velocity for significant entrainment as the intersection of these two lines, which occurs at $u^*_c = 0.0186$ m/s. We set the entrainment function to zero for $\tau < 0.58\tau_c$ to avoid unphysical negative entrainment rates. The non-zero entrainment rate for $0.58\tau_c < \tau < \tau_c$ is likely due to small mud aggregates produced by minor surface disturbance or incompletely settled or compacted grains. Similar low values of entrainment below a threshold value were observed in the experiments of Partheniades (1965).

8.7 Analysis

8.7.1 Comparing laboratory and field measurements

We compared the experimental model for bank erosion to field measurements of erosion rate and surveys of channel bankfull geometry (Fig. 8.15a). We applied our experimental sediment entrainment rate (Eq. 8.10) to the floods that occurred when we had recordings for river stage. We set $u_{bank}^* = 0$ for cases when the fluid shear velocity (calculated using Eq. (8.4) and (8.5)) is below u^*_c or the water depth is shallower than the height of the erosion pins above the bed. We used these water stage measurements and surveyed channel cross-sectional geometries and slopes to evaluate Eq. (8.2)-(8.4) and calculate near-bank fluid shear velocities throughout the floods (Fig. 8.15a). Modelled entrainment from two discrete floods agreed with erosion pin measurements over the same interval (Fig. 8.15b), indicating that our laboratory calibration of bank toe sediment entrainment produces accurate bank erosion rates under field conditions.

Since the HOBOware pressure sensors were not deployed during the bankfull flood in 2022, we do not have measurements of the local flood hydrograph and were not able to compare our modelled versus observed erosion rates through the complete hydrograph. However, we can use flood stage markers, such as strandlines and overhangs, to determine the peak flood

stage and estimate bankfull shear velocities. We found that bankfull flows have $u^*_{bf} = 0.0352$ m/s, above the threshold of significant mud erosion by a factor of 1.6, with predicted bankfull erosion rates of 7.3 mm/hr (Fig. 8.4f). During the bankfull flood, we observed a maximum of over 51 cm of erosion for one pin located 20 cm below the top of the cutbank. This implies that the river flowed near bankfull conditions for approximately 70 hours to erode this pin from the bank, or else that this upper portion of bank collapsed in a slump block during the flood. Excluding this maximum erosion measurement, the erosion pins recorded a mean erosion of 18.2 cm during the bankfull flood. This is consistent with less than 25 hours at bankfull conditions, and supports the hypothesis that the >51 cm of erosion occurred due to block failure and not direct fluvial entrainment. Therefore, we expect that our study reach experienced bankfull flow in fall 2022 lasting less than 1 day.
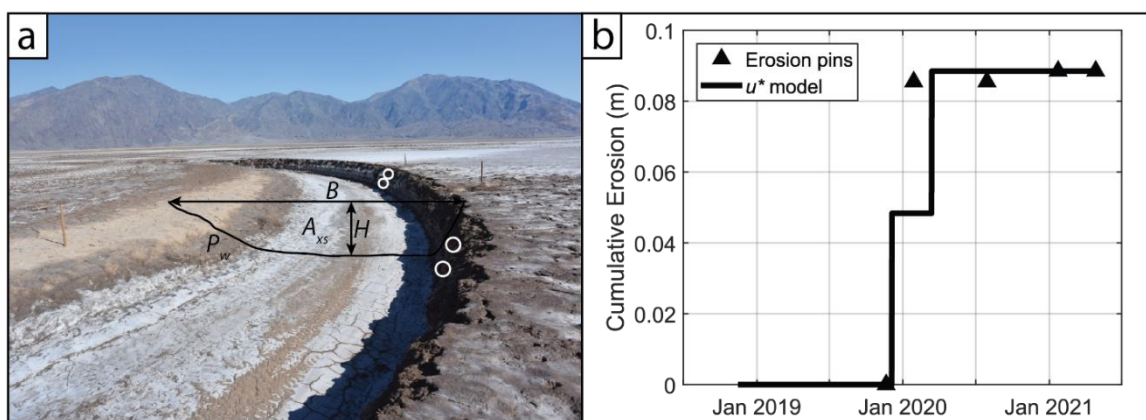
Figure 8.15: (a) Photo of Bend 2 cross-sectional geometry, with erosion pins circled in white. We used RTK GPS surveys to measure bankfull top-width B, maximum depth H, wetted perimeter P_w, and cross-sectional area A_{xs}. **(b)** Erosion pin measurements (black triangles) and cumulative bank erosion (black line) calculated using entrainment fluxes derived from mill experiments.

8.7.2 River migration over decadal timescales

In this section, we conduct analysis on remote sensing imagery and long-term precipitation and stream gage records to understand the Amargosa's evolution over decadal timescales. First, we scale the peak water discharge observed at the USGS Tecopa gage to our field observations and predict bank erosion rates along our study reach using our calibrated experimental model (Eq. 8.10). Then, we compare our predicted channel migration rates with satellite and aerial images of the channel to determine its behavior over time. Finally, we compare the Amargosa's flood frequency distribution with our bank erosion function to evaluate the flood magnitude responsible for most geomorphic work from bank erosion along sinuous reaches of the Amargosa.

To determine bank erosion rates along our study reach over decadal timescales, we develop a scaling relation between peak water discharge at the Tecopa stream gage (Q_{Tecopa}; m^3/s) and our study site (Q_{DEVA}; m^3/s). We were not able to establish a consistent time lag between high flow at the Tecopa gage and our study reach, so we developed a relation to correlate the

magnitude of peak discharge at each site. We assume that water discharge at each location follows a power-law relation with drainage area, as is typical for alluvial river systems (Luna Bergere Leopold et al., 1964).

$$Q_{DEVA} = K_{DEVA}A_{DEVA}^m \tag{8.11a}$$
$$Q_{Tecopa} = K_{Tecopa}A_{Tecopa}^n \tag{8.11b}$$

Here, A_{DEVA} (m^2) is the drainage area at our study site in Death Valley and K_{DEVA} (m/s) and m are empirical constants. Similarly, A_{Tecopa} (m^2) is the drainage area and K_{Tecopa} (m/s) and n are empirical constants for the USGS gage in Tecopa. We assume that water discharge at each site follows a similar power law scaling with drainage area, such that $K_{DEVA} = K_{Tecopa}$ and $m = n$. Dividing Eq. (8.11a) by Eq. (8.11b) yields:

$$Q_{DEVA} = Q_{Tecopa}\left(\frac{A_{DEVA}}{A_{Tecopa}}\right)^m. \tag{8.12}$$

Since the ratio of drainage area between our field site and Tecopa should be relatively constant over decadal timescales, Eq. (8.12) yields a linear relationship between Q_{DEVA} and Q_{Tecopa}.

We calculate the relative discharges at Tecopa and our monitoring site using the flow depths of the three main floods we observed, plus the ^{14}C dates from woody debris in the strandline. The radiocarbon dates match well with a large flood that occurred in 2017, indicating the maximum flow depth for this event (Table 8.2). Using these constraints, we calculate a ratio between the water discharge at Tecopa and our observation site (Fig. 8.16b).

Table 8.2. Radiocarbon dating results and conversion to calendar ages. The calendar date is reported for the most probable date calculated using 1SD of uncertainty on the measured fraction modern as well as the goodness of fit for all calibrated dates with >1% probability

Sample name	Fraction modern (Fm)	Date (AD)	Fitted dates (% probability)
DEVA-Plant1	1.0162±0.0021	2015 – 2018	2016.82 - 2018.11 (85.1%), 2018.54 - 2018.70 (9.0%), 2016.24 - 2016.32 (4.3%), 1955.45 - 1955.48 (1.6%)
DEVA-Plant2	1.0184±0.0022	2015 – 2018	2016.06 - 2017.01 (64.3%), 2017.43 - 2018.05 (24.8%), 1955.46 - 1955.66 (10.9%)
DEVA-Plant3	1.0156±0.0025	2015 – 2018	1989.88 - 1990.29 (76.4%), 2018.49 - 2018.77 (15.7%), 1955.39 - 1955.50 (5.3%)
DEVA-Strandline1	1.1596±0.0022	1989 – 1990	1989.88 - 1990.29 (76.4%), 1958.64 - 1958.84 (23.6%)
DEVA-Strandline2	0.9762±0.0020	1664 – 1668	1763.73 - 1785.21 (35.7%), 1663.78 - 1679.02 (24.8%), 1740.98 - 1751.68 (16.4%), 1794.09 - 1799.00 (8.6%), 1944.67 - 1949.60

			(7.3%), 1942.21 - 1944.29 (3.1%), 1950.03 - 1951.79 (2.4%), 1952.28 - 1953.07 (1.2%)
DEVA-Strandline3	1.3811±0.0027	1974 – 1975	1975.07 - 1975.30 (72.0%), 1975.80 - 1975.88 (20.5%), 1962.40 - 1962.43 (7.5%)

To understand which flood magnitude plays the most significant role in shaping the lower Amargosa River network, we calculate the bank erosion accomplished by each flood magnitude. First, we use peak annual discharge at Tecopa to calculate recurrence interval of observed and bankfull floods (Fig. 8.16a). The frequency of each flood (f; 1/yr) is calculated as the inverse of recurrence interval ($f = 1/RI$). Then, we multiply the event frequency distribution by the bank erosion rate at that discharge (E; mm/s) to calculate bank erosion potential (β; cm/min/yr):

$$\beta = \frac{E}{RI}. \tag{8.13}$$

Since the floodplain is very wide, we set all bank erosion potential for $H > H_{bf}$ equal to β_{bf}. We find that the highest bank erosion potential occurs at approximately 2/3 of bankfull discharge but that one flood magnitude does not dominate bank erosion in the system (Fig. 8.16c).
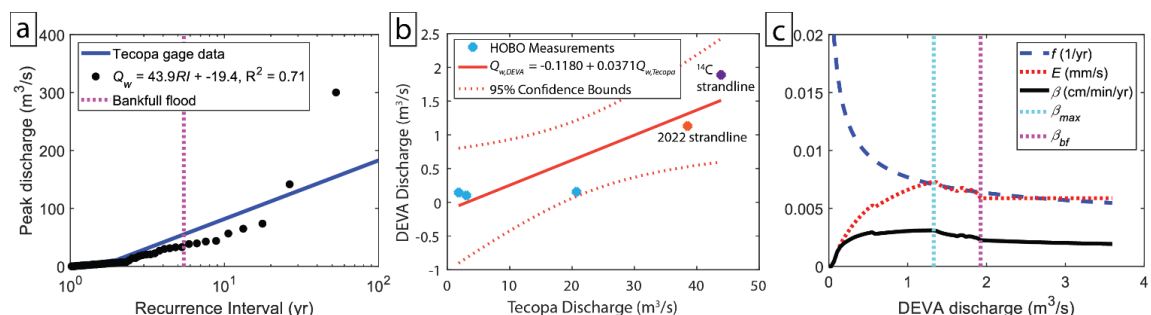
Figure 8.16: Comparison of our measurements with the long-term USGS stream gage record at Tecopa, CA to evaluate the frequency and amount of bank erosion caused by different flood magnitudes. **(a)** We fit a semi-logarithmic relation (blue line) between peak annual discharge and recurrence interval (RI) for the USGS gage (black circles) to calculate an event frequency model as 1/RI. The recurrence interval for a bankfull flood (5.45 years) is shown as a magenta dashed line. **(b)** Combining our discharge measurements from the pressure sensor (blue diamonds) with ^{14}C dating of woody debris in a channel strandline (orange diamond) and the 2022 flood strandline (purple diamond), we found a linear relationship (red line, 95% CI in dashed lines) between discharge at Tecopa and our monitoring site. **(c)** We multiplied the flood frequency (f; blue dashed line) by the function for bank erosion calculated from excess shear stress (E; red dashed line) to calculate the bank erosion potential that occurs in Death Valley (β; solid black line). The discharge which accomplishes most bank erosion (β_{max}) is shown as a dashed teal line and the bank erosion potential for a bankfull flood (β_{bf}) is shown by the magenta dashed line.

8.7.3 River depositional stratigraphy

To quantify the relative importance of channel lateral migration versus avulsion for the lower Amargosa, we calculate the channel mobility number (M) (Jerolmack & Mohrig, 2007). Substituting aggradation rates of $v_a = 7.7 \times 10^{-4}$ m/yr from the Badwater core (Lowenstein et al., 1999), a channel migration rate of $v_c = 0.05$ m/yr from erosion pins, and RTK GPS survey measurements of $H_{avg} = 0.38$ m and $B = 6.86$ m into Eq. (8.1) produces $M = 0.36$. The channel mobility number is defined so that river systems with $M > 1$ laterally migrate to re-surface their floodplain, while rivers with $M < 1$ form many branches with lower sinuosity and avulse frequently to maintain floodplain aggradation rates. Our calculation indicates that even the highest sinuosity and most rapidly migrating channels of the Amargosa cannot keep up with valley aggradation rates, so avulsion must dominate re-working of the floodplain.

A low channel mobility indicating frequent avulsions matches field and remote sensing observations of Death Valley. Lidar reveals abundant evidence of floodplain channel avulsion, infilling, re-occupation, and incision (Fig. 8.7). We observe that avulsions appear to occur preferentially to the eastern side of the valley, possibly due to higher tectonic subsidence rates on the eastern bounding fault (Hooke, 1972). Meandering must not be the dominant mechanism for floodplain resurfacing, because there are few visible cutoff bends in abandoned channels in the floodplain, implying that the river tends to avulse before it becomes too sinuous and cuts off. Evidence from hand auger cores support this interpretation, with sandy deposits ~1 m thick suspended in mud (Hooke, 1972). We interpret the auger stratigraphy to represent channel bodies, constructed as point bars and isolated by avulsion, suspended in a matrix of fine floodplain material. This coincides with the upper strata of the Badwater Basin core, which previous investigators interpreted as "mud flats" distinct from underlying Lake Manly deposits (Ku et al., 1998; Lowenstein et al., 1999). Therefore, plants are not needed to develop a stratigraphic architecture of channel-belt sandstones isolated within a mudstone matrix.

We speculate that rare bankfull floods may trigger avulsions across the floodplain and be a primary shaper of channel network topology, while sub-bankfull channels cause meandering. Potentially, the river rapidly erodes and carves new channels into the floodplain when it overtops its banks. Otherwise, our results indicate that channel banks are eroded very slowly, producing noticeable migration over decades that is insufficient to re-surface the floodplain. We also speculate that the Amargosa may experience discharge from rainfall sources locally from the floodplain that drains in channels, resulting in the abundant headward-migrating channels. These channels may also re-direct water outwards onto the floodplain during periods of high flow, lowering the threshold for avulsion to below bankfull flood stage.

8.8 Discussion

The lower Amargosa River is a modern example of a meandering river with a muddy, self-formed, largely unvegetated floodplain. There are very few plants growing on floodplain, and those present are on point bar or non-migrating active channels, and seldom grow on cutbanks. We observed very few plant roots in the floodplain stratigraphy, so this cannot be

a significant source of bank cohesion. However, our results support that the Amargosa is meandering despite its lack of plants, and not simply incising into paleolake deposits. We observed point bars with lateral accretion surfaces that contain ripple cross-strata and have active ripples migrating across their surfaces, indicating that point bars grow as the bends migrate. Ripple cross-strata are also visible in cutbanks, indicating that meanders are eroding into fluvial deposits, and not lake sediment deposited by Lake Manly. We observed cutbank erosion via collapse of subaerial slump blocks (on game camera timelapse) and direct fluid mobilization (from erosion pins), as well as 7 cm of mud deposition on the channel bed and point bars during a single flood event. We also see evidence for migration sufficient to form cutoffs and oxbow lakes, which are apparent in lidar imagery. Our results agree with previous cores taken in Badwater Basin, which indicate over 7.7 m of aggradation (~7 channel depths) since Lake Manly dried up, implying significant fluvial sediment deposition.

Our field and experimental results support that mud, and not salt, supplies the bank strength controlling the rate of lateral cutbank erosion. We found that water conductivity changed throughout a single flood event, implying that the river water did not reach salt saturation during floods. In channels where we observed flowing water, all salt crusts had been dissolved from the submerged channel bed and banks (Fig. 8.12c). We also observed pooled, stagnant water that remained from a flood in Bend 1 that had dissolved salt crusts on the bank and beds but left footprints and mud cracks intact (Fig. 8.8g). During our field site visit in March 2023, the salt crusts across the floodplain had completely dissolved and instead of 10-cm scale bumps and flakes the ground was entirely smooth with only a thin veneer of precipitated salt. Salt crusts might decrease the impact of small or short floods, which would not have time to dissolve all of the salt and erode underlying mud, but our results indicate that salt crusts do not significantly inhibit fluvial erosion. Instead, mud and cohesive sediment set the rate of cutbank erosion. Our experiments calculating mud entrainment accurately reproduce observed erosion pin rates. We also observed deposits of mud rip-up clasts that had been transported as bedload in the river, implying that cohesive mud limits erosion of channel bed and banks (Fig. 8.13c).

Our observed rates of channel migration were much slower than those reported in Ielpi (Ielpi, 2018). We recorded negligible erosion (<2 cm) over 3 years of observations and a maximum of 30.5 cm from the 2022 bankfull flood in our Bend 2, which was previously reported to migrate at 1.5 m/yr. The shear stresses required to produce erosion rates greater than 1 m/yr require a 5-year flood event to instead occur 3 times per year, which is not supported by historical records and observations. However, we observed annual changes to patterns of salt crusts and sedimentary bedforms, which would be readily visible in satellite imagery. We hypothesize that the change detection method used by Ielpi (2018) might erroneously register changes in the salt crusts as channel migration. In addition, slight issues in orthorectification of images (for Landsat, by 1 pixel) could lead to errors of 30 m over the Landsat record (1978-present), producing rates of ~1 m/yr. Our results imply that meander migration rates obtained using similar methods (e.g., Ielpi and Lapôtre, 2020) should be scrutinized to ensure accurate orthorectification and bank tracking.

Slow channel migration rates were supported by experimental results on bank sediment entrainment rates. Our experimental setup shows promise as a means of directly constraining erosion rates for cohesive riverbanks. Although we only examine one sample under a range of shear velocities, and floodplain stratigraphy is heterogeneous, the technique is encouraging because it matches direct measurements made using erosion pins and remote sensing. We found $u*_c = 0.0186$ m/s, corresponding to $\tau_c = 0.35$ Pa, within the range of values commonly reported for cohesive sediment, where 0.1 Pa $< \tau_c <$ 5 Pa (Winterwerp et al., 2012). For the coefficient for Eq. (8.10) (Partheniades, 1965), we found $\gamma = 3.19 \times 10^{-6}$ m/s. That is on the upper range of reported values, which span 6×10^{-9} m/s $< \gamma < 3 \times 10^{-7}$ m/s assuming a sediment bulk density of 1800 kg/m^3 (Winterwerp et al., 2012). Since other muddy channel banks are expected to have similar thresholds and rates of erosion, we speculate that slow migration rates may be present in other muddy environments, including drylands and estuaries.

We found that the Amargosa forms a channel cross-sectional geometry where bankfull flows exceed the threshold of erosion of the bank material. Bankfull flow occurred at 0.42 m average flow depth and 1.9 m^3/s water discharge, exerting approximately 1.6 times the critical shear stress to erode bank sediment, so sub-bankfull floods may shape the river system. Threshold channel theory posits that the critical stress to erode the toe of the riverbank sets the bankfull hydraulic geometry (Dunne & Jerolmack, 2020). Our analysis agrees within a factor of two, but the Amargosa exerts stresses much greater than the threshold for sediment entrainment during bankfull flows owing to the non-linear entrainment law. Wolman and Miller (1960) found that dryland rivers have hydraulic geometries such that bankfull floods occur less frequently than rivers in wetter climates. We concur with their assessment, since bankfull flows have a recurrence interval of 5.5 years but their recurrence interval for exceeding the threshold of sediment transport is similar to threshold channels (approximately every 2 years). Our study reach also aggraded 5-10% of its channel depth during the bankfull flood, so it may be out of equilibrium with its threshold state and slowly aggrading to the point where bankfull flows occur more frequently and the channel sits closer to a threshold geometry. However, the combination of tectonic tilting, net basin aggradation, and the ephemeral nature of the Amargosa may cause the channel to be out of equilibrium with its threshold geometry.

The Amargosa constructs its floodplain predominantly out of mud despite lacking vegetation, implying that processes not dependent on vegetation cause mud deposition and prevent its re-erosion. Death Valley is an endorheic basin, so all sediment must be deposited in the lower reaches of the Amargosa, and mud must end up in the floodplain deposits. Salt crusts may prevent this fine sediment from being eroded by wind between flood events, based on our observations that no sediment on the floodplain was mobilized by sustained 40 km/h winds except where salt crusts were broken or disrupted. In addition, trace organics may contribute to mud flocculation, increasing the settling velocity of sediment and promoting mud deposition across the floodplain (Nghiem et al., 2022; Zeichner et al., 2021). We observed abundant woody debris on the floodplain, including the strandline we sampled for radiocarbon dates, and the presence of upstream vegetation may indirectly affect sediment

dynamics along the unvegetated reaches of the Amargosa. We also infer the presence of algae and microbial communities living on the floodplain from the production of foam on the flowing river visible in game camera timelapses, which may influence sediment transport (see Supplemental Movie SM1). Flocculation can also be enhanced by high salinity, and we observed flocs in our experiments and in reaches of the channel with water (see Supplemental Movie SM2).

Our study of the Amargosa implies that single-threaded alluvial, meandering rivers can construct muddy floodplains without plants. Therefore, while the Amargosa provides a potential analog for environments on early Earth, its tectonically active location may make similar river systems less likely to be preserved in Earth's rock record. The Amargosa has a significantly different patterns of intermittency and bank erosion than vegetated rivers, with flows below bankfull accomplishing most riverbank erosion. This implies that much bank erosion on other unvegetated meandering rivers on Mars or early Earth may have been accomplished at sub-bankfull flows, potentially revising downward the amount of liquid water required to produce these deposits. The stratigraphic architecture produced by the Amargosa is also reminiscent of likely Martian inverted channels, where very narrow channel belts are preserved but the majority of floodplain sediment was highly erodible (presumably mud) and has been removed by wind.

8.9 Conclusions

We studied the Amargosa River on the floor of Death Valley and found that is actively meandering very slowly in Death Valley without plants on its cutbank. Stratigraphic evidence from point bar trenches, cut bank stratigraphic sections, and previously published cores indicate that the Amargosa is migrating through its own fluvial deposits, and not lacustrine deposits from Paleolake Manly. We used multiple years of field monitoring and remote sensing imagery to understand the processes and rates of riverbank erosion, and found that the most sinuous channel reaches migrate at ~5 cm/yr. We developed an experimental setup to calibrate a relation for bank erosion as a function of excess shear stress on cohesive mud that matched field observations well. We found that bank cohesion limiting fluvial erosion is provided by mud and not salt, which dissolves fully during flow events. Then, we developed a relation between discharge along our study reach and at the USGS gage in Tecopa and combined our observed floods with radiocarbon ages of sparse vegetation and observations of a bankfull flood strandline to determine the decadal-scale flood frequency and erosion rates. Despite localized meandering to form cutoffs, the Amargosa primarily re-surfaces its floodplain via avulsion and not lateral migration. This is because Death Valley is rapidly subsiding along its bounding faults and migration rates are insufficient to re-surface the floodplain, so the river primarily fills this accommodation space by avulsion, in the process forming a stratigraphic architecture with sandy lateral accretion sets isolated in a mud matrix.

8.10 Acknowledgements

8.11 Supplemental Materials

Supplemental Movie SM1. Flocculated sediment transported in a shallow flow in the lower Amargosa floodplain. A strong (~25 mph) wind blows left to right (upstream) across the movie, and transports floating clumps of sediment rapidly across the water surface. Deeper in the water, larger flocculated particles are visible rolling in the opposite direction, from left to right (downstream).

Supplemental Movie SM2. River water flows left to right (downstream) across the video, transporting thin mats of floating sediment.

Supplemental Movie SM3. Five-minute timelapse of a single river flow event from March 12-15, 2020 along the main study bend. The flood begins after dusk on March 12th and before dawn on the 13th, so its start is not recorded. Active erosion is observed as a slump block falls on March 13th as flow recedes. The channel appears to be brown and muddy when water flows through it, indicating that salt crusts are likely dissolved during floods. This flood is characteristic of flow events at our monitoring site along the lower Amargosa.

Table 8.S1. Channel cross-section measurements from March 3, 2023 used to calculate Manning's n.

Distance across channel (m)	Flow depth (m)
0.00	0.00
0.20	0.09
0.50	0.11
0.70	0.10
1.10	0.09
1.40	0.11
1.70	0.02
1.79	0.00

Table 8.S2. RTK cross-sections and channel slope survey measurements (UTM 11N, NAD83).

Point ID	Easting (m)	Northing (m)	Elevation (m)	Horizontal standard deviation (m)	Vertical standard deviation (m)
LongPro file1	399662 9.187	516595. 033	- 114.021	0.004	0.001
LongPro file2	399660 2.285	516663. 148	- 113.977	0.007	0.002
LongPro file3	399653 1.559	516606. 935	- 114.001	0.013	0.002
LongPro file4	399651 1.877	516553. 779	- 113.973	0.004	0.002
LongPro file5	399645 5.925	516621. 357	- 113.878	0.003	0.002
LongPro file6	399644 5.643	516677. 811	- 113.887	0.005	0.002
LongPro file7	399635 3.236	516659. 44	- 113.878	0.005	0.002
LongPro file8	399631 4.859	516656. 324	- 113.797	0.008	0.002
LongPro file9	399621 5.926	516736. 539	- 113.726	0.004	0.002
LongPro file10	399615 5.708	516686. 913	- 113.826	0.003	0.002
LongPro file11	399613 9.611	516667. 262	- 113.799	0.004	0.002
LongPro file12	399607 9.113	516685. 296	- 113.742	0.003	0.003
LongPro file13	399597 5.129	516671. 913	- 113.701	0.004	0.002
LongPro file14	399584 2.965	516636. 612	- 113.658	0.003	0.002
LongPro file15	399573 7.126	516621. 752	- 113.550	0.005	0.002
LongPro file16	399564 9.199	516624. 718	- 113.660	0.007	0.002
LongPro file17	399563 7.279	516638. 475	- 113.628	0.008	0.002
LongPro file18	399561 8.361	516651. 836	- 113.542	0.006	0.002
Bend1X S1	399658 8.466	516607. 107	- 112.816	0.005	0.003
Bend1X S2	399659 0.477	516614. 375	-112.87	0.012	0.006

Bend1X S3	399659 1.868	516619. 785	- 112.911	0.029	0.007
Bend1X S4	399659 2.193	516621. 138	- 112.917	0.008	0.003
Bend1X S5	399659 2.516	516622. 222	- 112.991	0.01	0.005
Bend1X S6	399659 2.695	516623. 1	- 113.008	0.016	0.004
Bend1X S7	399659 4.873	516631. 67	- 113.048	0.028	0.004
Bend1X S8	399659 7.078	516640. 333	- 113.053	0.02	0.002
Bend1X S9	399659 7.697	516642. 739	- 113.056	0.026	0.009
Bend1X S10	399659 9.857	516650. 462	- 113.014	0.004	0.003
Bend1X S11	399660 0.76	516654. 099	- 113.065	0.02	0.004
Bend1X S12	399660 0.936	516654. 852	- 113.127	0.04	0.003
Bend1X S13	399660 1.576	516657. 548	- 113.226	0.013	0.002
Bend1X S14	399660 1.969	516658. 068	- 113.312	0.007	0.012
Bend1X S15	399660 1.844	516658. 935	- 113.476	0.03	0.003
Bend1X S16	399660 2.119	516659. 389	- 113.499	0.017	0.002
Bend1X S17	399660 2.255	516659. 863	- 113.663	0.016	0.003
Bend1X S18	399660 2.208	516660. 625	- 113.815	0.027	0.002
Bend1X S19	399660 2.417	516660. 908	- 113.847	0.016	0.002
Bend1X S20	399660 2.483	516661. 219	- 113.897	0.02	0.002
Bend1X S21	399660 2.715	516661. 877	- 113.921	0.01	0.002
Bend1X S22	399660 2.818	516662. 982	- 113.992	0.014	0.004
Bend1X S23	399660 2.877	516663. 477	- 113.973	0.005	0.002
Bend1X S24	399660 2.79	516663. 79	- 113.844	0.009	0.003

Bend1X S25	399660 2.796	516664. 081	- 113.652	0.009	0.003
Bend1X S26	399660 3.048	516664. 282	- 112.776	0.009	0.003
Bend1X S27	399660 3.711	516665. 374	- 112.788	0.007	0.001
Bend2X S1	399544 4.430	516592. 488	- 112.447	0.001	0.001
Bend2X S2	399544 5.433	516592. 727	- 112.417	0.001	0.001
Bend2X S3	399544 5.726	516592. 770	- 112.600	0.001	0.001
Bend2X S4	399544 6.016	516592. 822	- 112.878	0.001	0.001
Bend2X S5	399544 6.141	516593. 137	- 113.417	0.001	0.001
Bend2X S6	399544 6.289	516593. 223	- 113.506	0.001	0.001
Bend2X S7	399544 6.550	516593. 264	- 113.531	0.001	0.001
Bend2X S8	399544 6.839	516593. 410	- 113.551	0.001	0.001
Bend2X S9	399544 7.053	516593. 593	- 113.529	0.001	0.001
Bend2X S10	399544 7.454	516593. 777	- 113.467	0.001	0.001
Bend2X S11	399544 8.320	516594. 059	- 113.374	0.001	0.002
Bend2X S12	399544 9.081	516594. 121	- 113.236	0.001	0.001

Table 8.S3. Distance of exposure measured for each erosion pin due to fluvial erosion of the riverbank.

Pin location	Height above thalweg (m)	Installation date	1/29/ 2019	3/27/ 2019	11/20/ 2019	1/28/ 2020	7/27/ 2020	1/23/ 2021	4/29/ 2021	3/5/2 023	Total	Erosion rate (cm/yr)
					Eroded distance (cm)							
Bend 1 downstream	0.94	11/14/2018	0.0	0.0	0.0	0.0	0.0	0.1	0.0	>51	>51.1	>11.9
Bend 1 downstream	0.33	11/20/2019	-	-	-	0.0	0.0	-1.2	0.0	15	13.8	4.2
Bend 1 downstream	0.11	11/20/2019	-	-	-	9.0	0.0	0.6	0.0	5	14.6	4.4

Location													
Bend upstream	1	0.93	11/14/2018	0.0	0.0	0.0	-1.0	0.0	0.0	0.0	18	17	3.9
Bend upstream	1	0.30	11/20/2019	-	-	-	0.0	0.0	0.0	0.0	14	14	4.3
Bend upstream	1	0.14	11/20/2019	-	-	-	8.2	0.0	0.0	0.0	7	15.2	4.6
Bend downstream	2	0.94	11/15/2018	0.0	1.5	0.0	0.0	0.0	0.0	0.0	29	30.5	7.1
Bend downstream	2	0.35	11/15/2018	0.0	2.8	0.0	0.0	0.0	0.0	0.0	8	10.8	2.5
Bend middle	2	0.74	11/15/2018	0.0	1.0	0.0	0.0	0.0	0.0	0.0	15	16	3.7
Bend middle	2	0.29	11/15/2018	0.0	3.0	0.0	0.0	0.0	0.0	0.0	15	18	4.2
Bend upstream	2	0.84	11/15/2018	0.0	3.0	0.0	0.0	0.0	0.0	0.0	24	27	6.3
Bend upstream	2	0.39	11/15/2018	0.0	2.3	0.0	0.0	0.0	0.0	0.0	21	23.3	5.4
												Mean	**5.2**

8.11.1 Experimental calibrations for RPM vs u^* with varying grain size

We calibrated a relation for rotations per minute (RPM) of the spinning plate with shear velocity in the mill using sand and gravel of known sizes and look for threshold of entrainment: when sediment is actively being exchanged with the bed across the entire diameter of the mill (Table 8.S4). Sediment median grain size (D_{50}; m) was measured using Wolman pebble counts (gravel) or the Camsizer X2 with XFall attachment (sand). Then, we used measured grain sizes with the Parker et al. (2003) relation to calculate the critical Shields number (τ_c^*; unitless) for entrainment for each grain size:

$$\tau_c^* = 0.11 Re_p^{-0.6} + 0.03 \times 10^{-7.7 Re_p^{-0.6}}. \tag{8.S1}$$

Here, the critical Shields number is formulated as a function of particle Reynolds number (Re_p), defined as:

$$Re_p = \sqrt{R g D_{50}^3}/\upsilon, \tag{8.S2}$$

where $R = (\rho_s-\rho)/\rho$ is the submerged specific gravity of sediment ($R = 1.65$) calculated from water density ($\rho = 1000$ kg/m^3) and sediment density ($\rho_s = 2650$ kg/m^3), g is gravitational acceleration (9.81 m/s^2), and υ is the fluid kinematic viscosity (10^{-6} m^2/s). Since the Shields number is defined as:

$$\tau^* = \frac{\tau_b}{(\rho_s - \rho) g D_{50}}. \tag{8.S3}$$

We use the definition of shear velocity shear velocity (u^*; m/s) as a function of basal shear stress (τ_b; Pa),

$$u^* \equiv \sqrt{\tau_b/\rho} \tag{8.S4}$$

to solve for shear velocity as a function of the Shields number:

$$u^* = \sqrt{RgD_{50}\tau^*}. \tag{8.S5}$$

By substituting Eq. (8.S2) into Eq. (8.S1), evaluating for critical Shields number, then substituting into Eq. (8.S5) we can determine the critical shear velocity for entrainment of each sediment grain size in our calibration.

Our experimental setup produced slightly lower shear velocities than previous work (Fig. 8.S4). We hypothesize this was due to the shallower depth of our setup (40 vs 50 cm), which would be expected to cause a ~20% decrease in shear stress and ~10% decrease in shear velocity; and using a flat plate instead of a propeller, which may change the shape of the water surface and change the structure of turbulence in the mill. A test using a propeller to determine the threshold of motion versus RPM found similar results to the flat plate, but particle motion was first observed at the outer edges of the mill compared to near the center, which was the case when a propeller was used. This observation indicates the structure of turbulence and secondary currents strongly depends on the propeller or plate geometry, and supports our use of a different calibration for our experimental setup.

Table 8.S4. Grain size and flow characteristics at threshold of entrainment for abrasion mill calibration experiments.

Grain description	Median grain size (mm)	Threshold u* for entrainment (m/s)	RPM ± 1SD at entrainment
Fine grey sand	1.1	0.018	333 ± 6
Yellow coarse sand	2.5	0.030	421 ± 4
Pea gravel	6	0.050	622 ± 6
Coarse gravel	29	0.12	1098 ± 11
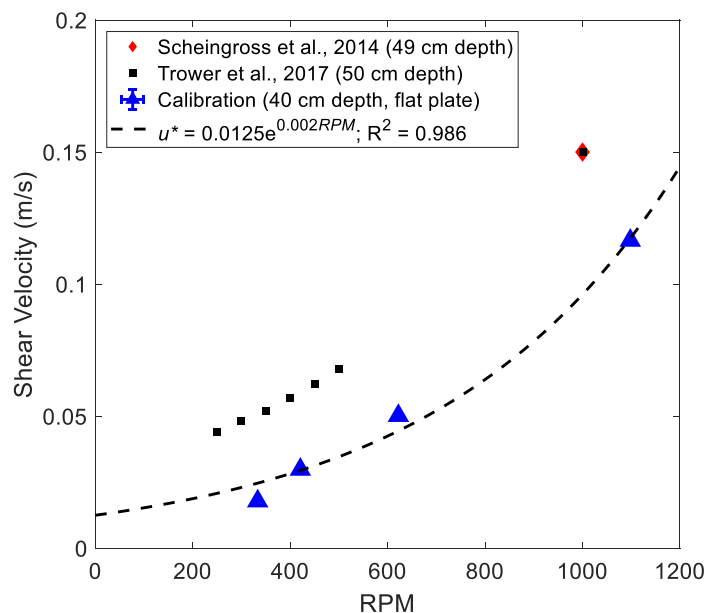
Figure 8.S1. A comparison of our calibrated shear velocities (u^*) versus RPM with previously published values. Our calibration points (blue triangles) enclose error bars representing 1 standard error of the mean for shear velocity and RPM.
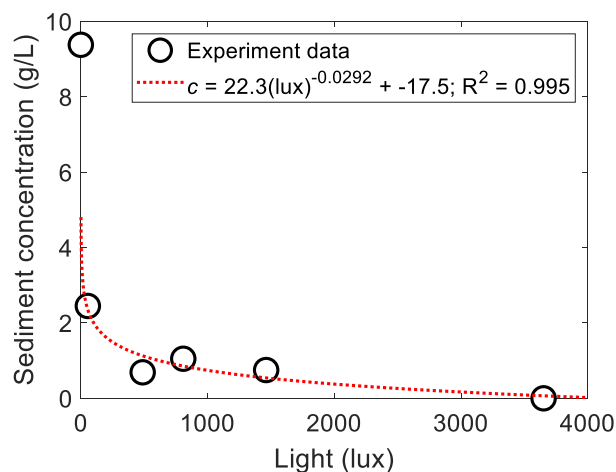
Figure 8.S2. Calibration of sediment concentration (c; g/L) as a function of light measurements (units of lux) by the sensor in the mill. The experiment data are from siphoned samples taken at the end of each experimental stage.

8.11.2 Detailed methods for abrasion mill experiments

In this section, we describe the detailed setup (Sect. 8.11.2.1) and calibration (Sect. 8.11.2.2) of the sediment entrainment mill experiments. Details on running the experiments are summarized in the main text (see Sect. 8.5.5).

8.11.2.1 Experimental setup

After retrieving an intact sample of the cutbank toe of the Amargosa River from the field, we prepared the sample for experimental runs. Between sample retrieval and experimental setup, the samples were stored covered by a damp rag and sealed from the atmosphere to avoid the bank mud cracking and drying out or forming salt crusts. To prepare the sample, first we used silicone sealant to attach the PVC mill that the sample was acquired in to an acrylic plate to form the base of the mill. Next, we marked the inside of the mill at 40 cm above the initial bed height and drilled holes for the light sensor mount, windows, and spigot centered at 10 cm above the initial bed height. We attached an adjustable metal spigot that is used to control siphon speed to match mean water velocity in mill and minimize grain size fractionation during sampling. We also used silicone sealant to attach acrylic windows (¾" acrylic with 3 3/8" diameter) that allow exterior lights to shine into the mill. Then, we sealed all gaps with epoxy and silicone sealant, letting these cure for at least 48 hours before filling the mill with fluid.

While the sealant was setting, we wiped down the interior of mill above the sediment sample, as well as a 5-gallon bucket with ethanol to kill any algae or microbes living on those surfaces. Next, we took a small sample (~0.1 g) of sediment from the base of the mill to run for grain size analysis and compare to sediment sampled from the bed after the experiment and from samples siphoned at the end of each experimental stage. We then dissolved salt crusts from channel in tapwater to ~30,000 µS/cm (representative value for Death Valley floods based off our field salinity meter is ~30,000 µS/cm) and let the saline solution sit for at least 22 hours for fine sediment to settle out of solution. The buckets are 44 cm deep to the rim, and this allows all sediment with grain size $D > 0.1$ µm to settle 40 cm distance (Dietrich, 1982). The saline solution was siphoned into the abrasion mill, filling it to the 40 cm mark. Then, we waited an additional 24 hours for any sediment disturbed by siphoning to settle out of the water column in the mill.

We set up the mill with two floodlights in fixed locations under a light-blocking cover to begin the experiments. We started the HOBOware pendant logging at a 10-sec interval and used wires to attach it to the wall of the mill 10 cm above the initial bed elevation. Then we attached the spinning plate to the motor and centered the mill so that the plate could spin freely without hitting the sides of the mill. Experimental runs and sample grain size analysis are described thoroughly in the main text of the manuscript.

Finally, we determined a relation between the measured sediment concentrations and light sensor measurements,

$$c = 22.3L^{-0.0292} - 17.5, \tag{8.S6}$$

where sediment concentration (c; g/L) is a function of light flux (L; lux), with a goodness of fit of $R^2 = 0.995$. We used this relation to calculate sediment concentration through time in the experiment.

8.11.2.2 Evaluating variation in sediment concentration with depth

Our analysis of sediment entrainment rate assumes that suspended sediment concentration is homogeneous throughout mill (see Sect 8.5.5). To evaluate this assumption, we determine the variation in sediment concentration with depth assuming that concentration follows a Rouse profile within the mill (Scheingross et al., 2014). In the derivation of the Rouse profile, sediment concentration reaches a time-invariant steady state when the amount of sediment lofted by fluid turbulence is balanced by the settling flux of sediment within the mill. At steady state, sediment concentration (c; unitless) is a function of height above the bed (z; m), such that

$$\frac{c(z)}{c(a)} = \left[\frac{\frac{H}{z}-1}{\frac{H}{a}-1}\right]^{P}. \tag{8.S7}$$

Sediment concentration depends on the flow depth (H; m), a reference height (a; m), the sediment concentration at that reference height ($c(a)$; unitless), and the dimensionless Rouse number (P). The Rouse number is defined as:

$$P = \frac{w_s}{\beta u^*}, \tag{8.S8}$$

where particle settling velocity (w_s; m) is divided by the fluid shear velocity (u^*; m/s) and an empirical factor accounting for differences between sediment turbulent diffusivity and the assumed fluid eddy viscosity model (β; unitless). We evaluate P using $\beta = 1$ because most existing models for β predict values of the same order of magnitude (de Leeuw et al., 2020).

Our assumption that sediment concentration does not change significantly with increasing depth in the mill requires that $P \ll 1$. We evaluate the Rouse number (equation (8.S8)) using representative values from our experiments of $w_s = 1.51 \times 10^{-4}$ m/s and $u^* = 0.0016$ m/s. These values indicate $P < 0.001$ for our experimental runs, supporting that a vertical sediment concentration gradient did not develop within the mill.

Chapter 9

THE INTERMITTENCY OF BEDROCK RIVER
INCISION BY ABRASION

Madison M. Douglas and Michael P. Lamb

Key Points:

- We invert the saltation abrasion model for bedrock incision intermittency using an erosion rate dataset.
- Bedrock rivers have a lower intermittency factor for channel-forming floods than alluvial rivers.
- Bedrock incising floods occur less frequently in steeper river channels.

9.1 Abstract

The saltation-abrasion model is the leading physics-based description of bedrock channel incision, but it is challenging to implement in landscape evolution models because the intermittency of channel-forming foods is unknown. We used hydraulics and channel-geometry relations combined with a global compilation of bedrock erosion rates to invert for a bedrock-incision intermittency factor (I) — the observed long-term erosion rate normalized by the rate predicted by the saltation-abrasion model for a characterisitic flood event. The best-fit bedrock-incision intermittency factor was $I = 4.50 \times 10^{-3}$ with sediment supply set to half the transport capacity. The intermittency factor declines with channel slope, indicating steeper rivers experience less frequent channel-forming floods. Bedrock rivers also have less frequent channel-forming floods than alluvial rivers of similar gradient and grain size. The bedrock incision intermittency factor helps bridge the gap between flood-scale erosion and landscape evolution.

9.2 Plain-language summary

Bedrock rivers are important because they transmit changes in climate, tectonics, and sediment supply across steep landscapes. However, the leading physical model for bedrock incision requires understanding flood frequency and sediment supply over geologic timescales, which poses a significant challenge. To constrain these parameters, we combined empiricisms for steep channel hydraulics with a global data compilation of bedrock river characteristics and erosion rates. This allowed us to assume a long-term sediment supply and constrain erosive flood frequency using our global compilation. We found that the frequency of erosive floods decreases for steep channels, and that bedrock rivers have less-frequent channel-forming floods than alluvial rivers with similar sediment size and channel slope. Constraining the value of erosion intermittency allows physics-based models of bedrock river erosion to be applied over geologic timescales.

9.3 Introduction

Bedrock river incision transmits signals of tectonics and base level change through steep landscapes, setting the boundary conditions for hillslope and mountain erosion (DiBiase et al., 2012; Whipple, 2004). Field and modeling work demonstrates that bedrock rivers respond to increased uplift rates by steepening their channels, offering a powerful tool to identify and determine the magnitude of offset for active fault systems (Wobus et al., 2006). Many processes cause bedrock incision, including abrasion, plucking, and cavitation (Lamb et al., 2015). While the relative rates of these processes remain uncertain, abrasion of bedrock by sediment transported as bedload is considered to be the dominant erosion mechanism in most bedrock rivers (Sklar & Dietrich, 2001, 2004, 2006). Physics-based models quantify wear from particle impacts on bedrock to calculate channel bed erosion rates (Lamb, Dietrich, & Sklar, 2008; Sklar & Dietrich, 2004; Turowski, 2020) and these models agree with experimental results (Scheingross et al., 2014; Shepherd & Schumm, 1974; Sklar & Dietrich, 2001). However, these models remain difficult to implement in long-timescale landscape evolution simulations because they require input variables, such as particle size, flood hydrographs, rock strength, and sediment supply, that are difficult to constrain over long timescales (Lague et al., 2005; Turowski, 2021). Consequently, most landscape evolution simulations continue to rely on the stream power model, which does not explicitly include physical processes (Howard & Kerby, 1983; Kirby & Whipple, 2001).

The most uncertain parameter in the saltation-abrasion model is the intermittency of bedrock incision (Sklar & Dietrich, 2006). Here, we define intermittency (I, dimensionless) as a multiplicative factor for erosion rates during a characteristic flood (E; m/s) to obtain long-term incision rates (E_L; m/s), so that $I=E_L/E$. (Figure 9.1). For comparison, the sediment transport intermittency of alluvial rivers is typically defined using the annual total bed-material load transport ($Q_{s,tot}$; m^3/s) and sediment transport capacity at bankfull conditions ($Q_{s,bf}$; m^3/s), so that $I=Q_{s,bf}/Q_{s,tot}$ (Hayden et al., 2021; Paola et al., 1992). The intermittency approach is asimplification, but one that is useful for modeling landscape evoution because it is difficult if not impossible to constrain the distribution of flood events beyond the historical record. While flood hydrographs remain unknown, the geometry of river channels often gives insight into the characteristic floods over geomorphic timescales (e.g., bankfull floods that accomplish the most geomorphic work) (Leopold et al., 1964). Thus, the intermittency-factor approach, as outlined by Paola et al. (1992), is to model landform evolution through a reoccuring characteristic event multiplied by an intermittency factor in an attempt to correct for the geomorphic work done during events other than the characteristic event.

Alluvial river intermittency varies over multiple orders of magnitude, though coarser gravel-bedded rivers generally have lower intermittency factors than sand-bedded rivers (Hayden et al., 2021; Paola et al., 1992). Field observations imply that most bedrock incision may be caused by infrequent, large floods (Lamb & Fonstad, 2010; Turowski, 2021) and localized flow focusing by topography and plunge pools that rapidly scours bedrock canyons (Cook et al., 2014; Venditti et al., 2014). The river must be able to mobilize sediment covering its bed to incise, so in some cases large boulders may shield the channel bed from incision (DiBiase

et al., 2018; Finnegan et al., 2017). Therefore, bedrock incision intermittency is expected to vary over orders of magnitude, but it has yet to be quantified, and is needed to apply the saltation abrasion model at scale.

To address this knowledge gap, we reformulated the saltation-abrasion model in terms of the intermittency factor of bedrock channel incision and other parameters that can be measured: channel slope, median grain size, and drainage area. We used this model with a global data compilation of channel characteristics and cosmogenic erosion rates to determine best-fit values of the intermittency factor and relative sediment supply.
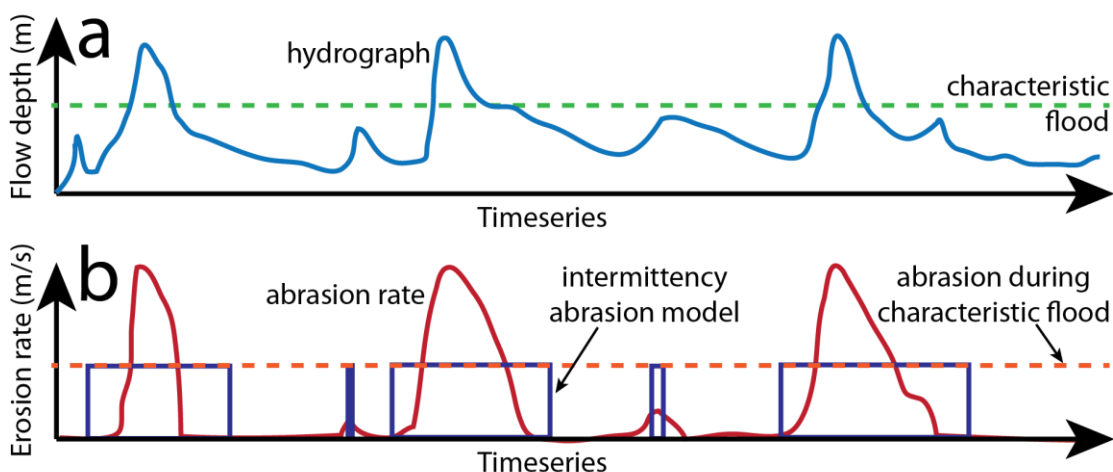
Figure 9.1. Schematic of a bedrock river hydrograph and abrasion rates overlain with the equivalent erosion rates produced by intermittent abrasion by a characteristic flood. (**a**) Flow depth varies through time (blue line) and the channel geometry reflects a characteristic flood magnitude (green dashed line). (**b**) Sediment abrasion cutting into the river bed (red line) happens irregularly in response to the changing hydrograph, but can be represented by intervals of time with constant abrasion rate (blue line) where the magnitude of the abrasion is equal to abrasion caused by the characteristic flood (orange dashed line).

9.4 Methods

9.4.1 Model Derivation

We used the saltation-abrasion model for bedload transport (Sklar & Dietrich, 2004) (Appendix 1). We do not address cases where gravel can be in suspension (Lamb et al., 2008) or where more complex treatments of bedrock cover (Turowski et al., 2007). Thus, the intermittency factors we derived should be used in conjunction with the Sklar and Dietrich (2004) model. We also do not address other erosion mechanisms, including plucking (Beer et al., 2017; Chatanantavet & Parker, 2009; Wilkinson et al., 2018), debris flows (Stock et al., 2005), plunge pool erosion (Scheingross & Lamb, 2017), and abrasion by cobbles and boulders rolling or sliding along the channel bed (Turowski et al., 2009) or suspended sediment during large floods (Lamb et al., 2008; Scheingross et al., 2014). Bedload abrasion by saltation is considered the dominant erosion mechanism in many rivers, and if other

processes are important, our exercise could be repeated to derive intermittency factors appropriate for those alternate erosion mechanisms.

The saltation-abrasion model predicts that local bedrock incision rate (E, m/s) is a product of the rate of bedload sediment impacts per area of channel bed (I_B, impacts/s/m^2), the volume of rock eroded per impact (V, m^3/impact), and the fraction of channel bed comprising exposed bedrock (F, dimensionless) (Sklar & Dietrich, 2004):

$$E = I_B V F. \tag{9.1}$$

Sklar and Dietrich parameterized each of these variables to derive

$$E = \frac{\rho_s q_b w_i^2 Y (1 - q_b/q_{bc})}{L_b k_v \sigma_T^2} \tag{9.2}$$

in which sediment density is ρ_s (kg/m^3), width-normalized bedload sediment transport and transport capacity (q_b and q_{bc}, m^2/s), Young's modulus of bedrock elasticity (Y, MPa), a rock erodibility constant (k_v, dimensionless), and the bedrock tensile strength (σ_T, MPa). The average saltation hop length (m) is:

$$L_b = 8.0 D \left(\frac{\tau^*}{\tau_c^*} - 1 \right)^{0.88}, \tag{9.3}$$

where D is the median bedload grain size (m). The average impact velocity for a single particle on the channel bed (m/s) is

$$w_i = 0.8 \sqrt{RgD} \left(\frac{\tau^*}{\tau_c^*} - 1 \right)^{0.18}, \tag{9.4}$$

dependent on gravitational acceleration (g, m/s^2), the sediment submerged specific gravity ($R = (\rho_s - \rho)/\rho$) where ρ is the density of water (kg/m^3)), the Shields stress (τ^*, dimensionless), and the critical Shields stress for sediment entrainment (τ^*_c, dimensionless). Sklar & Dietrich (2004) used Fernandez Luque & Van Beek (1976),

$$q_{bc} = 5.7 \sqrt{RgD^3 (\tau^* - \tau_c^*)^3}, \tag{9.5}$$

for bedload transport capacity. Substituting equations (9.3)-(9.5) into equation (9.2), multiplying by the right-hand side of equation (9.5), and dividing by q_{bc} yields the expression:

$$E = \frac{0.456 \rho_s Y (RgD\tau_c^*)^{3/2}}{k_v \sigma_T^2} \frac{q_b}{q_{bc}} \left(1 - \frac{q_b}{q_{bc}} \right) \left(\frac{\tau^*}{\tau_c^*} - 1 \right)^{0.98}. \tag{9.6}$$

To reformulate equation (9.6) so that it can be used more broadly in landscape evolution modeling, we made simplifying assumptions and applied empirical relations for steep

channel dynamics. The characteristic flood must have a Shields stress (τ^*) greater than the critical Shields stress (τ^*_c) to entrain sediment and the river must have sediment supply less than transport capacity ($q_b < q_{bc}$) to incise bedrock, so q_b/q_{bc} ranges from 0 to 1 and $\tau^*/\tau^*_c > 1$. We also introduced a bedrock incision intermittency factor $I=E_L/E$ (dimensionless), such that long-term incision rates occurring over multiple floods can be calculated by multiplying I by the instantaneous erosion rate for the characteristic flood, resulting in:

$$E_L = \frac{0.456\rho_s YI(RgD\tau^*_c)^{3/2}}{k_v \sigma_T^2} \frac{q_b}{q_{bc}}\left(1 - \frac{q_b}{q_{bc}}\right)\left(\frac{\tau^*}{\tau^*_c} - 1\right)^{0.98}. \tag{9.7}$$

We assumed normal flow conditions so that $\tau^*_c = HS/RD$, where H (m) is the cross-sectional averaged flow depth. To calculate the critical Shields stress, we used the slope-dependent formulation from Lamb et al. (2008) for the bedload median grain size:

$$\tau^*_c = \frac{2C_f}{C_D}\left(\frac{\tau_T}{\tau_T - \tau_M - \tau_W}\right)\left(\frac{tan\varphi_0 - S}{1 + (F_L/F_D)tan\varphi_0}\right)\left[\frac{V_p}{A_{xs}D}\frac{1}{R}\left(\frac{\rho_s}{\rho_a} - \frac{V_{ps}}{V_p}\right)\right], \tag{9.8}$$

in which V_p is the median grain size volume (m³), A_{xs} is the submerged cross-sectional area (m²), and V_{ps} is the submerged particle volume (m³). We calculated V_p and A_{xs} assuming a spherical grain shape following Lamb et al. (2008). We used a flow resistance relation for gravel- and boulder-bedded streams (Ferguson, 2007),

$$C_f = \frac{a_1^2 + a_2^2(H/D_{84})^{5/3}}{a_1^2 a_2^2 H^2/D_{84}^2} \tag{9.9}$$

with $a_1 = 6.5$, $a_2 = 2.5$, and $D_{84} = 2.2D$ (Rickenmann & Recking, 2011). We used the formula from Lamb et al. (2008) to account for flow aeration:

$$\rho_a = \rho(1 - 0.9\sin\beta) \tag{9.10}$$

where ρ_a was the aerated water density (kg/m³) and β was the channel slope (°, $S = \tan\beta$). In general, flow aeration is a minor effect and the threshold of sediment mobilization is primarily influenced by grain emergence and the fraction of shear stress dissipated by morphologic drag (Lamb et al., 2008). We calculated the critical Shields number for entrainment of sediment in a given bedrock river channel by iteratively solving equations (9.8)-(9.10), and then inserted the result into equation (9.8) to find E_L as a function of I.

9.4.2 Data compilation

To implement equation (9.8), we identified catchments where drainage area (A, m²), local slope (S, dimensionless), median grain size (D, m), long-term averaged erosion rates from cosmogenic nuclides (E_{10Be}, m/yr), and precipitation (P, m/yr) had been measured previously. This global compilation ($n=347$) spans -43° to 56° latitude and includes channels with a range of mean annual precipitation from 2 to 3431 mm/yr (Figure 9.2; Supplemental Table 9.S1).

We used stringent criteria for which catchments were considered fluvial channels incising into bedrock, only including sources that stated that the channel had a bedrock bed. We excluded measurements of grain size or cosmogenic erosion rates that were specifically collected from landslide or debris flow deposits, since these represent transient changes relative to bedrock incision timescales (Ansberque et al., 2015; Wang et al., 2015; Wang et al., 2017; West et al., 2014). We did not attempt to exclude catchments based on dominant erosion processes (e.g., plucking vs abrasion). Grain size data and cosmogenic erosion rates from the same site were combined from different published studies. For cases where multiple cosmogenic erosion rate measurements were made in one catchment, we selected the one along the same tributary closest to grain size measurements. One source of uncertainty is that [10]Be concentrations are typically measured for sand samples, and may not represent the residence time of coarse sediment in steep catchments. This is an active area of investigation, and while some studies have found that bulk measurements of cobbles and sand yield similar cosmogenic erosion rates (Neely & DiBiase, 2020) others have found variation in detrital sediment ages with grain size (Aguilar et al., 2014; van Dongen et al., 2019; Lavarini et al., 2018). We compiled drainage area and local channel slope (not the catchment-averaged slope) reported at sampling locations.
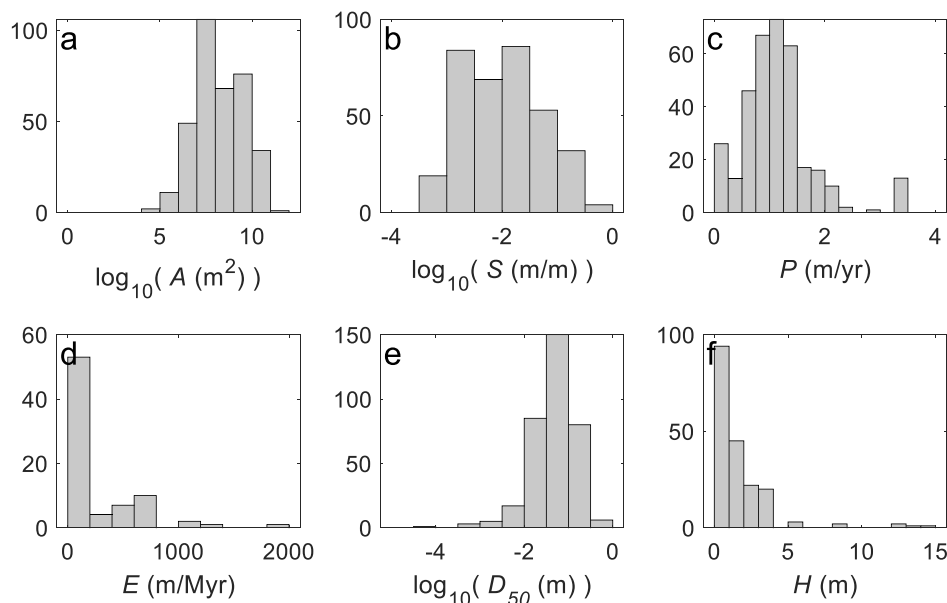
Figure 9.2. Histograms of compiled bedrock channel characteristics. Our global compilation spans multiple orders of magnitude of study site (**a**) drainage area, (**b**) local slope, (**c**) mean annual precipitation, (**d**) [10]Be cosmogenic erosion rate, (**e**) median bed grain size, and (**f**) channel depths.

Surprisingly, our data compilation was primarily limited by the availability of grain size data in bedrock catchments and not cosmogenic erosion rates. Some references also published

84th percentile grain size measurements (D_{84}, m), which we used to validate the relation $D_{84} = 2.2D$ from equation (9.9).

We used mean annual precipitation values at each sampling location taken from WorldClim 2 (Fick & Hijmans, 2017). This dataset reports bioclimatic variables averaging from 1970-2000 at 1 km^2 resolution over global land area. While the mean annual precipitation at the sampling location may not be representative of the whole catchment, our study catchments generally span less than 10 pixels of precipitation data (n=62 < 10 km^2, n=285 > 10 km^2 with n=179 > 100 km^2).

Where available, we also compiled channel width (W, m) and depth (H, m) data. It is challenging to determine the depth of a characteristic channel-incising flow from field observations, so we compiled reported bankfull depths. There was no consistent characterization for the bankfull depth of bedrock channels, and researchers used different methods including the height of well-established vegetation (Finnegan et al., 2017; Pike, 2008) as well as the height of sediment abrasion, flood strandlines, and boulder bleaching (Whittaker et al., 2007). In addition, many studies reported either the maximum bankfull depth or the cross-sectionally averaged bankfull depth.

9.4.3. Model implementation

To implement the model, we assumed a constant sediment density ($\rho_s = 2650$ kg/m^3) and water density ($\rho = 1000$ kg/m^3). Due to a lack of bedrock strength measurements, we selected a constant Young's modulus ($Y = 5 \times 10^4$ MPa), tensile strength ($\sigma_T = 7$ MPa), and erodibility coefficient ($k_v = 10^6$) as representative values for bedrock (Sklar & Dietrich, 2001). Since the erodibility of a single, unweathered rock type can vary by multiple orders of magnitude (Sklar & Dietrich, 2001) and is significantly influenced by the strength of sediment abrading the bedrock (Johnson et al., 2009), direct measurements of rock strength would be required to accurately parameterize these values for each catchment. Finally, long-term bedrock incision rates (E_L) were determined using previously reported catchment-averaged ^{10}Be cosmogenic erosion rates (E_{10Be}, m/kyr). Using an attenuation length for cosmogenic nuclide penetration into bedrock of ~0.6 m (Gosse & Phillips, 2001), we estimated that our compilation represents ^{10}Be erosion rates averaged over 0.14 – 60 kyr timescales. We evaluated the intermittency factor so that $I = E_{10Be}/E$.

To evaluate the critical Shields stress (equation (9.8)), we followed previous field measurements and experiments to model gravel entrainment in steep alluvial channels, assuming that 50% of the total shear stress (τ_T, Pa) was taken up by morphological drag (τ_M, Pa) and wall stresses were negligible ($\tau_W = 0$ Pa) (Prancevic & Lamb, 2015b). We selected an internal friction angle of $\varphi_0 = 60°$ (Wiberg & Smith, 1987), similar to the average value of 67° found from field measurements of steep channel networks in the San Gabriel mountains (Prancevic & Lamb, 2015a). We used a drag coefficient $C_D = 0.9$ and a ratio of the lift to drag force (F_L/F_D) of 0.85 (Lamb, Dietrich, & Venditti, 2008).

The critical Shields stress (equation (9.8)) and coefficient of friction (equation (9.9)) both depend on the depth of a characteristic flood (H, m). To determine H from our data compilation of bedrock channel geometries (Section 9.4.2), we used the conservation of mass for water during a characteristic flood,

$$Q = UHW \tag{9.11}$$

which depends on flood discharge (Q, m³/s), mean water velocity (U, m/s), and channel width (W, m) assuming a rectangular channel. We calculated the water discharge assuming a steady-state water balance as a function of drainage area (A, m²) and modern mean annual precipitation (P, m/yr) (Chatanantavet & Parker, 2009):

$$Q = K_w P A \tag{9.12}$$

and used K_w as a fitting parameter so that Q in equation (9.12) represents the characteristic flood discharge, as described below.

We used an empirical relation for coarse-grained, gravel bedded channels to calculate channel width (Parker et al., 2007). Bedrock channel width is known to change significantly along a river reach in response to forcings such as tectonics (Finnegan et al., 2005; Lavé & Avouac, 2001) and sediment supply (Turowski et al., 2015; Wright et al., 2022). However, scaling relations for the width of coarse-grained alluvial rivers as a function of discharge provide a first-order estimate of bedrock channel widths between river systems (Hack, 1957; Phillips & Jerolmack, 2019). We calculated channel width as a function of discharge, median grain size, and gravitational acceleration (g, m/s²):

$$W = \frac{4.63}{g^{1/5}} Q^{0.4} \left(\frac{Q}{\sqrt{g D D^2}} \right)^{0.0667}. \tag{9.13}$$

Combining equations (9.11)-(9.13), results in an estimate for the flow depth of a characteristic bedrock-incising flood:

$$H = \left[\frac{(K_w P A)^{0.5333} C_f^{0.5} D^{0.1667}}{4.63 g^{0.2667} S^{0.5}} \right]^{2/3} \tag{9.14}$$

using K_w as the precipitation coefficient, a dimensionless fitting parameter of order unity to account for uncertainty in the magnitude of the characteristic flood relative to P and fitting relations for W and C_f. Flow depth depends on the channel slope (S, dimensionless) and coefficient of friction (C_f). Therefore, we solved equations (9.8), (9.9), and (9.14) iteratively to calculate the bedrock channel characteristics.

Not all locations in the data compilation had previously published surveys of channel width and depth, so we tuned K_w based on locations where we had survey results and measured erosion rates (Supplemental Figure 9.S1). We iteratively solved equations (9.9) and (9.14)

and to model characteristic flow depth at each location using a fitted value of $K_w = 1.16$. Results show that modeled characteristic flow depth was correlated with the average surveyed channel depth at each location (Figure 9.3a) while this value of K_w generally over-estimated channel width (Figure 9.3b). This agrees with our derivation, where K_w should be of order unity and channel incision rate primarily depends on flow depth. Therefore, we solved the system of equations using $K_w = 1.16$ in equation (9.12) to iteratively solve the system of equations for H, C_f, and S and invert for plausible ranges of bedrock channel sediment supply, intermittency, and the supply-normalized intermittency factor.
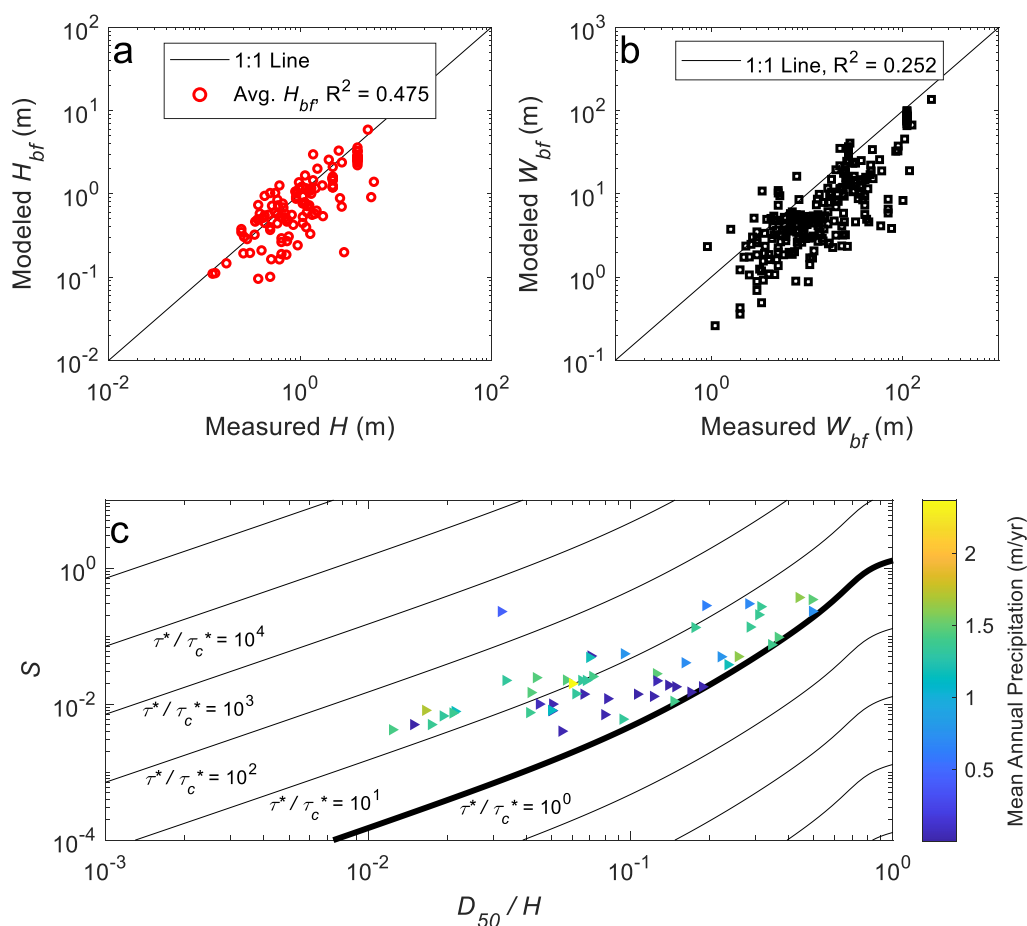
Figure 9.3. Evaluating bedrock channel geometry to fit characteristic flood discharge. (**a**) Fit of modeled versus measured average bankfull channel depths. (**b**) Best fit of measured versus modeled channel width. Panels (a) and (b) include all bedrock channel geometry data from our compilation to constrain general relations that we apply to sites with corresponding cosmogenic erosion rates and show R^2 values calculated in log-log space. (**c**) Channel slope plotted versus median grain size divided by average channel depth measured in the field or calculated from equation (9.14) for sites without measured depths. Points are color-coded by mean annual precipitation, and contour lines show τ^*/τ^*_c increasing as slope increases, with

$\tau^*/\tau^*_c = 1$ plotted as a thick black line, while thin black lines mark factors of 10 contour intervals and increase to the upper left of the plot.

Using this K_w, we compared modeled Shields numbers of characteristic floods for a channel versus the threshold critical Shields number for sediment entrainment. Based on the formulation of the Shields number and equation (9.10), we collapsed the model results by plotting our data in slope versus D/H space with contour lines of constant τ^*/τ^*_c (Figure 9.3c). Slope and grain size measurements were taken directly from the data compilation and used to solve for H iteratively via equations (9.10) and (9.14) for locations where H_{avg} measurements were not available. Results show that most bedrock rivers plot in our compilation near or above the critical Shields stress to mobilize the median grain size present on their beds (Figure 9.3c). We exclude sites with modeled $\tau^*/\tau^*_c < 1$ since these catchments may violate assumptions used to derive equation (9.14). For example, most of the sites with $\tau^*/\tau^*_c < 1$ had very large grain sizes, so sediment on the channel bed primarily transported by debris flows rather than as fluvial bedload, as was assumed in our derivation.

Two variables remain unconstrained: long-term sediment supply relative to bedload transport capacity (q_b/q_{bc}) and the characteristic erosion intermittency (I). Previous modeling efforts assumed values of bedrock erosion intermittency based on flood intermittency for modern hydrographs (Sklar & Dietrich, 2006). However, the intermittency of a characteristic flood does not reflect intermittency of erosion because incision scales nonlinearly with flood magnitude (flow depth and velocity; see equation (9.14) and Figure 9.1). Instead, we evaluated the model varying both q_b/q_{bc} and I for best fits and sensitivity to potential changes in sediment supply through time.

9.5 Results

We evaluated our model for a range of sediment supply (q_b/q_{bc}), flood intermittency (I), and supply-normalized intermittency ($I_s = I(q_b/q_{bc})(1 - q_b/q_{bc})$) and compared the modeled erosion rates (E) to cosmogenic erosion rates (E_{10Be}). We display results and calculate R^2 values in $\log_{10}$-$\log_{10}$ space because our data for D, E_{10Be}, and S span multiple orders of magnitude (Figure 9.4a). Best-fit values of intermittency and sediment supply covary, forming a concave-up quadratic function with a minimum I for moderate sediment supply. The goodness of fit is much less sensitive to sediment supply at moderate values of q_b/q_{bc}, while sediment supplies near zero or approaching the transport capacity had a narrower range of higher intermittency values that fit the data (Figure 9.4a). We found best-fit values for constant $q_b/q_{bc} = 0.5$ and $I = 4.50 \times 10^{-3}$, though these values explained very little variance of the data ($R^2 = 0.16$).

We examined the covariance of I_s with other parameters in our data compilation (D, E_{10Be}, A, S, and P) and found a significant negative correlation between I_s and channel-bed slope (Figure 9.4b). Fitting compiled data with a slope-dependent I_s, we obtained the relation,

$$I_s = 8.36 \times 10^{-5} S^{-0.712}. \tag{9.16}$$

This produced a significant fit between cosmogenic measurements and modeled bedrock incision rates with $R^2 = 0.49$ (Figure 9.4c). Thus, characteristic channel-incising floods occur less frequently in steep channels, which supports prior observations of mountainous channels (Montgomery & Buffington, 1997). I_s also has a slight negative correlation with median grain size, but that dependence was weaker than the slope dependence. Using equation (9.16) to solve for I_s, we substitute this into equation (9.8) to calculate erosion rates and compare them to measured rates (Figure 9.4c). There is some circularity in this result, since the relation for I_s is fit on the same data used to produce Figure 9.4b. However, this calculation demonstrates that accounting for slope-dependent I_s along with other variables measured in the field can explain much of the variance in cosmogenic erosion rate data.
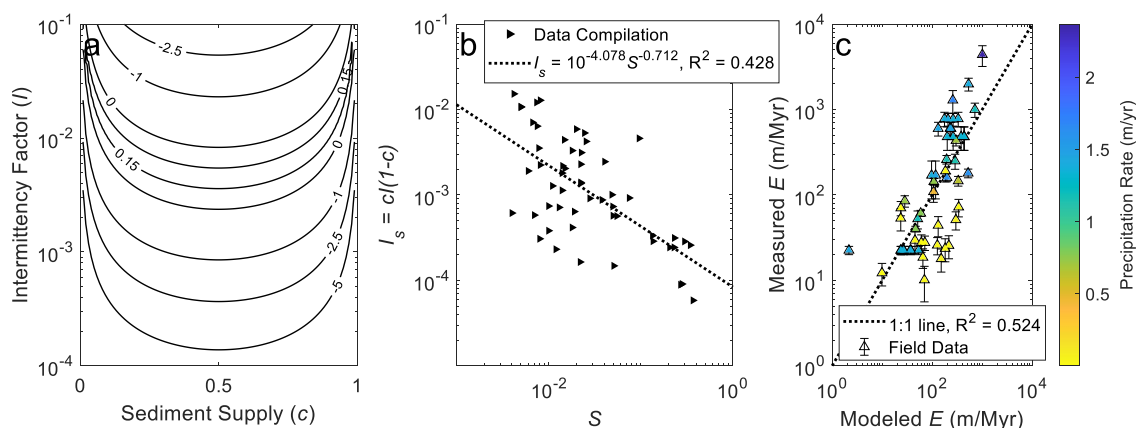
Figure 9.4. Supply-normalized intermittency depends on slope and sediment supply. (**a**) Contours of R^2 values (calculated in log-log space) for a range of q_b/q_{bc} and I inputs to the saltation-abrasion equation to calculate erosion rates (E, m/s) for comparison to cosmogenic erosion rates (E_{10Be}, m/s). The best-fit values occur at $q_b/q_{bc} = 0.5$ and $I = 4.50\times10^{-3}$, though $R^2=0.16$. (**b**) Best fit of supply-normalized intermittency ($I_s = I(q_b/q_{bc})(1 - q_b/q_{bc}) = 8.36\times10^{-5}S^{-0.712}$) versus slope. (**c**) Modeled versus measured erosion rates calculated from channel S and best-fit I_s (S), color-coded by mean annual precipitation.

We plotted best fit I for $q_b/q_{bc} = 0.5$ and found that for a given grain size, most bedrock rivers would have a lower intermittency factor than found for alluvial rivers (Hayden et al., 2021) (Figure 9.5a). While the intermittency of bedrock river incision and alluvial river sediment transport have different definitions, both intermittency factors provide an indirect measure of how frequently geomorphic work occurs in the sense of Leopold et al (1964). Of the variables they compiled, Hayden et al. (2021) only found a significant correlation between alluvial channel intermittency and the ratio of cosmogenic erosion rates from the catchment headwaters to mean annual precipitation (Figure 9.5b). They and others argued that precipitation provides a proxy for the ratio of physical versus chemical weathering intensity in bedrock river catchments (Ferrier, Huppert, et al., 2013; Ferrier, Perron, et al., 2013; Murphy et al., 2016). When plotted along the same axes (Figure 9.5b), our data generally had a higher ratio of cosmogenic erosion rate to mean annual precipitation. This implies

physical as opposed to chemical weathering dominates bedrock catchments, in line with expectations for catchments where soil production must be slow for exposed bedrock to persist. In line with expectations, bedrock catchments are generally steeper than alluvial catchments (Figure 9.5c). However, for river reaches with similar slopes, bedrock channels generally have lower intermittency than alluvial channels. This result implies that the threshold to mobilize the bed-material load is lower than the threshold to significantly abrade any underlying material.
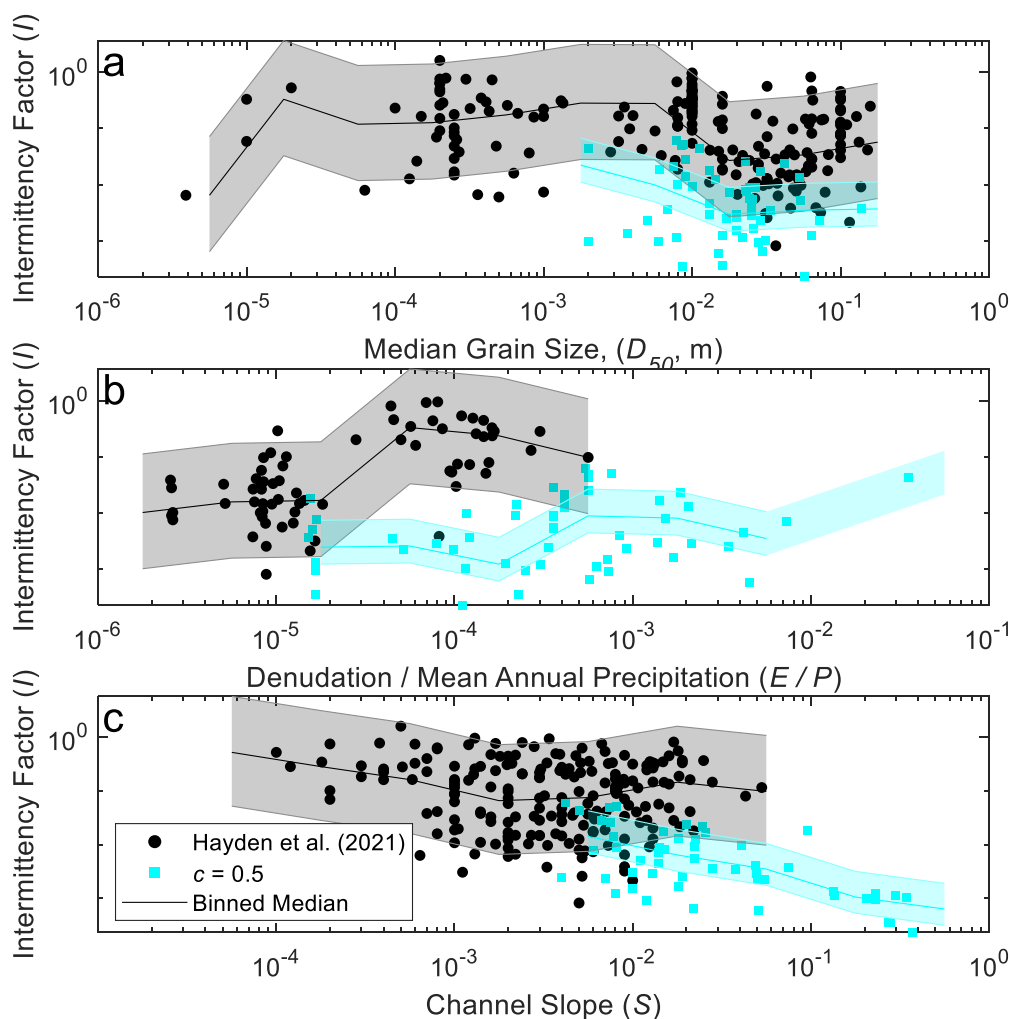
Figure 9.5. Comparison of best-fit intermittency factor from alluvial river compilation (Hayden et al., 2021) to best-fit intermittency (I) for bedrock river data compiled in this study. I was calculated using a fixed long-tern sediment supply, $q_b/q_{bc} = 0.5$, then dividing measured by modeled erosion rates. Intermittency rates are displayed versus **(a)** median bed grain size, **(b)** the ratio of cosmogenic erosion rate divided by precipitation rate, and **(c)** channel slope. Uncertainty (shown by shaded regions tracing the moving median of data) were estimated in

Hayden et al. (2021) as one order of magnitude, and we estimated uncertainty using a maximum cosmogenic erosion rate uncertainty from our compilation as a factor of 2 (50% measured value).

9.6 Discussion

We found that evaluating the saltation abrasion model using slope-dependent supply normalized intermittency, where $I_s = 8.36 \times 10^{-5} S^{-0.712}$ (equation (9.16)), can explain approximately half the variance in cosmogenic erosion rates ($R^2 = 0.52$). Intermittency and sediment supply co-vary, with model best-fits produced for moderate sediment supply (q_b/q_{bc} = 0.5) and a constant value of $I = 4.50 \times 10^{-3}$. Therefore, we recommend using equation (9.16) to calculate values of I_s with $q_b/q_{bc} = 0.5$ in landscape evolution models. Maintaining a moderate sediment supply allows rivers to adjust to rapidly adjust to changes in uplift and climate by changing their fraction of bed cover, so it makes sense that bedrock rivers maintain q_b/q_{bc} near 0.5. Our analysis follows efforts by Sklar and Dietrich (2006) to infer the intermittency of two channel-forming discharges (one low and the other exposing bedrock to be incised) along the Eel River. By partitioning the modern hydrograph in conjunction with measurements of instantaneous and long-term incision rates, they found a best-fit $I = 0.0437$ (Sklar & Dietrich, 2006), within the range of values from our global compilation (Figure 9.5). Sklar and Dietrich also found that sediment grain size was a dominant control on bedrock river channel geometry. This provides one possible explanation for the slope dependency of I_s: steeper catchments are dominated by coarse grains and boulders (Attal et al., 2015), which rarely move due to high critcal Shields numbers (Lamb et al., 2008). But when they do move, they have higher kinetic energy such that infrequent floods are sufficient to generate high erosion rates (Beer & Lamb, 2021; Turowski et al., 2015). Another explanation is that a rainstorm in a small, steep catchment would produce a short flood with very high flow velocities, while the equivalent rainstorm would produce a longer flood with deeper flows in a larger and flatter catchment. This hypothetical storm would produce high shear stresses in both catchments, but the duration of incision will be much shorter in the steep catchment than the low-slope catchment, producing a smaller intermittency value.

The best-fit parameter region had a quadratic dependence on q_b/q_{bc} and a linear dependence on I (Figure 9.4b). In general, bedrock channels have intermittencies much lower than values observed in alluvial channels (Hayden et al., 2021). This may be because bedrock channels do not have extensive floodplains, so floods with higher discharge are able to exert more shear stress on the channel bed and move more sediment than alluvial rivers, where increasing the flow depth above bankfull causes flooding and little increase in channel sediment transport capacity. Moreover, floods must be sufficient to strip the boulder cover and expose bedrock to wear to cause geomorphic work, whereas in alluvial channels only need to exceed the transport threshold. Alluvial rivers typically erode and deposit sediment simultaneously on opposite banks during their channel forming floods, and their channel geometry evolution can be driven by deposition as well as erosion. In contrast, bedrock channel geometries are shaped only by erosion and not deposition, and any sedimentary gravel bar deposits are transient features (Beer et al., 2017). Therefore, bedrock channels are

more sensitive to large erosional events that have a lower intermittency while alluvial rivers are sensitive to more frequent events that cause both erosion and deposition.

Our results indicate that bedrock river incision is highly intermittent, and that a characteristic bankfull flood lasting <0.5% of a year would be sufficient to produce average incision rates for bedrock rivers in our global compilation. This is much lower than alluvial river intermittencies, implying that bedrock channels will adjust their geometries over lower frequency, higher magnitude events when compared to downstream alluvial systems, even when their slope and bed grain sizes are similar. Alluvial rivers are typically shaped by more moderate floods, which accomplish the majority of sediment transport and geomorphic work in these systems (Leopold et al., 1964; Wolman & Miller, 1960), while these same floods would cause little change in channel geometry for upstream bedrock reaches. Instead, our model implies that large and infrequent floods should shape bedrock channels, in support of previous modeling efforts (DiBiase & Whipple, 2011; Lague et al., 2005; Sklar & Dietrich, 2006). The infrequency of these large floods means that their deposits in the downstream alluvial reach will be subsequently re-worked and deposits preserving more moderate events will be preserved in floodplain stratigraphic record (Ganti et al., 2020). Therefore, coupled bedrock and alluvial rivers are expected to be sensitive to different portions of river hydrographs and the bedrock-alluvial transition might be a key location where signals of changing climate become shredded and erased from the geologic record (Jerolmack & Paola, 2010).

9.7 Conclusions

In this study, we developed a closure for the saltation-abrasion model using bedrock channel hydraulics. We then used the saltation-abrasion model to calculate erosion rates from a global data compilation of co-located bedrock channel grain sizes and geometries, and compared modeled rates with ^{10}Be cosmogenic erosion rates to constrain the intermittency of bedrock river incision. Using a fitted relation where channel slope is inverse to characteristic flood intermittency accounted for approximately half the variance in measured erosion rates. Assuming a moderate sediment supply, we found that bedrock river systems had intermittency factors of order 10^{-3}. These intermittencies are lower than those for alluvial river bed-material load transport, indicating that alluvial rivers transport sediment with greater frequency than bedrock rivers incise their beds. Our supply-normalized intermittency relation enables landscape-scale modeling of bedrock river incision using the saltation-abrasion model.

9.8 Appendix 1

Table 9.1 Symbol definition list for model input and output parameters.

Variable	Parameter Name	Units	Value Used
ρ_s	Sediment density	kg/m^3	2650
ρ	Water density	kg/m^3	1000
R	Sediment submerged specific gravity, R $= (\rho_s - \rho)/\rho$	dimensionless	1.65

Y	Young's modulus	MPa	5×10^4
k_v	Rock erodibility coefficient	dimensionless	10^6
σ_T	Bedrock tensile strength	MPa	7
g	Gravitational acceleration	m/s^2	9.81
τ_T	Total shear stress	Pa	100
τ_W	Wall shear stress	Pa	50
τ_M	Morphological drag	Pa	0
φ_0	Internal friction angle	°	60°
a_1	Empirical coefficient in equation (9.9)	dimensionless	6.5
a_2	Empirical coefficient in equation (9.9)	dimensionless	2.5
C_D	Drag coefficient	dimensionless	0.9
F_L/F_D	Ratio of lift to drag force on particle	dimensionless	0.85
K_w	Fitted coefficient in equation (9.13)	dimensionless	1.16
H	Characteristic flood depth	m	Site-specific
W	Channel width	m	Site-specific
Q	Characteristic flood water discharge	m^3/s	Site-specific
S	Channel slope	m/m	Site-specific
β	Channel slope	°	Site-specifc
D	Median grain size	m	Site-specific
D_{84}	84th percentile grain size	m	Site-specific
C_f	Coefficient of friction	dimensionless	Site-specific
P	Mean annual precipitation	m/s	Site-specific
A	Drainage area	m^2	Site-specific
E_{10Be}	Cosmogenic erosion rate	m/s	Site-specific
q_{bc}	Bedload transport capacity	m^2/s	Site-specific
q_b	Bedload sediment flux	m^2/s	Unknown
I	Bedrock incision intermittency	dimensionless	Unknown
E	Instantaneous erosion rate	m/s	Model output
E_L	Long-term erosion rate	m/kyr	Model output
I_B	Saltation impacts per unit channel width	impacts/s/m^2	Model output
V	Volume of rock eroded per impact	m^3/impact	Model output
F	Fraction of exposed bedrock on channel bed	dimensionless	Model output
ρ_a	Aerated water density	kg/m^3	Model output
q_b	Width-normalized bedload transport	m^2/s	Model output
q_{bc}	Width-normalized bedload transport capacity	m^2/s	Model output
w_i	Sediment vertical impact velocity	m/s	Model output
I_s	Supply-normalized intermittency	dimensionless	Model output
L_b	Characteristic saltation hop length	m	Model output
τ^*	Shields stress	dimensionless	Model output
τ^*_c	Critical Shields stress	dimensionless	Model output
U	Mean water velocity	m/s	Model output
S_{crit}	Critical slope for sediment entrainment	m/m	Model output

9.9 Supplementary Materials
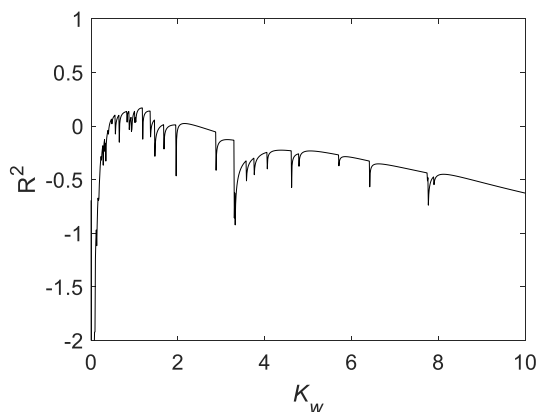
Figure 9.S1. Values of R^2 for fitting measured versus modeled erosion rates calculated with varying K_w and using $c = 0.5$, $I = 4.50 \times 10^{-3}$. The line is jagged because changing K_w alters the characteristic flow depth, and points with flow depths insufficient to mobilize their bed sediment are excluded from the fit.

Table 9.S1. The complete data compilation used in Chapter 9 analysis is available for download as "SupplementalTableS9_1.csv" at https://thesis.library.caltech.edu/.

C h a p t e r   1 0

CONCLUSIONS

In this thesis, I addressed three themes: permafrost fluvial morphodynamics and floodplain biogeochemistry, fluvial morphodynamics in the absence of plants, and the intermittency of bedrock river incision. Here, I summarize the main findings of each chapter and reflect on their broader implications for landscape evolution.

10.1 Permafrost riverbank erosion

In Chapters 2-4 of my thesis, I used physical experiments and numerical modeling to develop and test a model of permafrost riverbank erosion against field observations. I found that previous work had not accurately accounted for bank roughness in cases when bank erosion is thaw-limited (Chapter 3). However, using representative water temperature and discharge curves for the Yukon River at Stevens Village, I found that the calibrated thaw-limited erosion model significantly over-predicts bank erosion rates (Figure 10.1). Therefore, I proposed that bank erosion can be limited by sediment entrainment, which produces erosion rates within the range of observed values (Figure 10.1c). I then developed a model that tracks the bank front as well as the thaw front within the bank (Chapter 4). For unstable banks that collapse after thawing a small distance, the model predicts that rapid erosion sensitive to water temperature can occur, even when bank thaw is more rapid than sediment entrainment. Together, these models provide quantitative predictions of how bank erosion rates might respond to changes the magnitude and temporal patterns of river discharge and temperature.

These results imply that bank erosion rates will increase in tandem with rising Arctic river discharges and temperatures. Depending on whether bar deposition rates increase as well, it is possible that permafrost rivers will significantly widen over the coming years. For local communities, river widening and potential shallowing would decrease channel navigability, disrupt fish habitat, and potentially cause the formation of mid-channel bars. These changes would negatively impact the quality of life and access to natural and imported resources for remote communities. River widening would also have profound implications for Arctic biogeochemical cycles, as a pulse of sediment, organic carbon, and pollutants would originate from rapidly eroding banks. The duration of this pulse would reflect the time required for the river to adjust to its new characteristic width and depth. Depending on the transit times of water and sediment through Arctic catchments, it may take decades to centuries for the signal of this landscape change to reach active monitoring stations, which are primarily located near river deltas. Therefore, evidence of significant permafrost thaw and landscape change will only be detected using current monitoring networks long after these changes occur.
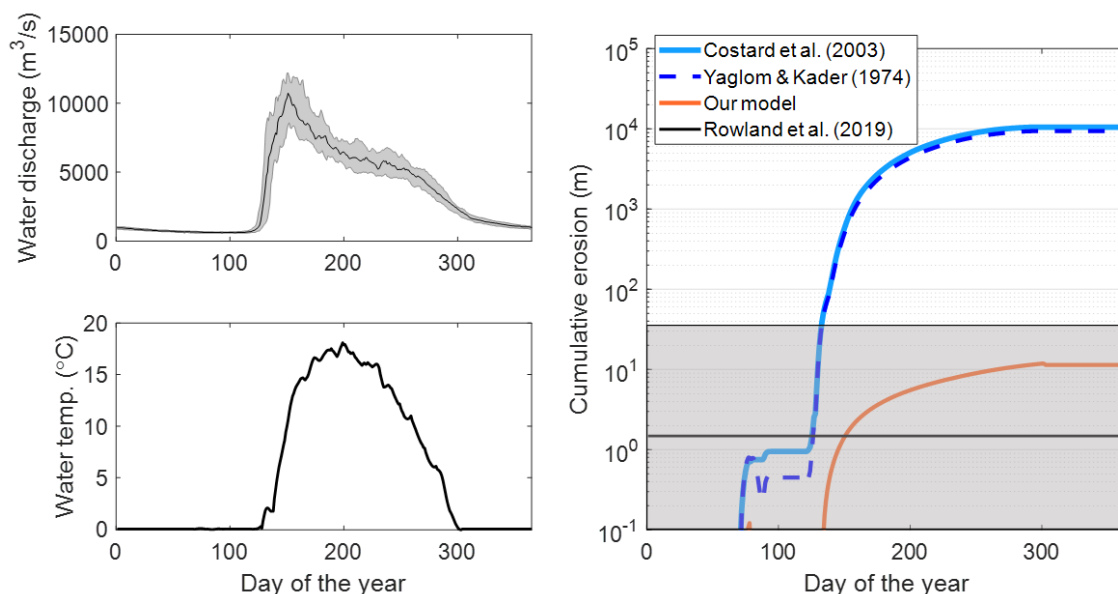
Figure 10.1. Predicted bank erosion rates for the Yukon River at Stevens Village, Alaska. **(a)** A median annual hydrograph from USGS gage data. **(b)** Median measured annual water temperature. **(c)** Cumulative bank erosion modeled using thaw-limited bank erosion with heat transfer parameterized by Costard et al. (2003) (previous state-of-the-art), thaw-limited erosion with heat transfer parameterized by Yaglom & Kader (1974) (from experiments in Chapter 3), and our model of thaw- and entrainment-limited erosion with heat transfer parameterized using Yaglom & Kader (1974) (from models in Chapters 2 and 4). The mean and range of observed riverbank erosion rates from 1978-2018 is shown as a black bar with a shaded grey band (Rowland et al., 2019).

10.2 Permafrost floodplain biogeochemistry

To investigate the relation between river channel migration and permafrost floodplain biogeochemistry, I conducted fieldwork and analyzed samples from the Koyukuk River floodplain near Huslia, Alaska. The key results of these studies included that permafrost and methanogenic microbes are more prevalent on older floodplain deposits compared to younger ones. In addition, organic carbon stocks were relatively similar across the floodplain, in part because a significant fraction of organic carbon eroded from riverbanks was subsequently deposited in bars.

Despite these contributions, significant work remains to understand the interplay between biogeochemical cycles and geomorphology in Arctic floodplains. While I documented the presence of microbial communities capable of producing methane located in permafrost regions of the floodplain, their activity must be demonstrated using in-situ flux chamber measurements. In addition, my discussion of organic carbon stocks across the floodplain did not include a detailed analysis of the variations in OC stock with landforms. Using correlations between floodplain landforms and OC stocks in combination with masks of channel erosion and deposition obtained from satellite imagery, a more complete 3D

understanding of particulate OC erosion and deposition in the Koyukuk can be obtained. Combining this analysis with consideration of OC stocks in above-ground biomass and woody debris transported by the river will allow a more complete understanding of floodplain carbon cycling to emerge.

10.3 River meandering without plants

Through long-term study of the Amargosa River in Death Valley, California, I found that cohesive mud enables channel meandering across a floodplain in the absence of plants. While salt crusts have also been proposed to stabilize riverbanks in arid environments that lack vegetation, I observed that salt completely dissolved during floods and did not limit fluvial sediment entrainment. This observation was supported by laboratory measurements of sediment entrainment rates made using a novel experimental setup, which matched entrainment rates calculated from field measurements.

The finding that fine sediment cohesion is sufficient to enable river meandering provides insight into hydrologic conditions on early Mars. Sinuous topographic features have been interpreted to represent inverted sedimentary deposits from early Martian rivers (Dickson et al., 2020), and some of these features appear to have barforms and cutoffs indicative of channel meandering (Matsubara et al., 2015). There is abundant evidence of clays and chemical weathering on Mars, and the formation of clay minerals might provide sufficient cohesion to enable meandering (Lapôtre et al., 2019). In addition, very fine silica powder has been successfully used to produce channel meandering in laboratory studies (Peakall et al., 2007), so very fine basalt dust produced by physical weathering might also have provided riverbank cohesion in early Mars. Further study of the deposits and basin stratigraphy in Death Valley and other arid catchments on Earth can provide analogs for fluvial deposits on Mars.

10.4 Drivers and limitations of bedrock incision

To investigate the intermittency of fluvial bedrock incision by bedload abrasion, I developed a method to solve the saltation-abrasion equation using parameters that can be measured in the field. Using catchment-averaged erosion rates calculated from [10]Be concentrations in river sediment, I inverted this method to calculate the intermittency of bedrock incision. This method provides an important step towards making physics-based bedrock erosion models applicable over landscape-scale spatial and temporal scales and moving beyond the heuristic stream power model.

Despite my contribution, significant work remains to better predict long-term erosion rates in bedrock catchments. My model only considers abrasion by bedload and needs to be extended to processes where erosion rates are well-understood (such as abrasion by suspended load) or poorly constrained (such as block plucking) depending on which processes are dominant in each catchment. In addition, my model relies on a characteristic flood shaping to river network, and it is unclear what the equivalent of a bankfull flood should be for bedrock channels, since defining the top of the riverbanks is challenging in canyon-

bound systems. While fitting long-term erosion rates to modern climates produces some agreement, there is significant scatter around this relation. I propose that one effect of changes in rainfall through climate cycles is to cause bedrock channel beds to be periodically shielded from erosion by sediment and eroded depending on the ratio of water and sediment supplied to the channel. Therefore, climates that are arid at present but were significantly wetter during glacial periods might preserve a record of larger characteristic floods through geometries that are currently protected by a thin veneer of sediment.

10.5 Reflections

This thesis examines river systems with varied climatic and tectonic histories but with striking similarities in form and process. Meandering rivers with banks stabilized by permafrost have similar hydraulic geometries to muddy, ephemeral channels on the floor of Death Valley. Despite evolving on much longer timescales, bedrock rivers follow similar hydraulic scaling relations to alluvial rivers (Phillips & Jerolmack, 2016; Whipple et al., 2013). From the Koyukuk to the Eel and Amargosa, terrestrial rivers record a history of climate and tectonics, writing in water and rock across landscapes. This thesis represents an incremental step towards reading these records to better understand Earth's past and predict its future.

REFERENCES

Afzal, N., Seena, A., & Bushra, A. (2013). Turbulent flow in a machine honed rough pipe for large Reynolds numbers: General roughness scaling laws. *Journal of Hydro-Environment Research*, *7*(1), 81–90. https://doi.org/10.1016/j.jher.2011.08.002

Aguilar, G., Carretier, S., Regard, V., Vassallo, R., Riquelme, R., & Martinod, J. (2014). Grain size-dependent 10Be concentrations in alluvial stream sediment of the Huasco Valley, a semi-arid Andes region. *Quaternary Geochronology*, *19*, 163–172. https://doi.org/10.1016/j.quageo.2013.01.011

Alaska-Pacific River Forecasting Center, N. (2023). Break Up Database [Data set]. NOAA's National Weather Service. Retrieved from https://www.weather.gov/aprfc/breakupDB?site=429

Alexander, M. T. (2008). *The Influence of Water Content on the Thermoerosion Rate of Frozen Sand in Moving Water* (Master of Science). University of Alaska, Anchorage, AK. Retrieved from https://www.proquest.com/openview/e6376000086472705b1b2e857adeba3f/1?pq-origsite=gscholar&cbl=18750

Allan, J., Ronholm, J., Mykytczuk, N. C. S., Greer, C. W., Onstott, T. C., & Whyte, L. G. (2014). Methanogen community composition and rates of methane consumption in Canadian High Arctic permafrost soils. *Environmental Microbiology Reports*, *6*(2), 136–144. https://doi.org/10.1111/1758-2229.12139

Alley, R. B. (2004). GISP2 ice core temperature and accumulation data. *IGBP PAGES/World Data Center for Paleoclimatology Data Contribution Series*, *13*, 2004.

Almeida, R. P. de, Marconato, A., Freitas, B. T., & Turra, B. B. (2016). The ancestors of meandering rivers. *Geology*, *44*(3), 203–206. https://doi.org/10.1130/G37534.1

Anderson, D. E. (2005). Holocene fluvial geomorphology of the Amargosa River through Amargosa Canyon, California. *Earth-Science Reviews*, *73*(1), 291–307. https://doi.org/10.1016/j.earscirev.2005.04.010

Anisimov, O. A., Shiklomanov, N. I., & Nelson, F. E. (1997). Global warming and active-layer thickness: results from transient general circulation models. *Global and Planetary Change*, *15*(3), 61–77. https://doi.org/10.1016/S0921-8181(97)00009-X

Ansberque, C., Godard, V., Bellier, O., De Sigoyer, J., Liu-Zeng, J., Xu, X., et al. (2015). Denudation pattern across the Longriba fault system and implications for the geomorphological evolution of the eastern Tibetan margin. *Geomorphology*, *246*, 542–557. https://doi.org/10.1016/j.geomorph.2015.07.017

Arcement, G. J., & Schneider, V. R. (1989). *Guide for selecting Manning's roughness coefficients for natural channels and flood plains* (No. 2339). *Water Supply Paper*. U.S. G.P.O.; U.S. Geological Survey,. https://doi.org/10.3133/wsp2339

Arenson, L. U., & Springman, S. M. (2005). Triaxial constant stress and constant strain rate tests on ice-rich permafrost samples. *Canadian Geotechnical Journal*, *42*(2), 412–430. https://doi.org/10.1139/t04-111

Arnold, L. J., & Roberts, R. G. (2009). Stochastic modelling of multi-grain equivalent dose (De) distributions: Implications for OSL dating of sediment mixtures. *Quaternary Geochronology*, *4*(3), 204–230. https://doi.org/10.1016/j.quageo.2008.12.001

Ashmore, P., & Church, M. (2001). *The Impact of Climate Change on Rivers and River Processes in Canada* (Geological Survey of Canada Bulletin No. 555) (p. 58). Canada: Natural Resources.

Ashton, G. D., & Kennedy, J. F. (1972). Ripples on underside of river ice covers. *Journal of the Hydraulics Division*, *98*(9), 1603–1624. https://doi.org/10.1061/JYCEAJ.0003407

Attal, M., Mudd, S. M., Hurst, M. D., Weinman, B., Yoo, K., & Naylor, M. (2015). Impact of change in erosion rate and landscape steepness on hillslope and fluvial sediments grain size in the Feather River basin (Sierra Nevada, California). *Earth Surface Dynamics*, *3*(1), 201–222. https://doi.org/10.5194/esurf-3-201-2015

Baldridge, A. M., Farmer, J. D., & Moersch, J. E. (2004). Mars remote-sensing analog studies in the Badwater Basin, Death Valley, California. *Journal of Geophysical Research: Planets*, *109*(E12). https://doi.org/10.1029/2004JE002315

Barbier, B. A., Dziduch, I., Liebner, S., Ganzert, L., Lantuit, H., Pollard, W., & Wagner, D. (2012). Methane-cycling communities in a permafrost-affected soil on Herschel Island, Western Canadian Arctic: Active layer profiling of mcrA and pmoA genes. *FEMS Microbiology Ecology*, *82*(2), 287–302. https://doi.org/10.1111/j.1574-6941.2012.01332.x

Barclay, D. J., Wiles, G. C., & Calkin, P. E. (2009). Holocene glacier fluctuations in Alaska. *Quaternary Science Reviews*, *28*(21), 2034–2048. https://doi.org/10.1016/j.quascirev.2009.01.016

Barnhart, K. R., Anderson, R. S., Overeem, I., Wobus, C., Clow, G. D., & Urban, F. E. (2014). Modeling erosion of ice-rich permafrost bluffs along the Alaskan Beaufort Sea coast. *Journal of Geophysical Research: Earth Surface*, *119*(5), 1155–1179. https://doi.org/10.1002/2013JF002845

Barree, R. D., & Conway, M. W. (2004). Beyond beta factors: A complete model for Darcy, Forchheimer, and trans-Forchheimer flow in porous media. Presented at the SPE Annual Technical Conference and Exhibition, OnePetro. https://doi.org/10.2118/89325-MS

Bear, J. (1972). *Dynamics of Fluids in Porous Media* (Vol. 61). Cambridge University Press. Retrieved from

https://www.cambridge.org/core/journals/journal-of-fluid-mechanics/article/dynamics-of-fluids-in-porous-media-by-jacob-bear-elsevier-1972-764-pp-dfk-9400-fundamentals-of-transport-phenomena-in-porous-media-elsevier-1972-392-pp-dfl-6500-differential-equations-of-hydraulic-transients-dispersion-and-ground-water-flow-by-wenhsiung-li-prenticehall-1972-316-pp-895/E8AAB08708A55D451C600A86AC144A53

Beckermann, C., & Viskanta, R. (1988). Natural convection solid/liquid phase change in porous media. *International Journal of Heat and Mass Transfer*, *31*(1), 35–46. https://doi.org/10.1016/0017-9310(88)90220-7

Beel, C. R., Lamoureux, S. F., Orwin, J. F., Pope, M. A., Lafrenière, M. J., & Scott, N. A. (2020). Differential impact of thermal and physical permafrost disturbances on High Arctic dissolved and particulate fluvial fluxes. *Scientific Reports*, *10*(1), 11836. https://doi.org/10.1038/s41598-020-68824-3

Beer, A. R., & Lamb, M. P. (2021). Abrasion regimes in fluvial bedrock incision. *Geology*, *49*(6), 682–386. https://doi.org/10.1130/G48466.1

Beer, Alexander. R., Turowski, J. M., & Kirchner, J. W. (2017). Spatial patterns of erosion in a bedrock gorge. *Journal of Geophysical Research: Earth Surface*, *122*(1), 191–214. https://doi.org/10.1002/2016JF003850

Behnke, M. I., McClelland, J. W., Tank, S. E., Kellerman, A. M., Holmes, R. M., Haghipour, N., et al. (2021). Pan-Arctic riverine dissolved organic matter: Synchronous molecular stability, shifting sources and subsidies. *Global Biogeochemical Cycles*, *35*(4), e2020GB006871. https://doi.org/10.1029/2020GB006871

Beltaos, S., & Burrell, B. C. (2021). Effects of river-ice breakup on sediment transport and implications to stream environments: A review. *Water*, *13*(18), 2541. https://doi.org/10.3390/w13182541

Best, J. (2019). Anthropogenic stresses on the world's big rivers. *Nature Geoscience*, *12*(1), 7–21. https://doi.org/10.1038/s41561-018-0262-x

Biskaborn, B. K., Lanckman, J.-P., Lantuit, H., Elger, K., Streletskiy, D. A., Cable, W. L., & Romanovsky, V. E. (2015). The new database of the Global Terrestrial Network for Permafrost (GTN-P). *Earth System Science Data*, *7*(2), 245–259. https://doi.org/10.5194/essd-7-245-2015

Biskaborn, Boris K., Smith, S. L., Noetzli, J., Matthes, H., Vieira, G., Streletskiy, D. A., et al. (2019). Permafrost is warming at a global scale. *Nature Communications*, *10*(1), 1–11. https://doi.org/10.1038/s41467-018-08240-4

Blaen, P. J., Hannah, D. M., Brown, L. E., & Milner, A. M. (2013). Water temperature dynamics in High Arctic river basins. *Hydrological Processes*, *27*(20), 2958–2972. https://doi.org/10.1002/hyp.9431

Blair, N. E., Leithold, E. L., Ford, S. T., Peeler, K. A., Holmes, J. C., & Perkey, D. W. (2003). The persistence of memory: The fate of ancient sedimentary organic carbon in a modern sedimentary system. *Geochimica et*

Cosmochimica Acta, *67*(1), 63–73. https://doi.org/10.1016/S0016-7037(02)01043-8

Blake, L. I., Tveit, A., Øvreås, L., Head, I. M., & Gray, N. D. (2015). Response of methanogens in arctic sediments to temperature and methanogenic substrate availability. *PLOS ONE*, *10*(6), e0129733. https://doi.org/10.1371/journal.pone.0129733

von Blanckenburg, F. (2005). The control mechanisms of erosion and weathering at basin scale from cosmogenic nuclides in river sediment. *Earth and Planetary Science Letters*, *237*(3–4), 462–479. https://doi.org/10.1016/j.epsl.2005.06.030

Blasius, H. (1950). *The Boundary Layers in Fluids with Little Friction* (No. NACA-TM-1256). Retrieved from https://ntrs.nasa.gov/citations/20050028493

Bonales, L. J., Rodriguez, A. C., & Sanz, P. D. (2017). Thermal conductivity of ice prepared under different conditions. *International Journal of Food Properties*, *20*(sup1), 610–619. https://doi.org/10.1080/10942912.2017.1306551

Bøtter-Jensen, L., Bulur, E., Duller, G. A. T., & Murray, A. S. (2000). Advances in luminescence instrument systems. *Radiation Measurements*, *32*(5), 523–528. https://doi.org/10.1016/S1350-4487(00)00039-1

Bøtter-Jensen, L., Andersen, C. E., Duller, G. A. T., & Murray, A. S. (2003). Developments in radiation, stimulation and observation facilities in luminescence measurements. *Radiation Measurements*, *37*(4), 535–541. https://doi.org/10.1016/S1350-4487(03)00020-9

Bouchez, J., Beyssac, O., Galy, V., Gaillardet, J., France-Lanord, C., Maurice, L., & Moreira-Turcq, P. (2010). Oxidation of petrogenic organic carbon in the Amazon floodplain as a source of atmospheric CO2. *Geology*, *38*(3), 255–258. https://doi.org/10.1130/G30608.1

Brabets, T. P., & Walvoord, M. A. (2009). Trends in streamflow in the Yukon River Basin from 1944 to 2005 and the influence of the Pacific Decadal Oscillation. *Journal of Hydrology*, *371*(1), 108–119. https://doi.org/10.1016/j.jhydrol.2009.03.018

Brabets, T. P., Wang, B., & Meade, R. H. (2000). *Environmental and hydrologic overview of the Yukon River Basin, Alaska and Canada* (Vol. 99). US Department of the Interior, US Geological Survey. Retrieved from https://pubs.usgs.gov/wri/wri994204/

Bragg, R. A., & Andersland, O. B. (1981). Strain rate, temperature, and sample size effects on compression and tensile properties of frozen sand. *Engineering Geology*, *18*(1), 35–46. https://doi.org/10.1016/0013-7952(81)90044-2

Braudrick, C. A., Dietrich, W. E., Leverich, G. T., & Sklar, L. S. (2009). Experimental evidence for the conditions necessary to sustain meandering in coarse-bedded rivers. *Proceedings of the National Academy of Sciences*, *106*(40), 16936–16941. https://doi.org/10.1073/pnas.0909417106

Bronen, R., & Chapin, F. S. (2013). Adaptive governance and institutional strategies for climate-induced community relocations in Alaska. *Proceedings of the National Academy of Sciences*, *110*(23), 9320–9325. https://doi.org/10.1073/pnas.1210508110

Burkert, A., Douglas, T. A., Waldrop, M. P., & Mackelprang, R. (2019). Changes in the active, dead, and dormant microbial community structure across a pleistocene permafrost chronosequence. *Applied and Environmental Microbiology*, *85*(7). https://doi.org/10.1128/AEM.02646-18

Bushuk, M., Holland, D. M., Stanton, T. P., Stern, A., & Gray, C. (2019). Ice scallops: A laboratory investigation of the ice–water interface. *Journal of Fluid Mechanics*, *873*, 942–976. https://doi.org/10.1017/jfm.2019.398

Camporeale, C., & Ridolfi, L. (2012). Ice ripple formation at large Reynolds numbers. *Journal of Fluid Mechanics*, *694*, 225–251. https://doi.org/10.1017/jfm.2011.540

Caporaso, J. G., Kuczynski, J., Stombaugh, J., Bittinger, K., Bushman, F. D., Costello, E. K., et al. (2010). QIIME allows analysis of high-throughput community sequencing data. *Nature Methods*, *7*(5), 335–336. https://doi.org/10.1038/nmeth.f.303

Chatanantavet, P., & Lamb, M. P. (2014). Sediment transport and topographic evolution of a coupled river and river plume system: An experimental and numerical study. *Journal of Geophysical Research: Earth Surface*, *119*(6), 1263–1282. https://doi.org/10.1002/2013JF002810

Chatanantavet, P., & Parker, G. (2008). Experimental study of bedrock channel alluviation under varied sediment supply and hydraulic conditions. *Water Resources Research*, *44*(12). https://doi.org/10.1029/2007WR006581

Chatanantavet, P., & Parker, G. (2009). Physically based modeling of bedrock incision by abrasion, plucking, and macroabrasion. *Journal of Geophysical Research: Earth Surface*, *114*(F4), F04018. https://doi.org/10.1029/2008JF001044

Chatanantavet, P., & Parker, G. (2011). Quantitative testing of model of bedrock channel incision by plucking and macroabrasion. *Journal of Hydraulic Engineering*, *137*(11), 1311–1317. https://doi.org/10.1061/(ASCE)HY.1943-7900.0000421

Clement, D. T. (1999). *Fluvial Geomorphology of the Yukon River, Yukon Flats, Alaska* (Master of Science). University of Calgary, Calgary, Alberta.

Colarossi, D., Duller, G. A. T., Roberts, H. M., Tooth, S., & Lyons, R. (2015). Comparison of paired quartz OSL and feldspar post-IR IRSL dose distributions in poorly bleached fluvial sediments from South Africa. *Quaternary Geochronology*, *30*, 233–238. https://doi.org/10.1016/j.quageo.2015.02.015

Cook, K. L., Turowski, J. M., & Hovius, N. (2014). River gorge eradication by downstream sweep erosion. *Nature Geoscience*, *7*(9), 682–686. https://doi.org/10.1038/ngeo2224

Coolen, M. J. L., & Orsi, W. D. (2015). The transcriptional response of microbial communities in thawing Alaskan permafrost soils. *Frontiers in Microbiology*, *6*. https://doi.org/10.3389/fmicb.2015.00197

Corenblit, D., & Steiger, J. (2009). Vegetation as a major conductor of geomorphic changes on the Earth surface: toward evolutionary geomorphology. *Earth Surface Processes and Landforms*, *34*(6), 891–896. https://doi.org/10.1002/esp.1788

Costard, F., Dupeyrat, L., Gautier, E., & Carey-Gailhardis, E. (2003). Fluvial thermal erosion investigations along a rapidly eroding river bank: Application to the Lena River (central Siberia). *Earth Surface Processes and Landforms*, *28*(12), 1349–1359. https://doi.org/10.1002/esp.592

Costard, F., Gautier, E., Fedorov, A., Konstantinov, P., & Dupeyrat, L. (2014). An assessment of the erosion potential of the fluvial thermal process during ice breakups of the Lena River (Siberia). *Permafrost and Periglacial Processes*, *25*(3), 162–171.

Crampton, C. B. (1979). Changes in permafrost distribution produced by a migrating river meander in the northern Yukon, Canada. *Arctic*, *32*(2), 148–151.

Crevecoeur, S., Vincent, W. F., Comte, J., Matveev, A., & Lovejoy, C. (2017). Diversity and potential activity of methanotrophs in high methane-emitting permafrost thaw ponds. *PLOS ONE*, *12*(11), e0188223. https://doi.org/10.1371/journal.pone.0188223

Cui, X., Bianchi, T. S., Jaeger, J. M., & Smith, R. W. (2016). Biospheric and petrogenic organic carbon flux along southeast Alaska. *Earth and Planetary Science Letters*, *452*, 238–246. https://doi.org/10.1016/j.epsl.2016.08.002

Cyr, A. J., Granger, D. E., Olivetti, V., & Molin, P. (2010). Quantifying rock uplift rates using channel steepness and cosmogenic nuclide–determined erosion rates: Examples from northern and southern Italy. *Lithosphere*, *2*(3), 188–198. https://doi.org/10.1130/L96.1

Czuba, J. A., David, S. R., Edmonds, D. A., & Ward, A. S. (2019). Dynamics of surface-water connectivity in a low-gradient meandering river floodplain. *Water Resources Research*, *55*(3), 1849–1870. https://doi.org/10.1029/2018WR023527

Daly, C., Smith, J. I., & Olson, K. V. (2015). Mapping atmospheric moisture climatologies across the co-terminous United States. *PLOS ONE*, *10*(10), e0141140. https://doi.org/10.1371/journal.pone.0141140

Daly, C., Smith, J., & Halbleib, M. (2018). 1981-2010 High-Resolution Temperature and Precipitation Maps for Alaska Final Report, 43.

Daniels, W. C., Russell, J. M., Morrill, C., Longo, W. M., Giblin, A. E., Holland-Stergar, P., et al. (2021). Lacustrine leaf wax hydrogen isotopes indicate strong regional climate feedbacks in Beringia since the last ice age. *Quaternary Science Reviews*, *269*, 107130. https://doi.org/10.1016/j.quascirev.2021.107130

Darby, S. E., Trieu, H. Q., Carling, P. A., Sarkkula, J., Koponen, J., Kummu, M., et al. (2010). A physically based model to predict hydraulic erosion of fine-grained riverbanks: The role of form roughness in limiting erosion. *Journal of Geophysical Research: Earth Surface*, *115*(F4). https://doi.org/10.1029/2010JF001708

David, S. R., Edmonds, D. A., & Letsinger, S. L. (2017). Controls on the occurrence and prevalence of floodplain channels in meandering rivers. *Earth Surface Processes and Landforms*, *42*(3), 460–472. https://doi.org/10.1002/esp.4002

Davidson, E. A., Janssens, I. A., & Luo, Y. (2006). On the variability of respiration in terrestrial ecosystems: moving beyond Q_{10}. *Global Change Biology*, *12*(2), 154–164. https://doi.org/10.1111/j.1365-2486.2005.01065.x

Davies, N. S., & Gibling, M. R. (2010a). Cambrian to Devonian evolution of alluvial systems: The sedimentological impact of the earliest land plants. *Earth-Science Reviews*, *98*(3), 171–200. https://doi.org/10.1016/j.earscirev.2009.11.002

Davies, N. S., & Gibling, M. R. (2010b). Paleozoic vegetation and the Siluro-Devonian rise of fluvial lateral accretion sets. *Geology*, *38*(1), 51–54. https://doi.org/10.1130/G30443.1

Day, G., Dietrich, W. E., Rowland, J. C., & Marshall, A. (2008). The depositional web on the floodplain of the Fly River, Papua New Guinea. *Journal of Geophysical Research: Earth Surface*, *113*(F1). https://doi.org/10.1029/2006JF000622

Delisle, G. (1998). Numerical simulation of permafrost growth and decay. *Journal of Quaternary Science*, *13*(4), 325–333. https://doi.org/10.1002/(SICI)1099-1417(199807/08)13:4<325::AID-JQS385>3.0.CO;2-A

Denfeld, B. A., Frey, K. E., Sobczak, W. V., Mann, P. J., & Holmes, R. M. (2013). Summer CO_2 evasion from streams and rivers in the Kolyma River basin, north-east Siberia. *Polar Research*, *32*(1), 19704. https://doi.org/10.3402/polar.v32i0.19704

Dethier, E. N., Renshaw, C. E., & Magilligan, F. J. (2022). Rapid changes to global river suspended sediment flux by humans. *Science*, *376*(6600), 1447–1452. https://doi.org/10.1126/science.abn7980

DiBiase, R. A., & Whipple, K. X. (2011). The influence of erosion thresholds and runoff variability on the relationships among topography, climate, and erosion rate. *Journal of Geophysical Research: Earth Surface*, *116*(F4). https://doi.org/10.1029/2011JF002095

DiBiase, R. A., Whipple, K. X., Heimsath, A. M., & Ouimet, W. B. (2010). Landscape form and millennial erosion rates in the San Gabriel Mountains, CA. *Earth and Planetary Science Letters*, *289*(1), 134–144. https://doi.org/10.1016/j.epsl.2009.10.036

DiBiase, R. A., Heimsath, A. M., & Whipple, K. X. (2012). Hillslope response to tectonic forcing in threshold landscapes. *Earth Surface Processes and Landforms*, *37*(8), 855–865. https://doi.org/10.1002/esp.3205

DiBiase, R. A., Rossi, M. W., & Neely, A. B. (2018). Fracture density and grain size controls on the relief structure of bedrock landscapes. *Geology*, *46*(5), 399–402. https://doi.org/10.1130/G40006.1

Dickson, J. L., Lamb, M. P., Williams, R. M. E., Hayden, A. T., & Fischer, W. W. (2020). The global distribution of depositional rivers on early Mars. *Geology*, *49*(5), 504–509. https://doi.org/10.1130/G48457.1

Dietrich, W. E. (1982). Settling velocity of natural particles. *Water Resources Research*, *18*(6), 1615–1626. https://doi.org/10.1029/WR018i006p01615

Dietrich, W. E., Smith, J. D., & Dunne, T. (1979). Flow and Sediment Transport in a Sand Bedded Meander. *The Journal of Geology*, *87*(3), 305–315. https://doi.org/10.1086/628419

van Dijk, W. M., van de Lageweg, W. I., & Kleinhans, M. G. (2012). Experimental meandering river with chute cutoffs. *Journal of Geophysical Research: Earth Surface*, *117*(F3). https://doi.org/10.1029/2011JF002314

van Dijk, Wout M., van de Lageweg, W. I., & Kleinhans, M. G. (2013). Formation of a cohesive floodplain in a dynamic experimental meandering river. *Earth Surface Processes and Landforms*, *38*(13), 1550–1565. https://doi.org/10.1002/esp.3400

Docherty, C. L., Dugdale, S. J., Milner, A. M., Abermann, J., Lund, M., & Hannah, D. M. (2019). Arctic river temperature dynamics in a changing climate. *River Research and Applications*, *35*(8), 1212–1227. https://doi.org/10.1002/rra.3537

Domine, F., Fourteau, K., Picard, G., Lackner, G., Sarrazin, D., & Poirier, M. (2022). Permafrost cooled in winter by thermal bridging through snow-covered shrub branches. *Nature Geoscience*, *15*(7), 554–560. https://doi.org/10.1038/s41561-022-00979-2

van Dongen, R., Scherler, D., Wittmann, H., & von Blanckenburg, F. (2019). Cosmogenic 10Be in river sediment: where grain size matters and why. *Earth Surface Dynamics*, *7*(2), 393–410. https://doi.org/10.5194/esurf-7-393-2019

Douglas, M. M., Lingappa, U. F., Lamb, M. P., Rowland, J. C., West, A. J., Li, G., et al. (2021). Impact of river channel lateral migration on microbial communities across a discontinuous permafrost floodplain. *Applied and Environmental Microbiology*, *87*(20), AEM.01339-21. https://doi.org/10.1128/AEM.01339-21

Douglas, M. M., Li, G. K., Fischer, W. W., Rowland, J. C., Kemeny, P. C., West, A. J., et al. (2022). Organic carbon burial by river meandering partially offsets bank erosion carbon fluxes in a discontinuous permafrost floodplain. *Earth Surface Dynamics*, *10*(3), 421–435. https://doi.org/10.5194/esurf-10-421-2022

Douglas, M. M., Dunne, K. B. J., & Lamb, M. P. (2023). Sediment Entrainment and Slump Blocks Limit Permafrost Riverbank Erosion. *Geophysical Research Letters*, *50*(11), e2023GL102974. https://doi.org/10.1029/2023GL102974

Dumoulin, J. A., Harris, A. G., Blome, C. D., & Young, L. E. (2004). Depositional settings, correlation, and age of Carboniferous rocks in the western Brooks Range, Alaska. *Economic Geology*, *99*(7), 1355–1384. https://doi.org/10.2113/gsecongeo.99.7.1355

Dunne, K. B. J., & Jerolmack, D. J. (2020). What sets river width? *Science Advances*, *6*(41), eabc1505. https://doi.org/10.1126/sciadv.abc1505

Dupeyrat, L., Costard, F., Randriamazaoro, R., Gailhardis, E., Gautier, E., & Fedorov, A. (2011). Effects of ice content on the thermal erosion of permafrost: Implications for coastal and fluvial erosion. *Permafrost and Periglacial Processes*, *22*(2), 179–187. https://doi.org/10.1002/ppp.722

Durcan, J. A., King, G. E., & Duller, G. A. T. (2015). DRAC: Dose Rate and Age Calculator for trapped charge dating. *Quaternary Geochronology*, *28*, 54–61. https://doi.org/10.1016/j.quageo.2015.03.012

Earth Resources Observation and Science (EROS) Center. (2017). Global 30 Arc-Second Elevation (GTOPO30) [Tiff]. Digital Elevation Model (DEM), U.S. Geological Survey. https://doi.org/10.5066/F7DF6PQS

Edgar, R. C. (2010). Search and clustering orders of magnitude faster than BLAST. *Bioinformatics*, *26*(19), 2460–2461. https://doi.org/10.1093/bioinformatics/btq461

Eke, E., Parker, G., & Shimizu, Y. (2014). Numerical modeling of erosional and depositional bank processes in migrating river bends with self-formed width: Morphodynamics of bar push and bank pull. *Journal of Geophysical Research: Earth Surface*, *119*(7), 1455–1483. https://doi.org/10.1002/2013JF003020

England, M. R., Eisenman, I., Lutsko, N. J., & Wagner, T. J. W. (2021). The recent emergence of Arctic amplification. *Geophysical Research Letters*, *48*(15), e2021GL094086. https://doi.org/10.1029/2021GL094086

Ensom, T. P., Burn, C. R., & Kokelj, S. V. (2012). Lake- and channel-bottom temperatures in the Mackenzie Delta, Northwest Territories1This article is one of a series of papers published in this CJES Special Issue on the theme of Fundamental and applied research on permafrost in Canada.2Polar Continental Shelf Project Contribution 03511. *Canadian Journal of Earth Sciences*, *49*(8), 963–978. https://doi.org/10.1139/e2012-001

Ewing, S. A., O'Donnell, J. A., Aiken, G. R., Butler, K., Butman, D., Windham-Myers, L., & Kanevskiy, M. Z. (2015). Long-term anoxia and release of ancient, labile carbon upon thaw of Pleistocene permafrost. *Geophysical Research Letters*, *42*(24), 10,730-10,738. https://doi.org/10.1002/2015GL066296

Farouki, O. T. (1981). The thermal properties of soils in cold regions. *Cold Regions Science and Technology*, *5*(1), 67–75. https://doi.org/10.1016/0165-232X(81)90041-0

Ferguson, R. (2007). Flow resistance equations for gravel- and boulder-bed streams. *Water Resources Research*, *43*(5). https://doi.org/10.1029/2006WR005422

Fernandez Luque, R., & Van Beek, R. (1976). Erosion and Transport Of Bed-Load Sediment. *Journal of Hydraulic Research*, *14*(2), 127–144. https://doi.org/10.1080/00221687609499677

Ferrier, K. L., Huppert, K. L., & Perron, J. T. (2013). Climatic control of bedrock river incision. *Nature*, *496*(7444), 206–209. https://doi.org/10.1038/nature11982

Ferrier, K. L., Perron, J. T., Mukhopadhyay, S., Rosener, M., Stock, J. D., Huppert, K. L., & Slosberg, M. (2013). Covariation of climate and long-term erosion rates across a steep rainfall gradient on the Hawaiian island of Kaua'i. *GSA Bulletin*, *125*(7–8), 1146–1163. https://doi.org/10.1130/B30726.1

Fick, S. E., & Hijmans, R. J. (2017). WorldClim 2: new 1-km spatial resolution climate surfaces for global land areas. *International Journal of Climatology*, *37*(12), 4302–4315. https://doi.org/10.1002/joc.5086

Finnegan, N. J., Roe, G., Montgomery, D. R., & Hallet, B. (2005). Controls on the channel width of rivers: Implications for modeling fluvial incision of bedrock. *Geology*, *33*(3), 229–232. https://doi.org/10.1130/G21171.1

Finnegan, N. J., Klier, R. A., Johnstone, S., Pfeiffer, A. M., & Johnson, K. (2017). Field evidence for the control of grain size and sediment supply on steady-state bedrock river channel slopes in a tectonically active setting: grain size and steady-state bedrock river channel slopes. *Earth Surface Processes and Landforms*, *42*(14), 2338–2349. https://doi.org/10.1002/esp.4187

Fox, M., Goren, L., May, D. A., & Willett, S. D. (2014). Inversion of fluvial channels for paleorock uplift rates in Taiwan. *Journal of Geophysical Research: Earth Surface*, *119*(9), 1853–1875. https://doi.org/10.1002/2014JF003196

French, H., & Shur, Y. (2010). The principles of cryostratigraphy. *Earth-Science Reviews*, *101*(3), 190–206. https://doi.org/10.1016/j.earscirev.2010.04.002

Fuchs, M., Nitze, I., Strauss, J., Günther, F., Wetterich, S., Kizyakov, A., et al. (2020). Rapid fluvio-thermal erosion of a yedoma permafrost cliff in the Lena River delta. *Frontiers in Earth Science*, *8*. https://doi.org/10.3389/feart.2020.00336

Furbish, D. J. (1988). River-bend curvature and migration: How are they related? *Geology*, *16*(8), 752–755. https://doi.org/10.1130/0091-7613(1988)016<0752:RBCAMH>2.3.CO;2

Galbraith, R. F., Roberts, R. G., Laslett, G. M., Yoshida, H., & Olley, J. M. (1999). Optical dating of single and multiple grains of quartz from

Jinmium Rock Shelter, Northern Australia: Part I, Experimental Design and Statistical Models. *Archaeometry*, *41*(2), 339–364. https://doi.org/10.1111/j.1475-4754.1999.tb00987.x

Galushko, A., & Kuever, J. (2019). Syntrophus. In *Bergey's Manual of Systematics of Archaea and Bacteria* (pp. 1–6). American Cancer Society. https://doi.org/10.1002/9781118960608.gbm01064.pub2

Galy, V., & Eglinton, T. (2011). Protracted storage of biospheric carbon in the Ganges–Brahmaputra basin. *Nature Geoscience*, *4*(12), 843–847. https://doi.org/10.1038/ngeo1293

Galy, V., France-Lanord, C., Beyssac, O., Faure, P., Kudrass, H., & Palhol, F. (2007). Efficient organic carbon burial in the Bengal fan sustained by the Himalayan erosional system. *Nature*, *450*(7168), 407–410. https://doi.org/10.1038/nature06273

Galy, V., France-Lanord, C., & Lartiges, B. (2008). Loading and fate of particulate organic carbon from the Himalaya to the Ganga–Brahmaputra delta. *Geochimica et Cosmochimica Acta*, *72*(7), 1767–1787. https://doi.org/10.1016/j.gca.2008.01.027

Galy, V., Peucker-Ehrenbrink, B., & Eglinton, T. (2015). Global carbon export from the terrestrial biosphere controlled by erosion. *Nature*, *521*(7551), 204–207. https://doi.org/10.1038/nature14400

Ganti, V., Whittaker, A. C., Lamb, M. P., & Fischer, W. W. (2019). Low-gradient, single-threaded rivers prior to greening of the continents. *Proceedings of the National Academy of Sciences*, *116*(24), 11652–11657. https://doi.org/10.1073/pnas.1901642116

Ganti, V., Hajek, E. A., Leary, K., Straub, K. M., & Paola, C. (2020). Morphodynamic Hierarchy and the Fabric of the Sedimentary Record. *Geophysical Research Letters*, *47*(14), e2020GL087921. https://doi.org/10.1029/2020GL087921

Garcia, M., & Parker, G. (1991). Entrainment of bed sediment into suspension. *Journal of Hydraulic Engineering*, *117*(4), 414–435. https://doi.org/10.1061/(ASCE)0733-9429(1991)117:4(414)

Gee, G. W., & Or, D. (2002). Particle-Size Analysis. In J. H. Dane & G. C. Topp (Eds.), *Methods of Soil Analysis Part 4: Physical Methods*. Madison, WI: Soil Science Society of America, Inc.

Ghisalberti, M. (2009). Obstructed shear flows: Similarities across systems and scales. *Journal of Fluid Mechanics*, *641*, 51–61. https://doi.org/10.1017/S0022112009992175

Gilbert, G. K. (1877). *Report on the geology of the Henry mountains*. Washington, Govt. print. off. Retrieved from http://archive.org/details/reportongeology00gilbgoog

Gill, D. (1973). Modification of northern alluvial habitats by river development. *The Canadian Geographer / Le Géographe Canadien*, *17*(2), 138–153. https://doi.org/10.1111/j.1541-0064.1973.tb00079.x

Gordeev, V. V. (2006). Fluvial sediment flux to the Arctic Ocean. *Geomorphology*, *80*(1), 94–104. https://doi.org/10.1016/j.geomorph.2005.09.008

Goren, L., Fox, M., & Willett, S. D. (2014). Tectonics from fluvial topography using formal linear inversion: Theory and applications to the Inyo Mountains, California. *Journal of Geophysical Research: Earth Surface*, *119*(8), 1651–1681. https://doi.org/10.1002/2014JF003079

Gosse, J. C., & Phillips, F. M. (2001). Terrestrial in situ cosmogenic nuclides: theory and application. *Quaternary Science Reviews*, *20*(14), 1475–1560. https://doi.org/10.1016/S0277-3791(00)00171-2

Greenwald, M. J., Bowden, W. B., Gooseff, M. N., Zarnetske, J. P., McNamara, J. P., Bradford, J. H., & Brosten, T. R. (2008). Hyporheic exchange and water chemistry of two arctic tundra streams of contrasting geomorphology. *Journal of Geophysical Research: Biogeosciences*, *113*(G2). https://doi.org/10.1029/2007JG000549

Guérin, G., Mercier, N., & Adamiec, G. (2011). Dose-rate conversion factors: update. *Ancient TL*, *29*(1), 5–8.

Gulley, J. D., Spellman, P. D., Covington, M. D., Martin, J. B., Benn, D. I., & Catania, G. (2014). Large values of hydraulic roughness in subglacial conduits during conduit enlargement: implications for modeling conduit evolution. *Earth Surface Processes and Landforms*, *39*(3), 296–310. https://doi.org/10.1002/esp.3447

Hack, J. T. (1957). *Studies of Longitudinal Stream Profiles in Virginia and Maryland*. U.S. Government Printing Office.

Hajek, E. A., Heller, P. L., & Sheets, B. A. (2010). Significance of channel-belt clustering in alluvial basins. *Geology*, *38*(6), 535–538. https://doi.org/10.1130/G30783.1

Hales, B. A., Edwards, C., Ritchie, D. A., Hall, G., Pickup, R. W., & Saunders, J. R. (1996). Isolation and identification of methanogen-specific DNA from blanket bog peat by PCR amplification and sequence analysis. *Applied and Environmental Microbiology*, *62*(2), 668–675.

Hanson, G. J., & Cook, K. R. (2004). Apparatus, test procedures, and analytical methods to measure soil erodibility in situ. *Applied Engineering in Agriculture*, *20*(4), 455–462.

Hanson, G. J., & Simon, A. (2001). Erodibility of cohesive streambeds in the loess area of the midwestern USA. *Hydrological Processes*, *15*(1), 23–38. https://doi.org/10.1002/hyp.149

Harel, M.-A., Mudd, S. M., & Attal, M. (2016). Global analysis of the stream power law parameters based on worldwide 10Be denudation rates. *Geomorphology*, *268*, 184–196. https://doi.org/10.1016/j.geomorph.2016.05.035

Haroon, M. F., Hu, S., Shi, Y., Imelfort, M., Keller, J., Hugenholtz, P., et al. (2013). Anaerobic oxidation of methane coupled to nitrate reduction in a

novel archaeal lineage. *Nature*, *500*(7464), 567–570. https://doi.org/10.1038/nature12375

Hayden, A. T., Lamb, M. P., & McElroy, B. J. (2021). Constraining the timespan of fluvial activity from the intermittency of sediment transport on Earth and Mars. *Geophysical Research Letters*, *48*(16), e2021GL092598. https://doi.org/10.1029/2021GL092598

Hemingway, J. D., Hilton, R. G., Hovius, N., Eglinton, T. I., Haghipour, N., Wacker, L., et al. (2018). Microbial oxidation of lithospheric organic carbon in rapidly eroding tropical mountain soils. *Science*, *360*(6385), 209–212. https://doi.org/10.1126/science.aao6463

Hilton, R. G., Galy, V., Gaillardet, J., Dellinger, M., Bryant, C., O'Regan, M., et al. (2015). Erosion of organic carbon in the Arctic as a geological carbon dioxide sink. *Nature*, *524*(7563), 84. https://doi.org/10.1038/nature14653

Hjort, J., Karjalainen, O., Aalto, J., Westermann, S., Romanovsky, V. E., Nelson, F. E., et al. (2018). Degrading permafrost puts Arctic infrastructure at risk by mid-century. *Nature Communications*, *9*(1), 5147. https://doi.org/10.1038/s41467-018-07557-4

Hodgkins, S. B., Chanton, J. P., Langford, L. C., McCalley, C. K., Saleska, S. R., Rich, V. I., et al. (2015). Soil incubations reproduce field methane dynamics in a subarctic wetland. *Biogeochemistry*, *126*(1), 241–249. https://doi.org/10.1007/s10533-015-0142-z

Hollingshead, G., L, S., & La, R. (1978). Permafrost Beneath Channels in the Mackenzie Delta, N.W.T., Canada, 406–412.

Holmes, R. M., McClelland, J. W., Peterson, B. J., Tank, S. E., Bulygina, E., Eglinton, T. I., et al. (2012). Seasonal and annual fluxes of nutrients and organic matter from large rivers to the Arctic Ocean and surrounding seas. *Estuaries and Coasts*, *35*(2), 369–382. https://doi.org/10.1007/s12237-011-9386-6

Hooke, R. L. (1972). Geomorphic evidence for late-Wisconsin and Holocene tectonic deformation, Death Valley, California. *GSA Bulletin*, *83*(7), 2073–2098. https://doi.org/10.1130/0016-7606(1972)83[2073:GEFLAH]2.0.CO;2

Horan, K., Hilton, R. G., Dellinger, M., Tipper, E., Galy, V., Calmels, D., et al. (2019). Carbon dioxide emissions by rock organic carbon oxidation and the net geochemical carbon budget of the Mackenzie River Basin. *American Journal of Science*, *319*(6), 473–499. https://doi.org/10.2475/06.2019.02

Howard, A. D., & Kerby, G. (1983). Channel changes in badlands. *GSA Bulletin*, *94*(6), 739–752. https://doi.org/10.1130/0016-7606(1983)94<739:CCIB>2.0.CO;2

Howard, A. D., & Knutson, T. R. (1984). Sufficient conditions for river meandering: A simulation approach. *Water Resources Research*, *20*(11), 1659–1667. https://doi.org/10.1029/WR020i011p01659

Hsu, C. T., & Cheng, P. (1990). Thermal dispersion in a porous medium. *International Journal of Heat and Mass Transfer*, *33*(8), 1587–1597.

Hua, Q., Turnbull, J. C., Santos, G. M., Rakowski, A. Z., Ancapichún, S., Pol-Holz, R. D., et al. (2022). Atmospheric radiocarbon for the period 1950–2019. *Radiocarbon*, *64*(4), 723–745. https://doi.org/10.1017/RDC.2021.95

Hugelius, G., Strauss, J., Zubrzycki, S., Harden, J. W., Schuur, E. a. G., Ping, C.-L., et al. (2014). Estimated stocks of circumpolar permafrost carbon with quantified uncertainty ranges and identified data gaps. *Biogeosciences*, *11*(23), 6573–6593. https://doi.org/10.5194/bg-11-6573-2014

Ielpi, A. (2018). Morphodynamics of meandering streams devoid of plant life: Amargosa River, Death Valley, California. *GSA Bulletin*, *131*(5–6), 782–802. https://doi.org/10.1130/B31960.1

Ielpi, A., & Lapôtre, M. G. A. (2019). Barren meandering streams in the modern Toiyabe Basin of Nevada, U.S.A., and their relevance to the study of the pre-vegetation rock record. *Journal of Sedimentary Research*, *89*(5), 399–415. https://doi.org/10.2110/jsr.2019.25

Ielpi, A., & Lapôtre, M. G. A. (2020). A tenfold slowdown in river meander migration driven by plant life. *Nature Geoscience*, *13*(1), 82–86. https://doi.org/10.1038/s41561-019-0491-7

Ielpi, A., Lapôtre, M. G. A., Finotello, A., Ghinassi, M., & D'Alpaos, A. (2020). Channel mobility drives a diverse stratigraphic architecture in the dryland Mojave River (California, USA). *Earth Surface Processes and Landforms*, *45*(8), 1717–1731. https://doi.org/10.1002/esp.4841

Ielpi, A., Lapôtre, M. G. A., Finotello, A., & Roy-Léveillée, P. (2023). Large sinuous rivers are slowing down in a warming Arctic. *Nature Climate Change*, 1–7. https://doi.org/10.1038/s41558-023-01620-9

Ielpi, Alessandro & Rainbird, Robert H. (2015). Architecture and morphodynamics of a 1.6 Ga fluvial sandstone: Ellice Formation of Elu Basin, Arctic Canada. *Sedimentology*, *62*(7), 1950–1977. https://doi.org/10.1111/sed.12211

Isaksen, K., Romanovsky, V., Smith, S. L., & Drozdov, D. S. (2016). Thermal state of permafrost across the circumpolar permafrost regions–results from the latest assessment report, the SWIPA update. In F. Günther & A. Morgenstern (Eds.), *XI International Conference on Permafrost, book of abstracts* (pp. 444–445). Potsdam, DE: Bibliothek Wissenschaftspark Albert Einstein.

Ishii, Y., & Hori, K. (2016). Formation and infilling of oxbow lakes in the Ishikari lowland, northern Japan. *Quaternary International*, *397*, 136–146. https://doi.org/10.1016/j.quaint.2015.06.016

Jafarov, E. E., Coon, E. T., Harp, D. R., Wilson, C. J., Painter, S. L., Atchley, A. L., & Romanovsky, V. E. (2018). Modeling the role of preferential snow accumulation in through talik development and hillslope groundwater flow in a transitional permafrost landscape. *Environmental Research Letters*, *13*(10), 105006. https://doi.org/10.1088/1748-9326/aadd30

Jain, M., Murray, A. S., & Botter-Jensen, L. (2004). Optically stimulated luminescence dating: how significant is incomplete light exposure in fluvial environments? [Datation par luminescence stimulée optiquement : quelle signification en cas de blanchiment incomplet des sédiments fluviatiles ?]. *Quaternaire*, *15*(1), 143–157. https://doi.org/10.3406/quate.2004.1762

Jansson, J. K., & Taş, N. (2014). The microbial ecology of permafrost. *Nature Reviews Microbiology*, *12*(6), 414–425. https://doi.org/10.1038/nrmicro3262

Jensen, B. J. L., Evans, M. E., Froese, D. G., & Kravchinsky, V. A. (2016). 150,000 years of loess accumulation in central Alaska. *Quaternary Science Reviews*, *135*, 1–23. https://doi.org/10.1016/j.quascirev.2016.01.001

Jerolmack, D. J., & Mohrig, D. (2007). Conditions for branching in depositional rivers. *Geology*, *35*(5), 463–466. https://doi.org/10.1130/G23308A.1

Jerolmack, D. J., & Paola, C. (2010). Shredding of environmental signals by sediment transport. *Geophysical Research Letters*, *37*(19). https://doi.org/10.1029/2010GL044638

Johnson, C. A., Dumoulin, J. A., Burruss, R. A., & Slack, J. F. (2015). Depositional conditions for the Kuna Formation, Red Dog Zn-Pb-Ag-Barite District, Alaska, inferred from isotopic and chemical proxies. *Economic Geology*, *110*(5), 1143–1156. https://doi.org/10.2113/econgeo.110.5.1143

Johnson, J. P. L., Whipple, K. X., Sklar, L. S., & Hanks, T. C. (2009). Transport slopes, sediment cover, and bedrock channel incision in the Henry Mountains, Utah. *Journal of Geophysical Research: Earth Surface*, *114*(F2). https://doi.org/10.1029/2007JF000862

Johnston, E. R., Hatt, J. K., He, Z., Wu, L., Guo, X., Luo, Y., et al. (2019). Responses of tundra soil microbial communities to half a decade of experimental warming at two critical depths. *Proceedings of the National Academy of Sciences*, *116*(30), 15096–15105. https://doi.org/10.1073/pnas.1901307116

Jorgenson, M. T., Shur, Y. L., & Walker, H. J. (1998). Evolution of a Permafrost-Dominated Landscape on the Colville River Delta, Northern Alaska. In *Proceedings of the 7th International Conference on Permafrost* (Vol. 55, pp. 523–529). Yellowknife, Canada: Collection Nordicana.

Jorgenson, M. T., Racine, C. H., Walters, J. C., & Osterkamp, T. E. (2001). Permafrost degradation and ecological changes associated with a warming climate in central Alaska. *Climatic Change*, *48*(4), 551–579. https://doi.org/10.1023/A:1005667424292

Jorgenson, M. T., Yoshikawa, K., Kanevskiy, M., Shur, Y., Romanovsky, V., Marchenko, S., et al. (2008). Permafrost characteristics of Alaska. University of Alaska: Fairbanks.

Jorgenson, M. Torre, & Shur, Y. (2007). Evolution of lakes and basins in northern Alaska and discussion of the thaw lake cycle. *Journal of Geophysical Research: Earth Surface*, *112*(F2). https://doi.org/10.1029/2006JF000531

Kader, B. A., & Yaglom, A. M. (1972). Heat and mass transfer laws for fully turbulent wall flows. *International Journal of Heat and Mass Transfer*, *15*(12), 2329–2351. https://doi.org/10.1016/0017-9310(72)90131-7

Kanevskiy, M., Jorgenson, T., Shur, Y., O'Donnell, J. A., Harden, J. W., Zhuang, Q., & Fortier, D. (2014). Cryostratigraphy and Permafrost Evolution in the Lacustrine Lowlands of West-Central Alaska. *Permafrost and Periglacial Processes*, *25*(1), 14–34.

Kanevskiy, M., Shur, Y., Strauss, J., Jorgenson, T., Fortier, D., Stephani, E., & Vasiliev, A. (2016). Patterns and rates of riverbank erosion involving ice-rich permafrost (yedoma) in northern Alaska. *Geomorphology*, *253*, 370–384. https://doi.org/10.1016/j.geomorph.2015.10.023

Karjalainen, O., Aalto, J., Luoto, M., Westermann, S., Romanovsky, V. E., Nelson, F. E., et al. (2019). Circumpolar permafrost maps and geohazard indices for near-future infrastructure risk assessments. *Scientific Data*, *6*(1), 1–16. https://doi.org/10.1038/sdata.2019.37

Karlstrom, L., Gajjar, P., & Manga, M. (2013). Meander formation in supraglacial streams. *Journal of Geophysical Research: Earth Surface*, *118*(3), 1897–1907. https://doi.org/10.1002/jgrf.20135

Kean, J. W., & Smith, J. D. (2006a). Form drag in rivers due to small-scale natural topographic features: 1. Regular sequences. *Journal of Geophysical Research: Earth Surface*, *111*(F4). https://doi.org/10.1029/2006JF000467

Kean, J. W., & Smith, J. D. (2006b). Form drag in rivers due to small-scale natural topographic features: 2. Irregular sequences. *Journal of Geophysical Research: Earth Surface*, *111*(F4). https://doi.org/10.1029/2006JF000490

Kim, H. M., Lee, M. J., Jung, J. Y., Hwang, C. Y., Kim, M., Ro, H.-M., et al. (2016). Vertical distribution of bacterial community is associated with the degree of soil organic matter decomposition in the active layer of moist acidic tundra. *Journal of Microbiology*, *54*(11), 713–723. https://doi.org/10.1007/s12275-016-6294-2

Kim, W., Connell, S. D., Steel, E., Smith, G. A., & Paola, C. (2011). Mass-balance control on the interaction of axial and transverse channel systems. *Geology*, *39*(7), 611–614. https://doi.org/10.1130/G31896.1

Kirby, E., & Whipple, K. (2001). Quantifying differential rock-uplift rates via stream profile analysis. *Geology*, *29*(5), 415–418. https://doi.org/10.1130/0091-7613(2001)029<0415:QDRURV>2.0.CO;2

Kleinhans, M. G., de Vries, B., Braat, L., & van Oorschot, M. (2018). Living landscapes: Muddy and vegetated floodplain effects on fluvial pattern in an incised river. *Earth Surface Processes and Landforms*, *43*(14), 2948–2963. https://doi.org/10.1002/esp.4437

Knoblauch, C., Beer, C., Sosnin, A., Wagner, D., & Pfeiffer, E.-M. (2013). Predicting long-term carbon mineralization and trace gas production from thawing permafrost of Northeast Siberia. *Global Change Biology*, *19*(4), 1160–1172. https://doi.org/10.1111/gcb.12116

Knoblauch, C., Beer, C., Liebner, S., Grigoriev, M. N., & Pfeiffer, E.-M. (2018). Methane production as key to the greenhouse gas budget of thawing permafrost. *Nature Climate Change*, *8*(4), 309–312. https://doi.org/10.1038/s41558-018-0095-z

Koch, J., Ewing, S., Striegl, R., & McKnight, D. (2013). Rapid runoff via shallow throughflow and deeper preferential flow in a boreal catchment underlain by frozen silt (Alaska, USA). *Hydrogeology Journal*, *21*(1). https://doi.org/10.1007/s10040-012-0934-3

Koch, J. C., Bogard, M. J., Butman, D. E., Finlay, K., Ebel, B., James, J., et al. (2022). Heterogeneous patterns of aged organic carbon export driven by hydrologic flow paths, soil texture, fire, and thaw in discontinuous permafrost headwaters. *Global Biogeochemical Cycles*, *36*(4), e2021GB007242. https://doi.org/10.1029/2021GB007242

Kokelj, S. V., & Burn, C. R. (2005). Geochemistry of the active layer and near-surface permafrost, Mackenzie delta region, Northwest Territories, Canada. *Canadian Journal of Earth Sciences*, *42*(1), 37–48. https://doi.org/10.1139/e04-089

Kokelj, S. V., Lacelle, D., Lantz, T. C., Tunnicliffe, J., Malone, L., Clark, I. D., & Chin, K. S. (2013). Thawing of massive ground ice in mega slumps drives increases in stream sediment and solute flux across a range of watershed scales. *Journal of Geophysical Research: Earth Surface*, *118*(2), 681–692. https://doi.org/10.1002/jgrf.20063

Kopp, J., & Kim, W. (2015). The effect of lateral tectonic tilting on fluviodeltaic surficial and stratal asymmetries: experiment and theory. *Basin Research*, *27*(4), 517–530. https://doi.org/10.1111/bre.12086

Kotsyurbenko, O. R., Chin, K.-J., Glagolev, M. V., Stubner, S., Simankova, M. V., Nozhevnikova, A. N., & Conrad, R. (2004). Acetoclastic and hydrogenotrophic methane production and methanogenic populations in an acidic West-Siberian peat bog. *Environmental Microbiology*, *6*(11), 1159–1173. https://doi.org/10.1111/j.1462-2920.2004.00634.x

Kreig, R. A., & Reger, R. D. (1982). *Air-photo analysis and summary of landform soil properties along the route of the Trans-Alaska Pipeline System*. Division of Geological & Geophysical Surveys.

Kreutzer, S., Schmidt, C., Fuchs, M. C., Dietze, M., Fischer, M., & Fuchs, M. (2012). Introducing an R package for luminescence dating analysis. *Ancient TL*, *30*(1), 1–8.

Ku, T.-L., Luo, S., Lowenstein, T. K., Li, J., & Spencer, R. J. (1998). U-Series chronology of lacustrine deposits in Death Valley, California. *Quaternary Research*, *50*(3), 261–275. https://doi.org/10.1006/qres.1998.1995

Kudryavtsev, V. A., Garagulya, L. S., & Melamed, V. G. (1977). *Fundamentals of Frost Forecasting in Geological Engineering Investigations (Osnovy Merzlotnogo Prognoza pri Inzhenerno-Geologicheskikh Issledovaniyakh).* Hanover, NH: Cold Regions Research and Engineering Lab.

Kuhn, M., Lundin, E. J., Giesler, R., Johansson, M., & Karlsson, J. (2018). Emissions from thaw ponds largely offset the carbon sink of northern permafrost wetlands. *Scientific Reports*, *8*(1), 1–7. https://doi.org/10.1038/s41598-018-27770-x

Kuwata, Y. (2021). Direct numerical simulation of turbulent heat transfer on the Reynolds analogy over irregular rough surfaces. *International Journal of Heat and Fluid Flow*, *92*, 108859. https://doi.org/10.1016/j.ijheatfluidflow.2021.108859

Lague, D., Hovius, N., & Davy, P. (2005). Discharge, discharge variability, and the bedrock channel profile. *Journal of Geophysical Research: Earth Surface*, *110*(F4). https://doi.org/10.1029/2004JF000259

Lamb, M. P., & Fonstad, M. A. (2010). Rapid formation of a modern bedrock canyon by a single flood event. *Nature Geoscience*, *3*(7), 477–481. https://doi.org/10.1038/ngeo894

Lamb, M. P., Dietrich, W. E., & Sklar, L. S. (2008). A model for fluvial bedrock incision by impacting suspended and bed load sediment. *Journal of Geophysical Research: Earth Surface*, *113*(F3). https://doi.org/10.1029/2007JF000915

Lamb, M. P., Dietrich, W. E., & Venditti, J. G. (2008). Is the critical Shields stress for incipient sediment motion dependent on channel-bed slope? *Journal of Geophysical Research: Earth Surface*, *113*(F2), F02008. https://doi.org/10.1029/2007JF000831

Lamb, M. P., Finnegan, N. J., Scheingross, J. S., & Sklar, L. S. (2015). New insights into the mechanics of fluvial bedrock erosion through flume experiments and theory. *Geomorphology*, *244*, 33–55. https://doi.org/10.1016/j.geomorph.2015.03.003

Lamb, M. P., Brun, F., & Fuller, B. M. (2017). Hydrodynamics of steep streams with planar coarse-grained beds: Turbulence, flow resistance, and implications for sediment transport. *Water Resources Research*, *53*(3), 2240–2263. https://doi.org/10.1002/2016WR019579

Lantz, T. C., & Kokelj, S. V. (2008). Increasing rates of retrogressive thaw slump activity in the Mackenzie Delta region, N.W.T., Canada. *Geophysical Research Letters*, *35*(6). https://doi.org/10.1029/2007GL032433

Lapotre, M. G., & Lamb, M. P. (2018). Substrate controls on valley formation by groundwater on Earth and Mars. *Geology*, *46*(6), 531–534. https://doi.org/10.1130/G40007.1

Lapôtre, M. G. A., Ielpi, A., Lamb, M. P., Williams, R. M. E., & Knoll, A. H. (2019). Model for the formation of single-thread rivers in barren landscapes and implications for pre-Silurian and Martian fluvial deposits.

Journal of Geophysical Research: Earth Surface, *124*(12), 2757–2777. https://doi.org/10.1029/2019JF005156

Lattaud, J., Bröder, L., Haghipour, N., Rickli, J., Giosan, L., & Eglinton, T. I. (2021). Influence of hydraulic connectivity on carbon burial efficiency in Mackenzie Delta lake sediments. *Journal of Geophysical Research: Biogeosciences*, *126*(3), e2020JG006054. https://doi.org/10.1029/2020JG006054

Lauer, J. W., & Parker, G. (2008a). Modeling framework for sediment deposition, storage, and evacuation in the floodplain of a meandering river: Application to the Clark Fork River, Montana. *Water Resources Research*, *44*(8). https://doi.org/10.1029/2006WR005529

Lauer, J. W., & Parker, G. (2008b). Net local removal of floodplain sediment by river meander migration. *Geomorphology*, *96*(1), 123–149. https://doi.org/10.1016/j.geomorph.2007.08.003

Lauer, J. W., & Willenbring, J. (2010). Steady state reach-scale theory for radioactive tracer concentration in a simple channel/floodplain system. *Journal of Geophysical Research: Earth Surface*, *115*(F4). https://doi.org/10.1029/2009JF001480

Lavarini, C., Attal, M., da Costa Filho, C. A., & Kirstein, L. A. (2018). Does pebble abrasion influence detrital age population statistics? A numerical investigation of natural data sets. *Journal of Geophysical Research: Earth Surface*, *123*(10), 2577–2601. https://doi.org/10.1029/2018JF004610

Lavé, J., & Avouac, J. P. (2001). Fluvial incision and tectonic uplift across the Himalayas of central Nepal. *Journal of Geophysical Research: Solid Earth*, *106*(B11), 26561–26591. https://doi.org/10.1029/2001JB000359

Laxton, S., & Coates, J. (2010). Geophysical and borehole investigations of permafrost conditions associated with compromised infrastructure in Dawson and Ross River, Yukon, 14.

de Leeuw, J., Lamb, M. P., Parker, G., Moodie, A. J., Haught, D., Venditti, J. G., & Nittrouer, J. A. (2020). Entrainment and suspension of sand and gravel. *Earth Surface Dynamics*, *8*(2), 485–504. https://doi.org/10.5194/esurf-8-485-2020

Lehner, B., Verdin, K., & Jarvis, A. (2008). New Global Hydrography Derived from Spaceborne Elevation Data. *Eos, Transactions, American Geophysical Union*, *89*(10), 93–94. https://doi.org/10.1029/2008EO100001

Leopold, Luna B., Wolman, M. G., & Miller, J. P. (1964). *Fluvial processes in geomorphology*. San Francisco: W. H. Freeman.

Leopold, Luna Bergere, Wolman, M. G., & Miller, J. P. (1964). Fluvial processes in geomorphology.

Li, J., Lowenstein, T. K., Brown, C. B., Ku, T.-L., & Luo, S. (1996). A 100 ka record of water tables and paleoclimates from salt cores, Death Valley, California. *Palaeogeography, Palaeoclimatology, Palaeoecology*, *123*(1), 179–203. https://doi.org/10.1016/0031-0182(95)00123-9

Liebner, S., & Wagner, D. (2007). Abundance, distribution and potential activity of methane oxidizing bacteria in permafrost soils from the Lena Delta, Siberia. *Environmental Microbiology*, *9*(1), 107–117. https://doi.org/10.1111/j.1462-2920.2006.01120.x

Liebner, S., Ganzert, L., Kiss, A., Yang, S., Wagner, D., & Svenning, M. M. (2015). Shifts in methanogenic community composition and methane fluxes along the degradation of discontinuous permafrost. *Frontiers in Microbiology*, *6*. https://doi.org/10.3389/fmicb.2015.00356

Lininger, K. B., Wohl, E., & Rose, J. R. (2018). Geomorphic controls on floodplain soil organic carbon in the Yukon Flats, interior Alaska, from reach to river basin scales. *Water Resources Research*, *54*(3), 1934–1951. https://doi.org/10.1002/2017WR022042

Lininger, K. B., Wohl, E., Rose, J. R., & Leisz, S. J. (2019). Significant floodplain soil organic carbon storage along a large high-latitude river and its tributaries. *Geophysical Research Letters*, *46*(4), 2121–2129. https://doi.org/10.1029/2018GL080996

Lininger, Katherine B., & Wohl, E. (2019). Floodplain dynamics in North American permafrost regions under a warming climate and implications for organic carbon stocks: A review and synthesis. *Earth-Science Reviews*, *193*, 24–44. https://doi.org/10.1016/j.earscirev.2019.02.024

Lipson, D. A., Raab, T. K., Parker, M., Kelley, S. T., Brislawn, C. J., & Jansson, J. (2015). Changes in microbial communities along redox gradients in polygonized Arctic wet tundra soils. *Environmental Microbiology Reports*, *7*(4), 649–657. https://doi.org/10.1111/1758-2229.12301

Littlefair, C. A., Tank, S. E., & Kokelj, S. V. (2017). Retrogressive thaw slumps temper dissolved organic carbon delivery to streams of the Peel Plateau, NWT, Canada. *Biogeosciences*, *14*(23), 5487–5505. https://doi.org/10.5194/bg-14-5487-2017

Liu, B., Yang, D., Ye, B., & Berezovskaya, S. (2005). Long-term open-water season stream temperature variations and changes over Lena River Basin in Siberia. *Global and Planetary Change*, *48*(1), 96–111. https://doi.org/10.1016/j.gloplacha.2004.12.007

Loiko, S. V., Pokrovsky, O. S., Raudina, T. V., Lim, A., Kolesnichenko, L. G., Shirokova, L. S., et al. (2017). Abrupt permafrost collapse enhances organic carbon, CO_2, nutrient and metal release into surface waters. *Chemical Geology*, *471*, 153–165. https://doi.org/10.1016/j.chemgeo.2017.10.002

Longo, W. M., Huang, Y., Russell, J. M., Morrill, C., Daniels, W. C., Giblin, A. E., & Crowther, J. (2020). Insolation and greenhouse gases drove Holocene winter and spring warming in Arctic Alaska. *Quaternary Science Reviews*, *242*, 106438. https://doi.org/10.1016/j.quascirev.2020.106438

Lowenstein, T. K., Li, J., Brown, C., Roberts, S. M., Ku, T.-L., Luo, S., & Yang, W. (1999). 200 k.y. paleoclimate record from Death Valley salt core.

Geology, *27*(1), 3–6. https://doi.org/10.1130/0091-7613(1999)027<0003:KYPRFD>2.3.CO;2

Lunardini, V. J. (1986). *Experimental determination of heat transfer coefficients in water flowing over a horizontal ice sheet* (CRREL Report No. 86–3). US Army Corps of Engineers, Cold Regions Research & Engineering Laboratory.

Luo, D., Wu, Q., Jin, H., Marchenko, S. S., Lü, L., & Gao, S. (2016). Recent changes in the active layer thickness across the northern hemisphere. *Environmental Earth Sciences*, *75*(7), 555.

Mackelprang, R., Waldrop, M. P., DeAngelis, K. M., David, M. M., Chavarria, K. L., Blazewicz, S. J., et al. (2011). Metagenomic analysis of a permafrost microbial community reveals a rapid response to thaw. *Nature*, *480*(7377), 368–371. https://doi.org/10.1038/nature10576

Mackelprang, R., Saleska, S. R., Jacobsen, C. S., Jansson, J. K., & Taş, N. (2016). Permafrost meta-omics and climate change. *Annual Review of Earth and Planetary Sciences*, *44*(1), 439–462. https://doi.org/10.1146/annurev-earth-060614-105126

Maldonado, J. K., Shearer, C., Bronen, R., Peterson, K., & Lazrus, H. (2013). The impact of climate change on tribal communities in the US: displacement, relocation, and human rights. *Climatic Change*, *120*(3), 601–614. https://doi.org/10.1007/s10584-013-0746-z

Malin, M. C., & Edgett, K. S. (2003). Evidence for persistent flow and aqueous sedimentation on early Mars. *Science*, *302*(5652), 1931–1934. https://doi.org/10.1126/science.1090544

Malmon, D. V., Dunne, T., & Reneau, S. L. (2003). Stochastic theory of particle trajectories through alluvial valley floors. *The Journal of Geology*, *111*(5), 525–542. https://doi.org/10.1086/376764

Malone, L., Lacelle, D., Kokelj, S., & Clark, I. D. (2013). Impacts of hillslope thaw slumps on the geochemistry of permafrost catchments (Stony Creek watershed, NWT, Canada). *Chemical Geology*, *356*, 38–49. https://doi.org/10.1016/j.chemgeo.2013.07.010

Malyarenko, A., Wells, A. J., Langhorne, P. J., Robinson, N. J., Williams, M. J. M., & Nicholls, K. W. (2020). A synthesis of thermodynamic ablation at ice–ocean interfaces from theory, observations and models. *Ocean Modelling*, *154*, 101692. https://doi.org/10.1016/j.ocemod.2020.101692

Mann, D. H., Fastie, C. L., Rowland, E. L., & Bigelow, N. H. (1995). Spruce succession, disturbance, and geomorphology on the Tanana River floodplain, Alaska. *Ecoscience*, *2*(2), 184–199.

Marsicek, J., Shuman, B. N., Bartlein, P. J., Shafer, S. L., & Brewer, S. (2018). Reconciling divergent trends and millennial variations in Holocene temperatures. *Nature*, *554*(7690), 92–96. https://doi.org/10.1038/nature25464

Mason, J., & Mohrig, D. (2019). Scroll bars are inner bank levees along meandering river bends. *Earth Surface Processes and Landforms*, *44*(13), 2649–2659. https://doi.org/10.1002/esp.4690

Mason, O. U., Case, D. H., Naehr, T. H., Lee, R. W., Thomas, R. B., Bailey, J. V., & Orphan, V. J. (2015). Comparison of archaeal and bacterial diversity in methane seep carbonate nodules and host sediments, Eel River Basin and Hydrate Ridge, USA. *Microbial Ecology*, *70*(3), 766–784. https://doi.org/10.1007/s00248-015-0615-6

Matsubara, Y., Howard, A. D., Burr, D. M., Williams, R. M. E., Dietrich, W. E., & Moore, J. M. (2015). River meandering on Earth and Mars: A comparative study of Aeolis Dorsa meanders, Mars and possible terrestrial analogs of the Usuktuk River, AK, and the Quinn River, NV. *Geomorphology*, *240*, 102–120. https://doi.org/10.1016/j.geomorph.2014.08.031

McCalley, C. K., Woodcroft, B. J., Hodgkins, S. B., Wehr, R. A., Kim, E.-H., Mondav, R., et al. (2014). Methane dynamics regulated by microbial community response to permafrost thaw. *Nature*, *514*(7523), 478–481. https://doi.org/10.1038/nature13798

McClelland, J. W., Holmes, R. M., Peterson, B. J., Raymond, P. A., Striegl, R. G., Zhulidov, A. V., et al. (2016). Particulate organic carbon and nitrogen export from major Arctic rivers. *Global Biogeochemical Cycles*, *30*(5), 629–643. https://doi.org/10.1002/2015GB005351

McMahon, W. J., & Davies, N. S. (2018). The shortage of geological evidence for pre-vegetation meandering rivers. In *Fluvial Meanders and Their Sedimentary Products in the Rock Record* (pp. 119–148). John Wiley & Sons, Ltd. https://doi.org/10.1002/9781119424437.ch5

McNamara, J. P., Oatley, J. A., Kane, D. L., & Hinzman, L. D. (2008). Case study of a large summer flood on the North Slope of Alaska: Bedload transport. *Hydrology Research*, *39*(4), 299–308. https://doi.org/10.2166/nh.2008.006

McPhee, M. G. (1992). Turbulent heat flux in the upper ocean under sea ice. *Journal of Geophysical Research: Oceans*, *97*(C4), 5365–5379. https://doi.org/10.1029/92JC00239

Meyer, H., Schirrmeister, L., Yoshikawa, K., Opel, T., Wetterich, S., Hubberten, H.-W., & Brown, J. (2010). Permafrost evidence for severe winter cooling during the Younger Dryas in northern Alaska. *Geophysical Research Letters*, *37*(3). https://doi.org/10.1029/2009GL041013

Miall, A. D. (2013). *Principles of Sedimentary Basin Analysis*. Springer Science & Business Media.

Mietta, F., Chassagne, C., Manning, A. J., & Winterwerp, J. C. (2009). Influence of shear rate, organic matter content, pH and salinity on mud flocculation. *Ocean Dynamics*, *59*(5), 751–763. https://doi.org/10.1007/s10236-009-0231-4

Millar, R. G. (2000). Influence of bank vegetation on alluvial channel patterns. *Water Resources Research*, *36*(4), 1109–1118. https://doi.org/10.1029/1999WR900346

Millar, R. G. (2005). Theoretical regime equations for mobile gravel-bed rivers with stable banks. *Geomorphology*, *64*(3), 207–220. https://doi.org/10.1016/j.geomorph.2004.07.001

Millar, R. G., & Quick, M. C. (1998). Stable width and depth of gravel-bed rivers with cohesive banks. *Journal of Hydraulic Engineering*, *124*(10), 1005–1013. https://doi.org/10.1061/(ASCE)0733-9429(1998)124:10(1005)

Miyake, Y., Tsujimoto, K., & Nakaji, M. (2001). Direct numerical simulation of rough-wall heat transfer in a turbulent channel flow. *International Journal of Heat and Fluid Flow*, *22*(3), 237–244. https://doi.org/10.1016/S0142-727X(01)00085-6

Mondav, R., Woodcroft, B. J., Kim, E.-H., McCalley, C. K., Hodgkins, S. B., Crill, P. M., et al. (2014). Discovery of a novel methanogen prevalent in thawing permafrost. *Nature Communications*, *5*, 3212. https://doi.org/10.1038/ncomms4212

Moni, C., Lerch, T. Z., Knoth de Zarruk, K., Strand, L. T., Forte, C., Certini, G., & Rasse, D. P. (2015). Temperature response of soil organic matter mineralisation in arctic soil profiles. *Soil Biology and Biochemistry*, *88*, 236–246. https://doi.org/10.1016/j.soilbio.2015.05.024

Monteux, S., Weedon, J. T., Blume-Werry, G., Gavazov, K., Jassey, V. E. J., Johansson, M., et al. (2018). Long-term in situ permafrost thaw effects on bacterial communities and potential aerobic respiration. *The ISME Journal*, *12*(9), 2129–2141. https://doi.org/10.1038/s41396-018-0176-z

Montgomery, D. R., & Buffington, J. M. (1997). Channel-reach morphology in mountain drainage basins. *GSA Bulletin*, *109*(5), 596–611. https://doi.org/10.1130/0016-7606(1997)109<0596:CRMIMD>2.3.CO;2

Morris, R., Schauer-Gimenez, A., Bhattad, U., Kearney, C., Struble, C. A., Zitomer, D., & Maki, J. S. (2014). Methyl coenzyme M reductase (mcrA) gene abundance correlates with activity measurements of methanogenic H_2/CO_2-enriched anaerobic biomass. *Microbial Biotechnology*, *7*(1), 77–84. https://doi.org/10.1111/1751-7915.12094

Murphy, B. P., Johnson, J. P. L., Gasparini, N. M., & Sklar, L. S. (2016). Chemical weathering as a mechanism for the climatic control of bedrock river incision. *Nature*, *532*(7598), 223–227. https://doi.org/10.1038/nature17449

Murray, A. S., & Wintle, A. G. (2000). Luminescence dating of quartz using an improved single-aliquot regenerative-dose protocol. *Radiation Measurements*, *32*(1), 57–73. https://doi.org/10.1016/S1350-4487(99)00253-X

Murray, A. S., & Wintle, A. G. (2003). The single aliquot regenerative dose protocol: potential for improvements in reliability. *Radiation*

Measurements, *37*(4), 377–381. https://doi.org/10.1016/S1350-4487(03)00053-2

Naito, K., & Parker, G. (2019). Can bankfull discharge and bankfull channel characteristics of an alluvial meandering river be cospecified from a flow duration curve? *Journal of Geophysical Research: Earth Surface*, *124*(10), 2381–2401. https://doi.org/10.1029/2018JF004971

Naito, K., & Parker, G. (2020). Adjustment of self-formed bankfull channel geometry of meandering rivers: modelling study. *Earth Surface Processes and Landforms*, *45*(13), 3313–3322. https://doi.org/10.1002/esp.4966

Neely, A. B., & DiBiase, R. A. (2020). Drainage area, bedrock fracture spacing, and weathering controls on landscape-scale patterns in surface sediment grain size. *Journal of Geophysical Research: Earth Surface*, *125*(10), e2020JF005560. https://doi.org/10.1029/2020JF005560

Nghiem, J. A., Fischer, W. W., Li, G. K., & Lamb, M. P. (2022). A mechanistic model for mud flocculation in freshwater rivers. *Journal of Geophysical Research: Earth Surface*, *127*(5), e2021JF006392. https://doi.org/10.1029/2021JF006392

Nield, D. A., & Bejan, A. (2017). *Convection in porous media* (5th ed., Vol. 3). Cham, Switzerland: Springer International Publishing.

Nowacki, G. J., Spencer, P., Fleming, M., Brock, T., & Jorgenson, T. (2003). *Unified Ecoregions of Alaska: 2001* (USGS Numbered Series No. 2002–297). Geological Survey (U.S.). Retrieved from http://pubs.er.usgs.gov/publication/ofr2002297

Obu, J. (2021). How Much of the Earth's Surface is Underlain by Permafrost? *Journal of Geophysical Research: Earth Surface*, *126*(5), e2021JF006123. https://doi.org/10.1029/2021JF006123

Obu, Jaroslav, Westermann, S., Bartsch, A., Berdnikov, N., Christiansen, H. H., Dashtseren, A., et al. (2019). Northern Hemisphere permafrost map based on TTOP modelling for 2000–2016 at 1 km^2 scale. *Earth-Science Reviews*, *193*, 299–316. https://doi.org/10.1016/j.earscirev.2019.04.023

O'Donnell, J. A., Aiken, G. R., Kane, E. S., & Jones, J. B. (2010). Source water controls on the character and origin of dissolved organic matter in streams of the Yukon River basin, Alaska. *Journal of Geophysical Research: Biogeosciences*, *115*(G3). https://doi.org/10.1029/2009JG001153

O'Donnell, J. A., Jorgenson, M. T., Harden, J. W., McGuire, A. D., Kanevskiy, M. Z., & Wickland, K. P. (2012). The effects of permafrost thaw on soil hydrologic, thermal, and carbon dynamics in an Alaskan peatland. *Ecosystems*, *15*(2), 213–229.

Ohara, N., Jones, B. M., Parsekian, A. D., Hinkel, K. M., Yamatani, K., Kanevskiy, M., et al. (2022). A new Stefan equation to characterize the evolution of thermokarst lake and talik geometry. *The Cryosphere*, *16*(4), 1247–1264. https://doi.org/10.5194/tc-16-1247-2022

OpenTopography. (2020). Meandering Channels in Death Valley, CA 2019. https://doi.org/10.5069/G96D5R55

Paola, C., Heller, P. L., & Angevine, C. L. (1992). The large-scale dynamics of grain-size variation in alluvial basins, 1: Theory. *Basin Research*, *4*(2), 73–90. https://doi.org/10.1111/j.1365-2117.1992.tb00145.x

Paola, C., Ganti, V., Mohrig, D., Runkel, A. C., & Straub, K. M. (2018). Time not our time: Physical controls on the preservation and measurement of geologic time. *Annual Review of Earth and Planetary Sciences*, *46*(1), 409–438. https://doi.org/10.1146/annurev-earth-082517-010129

Parada, A. E., Needham, D. M., & Fuhrman, J. A. (2016). Every base matters: Assessing small subunit rRNA primers for marine microbiomes with mock communities, time series and global field samples. *Environmental Microbiology*, *18*(5), 1403–1414. https://doi.org/10.1111/1462-2920.13023

Parker, G., Shimizu, Y., Wilkerson, G. V., Eke, E. C., Abad, J. D., Lauer, J. W., et al. (2011). A new framework for modeling the migration of meandering rivers. *Earth Surface Processes and Landforms*, *36*(1), 70–86. https://doi.org/10.1002/esp.2113

Parker, Gary. (1976). On the cause and characteristic scales of meandering and braiding in rivers. *Journal of Fluid Mechanics*, *76*(3), 457–480. https://doi.org/10.1017/S0022112076000748

Parker, Gary. (1978). Self-formed straight rivers with equilibrium banks and mobile bed. Part 2. The gravel river. *Journal of Fluid Mechanics*, *89*(1), 127–146. https://doi.org/10.1017/S0022112078002505

Parker, Gary, Toro-Escobar, C. M., Ramey, M., & Beck, S. (2003). Effect of floodwater extraction on mountain stream morphology. *Journal of Hydraulic Engineering*, *129*(11), 885–895. https://doi.org/10.1061/(ASCE)0733-9429(2003)129:11(885)

Parker, Gary, Wilcock, P. R., Paola, C., Dietrich, W. E., & Pitlick, J. (2007). Physical basis for quasi-universal relations describing bankfull hydraulic geometry of single-thread gravel bed rivers. *Journal of Geophysical Research: Earth Surface*, *112*(F4). https://doi.org/10.1029/2006JF000549

Parmentier, F.-J. W., Christensen, T. R., Rysgaard, S., Bendtsen, J., Glud, R. N., Else, B., et al. (2017). A synthesis of the arctic terrestrial and marine carbon cycles under pressure from a dwindling cryosphere. *Ambio*, *46*(Suppl 1), 53–69. https://doi.org/10.1007/s13280-016-0872-8

Partheniades, E. (1965). Erosion and deposition of cohesive soils. *Journal of the Hydraulics Division*, *91*(1), 105–139. https://doi.org/10.1061/JYCEAJ.0001165

Pastick, N. J., Jorgenson, M. T., Wylie, B. K., Rose, J. R., Rigge, M., & Walvoord, M. A. (2014). Spatial variability and landscape controls of near-surface permafrost within the Alaskan Yukon River Basin. *Journal of Geophysical Research: Biogeosciences*, *119*(6), 1244–1265. https://doi.org/10.1002/2013JG002594

Pastick, N. J., Jorgenson, M. T., Wylie, B. K., Nield, S. J., Johnson, K. D., & Finley, A. O. (2015). Distribution of near-surface permafrost in Alaska:

Estimates of present and future conditions. *Remote Sensing of Environment*, *168*, 301–315. https://doi.org/10.1016/j.rse.2015.07.019

Patsinghasanee, S., Kimura, I., Shimizu, Y., & Nabi, M. (2018). Experiments and modelling of cantilever failures for cohesive riverbanks. *Journal of Hydraulic Research*, *56*(1), 76–95.

Peakall, J., Ashworth, P. J., & Best, J. L. (2007). Meander-bend evolution, alluvial architecture, and the role of cohesion in sinuous river channels: A flume study. *Journal of Sedimentary Research*, *77*(3), 197–212. https://doi.org/10.2110/jsr.2007.017

Pekel, J.-F., Cottam, A., Gorelick, N., & Belward, A. S. (2016). High-resolution mapping of global surface water and its long-term changes. *Nature*, *540*(7633), 418–422. https://doi.org/10.1038/nature20584

Peterson, B. J., Holmes, R. M., McClelland, J. W., Vörösmarty, C. J., Lammers, R. B., Shiklomanov, A. I., et al. (2002). Increasing river discharge to the Arctic Ocean. *Science*, *298*(5601), 2171–2173. https://doi.org/10.1126/science.1077445

Péwé, T. L., Church, R. E., & Andresen, M. J. (1969). *Origin and Paleoclimatic Significance of Large-Scale Patterned Ground in the Donnelly Dome Area, Alaska*. Geological Society of America. https://doi.org/10.1130/SPE103

Phillips, C. B., & Jerolmack, D. J. (2019). Bankfull transport capacity and the threshold of motion in coarse-grained rivers. *Water Resources Research*, *55*(12), 11316–11330. https://doi.org/10.1029/2019WR025455

Pike, A. S. (2008). *Longitudinal Patterns in Stream Channel Geomorphology and Aquatic Habitat in the Luquillo Mountains of Puerto Rico* (PhD). University of Pennsylvania.

Pitlick, J., Marr, J., & Pizzuto, J. (2013). Width adjustment in experimental gravel-bed channels in response to overbank flows. *Journal of Geophysical Research: Earth Surface*, *118*(2), 553–570. https://doi.org/10.1002/jgrf.20059

Pizzuto, J. E. (2014). Long-term storage and transport length scale of fine sediment: Analysis of a mercury release into a river. *Geophysical Research Letters*, *41*(16), 5875–5882. https://doi.org/10.1002/2014GL060722

Plug, L. J., & Werner, B. T. (2002). Nonlinear dynamics of ice-wedge networks and resulting sensitivity to severe cooling events. *Nature*, *417*(6892), 929–933. https://doi.org/10.1038/nature00796

Pollen-Bankhead, N., & Simon, A. (2010). Hydrologic and hydraulic effects of riparian root networks on streambank stability: Is mechanical root-reinforcement the whole story? *Geomorphology*, *116*(3), 353–362. https://doi.org/10.1016/j.geomorph.2009.11.013

Portenga, E. W., & Bierman, P. R. (2011). Understanding Earth's eroding surface with 10Be. *GSA Today*, *21*(8), 4–10. https://doi.org/10.1130/G111A.1

Potter, C., Klooster, S., & Genovese, V. (2013). Alaska ecosystem carbon fluxes estimated from MODIS satellite data inputs from 2000 to 2010. *Carbon Balance and Management*, *8*(1), 12. https://doi.org/10.1186/1750-0680-8-12

Powell, R. W., Ho, C. Y., & Liley, P. E. (1966). *Thermal Conductivity of Selected Materials* (National Standard Reference Data System No. 8). Thermophysical Properties Research Center: US Department of Commerce, National Bureau of Standards. Retrieved from https://www.google.com/url?sa=t&rct=j&q=&esrc=s&source=web&cd=&ved=2ahUKEwi_m6vU5K78AhUNI0QIHcp3AFcQFnoECBUQAQ&url=https%3A%2F%2Fnvlpubs.nist.gov%2Fnistpubs%2Flegacy%2Fnsrds%2Fnbsnsrds8.pdf&usg=AOvVaw1ZwZoaMxACHvtf07HXT64w

Praetorius, S. K., & Mix, A. C. (2014). Synchronization of North Pacific and Greenland climates preceded abrupt deglacial warming. *Science*, *345*(6195), 444–448. https://doi.org/10.1126/science.1252000

Prancevic, J. P., & Lamb, M. P. (2015a). Particle friction angles in steep mountain channels. *Journal of Geophysical Research: Earth Surface*, *120*(2), 242–259. https://doi.org/10.1002/2014JF003286

Prancevic, J. P., & Lamb, M. P. (2015b). Unraveling bed slope from relative roughness in initial sediment motion. *Journal of Geophysical Research: Earth Surface*, *120*(3), 474–489. https://doi.org/10.1002/2014JF003323

Prescott, J. R., & Hutton, J. T. (1994). Cosmic ray contributions to dose rates for luminescence and ESR dating: Large depths and long-term time variations. *Radiation Measurements*, *23*(2), 497–500. https://doi.org/10.1016/1350-4487(94)90086-8

Quast, C., Pruesse, E., Yilmaz, P., Gerken, J., Schweer, T., Yarza, P., et al. (2013). The SILVA ribosomal RNA gene database project: Improved data processing and web-based tools. *Nucleic Acids Research*, *41*(D1), D590–D596. https://doi.org/10.1093/nar/gks1219

Randriamazaoro, R., Dupeyrat, L., Costard, F., & Gailhardis, E. C. (2007). Fluvial thermal erosion: Heat balance integral method. *Earth Surface Processes and Landforms*, *32*(12), 1828–1840. https://doi.org/10.1002/esp.1489

Reimer, P. J., Brown, T. A., & Reimer, R. W. (2004). Discussion: Reporting and calibration of post-bomb 14C data. *Radiocarbon*, *46*(3), 1299–1304. https://doi.org/10.1017/S0033822200033154

Reimer, P. J., Bard, E., Bayliss, A., Beck, J. W., Blackwell, P. G., Ramsey, C. B., et al. (2013). IntCal13 and Marine13 radiocarbon age calibration curves 0–50,000 years cal BP. *Radiocarbon*, *55*(4), 1869–1887. https://doi.org/10.2458/azu_js_rc.55.16947

Reimer, P. J., Austin, W. E. N., Bard, E., Bayliss, A., Blackwell, P. G., Ramsey, C. B., et al. (2020). The IntCal20 northern hemisphere radiocarbon age calibration curve (0–55 cal kBP). *Radiocarbon*, *62*(4), 725–757. https://doi.org/10.1017/RDC.2020.41

Reimer, R. W., & Reimer, P. J. (2023). CALIBomb. Retrieved from https://calib.org/CALIBomb/

Repasch, M., Wittmann, H., Scheingross, J. S., Sachse, D., Szupiany, R., Orfeo, O., et al. (2020). Sediment transit time and floodplain storage dynamics in alluvial rivers revealed by meteoric ^{10}Be. *Journal of Geophysical Research: Earth Surface*, *125*(7), e2019JF005419. https://doi.org/10.1029/2019JF005419

Repasch, M., Scheingross, J. S., Hovius, N., Lupker, M., Wittmann, H., Haghipour, N., et al. (2021). Fluvial organic carbon cycling regulated by sediment transit time and mineral protection. *Nature Geoscience*, *14*(11), 842–848. https://doi.org/10.1038/s41561-021-00845-7

Rickenmann, D., & Recking, A. (2011). Evaluation of flow resistance in gravel-bed rivers through a large field data set. *Water Resources Research*, *47*(7). https://doi.org/10.1029/2010WR009793

Ritter, B., Diederich-Leicher, J. L., Binnie, S. A., Stuart, F. M., Wennrich, V., Bolten, A., & Dunai, T. J. (2022). Impact of CaSO4-rich soil on Miocene surface preservation and Quaternary sinuous to meandering channel forms in the hyperarid Atacama Desert. *Scientific Reports*, *12*(1), 17951. https://doi.org/10.1038/s41598-022-22787-9

Roda-Boluda, D. C., D'Arcy, M., Whittaker, A. C., Gheorghiu, D. M., & Rodés, Á. (2019). 10Be erosion rates controlled by transient response to normal faulting through incision and landsliding. *Earth and Planetary Science Letters*, *507*, 140–153. https://doi.org/10.1016/j.epsl.2018.11.032

Romanovsky, V. E., Smith, S. L., & Christiansen, H. H. (2010). Permafrost thermal state in the polar Northern Hemisphere during the international polar year 2007–2009: a synthesis. *Permafrost and Periglacial Processes*, *21*(2), 106–116. https://doi.org/10.1002/ppp.689

Roux, N., Costard, F., & Grenier, C. (2017). Laboratory and numerical simulation of the evolution of a river's talik. *Permafrost and Periglacial Processes*, *28*(2), 460–469. https://doi.org/10.1002/ppp.1929

Rowland, J., & Stauffer, S. (2019). Classified channel masks of portions of 13 rivers across the Arctic and areas of floodplain erosion and accretion ranging from 1973 to 2016. Retrieved from https://data.ess-dive.lbl.gov/view/doi:10.15485/1571525

Rowland, J., Stauffer, S., & Schwenk, J. (2019). Pan-arctic river bank erosion and accretion, and planform metrics measured over intervals ranging from 1973 to 2016. Incorporating the Hydrological Controls on Carbon Cycling in Floodplain Ecosystems into Earth System Models (ESMs). https://doi.org/10.15485/1571527

Rowland, J. C., Dietrich, W. E., Day, G., & Parker, G. (2009). Formation and maintenance of single-thread tie channels entering floodplain lakes: Observations from three diverse river systems. *Journal of Geophysical Research: Earth Surface*, *114*(F2). https://doi.org/10.1029/2008JF001073

Rowland, Joel C., & Coon, E. T. (2016). From documentation to prediction: Raising the bar for thermokarst research. *Hydrogeology Journal*, *24*(3), 645–648. https://doi.org/10.1007/s10040-015-1331-5

Rowland, Joel C., Lepper, K., Dietrich, W. E., Wilson, C. J., & Sheldon, R. (2005). Tie channel sedimentation rates, oxbow formation age and channel migration rate from optically stimulated luminescence (OSL) analysis of floodplain deposits. *Earth Surface Processes and Landforms*, *30*(9), 1161–1179. https://doi.org/10.1002/esp.1268

Rowland, Joel C., Shelef, E., Pope, P. A., Muss, J., Gangodagamage, C., Brumby, S. P., & Wilson, C. J. (2016). A morphology independent methodology for quantifying planview river change and characteristics from remotely sensed imagery. *Remote Sensing of Environment*, *184*, 212–228. https://doi.org/10.1016/j.rse.2016.07.005

Rowland, Joel Carey, Schwenk, J., Shelef, E., Muss, J., Ahrens, D., Stauffer, S., et al. (2023). *Scale-dependent influence of permafrost on riverbank erosion rates* (preprint). Preprints. https://doi.org/10.22541/essoar.167591069.91968615/v1

Santos, M. G. M., & Owen, G. (2016). Heterolithic meandering-channel deposits from the Neoproterozoic of NW Scotland: Implications for palaeogeographic reconstructions of Precambrian sedimentary environments. *Precambrian Research*, *272*, 226–243. https://doi.org/10.1016/j.precamres.2015.11.003

Santos, M. G. M., Hartley, A. J., Mountney, N. P., Peakall, J., Owen, A., Merino, E. R., & Assine, M. L. (2019). Meandering rivers in modern desert basins: Implications for channel planform controls and prevegetation rivers. *Sedimentary Geology*, *385*, 1–14. https://doi.org/10.1016/j.sedgeo.2019.03.011

Schädel, C., Bader, M. K.-F., Schuur, E. A. G., Biasi, C., Bracho, R., Čapek, P., et al. (2016). Potential carbon emissions dominated by carbon dioxide from thawed permafrost soils. *Nature Climate Change*, *6*(10), 950–953. https://doi.org/10.1038/nclimate3054

Scheingross, J. S., Repasch, M. N., Hovius, N., Sachse, D., Lupker, M., Fuchs, M., et al. (2021). The fate of fluvially-deposited organic carbon during transient floodplain storage. *Earth and Planetary Science Letters*, *561*, 116822. https://doi.org/10.1016/j.epsl.2021.116822

Scheingross, Joel S., & Lamb, M. P. (2017). A Mechanistic Model of Waterfall Plunge Pool Erosion into Bedrock. *Journal of Geophysical Research: Earth Surface*, *122*(11), 2079–2104. https://doi.org/10.1002/2017JF004195

Scheingross, Joel S., Brun, F., Lo, D. Y., Omerdin, K., & Lamb, M. P. (2014). Experimental evidence for fluvial bedrock incision by suspended and bedload sediment. *Geology*, *42*(6), 523–526. https://doi.org/10.1130/G35432.1

Scheingross, Joel S., Lamb, M. P., & Fuller, B. M. (2019). Self-formed bedrock waterfalls. *Nature*, *567*(7747), 229–233. https://doi.org/10.1038/s41586-019-0991-z

Schostag, M., Stibal, M., Jacobsen, C. S., Bælum, J., Taş, N., Elberling, B., et al. (2015). Distinct summer and winter bacterial communities in the active layer of Svalbard permafrost revealed by DNA- and RNA-based analyses. *Frontiers in Microbiology*, *6*. https://doi.org/10.3389/fmicb.2015.00399

Schreiner, K. M., Bianchi, T. S., & Rosenheim, B. E. (2014). Evidence for permafrost thaw and transport from an Alaskan North Slope watershed. *Geophysical Research Letters*, *41*(9), 3117–3126. https://doi.org/10.1002/2014GL059514

Schulson, E. M., & Duval, P. (2009). *Creep and Fracture of Ice* (p. 416). Cambridge University Press. Retrieved from https://hal-insu.archives-ouvertes.fr/insu-00421610

Schuur, E. a. G., McGuire, A. D., Schädel, C., Grosse, G., Harden, J. W., Hayes, D. J., et al. (2015). Climate change and the permafrost carbon feedback. *Nature*, *520*(7546), 171–179. https://doi.org/10.1038/nature14338

Schwab, M. S., Hilton, R. G., Raymond, P. A., Haghipour, N., Amos, E., Tank, S. E., et al. (2020). An Abrupt Aging of Dissolved Organic Carbon in Large Arctic Rivers. *Geophysical Research Letters*, *47*(23), e2020GL088823. https://doi.org/10.1029/2020GL088823

Schwenk, J., Piliouras, A., Rowland, J., Douglas, M., Lamb, M., West, A. J., et al. (2023). *Observations and Machine-Learned Models of Near-Surface Permafrost along the Koyukuk River, Alaska, USA*. Environmental System Science Data Infrastructure for a Virtual Ecosystem (ESS-DIVE) (United States). https://doi.org/10.15485/1922517

Scott, K. M. (1978). *Effects of Permafrost on Stream Channel Behavior in Arctic Alaska* (Geological Survey Professional Paper No. 1068) (p. 19). Washington, D.C.: U.S. Geological Survey.

Serikova, S., Pokrovsky, O. S., Ala-Aho, P., Kazantsev, V., Kirpotin, S. N., Kopysov, S. G., et al. (2018). High riverine CO_2 emissions at the permafrost boundary of Western Siberia. *Nature Geoscience*, *11*(11), 825–829. https://doi.org/10.1038/s41561-018-0218-1

Serreze, M. C., & Barry, R. G. (2011). Processes and impacts of Arctic amplification: A research synthesis. *Global and Planetary Change*, *77*(1), 85–96. https://doi.org/10.1016/j.gloplacha.2011.03.004

Shakil, S., Tank, S. E., Kokelj, S. V., Vonk, J. E., & Zolkos, S. (2020). Particulate dominance of organic carbon mobilization from thaw slumps on the Peel Plateau, NT: Quantification and implications for stream systems and permafrost carbon release. *Environmental Research Letters*, *15*(11), 114019. https://doi.org/10.1088/1748-9326/abac36

Shepherd, R. G., & Schumm, S. A. (1974). Experimental study of river incision. *GSA Bulletin*, *85*(2), 257–268. https://doi.org/10.1130/0016-7606(1974)85<257:ESORI>2.0.CO;2

Shepherd, Russell G. (1989). Correlations of permeability and grain size. *Groundwater*, *27*(5), 633–638. https://doi.org/10.1111/j.1745-6584.1989.tb00476.x

Shishkina, O., & Wagner, C. (2011). Modelling the influence of wall roughness on heat transfer in thermal convection. *Journal of Fluid Mechanics*, *686*, 568–582. https://doi.org/10.1017/jfm.2011.348

Shur, Y., Jones, B. M., Kanevskiy, M., Jorgenson, T., Jones, M. K. W., Fortier, D., et al. (2021). Fluvio-thermal erosion and thermal denudation in the yedoma region of northern Alaska: Revisiting the Itkillik River exposure. *Permafrost and Periglacial Processes*, *32*(2), 277–298. https://doi.org/10.1002/ppp.2105

Shur, Y. L., & Jorgenson, M. T. (2007). Patterns of permafrost formation and degradation in relation to climate and ecosystems. *Permafrost and Periglacial Processes*, *18*(1), 7–19. https://doi.org/10.1002/ppp.582

Sklar, L. S., & Dietrich, W. E. (2001). Sediment and rock strength controls on river incision into bedrock. *Geology*, *29*(12), 1087–1090. https://doi.org/10.1130/0091-7613(2001)029<1087:SARSCO>2.0.CO;2

Sklar, L. S., & Dietrich, W. E. (2004). A mechanistic model for river incision into bedrock by saltating bed load. *Water Resources Research*, *40*(6), W06301. https://doi.org/10.1029/2003WR002496

Sklar, L. S., & Dietrich, W. E. (2006). The role of sediment in controlling steady-state bedrock channel slope: Implications of the saltation–abrasion incision model. *Geomorphology*, *82*(1), 58–83. https://doi.org/10.1016/j.geomorph.2005.08.019

Slack, J. F., Selby, D., & Dumoulin, J. A. (2015). Hydrothermal, biogenic, and seawater components in metalliferous black shales of the Brooks Range, Alaska: Synsedimentary metal enrichment in a carbonate ramp setting. *Economic Geology*, *110*(3), 653–675. https://doi.org/10.2113/econgeo.110.3.653

Slusarchuk, W. A., & Watson, G. H. (1975). Thermal conductivity of some ice-rich permafrost soils. *Canadian Geotechnical Journal*, *12*(3), 413–424. https://doi.org/10.1139/t75-045

Smith, M. (1976). *Permafrost in the Mackenzie Delta, Northwest Territories* (No. Paper 75-28). Geological Survey of Canada.

Smith, M. W. (1975). Microclimatic influences on ground temperatures and permafrost distribution, Mackenzie Delta, Northwest Territories. *Canadian Journal of Earth Sciences*, *12*(8), 1421–1438. https://doi.org/10.1139/e75-129

Snyder, N. P., Whipple, K. X., Tucker, G. E., & Merritts, D. J. (2000). Landscape response to tectonic forcing: Digital elevation model analysis of stream profiles in the Mendocino triple junction region, northern California. *GSA Bulletin*, *112*(8), 1250–1263. https://doi.org/10.1130/0016-7606(2000)112<1250:LRTTFD>2.0.CO;2

Spencer, R. G., Mann, P. J., Dittmar, T., Eglinton, T. I., McIntyre, C., Holmes, R. M., et al. (2015). Detecting the signature of permafrost thaw in Arctic rivers. *Geophysical Research Letters*, *42*(8), 2830–2835. https://doi.org/10.1002/2015GL063498

Steinberg, L. M., & Regan, J. M. (2009). mcrA-targeted real-time quantitative PCR method to examine methanogen communities. *Applied and Environmental Microbiology*, *75*(13), 4435–4442. https://doi.org/10.1128/AEM.02858-08

Stephani, E., Drage, J., Miller, D., Jones, B. M., & Kanevskiy, M. (2020). Taliks, cryopegs, and permafrost dynamics related to channel migration, Colville River Delta, Alaska. *Permafrost and Periglacial Processes*, *31*(2), 239–254. https://doi.org/10.1002/ppp.2046

Stock, J. D., Montgomery, D. R., Collins, B. D., Dietrich, W. E., & Sklar, L. (2005). Field measurements of incision rates following bedrock exposure: Implications for process controls on the long profiles of valleys cut by rivers and debris flows. *GSA Bulletin*, *117*(1–2), 174–194. https://doi.org/10.1130/B25560.1

Striegl, R. G., Dornblaser, M. M., McDonald, C. P., Rover, J. R., & Stets, E. G. (2012). Carbon dioxide and methane emissions from the Yukon River system. *Global Biogeochemical Cycles*, *26*(4). https://doi.org/10.1029/2012GB004306

Sutfin, N. A., & Wohl, E. (2017). Substantial soil organic carbon retention along floodplains of mountain streams. *Journal of Geophysical Research: Earth Surface*, *122*(7), 1325–1338. https://doi.org/10.1002/2016JF004004

Sylvester, Z., Durkin, P. R., Hubbard, S. M., & Mohrig, D. (2021). Autogenic translation and counter point bar deposition in meandering rivers. *GSA Bulletin*. https://doi.org/10.1130/B35829.1

Sylvester, Zoltán, Durkin, P., & Covault, J. A. (2019). High curvatures drive river meandering. *Geology*, *47*(3), 263–266. https://doi.org/10.1130/G45608.1

Syvitski, J., Cohen, S., Miara, A., & Best, J. (2019). River temperature and the thermal-dynamic transport of sediment. *Global and Planetary Change*, *178*, 168–183. https://doi.org/10.1016/j.gloplacha.2019.04.011

Tal, M., & Paola, C. (2007). Dynamic single-thread channels maintained by the interaction of flow and vegetation. *Geology*, *35*(4), 347–350. https://doi.org/10.1130/G23260A.1

Tal, M., & Paola, C. (2010). Effects of vegetation on channel morphodynamics: results and insights from laboratory experiments. *Earth Surface Processes and Landforms*, *35*(9), 1014–1028. https://doi.org/10.1002/esp.1908

Tananaev, N. I. (2016). Hydrological and sedimentary controls over fluvial thermal erosion, the Lena River, central Yakutia. *Geomorphology*, *253*, 524–533. https://doi.org/10.1016/j.geomorph.2015.11.009

Taş, N., Prestat, E., Wang, S., Wu, Y., Ulrich, C., Kneafsey, T., et al. (2018). Landscape topography structures the soil microbiome in arctic polygonal

tundra. *Nature Communications*, *9*(1), 1–13. https://doi.org/10.1038/s41467-018-03089-z

Ternat, F., Boyer, P., Anselmet, F., & Amielh, M. (2008). Erosion threshold of saturated natural cohesive sediments: Modeling and experiments. *Water Resources Research*, *44*(11). https://doi.org/10.1029/2007WR006537

Toohey, R. C., Herman-Mercer, N. M., Schuster, P. F., Mutter, E. A., & Koch, J. C. (2016). Multidecadal increases in the Yukon River Basin of chemical fluxes as indicators of changing flowpaths, groundwater, and permafrost. *Geophysical Research Letters*, *43*(23), 12,120-12,130. https://doi.org/10.1002/2016GL070817

Toonen, W. H. J., Kleinhans, M. G., & Cohen, K. M. (2012). Sedimentary architecture of abandoned channel fills. *Earth Surface Processes and Landforms*, *37*(4), 459–472. https://doi.org/10.1002/esp.3189

Torres, M. A., Limaye, A. B., Ganti, V., Lamb, M. P., West, A. J., & Fischer, W. W. (2017). Model predictions of long-lived storage of organic carbon in river deposits. *Earth Surface Dynamics*, *5*(4), 711–730. https://doi.org/10.5194/esurf-5-711-2017

Torres, M. A., Kemeny, P. C., Lamb, M. P., Cole, T. L., & Fischer, W. W. (2020). Long-term storage and age-biased export of fluvial organic carbon: Field evidence from west Iceland. *Geochemistry, Geophysics, Geosystems*, *21*(4), e2019GC008632. https://doi.org/10.1029/2019GC008632

Trampush, S. M., Huzurbazar, S., & McElroy, B. (2014). Empirical assessment of theory for bankfull characteristics of alluvial channels. *Water Resources Research*, *50*(12), 9211–9220. https://doi.org/10.1002/2014WR015597

Treat, C. C., Marushchak, M. E., Voigt, C., Zhang, Y., Tan, Z., Zhuang, Q., et al. (2018). Tundra landscape heterogeneity, not interannual variability, controls the decadal regional carbon balance in the Western Russian Arctic. *Global Change Biology*, *24*(11), 5188–5204. https://doi.org/10.1111/gcb.14421

Tripathi, B. M., Kim, M., Kim, Y., Byun, E., Yang, J.-W., Ahn, J., & Lee, Y. K. (2018). Variations in bacterial and archaeal communities along depth profiles of Alaskan soil cores. *Scientific Reports*, *8*(1), 1–11. https://doi.org/10.1038/s41598-017-18777-x

Trower, E. J., Lamb, M. P., & Fischer, W. W. (2017). Experimental evidence that ooid size reflects a dynamic equilibrium between rapid precipitation and abrasion rates. *Earth and Planetary Science Letters*, *468*, 112–118. https://doi.org/10.1016/j.epsl.2017.04.004

Turetsky, M. R., Abbott, B. W., Jones, M. C., Anthony, K. W., Olefeldt, D., Schuur, E. A., et al. (2020). Carbon release through abrupt permafrost thaw. *Nature Geoscience*, *13*(2), 138–143. https://doi.org/10.1038/s41561-019-0526-0

Turowski, J. M. (2021). Upscaling sediment-flux-dependent fluvial bedrock incision to long timescales. *Journal of Geophysical Research: Earth Surface*, *126*(5), e2020JF005880. https://doi.org/10.1029/2020JF005880

Turowski, Jens M., Lague, D., & Hovius, N. (2007). Cover effect in bedrock abrasion: A new derivation and its implications for the modeling of bedrock channel morphology. *Journal of Geophysical Research: Earth Surface*, *112*(F4). https://doi.org/10.1029/2006JF000697

Turowski, Jens M., Wyss, C. R., & Beer, A. R. (2015). Grain size effects on energy delivery to the streambed and links to bedrock erosion. *Geophysical Research Letters*, *42*(6), 1775–1780. https://doi.org/10.1002/2015GL063159

Turowski, Jens Martin. (2020). Mass balance, grade, and adjustment timescales in bedrock channels. *Earth Surface Dynamics*, *8*(1), 103–122. https://doi.org/10.5194/esurf-8-103-2020

UAF, & USACE. (2019). *Statewide Threat Assessment: Identification of Threats from Erosion, Flooding, and Thawing Permafrost in Remote Alaska Communities* (No. INE 19.03) (p. 99). Denali Commission.

del Valle, J. I., Guarín, J. R., & Sierra, C. A. (2014). Unambiguous and low-cost determination of growth rates and ages of tropical trees and palms. *Radiocarbon*, *56*(1), 39–52.

Vanoni, V. A. (2006). *Sedimentation Engineering*. American Society of Civil Engineers. https://doi.org/10.1061/9780784408230

Vanoni, V. A., & Brooks, N. H. (1957). *Laboratory studies of the roughness and suspended load of alluvial streams* (Report or Paper No. 11) (p. 130). Pasadena, CA: California Institute of Technology. Retrieved from https://resolver.caltech.edu/CaltechKHR:SedLabRpt-E-68

Venditti, J. G., Rennie, C. D., Bomhof, J., Bradley, R. W., Little, M., & Church, M. (2014). Flow in bedrock canyons. *Nature*, *513*(7519), 534–537. https://doi.org/10.1038/nature13779

Viereck, L. A. (1970). Forest succession and soil development adjacent to the Chena River in Interior Alaska. *Arctic and Alpine Research*, *2*(1), 1–26. https://doi.org/10.1080/00040851.1970.12003558

Vonk, J. E., Tank, S. E., Bowden, W. B., Laurion, I., Vincent, W. F., Alekseychik, P., et al. (2015). Reviews and syntheses: Effects of permafrost thaw on Arctic aquatic ecosystems. *Biogeosciences*, *12*(23), 7129–7167. https://doi.org/10.5194/bg-12-7129-2015

Vonk, J. E., Tank, S. E., & Walvoord, M. A. (2019). Integrating hydrology and biogeochemistry across frozen landscapes. *Nature Communications*, *10*(1), 1–4. https://doi.org/10.1038/s41467-019-13361-5

Wagner, A., Lohmann, G., & Prange, M. (2011). Arctic river discharge trends since 7ka BP. *Global and Planetary Change*, *79*(1), 48–60. https://doi.org/10.1016/j.gloplacha.2011.07.006

Wagner, D., Gattinger, A., Embacher, A., Pfeiffer, E.-M., Schloter, M., & Lipski, A. (2007). Methanogenic activity and biomass in Holocene permafrost deposits of the Lena Delta, Siberian Arctic and its implication for the global methane budget. *Global Change Biology*, *13*(5), 1089–1099. https://doi.org/10.1111/j.1365-2486.2007.01331.x

Waldrop, M. P., Wickland, K. P., Iii, R. W., Berhe, A. A., Harden, J. W., & Romanovsky, V. E. (2010). Molecular investigations into a globally important carbon pool: permafrost-protected carbon in Alaskan soils. *Global Change Biology*, *16*(9), 2543–2554. https://doi.org/10.1111/j.1365-2486.2009.02141.x

Walker, H. J., & Hudson, P. F. (2003). Hydrologic and geomorphic processes in the Colville River delta, Alaska. *Geomorphology*, *56*(3), 291–303. https://doi.org/10.1016/S0169-555X(03)00157-0

Walker, J., Arnborg, L., & Peippo, J. (1987). Riverbank erosion in the Colville Delta, Alaska. *Geografiska Annaler: Series A, Physical Geography*, *69*(1), 61–70. https://doi.org/10.1080/04353676.1987.11880197

Walvoord, M. A., & Kurylyk, B. L. (2016). Hydrologic impacts of thawing permafrost—A review. *Vadose Zone Journal*, *15*(6). https://doi.org/10.2136/vzj2016.01.0010

Walvoord, M. A., Voss, C. I., & Wellman, T. P. (2012). Influence of permafrost distribution on groundwater flow in the context of climate-driven permafrost thaw: Example from Yukon Flats Basin, Alaska, United States. *Water Resources Research*, *48*(7). https://doi.org/10.1029/2011WR011595

Wanders, N., van Vliet, M. T. H., Wada, Y., Bierkens, M. F. P., & van Beek, L. P. H. (Rens). (2019). High-resolution global water temperature modeling. *Water Resources Research*, *55*(4), 2760–2778. https://doi.org/10.1029/2018WR023250

Wang, D., Li, Z., Li, Z., Ma, W., Nie, X., & Yi, Y. (2020). Point bars retained particulate organic carbon within a meandering river corridor in Zoige Basin of the Tibetan Plateau. *Journal of Hydrology*, *588*, 125112. https://doi.org/10.1016/j.jhydrol.2020.125112

Wang, J., Jin, Z., Hilton, R. G., Zhang, F., Densmore, A. L., Li, G., & West, A. J. (2015). Controls on fluvial evacuation of sediment from earthquake-triggered landslides. *Geology*, *43*(2), 115–118. https://doi.org/10.1130/G36157.1

Wang, J., Hilton, R. G., Jin, Z., Zhang, F., Densmore, A. L., Gröcke, D. R., et al. (2019). The isotopic composition and fluxes of particulate organic carbon exported from the eastern margin of the Tibetan Plateau. *Geochimica et Cosmochimica Acta*, *252*, 1–15. https://doi.org/10.1016/j.gca.2019.02.031

Wang, K., Jafarov, E., & Overeem, I. (2020). Sensitivity evaluation of the Kudryavtsev permafrost model. *Science of The Total Environment*, *720*, 137538. https://doi.org/10.1016/j.scitotenv.2020.137538

Wang, W., Godard, V., Liu-Zeng, J., Scherler, D., Xu, C., Zhang, J., et al. (2017). Perturbation of fluvial sediment fluxes following the 2008 Wenchuan earthquake: Fluvial sediment fluxes following large-magnitude earthquake. *Earth Surface Processes and Landforms*, *42*(15), 2611–2622. https://doi.org/10.1002/esp.4210

Wankiewicz, A. (1984). Hydrothermal Processes Beneath Arctic River Channels. *Water Resources Research*, *20*(10), 1417–1426. https://doi.org/10.1029/WR020i010p01417

West, A. J., Hetzel, R., Li, G., Jin, Z., Zhang, F., Hilton, R. G., & Densmore, A. L. (2014). Dilution of 10Be in detrital quartz by earthquake-induced landslides: Implications for determining denudation rates and potential to provide insights into landslide sediment dynamics. *Earth and Planetary Science Letters*, *396*, 143–153. https://doi.org/10.1016/j.epsl.2014.03.058

Whipple, K. X. (2001). Fluvial Landscape Response Time: How Plausible Is Steady-State Denudation? *American Journal of Science*, *301*(4–5), 313–325. https://doi.org/10.2475/ajs.301.4-5.313

Whipple, K. X. (2004). Bedrock Rivers and the Geomorphology of Active Orogens. *Annual Review of Earth and Planetary Sciences*, *32*(1), 151–185. https://doi.org/10.1146/annurev.earth.32.101802.120356

Whipple, K. X., Kirby, E., & Brocklehurst, S. H. (1999). Geomorphic limits to climate-induced increases in topographic relief. *Nature*, *401*(6748), 39–43. https://doi.org/10.1038/43375

Whipple, K. X., Hancock, G. S., & Anderson, R. S. (2000). River incision into bedrock: Mechanics and relative efficacy of plucking, abrasion, and cavitation. *GSA Bulletin*, *112*(3), 490–503. https://doi.org/10.1130/0016-7606(2000)112<490:RIIBMA>2.0.CO;2

White, K. D., & Eames, H. J. (1999). *CRREL Ice Jam Database.* (No. CRREL-99-2). Cold Regions Research and Engineering Lab Hanover, NH. Retrieved from https://apps.dtic.mil/docs/citations/ADA362147

Whittaker, A. C., Cowie, P. A., Attal, M., Tucker, G. E., & Roberts, G. P. (2007). Contrasting transient and steady-state rivers crossing active normal faults: New field observations from the Central Apennines, Italy. *Basin Research*, *19*(4), 529–556. https://doi.org/10.1111/j.1365-2117.2007.00337.x

Wiberg, P. L., & Smith, J. D. (1987). Calculations of the critical shear stress for motion of uniform and heterogeneous sediments. *Water Resources Research*, *23*(8), 1471–1480. https://doi.org/10.1029/WR023i008p01471

Wickham, J., Stehman, S. V., Sorenson, D. G., Gass, L., & Dewitz, J. A. (2021). Thematic accuracy assessment of the NLCD 2016 land cover for the conterminous United States. *Remote Sensing of Environment*, *257*, 112357. https://doi.org/10.1016/j.rse.2021.112357

Wild, B., Andersson, A., Bröder, L., Vonk, J., Hugelius, G., McClelland, J. W., et al. (2019). Rivers across the Siberian Arctic unearth the patterns of carbon release from thawing permafrost. *Proceedings of the National Academy of Sciences*, *116*(21), 10280–10285. https://doi.org/10.1073/pnas.1811797116

Wilkinson, C., Harbor, D. J., Helgans, E., & Kuehner, J. P. (2018). Plucking phenomena in nonuniform flow. *Geosphere*, *14*(5), 2157–2170. https://doi.org/10.1130/GES01623.1

Willett, S. D., McCoy, S. W., Perron, J. T., Goren, L., & Chen, C.-Y. (2014). Dynamic reorganization of river basins. *Science*, *343*(6175), 1248765.

Willett, S. D., McCoy, S. W., & Beeson, H. W. (2018). Transience of the North American High Plains landscape and its impact on surface water. *Nature*, *561*(7724), 528–532. https://doi.org/10.1038/s41586-018-0532-1

Wilson, F. H., Hults, C. P., Mull, C. G., & Karl, S. M. (2015). *Geologic map of Alaska* (USGS Numbered Series No. 3340). *Geologic map of Alaska* (Vol. 3340). Reston, VA: U.S. Geological Survey. https://doi.org/10.3133/sim3340

Winterwerp, J. C., van Kesteren, W. G. M., van Prooijen, B., & Jacobs, W. (2012). A conceptual framework for shear flow–induced erosion of soft cohesive sediment beds. *Journal of Geophysical Research: Oceans*, *117*(C10). https://doi.org/10.1029/2012JC008072

Wobus, C., Whipple, K. X., Kirby, E., Snyder, N., Johnson, J., Spyropolou, K., et al. (2006). Tectonics from topography: Procedures, promise, and pitfalls. *Geological Society of America Special Papers*, *398*, 55–74.

Wolfe, L. H., & Thieme, J. O. (1964). Physical and thermal properties of frozen soil and ice. *Society of Petroleum Engineers Journal*, *4*(01), 67–72. https://doi.org/10.2118/675-PA

Wolman, M. G., & Miller, J. P. (1960). Magnitude and frequency of forces in geomorphic processes. *The Journal of Geology*, *68*(1), 54–74.

Wright, M., Venditti, J. G., Li, T., Hurson, M., Chartrand, S., Rennie, C., & Church, M. (2022). Covariation in width and depth in bedrock rivers. *Earth Surface Processes and Landforms*, *47*(6), 1570–1582. https://doi.org/10.1002/esp.5335

Wright, S., & Parker, G. (2004). Flow resistance and suspended load in sand-bed rivers: simplified stratification model. *Journal of Hydraulic Engineering*, *130*(8), 796–805. https://doi.org/10.1061/(ASCE)0733-9429(2004)130:8(796)

Yaglom, A. M., & Kader, B. A. (1974). Heat and mass transfer between a rough wall and turbulent fluid flow at high Reynolds and Peclet numbers. *Journal of Fluid Mechanics*, *62*(3), 601–623. https://doi.org/10.1017/S0022112074000838

Yamada, T., & Sekiguchi, Y. (2018). Anaerolineaceae. In *Bergey's Manual of Systematics of Archaea and Bacteria* (pp. 1–5). American Cancer Society. https://doi.org/10.1002/9781118960608.fbm00301

Yan, N., Colombera, L., & Mountney, N. P. (2021). Evaluation of morphodynamic controls on the preservation of fluvial meander-belt deposits. *Geophysical Research Letters*, *48*(16), e2021GL094622. https://doi.org/10.1029/2021GL094622

Yang, D., & Peterson, A. (2017). River Water Temperature in Relation to Local Air Temperature in the Mackenzie and Yukon Basins. *Arctic*, *70*(1), 47–58.

Yergeau, E., Hogues, H., Whyte, L. G., & Greer, C. W. (2010). The functional potential of high Arctic permafrost revealed by metagenomic sequencing, qPCR and microarray analyses. *The ISME Journal*, *4*(9), 1206–1214. https://doi.org/10.1038/ismej.2010.41

Zarnetske, J. P., Gooseff, M. N., Bowden, W. B., Greenwald, M. J., Brosten, T. R., Bradford, J. H., & McNamara, J. P. (2008). Influence of morphology and permafrost dynamics on hyporheic exchange in arctic headwater streams under warming climate conditions. *Geophysical Research Letters*, *35*(2). https://doi.org/10.1029/2007GL032049

Zeichner, S. S., Nghiem, J., Lamb, M. P., Takashima, N., de Leeuw, J., Ganti, V., & Fischer, W. W. (2021). Early plant organics increased global terrestrial mud deposition through enhanced flocculation. *Science*, *371*(6528), 526–529. https://doi.org/10.1126/science.abd0379

Zeleke, J., Lu, S.-L., Wang, J.-G., Huang, J.-X., Li, B., Ogram, A. V., & Quan, Z.-X. (2013). Methyl Coenzyme M Reductase A (mcrA) gene-based investigation of methanogens in the mudflat sediments of Yangtze River Estuary, China. *Microbial Ecology*, *66*(2), 257–267. https://doi.org/10.1007/s00248-012-0155-2

Zhang, K., Gong, Z., Zhao, K., Wang, K., Pan, S., & Coco, G. (2021). Experimental and Numerical Modeling of Overhanging Riverbank Stability. *Journal of Geophysical Research: Earth Surface*, *126*(10), e2021JF006109. https://doi.org/10.1029/2021JF006109

Zhang, T., Barry, R. G., Knowles, K., Heginbottom, J. A., & Brown, J. (1999). Statistics and characteristics of permafrost and ground-ice distribution in the Northern Hemisphere. *Polar Geography*, *23*(2), 132–154. https://doi.org/10.1080/10889379909377670

Zhang, X., Xu, S., Li, C., Zhao, L., Feng, H., Yue, G., et al. (2014). The soil carbon/nitrogen ratio and moisture affect microbial community structures in alkaline permafrost-affected soils with different vegetation types on the Tibetan plateau. *Research in Microbiology*, *165*(2), 128–139. https://doi.org/10.1016/j.resmic.2014.01.002

Zhang, Y., Jafarov, E., Piliouras, A., Jones, B. M., Rowland, J., & Moulton, D. (2023). The thermal response of permafrost to coastal floodplain flooding. *Environmental Research Letters*. https://doi.org/10.1088/1748-9326/acba32

Zhao, K., Lanzoni, S., Gong, Z., & Coco, G. (2021). A Numerical Model of Bank Collapse and River Meandering. *Geophysical Research Letters*, *48*(12). https://doi.org/10.1029/2021gl093516

Zheng, L., Overeem, I., Wang, K., & Clow, G. D. (2019). Changing Arctic river dynamics cause localized permafrost thaw. *Journal of Geophysical Research: Earth Surface*, *124*(9), 2324–2344. https://doi.org/10.1029/2019JF005060

Zhilyaev, S., & Fofonova, V. (2016). Numerical analysis and reconstruction of the temperature regime of the Lena River segment. In *2016 Third*

International Conference on Mathematics and Computers in Sciences and in Industry (MCSI) (pp. 224–228). https://doi.org/10.1109/MCSI.2016.049

Zona, D., Gioli, B., Commane, R., Lindaas, J., Wofsy, S. C., Miller, C. E., et al. (2016). Cold season emissions dominate the Arctic tundra methane budget. *Proceedings of the National Academy of Sciences*, *113*(1), 40–45. https://doi.org/10.1073/pnas.1516017113